Quantifying the dynamics and behaviour of ancient fluvial systems in space and time

Sinéad J. Lyster

Imperial College London

Department of Earth Science and Engineering

This thesis is submitted for the degree of *Doctor of Philosophy* in Earth Science and Engineering Research

20th April, 2022

Declarations

Declaration of originality

I declare that this thesis, submitted for the degree of Doctor of Philosophy at Imperial College London and Associateship of the Royal School of Mines, is original research that has been completed by me, and carried out under the supervision of Dr Alex Whittaker and Prof Peter Allison. All published and unpublished material used in this thesis has been appropriately referenced. None of this work has previously been submitted to Imperial College London or any other academic institution for a degree or diploma, or for any other qualification.

Sinéad J. Lyster

20th April, 2022

Copyright declaration

Abstract

The sedimentary record is a crucial archive of past surface processes, including ancient river dynamics, on Earth. Rivers are sensitive to allogenic (external) forcings, such as changes to tectonic and climatic boundary conditions, and can respond to these forcings by propagating environmental signals, such as changes to sediment supply and grain-size, throughout fluvial networks. In theory, environmental signals associated with these allogenic forcings are preserved in depositional stratigraphy. However, rivers are also sensitive to autogenic (internal) forcings, such as channel migration and avulsion, which generates "noise" in depositional stratigraphy. Stratigraphy therefore represents the time-integrated product of the movement of water and sediment, in response to both allogenic and autogenic forcing, across Earth's surface in the geological past. The ability to reconstruct mass fluxes in time and space from the continents, and to extract these signals from fluvial strata, provides unique insights into the dynamics and behaviour of the Earth system in the geological past.

In this thesis, I explore methods to investigate the dynamics and behaviour of ancient fluvial systems from fluvial strata. While qualitative methods (e.g., facies mapping, logging) provide useful insights, these insights are limited in the extent to which they can be used to investigate ancient river dynamics. Here I explore and develop quantitative methods to investigate ancient fluvial systems. Quantitative insights are crucial to constrain total water and sediment discharges, spatial and temporal trends in river dynamics, and the magnitudes and frequencies of river response to forcing. At large spatial and temporal scales, I present a new method to reconstruct water and sediment discharges in palaeo-catchments — this method exploits access to palaeo-digital elevation models and general circulation climate model results, both of which are now becoming increasingly sophisticated. At smaller spatial and temporal scales, I present a framework to reconstruct morphologic (e.g., flow depths, slopes) and hydrodynamic (e.g., flow velocities, water discharges) parameters from fluvial strata, and I present a new method to reconstruct river planform from field-derived observations. These methods and frameworks can provide a range of insights into ancient fluvial systems in general and, in this thesis, I successfully apply them to ancient fluvial systems in the Late Cretaceous North American continent.

Beyond the development of new methods and frameworks to investigate the behaviour of ancient fluvial systems, this thesis also presents unambiguous stratigraphic evidence for bedform preservation in non-steady, or disequilibrium, conditions for Upper Cretaceous fluvial deposits in North America. These observations challenge the use of steady-state bedform preservation models in palaeohydraulic reconstructions. My results highlight the importance of making systematic field measurements of cross-set geometries in fluvial strata to determine the nature of bedform preservation, and the importance of considering disequilibrium dynamics for palaeohydraulic reconstructions. Further, these results provide a potentially powerful avenue to quantify flood variability from fluvial strata, and I explore the necessary future work to achieve this research goal.

Together, the methods and frameworks that I present in this thesis advance our ability to extract quantitative information from fluvial strata. Further, in exemplifying these methods and frameworks for ancient fluvial systems of the Late Cretaceous North American continent, I highlight the advantages, limitations, and best practices associated with these approaches. These methods and frameworks can be implemented at a variety of spatial and temporal scales and can provide sophisticated insights into the dynamics and behaviour of ancient fluvial systems, both on Earth and other planets.

Acknowledgements

First and foremost, I would like to thank my supervisors Alex Whittaker and Peter Allison. Alex, thank you for your endless support, for guiding me to the researcher that I am today (including the "informal Whittaker training program"), for giving me the space and support to pursue my research ideas, and for always being there for me professionally, personally, and that one time my car caught fire in the middle of Utah (oops…). Peter, thank you for your curiosity and ideas which have led to many exciting and fruitful scientific discussions, for your encouragement and support over the years and, importantly, for providing me with many mid-lockdown knitting ideas. Alex, Peter, you have both been wonderful supervisors — I hope to carry forward the example you have set throughout my career.

Thank you to all of my other mentors, collaborators, and co-authors for useful discussions and support over the years. I want to highlight four people in particular. First, I want to thank Gary Hampson for his guidance and feedback on my work throughout the years, both as an assessor and, more recently, as a co-author, and for always being up for a chat and willing to share his extensive knowledge of Utah geology with me. Second, I want to thank Liz Hajek who, over recent years, I have sort of assumed (potentially against her will?) as an informal supervisor. I want to thank Liz for allowing me to be a part of her research group, for all of the conversations which, over an hour later, would end in a crisis about the rock record, and for always encouraging my chaotically tangential research ideas. Third, I want to thank my secondary school geography teacher, Miss Henry, and fourth, I want to thank Carmen Solana. In secondary school, Miss Henry was the teacher that inspired and motivated me to pursue geology and, at the age of 14, I went on to spend my mandatory "work experience" placement running around the corridors of the University of Portsmouth, getting various academics to show me crazy experiments, and insisting that I wanted to be a volcanologist one day. Here, Carmen Solana took me under her wing and mentored me (and let me do more crazy experiments). These two are one of the main reasons I pursued geology — I didn't quite end up in volcanology, but I did end up close by(?)! Also, thank you to everyone, past and present, in the Surface Processes Group at Imperial, thank you to everyone in the Earth & Planets group in general, thank you to Ale and Lewis, and thank you to everyone in the PSUPER SED Lab at Penn State. You are all fab.

Thank you to Ruth, Jenny, Bailey, Tom, Catherine, Cecily, Evie, Lucy, Sian, Harriet, Alex, Carla, Vic (my Surface Processes big sis), and Stephen (my Surface Processes big brother) for making my time at Imperial the absolute best, for always hyping me up, and for always being there whenever I needed a glass of wine (or three). I have to give a special shout out to Ruth, Jenny, Bailey, and Tom (a.k.a. the housemates of dreams); I will always laugh when I think about the year and a half that we spent stuck together at 91, "working" from home, slowly losing our minds, during three (how many were there?!) national lockdowns. Also, a rogue one, but thank you to Briony and the consultant whose name I cannot remember at Chelsea and Westminster Hospital for teaching me to speak again and for dealing with my bleeding neck (honestly second year was so chaotic it was comical).

Lastly, a huge thank you goes to my family. I'm pretty sure that none of you have any clue what I do ("How's your dirt project going?" is a personal favourite), but I appreciate your support and encouragement, nonetheless. My thanks go out to my parents, siblings, my dog (obviously), and all of my extended family in both England and Ireland. Sláinte.

Contents

CHAPTER 1: Introduction

1.1 Research problem and rationale

Sediment routing systems redistribute water and sediment across Earth's surface (Schumm, 1977; Allen, 1997; Allen, 2008a, 2008b, 2017). They are dynamic systems that integrate the production of sediment in erosional upland source regions, the transport and temporary storage of sediment in transfer zones, and the eventual long-term deposition of sediment in lowland and marine sinks (Meade, 1972; Schumm, 1977; Meade, 1982; Allen, 2008a, 2008b, 2017).

Within sediment routing systems, rivers are the primary conduit of water and sediment (Hinderer, 2012; Nyberg & Howell, 2015). Rivers are sensitive to allogenic (external) forcing and respond to changes in tectonic and/or climatic boundary conditions by propagating environmental signals, such as changes to sediment supply and grain-size distribution, throughout fluvial networks (Robinson & Slingerland, 1998; Whittaker et al., 2011; Parsons et al., 2012; Whittaker, 2012; Michael et al., 2014; Romans et al., 2016; D'Arcy et al., 2017; Watkins et al., 2018). Allogenic forcing includes long-period forcings ($>10^6$ yrs), which are typically governed by tectonic and climatic boundary conditions, and which influence source area denudation rates and spatio-temporal patterns in sediment routing (Allen, 1997; Allen, 2008b). Whereas short-period forcings ($<10^6$ yrs) are typically governed by perturbations, such as climate change events or drainage capture events (Blum & Pecha, 2014; Colombera et al., 2017; Chen et al., 2018; Duller et al., 2019). In theory, environmental signals associated with allogenic forcing can be preserved in depositional stratigraphy (Romans & Graham, 2013; Romans et al., 2016; Straub et al., 2020). However autogenic (internal) forcing, such as channel avulsion and migration (Jones & Hajek, 2007; Hajek & Wolinsky, 2012; Flood & Hampson, 2014; Hajek & Edmonds, 2014; Chamberlin & Hajek, 2015, 2019; Ganti, Lamb, et al., 2019) can generate "noise" in preserved depositional stratigraphy (Jerolmack & Sadler, 2007; Jerolmack & Paola, 2010; Straub et al., 2020).

Nonetheless, the sedimentary record is a crucial physical archive of past surface processes and represents the time-integrated product of the movement of water and sediment, in response to tectonic and climatic forcing, across Earth's surface in the geological past (Allen, 2008a, 2008b; Whittaker, 2012; Romans & Graham, 2013; Castelltort et al., 2015; Romans et al., 2016; Allen, 2017; Straub et al., 2020). To date, investigation of past surface processes in the geologic record has been limited by our understanding of how geomorphic processes are translated into the rock record, the controls on signal preservation in stratigraphy, and the extent to which the sedimentary record can be considered a reliable archive (Sadler, 1981; Jerolmack & Paola, 2010). Therefore, the aim of this thesis is to improve our ability to extract information about past surface processes from fluvial strata, particularly information pertaining to the dynamics and behaviour of ancient fluvial systems. This will enable us to build a complete and holistic picture of the movement of water and sediment across Earth's surface in the geological past.

Over the past century, the fields of process geomorphology, fluvial sedimentology, and quantitative sedimentology have significantly developed. The observation that fluvial systems, including their processes and products, are the result of tectonic and climatic forcing has long been known (e.g., Gilbert, 1914; Barrell, 1917; Howard, 1965) and has long been considered in the investigation of fluvial stratigraphy (Wheeler, 1964; Sloss, 1988). The concept of source-to-sink emerged in the seventies, with general partitioning of fluvial systems into three key zones, each of which is typically dominated by one key process: (1) the erosional source region; (2) the sediment transfer zone; and (3) the depositional sink region (Meade,1972; Schumm, 1977; Meade, 1982). Importantly, erosional source regions are inherently not preserved in the rock record (Romans & Graham, 2013; Romans et al., 2016); fluvial stratigraphers must therefore rely on preserved depositional stratigraphy, i.e., the depositional sink region, to make inference of water and sediment routing through the entire source-to-sink system (e.g., Poag & Sevon, 1989; Sømme et al., 2011; Sømme et al., 2013; Hampson et al., 2014). Depositional stratigraphy may capture elements of both the sediment transfer zone, i.e., alluvial rivers, and marine sinks, i.e., deltas and continental shelves. The field of fluvial sedimentology has therefore evolved with the goal of maximising the amount of information that can be retrieved from depositional stratigraphy.

Traditionally, fluvial sedimentology involves qualitative observations of fluvial strata such as facies mapping and sedimentary logging (examples of which include: Smith et al., 1989; Sellwood et al., 1993; Miall, 1994; Ryer & Anderson, 2004; Roberts, 2007; Fielding et al., 2009; Hampson et al., 2012; Huyghe et al., 2012; Hampson et al., 2013; Flood & Hampson, 2014; Ielpi & Ghinassi, 2014; Burns et al., 2017; Fielding et al., 2018). However, increasingly, stratigraphers and sedimentologists have looked to develop quantitative techniques to unravel the functioning of rivers in the geological past (Leclair & Bridge, 2001; Holbrook & Wanas, 2014; Trampush et al., 2014; Mahon & McElroy, 2018; Ganti, Whittaker, et al., 2019; Greenberg et al., 2021). Quantitative investigations of ancient fluvial systems are targeted at constraining (1) the morphologies and morphodynamics of ancient systems (e.g., Flood & Hampson, 2015; Ganti, Whittaker, et al., 2019) and (2) the hydrodynamics of ancient systems (e.g., Holbrook & Wanas, 2014). The overarching motivation to constrain parameters associated with these two "branches" is to gain insights into the dynamics and behaviour of ancient fluvial systems. However, each branch respectively entails its own motivations, and its own implications.

Constraints on ancient river morphologies and morphodynamics (e.g., flow depths, slopes, channel widths, river planform) can be used to build a complete and holistic picture of ancient fluvial landscapes. Of particular interest is building a picture of pre-vegetation fluvial landscapes on Earth (Ielpi & Ghinassi, 2015; Ielpi & Rainbird, 2016; Ganti, Whittaker, et al., 2019) and other planets (Lapôtre et al., 2019; Lapôtre & Ielpi, 2020). Importantly, constraints on river morphologies are crucial for subsequent reconstruction of river hydrodynamics — knowledge of river morphologies is crucial to estimate total water and sediment discharges.

Meanwhile, constraints on ancient river hydrodynamics (e.g., flow velocities, water discharges, flood durations) can be used to: (1) decipher prevailing flow conditions (Reesink & Bridge, 2007; Reesink & Bridge, 2009; Reesink et al., 2015; Ganti et al., 2020; Leary & Ganti, 2020); (2) estimate the magnitudes and characteristics of flood events (Leary & Ganti, 2020); (3) quantify sediment discharges (Holbrook & Wanas, 2014; Lin & Bhattacharya, 2017; Sharma et al., 2017; Brewer et al., 2020), and (4) reconstructing biogeochemical fluxes across Earth's surface in the geological past, such as organic carbon cycling (Blair et al., 2003; Blair et al., 2004; Hilton, 2008; Leithold et al., 2016). These constraints all have huge implications for investigating fluvial behaviour and landscape evolution in the geological past. For instance, constraints on water and sediment discharges facilitate the investigation of ancient rivers in palaeoclimates characterised by elevated atmospheric CO_2 concentrations and enable us to quantify the sensitivity and response of rivers to short-period climatic perturbations in the geological past, such as the Paleocene−Eocene Thermal Maximum (PETM) (Foreman et al., 2012; Foreman, 2014; Colombera et al., 2017; Chen et al., 2018).

More generally, constraints on river hydrodynamics provide additional insights into palaeo-catchment hydroclimate. Palaeoclimates are frequently modelled using general circulation models (GCMs) and validated using independent proxies. While sea surface temperatures generally agree between GCMs and marine proxies, terrestrial surface temperatures are generally inconsistent between GCMs and terrestrial proxies (Spicer et al., 2008; Upchurch Jr. et al., 2015; Tabor et al., 2016). This is partly due to the conflicting spatiotemporal resolution of GCMs and terrestrial proxies — GCMs do not capture the wide interannual range of terrestrial surface temperatures or the spatial heterogeneity that arises from local topography (e.g., Tabor et al., 2016). We lack terrestrial paleoclimate proxies that are more spatially and temporally averaged; however, constraints on river hydrodynamics, such as water discharges and flood magnitudes and frequencies, reflect catchment-averaged hydroclimate and therefore offer potentially useful terrestrial proxies of hydroclimate.

1.2 Investigation of ancient fluvial systems

Qualitative observations of fluvial strata (e.g., facies mapping, logging), in particular of channel architectural elements, provide crucial insights into the morphologies, morphodynamics, hydrodynamics, and sediment transport characteristics of ancient fluvial systems on Earth (e.g., Miall, 1994; Hampson et al., 2013; Flood & Hampson, 2014) and other planets (e.g., Davis et al., 2016; Cardenas et al., 2017; Edgar et al., 2018). Insights into channel morphologies and morphodynamics can include: (1) planform evolution, e.g., the nature of meander-bend transformations (Ghinassi et al., 2014; Ielpi & Ghinassi, 2014, 2015; Ielpi et al., 2018); (2) avulsion style (Smith et al., 1989; Mohrig et al., 2000; Jones & Hajek, 2007; Flood & Hampson, 2014; Hajek & Edmonds, 2014; Chamberlin & Hajek, 2015); and (3) channel reworking and lateral mobility (Hampson et al., 2012; Hampson et al., 2013; Flood & Hampson, 2014; Hampson, 2016; Chamberlin & Hajek, 2019). Whereas insights into channel hydrodynamics can include: (1) river discharge variability, e.g., whether rivers were associated with monsoonal/subtropical or perennial discharge regimes (Plink-Björklund, 2015; Fielding et al., 2018; Birgenheier et al., 2019; Herbert et al., 2020; Wang & Plink-Björklund, 2020); (2) backwater hydrodynamics (Kimmerle & Bhattacharya, 2018; Trower et al., 2018; Ganti, Lamb, et al., 2019); and (3) river runoff regimes, i.e., whether palaeocatchments were arid, semi-arid, or wet (Mack & James, 1994; Retallack, 1997; Tabor & Myers, 2014; Eide et al., 2018).

While qualitative observations of fluvial strata provide important insights into ancient fluvial systems, these insights are limited by both outcrop exposure and the extent to which they can be used to constrain ancient river dynamics. For instance, while we could attribute an interpreted change in variable discharge facies in fluvial strata to a change in river discharge variability (Plink-Björklund, 2015; Birgenheier et al., 2019; Wang & Plink-Björklund, 2020), we cannot quantify the magnitude or frequency of this change which limits our ability to quantify the response of ancient fluvial systems to tectonic and climatic perturbations. Whereas, with quantitative constraints on flow conditions associated with discharge variability, we could constrain the magnitude of fluvial response to perturbation, such as flood durations, discharges, and sediment transport capacities. Quantitative constraints are therefore a useful, and important, complement to qualitative insights.

Quantitative observations of fluvial strata include the use of detailed field measurements to gain sophisticated insights into the dynamics of ancient fluvial systems. For example, in the deposits of meandering rivers, systematic structural measurements of the dip and dip directions of lateral accretion surfaces and dune-scale cross-set lee slopes can be used to calculate flow divergence between bar accretion and local dune migration, and therefore infer channel sinuosity (Ghinassi et al., 2021). Another example includes making systematic measurements of the dimensions, abundances, and distributions of architectural elements, e.g., channelised sandstone bodies, to infer avulsion style and frequency, as well as relative rates of tectonic subsidence (Flood & Hampson, 2015; Chamberlin & Hajek, 2019). Importantly, quantitative observations of fluvial strata increasingly take advantage of high-resolution remote imagery and three-dimensional outcrop models (Hajek & Heller, 2012; Rittersbacher et al., 2014; Chamberlin & Hajek, 2019).

This facilitates efficient data collection from fluvial strata and, further, enables quantitative observations of fluvial strata on other planets from orbital imagery (Stepinski & Coradetti, 2004; Seybold et al., 2018; Hayden et al., 2019; Rivera-Hernández et al., 2020).

With detailed observations of fluvial strata, it becomes possible to apply various theoretically, empirically, and experimentally derived models (e.g., Parker, 1976; Paola & Borgman, 1991; Leclair & Bridge, 2001; Crosato & Mosselman, 2009; Trampush et al., 2014) to fluvial strata in order to reconstruct the morphologies, morphodynamics, hydrodynamics, and sediment transport characteristics of ancient rivers (e.g., Holbrook & Wanas, 2014; Bhattacharyya et al., 2015; Chen et al., 2018; Ganti, Whittaker, et al., 2019). In detail, application of these models to fluvial strata requires systematic measurements of grain-size, cross-set geometries, and channel architectural elements (Figure 1.1). For instance, measurements of cross-sets can be used to estimate original dune heights (Paola & Borgman, 1991; Leclair & Bridge, 2001) and then reconstruct flow depths (Bradley & Venditti, 2017), and measurements of fully preserved bars provide a direct proxy for flow depths (Hajek & Heller, 2012) (Figure 1.1). These constraints can then be coupled with grain-size measurements to estimate parameters such as palaeoslope (Trampush et al., 2014) and flow velocity (using formulae such as Manning's Equation or Chézy's Equation) (Figure 1.1). These models are typically borrowed from the fields of engineering and geomorphology and have been adapted for stratigraphic applications. However, in some instances, these models have been developed with specific stratigraphic applications in mind (Mahon & McElroy, 2018; Lapôtre et al., 2019; Greenberg et al., 2021).

Systematic measurements of grain-size, cross-set geometries, and channel architectural elements can involve a range of methods and measurement tools, each with different levels of precision. Measurements of grain-size and cross-set geometries are the most pertinent field data to this thesis, and the methods I use to collect these data are introduced and synthesised here.

Measurements of grain-size in fluvial strata are typically aimed at establishing grain-size distributions of particular fluvial facies, such as channel-fill deposits. From grain-size distributions, information such as the median grain size, D_{50}, can be extracted, as well as other grain-size percentiles including the oft-used 84th and 90th percentiles (D_{84} and D_{90}, respectively), and various measures of grain-size variability (e.g., the mean and standard deviation of grain-size). In the field, coarse-fraction (>2 mm in diameter) grain-size distributions can be established using the Wolman point count method, which involves repeated measurements of a particular axis of randomly selected clasts (Wolman, 1954) — this method is widely implemented in both geomorphic and stratigraphic studies (e.g., Whittaker et al., 2011; D'Arcy et al., 2017; Brooke et al., 2018). Whereas for sand-fractions (<2 mm in diameter), scaled photographs can be processed in an image analysis software, such as *ImageJ*, and grain-size can similarly be measured using a sampling method akin to the Wolman point count method. Alternatively, the median grain-size of sand-fractions can be estimated in the field using the Wentworth (1922) classification.

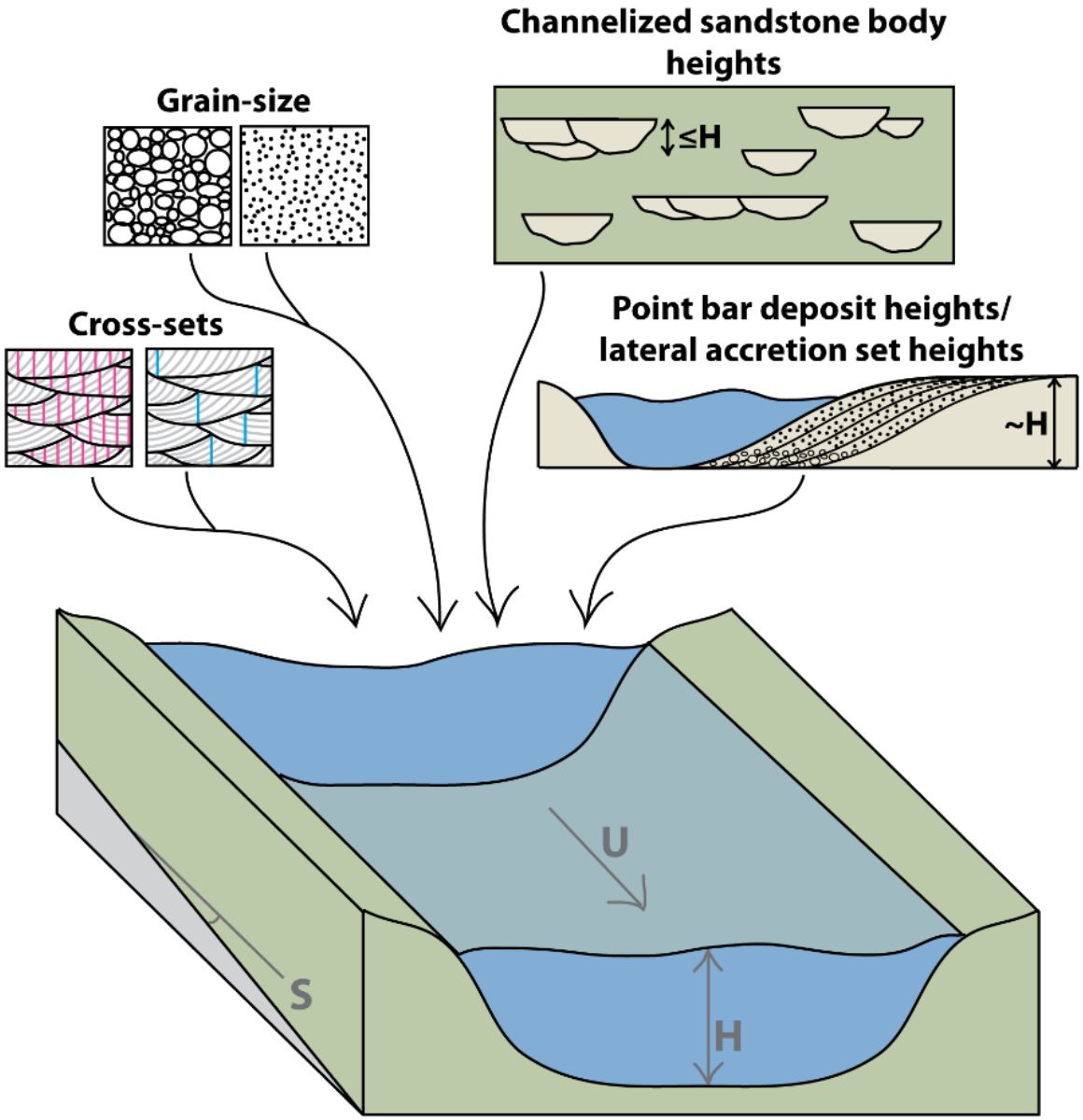

Figure 1.1 | A schematic showing that measurements of grain-size, cross-sets, and architectural elements in preserved fluvial strata can be used to reconstruct channel morphologies such as flow depths, *H*, and slopes, *S*, as well as hydrodynamic properties such as flow velocities, *U*.

Beyond measurements of grain-size, systematic measurements of cross-set geometries are also pertinent to this thesis (Figure 1.2). In the field, the most efficient means of measuring cross-sets is to measure the maximum height of individual cross-sets (Figure 1.2c,d). However, theory relating preserved cross-set thicknesses to original dune heights requires knowledge of the mean cross-set thickness, as opposed to the maximum cross-set thickness (Paola & Borgman, 1991; Leclair & Bridge, 2001). To determine the mean cross-set thickness, it is necessary to delineate cross-set boundaries (i.e., the lower, asymptotic bounding surface and the upper, erosional bounding surface) and to measure thicknesses at regular intervals along the entire width of the cross-set (Figure 1.2e,f). With the full distribution of thicknesses for individual cross-sets, the mean thickness of each cross-set can be established. This measurement procedure has been successfully implemented in both field stratigraphic examples (e.g., Ganti, Whittaker, et al., 2019) and in experimental (flume) settings (e.g., Leary & Ganti, 2020). It is important to note that this method of measuring mean cross-set thicknesses is not the same as methods to measure mean dune heights in experimental settings and in modern bathymetric datasets.

With interest in using mean cross-set thicknesses to estimate original dune heights, it is important that the measurement procedure outlined above is also consistent with the theory presented by Paola and Borgman (1991). Paola and Borgman (1991) considered bedform evolution and preserved cross-set geometries in two dimensions; the distribution of thicknesses within individual cross-sets should therefore be measured along the cross-set dip-section, i.e., parallel to the palaeoflow direction (cf. Paola & Borgman, 1991). However, measuring the dip-section is not always possible from outcrop, and it is often necessary to measure the thickness distribution along a slightly oblique section. The effect of measuring thickness distributions along oblique sections has not yet been documented but, geometrically, it is anticipated that the effect is minimal, although this is yet to be formally tested. Further, as Paola and Borgman (1991) considered bedform evolution and preserved cross-set geometries in two dimensions, it is not necessary to consider the shape of the bedform crest, which influences whether resultant cross-strata are planar or trough in shape. This is advantageous as it means that, when measuring thickness distributions within individual cross-sets, it is not necessary to consider whether strata are trough cross-bedded or planar cross-bedded.

Finally, quantitative investigation of ancient fluvial systems can be entirely independent of observations and measurements of fluvial strata, such as those described above, and can instead centre on numerical modelling. Examples include forward approaches to model fluvial stratigraphic architecture (Montero et al., 2021; Snieder et al., 2021; Yan et al., 2021), use of palaeogeographies and palaeo-digital elevation models to explore sediment routing (Bonne, 2014), inverse approaches such as the use of landscape evolution models to investigate fluvial landscapes and sediment routing on longer, geological timescales (Fernandes et al., 2019), and catchment-based models to reconstruct water and sediment discharges (Syvitski & Milliman, 2007; Allen et al., 2013; Watkins et al., 2018; Zhang et al., 2018; Brewer et al., 2020).

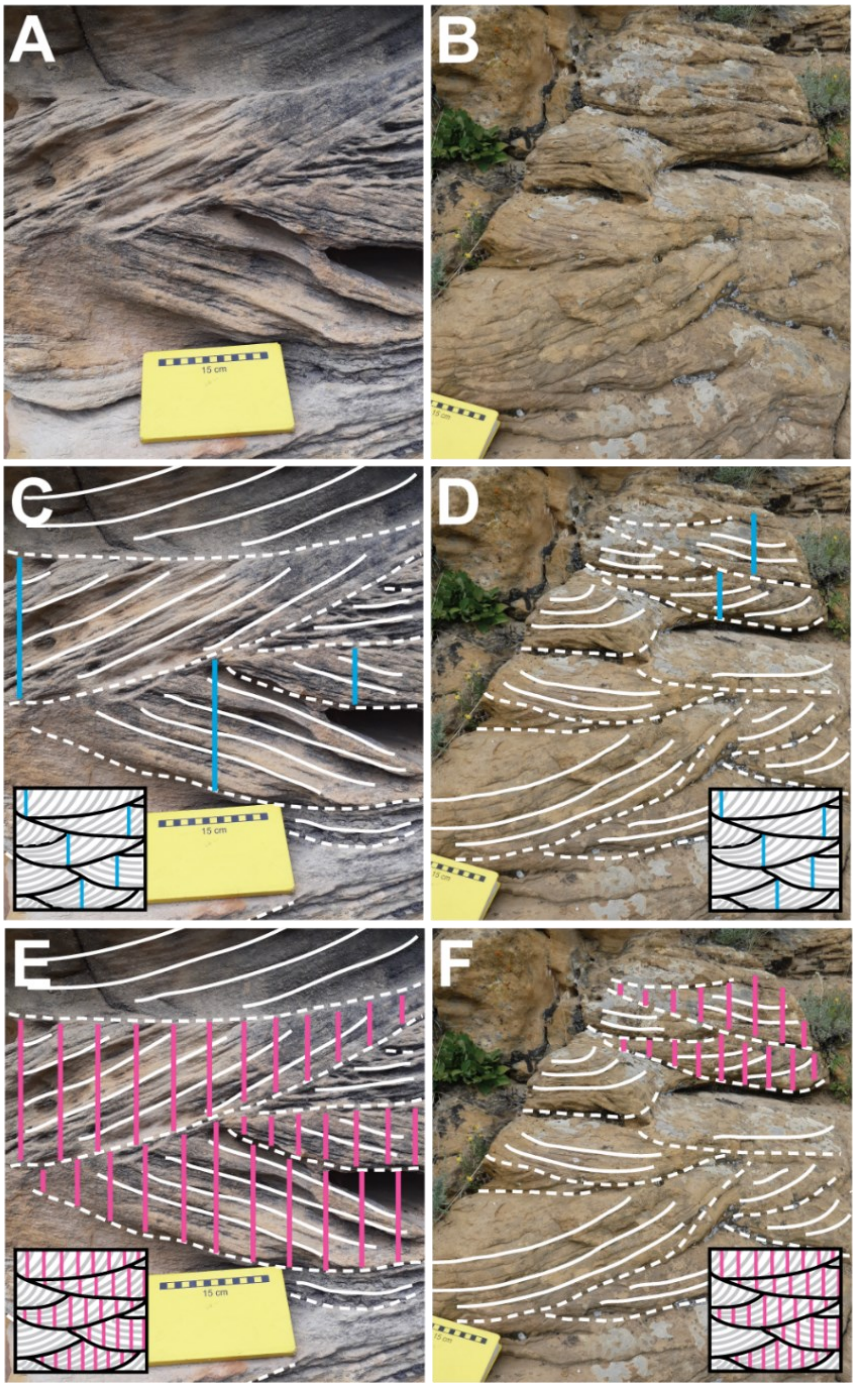

Figure 1.2 | A schematic demonstrating two different methods of measuring cross-set geometries. **A, B)** Uninterpreted photos of trough cross-sets in fluvial strata. **C, D)** Interpreted versions of parts **A** and **B** which demonstrate how and where maximum thicknesses of individual cross-sets are measured (solid blue lines). **E, F)** Interpreted versions of parts **A** and **B** which demonstrate how and where the distributions of thicknesses within individual cross-sets are measured (pink solid lines). Cross-set boundaries are delineated (i.e., the lower, asymptotic bounding surface and the upper, erosional bounding surface) and thicknesses are measured at regular intervals along the entire width of the cross-set dip-section. The mean thickness can then be calculated from the distribution of thicknesses. Dashed white lines in parts **C–F** indicate bounding surfaces of individual cross-sets and solid white lines indicate selected foresets within individual cross-sets. The insets in parts **C–F** demonstrate the measurement method as a schematic. This figure is adapted from method figures presented in Chapters 3 and 4.

1.3 Challenges of investigating of ancient fluvial systems

This thesis is primarily motivated by the observation that, despite the potentially far-reaching implications, morphologic, morphodynamic, hydrodynamic, and sediment transport models are seldom applied to fluvial strata. In addition, this thesis is motivated by the fact these models currently come with limitations which hinder their applicability to fluvial strata, and which hinder the extent to which they can be used to interpret fluvial strata.

i. Empirically derived models

Models that are often applied to fluvial strata can be empirically derived, theoretically derived, experimentally derived, or some combination of the three. Empirically derived models, i.e., models that are based on observations in modern rivers, include models that predict river morphologies such as flow depths, channel widths, slopes, and river planform (e.g., Leopold & Maddock Jr, 1953; Bridge & Mackey, 1993; van den Berg, 1995; Sømme et al., 2009; Trampush et al., 2014; Bradley & Venditti, 2017), as well as models that predict sediment transport characteristics, including sediment discharges and sediment transport intermittencies (e.g., Meybeck et al., 2003; Syvitski & Milliman, 2007; Sømme et al., 2009). While empirically derived models capture the wide variability of natural rivers, they are limited by the fact that their predictability power is poor and/or their uncertainty margins are wide. This may result in reconstruction of ancient river morphologies that are vastly different to true ancient river morphologies (Figure 1.3).

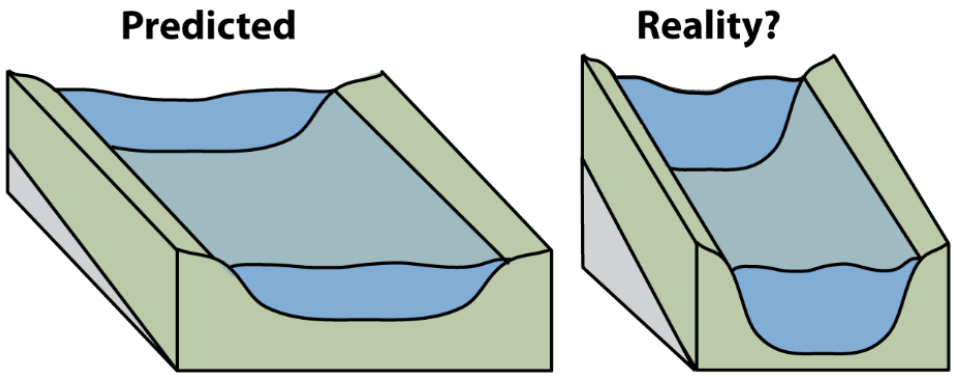

Figure 1.3 | A schematic showing how the predicted morphology (left) of an ancient river might differ from the true morphology (right) due to the errors/uncertainties associated with reconstruction methods.

ii. Theoretically derived models

Meanwhile, theoretically derived models are often effective at capturing process, and are often validated using experimental observations. However, theoretically derived models are limited by the assumptions that underpin them. For instance, theoretically derived models to predict river planform (e.g., Parker, 1976; Crosato & Mosselman, 2009) typically assume straight channels with rectangular cross-sections and non-erodible banks — this assumption is a major motivation for work presented in Chapter 5. Further,

theoretically derived models of bedform evolution and preservation often assume steady-state conditions in rivers (e.g., Paola & Borgman, 1991; Leclair & Bridge, 2001) — this assumption is a major motivation for work presented in Chapter 4.

To expand on the concept of steady-state conditions in rivers, this is an assumption that commonly underpins models of channel morphologies, morphodynamics, and hydrodynamics, and is therefore important to consider when using these models to quantify the dynamics and behaviour of ancient rivers. Steady-state conditions in rivers typically refer to channels in which flow is relatively uniform in space and/or time. Whereas non-steady conditions typically refer to channels in which flow is locally variable in space and/or time. Non-steady flow conditions may have multiple origins, including: (1) flow variability, which commonly refers to climatically driven discharge variability (Leary & Ganti, 2020), but also includes instantaneous discharge variability associated with channel avulsion and abandonment; (2) the effect of variable bed and bank topography on flow, which is linked to the presence and migration of bedforms and barforms in channels (Ganti et al., 2020; Wysocki & Hajek, 2021); and (3) the effect of backwater hydraulics on flow (Wu et al., 2020).

In steady-state conditions, the formative train of bedforms on a channel bed evolves with no-net aggradation and/or with small bedform climb angles ($<10^{-2}$; gradient in terms of y/x) (Paola & Borgman, 1991; Jerolmack & Mohrig, 2005). In these conditions, theoretical work, numerical models, and experimental observations all suggest that the bedform preservation ratio — which is the ratio of the average preserved cross-set thicknesses and the average original bedform heights — is a near-constant value of 0.3 (Paola & Borgman, 1991; Leclair & Bridge, 2001; Leclair, 2002; Jerolmack & Mohrig, 2005; Ganti et al., 2013; Leary & Ganti, 2020) (Figure 1.4). Further, these models predict that the coefficient of variation, *CV*, of preserved cross-set thicknesses has a constant value of 0.88 (Paola & Borgman, 1991; Leclair & Bridge, 2001; Leclair, 2002; Jerolmack & Mohrig, 2005; Ganti et al., 2013; Leary & Ganti, 2020) which is bounded by 0.88±0.30 Bridge (1997) (Figure 1.4). However, in non-steady flow conditions, the formative train of bedforms on a channel bed evolves with higher bedform climb angles, and localized increase in sedimentation rates relative to bedform migration rates results in enhanced preservation of bedforms (Reesink et al., 2015; Ganti et al., 2020; Leary & Ganti, 2020). In non-steady, or disequilibrium, conditions, the bedform preservation ratio is higher than 0.3, and the *CV* of preserved cross-set thicknesses is lower than 0.88 (Jerolmack & Mohrig, 2005; Reesink et al., 2015; Ganti et al., 2020; Leary & Ganti, 2020) (Figure 1.4). Ultimately, both steady-state and disequilibrium conditions leave potentially diagnostic cross-set geometries in fluvial strata.

Importantly, disequilibrium conditions associated with flow variability are increasingly recognised to be a fundamental control on river behaviour, fluvial landscape evolution, and, therefore, stratigraphic architecture (Leier et al., 2005; Fielding et al., 2009; Esposito et al., 2018; Ghinassi et al., 2018; Birgenheier et al., 2019; Hansford & Plink-Björklund, 2020; Herbert et al., 2020; Wang & Plink-Björklund, 2020). Further, recent insights into the role of bedform and barform migration on generating disequilibrium

conditions (e.g., Ganti et al., 2020; Wysocki & Hajek, 2021) has raised new questions as to whether steady-state assumptions are applicable to natural rivers. In extracting quantitative information from fluvial strata, it is therefore crucial to consider whether steady-state assumptions are appropriate, and the implications of steady-state assumptions on results.

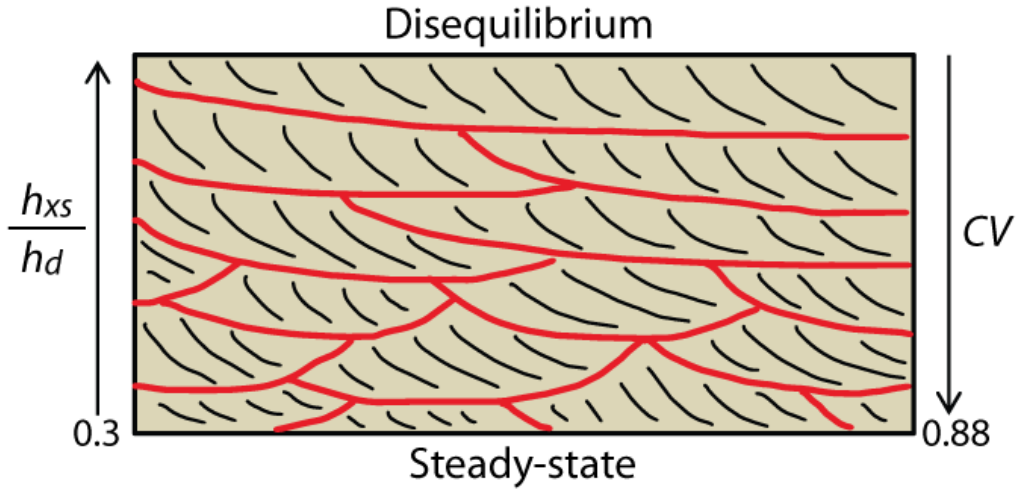

Figure 1.4 | Schematic that illustrates the nature of preserved cross-set geometries when bedform preservation occurs in steady-state *versus* disequilibrium conditions. In steady-state conditions, the bedform preservation ratio, h_{xs}/h_d, is 0.3, and is larger in disequilibrium conditions. Meanwhile in steady-state conditions, the coefficient of variation, CV, of preserved cross-set thicknesses is 0.88, and is smaller in disequilibrium conditions. Red solid lines indicate bounding surfaces between cross-sets. Black solid lines indicate individual cross-strata. This figure is replicated from Chapter 6, Figure 6.2.

iii. Numerical models

An alternative option to investigate the dynamics and behaviour of ancient fluvial systems is to implement models that are not directly tied to preserved fluvial strata, i.e., the use of models that describe sediment routing systems in the geological past, but which do not require direct observations or measurements of fluvial strata. These approaches may make use of palaeotopographic, palaeogeographic, and palaeoclimatic constraints (Markwick & Valdes, 2004; Hunter et al., 2008; Lunt et al., 2016; Markwick, 2018; Farnsworth et al., 2019), and are often focused on reconstructing water and sediment discharges in palaeocatchments that have been delimited using a wide range of techniques (Michael et al., 2014; Watkins et al., 2019). They include models such as the bulk diffusive model of Allen et al. (2013) and the empirical BQART model (Syvitski & Milliman, 2007). Approaches such as these represent catchment-based models that require knowledge of palaeogeographic boundary conditions, e.g., catchment areas, lengths, and relief, and are therefore limited by the difficulties associated with constraining these parameters. These parameters often have to be approximated using provenance data, catchment spacing ratios, slope–area relations, etc (e.g., Hovius, 1996; Lague & Davy, 2003). Further, catchment-based models usually require knowledge of palaeoclimatic boundary conditions, which is similarly difficult to constrain, and which may be temporally and spatially averaged. For instance, catchment palaeoclimates can be approximated using terrestrial

palaeoclimate proxies (Wolfe, 1993; Francis & Poole, 2002; Amiot et al., 2004; Poole et al., 2005; Craggs et al., 2012). However, use of terrestrial proxies is limited due to the wide interannual range in terrestrial surface temperature and precipitation rates, as well as spatial heterogeneity which arises from local topography (Tabor et al., 2016).

As the considerations outlined above show, quantifying the dynamics and behaviour of ancient fluvial systems remains a prominent research challenge — in this thesis I will use a suite a techniques to address this key challenge. I will use field observations and numerical and empirical models to evaluate the extent to which we can extract quantitative information from fluvial strata. Further, I will exploit access to high-resolution palaeogeographic reconstructions and GCM results, which are increasingly available and increasingly sophisticated, to implement and evaluate catchment-based approaches to investigate ancient river dynamics and behaviour.

1.4 Aims and objectives

Aims

Having emphasized the importance of quantitative insights, the overarching goal of this thesis is to improve our ability to quantify the dynamics and behaviour of ancient fluvial systems. This will enable us to build a more complete and holistic picture of the movement of water and sediment across Earth's surface in the geological past. To achieve this overarching research goal, I have developed three key aims that I will address in this thesis:

1. I will develop a new approach to quantify water and sediment discharges in the geological past, which exploits access to novel datasets (palaeo-digital elevation models and general circulation model outputs).
2. I will develop and refine a framework and methods to quantify channel morphologies (e.g., depths, widths, slopes), hydrodynamics (flow velocities, flow variability), and morphodynamics (e.g., planform morphologies, bedform migration, barform migration) from detailed field measurements of fluvial strata.
3. I will develop a new approach to assess planform morphology in ancient fluvial systems, using observations of hydraulic geometries and planform in modern fluvial systems.

These aims are all crucial to decipher the characteristics and behaviour of ancient fluvial systems, including quantification of their palaeo-water and sediment discharges. Further, these three aims all involve the development of new approaches to investigate ancient fluvial systems, and I will exemplify these approaches using geological examples. In this thesis, geological examples will focus on the Late Cretaceous North American continent, where palaeogeography and palaeodrainage are well-understood (Kauffman, 1977; Hay et al., 1993; Kauffman & Caldwell, 1993; Miall et al., 2008; Bhattacharya et al., 2016), and where exceptional preservation of fluvial strata enables detailed field investigation. However, in the future, I anticipate that these new methods can be implemented widely, in space and time, to investigate ancient fluvial systems on Earth and other planets.

To achieve these aims, I will exploit novel datasets which include: (1) palaeo-digital elevation models (palaeoDEMs), provided by *Getech Group Plc.*; and (2) general circulation model (GCM) outputs, provided by collaborators at the University of Bristol. I will also compile new datasets, which include: (3) a large stratigraphic dataset of quantitative sedimentological information, collected in the field; and (4) a large dataset of modern river observations, compiled using published literature.

Objectives

The key objectives of Aim 1 are:

1.1. Use palaeoDEMs and GIS techniques to delineate palaeocatchments in the Late Cretaceous North American continent and use spatial statistics to extract catchment geometries.

1.2. Use GCM outputs, GIS techniques and spatial statistics to extract catchment-averaged climate, including catchment water discharges.

1.3. Use the BQART model (Syvitski & Milliman, 2007) to reconstruct suspended sediment discharges in catchments.

1.4. Evaluate the efficacy of this new palaeoDEM–GCM–BQART approach by: (a) contrasting estimates of suspended sediment discharges with published estimates derived from independent approaches; (b) collecting my own field data and using these data to reconstruct suspended sediment discharges using an independent approach; (c) evaluating the univariate and multivariate sensitivity of the approach to uncertainties.

The key objectives of Aim 2 are:

2.1. Collect detailed field measurements of grain-size and cross-set geometries in fluvial strata, which can subsequently be used to reconstruct channel morphologies, hydrodynamics and morphodynamics.

2.2. Establish quantitative frameworks and/or methods that use field measurements of grain-size and cross-set geometries, and a series of empirically, theoretically, and experimentally derived equations, to reconstruct channel morphologies (e.g., depths, widths, slopes), hydrodynamics (flow velocities, flow variability), and morphodynamics (e.g., planform morphologies, bedform migration, barform migration).

2.3. Determine whether the steady-state assumptions made in these frameworks and/or methods are appropriate for the investigation of ancient fluvial systems and, where inappropriate, explore the implications.

2.4. Incorporate error analysis into these frameworks and/or methods to account for uncertainty.

2.5. Evaluate the efficacy of these frameworks and/or methods by: (1) contrasting estimates of morphologies, hydrodynamics, etc., with estimates derived using alternative approaches. For instance, estimates of slope derived using a Shields stress inversion can be contrasted with estimates of slope derived using empirical relations; (2) contrasting estimates of morphologies, hydrodynamics, etc., with stratigraphic observations and independent proxies. For instance, estimates of palaeoflow depth can be compared to independent palaeoflow depth proxies (e.g., bar clinoform heights), and insights into flow variability can be compared to facies interpretations using variable discharge facies models.

The key objectives of Aim 3 are:

3.1. Evaluate the efficacy of existing quantitative planform predictors (Parker, 1976; van den Berg, 1995; Crosato & Mosselman, 2009) for palaeo-planform prediction by comparing reconstructed planforms with stratigraphic interpretations of planform in geological examples, which were previously studied for Aim 2.

3.2. Compile a new dataset of hydraulic geometries in modern rivers and use these data to evaluate whether the thresholds associated with existing quantitative planform predictors are effective.

3.3. Use the same dataset to develop a new empirical approach to palaeo-planform prediction and establish new thresholds.

3.4. Evaluate the efficacy of this new empirical approach.

1.5 Study area

In this thesis I use geological examples to achieve the Aims and Objectives outlined in ***Section 1.4*** — these geological examples are focused on the Late Cretaceous North American continent where palaeogeography and palaeodrainage are well-understood (e.g., Kauffman, 1977; Hay et al., 1993; Kauffman & Caldwell, 1993; Miall et al., 2008; Bhattacharya et al., 2016) (Figures 1.5 and 1.6). These examples are focused on specific ancient fluvial systems and incorporate field measurements of preserved fluvial strata, which I collected during field campaigns in September 2018 and 2019. I collected field measurements from the Turonian Ferron Sandstone, Campanian Blackhawk Formation, Campanian Castlegate Sandstone, and Campanian Price River Formation, which all crop out in central Utah, USA (Figure 1.7). Fluvial strata in these formations are exceptionally well-preserved and accessible. Further, the stratigraphy is well-understood, particularly the nature of sediment routing and drainage patterns (e.g., Lawton, 1983, 1986b; Hampson et al., 2014; Bartschi et al., 2018; Pettit et al., 2019) (Figure 1.6), has been regionally correlated (e.g., Lawton, 1982; Robinson & Slingerland, 1998; Aschoff & Steel, 2011a, 2011b; Seymour & Fielding, 2013), and has robust age constraints (e.g., Fouch et al., 1983; Molenaar & Cobban, 1991; Cobban et al., 2006).

In each research chapter (Chapters 2–5), I provide a general overview of the study area. These overviews contain the necessary detail to support the research presented in that chapter, and typically include a brief description of the Late Cretaceous North American continent and/or Late Cretaceous central Utah, USA, and the local stratigraphy. Here, I provide a more detailed overview of the study area to complement the information provided in each research chapter, including detailed information pertaining to palaeogeography, palaeodrainage, and palaeoclimate, at both continental and regional scales, as well as detailed information pertaining to the stratigraphy and stratigraphic correlations.

Late Cretaceous North America: Palaeogeography

Key tectono-geographic features of the Late Cretaceous North American continent include the Sevier orogenic fold-and-thrust belt and its adjacent foreland basin, the Western Interior Basin (WIB) (Armstrong, 1968; Jordan, 1981; Cross, 1986; DeCelles, 1994) (Figure 1.5). The WIB formed due to eastward subduction of the Farallon plate beneath the western margin of the North American continent; subduction generated relatively uniform, long-wavelength dynamic subsidence across the continent (Liu et al., 2011; Liu, Nummedal, et al., 2014). Superimposed on this dynamic subsidence was a narrow 120–180 km region of more pronounced subsidence in the Sevier fold-and-thrust belt foredeep, which was driven by east–west crustal shortening and short-wavelength flexural loading (Kauffman, 1977; Pang & Nummedal, 1995; Liu & Nummedal, 2004). This subsidence, along with eustatic sea-level rise, led to flooding of the North American continent during the middle and Late Cretaceous (Albian−Maastrichtian stages) by the Western Interior Seaway (WIS), a north–south trending epicontinental seaway that extended 5000 km across the continent, connecting high latitude polar oceans in Arctic Canada with low latitude subtropical oceans in the Gulf of Mexico (Kauffman, 1977; Hay et al., 1993; Kauffman & Caldwell, 1993; Miall et al., 2008)

(Figure 1.5). This seaway divided the North American continent into two major landmasses, Laramidia (the western margin of the WIS) and Appalachia (the eastern margin of the WIS) (Figure 1.5).

The evolution of the WIS is characterized by transgressive–regressive episodes which occurred due to tectonic activity, eustatic sea level change, and variation in terrigenous sediment supply (Kauffman, 1977; Hay et al., 1993; Kauffman & Caldwell, 1993). The palaeoshoreline fluctuated west–east by hundreds of kilometres; at maximum transgression, which occurred during the Turonian, the WIS occupied a width of 1200–2000 km (Hay et al., 1993) (Figure 1.5).

On the western margin of the WIS (Laramidia), clastic sediments derived from the Sevier fold-and-thrust belt were transported eastwards to the WIS and deposited as a series of asymmetric clastic wedges which thin to the east, and which interfinger with marine strata (Lawton, 1986a; Kauffman & Caldwell, 1993; Aschoff & Steel, 2011a, 2011b). During periods of tectonic quiescence and/or high eustatic sea level, clastic sources were diminished and the WIB was dominated by deep marine deposits (Miall et al., 2008). Whereas, during periods of tectonic activity and/or low eustatic sea level, clastic sediment input dominated the WIB and, onshore, rivers coalesced in exposed lowland areas to form major fluvial drainage networks with large trunk rivers (Kauffman, 1977; Kauffman & Caldwell, 1993; Miall et al., 2008; Bhattacharya et al., 2016).

Conversely, the eastern margin of the WIS (Appalachia) was bounded by lowlands on the stable North American craton (Figure 1.5); sediment input was comparatively limited and resulted in accumulation of thin stratal sequences in the WIB (Hay et al., 1993; Miall et al., 2008). On the eastern margin, transcontinental fluvial systems transported Appalachian-derived sediments west, across these lowlands, to the back-bulge of the WIB and to the north (Finzel, 2014) (Figure 1.5). Further, the Appalachian–Ouachita cordillera formed a continental drainage divide that separated these systems from drainage to the Atlantic Ocean, Gulf of Mexico and the southeasternmost WIS margin (e.g., Adams & Carr, 2010; Blum et al., 2017) (Figure 1.5).

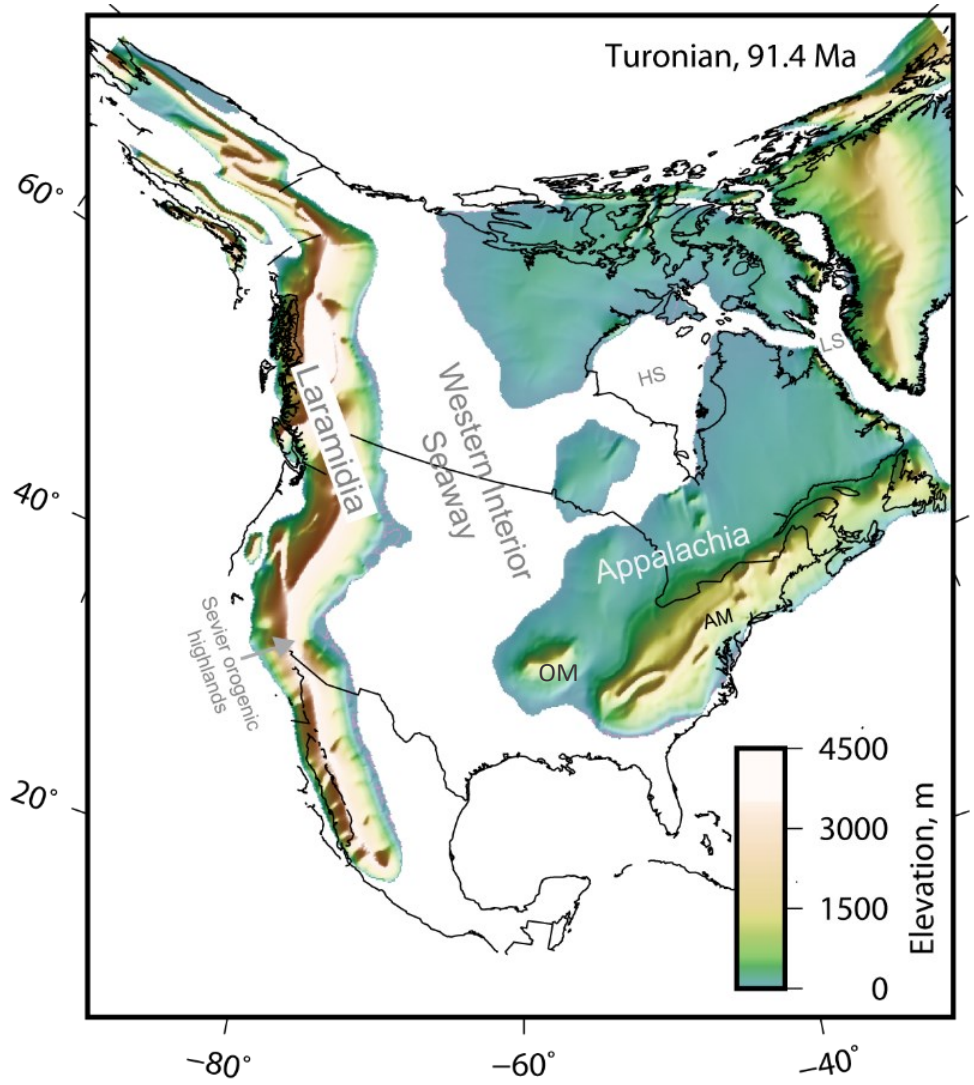

Figure 1.5 | Late Cretaceous North American palaeogeography. The example shown is for the Turonian stage of the Late Cretaceous and depicts an onshore palaeo-digital elevation model (palaeoDEM), including the highstand palaeogeography and palaeotopography, which was provided by *Getech Group Plc*. Key tectono-geographic features of the Late Cretaceous North American continent are depicted and labelled, including the Sevier orogenic highlands, Laramidian landmass, Western Interior Seaway (WIS), Appalachian landmass, Appalachian Mountains (AM), Ouachita Mountains (OM), Hudson Seaway (HS) and Labrador Seaway (LS). Modern North American coastlines and country borders (solid black lines) have been palaeo-rotated onto palaeoDEMs. This figure is replicated from Chapter 2, Figure 2.1 (part B).

Late Cretaceous North America: Palaeoclimate

The Cretaceous period (145–66 Ma) is characterized as one of the best examples of an ancient greenhouse climate and played host to the warmest climate states of the Phanerozoic eon (Frakes & Francis, 1988; Hay, 2008; Wade et al., 2019). Global temperatures were elevated and more equably distributed (Barron, 1983; Hallam, 1985; Barron et al., 1989; Caldeira & Rampino, 1991), and atmospheric CO_2 concentrations are estimated to have been 4–10 times higher than preindustrial levels of 280 ppm (Berner, 1994; Wang et al., 2014), which is akin to Intergovernmental Panel on Climate Change (IPCC) estimates for A.D. 2100 based on an unmitigated warming scenario (IPCC, 2014). In warm saline oceans, eustatic sea levels were 100–200 m higher than present day (Haq et al., 1987; Wolfe & Upchurch Jr., 1987). Further, in polar regions mean annual temperatures exceeded 14°C (Tarduno et al., 1998) and permanent ice sheets were absent — evidence of glacioeustacy favours episodic ice-sheet accumulation (Matthews & Poore, 1980; Miller et al., 1999; Stoll & Schrag, 2000; Miller et al., 2003), however permanent large continental ice sheets did not form until the middle Miocene (Savin et al., 1975; Shackleton & Kennett, 1975).

In general, Late Cretaceous North American climate is considered to have been warm and highly equable. Botanical evidence suggests that "megathermal" climates (mean annual temperatures >20°C) extended up to palaeolatitudes of ~40–50° north (Wolfe & Upchurch Jr., 1987) and that maximum mean monthly temperatures may have locally exceeded 30°C (Snell et al., 2014; Burgener et al., 2019). Latitudinal gradients were shallower in Late Cretaceous North America than in modern North America; latitudinal gradients of 0.3–0.4°C/1° latitude have been interpreted for the Campanian and Maastrichtian stages (Wolfe & Upchurch Jr., 1987; Amiot et al., 2004; Upchurch Jr. et al., 2015) whereas latitudinal gradients of 0.6–1.0°C/1° latitude have been documented for present day North America (Greenwood & Wing, 1995; Hay, 2008). Further, proxy reconstructions suggest a reduced mean annual range of temperature (MART) in Late Cretaceous North America (Wolfe & Upchurch Jr., 1987; Hunter et al., 2013; Burgener et al., 2019). Wolfe and Upchurch Jr. (1987) interpreted a MART of 8°C at palaeolatitudes of 52–55°N during the Campanian, Burgener et al. (2019) interpreted MARTs of 6−8°C at mid-latitudes during the Campanian (Burgener et al., 2019), and Hunter et al. (2013) interpreted a MART of ~10°C. These MARTs are much smaller than the MART of ~25−30°C that was estimated for modern North America at mid-latitudes of 50−55°N (Dee et al., 2011).

Late Cretaceous central Utah, USA: Palaeogeography and palaeoclimate

On the western margin of the WIS, major rivers drained the active Sevier orogenic fold-and-thrust belt and transported clastic sediments eastwards toward the WIS (Spieker, 1946; Armstrong, 1968; Kauffman, 1977; Hay et al., 1993; Kauffman & Caldwell, 1993) (Figure 1.6). In central Utah, Late Cretaceous fluvial systems are well-documented. Multiple transverse fluvial systems drained the Sevier fold-and-thrust belt (Lawton, 1983, 1986b; Bhattacharya et al., 2016; Bartschi et al., 2018; Kynaston, 2019; Pettit et al., 2019), and several studies have additionally interpreted an axial, or longitudinal, fluvial system that drained north–northeast

from the Mogollon Highlands (present day central Arizona) and Cordilleran magmatic arc (Lawton et al., 2003; Jinnah et al., 2009; Szwarc et al., 2015; Kynaston, 2019) (Figure 1.6). In close proximity to the Sevier thrust front, transverse rivers were dominated by a thrust-belt source (Bartschi et al., 2018; Pettit et al., 2019), whereas in more southerly rivers the longitudinal component of drainage interacted with these transverse systems and led to downsystem sediment mixing (Bartschi et al., 2018; Pettit et al., 2019) (Figure 1.6).

Tectonic forcing in this region is well studied (e.g., DeCelles, 1994, 2004; DeCelles & Coogan, 2006). In Utah, eastward propagation of the Sevier fold-and-thrust belt (due to continued eastward subduction of the Farallon plate) resulted in thin-skinned deformation and movement on the north–south trending Canyon (~145−110 Ma), Pahvant (~110−86 Ma), Paxton (86−75 Ma), and Gunnison (75−65 Ma) thrust systems (DeCelles, 1994, 2004; DeCelles & Coogan, 2006) (Figure 1.4). Exhumation associated with tectonic forcing created substantial topographic relief in the Sevier mountains, which has been described as "Andean" in scale (Sewall & Fricke, 2013; Foreman et al., 2015). Behind the Sevier front, existence of a high-elevation plateau known as "Nevadaplano" is inferred (Allmendinger, 1992; DeCelles, 1994, 2004; DeCelles & Coogan, 2006), which has been likened to the modern high-elevation plateau, Altiplano, of the central Andes. Palaeo-elevations in the Sevier highlands and Nevadaplano are argued to be 3 to >4 km — these values have been deduced from a combination of climate modelling studies (Sewall & Fricke, 2013; Foreman et al., 2015), kinematic reconstructions (DeCelles, 1994, 2004; DeCelles & Coogan, 2006) and other data, including palaeoflora (Chase et al., 1998).

Palaeoclimate in this region is also well studied, and proxy reconstructions have been conducted for the Campanian Kaiparowits Formation in south-central Utah, which crops out just south of my study area. Insights into palaeoclimate from the Campanian Kaiparowits Formation shed light on regional palaeoclimate during deposition of the Blackhawk Formation, Castlegate Sandstone, and Price River Formation. In the Kaiparowits Formation, observation of extensive floodbasin pond deposits, abundant flora and fauna, poorly developed hydromorphic paleosols, and evidence of rapid sedimentation rates all point to a relatively wet and subhumid climates (Roberts, 2007). Moreover, clumped isotope analysis of paleosol carbonate nodules indicate mean annual temperatures spanning 21 to 29°C (MART of ~8°C) and maximum monthly mean temperatures of 32 to 35±4°C (Burgener et al., 2019). Further, GCMs predict that a strong monsoon prevailed along the eastern flank of the Sevier mountains, and this prediction is corroborated by oxygen isotope data from bivalve shells and paleosol carbonates (Fricke et al., 2010). In detail, isotopic data indicate an east to west movement of water vapour, reflecting the movement of water vapour from low elevations (WIS) to high elevations (Sevier mountains) (Figures 1.5 and 1.6), and indicate the recharge of rivers in the foreland basin by high elevation precipitation (Fricke et al., 2010).

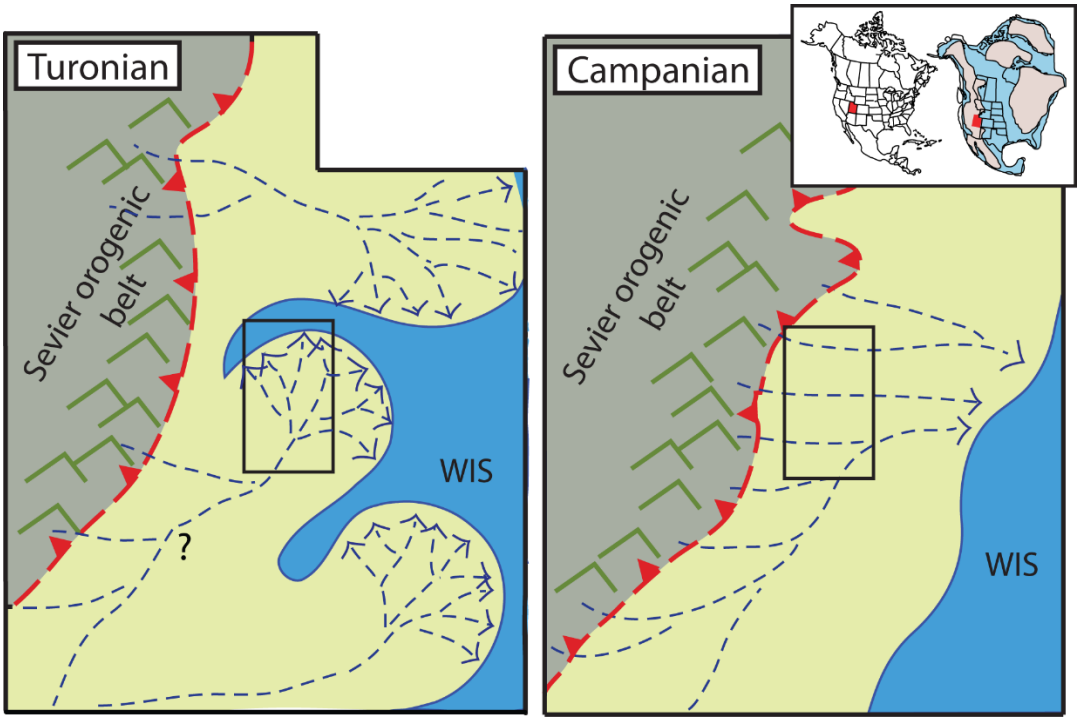

Figure 1.6 | Conceptual diagrams of Utah palaeogeography and palaeodrainage in the Turonian (left) and Campanian (right) stages of the Late Cretaceous. The dashed red lines with barbs indicate the approximate location of the Sevier thrust front. The dashed blue lines with arrows indicate the likely palaeodrainage configurations (and delta progradation) in the Sevier foreland. The black outlined boxes indicate the approximate position and extent of the study area (see Figure 1.7). The inset in the top right corner indicates the location of Utah relative to the modern North American continent (left) and the Late Cretaceous North American continent (right) — Utah is highlighted as a red box. WIS = Western Interior Seaway. Figure adapted from Chapters 3–5.

Late Cretaceous central Utah, USA: Regional stratigraphy

Rivers traversing the Sevier foreland during the Late Cretaceous transported large volumes of sediment eastward towards the WIS (Figure 1.6); these sediments were deposited on the western WIS margin and led to progradation of a large, asymmetric clastic wedge in the WIB (Lawton, 1986a; van Wagoner, 1995; Aschoff & Steel, 2011a, 2011b; Hampson et al., 2013) (Figure 1.8). Today, fluvial strata associated with these ancient rivers crop out extensively across midwest USA and Canada. These fluvial strata are exceptionally well-preserved in Utah and neighbouring states and are widely accessible (Figure 1.7). Further, these strata are well-documented, in term of their lithofacies and facies associations (e.g., Lawton, 1982, 1983, 1986a, 1986b; Miall, 1994; van Wagoner, 1995; Yoshida et al., 1996; Adams & Bhattacharya, 2005; Hampson, 2010; Hampson et al., 2012; Hampson et al., 2013; Flood & Hampson, 2014), have been regionally correlated (e.g., Lawton, 1982; Robinson & Slingerland, 1998; Aschoff & Steel, 2011a, 2011b; Seymour & Fielding, 2013), and have robust age constraints (e.g., Fouch et al., 1983; Molenaar & Cobban, 1991; Cobban et al., 2006).

In this thesis I focus on several geologic formations that crop out in central Utah, USA (Figure 1.7). In Chapter 3 I focus on the Campanian Blackhawk Formation, Castlegate Sandstone, and Price River Formation (Figure 1.8), as well as their upstream equivalents, which include the Sixmile Canyon Formation of the Indianola Group and the Price River Conglomerate (Figure 1.8). Whereas, in Chapters 4 and 5 I focus solely on the Campanian Blackhawk Formation and Castlegate Sandstone, and I additionally focus on the Turonian Ferron Sandstone (Figure 1.8). In Figure 1.7, I highlight the core field areas associated with Turonian age strata (black-outlined, white-filled circles) and Campanian age strata (black-outlined, black-filled circles). Turonian age strata belong to the Mancos Shale (or Mancos Group), and Campanian age strata belong to the Mesaverde Group (Figure 1.7b). Data from these field areas are presented in Chapters 3, 4, and 5. In Chapter 3, there are 5 additional field areas on the western and central Wasatch Plateau and to the west of the Wasatch Plateau (see Chapter 3; Figure 3.1). Below, I provide a detailed overview of these strata.

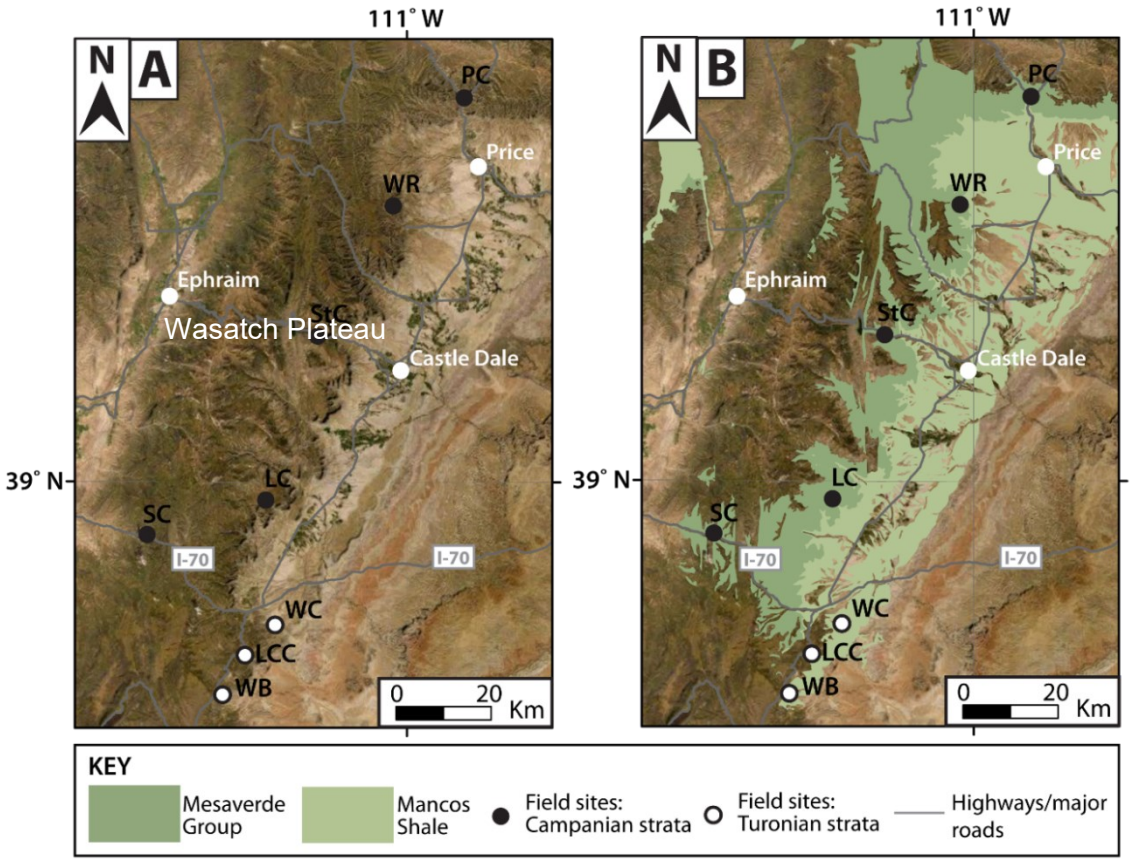

Figure 1.7 | Core field areas in central Utah, USA. **A)** Study area highlighting the location of field sites relative to towns (white-outlined, white-filled circles), highways/major roads, and the Wasatch Plateau. **B)** Study area highlighting the location of field sites relative to the Mesaverde Group and Mancos Shale. Field sites include Last Chance Creek (LCC), Link Canyon (LC), Price Canyon (PC), Salina Canyon (SC), Straight Canyon (StC), Wattis Road (WR), Willow Basin (WB) and Willow Creek (WC). LCC, WB and WC are field sites associated with Turonian age strata (Mancos Shale; black outlined, white-filled circles). LC, PC, SC, StC and WR are field sites associated with Campanian age strata (Mesaverde Group; black outlined, black-filled circles). Note: the black outlined boxes in Figure 1.6 indicate the approximate position and geographic extent of parts **A** and **B** in this figure.

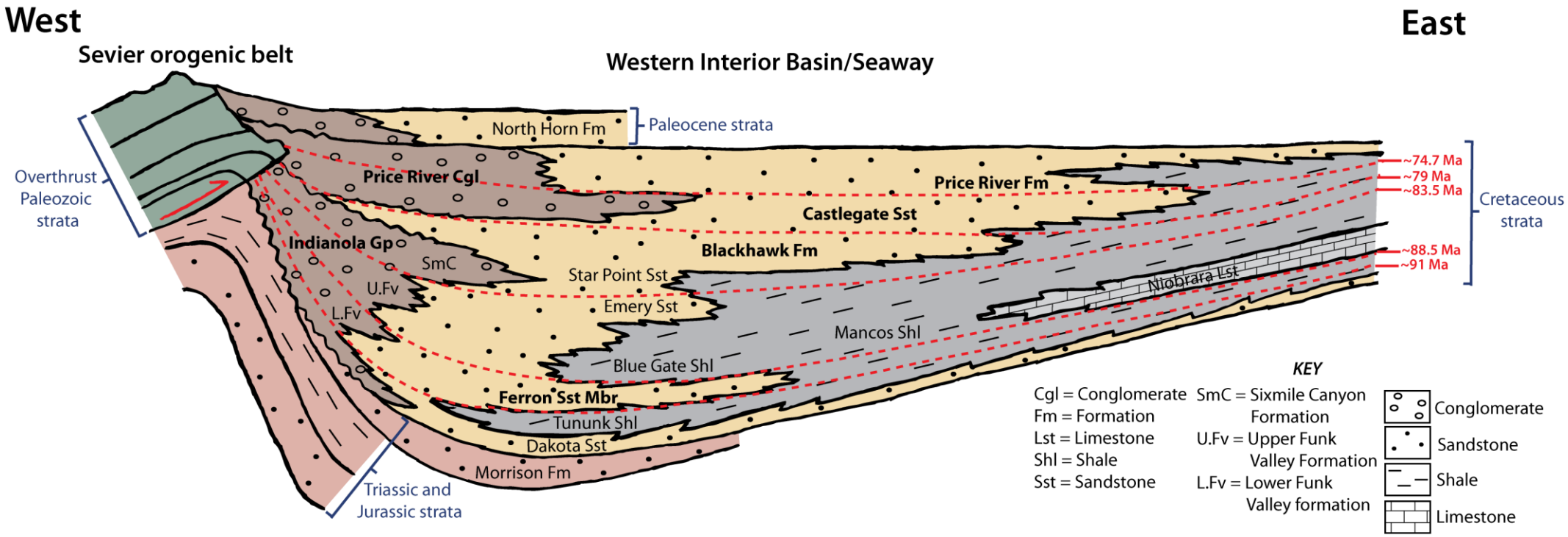

Figure 1.8 | Stratigraphic cross-section of the Western Interior Basin (WIB) from west-central Utah (West) to western Colorado (East), USA. The cross-section depicts the Sevier orogenic belt and the asymmetric clastic wedge that developed in the Sevier foreland basin as rivers draining the Sevier highlands transported sediment eastwards towards the Western Interior Seaway (WIS). The cross-section is therefore aligned with the regional palaeoflow direction (west to east). The dominant lithologies of strata are indicated on the figure (see Key) and, for strata relevant to this thesis, i.e., strata from which data are collected, their names are in **bold**. Further, the ages of strata are noted on the figure, and the ages of key horizons (indicated by dashed red lines) are also noted on the figure. Note: Figure is not to scale — dashed red lines are therefore approximate. Figure adapted from Armstrong (1968) and Howell et al., (2008).

i. Campanian stage

The Campanian stage of the Late Cretaceous spanned a duration of 11.5 Myr (83.6±0.2 to 72.1±0.2 Ma). In Chapter 3 of this thesis, I present field data from the Campanian Blackhawk Formation, Castlegate Sandstone, and Price River Formation, collected from the eastern Wasatch Plateau, central Utah, USA (Figures 1.7 and 1.8). In addition, I present field data from the upstream equivalents of these strata, the Indianola Group (specifically, the Sixmile Canyon Formation) and Price River Conglomerate, collected from the western and central Wasatch Plateau (Figures 1.7 and 1.8). Age constraints for these strata are derived from correlation with ammonite biozones in the distal Mancos Shale, which have been age-constrained by radiometric dating of volcanic ash beds (Gill & Hail Jr., 1975; Fouch et al., 1983; Cobban et al., 2006) — see recent review by Seymour and Fielding (2013).

Relatively distal

In this thesis, relatively distal (or downstream) field sites include Salina Canyon, Link Canyon, Straight Canyon, Wattis Road, and Price Canyon (Figure 1.7). At each of these field sites, the stratigraphy passes up-section through the Blackhawk Formation, Castlegate Sandstone, and Price River Formation (Figures 1.8 and 1.9).

The lower–middle Campanian Blackhawk Formation represents deposition on coastal plains behind wave-dominated deltaic shorelines which, up-section, pass landward into alluvial and fluvial plains (Hampson, 2010; Hampson et al., 2012; Hampson et al., 2013). The lowermost Blackhawk Formation is correlated with the *Scaphites hippocrepis II* zone (83.5±0.7–81.86±0.36 Ma), the middle Blackhawk Formation is correlated with the *Baculites obtusus* zone (80.58±0.55 Ma), and the top of the Blackhawk Formation is correlated with the *Baculites asperiformis* zone (79 Ma) (Fouch et al., 1983; Cobban et al., 2006). The eastern front of the Wasatch Plateau trends south-southwest to north-northeast, and exposures of the Blackhawk Formation along this front (exposed in cliff faces and canyons) form a transect which is broadly parallel (but slightly oblique) to the depositional strike, i.e., broadly parallel (but slightly oblique) to the palaeoshoreline (Figures 1.6, right, 1.7, and 1.10, left). Along the eastern front of the Wasatch Plateau, the size and abundance of channelized fluvial sandstone bodies (deposited by both single- and multi-thread rivers) in the Blackhawk Formation increases up-section (Adams & Bhattacharya, 2005; Hampson et al., 2012; Hampson et al., 2013; Flood & Hampson, 2015). These strata also become more palaeolandward up-section. In addition, the Blackhawk Formation is characterized by the presence and abundance of coal zones — these coal zones are associated with the lower and middle Blackhawk Formation but are most abundant in the lower Blackhawk Formation (Flood & Hampson, 2014, 2015) (Figure 1.10).

The middle–upper Campanian Castlegate Sandstone is situated atop the Blackhawk Formation and is an extensive and easily recognisable cliff-forming deposit — the basal contact separates mostly braided fluvial deposits from underlying coastal plain deposits of the Blackhawk Formation (van Wagoner, 1995; Yoshida et al., 1996) (Figure 1.10). The lower and middle Castlegate Sandstone are correlated with the *Baculites*

perplexus, *Baculites scotti* (75.84±0.26/75.56±0.11 Ma), *Didymoceras nebrascense* and *Didymoceras stevensoni* (75.19±0.28 Ma) zones, and the upper Castlegate Sandstone is correlated with the *Exiteloceras jenneyi* zone (75.08±0.11 Ma) (Fouch et al., 1983; Cobban et al., 2006). The lower and upper Castlegate Sandstone has been interpreted to comprise amalgamated braided fluvial channel-belt deposits, whereas the middle Castlegate Sandstone has been interpreted to comprise less amalgamated, more meandering/sinuous, fluvial channel-belt deposits with interbedded mudstones (Fouch et al., 1983; Lawton, 1986b; Miall, 1994; Yoshida et al., 1996; Miall & Arush, 2001).

The ledge-forming upper Campanian Price River Formation conformably overlies the Castlegate Sandstone and is recognised by transition from amalgamated fluvial channel-belt deposits of the upper Castlegate Sandstone to large, channelized sandstone bodies (~10–30m thick) with interbedded siltstones and mudstones — channelized sandstone bodies form ~75% of the formation (Lawton, 1983, 1986b). This transition is also recognised by a break in slope. The Price River Formation is correlated with the *Didymoceras cheyennense* and *Baculites jenseni* zones (74.67±0.15–71.98±0.31 Ma) (Fouch et al., 1983; Cobban et al., 2006).

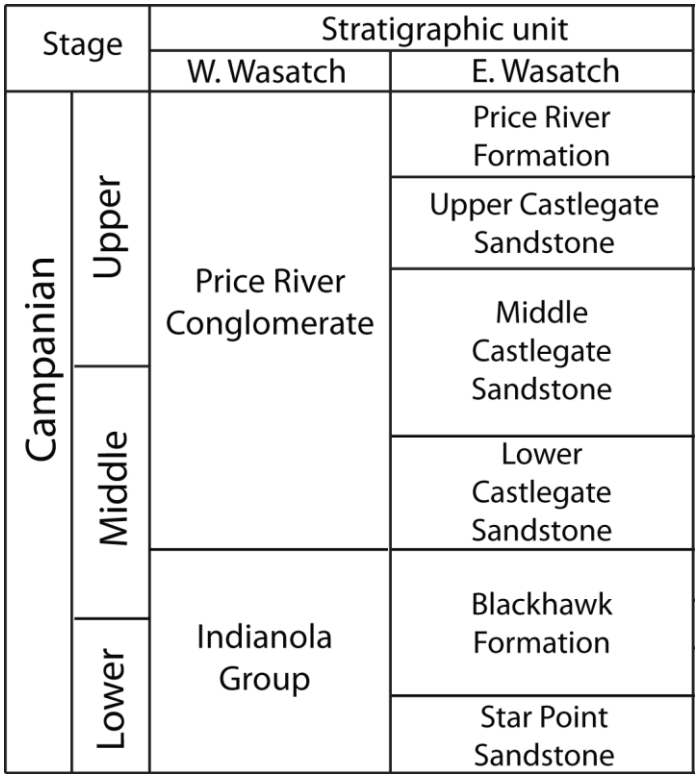

Figure 1.9 | Regional stratigraphy of the Mesaverde Group, including proximal (western Wasatch Plateau) to distal (eastern Wasatch Plateau) stratigraphic correlation. Modified and compiled using data from: Fouch et al. (1983); Robinson & Slingerland (1998); Miall & Arush (2001); Horton et al. (2004); Cobban et al. (2006); Aschoff & Steel (2011a, 2011b); Bartschi et al. (2018). Price River Conglomerate nomenclature follows Aschoff & Steel (2011a, 2011b). Note: The Price River Conglomerate may be referred to elsewhere as the Conglomerate of Thistle. This figure is adapted from Chapter 3, Figure 3.2.

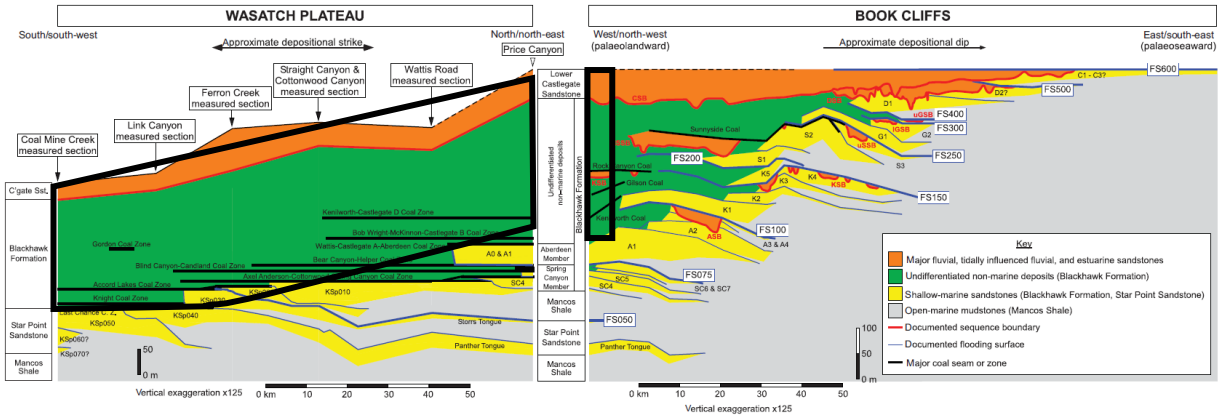

Figure 1.10 | Summary cross-sections of the stratigraphy of the Blackhawk Formation and Castlegate Sandstone, central Utah, USA. The cross-section on the lefthand side depicts a (slightly oblique) depositional strike transect and is the same depositional strike transect implemented in Chapter 3 of this thesis (Link Canyon, Straight Canyon, Wattis Road, and Price Canyon are all depicted on the lefthand cross-section and are also incorporated in the depositional strike transect implemented in Chapter 3; see Figure 3.1a). The black box highlights the area in which my field sites are situated, i.e., my field sites are restricted to terrestrial and nonmarine deposits. Meanwhile, the cross-section on the righthand side depicts a depositional dip, or proximal to distal, transect from Price Canyon (lefthand edge) to the eastern edge of Utah state (righthand edge). The most distal field site implemented in this thesis is Price Canyon, which is highlighted in the black box. More proximal field sites are not depicted in the righthand side cross-section. Figure adapted from Hampson et al., (2012). Refer to Hampson et al., (2012) for detailed information as to the notations depicted in this figure.

Relatively proximal

In this thesis, relatively proximal (or upstream) field sites include Mellor Canyon, Sixmile Canyon, Dry Hollow, Lake Fork, and Bear Canyon (Figure 1.7). At these upstream field sites, situated on the western and central Wasatch Plateau, correlative strata include more proximal sediments of the uppermost Indianola Group (specifically the upper Sixmile Canyon Formation) and the Price River Conglomerate (Figure 1.8). The Price River Conglomerate was formerly known as the Price River Formation but is now known to not be time-equivalent with the more distal Price River Formation exposed near Price, Utah (Robinson & Slingerland, 1998; Horton et al., 2004; Aschoff & Steel, 2011a, 2011b). Work by Robinson and Slingerland (1998) used palynology to establish correlation of the proximal "Price River Formation" in the western and central Wasatch Plateau with the more distal Castlegate–Price River succession in the Book Cliffs to the east (eastern Wasatch Plateau). This correlation is corroborated by field observations, e.g., correlation of a white, quartzite-dominated, cobble–boulder conglomerate in the Charleston–Nebo Salient of the Sevier thrust belt with the Castlegate–Price River succession in the Book Cliffs and can also be traced in seismic reflection data (Robinson & Slingerland, 1998; Horton et al., 2004). To avoid confusion, I refer to the proximal "Price River Formation" as the Price River Conglomerate in this thesis, following Aschoff and Steel (2011a, 2011b) (Figures 1.8 and 1.9). However, it should be noted that the Price River Conglomerate has elsewhere been referred to as the Conglomerate of Thistle (e.g., Valora, 2010).

The proximal Price River Conglomerate is characterised by quartzite-dominated synorogenic fanglomerates in which debris flow deposits interact with gravel–sand fluvial deposits (Robinson & Slingerland, 1998; Aschoff & Steel, 2011a, 2011b). As mentioned, the Price River Conglomerate is time-correlative with the more distal lower, middle, and upper Castlegate Sandstone, and Price River Formation (Robinson & Slingerland, 1998; Horton et al., 2004) (Figures 1.8 and 1.9). Meanwhile the proximal upper Sixmile Canyon Formation (uppermost Indianola Group) is predominantly characterised by synorogenic gravel–sand fluvial deposits, spanning polymictic fluvial conglomerates to medium–coarse-grained sandstones (Lawton, 1982, 1986a, 1986b). The upper Sixmile Canyon Formation is time-correlative with the Blackhawk Formation (Lawton, 1982; Fouch et al., 1983; Lawton, 1986b) (Figures 1.8 and 1.9).

ii. Turonian stage

The Turonian stage of the Late Cretaceous spanned a duration of 4.1 Myr (93.9–89.8±0.3 Ma) and, in this thesis, I focus on deposits of the upper Turonian Ferron Sandstone which crop out in central Utah, USA (Figures 1.7 and 1.8). The Ferron Sandstone preserves deposits of the ancient Last Chance, Notom, and Vernal fluvio-deltaic systems (e.g., Cotter, 1975a, 1975b, 1976; Chidsey et al., 2004). These systems were fed by rivers that drained the Sevier mountains toward the WIS, and which may have featured an additional/intermittent longitudinal component of drainage from the Mogollan highlands (Arizona) and/or the cordilleran magmatic arc (California) in the south-southwest (Kynaston, 2019) (Figure 1.6; left).

In Chapters 4 and 5 of this thesis, I present field data from deposits of the Last Chance fluvio-deltaic system. I focus on the Last Chance Ferron Sandstone because stratigraphic thicknesses and depositional sequence stratigraphy are well-documented (Garrison Jr et al., 1997; Anderson & Ryer, 2004; Gardner et al., 2004; Garrison Jr & van den Bergh, 2004; van den Bergh & Garrison Jr, 2004) (Figure 1.11) and because its age and depositional timespan are well-constrained. Garrison Jr and van den Bergh (2004) compiled biostratigraphic and stratigraphic correlation charts (Molenaar & Cobban, 1991; Kauffman & Caldwell, 1993; Gardner, 1995; Shanley & McCabe, 1995), which they calibrated using $^{40}Ar/^{39}Ar$ isotopic data (Obradovich, 1993), to determine that the Last Chance Ferron Sandstone was deposited over a period of 1.7 million years, between 90.3−88.6 Ma.

In detail, the Last Chance Ferron Sandstone comprises a clastic wedge that is orientated southwest to northeast, and which extends over ~60 km in length (Figure 1.11). In the southwest, deposits of the Last Chance Ferron Sandstone comprise palaeolandward terrestrial fluvial strata, whereas, to the northeast, deposits grade into deltaic facies (Figure 1.11). In this thesis, I present data collected from palaeolandward terrestrial fluvial facies. At the most palaeolandward field sites, i.e., the southwestern end of this clastic wedge (Figures 1.7 and 1.11), the Last Chance Ferron Sandstone is predominantly fluvial in origin and is characterised by major channelized sandstone bodies which are surrounded by abundant floodplain sediments and coals (Cotter, 1971; Chidsey et al., 2004) (Figure 1.11). These channelized sandstone bodies

represent the deposits of major meandering trunk channels, which is evidenced by abundant laterally accreted point bar deposits (Cotter, 1971; Chidsey et al., 2004).

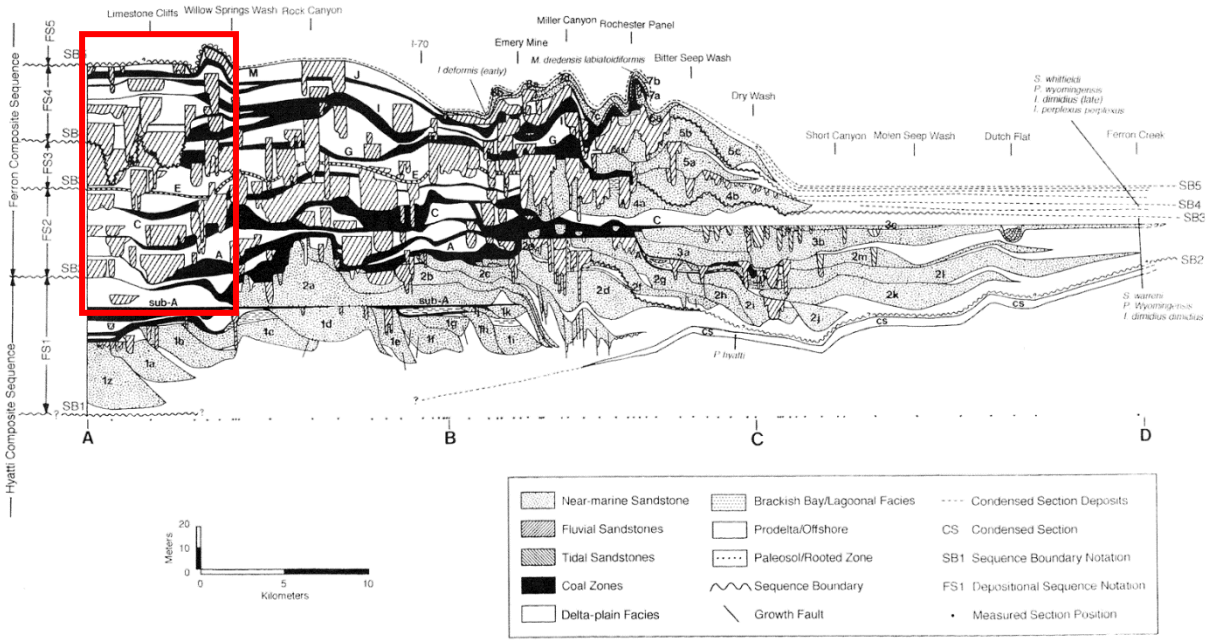

Figure 1.11 | Proximal to distal cross-section of the depositional sequence stratigraphy of the Upper Ferron Sandstone Last Chance Delta clastic wedge in Utah, USA. The Last Chance Delta clastic wedge is orientated southwest to northeast; the lefthand side of the cross-section (southwest) depicts the most proximal strata, whereas the righthand side of the cross-section (northeast) depicts the most distal strata. In this thesis, I collected field data from the most palaeolandward terrestrial fluvial strata of the Last Chance Ferron Sandstone. My field sites are all situated between the lefthand edge of the cross-section and Willow Springs Wash (a.k.a. Willow Creek; see Figure 1.7), as highlighted by the red box. At these field sites, the Last Chance Ferron Sandstone is predominantly fluvial in origin and is characterised by fluvial sandstones, which occur as major channelized sandstone bodies, and which are surrounded by abundant floodplain sediments and coals. Figure adapted from Garrison Jr and van den Bergh (2004). Refer to Garrison Jr and van den Bergh (2004) for detailed information as to the notations depicted in this figure.

1.6 Thesis outline

This thesis contains four research chapters, which follow this introduction, as well as a synthetic discussion and a conclusion. Each research chapter can be read as a standalone paper but, together, these chapters collectively address the aims and objectives outlined above.

Chapter 2

Chapter 2 of this thesis tackles Aim 1 and explores the reconstruction of sediment supply at large spatial and temporal scales in the geological past. I present a novel approach to reconstruct suspended sediment discharges using palaeoDEMs, GCM outputs, and the BQART suspended sediment discharge model (Syvitski & Milliman, 2007), and I exemplify this approach for the Cenomanian and Turonian North American continent. Using palaeoDEMs, I reconstruct catchments across the entire continent (n>1500) and I use GCM outputs to determine catchment climates and water discharges. I then use the BQART model to recover estimates of mean annual suspended sediment discharges for individual catchments, and I use these estimates to map spatial and temporal trends in sediment supply across the continent. Finally, I evaluate the efficacy of this approach. I show that estimates of suspended sediment discharges derived using this approach are in good agreement with estimates derived using independent approaches (e.g., Holbrook & Wanas, 2014) and, in evaluating the sensitivity of this approach to uncertainty, I show that this approach successfully provides first order approximations of suspended sediment discharges in the geological past.

This research chapter was published in ***Basin Research*** in February 2020. All of this published work was conceptualised, completed, and written by me, with supervision, review and editing by my supervisors and co-authors Dr Alex Whittaker and Prof Peter Allison, and with review and editing by my co-authors Prof Dan Lunt and Dr Alex Farnsworth.

Chapter 3

Chapter 3 of this thesis tackles Aim 2 and explores the reconstruction of morphologies, hydrodynamics and morphodynamics in ancient fluvial systems, which are intrinsically linked with water and sediment discharges (Chen et al., 2001; Liu, Yang, et al., 2014; Fielding et al., 2018; Chen et al., 2020; Herbert et al., 2020). I present a quantitative framework to reconstruct the morphologies and hydrodynamics from fluvial strata, and I apply this framework to Upper Cretaceous fluvial strata in central Utah, USA. To apply this framework, I collected field measurements of grain-size (>20,000), cross-set geometries (~7000 measurements across 470 cross-sets), maximum cross-set thicknesses (>4000), and architectural elements (>75) in the Late Cretaceous Blackhawk Formation, Castlegate Sandstone, and Price River Formation, central Utah, USA. Using these field measurements and new quantitative framework, I present the implied morphologies and hydrodynamics of ancient rivers in space, across five parallel fluvial systems, and in time, across seven stratigraphic intervals. Moreover, I evaluate the efficacy of this framework by contrasting different methods to check for consistency, and by contrasting reconstructed values with stratigraphic

observations, e.g., comparison of reconstructed palaeoflow depths with independent palaeoflow depth proxies (Adams & Bhattacharya, 2005; Lynds & Hajek, 2006; Hajek & Heller, 2012; Flood & Hampson, 2015; Chamberlin & Hajek, 2019). The results of Chapter 3 indicate that this quantitative framework can successfully recover spatiotemporal trends in the morphologies and hydrodynamics of ancient rivers, and that reconstructed values are reasonable when compared to stratigraphic and modern observations.

This research chapter was published in ***Sedimentology*** in April 2021. All of this published work was conceptualised, completed, and written by me, with supervision, review and editing by my supervisors and co-authors Dr Alex Whittaker and Prof Peter Allison, with review and editing by my co-authors Prof Gary Hampson and Dr Elizabeth Hajek, and with field assistance by Mx Bailey Lathrop.

Chapter 4

Chapter 4 in this thesis also tackles Aim 2, and explores our ability to reconstruct morphologies, hydrodynamics and morphodynamics of ancient fluvial systems in non-steady flow conditions. This chapter is motivated by the fact that methods to reconstruct morphologies, etc., from fluvial strata typically assume steady-state flow conditions (e.g., Paola & Borgman, 1991; Leclair, 2002), but that a plethora of theoretical, experimental and field observations all suggest that fluvial deposits may be dominated by preservation in non-steady, or disequilibrium, conditions (Ten Brinke et al., 1999; Jerolmack & Mohrig, 2005; Reesink & Bridge, 2007; Reesink & Bridge, 2009; Reesink et al., 2015; Fielding et al., 2018; Herbert et al., 2020; Leary & Ganti, 2020). These observations suggest that methods underpinned by steady-state assumptions may not be fully appropriate for the investigation of ancient fluvial systems.

In Chapter 4, I use field measurements of cross-set geometries and maximum cross-set thicknesses in the Ferron Sandstone, Blackhawk Formation and Castlegate Sandstone, to present unambiguous evidence for bedform preservation in disequilibrium conditions. I then use these field data to reconstruct the migration timescales of bedforms, and I use recent experimental observations made by Leary and Ganti (2020) to demonstrate a novel approach to extracting quantitative information pertaining to flow variability from fluvial strata. This may offer a potentially powerful approach to quantify flow variability in ancient fluvial systems, however it assumes that flow variability is the only control on bedform preservation in disequilibrium conditions, when in fact both flow variability and bar migration exert control on bedform preservation in disequilibrium conditions (Ganti et al., 2020; Leary & Ganti, 2020). Further investigation is therefore required to disentangle the relative role of these controls, to achieve the long-term goal of quantifying flow variability from fluvial strata, and I outline the necessary future work in ***Section 6.4***.

This research chapter was published in the February 2022 edition of ***Earth and Planetary Science Letters***. All of this work was conceptualised, completed, and written by me, with supervision, review and editing by my supervisor and co-author Dr Alex Whittaker, and with review and editing by my co-authors Dr Elizabeth Hajek and Dr Vamsi Ganti.

Chapter 5

Chapter 5 of this thesis tackles Aim 3 and is motivated by the importance of knowing ancient river planform for the reconstruction of palaeo-water and sediment discharges. However, Chapter 5 is also motivated by observations made in Chapter 3, and by Ganti, Whittaker, et al. (2019), that quantitative reconstructions of planform using the theoretically derived predictor of Parker (1976) are inconsistent with facies-based interpretations of planform. In Chapter 5, I present an evaluation of three well-known, and widely used, quantitative planform predictors (Parker, 1976; van den Berg, 1995; Crosato & Mosselman, 2009). I apply these predictors to field measurements of the Ferron Sandstone, Blackhawk Formation, and Castlegate Sandstone (presented in chapters 3 and 4 of the thesis), and I show that the results of each predictor are inconsistent with each other and with stratigraphic consensus for all three formations. As these predictors are typically tested using few observations of hydraulic geometries in natural rivers (e.g., n = 53 in Parker (1976)), I compile and present a new, and much larger, database of hydraulic geometries in natural rivers, with focus on rivers that are appropriate modern analogues for rivers preserved in the rock record (n = 1688). I use these data to evaluate the efficacy of the existing Parker (1976) predictor, and I present new criteria for palaeo-planform prediction which successfully predict planform in modern rivers and in three geologic examples.

A version of this research chapter was accepted for publication in ***Geology*** in February 2022. All of this work was conceptualised, completed, and written by me, with supervision, review and editing by my supervisor and co-author Dr Alex Whittaker, and with review and editing by my co-author Dr Elizabeth Hajek.

Chapter 6 (Discussion)

The final part of this thesis is a discussion. First, I present a general synthesis of my research, which includes a synopsis of each research chapter and highlights how each research chapter addresses the aims and objectives, to synthesise the key findings. I then discuss a number of cross-cutting themes that occur throughout the thesis, which are common to two or more research chapters. These cross-cutting themes are: (1) Importance of spatial and temporal scales; (2) Quantitative palaeohydrology versus qualitative palaeohydrology; (3) Errors and uncertainties of quantitative reconstruction methods; (4) Steady-state versus non-steady state; and (5) Multiple approaches to water and sediment discharge reconstruction. Then, I discuss my current and ongoing research and I outline prospective directions for future research, both of which are directly motivated by these cross-cutting themes. Finally, I provide a series of conclusions.

The research chapters in this thesis use either 'we/our' pronouns or the passive voice, in recognition of co-authors who appear (or who will appear) on the published version of each chapter. In the case of each research chapter, I confirm that I conceptualized and developed the research, conducted the data collection and data analysis, produced the figures and tables, and wrote the manuscripts. The contributions of co-authors Dr Alex Whittaker (Chapters 2–5) and Prof Peter Allison (Chapters 2, 3) included PhD supervision,

as well as review and editing of manuscripts (i.e., the research chapters). The contributions of co-authors Prof Dan Lunt (Chapter 2), Dr Alex Farnsworth (Chapter 2), Prof Gary Hampson (Chapter 3), Dr Elizabeth Hajek (Chapters 3–5), and Dr Vamsi Ganti (Chapter 4) included review and editing of manuscripts. The contributions of co-author Dr Bailey Lathrop (Chapter 3) included field assistance.

CHAPTER 2: Predicting sediment discharges and erosion rates in deep time — examples from the late Cretaceous North American continent[1]

ABSTRACT

Depositional stratigraphy represents the only physical archive of palaeo-sediment routing and this limits analysis of ancient source-to-sink systems in both space and time. Here we use palaeo-digital elevation models (palaeoDEMs; based on high-resolution palaeogeographic reconstructions), HadCM3L general circulation model (GCM) climate data and the BQART suspended sediment discharge model to demonstrate a predictive, forward approach to palaeo-sediment routing system analysis. To exemplify our approach, we use palaeoDEMs and HadCM3L data to predict the configurations, geometries and climates of large continental catchments in the Cenomanian and Turonian North American continent. Then, we use BQART to estimate suspended sediment discharges and catchment-averaged erosion rates and we map their spatial distributions. We validate our estimates with published geologic constraints from the Cenomanian Dunvegan Formation, Alberta, Canada, and the Turonian Ferron Sandstone, Utah, USA, and find that estimates are consistent or within a factor of two to three. We then evaluate the univariate and multivariate sensitivity of our estimates to a range of uncertainty margins on palaeogeographic and palaeoclimatic boundary conditions; large uncertainty margins (≤50%/±5°C) still recover estimates of suspended sediment discharge within an order of magnitude of published constraints. PalaeoDEMs are therefore suitable as a first-order investigative tool in palaeo-sediment routing system analysis and are particularly useful where stratigraphic records are incomplete. We highlight the potential of this approach to predict the global spatio-temporal response of suspended sediment discharges and catchment-averaged erosion rates to long-period tectonic and climatic forcing in the geologic past.

2.1 Introduction

2.1.1 Study rationale

Erosion and sediment discharge is an intrinsic part of the Earth surface system, with impacts on climate (Molnar & England, 1990), biogeochemical fluxes (Beusen et al., 2009; Bernard et al., 2011; Dürr et al., 2011) and long-term carbon cycling (Blair et al., 2004; Leithold et al., 2016), as well as feedbacks between tectonics and topography at Earth's surface (Willett, 1999; Wobus et al., 2006; Allen, 2008a, 2008b). As such, reconstruction of sediment routing and sediment discharges is essential to understanding the coupling of climate, tectonics, and surface processes over geological timescales (Whipple & Meade, 2006; Allen, 2008a; Whipple, 2009; Whittaker, 2012).

[1] A version of this chapter has been published in ***Basin Research***:

Lyster, S. J., Whittaker, A. C., Allison, P. A., Lunt, D. J. and Farnsworth, A. (2020) Predicting sediment discharges and erosion rates in deep time—examples from the late Cretaceous North American continent. ***Basin Research***, **32**, 1547– 1573, doi:10.1111/bre.12442

Depositional stratigraphy represents the time-integrated product of mass transfer across Earth's surface via palaeo-sediment routing systems (Allen, 2008a; Romans & Graham, 2013; Romans et al., 2016). In principle, it can be used to decipher catchment, erosion, and sediment discharge characteristics (Allen et al., 2013; Holbrook & Wanas, 2014; Michael et al., 2014), as well as tectonic and climatic events in the geologic past (Duller et al., 2010; Armitage et al., 2011; Whittaker et al., 2011). However, palaeo-sediment routing system analysis is typically limited by the incomplete or absent geologic record of terrestrial catchments (Sadler, 1981; Romans & Graham, 2013; Romans et al., 2016).

Techniques to quantitatively constrain sediment discharges and erosion rates in deep time include use of time-constrained sediment thicknesses/volumes (Walford et al., 2005; Galloway et al., 2011; Hampson et al., 2014), channel-fill palaeohydrology (Holbrook & Wanas, 2014; Lin & Bhattacharya, 2017; Sharma et al., 2017), grain-size sequestration trends (Duller et al., 2010; Whittaker et al., 2011; Michael et al., 2014), and reconstructed palaeocatchment characteristics (Sømme et al., 2009; Allen et al., 2013). This latter approach also includes the application of empirical sediment discharge models to ancient systems (Allen et al., 2013; Lin & Bhattacharya, 2017; Zhang et al., 2018). Additional approaches include techniques to constrain denudation rates using apatite fission track (AFT) ages (Tinker et al., 2008; Vernon et al., 2008; Cederbom et al., 2011; Painter et al., 2014) and large-scale fluvial inversion models based on present-day river long profiles (Paul et al., 2014; Stephenson et al., 2014). These methods are all useful but are subject to caveats associated with methodological assumptions, errors and uncertainties of measurement tools, and the restricted spatial and temporal resolution of data. Consequently, investigating sediment routing at continental and global scales in the geologic past remains a pre-eminent research challenge.

In this study we evaluate high-resolution palaeogeographies as a first-order investigative tool in palaeo-sediment routing system analysis. Palaeogeographic reconstructions offer a conceptual model of Earth's topography during time-integrated 'slices' of the geologic past (Markwick & Valdes, 2004; Markwick, 2018) and improvements to reconstruction methods and data sets over recent decades (see review in Markwick, 2018) have significantly enhanced our understanding of palaeotopography. Digitisation of these models as palaeo-digital elevation models (palaeoDEMs) is now employed by various research communities (e.g., Bonne, 2014; Lunt et al., 2016; Chiarenza et al., 2019) and routine application of palaeoDEMs to palaeoclimate modelling experiments (tested and calibrated against proxy records) suggests robustness at coarse resolution (Hunter et al., 2008; Tindall et al., 2010; Craggs et al., 2012; Tabor et al., 2016). Coupling of palaeoDEMs with palaeoclimate data therefore offers novel opportunities to explore Earth surface processes in the geologic past.

Here, we (1) use palaeoDEMs to reconstruct large continental palaeocatchments in North America during the Cenomanian and Turonian stages of the late Cretaceous; (2) predict suspended sediment discharges and erosion rates using data from HadCM3L, a coupled atmosphere–ocean general circulation model (GCM), and the BQART sediment discharge model (Syvitski & Milliman, 2007); (3) compare estimates of suspended sediment discharges with predictions derived from previous field-based approaches; and (4) test the

univariate and multivariate sensitivity of our approach. Our results provide insights to the utility (and fidelity) of palaeogeographic reconstructions within a predictive, forward approach to palaeo-sediment routing system analysis. Further, sensitivity analysis defines the limits and applications of our approach. We deliver first-order estimates of palaeodrainage networks, suspended sediment discharges and erosion rates in the Cenomanian and Turonian North American continent, which coincide with the Cretaceous Thermal Maximum.

2.1.2 Research background

Reconstructing sediment discharges in ancient source-to-sink systems

Techniques to reconstruct sediment discharges in the geologic past have generally focused on the thickness, volume, and characteristics of time-constrained depositional stratigraphy to estimate, or back-calculate, onshore sediment discharges (e.g., Walford et al., 2005; Galloway et al., 2011; Hampson et al., 2014). For example, Galloway et al. (2011) constrained sediment discharges to the Gulf of Mexico during the Cenozoic, which have since been corroborated by independent approaches (e.g., Petter et al., 2013; Zhang et al., 2018). A closed system is often assumed, but efforts have been made to account for along-strike sediment transport where the source-to-sink system is not fully closed (e.g., Hampson et al., 2014).

Alternatively, Holbrook and Wanas (2014) demonstrated use of channel palaeohydrology in fluvial stratigraphy to estimate sediment discharges in ancient source-to-sink systems of the Cenomanian Bahariya Formation, Egypt. This approach has also been used to understand sediment routing in late Cretaceous North America (Lin & Bhattacharya, 2017; Sharma et al., 2017), which we explore later in this study. While this method does not require a closed system, it assumes that, for a given time interval, the total sediment volume passing through a cross section of the trunk channel is equal to the sediment volume contributed by the source area and the sediment volume deposited in the sink region (Holbrook & Wanas, 2014). This method therefore requires preservation of a trunk channel significantly inland of the palaeoshoreline.

Measures of sediment calibre can be used to calculate grain-size fining rates, which are dependent on the distribution of tectonic subsidence (Whittaker et al., 2010) and sediment discharge (Fedele & Paola, 2007; Duller et al., 2010; Whittaker et al., 2011). While quantitative inversion of grain-size fining trends in fluvial stratigraphy can successfully recover spatio-temporal variations in sediment discharge and tectonic subsidence (Duller et al., 2010; Whittaker et al., 2011), this approach requires significant preservation of the sediment routing system in space and time.

Ultimately, all stratigraphic methods are limited by the need for well-preserved and age-constrained outcrop/subsurface data that ideally represent a closed or partially-closed system. Stratigraphic methods (particularly field-based methods) are also inherently time consuming and often recover estimates that are precise to only one order of magnitude.

An alternative, catchment-based, strategy is to forward model sediment discharges using the geometries and characteristics of ancient terrestrial catchments. Allen et al. (2013) made first-order estimates of sediment discharges from Paleogene palaeocatchments in the Pyrenees, Spain, by reconstructing catchment characteristics from field observations and applying a bulk diffusive model. In their model, sediment discharge is the product of an incising drainage network, where bulk diffusivity is controlled by mean annual precipitation and the length over which precipitation is concentrated. However, this model (as well as others) requires long term erosional parameters to be deduced *a priori*. Alternatively, catchment-based forward estimates of sediment discharge can also be made by relatively simple sediment discharge models such as BQART (Syvitski & Milliman, 2007). BQART is an empirically derived multiple regression model of long-term (>30 years) average suspended sediment load. Mean annual suspended sediment load, Q_s, can be approximated by

$$Q_s = \omega \mathrm{B} \mathrm{Q}^{0.31} \mathrm{A}^{0.5} \mathrm{R} \mathrm{T} \text{ for } \mathrm{T} \geq 2°\mathrm{C}, \quad \text{Eq. 2.1a}$$

$$Q_s = 2\omega \mathrm{B} \mathrm{Q}^{0.31} \mathrm{A}^{0.5} \mathrm{R} \text{ for } \mathrm{T} < 2°\mathrm{C}, \quad \text{Eq. 2.1b}$$

where Q_s is in units of MT/yr (1 MT = 10^9 kg), ω is a unit conversion constant of 0.0006, Q is water discharge (km^3/yr), A is drainage area (km^2), R is maximum relief (km), and T is mean annual temperature (°C). B is a glacial, lithologic, and anthropogenic factor (see Syvitski and Milliman, 2007). Syvitski and Milliman (2007) tested BQART on a global database of 488 rivers that drain 63% of Earth's surface and showed that BQART accounts for 96% of variance in observed Q_s. When B is set to 1, Syvitski and Milliman (2007) showed that BQART explains 66% of variance in observed Q_s, and that estimates of Q_s are calculated within one order of magnitude, and most within a factor of five, of observed Q_s.

Relative to other suspended sediment discharge models (e.g., Pelletier, 2012; Cohen et al., 2013), BQART is well-suited to geologic application as it has comparatively low data requirements (see discussion in Allen et al., 2013; Helland-Hansen et al., 2016; Eide et al., 2018) — this is ideal when one is dealing with an incomplete rock record as it minimises assumptions. Various authors have used BQART to model Q_s in Quaternary systems on 10^2–10^5 yr timescales and have calibrated BQART estimates with preserved sediment thicknesses (Sømme et al., 2011; Watkins et al., 2018) or catchment-averaged denudation rates derived from cosmogenic ^{10}Be (Hidy et al., 2014). In particular, BQART has been used to investigate temporal variation in Q_s across glacial–interglacial periods (Garvin, 2008; Hidy et al., 2014; Watkins et al., 2018). To date, translation of BQART to ancient systems on 10^6–10^8 yr timescales includes comparison of BQART with Q_s estimates derived from alternative methods (Allen et al., 2013; Lin & Bhattacharya, 2017), use of BQART where regional palaeogeography is well-understood (Zhang et al., 2018), and inverse applications, where constraints and/or estimates of Q_s from depositional stratigraphy have been used to predict palaeotopography (e.g., Carvajal & Steel, 2012; Sømme et al., 2013).

Application of BQART to ancient systems is infrequent as it requires constraints on palaeocatchment drainage area, maximum relief, temperature, and water discharge; deducing these parameters from

depositional stratigraphy at continental scales is not usually possible as the geologic record of terrestrial catchments is incomplete (and erosional source regions are inherently not preserved). In this study we translate BQART to ancient systems on continental scales; to achieve this we require robust palaeogeographies, to characterise palaeodrainage, and robust palaeoclimate estimates.

Palaeogeographies and HadCM3L

Access to palaeoDEMs and palaeoclimate modelling results offers new opportunities to constrain BQART input parameters, especially on large spatio-temporal scales. Coupling of these novel data sets enables us to reconstruct catchment geometries and catchment-averaged palaeoclimates; with BQART we can then model both *Qs* and catchment-averaged erosion rates on a variety of spatial and temporal scales.

Palaeogeographic reconstructions are of increasing scientific importance across fields such as pre-Quaternary palaeoclimate modelling and hydrocarbon exploration (evaluation of play element distributions, e.g., Markwick, 2018). Major advances to the resolution of palaeogeographies are attributed to growth of the extensive lithologic, tectonic and palaeontologic data sets that underpin them (see discussion in Markwick & Valdes, 2004; Markwick, 2018). Markwick and Valdes (2004) developed a method that uses geographic information systems (GIS) to digitise high-resolution palaeogeographies as palaeoDEMs and facilitate their use in palaeoclimate modelling, lithofacies retrodiction and source-to-sink analysis. These palaeoDEMs can subsequently be used as palaeogeographic boundary conditions in GCMs such as HadCM3L (e.g., Lunt et al., 2016).

HadCM3L is a coupled atmosphere–ocean GCM that was developed at the Hadley Centre for Climate Prediction and Research at the UK Meteorological Office; it comprises linked atmosphere, ocean, vegetation, and sea-ice models and is one of the earliest GCMs to prevent climate drift without requirement of flux adjustments (Gordon et al., 2000; Pope et al., 2000). Relative to more recent and/or higher resolution GCMs, HadCM3L is fast and allows millennial and multi-millennial-scale integrations (Farnsworth et al., 2019), which is essential for deep-time modelling work where the initial condition may be far from the final equilibrium state — HadCM3L has been used in numerous pre-Quaternary palaeoclimate studies (Lunt et al., 2007; Tindall et al., 2010; Craggs et al., 2012; Lunt et al., 2016).

2.2 Study area

We focus on the Cenomanian and Turonian North American continent, where published estimates of *Qs* offer opportunities to validate our palaeoDEM–HadCM3L–BQART approach. Key tectono-geographic features of this region include the Sevier orogenic fold-and-thrust belt and its adjacent foreland basin, the Western Interior Basin (WIB; Figure 2.1) (Armstrong, 1968; Jordan, 1981; Cross, 1986; DeCelles, 1994). The WIB formed from eastward subduction of the Farallon plate beneath the western margin of North America, which generated relatively uniform, long-wavelength dynamic subsidence across the continent (Liu et al., 2011; Liu et al., 2014). Superimposed on this was a narrow 120–180 km region of more

pronounced subsidence in the Sevier fold-and-thrust belt foredeep, driven by east–west crustal shortening and short-wavelength flexural loading (Kauffman, 1977; Pang & Nummedal, 1995; Liu & Nummedal, 2004). This led to flooding of the continent during the middle and late Cretaceous by the Western Interior Seaway (WIS) (Figure 2.1), a north–south trending epicontinental seaway that connected polar oceans in Arctic Canada with subtropical oceans in the Gulf of Mexico (Kauffman, 1977; Hay et al., 1993; Kauffman & Caldwell, 1993; Miall et al., 2008).

The palaeogeographic evolution of the Cretaceous North American continent is well-understood and has been comprehensively reviewed (Kauffman & Caldwell, 1993; Roberts & Kirschbaum, 1995; Hay et al., 1999; Miall et al., 2008), especially in the context of palaeodrainage evolution (Bhattacharya et al., 2016). This has largely been constrained by depositional stratigraphy and detrital zircon (DZ) geochronology, at both regional (Szwarc et al., 2015; Bartschi et al., 2018; Pettit et al., 2019) and continental scales (Roberts & Kirschbaum, 1995; Benyon et al., 2014; Blum & Pecha, 2014; Finzel, 2014). Clastic sediment input from the western WIS margin dominated the WIB and, at lowstand, rivers coalesced to form major fluvial drainage networks (Miall et al., 2008; Bhattacharya et al., 2016). Whereas the eastern WIS margin was bounded by lowlands on the stable North American craton; sediment input here was comparatively limited and resulted in accumulation of thin stratal sequences (Witzke et al., 1983; Hay et al., 1993; Witzke & Ludvigson, 1994; Brenner et al., 2003; Miall et al., 2008). On this eastern margin, transcontinental fluvial systems transported Appalachian-derived sediment west to the WIB back-bulge and also to the north (Finzel, 2014). The Appalachian–Ouachita cordillera formed a continental drainage divide that separated these systems from drainage to the Atlantic Ocean, Gulf of Mexico (GoM), and the southeasternmost WIS margin (e.g., Adams & Carr, 2010; Blum et al., 2017).

While late Cretaceous North American climate remains unresolved (due to the uncertain influence of epicontinental seaways) (DeConto et al., 1999; Hay, 2017), it is accepted that temperatures were elevated and more equably distributed (Barron, 1983; Hallam, 1985), with poleward isotherm displacement (Barron, 1983). Atmospheric CO_2 concentrations are estimated to have been 4–10 times higher than preindustrial levels of 280 ppmv (see review by Wang et al., 2014), with eustatic sea levels 100–200 m higher than present day (Haq et al., 1987) and an absence of permanent ice sheets (Savin et al., 1975; Shackleton & Kennett, 1975; Miller et al., 1999; Stoll & Schrag, 2000; Miller et al., 2003). As such, lack of permanent ice was conducive to the existence of major fluvial systems in Greenland (e.g., Pedersen & Pulvertaft, 1992; Jensen & Pedersen, 2010).

With a robust understanding of palaeogeography, extensive and well-documented exposures of Cretaceous strata, and a highly-refined chronology (Kauffman, 1977; Kauffman & Caldwell, 1993; Miall et al., 2008), the late Cretaceous North American continent, in particular the WIB, is an ideal natural laboratory for studying ancient source-to-sink systems and evaluating our approach.

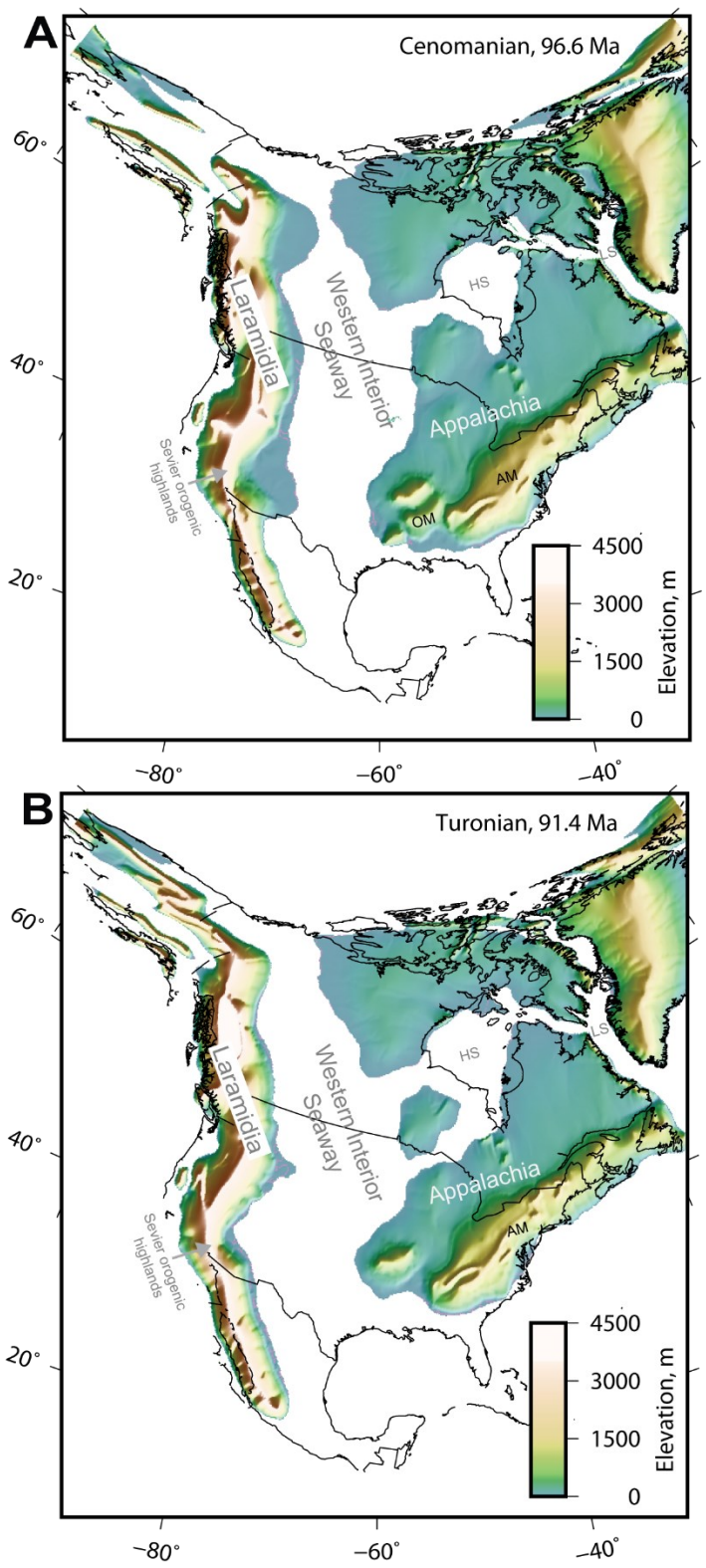

Figure 2.1 | Onshore palaeo-digital elevation models (palaeoDEMs) for the Cenomanian (part **A**) and Turonian (part **B**) North American continent. Key palaeogeographic features are labelled, including the Sevier orogenic highlands, Laramidian landmass, Western Interior Seaway (WIS), Appalachian landmass, Appalachian Mountains (AM), Ouachita Mountains (OM), Hudson Seaway (HS) and Labrador Seaway (LS). Modern North American coastlines and country borders (solid black lines) have been palaeo-rotated onto palaeoDEMs.

2.3 Data sets and methods

2.3.1 Palaeogeographies and palaeoDEMs

PalaeoDEMs were provided by Getech Group Plc for Cenomanian and Turonian time slices (Table 2.1) and are *time-averaged* representations of palaeogeography and palaeotopography — palaeoDEMs are time-averaged across the entire length of the stage (see discussion in Markwick and Valdes, 2004). Each palaeoDEM comprises a single elevation raster with a spatial resolution of 0.1° latitude × 0.1° longitude, which equates to a cell size of ~11 × 11 km (Figure 2.1). Getech construct palaeoDEMs using the methodology of Markwick and Valdes (2004) and Markwick (2018), based on concepts developed by Ziegler et al. (1985). Getech palaeoDEMs have been used in a number of studies on pre-Quaternary palaeoclimate (e.g., Craggs et al., 2012; Hunter et al., 2013; Armstrong et al., 2016; Lunt et al., 2016; Tabor et al., 2016) and palaeo-sediment routing (Bonne, 2014).

Getech has generated an in-house global plate model, underpinned by knowledge of crustal architecture (i.e., the origin, composition, and thickness of crust, as well as its structural framework) and geodynamic history, which is interpreted from data pertaining to igneous/sedimentary history, geochronology, palaeomagnetism, and structural geology. Tectonic blocks are assigned, each with unique geologic histories (including rift, drift, and accretion histories) and unique rotation parameters; relative motions are calculated within the Global Hybrid Reference Frame of Torsvik et al. (2008). Other useful data, such as lithologic, palaeontologic, or tectonic information are added into GIS compatible global databases. These are predominantly taken from the public domain and include data from publications, programmes (such as Deep Sea Drilling Project (DSDP) and Ocean Drilling Program (ODP)) and other sources, such as national geological surveys. Once collated these data are reconstructed back to their palaeo-coordinates using the plate model. These constraints are used to classify net-depositional environments and interpret contemporary base level, which separates net-depositional environments (below base level) and net-erosional, 'tectonophysiographic' terranes (above base level; see discussion of contemporary base level in Markwick and Valdes, 2004). This facilitates reconstruction of the relative distribution of relief. To reconstruct maximum elevation, Getech use analogue elevation distributions of modern tectonic settings and models of orogen growth and decay. In contrast, minimum elevation is reconstructed using depositional lithofacies and marine fossil occurrences to identify highstand palaeoshorelines (throughout this manuscript we refer to highstands and lowstands in terms of third- and fourth-order cycles, on 10^5–10^6 myr timescales). Getech use palaeodrainage information, where available, from sedimentologic, stratigraphic, and provenance studies, to guide interpolation of base contours (minimum elevation, contemporary base level, and maximum elevation) to an elevation raster. The end product is nine global, terrestrial contours that have been interpolated, using the palaeodrainage network, to an elevation raster with a cell size of 0.1° latitude × 0.1° longitude. For full, detailed information on palaeogeographic mapping workflow, see Markwick and Valdes (2004) and Markwick (2018).

Table 2.1 | Durations of Cenomanian and Turonian stages and the reconstruction ages of their associated palaeo-digital elevation models (palaeoDEMs).

	Stage age (Ma)	**Stage duration (Myr)**	**PalaeoDEM reconstruction age (Ma)**
Cenomanian	93.9–100.5	6.6	96.6
Turonian	89.8–93.9	4.1	91.4

2.3.2 HadCM3L GCM

HadCM3L GCM palaeoclimate data are time-averaged representations of Cenomanian and Turonian palaeoclimate and include mean annual air temperature at 1.5 m above the local surface and mean annual precipitation (Figure 2.2). These data have a spatial resolution of 2.5° latitude × 3.75° longitude, which equates to a cell size of 278 × 417 km at the equator and 278 × 295 km at 45° latitude (Gordon et al., 2000; Hunter et al., 2008), and the same stage-length temporal resolution as the Cenomanian and Turonian palaeoDEMs.

Cenomanian and Turonian palaeoclimate data are identical to those presented and described in Farnsworth et al. (2019), with atmospheric CO_2 set at 1120 ppmv (×4 preindustrial atmospheric CO_2) and using Cenomanian and Turonian palaeoDEMs as boundary conditions. The model used is very similar to the HadCM3BLM2.1aD model that is described and evaluated under modern climate configuration in Valdes et al. (2017), except that it includes a modification to the ozone profile which ensures that the model does not develop a runaway warming at ×4 preindustrial atmospheric CO_2, as discussed in Lunt et al. (2016). For further information on boundary conditions used in HadCM3L simulations see Appendix A1 and Farnsworth et al. (2019). Additional information on HadCM3L boundary conditions, assumptions and xperimental design in pre-Quaternary palaeoclimate modelling is discussed in Lunt et al. (2016).

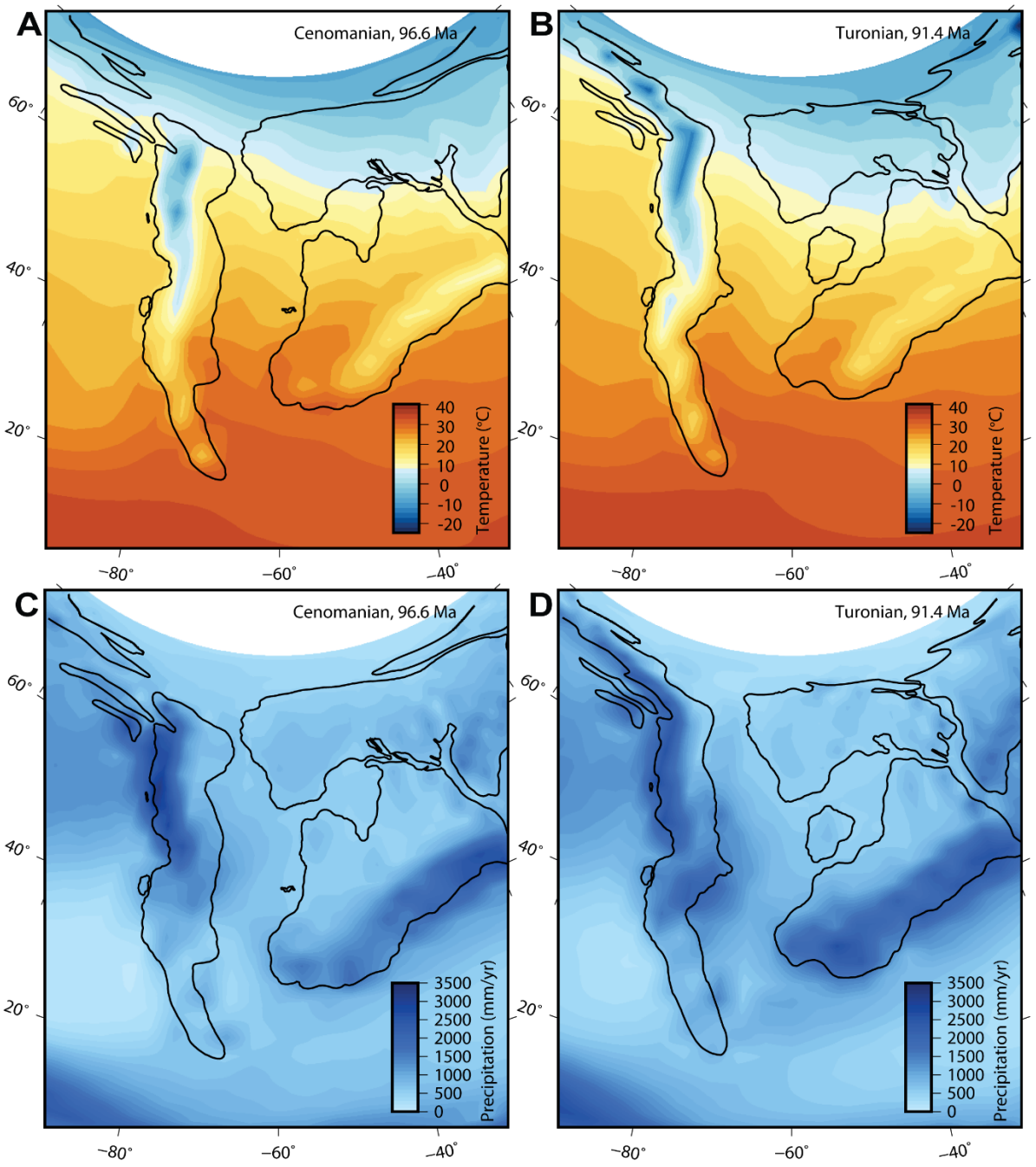

Figure 2.2 | Palaeoclimate data from the HadCM3L general circulation model (GCM), which includes mean annual temperature at Earth's surface for the Cenomanian (part **A**) and Turonian (part **B**) North American continent and mean annual precipitation for the Cenomanian (part **C**) and Turonian (part **D**) North American continent. Solid black lines illustrate (highstand) palaeoshorelines of palaeo-digital elevation models (palaeoDEMs).

2.3.3 Reconstructing palaeocatchments and extracting catchment geometries

We define the extent of the North American palaeo-continent as encompassing the palaeo-position of Greenland, Canada, U.S.A, Mexico, and Central America. To reconstruct the size and distribution of Cenomanian and Turonian palaeocatchments, we analysed the two palaeoDEMs in ArcGIS 10.5.1 (using the hydrological toolbox) to establish large channel networks and delineate palaeocatchment boundaries (Figures 2.3 and 2.4; for a detailed ArcGIS workflow, see Appendix A2). For each reconstructed palaeocatchment, we used zonal statistics to extract palaeocatchment geometries, which included drainage area (A) and maximum relief (R).

Interpolation between base contours during palaeoDEM construction results in low-lying areas adjacent to the palaeoshoreline that do not preserve relief (see Appendix A2) — these palaeocatchments are mostly small with drainage areas ≤500km^2. At this point we therefore omitted palaeocatchments with drainage areas ≤500km^2 (as well as larger palaeocatchments with zero/negligible relief). Removed palaeocatchments make up 1.5–2% of the total continental area and do not impact modelled estimates of total continental Qs as, with zero/negligible relief, they recover zero/negligible Qs (Equation 2.1). Our investigations are therefore focused on large reconstructed palaeocatchments with drainage areas ≥500 km^2. Independently validating these ancient catchments for the whole Cenomanian and Turonian North American continent is impossible due to the incomplete geologic record; instead, we compare palaeocatchment geometries, where possible, with estimates of drainage area, provenance, and palaeo-elevation (e.g., Chase et al., 1998; DeCelles, 2004; DeCelles & Coogan, 2006) in published literature.

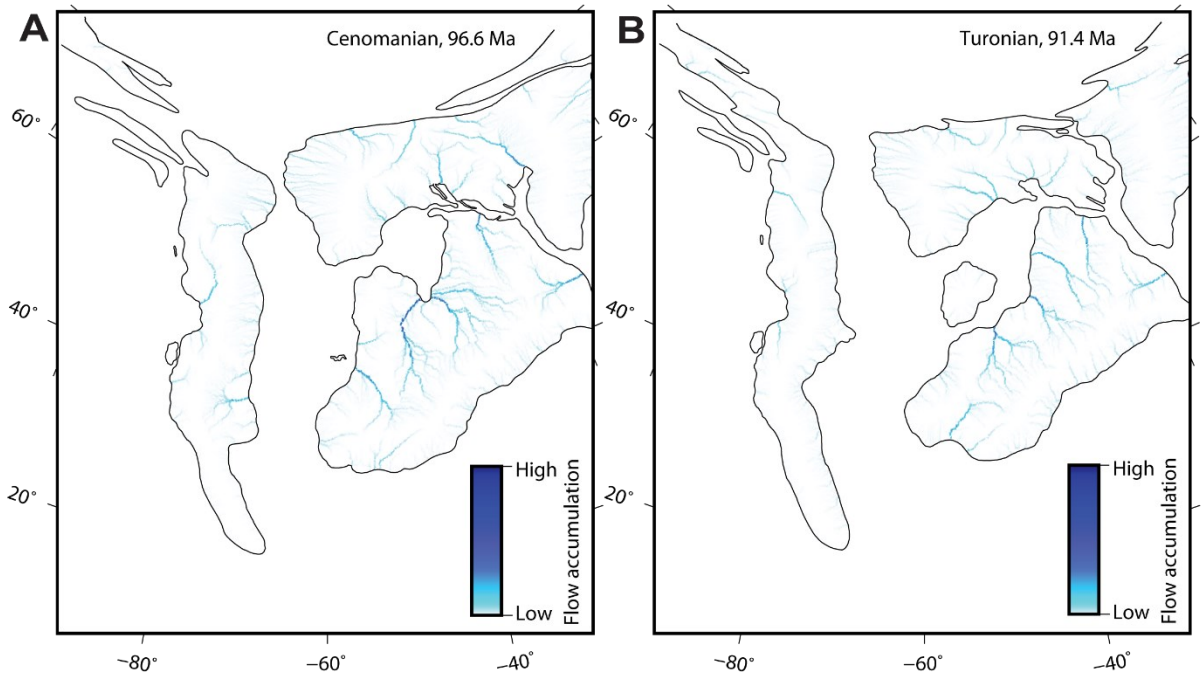

Figure 2.3 | Reconstructed location of major drainage systems across the Cenomanian (part **A**) and Turonian (part **B**) North American continent, from calculation of flow accumulation in palaeo-digital elevation models (palaeoDEMs). Flow accumulation is a measure of how many cells flow into each downslope cell. In the figure, flow accumulation ranges from low, 0 cells, to high, 8000 cells (palaeoDEM cells have a resolution of ~11 × 11 km, or 0.1°), and high flow accumulations are therefore predictive of the location of relatively major drainage networks. Solid black lines illustrate (highstand) palaeoshorelines of palaeoDEMs.

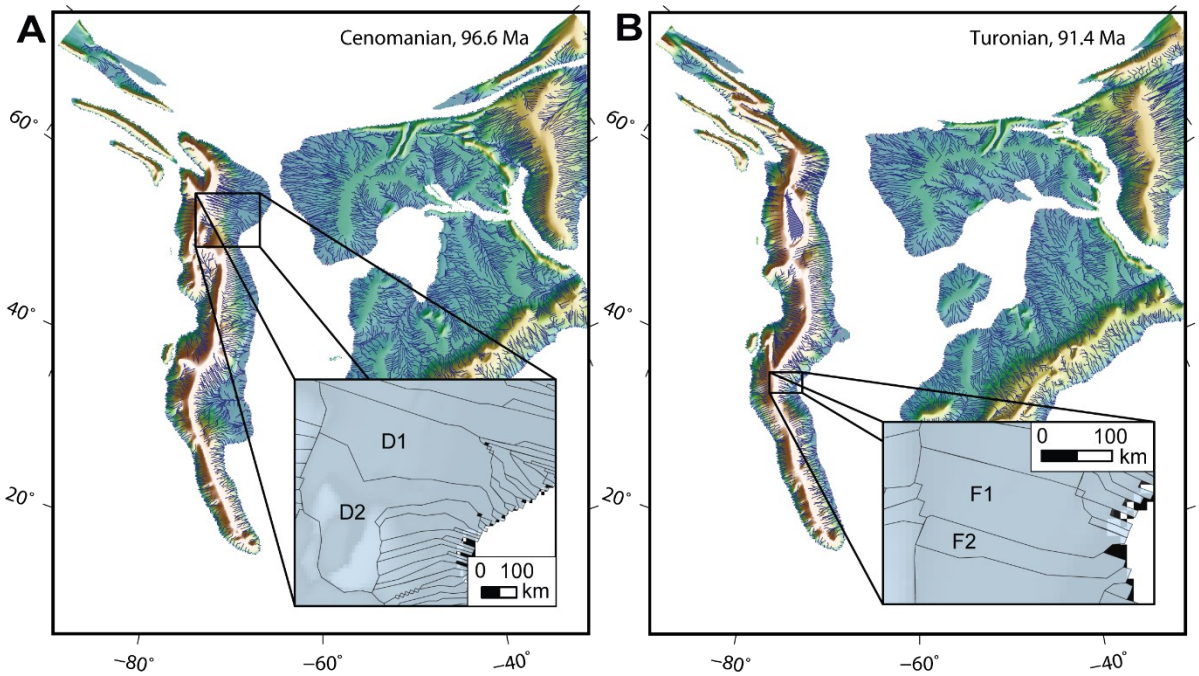

Figure 2.4 | Palaeodrainage networks derived for the Cenomanian (part **A**) and Turonian (part **B**) North American continent, which are considered to broadly reflect true palaeodrainage network configurations. Part **A**, inset, illustrates palaeocatchments that are reconstructed from the Cenomanian palaeo-digital elevation model (palaeoDEM) whereas part **B**, inset, illustrates palaeocatchments that are reconstructed from the Turonian palaeoDEM. Suspended sediment discharges (Q_s) in palaeocatchments labelled D1, D2, F1 and F2 are compared with published constraints in the Results section. Note that scale bars in the insets are approximate due to use of a conic projection.

2.3.4 Reconstructing catchment palaeoclimate variables

Palaeoclimate data from HadCM3L were resampled to the spatial resolution of palaeoDEMs using a bilinear resampling technique (Figure 2.2). We then used zonal statistics to derive the catchment-averaged mean annual temperature (T) and mean annual precipitation (P) of each palaeocatchment.

We require mean annual water discharge (Q) of each palaeocatchment to estimate Q_s. To estimate Q, we multiplied drainage area by modelled mean annual precipitation. This method is simple, repeatable and minimises assumptions in our approach — our water discharge values are therefore maximum estimates because they effectively assume that evaporation and storage is zero. Subsurface and surface runoff data are actually available from HadCM3L simulations (see Appendix A3), which has a full hydrological cycle including precipitation, evaporation, and runoff. However, we are presenting a methodology in which we model input parameters, and we therefore need to be able to somewhat constrain or corroborate these values with geologic evidence. In some other applications only data for precipitation may be available (such as when precipitation is estimated from proxy records, e.g., White et al., 2001); as such, here we use precipitation only. Nevertheless, we tested the sensitivity of using modelled subsurface and surface runoff data to estimate Q and Q_s and we present these results in Appendix A3. We suggest that use of subsurface and surface runoff data to estimate Q and Q_s can be applied at catchment-scales where runoff-derived Q estimates can be corroborated by geological evidence (e.g., identification of catchment runoff class from geological indicators, as discussed in Eide et al., 2018).

2.3.5 Comparison of palaeocatchments with modern catchments

We compared palaeotopography with modern topography to probe whether the palaeocatchment and palaeoclimate data that we extract are reasonable and in line with expectation, particularly the spread of data across the continent. To do this we used the same workflow to derive catchment geometries and catchment-averaged climate in the modern North American continent from ASTER and GTOPO30 global digital elevation models (GDEMs), decimated to the same 0.1° resolution as palaeoDEMs. We excluded Greenland (now ice-covered, but not during the Cretaceous) from comparison of palaeo- and modern topography. As we use smoothed and filled modern topographies, we included the GTOPO30 GDEM used to derive the USGS HYDRO1k database, which permits comparison of modelled drainage with actual drainage. To retrieve modern distributions of catchment-averaged climate, we used WorldClim mean annual temperature and total annual precipitation data sets, compiled from global weather stations between 1960–1990 and interpolated to a spatial resolution of 30 arc seconds, or 2.5, 5, and 10 arc minutes (see Hijmans et al., 2005). WorldClim data sets are averaged over decadal time scales, which is consistent with HadCM3L experiment outputs.

For palaeo- and modern DEMs, we plotted the cumulative frequency of catchments relative to their drainage area, maximum relief, mean annual temperature, and mean annual precipitation, ordered from

smallest to largest in each instance. This facilitates comparison and additionally aids visualisation of the data that we extracted from palaeoDEMs and HadCM3L outputs.

2.3.6 BQART suspended sediment discharge model

We used BQART (Equations 2.1a and 2.1b) to predict time-averaged suspended sediment load, Qs, for all reconstructed palaeocatchments with areas ≥500 km^2 in the Cenomanian and Turonian North American continent. To implement BQART, we extracted A, R, T, and P (hence Q) for each palaeocatchment, as previously described. We set B equal to 1 in all analyses as it is not necessary to consider glacial and anthropogenic impact in the Cretaceous. While lithology is considered in B, Syvitski and Milliman (2007) indicate the global mean is 1, so for simplicity and to avoid the introduction of unconstrained variables we maintain this value here. We converted Qs from a suspended sediment load with units of megatonnes per year (MT/yr) to a suspended sediment discharge with units of cubic metres per year (m^3/yr). For this conversion we used a plausible sediment porosity of 40% and a sediment grain density of 2650 kg/m^3; unconsolidated sediments typically have a porosity of at least 40% (Manger, 1963) so we have used this as a minimum estimate. Qs would vary proportionally if a different porosity or grain density were known to be more appropriate for a regional/catchment-scale study. With Qs quoted in units of volume per unit of time, we did a straight volume shift and divided palaeocatchment Qs values by their respective drainage area values to calculate catchment-averaged erosion rates (i.e., catchment-averaged denudation rates) — they are therefore functionally equivalent to sediment yields. The workflow required to reconstruct Qs and catchment-averaged erosion rates from palaeoDEMs and GCM data is summarised diagrammatically in Figure 2.5.

With estimates of Qs and catchment-averaged erosion rate for Cenomanian and Turonian palaeocatchments, we mapped their spatial distributions across the North American continent. We also plotted north–south transects depicting latitudinal variations in Qs and catchment-averaged erosion rates along the western WIS margin. Latitudinal variations were assessed by dividing the western WIS margin into 5° latitudinal bins and calculating the sum of Qs and the mean catchment-averaged erosion rate for all catchments that drain to a catchment outflow point within the limits of a specified latitudinal bin.

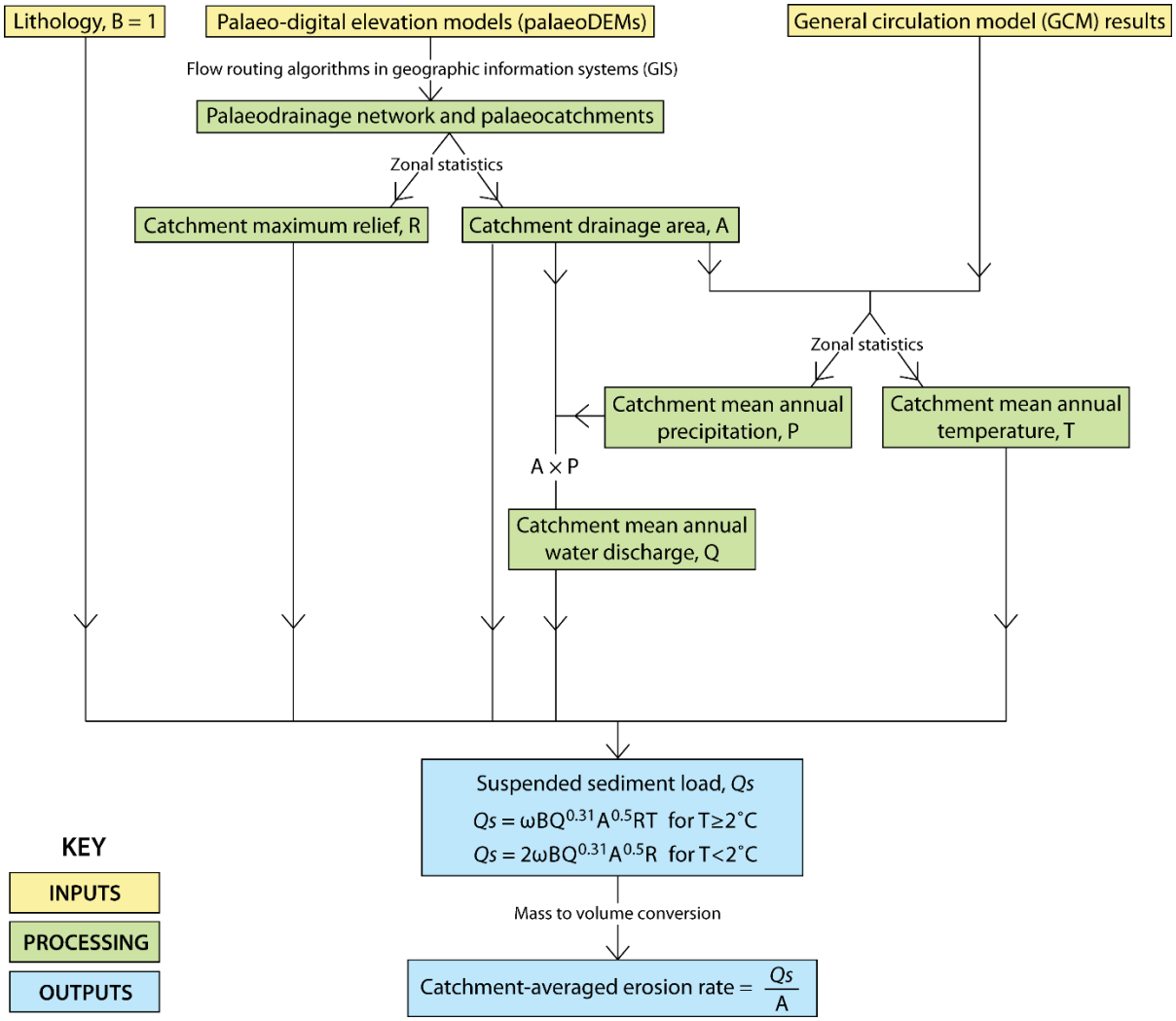

Figure 2.5 | Workflow diagram summarising the method to reconstruct suspended sediment discharges (*Qs*) and catchment-averaged erosion rates from palaeo-digital elevation models (palaeoDEMs) and general circulation model (GCM) results using the BQART model (Equation 2.1).

2.3.7 Uncertainties and comparison with previous studies

A formal analysis of the uncertainty of palaeogeographic reconstructions is not possible because we cannot know the real palaeotopography, and because palaeogeographies are time-averaged. Subsequently, we compared our *Qs* estimates with published estimates for two sediment routing systems in the Cenomanian and Turonian that drained to the WIS:

Dunvegan delta

The middle Cenomanian Dunvegan Formation, Canada, represents the earliest appearance of southeast-flowing rivers that drained to the western WIS margin; the southeast-thinning clastic wedge contains palaeovalley systems which have been interpreted as representing a network of tributaries that merge to form trunk valleys (Plint, 2002; Plint & Wadsworth, 2003; Bhattacharya et al., 2016). The ancient trunk channel of the Dunvegan Formation is considered to have drained an area of order 10^5 km^2 (Bhattacharya et al., 2016; Lin & Bhattacharya, 2017); Lin and Bhattacharya (2017) used the channel palaeohydrologic approach of Holbrook and Wanas (2014) to estimate a mean annual *Qs* of 5.2 $\times 10^6$ to 11.9 $\times 10^6$ m^3 for this system.

Ferron Notom delta

The middle Turonian Ferron Sandstone of Utah, USA, comprises three deltaic clastic wedges that were fed by rivers draining the Sevier orogenic belt to the western WIS margin, from which the Vernal, Last Chance, and Notom deltas have been described (Cotter, 1975) and extensively studied (see papers in volume edited by Chidsey et al., 2004). Recent work has focused extensively on characterising channel geometries and hydrology in palaeochannels draining to the Ferron Notom delta (e.g., Bhattacharyya et al., 2015; Kimmerle & Bhattacharya, 2018; Li et al., 2018); in particular, Sharma et al. (2017) also used the channel palaeohydrologic approach of Holbrook and Wanas (2014) to estimate a mean annual *Qs* of 1.5 $\times 10^6$ to 4.4 $\times 10^6$ m^3.

For comparison with published estimates, we identified the most plausible representative palaeocatchments in our model, based on published palaeolatitude, drainage area and palaeoflow direction, as well as palaeogeographic reconstructions (such as those reproduced in Bhattacharya et al., 2016). We then compared BQART-derived estimates of *Qs* for our 'candidate' catchments with published estimates. We subsequently evaluated how uncertain our palaeogeographic and palaeoclimatic boundary conditions (P, hence Q, A, R, and T) must be before BQART-derived estimates of *Qs* are inconsistent with published estimates of *Qs* from Lin and Bhattacharya (2017) and Sharma et al. (2017) respectively. We evaluated the univariate sensitivity of *Qs* values by applying 10%, 20%, 30%, 40%, and 50% uncertainty margins to each parameter, one at a time. Then, we evaluated the multivariate sensitivity of *Qs* values by applying 10%, 20%, 30%, 40%, and 50% uncertainty margins to all parameters at the same time. However, as temperature is a scale with an arbitrary zero value, we instead apply ±1°C, ±2°C, ±3°C, ±4°C, and ±5°C uncertainty margins

to mean annual temperature in sensitivity analyses. We contrasted ranges in Qs values associated with univariate and multivariate sensitivity with minimum and maximum Qs values estimated by Lin and Bhattacharya (2017) and Sharma et al. (2017).

Beyond uncertainty in palaeogeographic and palaeoclimatic boundary conditions, we must also consider that palaeoDEMs depict highstand palaeoshorelines. In this study we do not change palaeogeographic boundary conditions to accommodate lowstand conditions as this requires information on lowstand catchment geometries, which are not well-known at continental scales, and would require that HadCM3L is re-run (changes to land–sea configurations could change local/regional climate). Instead, we consider the implication of this on a case-by-case basis using sensitivity results.

2.4 Results

2.4.1 Palaeocatchment geometries and palaeoclimate

For the North American continent, we reconstructed 1623 Cenomanian palaeocatchments and 1742 Turonian palaeocatchments with areas ≥500 km^2 (Appendix Figure A1). Maximum drainage areas in the Cenomanian and Turonian are of order 990,000 km^2 and 830,000 km^2, respectively, which reflect large continental catchments comparable in size to drainage areas of the modern Rio Grande and Yukon rivers of North America (Milliman & Farnsworth, 2013). Palaeocatchment data are summarised in Tables 2.2 and 2.3 — note that these data include Greenland, whereas subsequent comparison of palaeo- and modern topography does not.

For catchment drainage areas, the 25th, 50th, and 75th percentiles are all higher in the palaeo-continent than the modern continent; median drainage areas in the Cenomanian and Turonian are 2560 km^2 and 2750 km^2, respectively, whereas modern, smoothed DEMs recover median drainage areas of 1680 km^2 and 1570 km^2 (Figure 2.6a, Table 2.2). This is expected as, in the absence of the WIS, modern North America is dominated by large, continental-scale drainage networks which results in a higher relative frequency of smaller catchments. For catchment maximum relief, the 25th percentile is higher in the modern continent than the palaeo-continent (Cenomanian = 59m, Turonian = 74m, modern = 153m or 172m; Figure 2.6b, Table 2.2). This is likely due to interpolation of contours during palaeoDEM reconstruction which results in abundant low-lying catchments with low relief. Whereas the 75th percentile is roughly three times higher in the palaeo-continent than in the modern continent (Cenomanian = 2280m, Turonian = 2270m, modern = 684m or 790m; Figure 2.6b, Table 2.2). This is likely the result of land–sea configurations associated with the WIS which forced abundant catchments along the western WIS margin — these catchments all have high maximum relief associated with the Sevier orogenic fold-and-thrust belt.

For catchment mean annual temperatures the 25th, 50th, and 75th percentiles are all higher in the palaeo-continent than the modern continent. Median catchment mean annual temperatures for the Cenomanian and Turonian are 11.5°C and 9.1°C, respectively, whereas modern DEMs and WorldClim data sets recover median values of 1.8°C and 0°C. Distributions converge toward the 75th percentile (Cenomanian = 19.2°C, Turonian = 17.5°C, modern = 16.3°C or 11.6°C; Figure 2.6c, Table 2.3). Higher catchment mean annual temperatures in the palaeo-continent are consistent with a warmer, more equable late Cretaceous greenhouse climate (Farnsworth et al., 2019), rather than the modern icehouse climate. Narrower 10–90 percentile ranges for catchment mean annual temperatures in the palaeo-continent are also consistent with a more equable climate (Cenomanian = 23.3°C, Turonian = 26.3°C, modern = 39.2°C or 42.1°C). For catchment mean annual precipitation, the 25th percentile is higher in the palaeo-continent than the modern continent (Cenomanian = 617 mm/yr, Turonian = 572 mm/yr, modern = 227 mm/yr or 184 mm/yr) and distributions converge towards the 50th and 75th percentiles (Figure 2.6d, Table 2.3). This is also consistent with a late Cretaceous greenhouse climate with intensified precipitation.

Table 2.2 | A summary of catchment geometries in Cenomanian and Turonian North American palaeocatchments, derived from analysis of palaeo-digital elevation models (palaeoDEMs). These data include Greenland.

	Number of palaeocatchments reconstructed	**Drainage area (km²)**			**Maximum relief (m)**		
		Mininmum–maximum	Median	Mean	Minimum–maximum	Median	Mean
Cenomanian	1623	510–993,000	2,680	10,800	1–4,240	460	1,180
Turonian	1742	510–830,000	2,890	9,290	1–4,310	649	1,240

Table 2.3 | A summary of catchment-averaged palaeoclimate in Cenomanian and Turonian North American palaeocatchments, derived from analysis of palaeo-digital elevation models (palaeoDEMs) and HadCM3L general circulation model (GCM) data. These data include Greenland.

	Mean annual temperature (°C)			**Mean annual precipitation (mm/yr)**		
	Minimum–maximum	Median	Mean	Minimum–maximum	Median	Mean
Cenomanian	−6.3–30.3	9.7	11.0	317–3,090	800	969
Turonian	−10.2–29.8	7.7	8.7	260–2,510	852	1,050

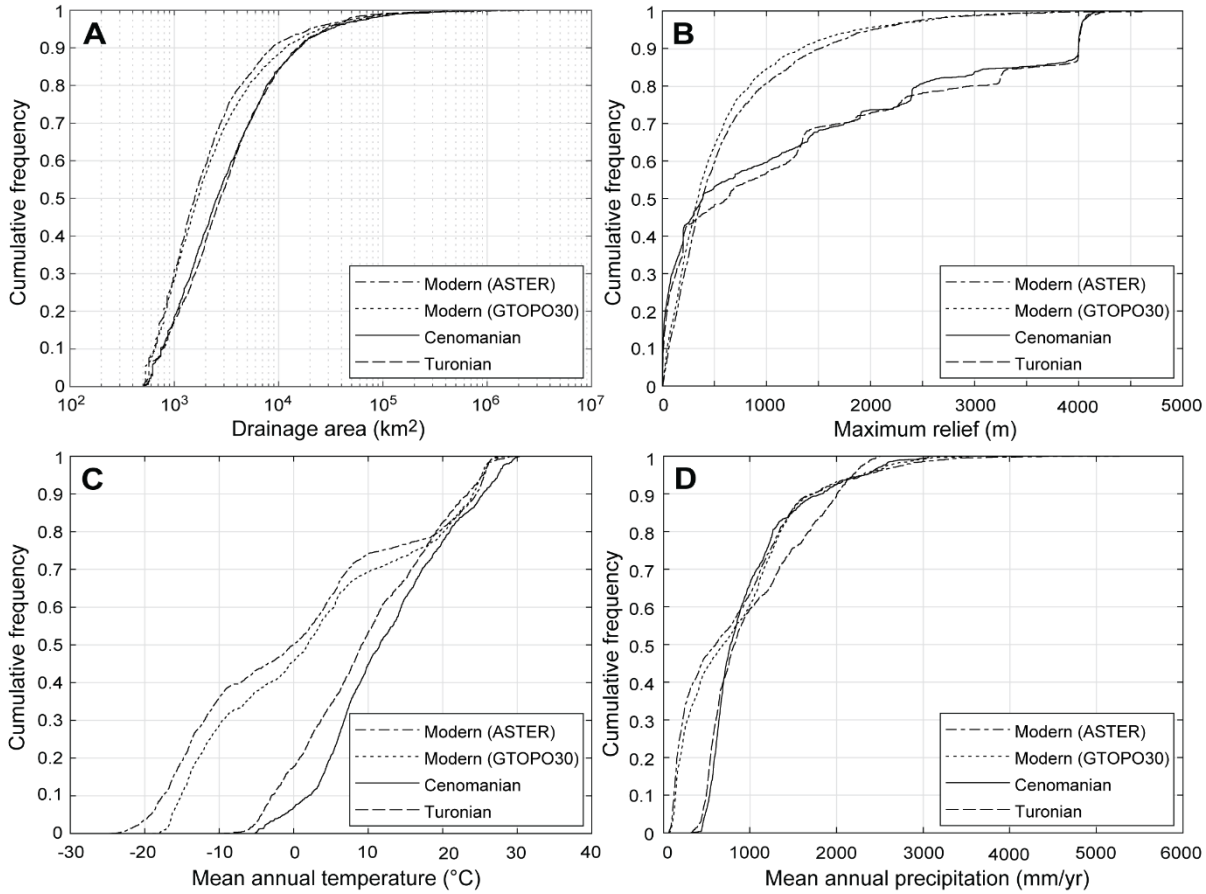

Figure 2.6 | Cumulative frequencies of catchments relative to their drainage area (part **A**), maximum relief (part **B**), mean annual temperature (part **C**) and mean annual precipitation (part **D**), ordered from smallest to largest, for the Cenomanian, Turonian and modern (ASTER, GTOPO30) North American continent. Catchment geometries and climates are derived from palaeo-digital elevation models (palaeoDEMs) and HadCM3L general circulation model (GCM) data for the Cenomanian and Turonian North American continent, and from the ASTER and GTOPO30 global DEMs (GDEMs) and WorldClim data sets for the modern North American continent.

2.4.2 Comparison with published palaeocatchments and estimates of *Qs*

Case study 1: Dunvegan delta, Lin and Bhattacharya (2017)

Rivers draining the Cenomanian Dunvegan Formation had a palaeolatitude of ~65° (Bhattacharya et al., 2016) and an estimated drainage area of order 140,000–180,000 km^2 (Lin & Bhattacharya, 2017). We identify two plausible catchments, Dunvegan 1 (D1) and Dunvegan 2 (D2), in our model (Figure 2.4a) which lie at the correct palaeolatitude and could have sourced the sediments draining the Dunvegan system. Palaeocatchments D1 and D2 have areas of 113,200 km^2 and 123,400 km^2 respectively, similar to that predicted by Lin and Bhattacharya (2017). Based on channel-fill palaeohydrology the authors predicted a mean annual *Qs* of 5.2 ×10^6 m^3 to 11.9 ×10^6 m^3. We reconstruct *Qs* values of 6.6 ×10^6 m^3/yr and 4.7 ×10^6 m^3/yr for catchments D1 and D2, respectively. D1 *Qs* falls within the predicted range derived from geologic evidence, meanwhile D2 *Qs* is the same order of magnitude as, and within a factor of two of, the lower value of the predicted range.

Case study 2: Ferron Notom delta, Sharma et al. (2017)

The Notom delta complex of the Turonian Ferron Sandstone had a palaeolatitude of ~45° (Bhattacharya et al., 2016) and is believed to have drained an area of order 10^4 km^2. Bhattacharya and Tye (2004) estimated that the drainage area for the Last Chance delta complex of the Ferron Sandstone was of order 50,000 km^2, with both the Vernal (relatively larger drainage area) and Notom (relatively smaller drainage area) delta complexes also draining an area 10^4 km^2. We identify two catchments with the correct palaeolatitude and palaeoflow direction that could plausibly have drained to the Notom delta, Ferron Notom 1 (F1) and Ferron Notom 2 (F2), which drain areas of 26,000 km^2 and 11,100 km^2 respectively (Figure 2.4b). Sharma et al. (2017) similarly used channel-fill palaeohydrology to reconstruct *Qs* to the Ferron Notom delta and reconstructed a mean annual *Qs* of 1.5 ×10^6 to 4.4 ×10^6 m^3. We reconstructed *Qs* values of 9.7 ×10^6 m^3/yr and 5.2 ×10^6 m^3/yr for catchments F1 and F2, respectively. F1 and F2 *Qs* values are both greater than the predicted range derived from geologic evidence but, at maximum, within a factor of two to three of the upper value of the predicted range. Our *Qs* estimates are more consistent with the estimates of Sharma et al. (2017) when the smaller F2 catchment draining to the Ferron is assumed.

2.4.3 Sensitivity of our approach

Results from our two case studies suggest our approach produces plausible first-order estimates of *Qs*. However, it is important that we quantify the univariate and multivariate sensitivity of our *Qs* estimates to unknown uncertainties in palaeogeographic (A, R) and palaeoclimatic (P, T) boundary conditions (Figure 2.7).

Univariate and multivariate sensitivity in Dunvegan case study

We retrieve palaeogeographic and palaeoclimatic boundary conditions from our two candidate catchments, D1 and D2, for the Cenomanian Dunvegan Formation. In D1, A is 113,200 km^2, R is 4150 m, T is 3.4°C and P is 1090 mm/yr. Whereas in D2, A is 123,400 km^2, R is 4230 m, T is −0.6°C and P is 1430 mm/yr. In our univariate analysis, to obtain estimates of *Qs* that are either consistent with Lin & Bhattacharya's (2017) range, or within a factor of two bigger than the maximum bound/a factor of two smaller than the minimum bound of this range, we can apply uncertainty margins of 40–50% to A, R and P, or ±5°C to T, for both D1 and D2 (Figure 2.7a,c).

For our multivariate analysis, to retrieve estimates of *Qs* that are either consistent with Lin & Bhattacharya's (2017) range, or within a factor of two bigger/smaller than the maximum/minimum bounds of this range, we can apply uncertainty margins of up to 20–30%/±2–3°C to all parameters in D1 and D2 (Figure 2.7b,d). We also note that with 50%/±5°C uncertainty margins on all parameters, *Qs* estimates are still within one order of magnitude, and within a factor of five to six, of the author's maximum/minimum bounds for both D1 and D2 (Figure 2.7b,d).

Univariate and multivariate sensitivity in Ferron case study

For the Turonian Ferron Sandstone, we also retrieve palaeogeographic and palaeoclimatic boundary conditions for our two candidate catchments, F1 and F2. In F1, A is 26,000 km^2, R is 4000 m, T is 14.9°C, and P is 1580 mm/yr. Whereas in F2, A is 11,110 km^2, R is 4010 m, T is 16.4°C and P is 1470 mm/yr. For the univariate sensitivity analysis, to obtain estimates of *Qs* that are either consistent with the range predicted by Sharma et al. (2017), or within a factor of two bigger than the maximum bound/a factor of two smaller than the minimum bound of this range, we can apply uncertainty margins of 50% /±5°C to A, R, T, and P in F2 (Figure 2.7g). Whereas for F1, these same uncertainty margins retrieve estimates of *Qs* that are within a factor of three to four bigger than the maximum bound (Figure 2.7e).

In our multivariate analysis, to retrieve estimates of *Qs* that are either consistent with the range that Sharma et al. (2017) predicted, or within a factor of two bigger than the maximum bound/a factor of two smaller than the minimum bound of this range, we can apply uncertainty margins of up to ~30%/±3°C to all parameters in F2 (Figure 2.7h), whereas in F1 these error margins recover estimates of *Qs* that are within a factor of ~four bigger than the maximum bound (Figure 2.7f). We also note that with 50%/±5°C uncertainty margins on all parameters, *Qs* estimates are still within one order of magnitude of the author's maximum and minimum bounds for both F1 and F2, and are within a factor of four for F2 and a factor of seven for F1 (Figure 2.7f,h).

Our case studies and sensitivity analyses suggest that our approach is suitable for making first-order approximations of *Qs* in ancient source-to-sink systems. In detail, uncertainty margins of up to 50%/±5°C on all palaeogeographic and palaeoclimatic boundary conditions still reconstruct *Qs* values that are within one order of magnitude of, and within a factor of four to seven of, published constraints. As expected

analytically in BQART (Equation 2.1), we also observe that *Qs* estimates are least sensitive to uncertainties in precipitation estimates (which are multiplied by drainage area to estimate water discharge) and are more sensitive to uncertainty in temperature in cooler catchments than warmer catchments.

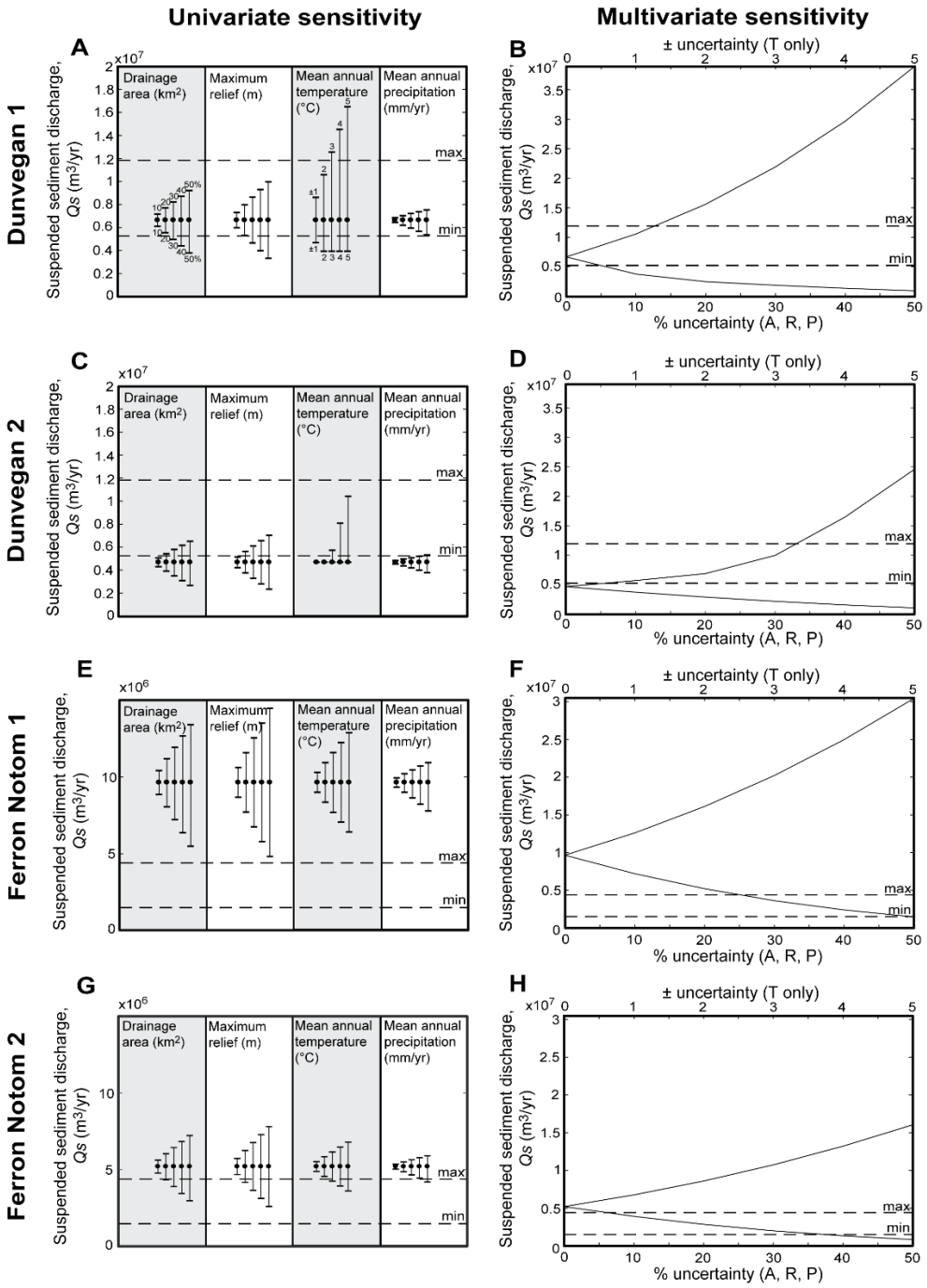

Figure 2.7 | Univariate and multivariate sensitivity of our approach to unknown uncertainties in palaeogeographic and palaeoclimatic boundary conditions. We show the univariate (parts **A**, **C, E, G**) and multivariate (parts **B**, **D, F, H**) sensitivity of our *Qs* estimates to 10%, 20%, 30%, 40% and 50% uncertainty margins on A, R, and P, and to ±1, ±2, ±3, ±4, ±5 uncertainty margins on T. Solid black lines represent the minimum and maximum *Qs* values predicted in this study when using a range of error margins on boundary conditions for D1, D2, F1 and F2. For univariate sensitivity, solid black lines are presented as error bars, and uncertainty margins increase, left to right, from 10% to 50%/±1 to ±5 for each parameter. For multivariate sensitivity, solid black lines are presented as minimum and maximum curves, and uncertainty margins are depicted on the X axis. Dashed black lines represent the minimum and maximum values of suspended sediment discharge (*Qs*) predicted in published literature for both the Cenomanian Dunvegan Formation, Alberta, Canada (parts **A–D**), and the Turonian Notom delta complex of the Ferron Sandstone, Utah, USA (parts **E–H**).

2.4.4 *Qs* and catchment-averaged erosion rates in the Cenomanian and Turonian North American continent

Assuming our approach has merit, we find that spatial distributions of *Qs* were highly variable across Cenomanian and Turonian North American catchments (Figure 2.8). During the Cenomanian, *Qs* spanned 7 orders of magnitude, up to 9.7 $\times 10^7$ m^3/yr with a median of 8.8 $\times 10^4$ m^3/yr (Figure 2.9). Whereas during the Turonian, *Qs* spanned 7 orders of magnitude up to 8.9 $\times 10^7$ m^3/yr with a median of 9.2 $\times 10^4$ m^3/yr (Figure 2.9). For the whole continent, we estimate total suspended sediment loads of 3.4 GT/yr and 3.2 GT/yr (or 1.8 $\times 10^9$ m^3/yr and 1.7 $\times 10^9$ m^3/yr) in the Cenomanian and Turonian, respectively.

Qs values demonstrate an overall increase towards low latitudes (Figure 2.8a,b), with high *Qs* values in large continental palaeocatchments, particularly in Appalachia and at high latitudes around Greenland. There is also a significant difference in total *Qs* input on either side of the WIS. We calculate that the western WIS margin contributes approximately three times more sediment to the WIS than the eastern margin. High *Qs* values in excess of 10^6 m^3/yr persist along the western WIS margin, whereas on the eastern margin high *Qs* values are only reconstructed in low latitude catchments that drain from the Appalachians to the Gulf of Mexico and the Atlantic.

Our results also imply that catchment-averaged erosion rates were highly variable across the Cenomanian and Turonian North American continent. Median catchment-averaged erosion rates of 0.02 mm/yr, and average catchment-averaged erosion rates of 0.1 mm/yr, are obtained for the Cenomanian and Turonian, with maximum catchment-averaged erosion rates of 0.8 mm/yr and 0.9 mm/yr for the two time intervals, respectively.

Similar to *Qs*, catchment-averaged erosion rates increase towards low latitudes (Figure 2.8c,d); this increase is pronounced on the western margin of the WIS, whereas on the eastern margin they remain low (<0.2 mm/yr), except in low latitude catchments draining from the Appalachians to the Atlantic, and sparse catchments draining to the Gulf of Mexico. However, erosion rate trends are discrepant with *Qs* trends in large continental palaeocatchments where *Qs* values are high (>10^6 m^3/yr at high latitudes and >10^7 m^3/yr at low latitudes) yet catchment-averaged erosion rates are low (<0.2 mm/yr).

While there are small differences in the spatial variation of *Qs* and catchment-averaged erosion rates between the Cenomanian and Turonian, we find that distributions of catchments relative to *Qs* and catchment-averaged erosion rate are almost identical for both time slices (Figure 2.9).

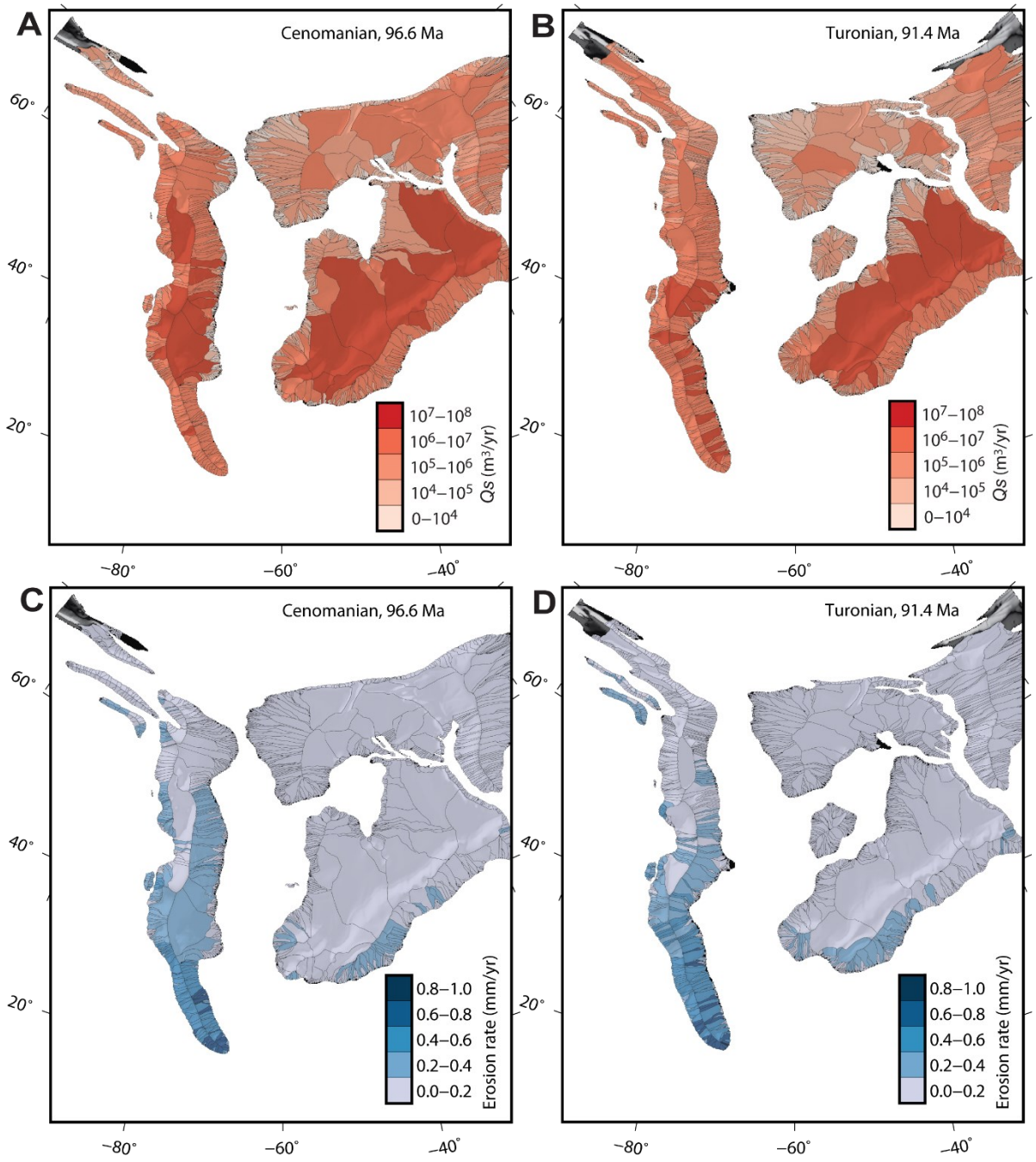

Figure 2.8 | Spatial distributions of suspended sediment discharges (*Qs*) for the Cenomanian (part **A**) and Turonian (part **B**) North American continent, as well as spatial distributions of catchment-averaged erosion rates for the Cenomanian (part **C**) and Turonian (part **D**) North American continent. *Qs* values are grouped by orders of magnitude whereas catchment-averaged erosion rates are grouped by equal intervals (see colour ramps). *Qs* values and catchment-averaged erosion rates overlay palaeo-digital elevation model (palaeoDEM) hillshades for comparison with palaeotopography.

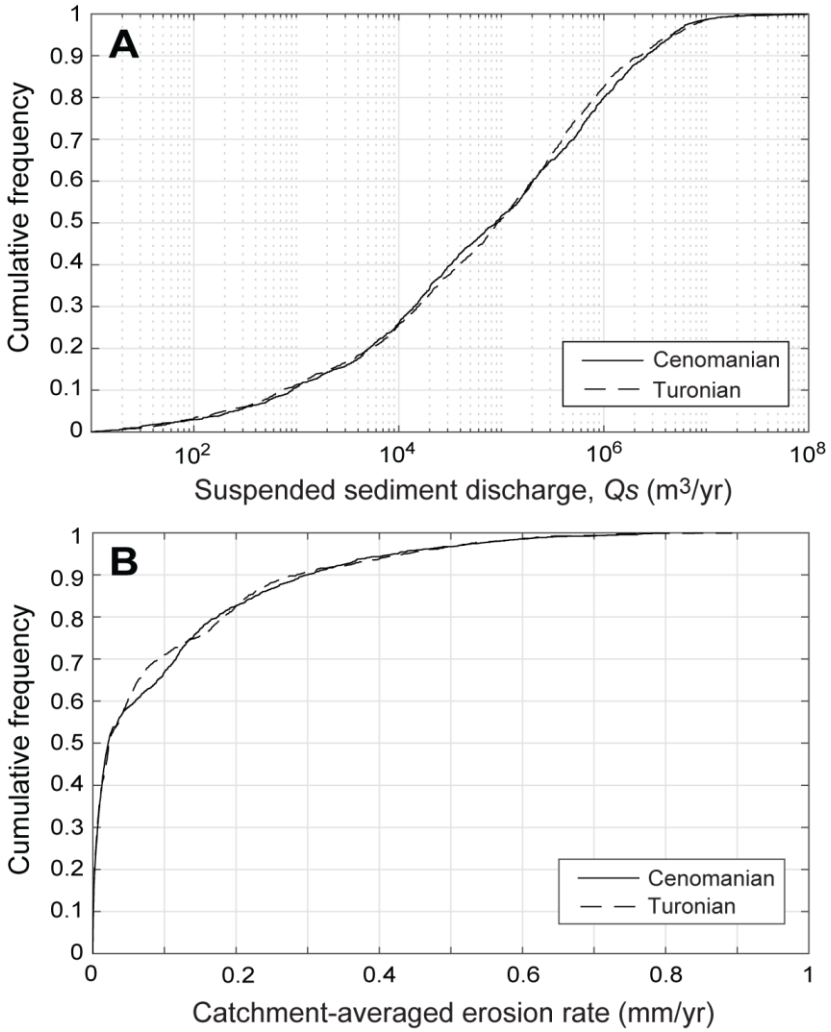

Figure 2.9 | The cumulative frequency of palaeocatchments relative to their suspended sediment discharges (*Qs*) values (part **A**) and catchment-averaged erosion rates (part **B**), ordered from smallest to largest, for both the Cenomanian and Turonian North American continent.

2.4.5 Latitudinal trends in *Qs* and catchment-averaged erosion rates along the western WIS margin

Following observed latitudinal variability in sediment supply across the continent, north–south transects along the western WIS margin (Figure 2.10) offer more refined observations. We predict that export of sediment to the western WIS margin is lowest at high latitudes and increases towards mid-latitudes, with maximum sediment export between 35°N and 40°N in both the Cenomanian and Turonian. For the Cenomanian, *Qs* values increase by a factor of five, from 1.8 $\times 10^7$ m^3/yr at 65–70°N to 9.5 $\times 10^7$ m^3/yr at 35–40°N. Whereas for the Turonian, *Qs* values increase by a factor of 22, from 4.9 $\times 10^6$ m^3/yr at 70–75°N to 1.1 $\times 10^8$ m^3/yr at 35–40°N. After *Qs* peaks at 35–40°N, *Qs* is projected to decrease by less than a factor of two towards low latitudes (20–25°N) in both the Cenomanian and Turonian. Catchment-averaged erosion rates increase from north to south, with maximum catchment-averaged erosion rates at the southernmost tip of the continent, between 20°N and 25°N, and an additional smaller peak between 50°N and 60°N (Figure 2.10c,d). For both the Cenomanian and Turonian, catchment-averaged erosion rates increase north to south by just over one order of magnitude, from 0.05 mm/yr at 65–70°N to 0.57 mm/yr at 20–25°N in the Cenomanian, and from 0.04 mm/yr at 70–75°N to 0.48 mm/yr at 20–25°N in the Turonian.

The sensitivity of north–south latitudinal trends to uncertainty is also illustrated (Figure 2.10). The presented uncertainty margins are based on adoption of 10%/±1°C uncertainty on all boundary conditions; it is impossible to know the actual uncertainties, but we note that it is not possible to make all palaeocatchments 20% or 30% larger, or increase the relief of all catchments by similar margins, without producing unrealistic values for the size and elevations of the North American continent. The most notable effect of adopting 10%/±1°C uncertainty on trends is that sensitivity is not uniform along the north–south latitudinal transect. Sensitivity increases towards low latitudes; *Qs* and catchment-averaged erosion rates are most sensitive to uncertainty at mid- to low latitudes, between 20° and 45° where mean annual temperature and mean annual precipitation are higher, which is expected analytically (see Equations 2.1a and 2.1b).

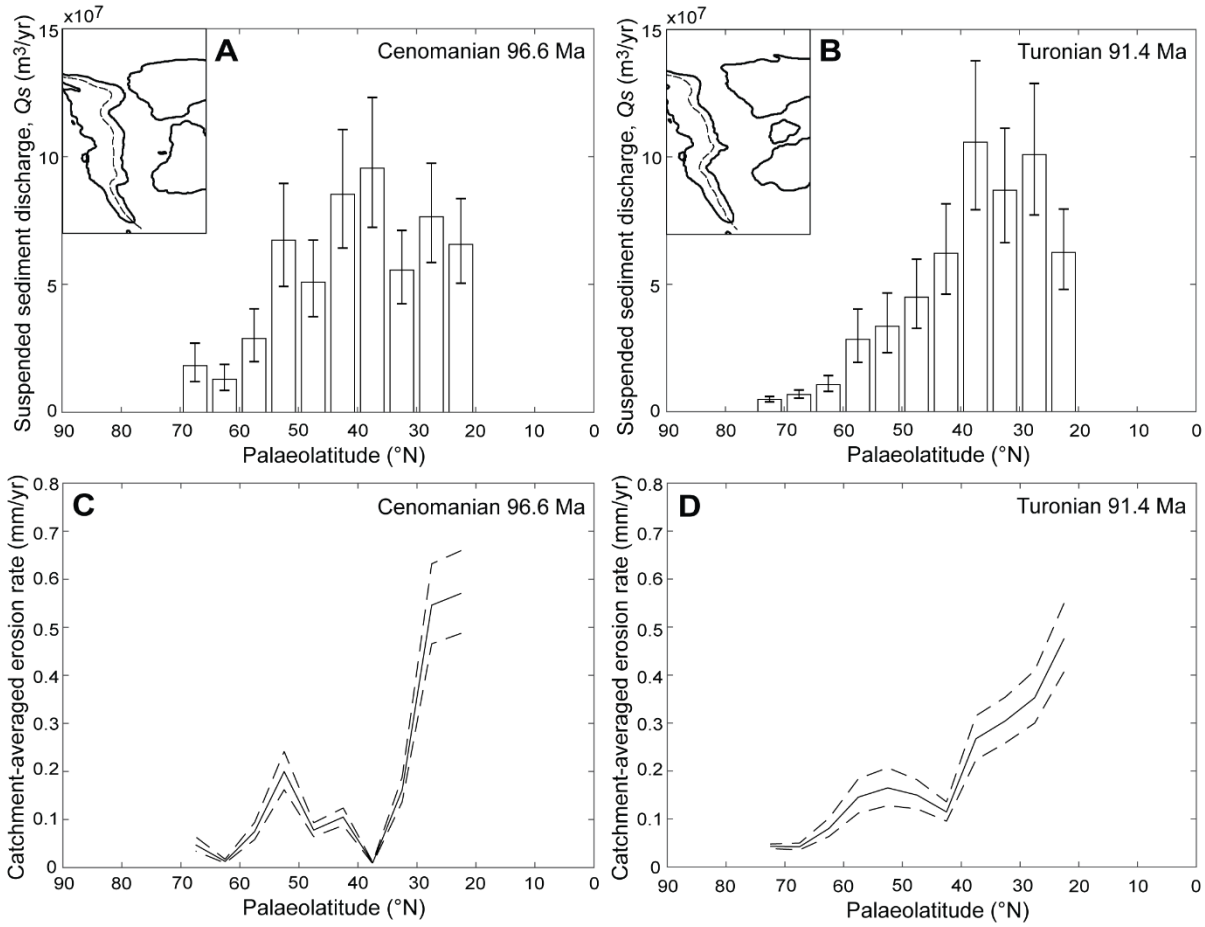

Figure 2.10 | Latitudinal variation in suspended sediment discharges (*Qs*) and catchment-averaged erosion rates for a north–south transect along the western margin of the Western Interior Seaway (WIS). Latitudinal variation in *Qs* values are depicted for the Cenomanian (part **A**) and Turonian (part **B**), and latitudinal variation in catchment-averaged erosion rates are also depicted for the Cenomanian (part **C**) and Turonian (part **D**). Insets in parts **A** and **B** illustrate highstand palaeoshorelines of the Cenomanian and Turonian North American continent (solid black lines) and the transect location (dashed black line). Uncertainty margins are plotted (bars in parts **A** and **B**, dashed lines in parts **C** and **D**) based on adoption of 10%/±1° uncertainty on all palaeogeographic and palaeoclimatic boundary conditions.

2.5 Discussion

2.5.1 Are reconstructed palaeocatchments reasonable? What are the wider uncertainties of this approach?

Are our reconstructions of continental drainage in the late Cretaceous realistic? Along the western WIS margin, a north–south trending drainage divide associated with the Sevier orogenic belt separates short steep catchments that drain to the Pacific Ocean and short steep catchments that drain to the WIS. Of catchments that drain to the WIS, their configurations are consistent with several well-studied ancient source-to-sink systems. These include published palaeogeographic reconstructions of fluvial systems that fed the Dunvegan Formation, Alberta, Canada (e.g., Plint & Wadsworth, 2003, 2006), the Cardium Formation, Alberta (e.g., Krause et al., 1994), the Vernal, Last Chance and Notom deltaic complexes of the Ferron Sandstone, Utah (e.g., Cotter, 1975), the Frontier Formation, Wyoming, USA, the Kaiparowits Formation, Utah, and the Gallup Sandstone, New Mexico (see Bhattacharya et al., 2016, and references therein).

On the eastern WIS margin, the Appalachian drainage divide separates short steep catchments that drain to the Atlantic and larger continental-scale catchments that drain to the eastern WIS margin and Hudson Seaway. The Woodbine Formation, Texas, and Tuscaloosa Formation, Alabama–Mississippi, represent southwestward drainage from the Appalachians to the Gulf of Mexico (Adams & Carr, 2010; Blum et al., 2017) — this is consistent with palaeocatchments that we reconstruct for this region. Moreover, our palaeocatchment configurations on the eastern WIS margin are consistent with published models of large continental drainages, which have been inferred from studies of the Dakota Sandstone, western Iowa and eastern Nebraska, where analysis of detrital zircons indicates continental-scale drainage from the Appalachians to the WIS (Finzel, 2014) (Figure 2.3). While we do not expect our reconstructed palaeocatchments to be in any way a perfect representation of palaeodrainage, we conclude that, to first order, their configurations are reasonable (Figure 2.3; Appendix Figure A1).

One limitation of our reconstructed palaeocatchments is that they are derived from palaeoDEMs that represent highstand conditions, which is typical practice in palaeoDEM construction for purposes of hydrocarbon exploration (Markwick, 2018). In this study we compare our Qs estimates with constraints from the Dunvegan Formation and Ferron Sandstone. However, the Dunvegan Formation was deposited at lowstand conditions when the palaeoshoreline likely advanced (Roberts & Kirschbaum, 1995); at lowstand conditions we expect drainage length to increase, and we also expect drainage area to increase as low-lying rivers coalesce. This has been observed extensively in Quaternary studies, such that rivers in northwest Europe (e.g., Thames, Rhine) were formerly tributaries of the lowstand Channel River that drained westward through the English Channel to the Atlantic (e.g., Gibbard, 1988; Lericolais et al., 2003). The implication of this is that our estimates of drainage area from the palaeoDEM, and therefore estimates of Qs, are underpredicted. We consider the implications of this on Qs estimates using results of our

univariate sensitivity analyses where we showed that increasing drainage area up to ~50% and beyond renders *Qs* values that are still consistent with published field constraints (Figure 2.7a,c). It is also entirely possible that palaeocatchments D1 and D2 (Section 4.2) could have coalesced at lowstand to feed the Dunvegan deltas. The combined sediment discharge of D1 and D2 is 11.3 $\times 10^6$ m^3/yr (which is still consistent with the range of values estimated by Lin and Bhattacharya, 2017) so, with a greater drainage area at lowstand, we may expect sediment discharges to be greater than this, but perhaps of the same order. Conversely, during the Turonian, the palaeoshoreline in central Utah remained in a relative highstand position, despite sea level change, which has been attributed to local subsidence keeping pace with rates of sediment accumulation (Roberts & Kirschbaum, 1995). This supports use of a highstand palaeoDEM to estimate *Qs* to the Ferron depocentre. Drainage capture or episodic sediment transport from different source regions may also lead to underprediction of drainage area. For example, in Utah, provenance studies on strata both time-correlative and younger/older than the Ferron Sandstone have suggested intermittent sourcing from the Mogollon Highlands (Arizona) and Cordilleran magmatic arc to the south (Owen et al., 2015; Szwarc et al., 2015; Bartschi et al., 2018; Primm et al., 2018), which may also potentially be true for the Ferron. These examples highlight the necessity of considering the implications of highstand palaeoshorelines and drainage areas on a case-by-case basis, in conjunction with sensitivity analyses, where the interest is in catchment/regional scale studies. At minimum, palaeoDEMs with highstand palaeoshorelines will recover estimates of minimum *Qs*.

Wider uncertainties in palaeocatchment configurations and drainage areas are centred on uncertainty in the position of palaeoshorelines and drainage divides in palaeoDEMs, as well as the palaeodrainage used to interpolate contours in palaeoDEM construction. Meanwhile, sources of uncertainty in maximum relief include the position and height of the maximum elevation contour in palaeoDEMs. To expand further, the two main sources of error in HadCM3L simulations, and therefore catchment-averaged temperature and precipitation estimates, are centred on the model itself (the magnitude of which can be estimated by assessing the model's ability to represent modern climate, as in Valdes et al., 2017) and the model boundary conditions which, for the timescales addressed here, are centred on the prescribed atmospheric CO_2 concentration and the palaeoDEM used (for further discussion refer to Appendix A1). Assessing the likely uncertainty should be tackled on a case-by-case basis at regional/catchment scales using knowledge of the likely sources and magnitudes of uncertainty, geologic evidence, and sensitivity results. We advise that, given unknown uncertainties and the current spatio-temporal resolution of data, but with consistency with published estimates and reasonably (and increasingly) advanced knowledge of palaeotopography, *Qs* estimates can be considered first-order estimates that are likely precise to within one order of magnitude.

2.5.2 How suitable is BQART for ancient source-to-sink analysis?

Application of BQART to ancient source-to-sink systems requires constraints on palaeocatchment drainage area, maximum relief, mean annual temperature and mean annual precipitation, and a defined B factor. Syvitski and Milliman (2007) showed that when B is set to 1, BQART explains 66% of variance in *Qs* in

modern systems, whereas when B is adjusted to reflect glacial, anthropogenic and lithologic conditions, BQART explains 96% of variance. However, BQART was originally developed from a modern global river data set (n=488) in which glacial coverage and anthropogenic activity, e.g., artificial sediment trapping and land use, are ubiquitous. Glacial coverage and anthropogenic activity are both major controls on Qs (e.g., Hallet et al., 1996; Syvitski et al., 2005) and are accounted for by Syvitski and Milliman (2007) in B. So, while setting B to 1 results in BQART explaining 66% of variance in Qs in modern systems, we might expect it to explain more variance in ancient systems, especially in the Cretaceous where glacial coverage and anthropogenic activity do not control Qs. However, this is difficult to test with data sets of modern source-to-sink systems as most large global rivers are affected by anthropogenic activity.

Having used BQART to estimate Qs in the Cenomanian and Turonian North American continent, there are, of course, issues to consider when validating BQART-derived Qs estimates with published constraints. BQART is used to estimate suspended load, which typically comprises silts and fine sands; this varies in global rivers, however, as many rivers may carry coarser grade sands in suspension. In this study we compare BQART-derived Qs estimates with published estimates from systems in which sands may or may not have been carried in suspension — depositional stratigraphy can be used to constrain mode of sediment transport in individual instances (Lin & Bhattacharya, 2017; Sharma et al., 2017). Moreover, while BQART estimates suspended load, bedload is also a potentially significant component of fluvial sediment discharge (Turowski et al., 2010). However, bedload fractions are difficult to constrain in modern systems, let alone ancient systems, and the empirical basis of various methods is often derived from small data sets (e.g., Schlunegger & Hinderer, 2003; Syvitski & Saito, 2007). One influence that inability to constrain bedload will have on our results is that catchment-averaged erosion rates are underpredicted.

Any comparison of BQART-derived Qs estimates with published constraints implicitly assumes that the previously published Qs estimates are robust themselves. In this study we use constraints derived from channel-fill palaeohydrology — this approach is not exact, with uncertainties centred on flow transport calculations (see Holbrook & Wanas, 2014). Nevertheless, the ability to recover estimates that are consistent with field data highlights potential to use BQART to make first-order approximations, particularly where we do not have access to outcrop data or where the geologic record is incomplete. In fact, if we assume published constraints are correct, then BQART estimates that are consistent with, or within a factor of two to three of, these constraints should be considered a successful result.

2.5.3 Suspended sediment discharges in the Cenomanian and Turonian North American continent

We estimate total continental Qs of 3.4 GT/yr and 3.2 GT/yr (or 1.8×10^9 m^3/yr and 1.7×10^9 m^3/yr) in the Cenomanian and Turonian, respectively. This implies that total continental Qs was a factor of two bigger in the Cenomanian and Turonian North American continent than the modern continent, when compared with Holocene pre-anthropogenic continental Qs estimates of 1.7 GT/yr (Syvitski & Kettner, 2011), which were similarly derived using BQART. Further, we are comparing total continental Qs during the ancient

Zuñi sequence highstand with the current Tejas sequence lowstand (in this specific instance we instead are referring to longer, second-order cycles, on 10^7–10^8 myr timescales) — we are not just predicting that twice as much sediment exported to oceans, we are also implying that it was exported from half of the land. Therefore, sediment yields (T/ km^2/yr) in the Cenomanian and Turonian North American continent may have been up to four times greater than today.

We find that *Qs* is highly variable across the North American continent, spanning seven orders of magnitude (in units of m^3/yr). The western WIS margin is an important source of sediment along its entire north–south transect, and generally increases towards low latitudes (which is likely due to increased mean annual precipitation towards the tropics). However, we note that BQART is more sensitive to uncertainty in palaeogeographic and palaeoclimatic boundary conditions at mid- to low latitudes. Whereas the eastern WIS margin is only an important source of sediment at low latitudes in catchments draining southwestward from the Appalachians to the Gulf of Mexico.

Catchment-averaged erosion rates increase towards low latitudes — however we expect these values to be an underprediction as bedload is not accounted for. Further, when we consider our catchment-averaged erosion rates, we expect source-area denudation rates to be higher as we focus on large catchments in which sediment trapping in low-lying areas is expected to be prominent. Painter et al. (2014) used AFT ages and DZ analysis to estimate local erosion rates >1 mm/yr in the Sevier orogenic fold-and-thrust belt, western U.S.A, whereas we reconstruct maximum catchment-averaged erosion rates of 0.5–0.6 mm/yr along the U.S.A portion of the western WIS margin.

Our estimates and spatial distributions of *Qs* and catchment-averaged erosion rates offer opportunities to exploit new lines of enquiry in the Cretaceous North American continent. In conjunction with palaeogeographic reconstructions, our results can be considered in the context of the long-term carbon cycle and organic carbon burial where, generally speaking, the efficiency of organic carbon burial is greater in small, active margin systems than large, passive margin systems (Blair et al., 2004; Leithold et al., 2016). Other avenues to consider include chemical weathering and nutrient fluxes in systems where source rock lithologies are known — recent work suggests an important link between palaeogeography and global weatherability throughout the Phanerozoic (Kent & Muttoni, 2013; Goddéris et al., 2017; Macdonald et al., 2019). Moreover, we have provided first-order estimates of Cenomanian and Turonian palaeodrainage networks (Figure 2.3), which is useful to field geologists interested in conducting regional source-to-sink studies. These opportunities are associated with the spatial and temporal scale of this study; extrapolation of our approach to different spatial and temporal scales offers further opportunities, but also requires adaptation to minimise uncertainties.

2.5.4 The future: opportunities and suitability of our approach at different spatial and temporal scales

We consider our approach suitable for making first-order approximations of *Qs* at continental scales. However, targeted interest in reconstructing *Qs* at catchment/regional scales requires further efforts to constrain palaeogeographic and palaeoclimatic boundary conditions using geological evidence, or to calibrate *Qs* estimates with field data. Results of our univariate sensitivity analyses highlight advantages of constraining boundary conditions using geological evidence, where possible, however we acknowledge that the feasibility of this decreases as spatial scale increases. We suggest that, for catchment/regional scales, palaeocatchment configurations and geometries should be augmented by published provenance analyses, where chronometric techniques such as U–Pb ages of detrital zircons are used to identify and characterise source areas (e.g., Blum & Pecha, 2014; Spencer et al., 2014). Moreover, estimates of maximum relief in palaeocatchments may potentially be refined, or supported, using stable-isotope based palaeoaltimetry (e.g., Chamberlain & Poage, 2000; Rowley et al., 2001; Rowley & Currie, 2006; Rowley & Garzione, 2007).

To refine catchment-averaged palaeoclimate at catchment/regional scales, water discharge and mean annual temperature estimates can be supported using Cretaceous climate zone maps deduced from large palaeontological, sedimentological, and mineralogical data sets (Chumakov et al., 1995), which have since been reproduced (Skelton et al., 2003; Hay & Floegel, 2012). Also, where broad estimates of palaeoclimate can be inferred from preservation of climatically sensitive sediments etc., water discharge can be estimated using drainage area and one of four runoff categories, following Eide et al. (2018). Beyond water discharge estimates, constraints on catchment-averaged temperature might be inferred from terrestrial surface temperature proxies (see Appendix A1).

PalaeoDEMs offer time-averaged "snapshots" of palaeogeography and palaeotopography (Markwick & Valdes, 2004) so are well-suited to investigation of long-period forcings (but require careful consideration if investigating short-period, high-frequency forcings). We consider change across time slices to represent broad change in *Qs* and catchment-averaged erosion rates on multimillion, 10^6–10^7, year timescales, which reflects environmental signals associated with long-period forcings such as orogenic cycles, uplift, and major shifts in global climate (Allen, 2008b; Romans et al., 2016). Long-period forcings are recorded in palaeogeographic reconstructions by changes to continental configurations and changes to elevation associated with orogenic growth and decay, which, as boundary conditions, then affect output of HadCM3L climate simulations (Markwick & Valdes, 2004; Markwick, 2018).

Incorporation of more time slices into analyses could expand the temporal scale of investigation to 10^7–10^8 yr timescales, which would additionally reflect environmental signals associated with supercontinental cycles, i.e., the effect of changing land–sea configurations as ocean basins open and close (Wilson, 1966). Moreover, at this temporal scale it is possible to capture signals associated with global shift from greenhouse to icehouse climate states, such as transition from Cretaceous–Eocene greenhouse conditions to Oligocene–present icehouse conditions (e.g., Zachos et al., 2008). However, investigation on 10^7–10^8 yr

timescales requires adaptation of HadCM3L boundary conditions (see Appendix A1) to reflect coeval changes to atmospheric CO_2 and other greenhouse gases before, during and after major climatic shifts (Foster et al., 2017). This ensures that palaeoclimate reconstructed by HadCM3L, using palaeoDEMs as boundary conditions, is not solely driven by changing palaeogeography. Other climatic forcings that may be captured as temporal (and spatial) scale increases include the supercontinent effect; previous studies suggest that supercontinents likely featured arid interiors with much larger interannual temperature ranges than present (Crowley et al., 1987; Crowley et al., 1989), these ranges being more closely related to solar forcing than ocean forcing (Otto-Bliesner & Houghton, 1986), and that monsoonal climates were likely restricted to coastal regions (Kutzbach et al., 1993).

Other opportunities associated with expanding temporal scale include investigation of provenance during WIB evolution. Our spatial variations in *Qs* on either side of the WIS are consistent with models of foreland basin evolution, in which the western WIS margin (fold-and-thrust belt) contributes more sediment than the eastern margin (stable continental craton). However, work in the northern Andean foreland basin demonstrates that sediment derived from the stable continental craton might be an important source of sediment during early foreland basin evolution (Horton, Parra, et al., 2010; Horton, Saylor, et al., 2010), which could also be explored during WIB evolution using appropriate Cretaceous palaeogeographic time slices.

Conversely, it may be possible to narrow the temporal scale of analysis by changing palaeogeographic and palaeoclimatic boundary conditions associated with each time slice to accommodate highstand vs. lowstand conditions, where fully understood, or rapid continental-scale palaeodrainage reorganisation (e.g., Galloway et al., 2011) . In particular, palaeoclimatic boundary conditions could be tweaked in line with published constraints to explore changes in *Qs* and catchment-averaged erosion rates over orbital cycles or periods of environmental change, such as the Cenomanian–Turonian oceanic anoxic event (OAE) or the Cretaceous–Paleogene (K–Pg) extinction event.

2.6 Conclusions

We evaluated high-resolution palaeogeographic reconstructions as a first-order investigative tool in palaeo-sediment routing system analysis. We used palaeoDEMs, HadCM3L data, and BQART to estimate palaeodrainage networks, *Qs* and catchment-averaged erosion rates in the Cenomanian and Turonian North American continent, and our results show that:

(1) The palaeocatchment geometries and climates that we reconstructed are reasonable compared to palaeogeographic reconstructions of ancient source-to-sink systems in published literature, as well as the distributions of catchment geometries and climates in the modern North American continent.
(2) Our BQART-derived *Qs* estimates are consistent with published constraints for the Cenomanian Dunvegan Formation in Alberta, Canada, and the Turonian Ferron Sandstone in Utah, USA. Our

estimates are the same order of magnitude as, and are either consistent or within a factor of two to three of, published estimates in both instances.

(3) Univariate sensitivity of BQART to palaeogeographic and palaeoclimatic boundary conditions supports use of our approach at catchment scales. It also highlights the potential to use geological evidence, where available, to refine palaeogeographic or palaeoclimatic boundary conditions and minimise uncertainty.

(4) Multivariate sensitivity of BQART to palaeogeographic and palaeoclimatic boundary conditions demonstrates that, despite unquantifiable uncertainties associated with palaeogeographic reconstructions, our approach can be used to make first-order approximations of Qs. We found that adoption of large uncertainties (≤50%/±5°C) for all palaeogeographic and palaeoclimatic boundary conditions recovers BQART-derived Qs estimates that are still within an order of magnitude of, and within a factor of four to seven of, published constraints.

(5) Qs and catchment-averaged erosion rates are highly variable across the Cenomanian and Turonian North American continent, with overall increase towards low latitudes. Moreover, the western WIS margin may have contributed three times more suspended sediment to the WIS than the eastern margin.

(6) Total continental Qs may have been up to a factor of two bigger in the Cenomanian and Turonian stages than estimates of Holocene pre-anthropogenic continental Qs. This invites investigation regarding the relative role of palaeogeographic change and major climate shifts in determining continental Qs over 10^7–10^8 yr time scales.

Our results demonstrate that high-resolution palaeogeographies can be used to make first-order approximations of fluvial suspended sediment discharges in the geologic past on a variety of spatial and temporal scales and will be particularly useful where stratigraphic records are incomplete. However, we stress that calibration with geological evidence, where possible, is crucial to minimising uncertainty. Moreover, we highlight the potential to use this approach to address some of the grand challenges in the geosciences, such as the global spatio-temporal response of Qs and catchment-averaged erosion rates to long-period tectonic and climatic forcing in the geologic past.

CHAPTER 3: Reconstructing the morphologies and hydrodynamics of ancient rivers from source to sink: Cretaceous Western Interior Basin, Utah, USA[1]

ABSTRACT

Quantitative reconstruction of palaeohydrology from fluvial stratigraphy provides sophisticated insights into the response, and relative impact, of tectonic and climatic drivers on ancient fluvial landscapes. Here, field measurements and a suite of quantitative approaches are used to develop a four-dimensional (space and time) reconstruction of palaeohydrology in Late Cretaceous palaeorivers of central Utah, USA — these rivers drained the Sevier mountains to the Western Interior Seaway. Field data include grain-size and cross-set measurements and span five parallel fluvial systems, two of which include proximal to distal transects, across seven stratigraphic intervals through the Blackhawk Formation, Castlegate Sandstone and Price River Formation. Reconstructed palaeohydrological parameters include fluvial morphologies (flow depths, palaeoslopes, alluvial palaeorelief, and planform morphologies) and various hydrodynamic properties (flow velocities, water discharges, and sediment transport modes). Results suggest that fluvial morphologies were similar in space and time; median flow depths spanned 2–4 m with marginally greater flow depths in southerly systems. Meanwhile palaeoslopes spanned 10^{-3} to 10^{-4}, decreasing downstream by an order of magnitude. The most prominent spatio-temporal change is an up to four-fold increase in palaeoslope at the Blackhawk–Castlegate transition; associated alluvial palaeorelief is tens of metres during Blackhawk deposition and >100 m during Castlegate Sandstone deposition. We observed no change in unit water discharges at the Blackhawk–Castlegate transition, which argues against a climatically driven increase in palaeoslope and channel steepness. These findings instead point to a tectonically driven palaeoslope increase, although one limitation in this study is uncertainty in palaeochannel widths, which directly influences total water discharges. These reconstructions complement and expand on extensive previous work in this region, which enables us to test the efficacy of quantitative reconstruction tools. Comparison of results with facies-based interpretations indicates that quantitative tools work well, but inconsistencies in more complex reconstructions (e.g., planform morphologies) highlight the need for further work.

3.1 Introduction

The stratigraphic record is a fundamental archive of Earth surface processes in space and time (Wobus et al., 2006; Allen, 2008a, 2008b; Armitage et al., 2011; Whittaker, 2012). A key research challenge is to decode this archive to reconstruct the movement of water and sediment across Earth's surface in the geological past (Castelltort & Van Den Driessche, 2003; Jerolmack & Paola, 2010; Ganti et al., 2014; Romans et al., 2016; Straub et al., 2020) — effective quantification of palaeohydrology from fluvial stratigraphy is crucial

[1] A version of this chapter has been published in ***Sedimentology***:

Lyster, S. J., Whittaker, A. C., Hampson, G. J., Hajek, E. A., Allison, P. A., and Lathrop, B. A. (2021) Reconstructing the morphologies and hydrodynamics of ancient rivers from source to sink: Cretaceous Western Interior Basin, Utah, USA. ***Sedimentology***, **68**, 2854–2886, doi:10.1111/sed.12877

to achieve this goal. Constraints on the morphologies and hydrodynamics of palaeorivers can be used to: resolve the size and scale of ancient catchments (Bhattacharya & Tye, 2004; Bhattacharya et al., 2016; Eide et al., 2018; Lyster et al., 2020); quantify sediment transport capacities and the magnitudes of sediment exported to oceans (Allen et al., 2013; Holbrook & Wanas, 2014; Lin & Bhattacharya, 2017; Sharma et al., 2017); decipher fluvial response to perturbation (Foreman et al., 2012; Foreman, 2014; Colombera et al., 2017; Chen et al., 2018); and reconstruct local palaeogeographies (Li et al., 2018). Importantly, these constraints can be used to investigate hydrological response to long-period forcing (>10^6 yrs) as river behaviour is intrinsically linked to tectono-climatic boundary conditions over geological timescales (Duller et al., 2010; Whitchurch et al., 2011; Whittaker et al., 2011; Castelltort et al., 2012; Hampson et al., 2013).

However, palaeohydrology is limited by incomplete (or absent) records of palaeorivers (Sadler, 1981; Jerolmack & Sadler, 2007), uncertainty as to what information fluvial stratigraphy actually preserves (Castelltort & Van Den Driessche, 2003; Jerolmack & Paola, 2010; Romans et al., 2016; Straub et al., 2020), and uncertainties associated with data type, data measurement, and reconstruction tools (e.g., Bridge & Tye, 2000). Where it is possible to overcome these challenges, the ability to decipher palaeohydrological information with high fidelity can enable sophisticated insights to be drawn about the sensitivity and response of ancient fluvial systems to tectonic and climatic drivers.

Here, a quantitative framework is used to reconstruct the palaeohydrological evolution of well-known source-to-sink systems of Late Cretaceous central Utah, USA. The focus of this study is the Blackhawk Formation–Castlegate Sandstone–Price River Formation fluvial succession as outcrops are extensive and well-documented (Kauffman, 1977; Kauffman & Caldwell, 1993; Cobban et al., 2006). These strata represent eastward flowing palaeorivers that drained the Sevier orogenic fold-and-thrust belt to the Western Interior Seaway (WIS). Previous work has primarily focused on *qualitative* inferences of palaeohydrology in these systems (Miall, 1994; Miall & Arush, 2001; Adams & Bhattacharya, 2005; McLaurin & Steel, 2007; Hampson et al., 2012; Flood & Hampson, 2014), which are sometimes complimented by simple quantitative reconstructions (e.g., Hampson et al., 2013). Meanwhile, *quantitative* work has mostly focused on architectural-scale elements in these systems, including preservation of channelized bodies and bars and associated autogenic processes, such as avulsion and backwater dynamics (Hajek et al., 2010; Hajek & Wolinsky, 2012; Flood & Hampson, 2015; Trower et al., 2018; Chamberlin & Hajek, 2019; Ganti, Lamb, et al., 2019). The palaeohydrological evolution of these rivers at the system scale has not been comprehensively addressed using quantitative tools — this study addresses this outstanding research challenge to shed new light on these ancient systems.

Palaeohydrological field data were collected for 5 parallel transverse fluvial systems (spaced ~20–25 km apart) across 7 stratigraphic intervals within the Campanian stage (83.6±0.2 to 72.1±0.2 Ma) of the Late Cretaceous, which spanned 11.5 Myr (Figures 3.1, 3.2). These data allow for high resolution spatio-temporal reconstructions of these systems, both upstream to downstream and along depositional strike (Figure 3.1). Reconstructed palaeohydrologic parameters include: flow depths; palaeoslopes and alluvial palaeorelief (i.e.,

relief specific to the alluvial domain); hydrodynamic properties, including flow velocities, water discharges and sediment transport modes; and planform morphologies. First and foremost, results show how the morphologies and hydrodynamic properties of these palaeorivers varied in space and time. Moreover, reconstruction of palaeoslopes and palaeorelief in the alluvial domain enable evaluation of the competing roles of tectonic and climatic drivers on the evolution of these ancient rivers. Finally, the results provide new insights regarding the extent to which quantitative palaeohydrologic methods (which are increasingly borrowed from the field of engineering) can be reconciled with sedimentological observables.

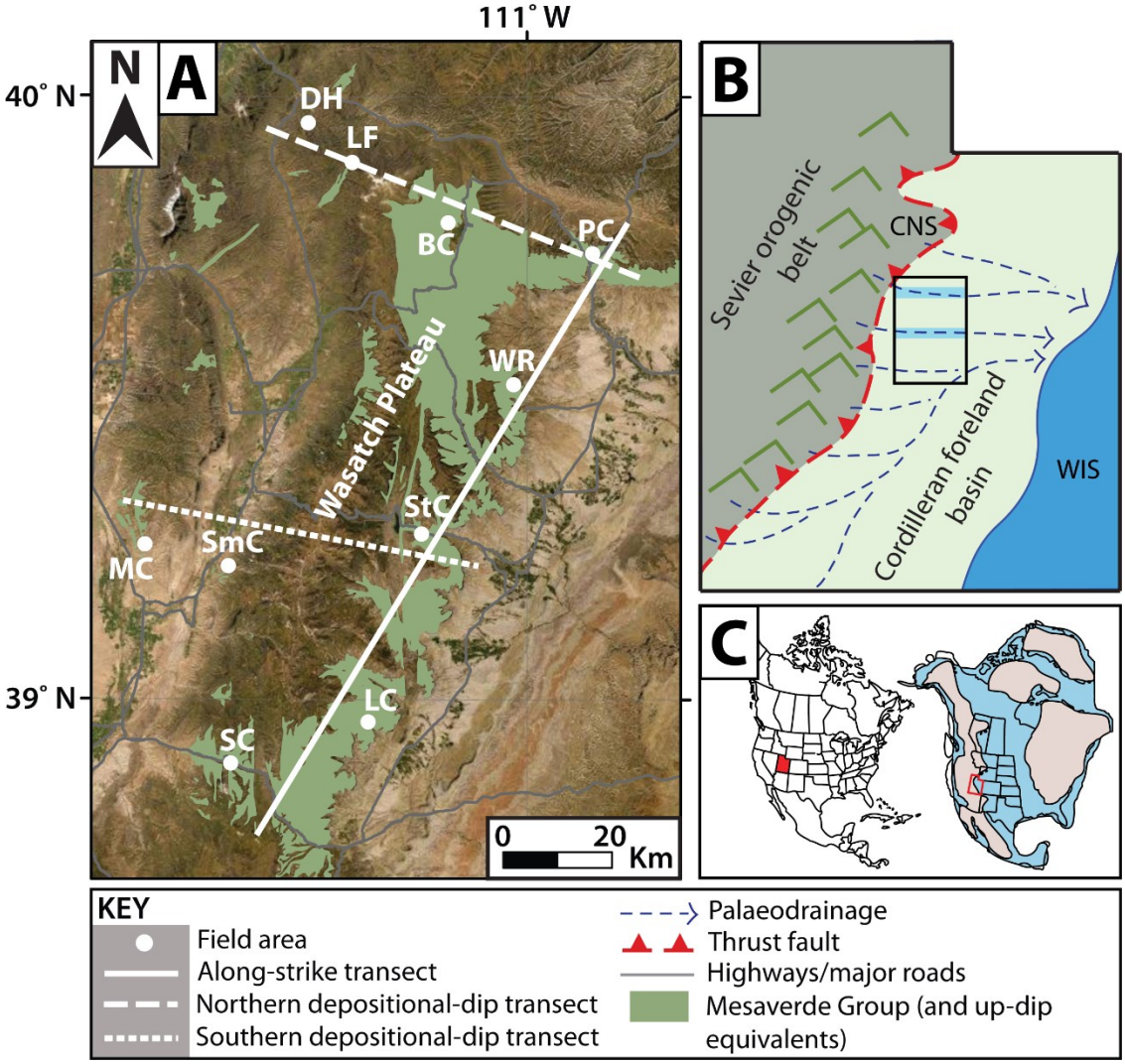

Figure 3.1 | Study area. Part **A**) Field areas in central Utah, USA, which include Bear Canyon (BC), Dry Hollow (DH), Lake Fork (LF), Link Canyon (LC), Mellor Canyon (MC), Price Canyon (PC), Salina Canyon (SC), Sixmile Canyon (SmC), Straight Canyon (StC) and Wattis Road (WR). The solid white line indicates the along-depositional-strike transect defined in this study, the dashed white line indicates the northern proximal–distal transect defined in this study, and the dotted white line indicates the southern proximal–distal transect defined in this study. Part **B**) A conceptual diagram of Utah palaeogeography and palaeodrainage in the Campanian (Late Cretaceous). Likely configurations of drainage toward the Western Interior Seaway (WIS) are indicated by dashed blue lines. CNS = Charleston–Nebo Salient. The black outlined box indicates the study area (i.e., part **A**), and the two highlighted drainage routes (shaded blue) represent the northern and southern proximal–distal transects defined in this study (see part **A**). Part **C**) The location of Utah relative to the modern North American continent (left) and the Late Cretaceous North American continent (right), which features the Western Interior Seaway (blue). Utah is highlighted as a red box.

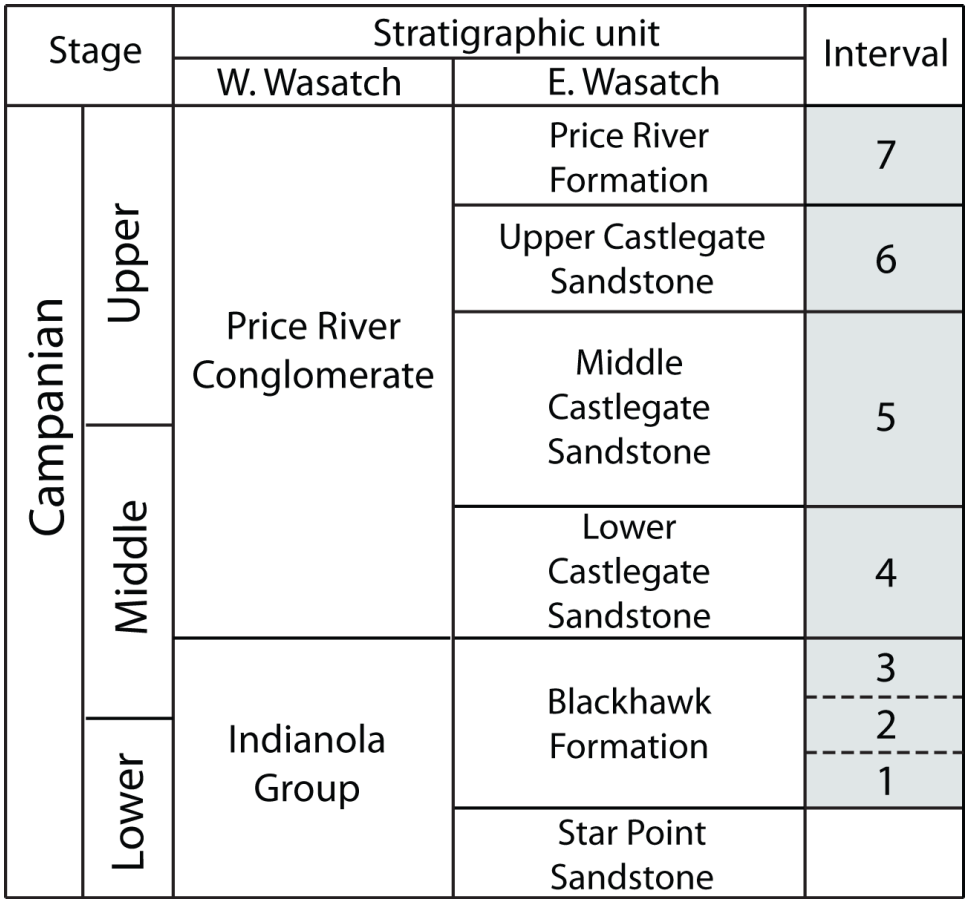

Figure 3.2 | Regional stratigraphy and proximal (western Wasatch Plateau) to distal (eastern Wasatch Plateau) stratigraphic correlation followed in this study. Shaded intervals indicate the stratigraphic intervals used in this study (note that they are not of equal duration). 1 = lower Blackhawk Formation; 2 = middle Blackhawk Formation; 3 = upper Blackhawk Formation; 4 = lower Castlegate Sandstone; 5 = middle Castlegate Sandstone; 6 = upper Castlegate Sandstone; 7 = (lowermost) Price River Formation. Dashed lines indicate an approximate interval boundary. Modified and compiled using data from: Fouch et al. (1983); Robinson & Slingerland (1998); Miall & Arush (2001); Horton et al. (2004); Cobban et al. (2006); Aschoff & Steel (2011a, 2011b); Bartschi et al. (2018). Price River Conglomerate nomenclature follows Aschoff & Steel (2011a, 2011b).

3.2 Research background

3.2.1 Palaeohydrology

Palaeohydrological interpretations traditionally derive from analysis of facies associations in fluvial strata, particularly of architectural-scale elements (Miall, 1994; Miall & Arush, 2001; Adams & Bhattacharya, 2005; McLaurin & Steel, 2007; Hampson et al., 2012; Hampson et al., 2013; Flood & Hampson, 2014), and increasingly take advantage of high-resolution remote imagery and three-dimensional outcrop models (Hajek & Heller, 2012; Rittersbacher et al., 2014; Chamberlin & Hajek, 2019). However, a combination of empirical, theoretical, and experimental work has led to the development of fluid and sediment transport models that are applicable to geologic questions (e.g., van Rijn, 1984b; Ferguson & Church, 2004; Parker, 2004; Wright & Parker, 2004; Mahon & McElroy, 2018), enabling more sophisticated inferences of palaeohydrology from the rock record.

Recent quantitative research has focused on maximising the ability to accurately reconstruct the evolution of fluvial landscapes in the geologic past. Some efforts have centred on connecting landscape surface kinematics to stratal preservation (Paola & Borgman, 1991; Castelltort & Van Den Driessche, 2003; Jerolmack & Mohrig, 2005; Jerolmack & Paola, 2010; Hajek & Wolinsky, 2012; Ganti et al., 2013; Ganti et al., 2014; Reesink et al., 2015; Romans et al., 2016; Ganti et al., 2020; Leary & Ganti, 2020; Straub et al., 2020) and a number of these studies have focused on Upper Cretaceous fluvial strata in central Utah (Flood & Hampson, 2015; Trower et al., 2018; Chamberlin & Hajek, 2019; Ganti, Lamb, et al., 2019). Meanwhile, other quantitative work has applied fluid and sediment transport models to stratigraphic field data, with an overarching goal of constraining the characteristics of catchments, regional systems, or entire fluvial landscapes in the geological past (Ganti, Whittaker, et al., 2019; Lapôtre et al., 2019), or even on other planetary bodies (Lamb et al., 2012; Buhler et al., 2014; Hayden et al., 2019; Lapôtre et al., 2019). This includes using quantitative palaeohydrological tools to reconstruct water and sediment discharges within mass balance frameworks (Holbrook & Wanas, 2014; Lin & Bhattacharya, 2017; Sharma et al., 2017), decipher local palaeogeographies (Bhattacharyya et al., 2015; Li et al., 2018), characterise pre-vegetation rivers (Ganti, Whittaker, et al., 2019), and reconstruct fluvial response to climatic perturbations for well-preserved fluvial strata straddling events such as the Paleocene–Eocene Thermal Maximum (PETM) (Foreman et al., 2012; Foreman, 2014; Colombera et al., 2017; Chen et al., 2018; Duller et al., 2019).

Despite the breadth of quantitative palaeohydrological tools available, previous applications to fluvial stratigraphic field data have typically centred on individual catchments and instantaneous or short-period intervals (i.e., individual discharge events and mean annual discharges) (Holbrook & Wanas, 2014; Lin & Bhattacharya, 2017; Sharma et al., 2017), or reconstructions across stratigraphic boundaries and short-period tectono-climatic events, such as the PETM (Foreman et al., 2012; Foreman, 2014; Colombera et al., 2017; Chen et al., 2018; Duller et al., 2019). Far fewer studies have focused on long-period intervals, such as the evolution of source-to-sink systems across geologic timescales (>10^6 yrs). This outstanding

opportunity can be exploited in Late Cretaceous fluvial systems of central Utah, where outcrop availability supports a four-dimensional (space and time) study in a region subject to active tectonics, spanning both Sevier and Laramide deformation.

3.2.2 Tectono-geographic setting and palaeodrainage

Input of sediment to the Late Cretaceous WIS was dominated by the western margin, where rivers draining the active Sevier fold-and-thrust belt eroded and transported huge volumes of clastic sediments eastwards into the foreland basin (Spieker, 1946; Armstrong, 1968; Kauffman, 1977; Hay et al., 1993; Kauffman & Caldwell, 1993) (Figure 3.1b,c). This led to the deposition and progradation of a large, asymmetric clastic wedge on the western WIS margin. This study focuses on Campanian non-marine clastic sediments of this wedge in central Utah, USA (Figures 3.1–3.3), where palaeodrainage is relatively well-constrained (Bartschi et al., 2018; Pettit et al., 2019). Multiple transverse fluvial systems drained the Sevier thrust belt in this area (Figure 3.1b). Several studies have additionally interpreted an axial, or longitudinal, fluvial system that drained north–northeast from the Mogollon Highlands (present day central Arizona) and Cordilleran magmatic arc, which interacted with transverse systems of the Sevier thrust belt (Lawton et al., 2003; Jinnah et al., 2009; Szwarc et al., 2015) (Figure 3.1b) and led to downsystem sediment mixing (Bartschi et al., 2018; Pettit et al., 2019). Detrital zircon data (Bartschi et al., 2018) indicate that these fluvial systems were dominated by a thrust-belt source in close proximity to the Sevier thrust front, but that more southerly transverse systems may have additionally featured a longitudinal component of drainage (Bartschi et al., 2018; Pettit et al., 2019). Herein, focus is on transverse fluvial systems that predominantly drained the Sevier mountains (Figure 3.1).

Tectonic forcing in this region is well studied (DeCelles, 1994, 2004; DeCelles & Coogan, 2006) and palaeoclimate has been reconstructed from a variety of palaeontological, geochemical-proxy and modelling studies (e.g., Wolfe & Upchurch Jr., 1987; Fricke et al., 2010; Miller et al., 2013; Sewall & Fricke, 2013; Foreman et al., 2015). In central Utah, eastward propagation of the Sevier thrust belt (due to eastward subduction of the Farallon plate) resulted in thin-skinned deformation and movement on the north–south trending Canyon (~145−110 Ma), Pahvant (~110−86 Ma), Paxton (86−75 Ma), and Gunnison (75−65 Ma) thrust systems (DeCelles, 1994, 2004; DeCelles & Coogan, 2006). Associated exhumation created substantial topographic relief in the Sevier mountains, which has been described as "Andean" in scale with mean elevations approaching near 4000 m (Sewall & Fricke, 2013; Foreman et al., 2015). Modelling results and stable isotope evidence suggest a strong monsoonal precipitation along the eastern flank of the Sevier mountains and seasonal flooding across low-relief regions (Roberts, 2007; Roberts et al., 2008; Fricke et al., 2010; Sewall & Fricke, 2013). The tectono-geographic set-up of the Western Interior was particularly conducive to a monsoonal climate — the proximity of a warm sea to high elevation mountains commonly results in strong seasonal precipitation and convective circulation (e.g., Zhisheng et al., 2001). A seasonal temperate-to-subtropical climate therefore prevailed throughout Campanian deposition (Parker, 1976b; Kauffman & Caldwell, 1993; Roberts & Kirschbaum, 1995). The Campanian onset of thick-skinned

deformation as the subducting Farallon plate transitioned to lower-angle, or flat-slab, subduction (DeCelles, 2004) began to manifest as basement-cored Laramide uplifts (e.g., San Rafael Swell, central Utah, and Uinta Mountains, northern Utah), which partitioned the Sevier foreland basin and disrupted patterns of both regional subsidence and drainage (Bartschi et al., 2018; Pettit et al., 2019).

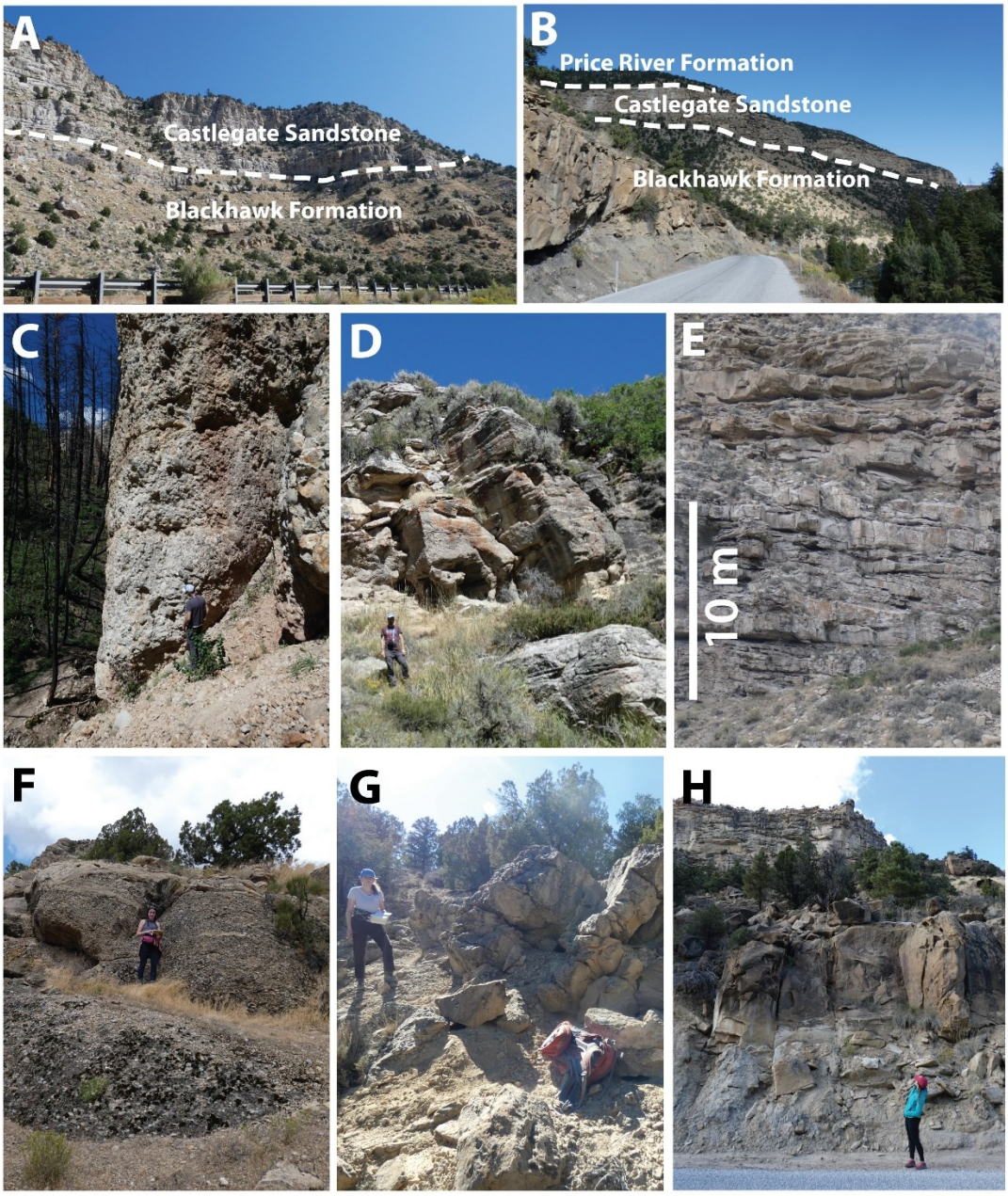

Figure 3.3 | An overview of fluvial strata from which palaeohydrological field data were collected. Data were collected for 5 parallel palaeorivers in Late Cretaceous central Utah, USA. These 5 palaeorivers cropped out in canyons on the eastern front of the Wasatch Plateau — parts **A** and **B** show typical exposure of the Blackhawk Formation, Castlegate Sandstone, and Price River Formation in these canyons. Specifically, part **A** shows strata in Salina Canyon and part **B** shows strata in Straight Canyon (see Figure 3.1), and dashed white lines indicate lithostratigraphic boundaries. For two of these 5 palaeorivers, data were additionally collected upstream to downstream along defined proximal–distal transects (see Figure 3.1). Parts **C–E** show deposits on the northern proximal–distal transect. From proximal to distal, part **C** shows debris flow facies of the Price River Conglomerate, part **D** shows amalgamated fluvial gravels and sands of the Castlegate Sandstone near Bear Canyon, and part **E** shows amalgamated fluvial sands of the Castlegate Sandstone in Price Canyon. Parts **F–H** show deposits on the southern proximal–distal transect, for older sediments. From proximal to distal, part **F** shows channelized fluvial gravel–sand bodies of the upper Sixmile Canyon Formation in Mellor Canyon, part **G** shows a small, channelized sandstone body of the upper Sixmile Canyon Formation in Sixmile Canyon, and part **H** shows a large, channelized sand body of the Blackhawk Formation in Straight Canyon (in the background the Castlegate Sandstone is visible).

3.2.3 Stratigraphic framework

Establishing a consistent stratigraphic framework in space and time is crucial for system scale palaeohydrological reconstructions. Here, focus is on the Upper Cretaceous Mesaverde Group and its proximal equivalents (Figures 3.1, 3.2) in central Utah, USA, specifically fluvial sediments situated less than ~100 km from the Sevier orogenic front (DeCelles & Coogan, 2006) in the flexurally subsiding foredeep (Figure 3.3). These sediments include the Blackhawk Formation, Castlegate Sandstone, and Price River Formation along the eastern front of the Wasatch Plateau (Figures 3.1–3.3). Proximally, on the western Wasatch Plateau, the Blackhawk–Castlegate–Price River succession is correlated with the Sixmile Canyon Formation (Indianola Group) and the Price River Conglomerate (following Robinson and Slingerland (1998); Horton et al. (2004); Aschoff & Steel (2011a, 2011b)) (Figures 3.1–3.3). From proximal to distal, these sediments encompass the entire alluvial domain of these palaeorivers draining the Sevier highlands. A broad summary of field sites and the stratigraphic framework (Figures 3.1, 3.2) is given below — extended information regarding regional stratigraphy and correlations is provided in Appendix B.

Distal field sites were grouped spatially into 5 field areas that represent 5 parallel transverse fluvial systems draining the Sevier thrust front: Price Canyon, Wattis Road, Straight Canyon (including Joe's Valley Reservoir), Link Canyon, and Salina Canyon (Figures 3.1, 3.3). These 5 field areas are approximately ~50 km from proximal alluvial fan lobes (Figures 3.1, 3.3). Assuming typical outlet spacings of rivers draining orogenic fronts (~25 km) (Hovius, 1996), it is likely that these field areas represent 5 distinct palaeorivers and form a ~125 km transect along depositional strike. For the 2 proximal–distal transects (Figure 3.1), the northern transect included 4 field areas: Dry Hollow, Lake Fork, Bear Canyon, and terminating at Price Canyon (Figure 3.3c–e), and the southern transect included 3 field areas: Mellor Canyon, Sixmile Canyon, and terminating at Straight Canyon (Figure 3.3d–f). These transects follow those widely implemented in previous work, both along strike (Hampson et al., 2012; Hampson et al., 2013; Flood & Hampson, 2014, 2015; Chamberlin & Hajek, 2019) and proximal to distal (Robinson & Slingerland, 1998; Horton et al., 2004; Aschoff & Steel, 2011a, 2011b).

In addition to grouping field sites in space, they were also grouped in time. In this study 7 stratigraphic intervals were defined: 1 = lower Blackhawk Formation; 2 = middle Blackhawk Formation; 3 = upper Blackhawk Formation; 4 = lower Castlegate Sandstone; 5 = middle Castlegate Sandstone; 6 = upper Castlegate Sandstone; 7 = (lowermost) Price River Formation (Figure 3.2).

At distal field sites, on the eastern front of the Wasatch Plateau, it is straightforward to assign sediments of the Blackhawk–Castlegate–Price River succession to the appropriate "space–time" interval by facies associations, following extensive work that has been undertaken in this region (Lawton, 1983, 1986b; Miall, 1994; van Wagoner, 1995; Yoshida et al., 1996; Miall & Arush, 2001; Lawton et al., 2003; Adams & Bhattacharya, 2005; Hampson et al., 2012; Hampson et al., 2013; Flood & Hampson, 2014; Hampson et al., 2014; Flood & Hampson, 2015). The lower–middle Campanian Blackhawk Formation represents deposition on coastal plains behind wave-dominated deltaic shorelines which, up-section, pass landward

into alluvial and fluvial plains (Hampson, 2010; Hampson et al., 2012; Hampson et al., 2013). The size and abundance of channelized fluvial sand bodies (deposited by both single- and multi-thread rivers) increase from base to top of the Blackhawk Formation (Adams & Bhattacharya, 2005; Hampson et al., 2012; Hampson et al., 2013; Flood & Hampson, 2015). The middle–upper Campanian Castlegate Sandstone is situated atop the Blackhawk Formation and is an extensive, cliff-forming river-dominated deposit. The lower Castlegate Sandstone and upper Castlegate Sandstone (elsewhere referred to as the Bluecastle Tongue) comprise amalgamated braided fluvial channel-belt deposits, whereas the middle Castlegate Sandstone comprises less amalgamated, more meandering, fluvial channel-belt deposits with interbedded mudstones (Fouch et al., 1983; Lawton, 1986b; Miall, 1994; van Wagoner, 1995; Yoshida et al., 1996; Miall & Arush, 2001). The ledge-forming upper Campanian Price River Formation sits conformably atop the Castlegate Sandstone and comprises large, channelized sand bodies with interbedded siltstones and mudstones — channelized sand bodies form ~75% of the formation (Lawton, 1983, 1986b). Fluvial sediments of the Price River Formation represent the end of Sevier thrusting; the late Maastrichtian–Eocene North Horn Formation unconformably overlies the Price River Formation.

At proximal field sites, on the western Wasatch Plateau, correlative strata include sediments of the Indianola Group and Price River Formation, which is now known to not be time-equivalent with the more distal Price River Formation exposed near Price, Utah (Robinson & Slingerland, 1998; Horton et al., 2004; Aschoff & Steel, 2011a, 2011b). To avoid confusion, these proximal strata are here referred to as the Price River Conglomerate, following Aschoff and Steel (2011a, 2011b). Proximal to distal correlations are limited by incomplete exposure on the western Wasatch Plateau and difficulty in dating conglomerates (see Appendix B). Nevertheless, Robinson and Slingerland (1998) used palynology to correlate these strata across a variety of localities on the Wasatch Plateau (Figure 3.2), which can be traced in seismic reflection data (Horton et al., 2004). The proximal Price River Conglomerate is time-correlative with the more distal lower, middle, and upper Castlegate Sandstone, and Price River Formation (Robinson & Slingerland, 1998; Horton et al., 2004; Aschoff & Steel, 2011a, 2011b), and is characterised by quartzite-dominated synorogenic fanglomerates and few gravel–sand fluvial bodies (Robinson & Slingerland, 1998; Aschoff & Steel, 2011a, 2011b). Of the Indianola Group, the upper Sixmile Canyon Formation is time-correlative with the Blackhawk Formation (Lawton, 1982; Fouch et al., 1983; Lawton, 1986b) and is predominantly characterised by synorogenic gravel–sand fluvial facies, spanning polymictic fluvial conglomerates to medium–coarse-grained sandstones (Lawton, 1982, 1986a, 1986b). Here a conservative approach is taken to proximal to distal correlations; the upper Sixmile Canyon Formation of the Indianola Group (intervals 1–3) is time-averaged, and the Price River Conglomerate (intervals 4–7) is also time-averaged, but exceptions were made where field sites were known to be situated at either the top of the upper Sixmile Canyon Formation or at the top/base of the Price River Conglomerate. A full description of these correlations, including new logging in Mellor Canyon, is presented in Appendix B.

Each proximal–distal transect is pinned at the most downstream location, i.e., it is assumed that the most distal sites in each transect (Price Canyon and Straight Canyon) are approximately parallel and at the same

downstream distance. Transects then work upstream, such that the most proximal field site (Dry Hollow; northern transect) is at a downstream distance of 0 km. Downstream distances follow Robinson & Slingerland (1998) — post-depositional extension is not corrected for. Alternatively, when reconstructing along-depositional-strike transects, transects are pinned at the most northern location (Price Canyon) with an along-strike distance of 0 km, meanwhile southern locations have along-depositional-strike distances up to 125 km.

3.3 Methods

Data were collected from channel-fill stratigraphy (cross-stratified sandstone and gravel deposits are interpreted as channel floor deposits) and were time-averaged across each stratigraphic space–time interval (field sites are listed in Appendix Table B2). These field data, including uncertainties, were propagated through a quantitative framework to reconstruct the morphologies and hydrodynamics (flow depths, palaeoslopes, alluvial river long profiles, flow velocities and discharges, sediment transport modes and likely planform morphologies) of palaeorivers in both space and time.

3.3.1 Field observations

Grain size

At each field site the coarse-fraction (>2 mm in diameter) and sand-fraction (<2 mm in diameter) grain-sizes of channel-fill deposits were established (Figure 3.4a,b). For coarse-fractions, grain-size distributions were measured via Wolman point counts (Wolman, 1954) (Figure 3.4a); this technique has been successfully used to decode spatio-temporal trends in grain-size (e.g., Whittaker et al., 2011; D'Arcy et al., 2017; Brooke et al., 2018). For sand-fractions, scaled photographs were processed in *ImageJ* software and, similarly, the long axis of a minimum of 50 randomly selected grains was measured to recover grain-size distributions (Figure 3.4b). From each measured grain-size distribution, the median grain-size, D_{50}, and 84th percentile, D_{84}, were extracted. Where grain-size facies were disparate, e.g., gravel topped with sand, data were collected for each grain-size facies and the proportions of each were estimated (Figure 3.4c).

In order to achieve representative sampling for spatio-temporal grain-size trends, multiple grain-size observations were collected at each field site. Not only were data collected for each grain-size facies (Figure 3.4a–c) but, depending on overall outcrop extent, Wolman point counts were repeated and/or additional scaled photographs were taken for *ImageJ* processing at intermittent stratigraphic intervals (e.g., one count per 5–10 m of strata or per channelized body). The extent of each field site can be approximated as the extent of outcrop apparent in Figure 3.3c–h. From these data an average grain-size was produced for both the sand-fraction and gravel-fraction at each field site. As each space–time interval includes multiple field sites, this results in multiple average sand- and gravel-fraction grain-sizes, capturing channel-fill deposits from several channelized bodies. Finally, a bulk-grain-size was produced for each space–time interval using the gravel-to-sand proportions at each field site — each site within a space–time interval was assigned equal

weighting. Further information regarding grain-size data collection, including axis selection, sample size sufficiency and weighting, is presented in the Appendix B.

Cross-sets

Cross-set heights were measured as these data can be used to reconstruct original bedform heights and formative flow depths. Trough- and planar-cross bedding, which are inherently indicative of bedload transport, were present at nearly all field sites. They occurred predominantly in sand-grade deposits, but also in granule- to pebble-grade deposits (Figure 3.4d–f). To establish mean cross-set heights, the sampling strategy of Ganti, Whittaker, et al. (2019) was followed. Cross-set boundaries (i.e., the lower, asymptotic bounding surface and the upper, erosional bounding surface) were delineated and then heights were measured at regular intervals along the entire width of the cross-set dip-section (Figure 3.4g–i). Measurements were made to a precision of ±5 mm. This protocol was repeated for individual cross-sets within co-sets to establish a mean cross-set height for each individual cross-set. Subsequently, maximum cross-set heights (i.e., the maximum distance between lower and upper bounding surfaces) were measured for a representative sample across the exposed outcrop (usually n=25–50).

From cross-sets for which height distributions were measured (n=470), the mean, 84th percentile (P_{84}), and maximum heights of each individual cross-set were extracted. From these data, the relationship between maximum and mean cross-set heights was established. This new relationship was then used to estimate mean cross-set heights from all measured maximum cross-set heights (n=4053). This maximised the amount of field data that could be collected, and therefore analysed, at each field site — it is more efficient to measure maximum cross-set heights than height distributions of individual cross-sets. These estimates of mean cross-set heights were propagated through subsequent calculations, as measurements of mean cross-set heights are more appropriate than maximum cross-set heights in reconstruction of palaeohydrologic parameters (e.g., Equation 3.1).

Channel geometry and architectural element data

Above grain- and bedform-scales, channel geometries and major architectural elements were also measured, where possible, using a Haglof Laser Geo laser range finder to a precision of ±5 cm. This included maximum channel body/story thicknesses and bar-scale clinoform heights. Previous work in this region has documented the dimensions and distributions of fluvial architectural elements using high-resolution imagery and 3D outcrop models (Hajek & Heller, 2012; Rittersbacher et al., 2014; Flood & Hampson, 2015; Chamberlin & Hajek, 2019). Field data collection therefore focused on grain-size and cross-set measurements, with compilation of published secondary data (alongside new data from this study) to augment field data and evaluate our palaeohydrological reconstructions (see Appendix Tables B4, B5).

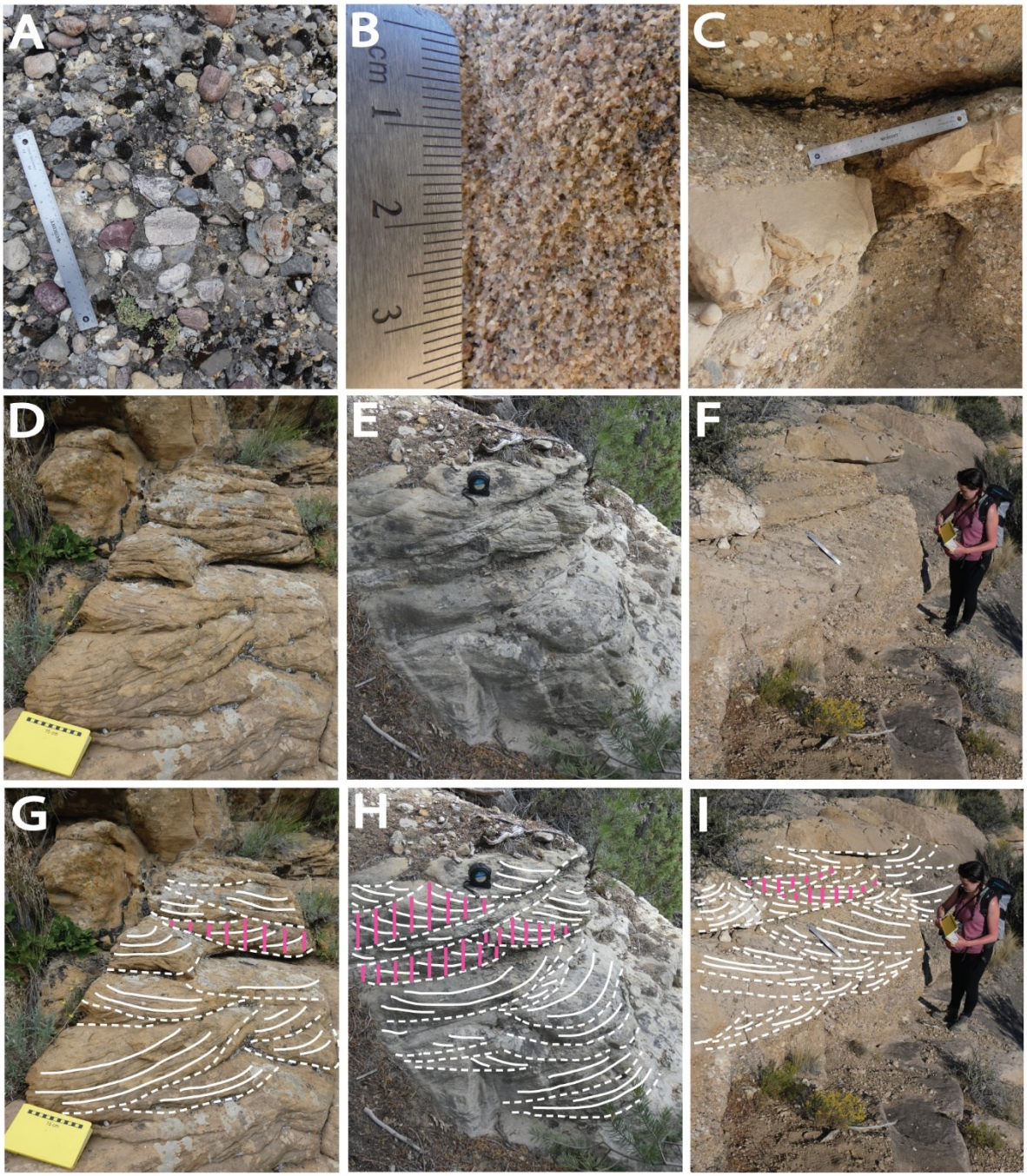

Figure 3.4 | Field data collection included grain-size measurements for (part **A**) gravel and (part **B**) sand fractions, as well as (part **C**) estimates of the proportions of different grain-size facies. Parts **D–F** depict cross-bedding, and parts **G–I** depict interpreted versions of the same images. Dashed white lines indicate bounding surfaces of individual cross-sets and solid white lines indicate selected foresets within individual cross-sets. To exemplify sampling procedure when determining mean cross-set height, solid pink lines demonstrate how heights are measured for selected cross-set dip sections. Field notebook with 15 cm scale, tape measure, and 30 cm rule for scale.

3.3.2 Quantitative palaeohydrology

Channel geometries

To calculate original bedform heights from cross-set measurements, the relation of Leclair and Bridge (2001) was used, which is based on theoretical work by Paola and Borgman (1991). Leclair and Bridge (2001) showed that mean bedform (i.e., dune) height, h_d, can be approximated as a function of mean cross-set height, h_{xs}, as

$$h_d = 2.9(\pm 0.7)h_{xs}, \quad \text{Eq. 3.1}$$

where 2.9 is the mean and 0.7 is the standard deviation. Given that exact error margins of palaeohydrologic inversion methods cannot be known, a Monte Carlo uncertainty propagation method is used in this study to estimate uncertainty and offer plausible spreads of values for each reconstructed palaeohydrological parameter. In Equation 3.1, uncertainty is represented as the mean (μ) and one standard deviation (σ). As such, 10^6 random samples were generated between bounds defined by $\mu-\sigma$ and $\mu+\sigma$. Samples were generated from a uniform distribution as the shape and the scale of the full distribution of the data is not known — this approach avoids introduction of additional assumptions. These values are then propagated through subsequent calculations.

While bedform height generally scales with flow depth, the mechanistic explanation for this is not fully resolved. As such, many scaling relations simply relate bedform height and flow depth (e.g., Yalin, 1964), whereas some incorporate additional parameters such as Froude number, D_{50}, and transport stage (e.g., Gill, 1971; van Rijn, 1984a), however their incorporation does not improve predictive power. Bradley and Venditti (2017) revisited previous bedform height−flow-depth scaling relations and derived a new relation between h_d and median formative flow depth, H, based on >380 field observations, where

$$H = 6.7h_d. \quad \text{Eq. 3.2}$$

In detail, Bradley and Venditti (2017) derived two relations to reconstruct H from h_d. Their first relation was derived from regression analysis and recovered μ and σ, however the authors argued that this relation is not useful as the data are not normally- or log-normally distributed, and that the tails of the distribution are not fully represented (Bradley & Venditti, 2017). The authors additionally presented a non-parametric relation to derive median H (Equation 3.2) with a probabilistic uncertainty estimator in which the 1st and 3rd quartiles of H are given by $H=4.4h_d$ and $H=10.1h_d$, respectively (Bradley & Venditti, 2017). Bradley and Venditti (2017) noted that this probabilistic uncertainty estimator better represented their data, as it does not assume an underlying distribution. This relation is more appropriate in palaeohydrologic reconstructions as, with a larger uncertainty estimate, it offers a broader spread of possible H values. As such, 10^6 uniformly distributed random samples were generated between 4.4 and 10.1, and these model parameter values were used to generate likely palaeoflow depths in these ancient systems. Where cross-

bedding was absent (i.e., the most proximal field sites), channel-body thicknesses were used as a proxy for flow depth.

Similar to H, channel width, W, can be estimated using scaling relations as direct measurement is not normally possible from outcrop. Bridge and Mackey (1993) proposed the relation $W=8.8H^{1.82}$ for single-thread channels. Alternatively, widths of fully-braided channel systems can be approximated as, for example, $W=42H^{1.11}$ (Leopold & Maddock Jr, 1953). However, estimates of W from outcrop data and scaling relations are particularly tentative and, where systems are braided, subject to further uncertainty pertaining to the number of threads. As such, results in this study are reported per unit width.

Palaeoslopes and alluvial palaeorelief

Palaeoslopes were estimated using 2 independent methodologies, adapted from Ganti, Lamb, et al. (2019). First, Shields stress, τ^*, was estimated using the bedform stability diagram of Carling (1999), which expresses bedform stability in terms of τ^* and D_{50} (for $D_{50} < 33$ mm). Minimum and maximum bounds of τ^* for the stable existence of dunes were then identified for a range of D_{50} values. Then, 10^6 uniformly distributed random samples of τ^* were generated between these grain-size-dependent bounds. Where D_{50} exceeded 33 mm, and in the absence of bedforms, possible τ^* values of 0.03–0.06 were assigned. To reconstruct palaeoslope, S, the bed shear stress, τ_b, was approximated as the depth–slope product ($\tau_b=\varrho gHS$) and then S can be given as

$$S = \frac{RD_{50}\tau^*}{H}, \qquad \text{Eq. 3.3}$$

where R is the dimensionless submerged specific gravity of sediment in water (1.65 for quartz) and H is the flow depth (ϱ is density and g is acceleration due to gravity). For the second approach, the method of Trampush et al. (2014) was used, which is based on Bayesian regression analysis of bankfull measurements in modern alluvial rivers (n=541); here slope is expressed as

$$\log S = \alpha_0 + \alpha_1 \log D_{50} + \alpha_2 \log H, \qquad \text{Eq. 3.4}$$

where the constants are given by $a_0 = -2.08\pm0.036$, $a_1 = 0.254\pm0.016$, and $a_2 = -1.09\pm0.044$. Again, 10^6 values of a_0, a_1, and a_2 were generated (uniformly distributed random samples between $\mu-\sigma$ and $\mu+\sigma$). Having propagated 10^6 values of τ^*, H, a_0, a_1, and a_2 into these calculations, 10^6 values of S were recovered for both Equations 3.3 and 3.4, which can then be contrasted.

Along proximal–distal transects, palaeoslope estimates can be used to infer the shape of the river long profile, and therefore palaeorelief, in the alluvial domain. Alluvial palaeorelief was reconstructed using estimates of S from Equations 3.3 and 3.4. For simplicity, median S was extracted from these values and used to derive alluvial palaeorelief. The local slope at downstream position x, S_x, can be related to its upstream contributing catchment area, A_x, (Hack, 1973; Flint, 1974; Whipple, 2004) as

$$S_x = k_s A_x^{-\theta}, \quad \text{Eq. 3.5}$$

where k_s is the steepness index and θ is the concavity, typically between 0.4 and 0.7 (Tucker & Whipple, 2002). Given that the palaeo-concavity is unknown, a range of plausible concavities (0.4, 0.5, and 0.6) were tested to gauge the spread of possible results. Following Hack's law, local catchment length, L_x, is related to A_x by $L_x = c_H A_x^h$, where c_H is the Hack coefficient, commonly taken as near 2 when L_x and A_x are in units of km^2 (Castelltort et al., 2009), and h is the Hack exponent, commonly taken as 0.5 (Hack, 1957). Using Hack's law, local slope can instead be estimated as a function of downstream distance, where

$$S_x = k_s L_x^{-\theta/h}. \quad \text{Eq. 3.6}$$

k_s is calculated from field data using downsystem palaeoslope estimates and knowledge of catchment lengths at each downstream location. As this study solely focuses on the alluvial domain, this means that proximal fan apexes would have a catchment length of 0 km. Here, the most proximal field sites are set as having a catchment length of 5 km to allow for additional upstream fan length. Knowledge of distance to the coeval palaeoshoreline from our most distal sites (Price Canyon and Straight Canyon) is also required. Based on previous studies, approximate distances to the palaeoshoreline are set as ~10 km for the lower Blackhawk Formation, ~35 km for the middle Blackhawk Formation, ~50 km for the upper Blackhawk Formation, ~110 km for the Castlegate Sandstone (Hampson et al., 2012; Hampson et al., 2013), and ~200 km for the Price River Formation (Hettinger & Kirschbaum, 2002; Aschoff & Steel, 2011b). A nonlinear least squares regression was used to find best fit palaeoslope profiles (Equation 3.6) for both the northern and southern transects at each time interval. Palaeoslope profiles were then transformed into alluvial river long profiles by summing elevation increments along the downstream length to the palaeoshoreline. This elevation decrease is indicative of the likely relief in the alluvial domain of these palaeorivers.

Hydrodynamics

In subsequent calculations, values derived from Monte Carlo uncertainty propagation were used, i.e., 10^6 estimates of H, S, etc. Specifically, estimates of S derived from the Shields stress inversion (Equation 3.3) were carried forward. Flow velocities, U, were calculated following Manning's Equation, where

$$U = \frac{1}{n} H^{\frac{2}{3}} S^{\frac{1}{2}} \quad \text{Eq. 3.7}$$

and n is Manning's constant, set as 0.03. Water discharges were then estimated by multiplying flow velocity by flow depth, to obtain discharge per unit width ($Q=UH$).

To determine dominant mode of sediment transport, the Rouse number, Z, was calculated as

$$Z = \frac{w_s}{\beta \kappa u_*} \quad \text{Eq. 3.8}$$

where β is a constant that correlates eddy viscosity to eddy diffusivity, typically taken as 1, $\varkappa$ is the von Karman constant, taken as 0.4, and u^* is the bed shear velocity ($gHS^{0.5}$). Sediment settling velocity, w_s, was calculated as a function of grain size following Ferguson and Church (2004),

$$w_s = \frac{RgD_{50}{}^2}{C_1\nu + (0.75C_2RgD_{50}{}^3)^{0.5}}, \quad \text{Eq. 3.9}$$

where ν is the kinematic viscosity of water (1×10^{-6} m^2/s for water at 20°C) and C_1=18 and C_2=1 are constants associated with grain sphericity and roundness. With Z, dominant mode of sediment transport is typically wash load for $Z < 0.8$, 100% suspended load for $0.8 < Z < 1.2$, 50% suspended load (i.e., mixed load) for $1.2 < Z < 2.5$, and bedload for $Z > 2.5$. To corroborate inferred sediment transport modes, the particle Reynolds number, Re_p, was additionally calculated in line with previous work (cf. Parker, 2004) as

$$Re_p = \frac{\sqrt{RgD_{50}}D_{50}}{\nu} \quad \text{Eq. 3.10}$$

and plotted as a function of τ^*, following Dade and Friend (1998). This enables field results to be contrasted with data that are typical of either suspended, mixed, or bedload sediments (Leopold & Wolman, 1957; Schumm, 1968; Chitale, 1970; Church & Rood, 1983; Andrews, 1984), and to identify where these data are positioned among characteristic flow regimes (no sediment transport; ripples and dunes; upper plane beds) following Allen (1982a, 1982b).

Fluvial style

Fluvial style (i.e., planform morphology) of Blackhawk–Castlegate rivers has been described qualitatively from outcrop architecture (Miall, 1994; Miall & Arush, 2001; Adams & Bhattacharya, 2005; Hampson et al., 2013). Here, a quantitative approach is implemented to decipher fluvial style to complement these works, check for consistency, and interpret the interplay between different planform morphologies and the tectono-geographic setting. This is carried out for field areas along the eastern Wasatch Plateau. First, Froude number, Fr, is calculated as

$$Fr = \frac{U}{\sqrt{gH}} \quad \text{Eq. 3.11}$$

and, then, depth/width ratios were plotted against palaeoslope/Froude ratios (Parker, 1976). Various flow widths were assigned to determine what depth/width ratios are required such that the data fall within the theoretical stability fields for single-thread and multi-thread fluvial planform morphologies. These flow widths are then contrasted with estimates of apparent maximum flow width from architectural analysis of channelized sandstone bodies (e.g., Flood & Hampson, 2015) and field interpretations of fluvial style (Miall, 1994; Miall & Arush, 2001; Adams & Bhattacharya, 2005; Hampson et al., 2013).

For all palaeohydrological parameters the median (2nd quartile) result is presented. Where minima and maxima are presented, these bounds reflect the full spread of recovered values. These are offered as plausible minimum and maximum values for the median, derived from propagation of uncertainty margins. In instances where a 1st–3rd interquartile range is additionally presented, specifically in box-and-whisker plots, this is the 1st–3rd interquartile range that has been extracted for each parameter from the 10^6 values recovered by Monte Carlo error propagation. The whiskers in these plots effectively describe the minimum and maximum values of the data and can also be considered as plausible minimum and maximum values for the median.

3.4 Results

3.4.1 Channel geometries

Linear relationships between maximum cross-set height and both the mean and the P_{84} cross-set height were established from measured cross-set distributions (n=470) for our field area (Figure 3.5a,b). Maximum and mean cross-set heights are well-correlated (R^2=0.88) and 95% of observed mean cross-set heights fall within ~3 cm of the predicted mean cross-set height. Using these new relationships, mean cross-set heights were estimated for all (n=4053) measured maximum cross-set heights (Figure 3.5c–e; Appendix Table B3).

Maximum cross-set heights typically span 0.1–0.35 m — these field data are comparable to the results of previous work (e.g., Adams & Bhattacharya, 2005). From maximum cross-set heights, mean cross-set heights spanning 0.07–0.25 m are estimated, which correspond with original bedform heights of 0.2–0.75 m. Flow depths for the along-depositional-strike transect suggest that, in both space and time, these 5 transverse fluvial systems maintained median flow depths of 2–4 m, with a range of 1–7 m (Figure 3.6). Overall, flow depths do not change across the Blackhawk–Castlegate transition but exhibit a marginal decrease during middle Castlegate Sandstone deposition of <0.5 m. Flow depths are also projected to be overall <1 m greater in southern fluvial systems (Figure 3.6). However, these observed differences all lie within the uncertainty margins of calculations, suggesting these systems were similar to each other.

Reconstructed palaeoflow depths are consistent with independent palaeoflow depth proxies (Appendix Table B4), which demonstrates applicability of cross-set scaling relations in the absence of well-preserved macroforms. Bar heights, where available, are consistent with projected flow depths of 2–4 m across field sites. For instance, Chamberlin and Hajek (2019) reported mean bar heights of 2.6 m, 3.6 m and 3.9 m for the entire Castlegate Sandstone at Price Canyon, Straight Canyon, and Salina Canyon, respectively. At Price Canyon, both Lynds and Hajek (2006) and Hajek and Heller (2012) reported greater mean bar heights of 4.1 m specifically for the lower Castlegate Sandstone, with a typical span of 1–8 m (Lynds & Hajek, 2006; McLaurin & Steel, 2007) — we note that the full range of our reconstructed palaeoflow depths is typically 1–7 m and therefore agrees with this range. Meanwhile, channelized fluvial sandstone bodies are more extensively documented for the Blackhawk Formation and their heights offer a maximum limit on palaeoflow depths. Flood and Hampson (2015) recovered mean apparent heights for channelized sandstone

bodies of 6–8 m across the entire Blackhawk Formation between Straight Canyon and Salina Canyon. As maximum bounds on palaeoflow depth, these values are also in good agreement with the upper bounds of estimated palaeoflow depths.

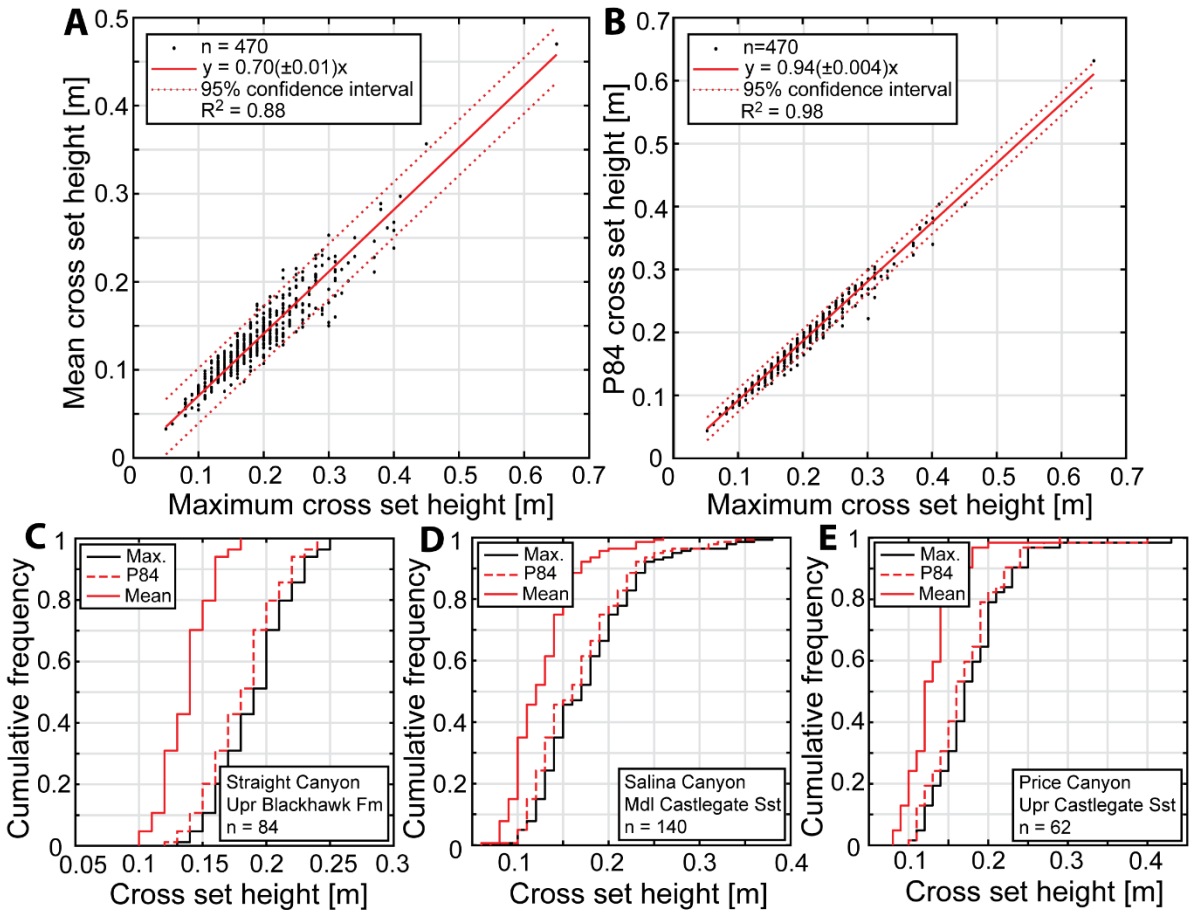

Figure 3.5 | Part **A**) Relationship between maximum cross-set height and mean cross-set height. Part **B**) Relationship between maximum cross-set height and the 84th percentile (P_{84}) of cross-set height. Data are based on 470 measured cross-set distributions. Errors reported in the fits are 95% confidence intervals. Parts **C–E**) Examples of the use of these new relations (parts **A** and **B**) to predict the mean and P_{84} cross-set height from maximum cross-set heights. Examples are for the upper Blackhawk Formation in Straight Canyon (part **C**), the middle Castlegate Sandstone in Salina Canyon (part **D**), and the upper Castlegate Sandstone in Price Canyon (part **E**). In parts **C–E**, n indicates the number of maximum cross-set heights used to predict mean and P_{84} cross-set heights. Full cross set data for each field site, through each stratigraphic interval, are located in Appendix Table B3.

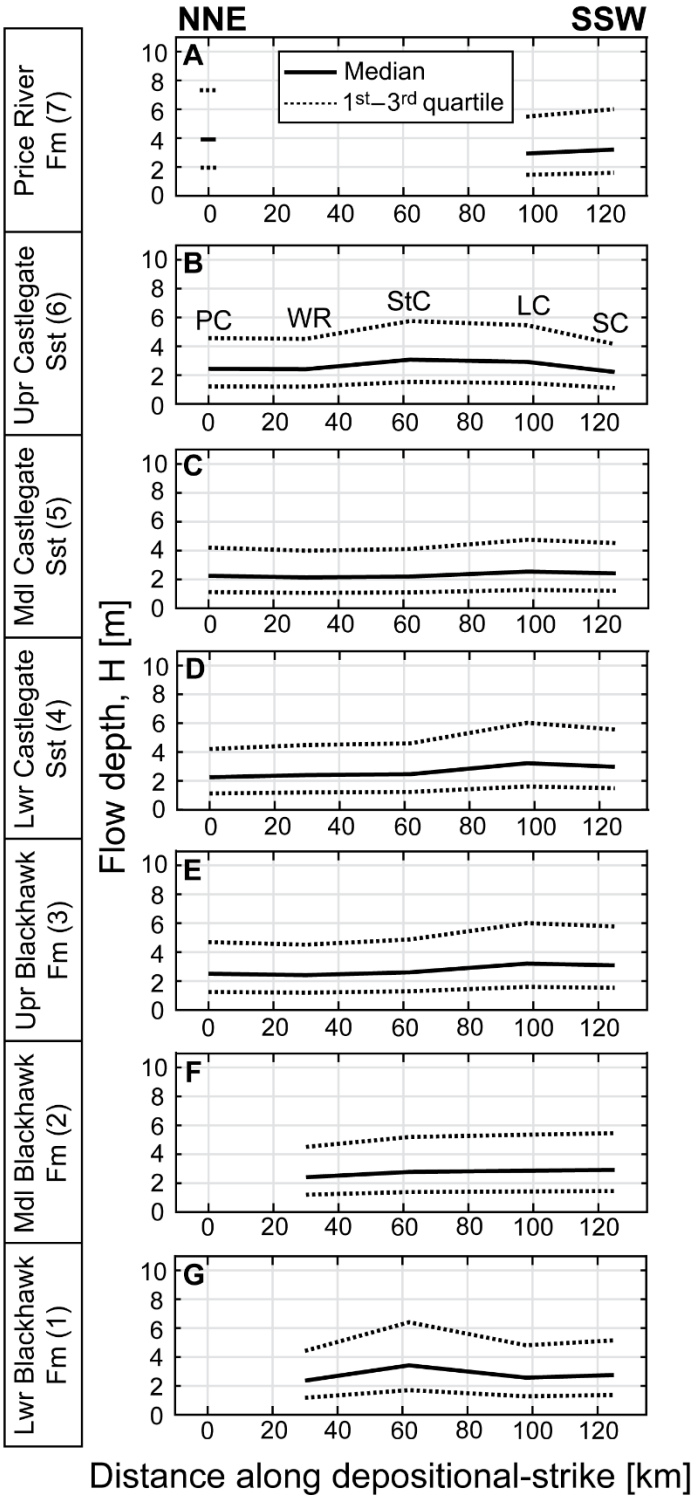

Figure 3.6 | Reconstructed palaeoflow depths for the 5 parallel fluvial systems, for each stratigraphic interval (parts **A–G**), where possible, using mean cross-set heights. Results are presented as along-depositional strike transects from NNE (left; 0 km) to SSW (right; 125 km). Field sites span Price Canyon (PC), Wattis Road (WR), Straight Canyon (StC), Link Canyon (LC), and Salina Canyon (SC). Solid lines indicate median palaeoflow depths and dashed lines indicated plausible minimum and maximum values for median palaeoflow depths using uncertainty margins of Equation 3.2. This figure is replicated in Appendix B alongside palaeoflow depths reconstructed from maximum cross-set heights (Appendix Figure B3).

3.4.2 Palaeoslopes and alluvial palaeorelief

Palaeoslope estimates for our northern (Figure 3.7a–f) and southern (Figure 3.7g–m) proximal–distal transects and results from each method (Equations 3.3 and 3.4) were compared (Figure 3.7). Palaeoslopes are presented as y/x — a palaeoslope of 0.001 results in an elevation decrease of 1 m per 1000 m and is equivalent to 0.057°. Maximum (more proximal) palaeoslopes of 5×10^{-3} are equivalent to slopes of ~0.3°; these magnitudes of palaeoslope are comparable with the slopes of modern rivers, including middle–upper reaches of the Colorado (USA) and upper reaches of the Niger (west Africa) (Roberts et al., 2012; Paul et al., 2014; Fernandes et al., 2019). Minimum (more distal) palaeoslopes of $\sim 5 \times 10^{-5}$ are equivalent to slopes of ~0.003°; palaeoslopes in the range 10^{-5} to 10^{-4} are characteristic of lowland/low-slope rivers, such as lower reaches of the Mississippi (USA), Ebro (Spain), Nile (northeast Africa), and Murray–Darling (Australia) (Carlston, 1969; Rudge et al., 2015; Fernandes et al., 2019; Roberts et al., 2019; Soria-Jáuregui et al., 2019).

At proximal field sites, palaeoslopes are consistently of order 10^{-3} (Figure 3.7), with the exception of the Blackhawk Formation in the southern transect where the 1st–3rd interquartile range of recovered palaeoslope values extends down to 7×10^{-4} (Figure 3.7k–m). Importantly, an order of magnitude decrease in palaeoslope is reconstructed between a down-system distance of 10 and 25 km; this occurs in all stratigraphic intervals, at the same downstream distance, for both the northern and southern transects (Figure 3.7). At more distal field sites, from ~25 km onwards, palaeoslopes are flatter and typically span 5×10^{-5} to 5×10^{-4}. In these lower gradient regions, there is an apparent downstream increase in palaeoslope in Figure 3.7b,c,i–m. However, this apparent increase is within the 1st–3rd interquartile range of values and may not be significant. Proximal to distal palaeoslope estimates derived from Equations 3.3 and 3.4 are broadly consistent with one another — they are the same order of magnitude and the 1st–3rd interquartile ranges either overlap with or are within a factor of 2–3 of one another. However, Equation 3.3 overpredicts and underpredicts palaeoslope relative to Equation 3.4, such that palaeoslope estimates derived from Equation 3.3 imply higher topographic relief and estimates derived from Equation 3.4 imply lower topographic relief (Figure 3.7).

To constrain temporal changes in palaeoslope, the palaeoslope evolution at the most proximal locations of both the northern and southern transects can be compared (Figure 3.8). Palaeoslopes increase at the onset of Castlegate Sandstone deposition (intervals 4–6) and the magnitude of this increase differs between the north and the south (Figure 3.8). In the north, the initial palaeoslope is higher ($\sim 2 \times 10^{-3}$) and increases by a factor of 1.5 to $\sim 3 \times 10^{-3}$ (Figure 3.8a), whereas, in the south, the initial palaeoslope is lower ($\sim 1 \times 10^{-3}$) and increases by a factor of up to 4, to $\sim 4 \times 10^{-3}$ (Figure 3.8b). This implies a coeval increase in palaeoslope at the onset of Castlegate Sandstone deposition which was more pronounced in the south. Again, estimates derived from Equation 3.4 dampen this increase relative to estimates derived from Equation 3.3.

With proximal to distal palaeoslope estimates for both the northern and southern transects, best-fit palaeoslope profiles were derived as a function of downstream distance (Equation 3.7; Appendix Table B6).

Palaeoslope profiles generally fit reconstructed palaeoslopes well, with typical R^2 values >0.85, and it is noted that of 3 reference concavities, θ, used, the higher value of θ=0.6 typically recovered the best fits (Appendix Table B6). A notable exception to this is palaeoslope profiles reconstructed from Shields stress palaeoslope estimates for the Castlegate Sandstone in the northern proximal–distal transect — the lower θ=0.4 value generates the best fit and this fit is relatively poor (R^2 of 0.35–0.6). However, palaeoslope profiles for these same space–time intervals derived from alternative palaeoslope estimates (Equation 3.4) fit well (R^2 >0.9; Appendix Table B6).

In reconstructing palaeoslope profiles steepness index, k_s, values were recovered for each stratigraphic interval (for θ=0.5), which were mostly between ~5 and 35 m (Appendix Table B6). There is an increase in reconstructed k_s values across the Blackhawk–Castlegate transition for both methods of palaeoslope estimation. For estimates derived from Equation 3.3, k_s values increase across the Blackhawk–Castlegate transition by a factor of ~2–3 in the northern transect, and by a factor of ~4–5 in the southern transect. In contrast, for estimates derived Equation 3.4, k_s values increase across the Blackhawk–Castlegate transition by a factor of <1.5 in the northern transect, and by a factor of ~2 in the southern transect (Appendix Table B6).

Palaeoslope profiles were transformed into alluvial river long profiles, which are indicative of the palaeorelief in the alluvial domain, or depositional reaches, of Blackhawk–Castlegate–Price River fluvial systems only (Figure 3.9). Given that the concavities of these ancient rivers are not known, implementing plausible concavities of 0.4, 0.5 and 0.6 enabled a likely spread of values for alluvial palaeorelief to be constrained (Figure 3.9). Results indicate that different concavities recover similar values for alluvial palaeorelief; total estimates vary within a factor of ~2, between a concavity of 0.4 and 0.6 (Figure 3.9).

Using palaeoslope estimates derived from Equation 3.3, alluvial palaeorelief during Blackhawk deposition was estimated as ~40–60 m in the northern transect (Figure 3.9e,f) and 15–25 m in the southern transect (Figure 3.9k–m). During Castlegate Sandstone deposition, alluvial palaeorelief increased by a factor of 1.5–2.5 in the northern transect, to an estimated 65–145 m of alluvial palaeorelief, whereas it increased by a factor of 5–6 in the southern transect, to an estimated 90–130 m of alluvial palaeorelief. Alternatively, using palaeoslope estimates derived from Equation 3.4, alluvial palaeorelief during Blackhawk Formation deposition was estimated as ~30–50 m in the northern transect (Figure 3.9e,f) and 15–25 m in the southern transect (Figure 3.9k–m). During Castlegate Sandstone deposition, alluvial palaeorelief increased by a factor of ~1.8 in the northern transect, to an estimated 55–90 m of alluvial palaeorelief, whereas it increases by a factor of 2 in the southern transect, to an estimated 30–50 m of alluvial palaeorelief. In detail, alluvial palaeorelief implied by Equation 3.3 (Shields) is up to a factor of 2 greater than the alluvial palaeorelief implied by Equation 3.4 (Trampush). This higher alluvial palaeorelief during Castlegate Sandstone deposition is sustained into Price River Formation times. It is stressed that these estimates refer to the alluvial domain only.

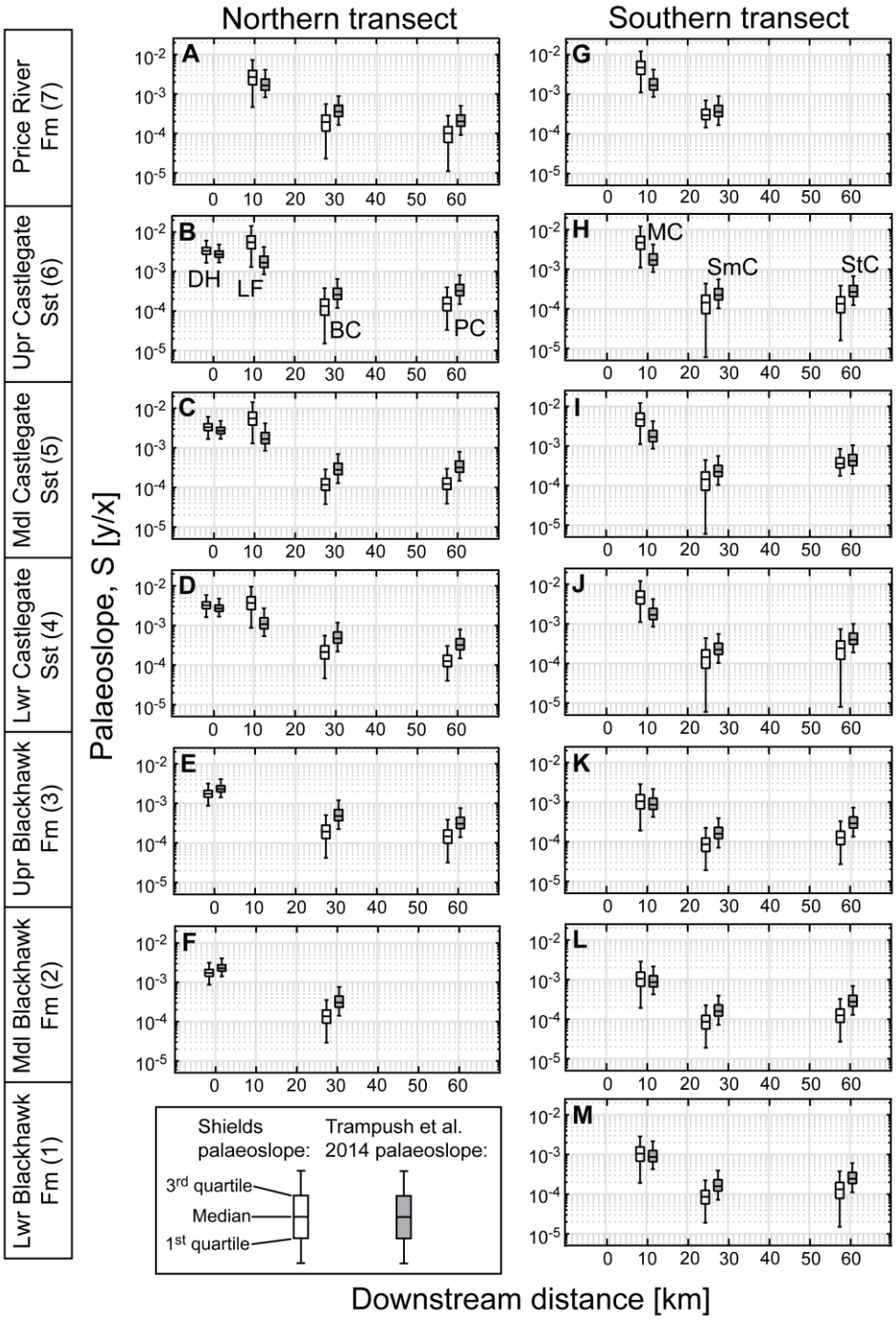

Figure 3.7 | Proximal to distal palaeoslope estimates for the defined northern and southern transects, using bulk grain-size data, for each stratigraphic interval (1–7), where possible. Parts **A–F** represent proximal to distal palaeoslopes for the northern transect, from the middle Blackhawk Formation to the Price River Formation. Parts **G–M** represent proximal to distal palaeoslopes for the southern transect, from the lower Blackhawk Formation to the Price River Formation. The central mark of each box indicates the median estimate, and the bottom and top edges of each box indicate the 1st and 3rd quartiles (or 25th and 75th percentiles), respectively. The whiskers extend to the most extreme estimates that are not considered to be outliers. Palaeoslope estimates are derived from 2 independent approaches; boxes with no fill indicate estimates of palaeoslope derived using a Shields stress inversion (Equation 3.3) and boxes with grey fill indicate estimates derived from the method of Trampush et al. (2014) (Equation 3.4). BC = Bear Canyon; DH = Dry Hollow; LF = Lake Fork; MC = Mellor Canyon; PC = Price Canyon; SmC = Sixmile Canyon; StC = Straight Canyon.

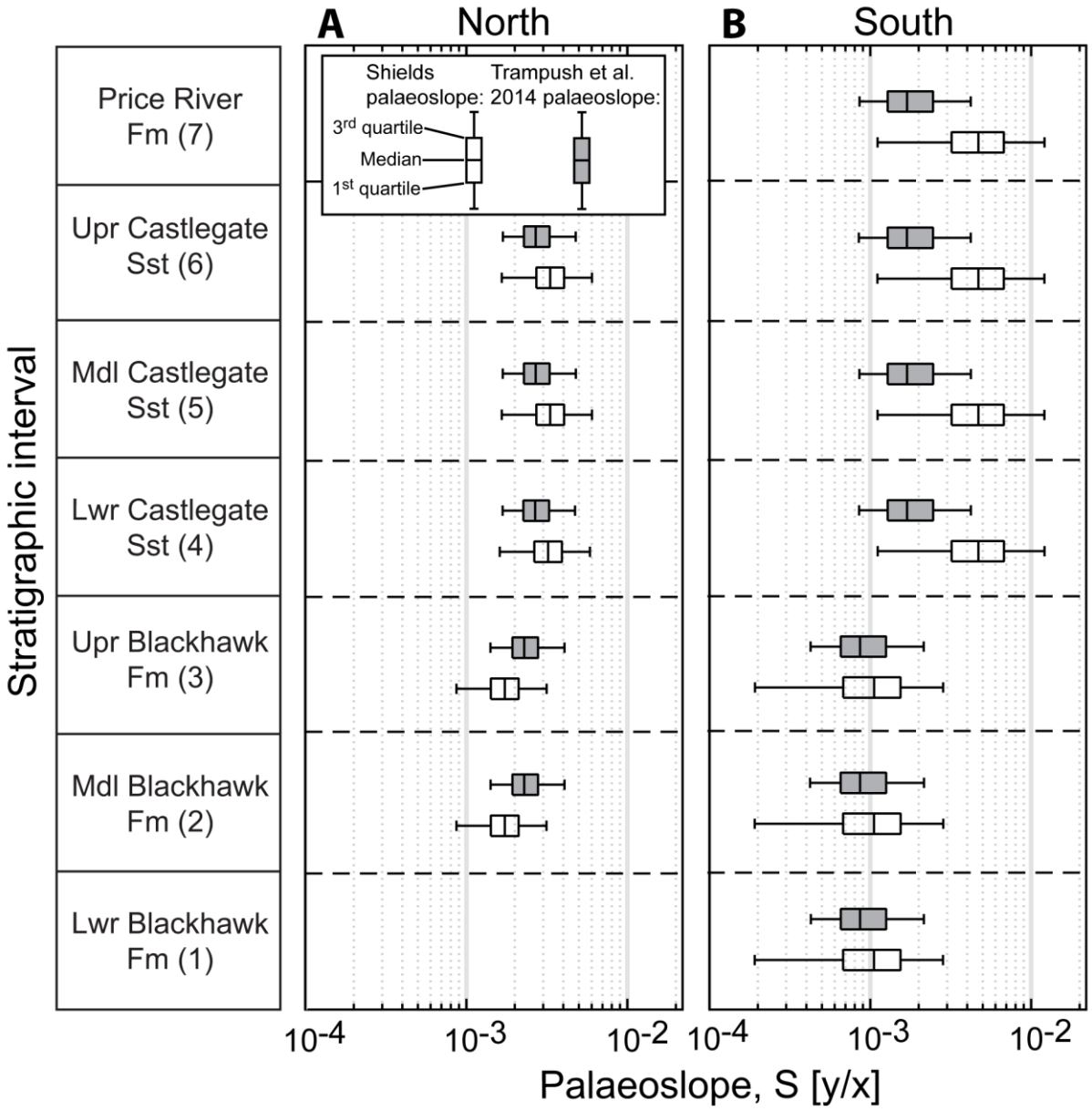

Figure 3.8 | Palaeoslope estimates for the most proximal location of the defined northern (part **A**) and southern (part **B**) proximal–distal transects, for each stratigraphic interval (1–7), where possible, using bulk grain-size data. The central mark of each box indicates the median estimate, and the edges of each box indicate the 1st and 3rd quartiles (or 25th and 75th percentiles) of estimates. The whiskers extend to the most extreme estimates that are not considered to be outliers. Palaeoslope estimates are derived from 2 independent approaches; boxes with no fill indicate estimates of palaeoslope derived using a Shields stress inversion (Equation 3.3) and boxes with grey fill indicate estimates derived from the method of Trampush et al. (2014) (Equation 3.4).

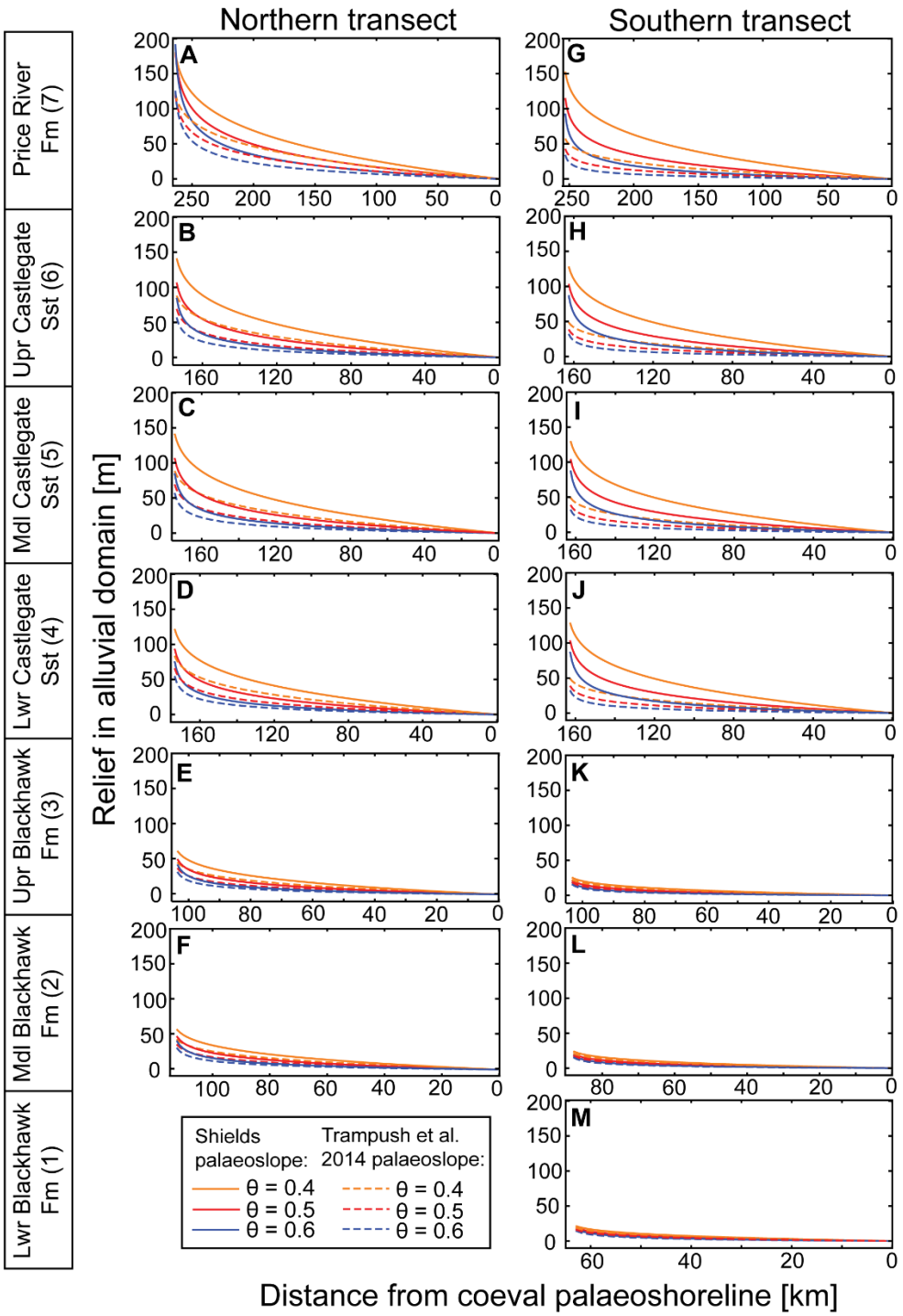

Figure 3.9 | Estimated palaeorelief in the alluvial domain for the defined northern and southern transects, using bulk grain-size data, for each stratigraphic interval (1–7), where possible. Parts **A–F** depict estimated alluvial palaeorelief for the northern transect, from the middle Blackhawk Formation to the Price River Formation. Parts **G–M** depict estimated alluvial palaeorelief for the southern transect, from the lower Blackhawk Formation to the Price River Formation. Alluvial palaeorelief estimates are derived using palaeoslope estimates from 2 independent approaches; palaeoslopes from a Shields stress inversion (Equation 3.3) and palaeoslopes from the method of Trampush et al. (2014) (Equation 3.4). In addition, alluvial palaeorelief is estimated using a plausible range of values for the concavity index, θ. Unlike other proximal–distal transects depicted in this study, the x axis instead depicts distance from the coeval palaeoshoreline (following Hettinger and Kirschbaum, 2002; Hampson et al., 2012; Hampson et al., 2013).

3.4.3 Hydrodynamics and sediment transport

Median flow velocities of 0.8 m/s, with a median plausible range of 0.4–1.6 m/s, are deduced across all field data (Figure 3.10a), as well as median unit discharges of 2.5 m^2/s with a median plausible range of 1–10 m^2/s (Figure 3.10b). Using plausible single-thread channel widths of 100–500 m at more distal locations (see *Planform morphologies*), this would imply median total discharges between 250–1250 m^3/s, which is comparable with total discharges of well-known North American rivers such as the Platte, Hudson, Colorado, Arkansas, and Susquehanna. However, if multi-thread rivers are assumed to possess >1 branch/braid, total discharges would have been several times greater. With a reconstructed increase in palaeoslope at the Blackhawk–Castlegate transition, a coeval increase in flow velocities and unit water discharges is expected analytically. Here, across all proximal field areas, flow velocities are overall greater during Castlegate Sandstone deposition, up to a factor of 2 to 3 (Figure 3.10c), relative to Blackhawk Formation deposition, whereas, at distal field areas, flow velocities are broadly the same through time (Figure 3.10d). At both proximal and distal field areas, unit water discharges overall do not change at the Blackhawk–Castlegate transition (Figure 3.10e,f). To offer a specific example for the Blackhawk–Castlegate transition (intervals 3 and 4), at Mellor Canyon, median flow velocity, U, increased from 1.9 to 3.0 m/s, and median unit water discharge, Q, only increased marginally from 4.4 to 4.6 m^2/s.

Reconstructed Rouse numbers, Z, indicate that dominant transport modes of bed-material varied in space and time (Figure 3.11). Proximal field sites consistently exhibit high Z values for both the median and 1st–3rd interquartile range, indicating predominant bedload transport (Figure 3.11). Median Z values then decrease by a downstream distance of 30 km, indicating local transition to predominantly mixed load systems, however the likely spread of values indicated by the interquartile ranges implies that dominant transport modes at this downstream distance may have spanned both mixed load and a near entirely suspended load (Figure 3.11). A crucial exception to this observation is for Castlegate Sandstone deposition in the southern transect (intervals 4–6) where, at a downstream distance of 30 km, median Z values suggest bedload remains the most important transport mode (Figure 3.11g–i). At downstream distances associated with the most distal field sites, median Z values have further decreased, however 1st–3rd interquartile ranges mostly still span both the mixed load and entirely suspended load domains.

The inferred dominant sediment transport modes are corroborated with results in Figure 3.12, in which Shields stress, τ^*, is plotted as a function of particle Reynolds number, Re_p, for each field site. These data are plotted alongside observed data that are characteristic of suspended load, mixed load, and bedload regimes (Leopold & Wolman, 1957; Schumm, 1968; Chitale, 1970; Church & Rood, 1983; Andrews, 1984). Proximal field sites (Dry Canyon, Lake Fork, Mellor Canyon) plot among secondary data that are typical for bedload rivers, meanwhile all other field sites plot in the mixed-load realm (Figure 3.12). Of field sites dominated by a mixed load, data from Sixmile Canyon and Straight Canyon plot closest to the bedload realm, which is consistent with observations in Figure 3.11, where results suggest that bedload transport remained important in the southern transect during Castlegate Sandstone deposition (intervals 4–6).

Overall, results in Figure 3.12 suggest that, downstream, field sites are firmly in the mixed load range — it is unlikely that bed-material loads were predominantly suspended. In contrast, the 1st–3rd interquartile ranges in Figure 3.11 suggest that dominant sediment transport modes may have spanned the mixed load/predominantly suspended domain. Downstream, all field sites straddle the bounds between the stability fields for ripples and dunes and upper-stage plane beds (Figure 3.12), which implies unidirectional flow and high sediment transport rates (both suspended transport and bedload transport).

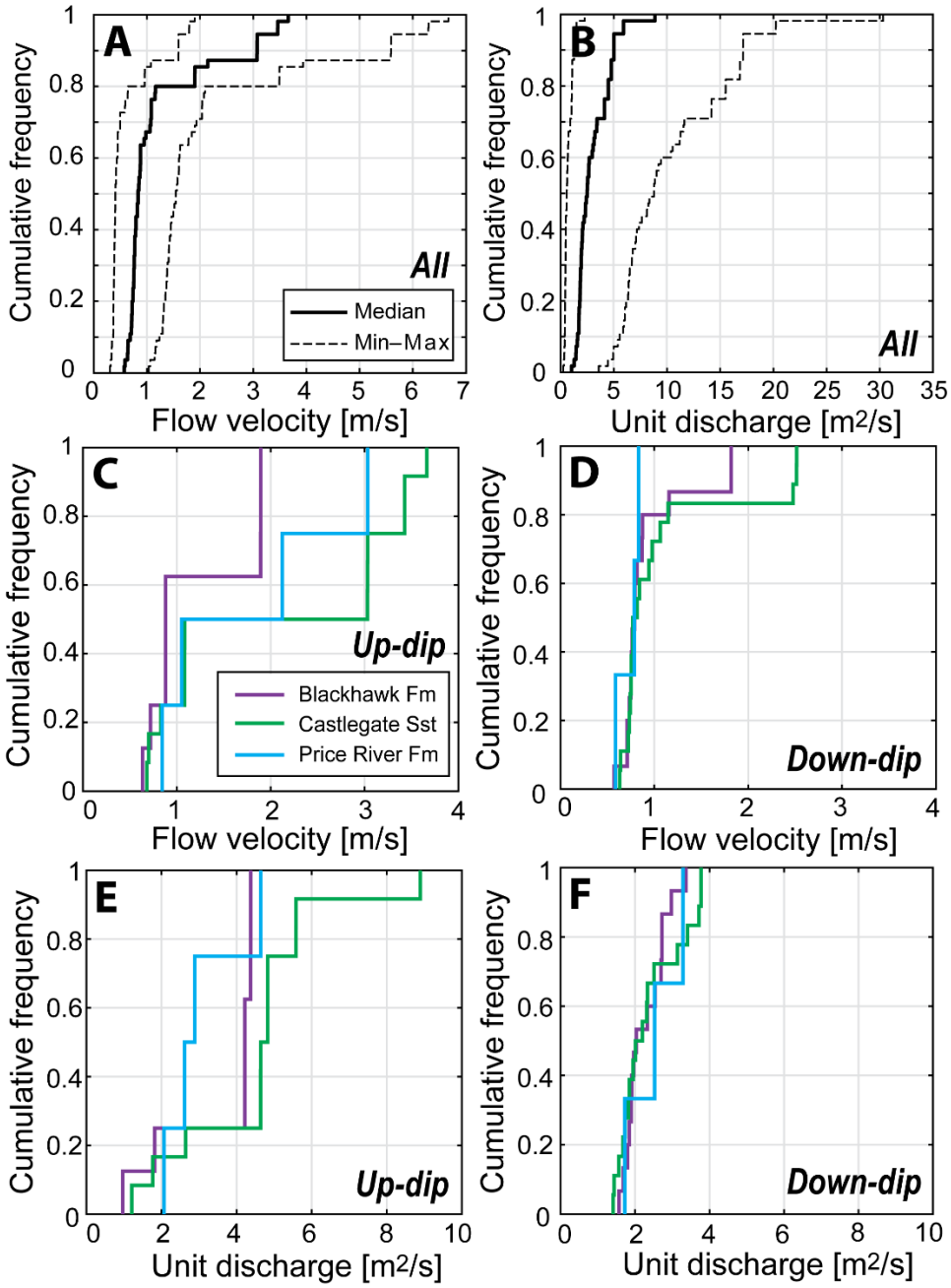

Figure 3.10 | Cumulative frequency distributions of (part **A**) reconstructed flow velocities across all field areas and (part **B**) reconstructed water discharges, per unit width, across all field areas. Solid lines indicate median values and dashed lines indicate plausible minimum and maximum values for the median, derived from propagated uncertainty margins. Flow velocities are derived using Manning's formula (Equation 3.7), as described in the Methods section. Parts **C–F** depict flow velocities and unit water discharges split into proximal (up-dip) and distal (down-dip) field sites. Distal field areas include field areas on the along-strike depositional transect (Price Canyon, Wattis Road, Straight Canyon, Link Canyon, and Salina Canyon), meanwhile proximal field areas include all those that are relatively proximal (Dry Hollow, Lake Fork, Bear Canyon, Mellor Canyon, and Sixmile Canyon). Field areas were also split into the Blackhawk Formation (and proximal equivalents, i.e., intervals 1–3), Castlegate Sandstone (and proximal equivalents, i.e., intervals 4–6), and Price River Formation (and proximal equivalents, i.e., interval 7). Parts **C** and **D** depict cumulative frequency distributions of reconstructed flow velocities for proximal (part **C**) and distal (part **D**) field areas, respectively. Parts **E** and **F** depict cumulative frequency distributions of reconstructed unit water discharges for proximal (part **E**) and distal (part **F**) field areas, respectively.

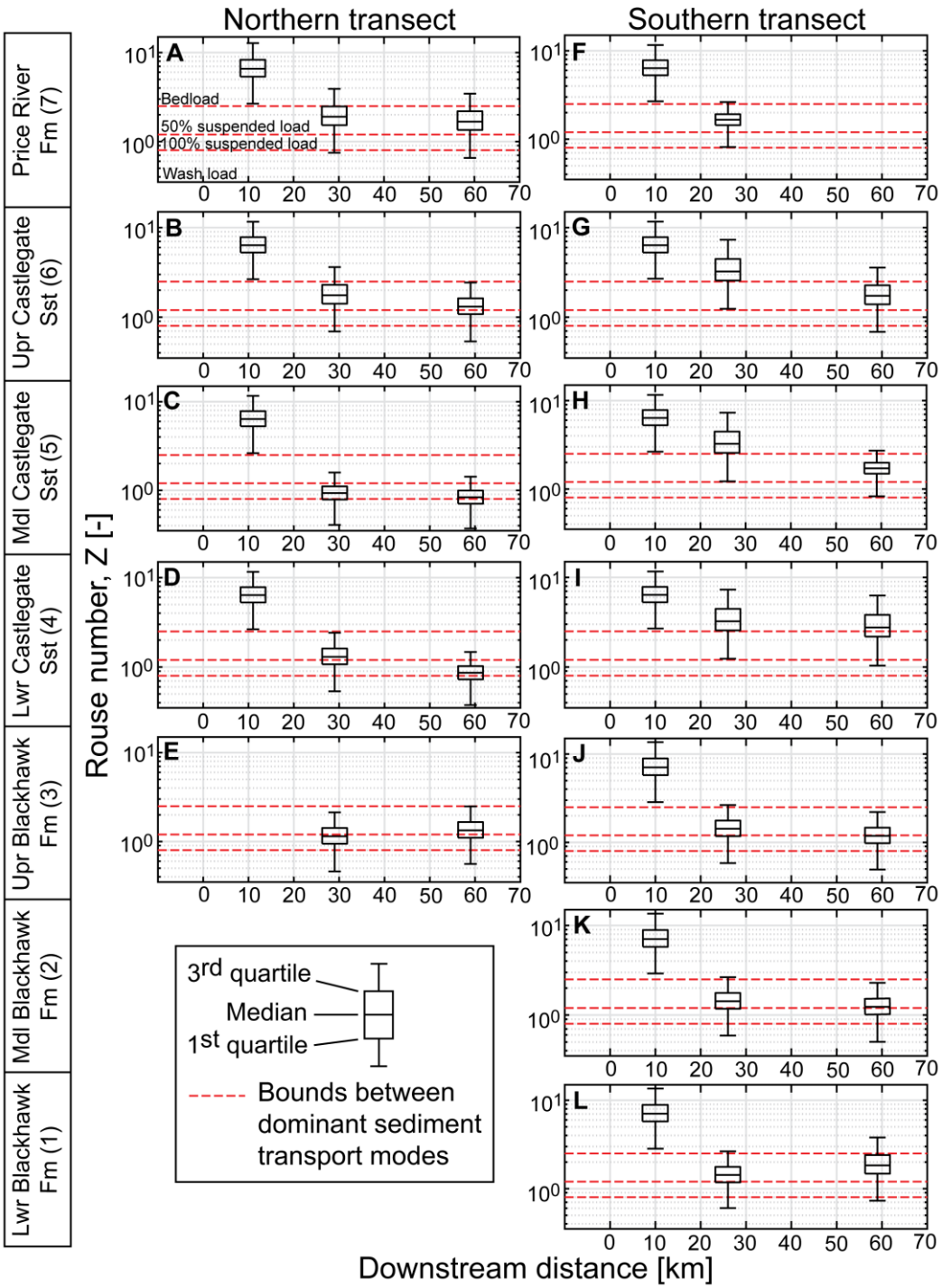

Figure 3.11 | Estimated Rouse numbers, *Z*, for the defined northern and southern transects, using bulk grain-size data, for each stratigraphic interval (1–7), where possible. Dominant mode of sediment transport is typically wash load for $Z < 0.8$, 100% suspended load for $0.8 < Z < 1.2$, 50% suspended load (i.e., mixed load) for $1.2 < Z < 2.5$, and bedload for $Z > 2.5$. Parts **A–E** represent proximal to distal Rouse numbers for the northern transect, from the upper Blackhawk Formation to the Price River Formation. Parts **F–L** represent proximal to distal Rouse numbers for the southern transect, from the lower Blackhawk Formation to the Price River Formation. The central mark of each box indicates the median estimate, and the bottom and top edges of each box indicate the 1st and 3rd quartiles (or 25th and 75th percentiles), respectively. The whiskers extend to the most extreme estimates that are not considered to be outliers. Dashed red lines indicate the bounds between differing dominant sediment transport modes, as labelled in part **A**.

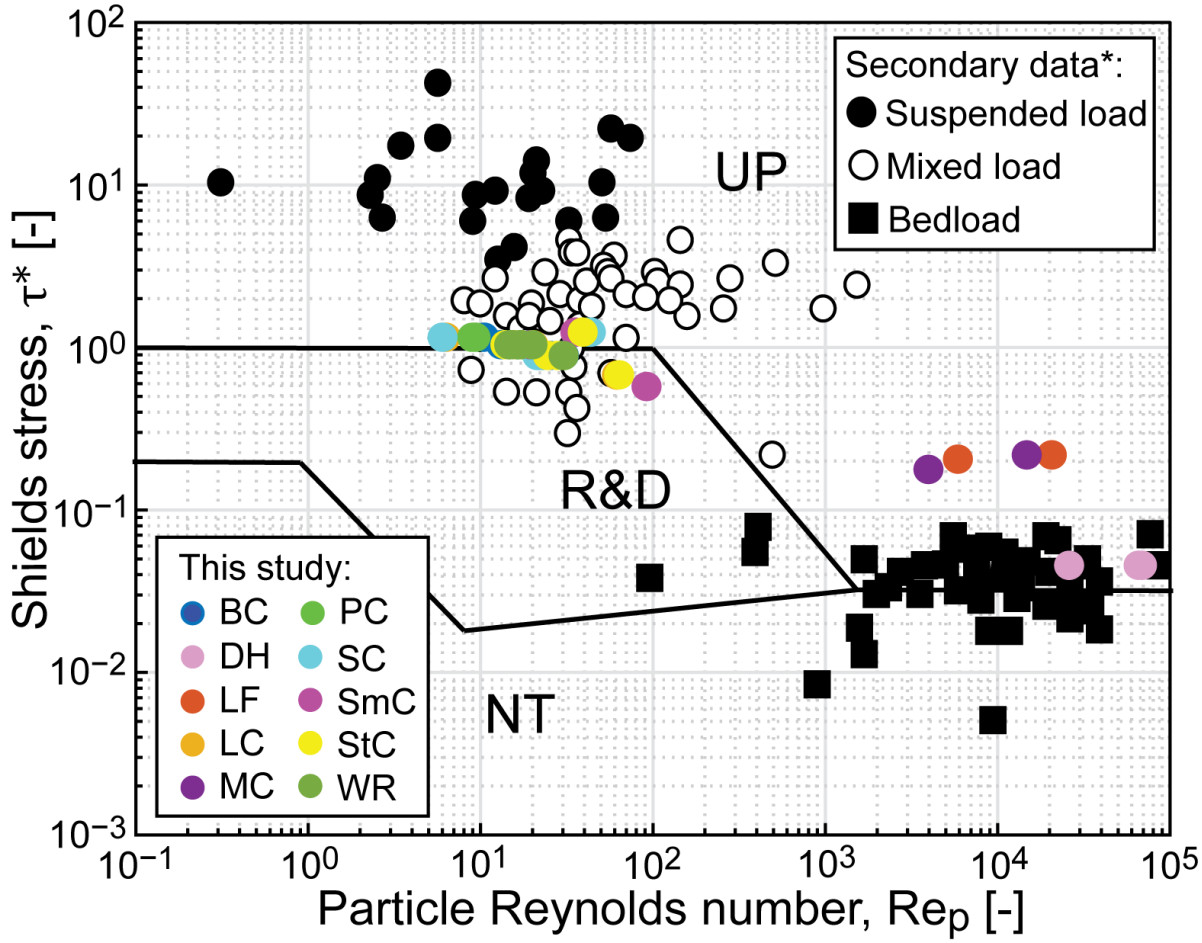

Figure 3.12 | Shields stress, τ^*, plotted as a function of particle Reynold's number, Re_p, for all field sites and for each stratigraphic interval (1–7), where possible, using bulk grain size data. Colour-filled circles indicate field results from this study for Bear Canyon (BC), Dry Hollow (DH), Lake Fork (LF), Link Canyon (LC), Mellor Canyon (MC), Price Canyon (PC), Salina Canyon (SC), Sixmile Canyon (SmC), Straight Canyon (StC) and Wattis Road (WR). *For comparison, this plot includes secondary data, originally compiled by Dade and Friend (1998), from Leopold and Wolman (1957); Schumm (1968); Chitale (1970); Church and Rood (1983); Andrews (1984), for characteristic dominant transport modes. Black squares indicate bedload, white circles indicate mixed load, and black circles indicate suspended load. Solid black lines indicate stability fields of different flow regimes: no sediment transport (NT), ripples and dunes (R&D) and upper-stage plane beds (UP), in line with Allen (1982a, 1982b).

3.4.4 Planform morphologies

Finally, these data provide insights into the implied planform morphology of these ancient fluvial systems. However, to do this effectively estimates of palaeochannel widths are needed. Widths are difficult to constrain with confidence from field observations and estimates from empirical scaling relations are tentative. Assuming single-thread channels, reconstructed median flow depths of 2–4 m might suggest channel widths of order 30–110 m and, using the upper bound of the 1–7 m range, widths up to ~300 m (following Bridge and Mackey, 1993). In contrast, if multi-thread channel belts are assumed, then channel belt widths of order 90–200 m, and up to ~400 m, might be expected (following Leopold and Maddock Jr, 1953).

For a range of possible widths, palaeoslope/Froude ratios were plotted against channel depth/width ratios (cf. Parker, 1976; Ganti, Whittaker, et al., 2019) (Figure 3.13). Results imply that, for Blackhawk–Castlegate–Price River fluvial systems, single-thread planforms would be stable at channel widths <1 km; channel and channel-belt widths >1 km would have been required to instigate formation of bars and support transition to multi-thread systems, forming vast channel-belt complexes (Figure 3.13a–d). However, planform reconstructions are very dependent on grain-size, a factor which is often not evaluated systematically. Bulk grain-sizes were used in initial calculations (Figure 3.13a–d; see *Methods*). However, when using gravel-fraction grain-sizes, which can be associated with tectonic or climatic perturbations (e.g., increased palaeoslope or high-magnitude low-frequency discharge events), the results show that multi-thread planforms were more likely (Figure 3.13e–h). For gravel-fraction grain-sizes, results imply that single-thread planforms were likely stable at channel widths <500 m, and that channel and channel-belt widths >500 m would have supported transition to multi-thread systems (Figure 3.13b).

Of the Blackhawk–Castlegate–Price River fluvial systems, field results for the Castlegate Sandstone plot closest to the single-thread–multi-thread transition, whereas field results for the Price River Formation plot furthest from this transition (Figure 3.13). This indicates the relatively high propensity of Castlegate fluvial systems to braiding, relative to Blackhawk and Price River systems.

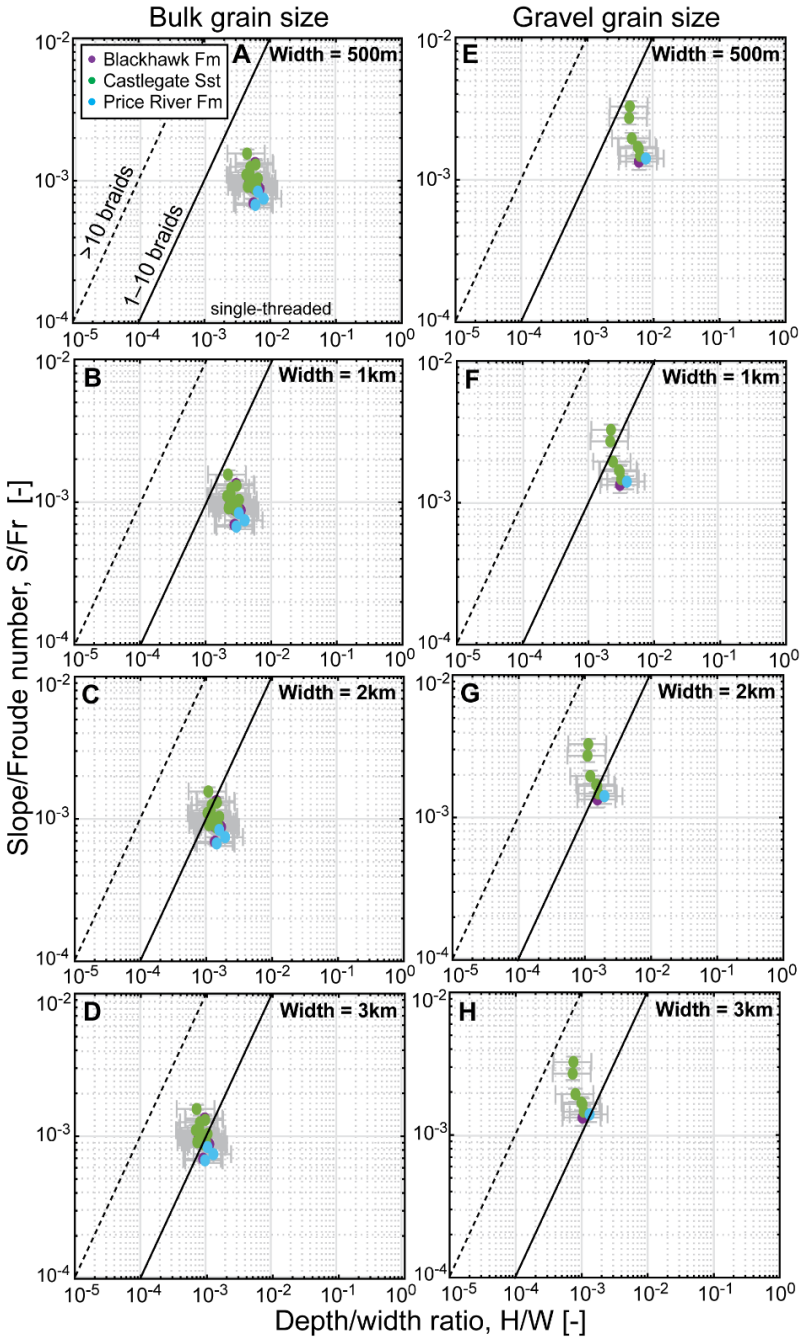

Figure 3.13 | Theoretical stability fields of fluvial planform morphologies, i.e., single-thread and multi-thread planforms, for both bulk grain-sizes (parts **A–D**) and gravel fraction grain-sizes (parts **E–H**), where present (not all field localities possessed a gravel fraction). For both bulk and gravel grain-size fractions, a range of river widths are assumed (500 m, 1 km, 2 km, and 3 km) and used to calculate the depth/width ratio. Data points are for all localities, in space and time, along the defined along-depositional strike transect, i.e., these data points represent the five parallel fluvial systems and do not consider more proximal localities. Data are further subdivided into the Blackhawk Formation (intervals 1–3), Castlegate Sandstone (intervals 4–6), and Price River Formation (interval 7). Coloured markers indicate the median value and error bars represent plausible minimum and maximum values for the median, derived from propagated uncertainty margins. Solid black lines indicate the bounds of each stability field, and therefore the predicted transition from single-thread (straight/meandering) to multi-thread (anabranching/braided) planform morphology. Dashed black lines indicate a potential transition from 1–10 threads to >10 threads, based on modern data (Parker, 1976).

3.5 Discussion

3.5.1 What did Campanian palaeorivers look like?

These analyses provide new insights that build on previous work characterising ancient rivers in the Campanian of central Utah as a series of distinct parallel transverse systems draining the Sevier front (Robinson & Slingerland, 1998; Bartschi et al., 2018; Chamberlin & Hajek, 2019; Pettit et al., 2019). These rivers traversed a low-gradient landscape; alluvial palaeorelief was 10s of metres to c. 100 m, and the length scale of the alluvial domain (i.e., the distance from fan apexes to the palaeoshoreline) varied from as little as ~70 km during lower Blackhawk Formation deposition, up to and in excess of 250 km during Price River Formation deposition (Hettinger & Kirschbaum, 2002; Aschoff & Steel, 2011b; Hampson et al., 2012; Hampson et al., 2013). Alluvial palaeorelief was 10s of metres during Blackhawk deposition, when the length scale of the alluvial domain was at its narrowest. At the onset of Castlegate Sandstone deposition an increase in palaeoslope is documented, with alluvial palaeorelief increasing to c. 100 metres, which persisted into Price River deposition (Figures 3.7–3.9). For comparative purposes, such values of palaeoslope and alluvial palaeorelief are characteristic of the Mississippi river and downstream reaches of its principal tributaries e.g., the Missouri, Tennessee, Arkansas, and Red rivers (Carlston, 1969; Fernandes et al., 2019).

Results imply that palaeoriver morphologies were similar in space and time, with palaeoflow depths of order 2–4 m (Figure 3.6). Previous detrital zircon results suggest that northerly field sites (Price Canyon and Wattis Road) represent smaller transverse systems and that southerly field sites (Straight Canyon, Link Canyon, and Salina Canyon) represent larger systems that include a longitudinal drainage component (Bartschi et al., 2018; Pettit et al., 2019). These results indicate that size disparities between these 5 systems were not statistically significant — reconstructed variations in palaeoflow depths are within the full range of plausible values. However, palaeoflow depths appear to have been marginally greater in southerly systems (Figure 3.6). If true, this may be attributed to the possible longitudinal drainage component (Bartschi et al., 2018; Pettit et al., 2019).

Comparisons with modern rivers suggest that these 5 parallel palaeorivers (being ~25 km apart) were substantial systems. Reconstructed hydrodynamic properties, such as flow velocities and unit water discharges, are consistent with the ranges of values of modern systems with similar outlet spacings and similar distances to range fronts (Perry et al., 1996; Schulze et al., 2005; Milliman & Farnsworth, 2013; Global Runoff Data Centre). Notably, unit discharges are overall constant in time — there is no apparent increase in unit discharge at the Blackhawk–Castlegate transition (coeval with palaeoslope increase). This raises questions as to the nature of down-system width evolution and has implications for total discharge — plausible single-thread river widths of 100–500 m at distal locations would imply median total discharges of 250–1250 m^3/s.

Bedload transport was dominant at gravel-dominated upstream localities, as expected, and suspended- and mixed-load systems prevailed further downstream, with some localised variations (Figures 3.11, 3.12). For

example, results highlight the importance of bedload transport during Castlegate Sandstone deposition in the southern transect (Figures 3.11, 3.12). With this information it is possible to map out how river behaviour varied spatially within catchments, and this informs best practices when it comes to reconstructing sediment discharges. This is especially important where interested in reconstructing the entire sediment load of an ancient system. For instance, channel palaeohydrologic approaches are often used to reconstruct sediment discharges in ancient source-to-sink systems (Holbrook & Wanas, 2014; Lin & Bhattacharya, 2017; Sharma et al., 2017), however these reconstruction tools solely reconstruct the bedload fraction and the suspended fraction of the bed material load (van Rijn, 1984b; Wright & Parker, 2004), i.e., the portion of the suspended load that interacts with the bed. As such, these reconstruction tools are not appropriate, by themselves, for reconstructing the total sediment load of a wash load-dominated system, for example. Knowledge of prevailing sediment transport modes is important for evaluating whether different sediment discharge reconstruction methods are consistent with one another, as studies that reconstruct sediment discharges often corroborate results with an independent approach (Lin & Bhattacharya, 2017; Watkins et al., 2018; Zhang et al., 2018; Brewer et al., 2020; Chapter 2 (Lyster et al., 2020)).

Here, reconstructions of planform morphology, following Parker (1976), and assuming channel widths <1 km, imply that single-thread rivers would have prevailed throughout Blackhawk–Castlegate–Price River deposition. Localized or intermittent transitions to braided planforms may have been associated with tectonic or climatic perturbations, such as increased palaeoslope or high-magnitude, low-frequency discharge events (Figure 3.13). In detail, these perturbations (which can be associated with the gravel-fraction grain-size) can support braiding at narrower channel/channel-belt widths of order 500 m. Of these fluvial systems, Castlegate systems had a higher propensity to braiding. At this point, it is important to flag that traditional bipartite classification of fluvial systems aims to define fluvial systems as either straight/meandering or braided/anabranching end members (Leopold & Wolman, 1957). However, these are not mutually exclusive; both straight/meandering and braided/anabranching planforms can co-exist at reach scales. These reconstructions can be contextualised by field evidence; however, field observations point to a discrepancy and this topic is returned to in the final discussion section.

To create a holistic view as to the nature of these ancient fluvial landscapes, various modern analogues can be considered. In the Amazon basin, several of the most up-system tributaries axially drain the central and eastern Andean cordillera. For example, the Huallaga River, Peru, is an axial river fed by transverse systems draining the eastern Andean range front. These transverse rivers have regular outlet spacings, channel-belt widths of order 100s of metres (up to 1 km) and combine both single- and multi-thread planforms which vary at reach-scales. In the eastern Himalayas, transverse systems draining the range front into the axial Brahmaputra (Assam Valley) provide another modern analogue for the pattern and style of these ancient fluvial systems, despite the larger scale of this system.

3.5.2 What drove spatio-temporal changes in morphologic properties?

A key result in this study is quantification of an increase in palaeoslope at the Blackhawk–Castlegate transition by a factor of 1.5–4, as well as the associated increase in alluvial palaeorelief (Figures 3.7–3.9). Increased palaeoslopes have implications for the morphologic and hydrodynamic properties of these palaeorivers, including their flow velocities and unit discharges. In this study, the increase in palaeoslope and alluvial palaeorelief implies that rivers were actively responding to changes in uplift rate in the hinterland region.

At the Blackhawk–Castlegate transition, alluvial palaeorelief increased from 10s of metres to c. 100 m (Figure 3.9). An important point to remember is that these estimates are specific to the alluvial domain only. Behind the Sevier front, existence of a high-elevation plateau known as "Nevadaplano" is inferred (Allmendinger, 1992; DeCelles, 1994, 2004; DeCelles & Coogan, 2006), which has been likened to the modern high-elevation plateau, Altiplano, of the central Andes. Palaeo-elevations in the Sevier highlands and Nevadaplano are argued to be 3 to >4 km — these values have been deduced from a combination of climate modelling studies (Sewall & Fricke, 2013; Foreman et al., 2015), kinematic reconstructions (DeCelles, 1994, 2004; DeCelles & Coogan, 2006) and other data, including palaeoflora (Chase et al., 1998). Here, alluvial palaeorelief of order 100 m is reconstructed. Given that the low-lying alluvial domain of these palaeorivers has a length scale of order 70–250 km, and given proximity to high-elevation Sevier highlands, the entire river long profile is inferred to have likely been highly concave. This is supported in part by the fact that, in reconstructing palaeoslope profiles, the best fits were recovered when using a higher reference concavity of 0.6 (Appendix Table B6). If best-fit palaeoslope profiles were projected upstream into the Sevier hinterland, palaeoslopes of 10^{-1} might be reached within as little as 10 km of the most proximal field area, and therefore elevations in excess of 1 km might be reached within a further 10 km. To again use the modern Andes as an analogue, a longitudinal river profile from the Peruvian shoreline to the western Andean cordillera and Altiplano would have a length scale of 50–150 km, with 0.5–1 km of relief in the alluvial domain and elevations >3 km in the western cordillera and Altiplano. With a similar tectono-geographic setting in Late Cretaceous Utah, this comparison can also be used to highlight the potential high concavity of these ancient river profiles.

In reconstructing alluvial palaeorelief, steepness indexes, k_s, were also recovered for northern and southern transects (Equations 3.5 and 3.6) (Appendix Table B6). While k_s was solved for using field data and a nonlinear least squares regression, k_s values are often estimated (albeit tenuously) as a function of known uplift rate and erodibility in bedrock channels, but additionally (although less frequently) in downstream alluvial reaches (Kirby & Whipple, 2012; Pederson & Tressler, 2012; Stucky de Quay et al., 2019). Inversely, where k_s can be measured, and where erodibility is known, first-order estimates of uplift rate can be made. Steepness indexes recovered in this study were typically ~5–35 m (for a reference concavity, θ, of 0.5) and, despite unknown erodibility, global data compilations indicate that low uplift rates of order 0.01–0.1 mm/yr are generally associated with these kinds of values (Kirby & Whipple, 2012). Despite overall low k_s values,

it is important to note the relative increase in k_s by a factor of <1.5 to 5 at the Blackhawk–Castlegate transition. While these are first-order estimates, and are derived solely for the alluvial domain, an increase in k_s (and alluvial palaeorelief) can be attributed to a relative increase in uplift rate in the hinterland region. Here, this increase might be attributed to frontal thrust migration, or thrust initiation in the Sevier highlands (DeCelles, 2004; DeCelles & Coogan, 2006). This includes Sevier shortening in the Charleston–Nebo Salient (CNS), an eastward convex portion of the Sevier thrust front in north-central Utah (Figure 3.1b) (Bruhn et al., 1986; Bryant & Nichols, 1988; Constenius et al., 2003; Bartschi et al., 2018), which is commonly attributed to the influx of quartzite-dominated coarse-grained detritus associated with Castlegate Sandstone progradation (Robinson & Slingerland, 1998; Horton et al., 2004). For Castlegate Sandstone deposition in the northern transect, results show that palaeoslope profiles did not fit reconstructed palaeoslopes well and favoured lower concavities (which also did not fit well). Our interpretation is that shortening in the CNS, which has been structurally linked with coeval basement Laramide uplifts in northern Utah (Bruhn et al., 1986; Bryant & Nichols, 1988; Constenius et al., 2003; Bartschi et al., 2018), may have significantly influenced river long profiles associated with northerly Castlegate fluvial systems near Price, and locally lowered their concavities. Whereas ~60 km south in the southern transect, higher concavity values of 0.6 deliver best fitting palaeoslope profiles through all 7 stratigraphic intervals (Appendix Table B6).

While tectonic drivers are commonly attributed to variations in channel steepness (Kirby & Whipple, 2001; Kirby et al., 2003; Wobus et al., 2006; Boulton & Whittaker, 2009; DiBiase et al., 2010), climatic drivers, especially precipitation rates, also play a crucial role but are notoriously difficult to disentangle from their tectonic counterpart (Wobus et al., 2010; DiBiase & Whipple, 2011; Champagnac et al., 2012; Whittaker, 2012; D'Arcy & Whittaker, 2014). The role of climate is important to consider here, given the assumed monsoonal climate and, therefore, highly seasonal discharge variability (Roberts, 2007; Roberts et al., 2008; Fricke et al., 2010; Sewall & Fricke, 2013). Previous work shows that precipitation rates have a discernible role on steepness indexes (Champagnac et al., 2012; D'Arcy & Whittaker, 2014); analytically, an increase in channel steepness and palaeoslope can be attributed to a decrease in precipitation rate (to maintain similar total water discharge) (D'Arcy & Whittaker, 2014). To reduce palaeoslopes by a factor of 2 precipitation rate must typically be quadrupled (D'Arcy & Whittaker, 2014). Despite the supposed warm and wet climate (Parker, 1976b; Kauffman & Caldwell, 1993; Roberts & Kirschbaum, 1995), few workers have argued for, or investigated, the possibility of increased aridity at the Blackhawk–Castlegate transition (van Wagoner, 1995; Adams & Bhattacharya, 2005). In theory, increased palaeoslopes can be explained by decreased precipitation (D'Arcy & Whittaker, 2014), however, here, no decrease in either flow velocities or unit discharges is reconstructed at the Blackhawk–Castlegate transition (Figure 3.10). Generally, at more distal locations, flow velocities and unit discharges are constant across this interval (Figure 3.10d,f). At more proximal field sites, however, flow velocities are overall slightly greater during Castlegate Sandstone deposition relative to Blackhawk Formation deposition, but unit discharges remain similar for both.

With unit discharges constant in space and time, the crucial unknown is palaeochannel width. At minimum, channel widths can be considered as broadly the same across the Blackhawk–Castlegate transition. During Blackhawk Formation deposition, channelized sandbody widths of order 350–420 m offer a maximum limit on palaeochannel widths (Hampson et al., 2013; Flood & Hampson, 2015). Meanwhile, during Castlegate Sandstone deposition, bar package widths are between ~60–180 m (Chamberlin & Hajek, 2019); assuming 2–3 threads, these bar widths might imply channel belt widths of order half a kilometre. However, planform stability estimates based on Parker (1976) indicate that these rivers could have possessed anywhere between 1–10 threads (Figure 3.13), which could result in channel-belt widths up to and in excess of 1 km. At maximum, this implies increased channel widths at the Blackhawk–Castlegate transition. Unless a significant decline in river widths is projected, then field results do not directly support a climatic driver. Consequently, our interpretation is that increased channel steepness and palaeoslope at the Blackhawk–Castlegate transition is due to tectonically driven uplift in hinterland regions.

3.5.3 Effectiveness of palaeohydrological and palaeomorphological reconstructions

While quantitative reconstructions have led to significant advances in both the quantity and level of detailed information that can be extracted from fluvial strata (e.g., Ganti, Whittaker, et al., 2019), it is unclear how accurately these tools characterise ancient systems. Addressing this question is particularly important as sedimentology becomes increasingly numerical and it becomes easier to apply quantitative tools to stratigraphy (Duller et al., 2010; Whittaker et al., 2011; Holbrook & Wanas, 2014; Ganti, Whittaker, et al., 2019). With extensive existing work on Late Cretaceous fluvial systems of central Utah, results in this study offer a unique opportunity to highlight consistencies and discrepancies between quantitative interpretations of fluvial palaeohydrology and more qualitative field-based facies and architectural interpretations.

To first order, whether point reconstructions of various morphologic and hydrodynamic parameters agree with qualitative interpretations can be evaluated using independent proxies (derived from field measurements or facies interpretations). As previously mentioned, reconstructed flow depths agree with several secondary observations of bar heights (Adams & Bhattacharya, 2005; Lynds & Hajek, 2006; McLaurin & Steel, 2007; Hajek & Heller, 2012; Chamberlin & Hajek, 2019) (Appendix Table B4), which can be used as a direct proxy for flow depth (Bridge & Tye, 2000; Hajek & Heller, 2012). This agreement indicates that the uncertainty estimator in Equation 3.2 is reasonable, and that cross-set heights can therefore be used to reconstruct reasonable flow-depth constraints and are useful as a bedform-scale approach. Such an approach is particularly useful in core data, locations with limited outcrop exposure, or deposits where the degree of bar preservation is poor. It is noted that scaling relations that relate cross-set heights with original bedform heights (and subsequently formative flow depths) are derived from theory and experiments that assume statistical steady state, in which flow is constant (Paola & Borgman, 1991; Leclair, 2002; Jerolmack & Mohrig, 2005). As such, agreement of flow depth reconstructions with bar heights might therefore imply that these dunes were formed in steady flow conditions (Ganti et al., 2020).

This contrasts with literature that alludes to the preferential preservation of dunes in unsteady flow conditions (Reesink & Bridge, 2007; Reesink & Bridge, 2009; Reesink et al., 2015; Leary & Ganti, 2020), and merits further work regarding the kinematic controls on dune preservation in this region.

For more complex palaeohydrologic reconstructions, such as palaeoslopes and alluvial palaeorelief (Figures 3.7–3.9), it is not possible to directly corroborate estimates with independent proxies derived from field data. Nevertheless, it is still possible to evaluate reconstruction tools by contrasting commonly used methods. In this study the first approach used a theoretically-based Shields stress inversion (Equation 3.3), whereas the second approach used the empirically-derived model (Equation 3.4) of Trampush et al. (2014). Palaeoslope estimates derived from each approach are in broad agreement with one another. Each method typically recovers estimates of the same order of magnitude — in many cases the interquartile ranges of values overlap, and, in all cases, the full ranges of plausible values overlap (i.e., the whiskers in Figure 3.7 and 8). These point comparisons between the 2 methods are promising, and in line with comparisons made elsewhere (e.g., Ganti, Lamb, et al., 2019). However, there are implications when larger spatial scales are concerned, imparting uncertainty that must be carried forward in interpretation of alluvial palaeorelief in the depositional reaches of these systems. Along the northern and southern transects, Shields stress inversion estimates consistently show higher differences in palaeoslope (i.e., higher slopes upstream and lower slopes downstream) relative to palaeoslopes derived from the Trampush et al. (2014) method. This difference is likely an outcome of the Trampush et al. (2014) method using a continuous function to estimate slope, whereas the Shields stress inversion relies on a step-change empirical estimate for gravel or sand-bed rivers. Regardless of the method used, palaeoslope reconstructions are dependent on grain-size and flow-depth estimates. Because flow depths did not appreciably change in Blackhawk and Castlegate palaeorivers, variations in reconstructed slopes and derivative estimates (e.g., water and sediment discharge) are largely driven by observed differences in grain-size.

Despite the differences of the 2 methodologies on alluvial palaeorelief, estimates of alluvial palaeorelief can be compared with relief in modern systems possessing similar tectono-geographic set-ups. Palaeorelief estimates between 50 and 100 m in depositional reaches of these ancient fluvial systems are reasonable when compared with relief in depositional reaches of modern systems with a similar tectono-geographic setting. For example, one can return to the Andean analogue, but cross over to the eastern Andean cordillera and into the foreland basin and low-lying plains of the Amazon River. For most of its course, the Amazon long profile has a relief of less than 100 m (Milliman & Farnsworth, 2013) — relief only exceeds 100 m in proximity to the range front (Milliman & Farnsworth, 2013).

Finally, these results complement field evaluation of the nature of Blackhawk Formation and Castlegate Sandstone planforms, but also raise new questions. Channelized sandstone bodies of the Blackhawk Formation are typically 350–420 m wide (Adams & Bhattacharya, 2005; Hampson et al., 2013; Flood & Hampson, 2015), although a small proportion are much larger and some exceed 1 km (Flood & Hampson, 2015). These sandstone bodies offer a maximum cap on palaeoflow width. The Blackhawk Formation is

considered to mostly represent single-thread systems, which results in this study agree with. However, there is significant field evidence that many channelized sandstone bodies of the Blackhawk Formation represent multi-thread systems with mid-channel bars, based on bar facies observations (Adams & Bhattacharya, 2005; Hampson et al., 2013; Flood & Hampson, 2015). Field observations of multi-thread Blackhawk fluvial systems of order 100s of metres are inconsistent with our results, which suggest multi-thread systems would not have been stable (Figure 3.13). Meanwhile, the Castlegate Sandstone is interpreted to be fully-braided from facies observations (Miall, 1993, 1994; Miall & Arush, 2001; McLaurin & Steel, 2007). Reported mean bar package widths of order 60–180 m for the Castlegate Sandstone (Chamberlin & Hajek, 2019) would imply total channel widths <1 km (assuming a few braids); our reconstructed planform stability estimates, which indicate that Castlegate systems should have been single-threaded, are again inconsistent with sedimentological facies and architectural interpretations. Other quantitative reconstructions of planform have contradicted traditional field-based facies observations (Ganti, Whittaker, et al., 2019), and these inconsistencies must be treated carefully. The main limitation to reconstructing ancient channel planforms is a lack of reliable methods for estimating palaeochannel widths. Interpreting palaeochannel planforms from facies associations and stratigraphic-architectural data is not trivial, particularly where outcrop is limited or where observations are equivocal. But, in this case, a number of workers have concluded that braided conditions prevailed at the time of Castlegate Sandstone deposition (Lawton, 1986b; Miall, 1994; van Wagoner, 1995; Miall & Arush, 2001) and occurred at times during Blackhawk Formation deposition (Adams & Bhattacharya, 2005; Hampson et al., 2013; Flood & Hampson, 2014, 2015). As such, it can be argued that further detailed work to test and reconcile facies-based and hydraulically derived interpretations of channel planforms is a pressing research goal.

3.6 Conclusions

Here a four-dimensional reconstruction of palaeohydrology in Late Cretaceous palaeorivers of central Utah, USA, is presented, using field data and a well-established quantitative framework. Overall, fluvial morphologies were similar in space and time, although marginally greater reconstructions of flow depths in southerly systems likely reflect the contribution of a longitudinal drainage component. The most prominent spatio-temporal change is an increase in palaeoslope at the Blackhawk–Castlegate transition by a factor of 1.5–4; this reflects an increase in palaeorelief (in the alluvial domain) from 10s of metres during Blackhawk Formation deposition up to, and in excess of, 100 m during Castlegate Sandstone deposition, which persisted into Price River Formation times. The observation that unit water discharges do not change at the Blackhawk–Castlegate transition does not support a climatically driven increase in palaeoslope and channel steepness. Results therefore point to a tectonically driven palaeoslope increase. In deciphering the relative role of tectonic and climatic drivers, the main limitation in this study is uncertainty in palaeochannel widths, which directly affect total water discharges. Palaeochannel width reconstructions therefore remain a prominent research challenge.

Results complement and expand on extensive facies-based interpretations of these systems, which offers unique opportunity to evaluate the efficacy of quantitative palaeohydrological reconstruction tools. Bedform-scale palaeoflow depth reconstructions are in good agreement with observations of preserved barforms. Moreover, while different palaeoslope reconstruction methods produce results that broadly agree, the results show that at larger spatial scales they over- and under-predict alluvial palaeorelief relative to one another, which has implications for quantifying alluvial palaeorelief and, therefore, the magnitude of change in alluvial palaeorelief at the Blackhawk–Castlegate transition. Finally, quantitative hydraulic reconstructions of planform somewhat disagree with facies-based interpretations. While this discrepancy ties back to uncertainty in palaeochannel widths, these results highlight that further work is required to reconcile hydraulically- and facies-based approaches in order to facilitate their application in the geological past.

CHAPTER 4: Field evidence for disequilibrium dynamics in preserved fluvial cross-strata: A record of discharge variability or morphodynamic hierarchy?[1]

ABSTRACT

Bedforms preserved in the rock record can provide detailed information on the morphologies and hydrodynamics of ancient fluvial systems on Earth and other planets. Existing process–product relations for bedform preservation assume that fluvial cross strata reflect conditions under which bedforms were equilibrated with the prevailing flow, i.e., steady-state conditions. However, recent theoretical and experimental observations indicate that enhanced bedform preservation can occur in non-steady state, or disequilibrium, conditions, and it is currently unclear how prevalent disequilibrium dynamics are in preserved fluvial strata at outcrop scale. Here we explore whether steady-state assumptions are appropriate for ancient fluvial systems by evaluating the nature of bedform preservation in well studied fluvial deposits of three Upper Cretaceous (Turonian and Campanian) geologic formations in central Utah, USA: the Blackhawk Formation, Castlegate Sandstone, and Ferron Sandstone. In the field, we made systematic measurements of dune-scale cross-strata to quantify the extent to which preserved cross-sets reflect dune preservation in steady-state conditions. Across the three formations, consistently low coefficients of variation in preserved cross-set thicknesses of 0.25–0.5 are inconsistent with bedform preservation in steady-state conditions, and instead point to fluvial systems in which enhanced bedform preservation occurred in disequilibrium conditions.

Enhanced bedform preservation in dune-scale cross-stratification can be explained by two independent hypotheses: the effect of flashy flood hydrographs on bedform preservation (*flood hypothesis*) or bedform preservation in the presence of larger migrating barforms (*hierarchy hypothesis*). We estimated bedform turnover timescales to quantitatively assess these competing hypotheses and contextualize their implications. Under the flood hypothesis, field measurements are consistent with enhanced bedform preservation driven by flashy flood hydrographs with flood durations ranging on the order of hours to a few days, which are consistent with perennial fluvial systems subject to heavy rains and tropical storms. Alternatively, under the hierarchy hypothesis, field measurements are consistent with bedform climb angles that range from 10^{-2} to 10^{-1}, reflecting rapid bar migration. Our work provides a novel way of investigating fluvial discharge variability in the geologic past, and we outline the potential next steps to disentangle the relative controls of flow variability and morphodynamic hierarchy in controlling bedform preservation in ancient fluvial systems.

[1] A version of this chapter is published in ***Earth and Planetary Science Letters***:

Lyster, S. J., Whittaker, A. C., Hajek, E. A., and Ganti, V. (2022) Field evidence for disequilibrium dynamics in preserved fluvial cross-strata: A record of discharge variability or morphodynamic hierarchy? ***Earth and Planetary Science Letters***, 579, 117355, DOI: 10.1016/j.epsl.2021.117355

4.1 Introduction

Quantitative reconstructions of palaeohydraulics from fluvial stratigraphy complement qualitative observations of sedimentary facies to build more complete pictures of palaeo-landscapes on Earth and other planets. In fluvial strata, preserved bedforms, which include ripples, dunes, and unit bars, are crucial to these reconstructions. Bedforms are readily formed on riverbeds across a range of grain sizes (e.g., Carling, 1999; Best, 2005) and their evolution generates cross-stratification — the resultant cross-strata are a fundamental building block of alluvium on planetary surfaces (e.g., Allen, 1982; Edgar et al., 2018). Cross-strata provide a window to formative conditions in ancient fluvial systems and are routinely used to reconstruct morphologies and hydrodynamics (Holbrook & Wanas, 2014; Ganti et al., 2019; Wang et al., 2020; Chapter 3 (Lyster et al., 2021)); for instance, measurements of dune-scale cross-set thicknesses provide a mechanism to estimate the sizes of dunes active on ancient riverbeds and, therefore, palaeoflow depths (Leclair & Bridge, 2001; Bradley & Venditti, 2017). Moreover, bedform kinematics respond to spatial and temporal changes in flow and sediment transport conditions (e.g., Ten Brinke et al., 1999; Martin & Jerolmack, 2013; Wu et al., 2020), and recent research has highlighted that these changes may be recorded in preserved cross-set geometries (Leary & Ganti, 2020). If we can use geometries of cross-stratification to extract information about water and sediment discharge variability, this would significantly improve our understanding of ancient fluvial systems, including river response to climatic perturbation (e.g., Foreman et al., 2012; Colombera et al., 2017). However, a crucial outstanding challenge in this field of research involves adapting engineering-scale insights, which are typically founded in precisely defined boundary conditions (and which underpin palaeohydraulic reconstructions), to geological scales over which more variability in environmental conditions is typically assumed due to issues of time-averaging and temporal incompleteness in the rock record (e.g., Romans et al., 2016; Straub et al., 2020).

Process–product relationships between bedform evolution and cross-stratal geometries have primarily been studied using small-scale physical experiments and numerical models (Paola & Borgman, 1991; Bridge, 1997; Leclair, 2002; Jerolmack & Mohrig, 2005; Ganti et al., 2013; Wu et al., 2020). Existing models that relate cross-set thicknesses to original bedform heights rely on the assumption that the formative train of bedforms evolved in steady-state conditions under no-net aggradation or with a small bedform climb angle ($<10^{-2}$; gradient in terms of y/x) (Paola & Borgman, 1991; Jerolmack & Mohrig, 2005). For a range of these formative conditions, theory, numerical models, and experimental observations suggest the bedform preservation ratio — defined as the ratio of the average preserved cross-set thicknesses and the average original bedform heights — is a near-constant value of 0.3 (Paola & Borgman, 1991; Leclair & Bridge, 2001; Leclair, 2002; Jerolmack & Mohrig, 2005). Further, these models predict that the coefficient of variation, CV, of cross-set thicknesses has a constant value of 0.88 (Paola & Borgman, 1991; Leclair & Bridge, 2001; Leclair, 2002; Jerolmack & Mohrig, 2005), with Bridge (1997) suggesting that the steady-state model for bedform preservation can be applied so long as the CV of cross-set thicknesses is bounded by 0.88 ± 0.30. While these insights have primarily been supported by numerical and experimental studies under steady-

state conditions (e.g., Leclair, 2002; Ganti et al., 2013; Leary & Ganti, 2020), they are widely applied in field-scale palaeohydrological studies (e.g., Holbrook & Wanas, 2014; Ganti et al., 2019; Wang et al., 2020; Chapter 3 (Lyster et al., 2021)).

However, steady-state conditions, strictly defined, are not commonly observed in natural systems when discharge is variable (e.g., Fielding et al., 2018; Ghinassi et al., 2018; Herbert et al., 2020), or under relatively constant flow conditions in which spontaneously developed features, such as bars, establish complex and locally variable flow conditions that change as bars shift and channels migrate (Reesink et al., 2015; Chamberlin & Hajek, 2019; Ganti et al., 2020; Wysocki & Hajek, 2021). These non-steady, or disequilibrium, conditions are increasingly recognized to be fundamental controls on fluvial behaviour and stratigraphic architecture (Plink-Björklund, 2015; Reesink et al., 2015; Fielding et al., 2018; Ghinassi et al., 2018; Ganti et al., 2020; Herbert et al., 2020; Leary & Ganti, 2020; Wysocki & Hajek, 2021). At the bedform scale, recent theoretical and experimental observations indicate that fluvial cross-strata may preferentially record bedform dynamics in disequilibrium conditions (Reesink et al., 2015; Ganti et al., 2020; Leary & Ganti, 2020), i.e., when flow and bedform evolution are out of phase (c.f. Myrow et al., 2018). Bedform disequilibrium conditions are characterized by localized increase in sedimentation rates relative to bedform migration rates, which enhances the preservation of bedforms (Reesink et al., 2015; Ganti et al., 2020; Leary & Ganti, 2020). Cross-sets preserved in disequilibrium conditions have diagnostic geometries that deviate from cross-sets preserved in steady-state conditions: a) restricted range of cross-set thickness distributions such that $CV<0.88$ and b) elevated bedform preservation ratios (>0.3) such that a larger fraction of the formative topography is preserved in the stratigraphy (Jerolmack & Mohrig, 2005; Leary & Ganti, 2020; Wu et al., 2020).

Two distinct disequilibrium conditions lead to enhanced bedform preservation. First, Leary and Ganti (2020) used experimental data to show that characteristic patterns of dune preservation are found under different conditions of formative flow variability (i.e., the near-instantaneous short-term discharge variability associated with the magnitudes and timescales of individual floods). They demonstrated that dune preservation preferentially occurs during flood recession, and that preserved cross-sets only have geometries that are consistent with steady-state conditions when the formative flow duration (T_f), i.e., the flood recession, is greater than the bedform turnover timescale (T_t) — defined as the time it takes to displace the volume of sediment in a bedform (Myrow et al., 2018). Conversely, when the flood recession is shorter than the bedform turnover timescale, the larger peak flood-equilibrated dunes get abandoned and are minimally reworked during the flood recession and subsequent low flow conditions, which results in a high bedform preservation ratio and low CV for preserved cross-sets (Leary & Ganti, 2020). These conditions are typical in rivers with flashy flood hydrographs (relative to bedform turnover timescales), which are characterised by rapid flow deceleration and, therefore, short flood recessions. We term this the *flood hypothesis* for enhanced bedform preservation. Moreover, Leary and Ganti (2020) showed that it is possible to estimate formative flow durations from preserved cross-sets — this may enable quantitative

reconstructions of flood variability from the rock record and augment traditional qualitative methods that rely on facies and architectural models (e.g., Plink-Björklund, 2015). Alternatively, the self-organization of fluvial systems into a morphodynamic hierarchy (e.g., dunes, bars, channels, channel belts) can also result in enhanced preservation of the topography associated with each hierarchical level (Ganti et al., 2020). In this scenario, high bedform preservation ratio and low *CV* can occur due to localized increase in the angle of climb of bedforms associated with, for example, concurrent migration of dunes and bars (Jerolmack & Mohrig, 2005; Ganti et al., 2013; Reesink et al., 2015; Ganti et al., 2020), which include both unit bars and longer-lived compound bar features. We term this the *hierarchy hypothesis* for enhanced bedform preservation. In both of these scenarios, cross-strata are expected to encode more detailed information about morphodynamic conditions in ancient fluvial systems, which are not accounted for in models that assume bedform preservation occurred in steady-state conditions.

Despite advances in understanding bedform dynamics, the prevalence of bedform disequilibrium dynamics in preserved fluvial strata is currently unclear, partly because we lack detailed field measurements of cross-set geometries and their statistical nature. While a handful of field studies have documented low *CV* (0.3–0.7) in fluvial cross-strata (Jerolmack & Mohrig, 2005; Colombera et al., 2017; Cardenas et al., 2020; Wang et al., 2020), consistent with bedform disequilibrium dynamics, these data are usually limited to a few outcrop observations for individual geologic formations. Here, we systematically characterize the geometries and statistical nature of dune-scale cross-strata for three Upper Cretaceous geologic formations in central Utah, USA (Figures 4.1, 4.2), to assess the nature of dune preservation. Across all three formations, we show that dune-scale cross-strata are dominated by the preservation of bedform disequilibrium dynamics, which calls into question the use of steady-state assumptions in palaeohydraulic reconstructions. Using these field observations, we reconstruct bedform kinematics (i.e., turnover timescales) and quantify the formative conditions that are consistent with field data under both the flood and hierarchy hypotheses (i.e., flood durations, migration rates). Finally, we evaluate whether it is possible to deconvolve the relative roles of flow variability and morphodynamic hierarchy on enhanced bedform preservation, which may provide a potentially powerful pathway to reconstruct flood variability in ancient fluvial systems, and to evaluate the nature of interactions between dunes, bars, channel migration and channel avulsion in palaeo-channel networks.

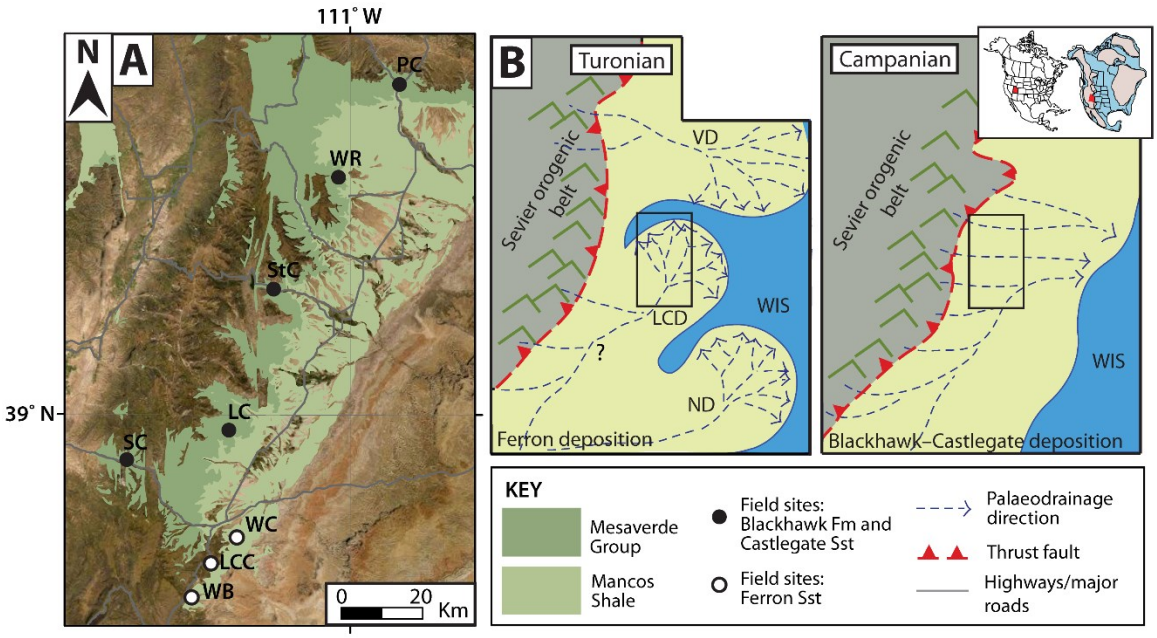

Figure 4.1 | Study area. **A**) Field areas in central Utah, U.S.A., which include Last Chance Creek (LCC), Link Canyon (LC), Price Canyon (PC), Salina Canyon (SC), Straight Canyon (StC), Wattis Road (WR), Willow Basin (WB) and Willow Creek (WC). LC, PC, SC, StC and WR are field sites from which we obtained data for the Blackhawk Formation and Castlegate Sandstone (Mesaverde Group; black-filled circles). LCC, WB and WC are field sites from which we obtained data for the Ferron Sandstone (Mancos Shale; white-filled circles). **B**) A conceptual diagram of Utah palaeogeography and palaeodrainage in both the Turonian (left) and Campanian (right). Likely palaeodrainage configurations (and delta progradation) are indicated by dashed blue lines with arrows. The black outlined box in the centre of each palaeogeography indicates the study area (i.e., the approximate position and extent of **A**). The location of Utah relative to the modern North American continent (left) and the Late Cretaceous North American continent (right) is shown in the inset figure — Utah is highlighted as a red box. LCD = Last Chance delta; ND = Notom delta; VD = Vernal delta; WIS = Western Interior Seaway. Figure adapted from Chapter 3 (Lyster et al., 2021).

4.2 Study area

In the Late Cretaceous North American continent, rivers draining the Sevier orogenic fold-and-thrust belt delivered sediment to the Western Interior Seaway (WIS) (e.g., Kauffman & Caldwell, 1993) (Figure 4.1). We focus on well-studied fluvial strata of the Upper Cretaceous Blackhawk Formation, Castlegate Sandstone and Ferron Sandstone in central Utah, USA (Figures 4.1, 4.2) (c.f. Chapter 3 (Lyster et al., 2021)). These strata have distinct architectures and are interpreted to preserve differing fluvial styles; the Ferron Sandstone preserves major meandering trunk channels (Cotter, 1971; Chidsey et al., 2004), while, at the Blackhawk–Castlegate transition, the deposits of single- and multi-thread channels of the Blackhawk Formation (Adams & Bhattacharya, 2005; Hampson et al., 2013; Flood & Hampson, 2014) are capped by the deposits of predominantly braided channels of the Castlegate Sandstone (e.g., Miall, 1993, 1994) (Figures 4.1, 4.2). Moreover, these systems are potentially linked with a monsoonal climate (Fricke et al., 2010; Sewall & Fricke, 2013).

4.2.1 Blackhawk Formation and Castlegate Sandstone, Mesaverde Group

The Campanian Blackhawk Formation and Castlegate Sandstone (Figures 4.1, 4.2) represent a series of transverse fluvial systems draining the Sevier orogenic front to the WIS (Pettit et al., 2019), with an additional longitudinal component of drainage from the south-southwest (e.g., Szwarc et al., 2015; Pettit et al., 2019) (Figure 4.1b). The lower–middle Campanian Blackhawk Formation is a ledge-forming succession characterized by large fluvial channelized sandstone bodies and abundant floodplain sediments (e.g., Adams & Bhattacharya, 2005; Hampson et al., 2013; Flood & Hampson, 2014) (Figure 4.2a–c). These sandstone bodies represent both single- and multi-thread systems, as interpreted from bar architectures (Adams & Bhattacharya, 2005; Hampson et al., 2013). Meanwhile the middle–upper Campanian Castlegate Sandstone is a cliff-forming succession situated above the Blackhawk Formation (Figure 4.2a) and is characterized by amalgamated fluvial channel-belt deposits, which are interpreted to preserve braided rivers (e.g., Miall, 1993, 1994). In the middle of the Castlegate Sandstone these sands are less amalgamated, with interbedded mudstones, and are interpreted to preserve more sinuous/meandering channels (e.g., Miall, 1993, 1994). We collected data for the Blackhawk Formation and Castlegate Sandstone from five canyons along the eastern Wasatch Plateau front (Figure 4.1a; c.f. Chapter 3 (Lyster et al. (2021)). Dune-scale cross-strata in the Blackhawk Formation are generally associated with bar deposits, as well as lower bar, channel floor or thalweg deposits, whereas dune-scale cross-strata in the Castlegate Sandstone are predominantly associated with bar deposits (Miall, 1993, 1994; Adams & Bhattacharya, 2005; Hampson et al., 2013; Flood & Hampson, 2014).

4.2.2 Ferron Sandstone, Mancos Shale

The Turonian Ferron Sandstone comprises three deltaic clastic wedges (Cotter, 1971; Chidsey et al., 2004) (Figure 4.1b). These deltas were fed by rivers draining the Sevier orogenic front to the WIS and may have

also featured an additional/intermittent longitudinal component of drainage from the south-southwest, as observed for the Blackhawk Formation–Castlegate Sandstone succession (e.g., Szwarc et al., 2015; Pettit et al., 2019). We focus on the Last Chance deltaic complex, using data from three canyons in southwestern Castle Valley (Figure 4.1). These canyons preserve the most palaeo-landward terrestrial fluvial facies of the Last Chance delta and are characterized by major channelized sandstone bodies and abundant floodplain sediments and palaeosols (Cotter, 1971; Chidsey et al., 2004) (Figure 4.2d–f). These strata preserve the major meandering trunk channels that fed the Last Chance delta, which is evidenced by abundant laterally accreted point bar deposits (Cotter, 1971; Chidsey et al., 2004) (Figure 4.2f). Dune-scale cross-strata in the Ferron Sandstone are generally associated with point bar deposits, as well as lower bar, channel floor, or thalweg deposits (Cotter, 1971; Chidsey et al., 2004).

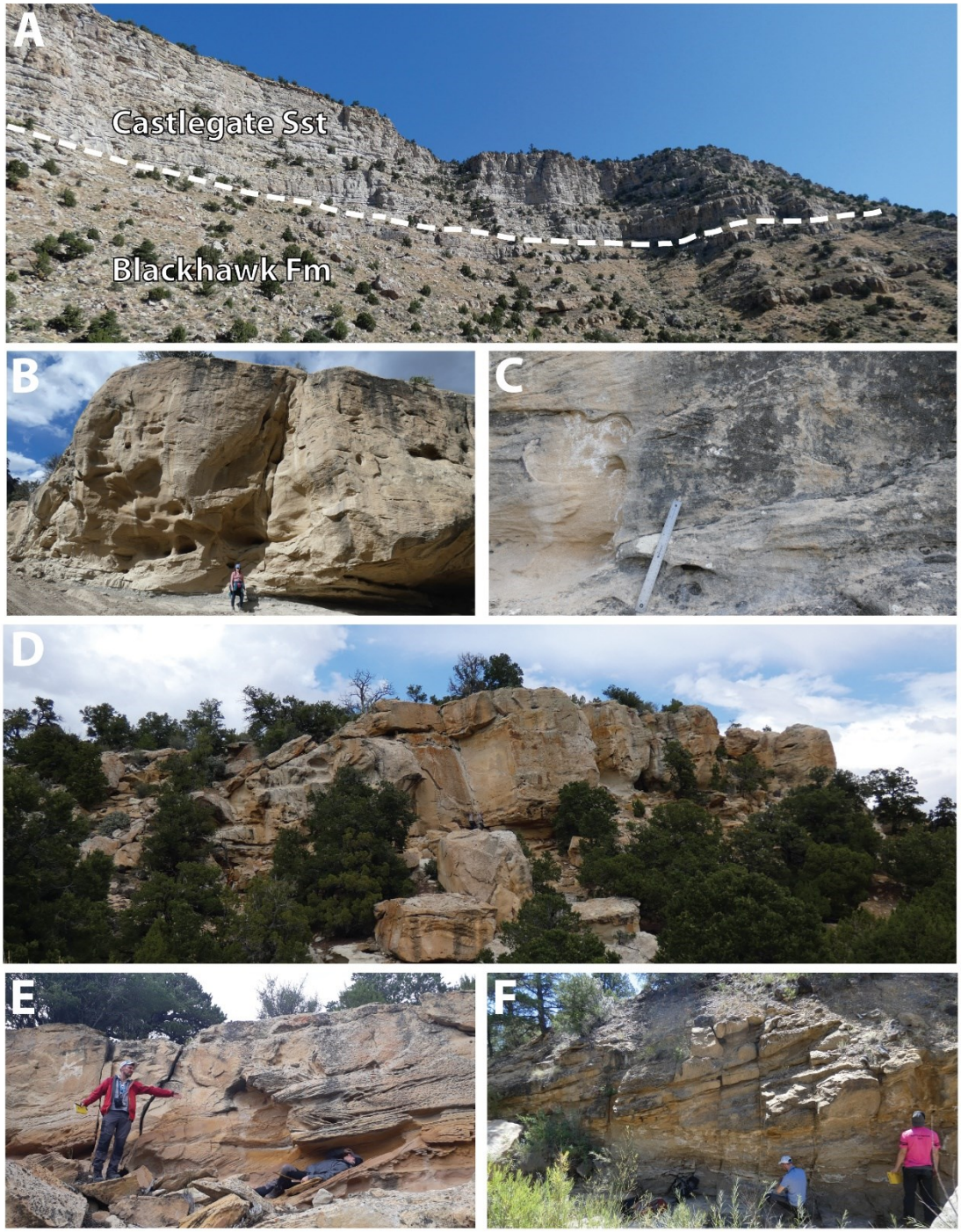

Figure 4.2 | An overview of Upper Cretaceous fluvial strata from which we collected field data in central Utah, USA. **A**) Example of typical exposure of the Blackhawk Formation and Castlegate Sandstone (at Salina Canyon; SC; Figure 4.1) which crops out in canyons along the eastern Wasatch front. Dashed white line indicates the lithostratigraphic boundary between the Blackhawk Formation and Castlegate Sandstone. Thickness of the Castlegate Sandstone is *ca* 85 m. **B**) Example of a major channelized fluvial sandstone body of the Blackhawk Formation at Link Canyon (LC; Figure 4.1). **C**) Crude cross-stratification of amalgamated fluvial deposits of the Castlegate Sandstone at Price Canyon (PC; Figure 4.1). **D**) Example of a major channelized sandstone body of the Ferron Sandstone at Last Chance Creek (LCC; Figure 4.1). Persons for scale in centre of image. Thickness of channelized sandstone body in centre of image is *ca* 12 m. **E**) Cross-stratified fluvial strata of the Ferron Sandstone at LCC (with some soft-sediment deformation apparent). **F**) Laterally accreted point bar deposits of the Ferron Sandstone at LCC.

4.3 Methods

At field localities, we measured the geometries of dune-scale cross-sets. Trough and planar cross-sets occurred predominantly in sand-grade sediments and occasionally in coarser granule-grade sediments (Figure 4.3). To measure the distribution of thicknesses within individual cross-sets we delineated cross-set boundaries (i.e., the lower, asymptotic bounding surface and the upper, erosional bounding surface) and measured cross-set thickness with a vertical precision of ±5 mm at regular intervals along the entire width of the cross-set dip-section (n=5–15 measurements) (Figure 4.3e,f), in line with methods outlined in Paola and Borgman (1991), Ganti et al. (2019), and in Chapter 3 (Lyster et al., 2021). We then estimated the median grain-size (D_{50}) using size terms of the Wentworth (1922) classification (Figure 4.3a,b). When converted to numerical values, we assigned the middle value for each size term or, where grain-size straddled two size terms, we used the boundary value, e.g., D_{50} of medium-grade sand = 0.375 mm and medium–coarse-grade sand = 0.5 mm (Wentworth, 1922). We repeated this for multiple cross-sets within co-sets. Having measured thickness distributions within individual cross-sets, we then measured a sample of maximum cross-set thicknesses (i.e., the maximum distance between lower and upper bounding surfaces) of cross-sets at each locality (n=~25–75). These cross-sets were all related, spanning multiple co-sets that were confined, where possible, to a single channelized sandstone body.

For each individual cross-set, we calculated the mean cross-set thickness, h_{xs}, the maximum thickness, and the *CV* of the internal thickness distribution ($CV(h_{xs})$) — a key parameter to test whether the bedforms are preserved in steady-state or disequilibrium conditions. For each sample of maximum cross-set thicknesses, we similarly calculated the mean maximum cross-set thickness, h_p, and the *CV* of the entire sample ($CV(h_p)$), and we additionally analysed the shape of each distribution.

We then propagated mean thicknesses of individually measured cross-sets (and their respective grain-sizes) through a well-established quantitative framework (c.f. Ganti et al., (2019); Chapter 3 (Lyster et al., 2021); Appendix C2) and used these values to reconstruct bedform turnover timescales — we can use turnover timescales to contextualise the implications of the flood and hierarchy hypotheses. For instance, under the flood hypothesis we expect waning flow durations to be shorter than turnover timescales, whereas under the hierarchy hypothesis we expect bars to be migrating at rates that approach the rates of bedform turnover, i.e., the rates of bedform migration. We reconstructed turnover timescales, T_t, i.e., the time taken to displace the volume of sediment of the bedform (per unit width), following Martin and Jerolmack (2013), Myrow et al. (2018), and Leary and Ganti (2020) as:

$$T_t = \frac{\lambda h_d \beta}{q_b}, \qquad \text{Eq. 4.1}$$

where λ is bedform wavelength, which we estimated using the depth scaling relation of van Rijn (1984), h_d is bedform (i.e., dune) height, which we calculated using the relation of Leclair and Bridge (2001), β ~0.55

is the bedform shape factor, and q_b is the unit bedload flux. We calculated q_b using the method of Mahon and McElroy (2018), in which q_b is calculated as a function of bed porosity, bedform height, and bedform migration velocity (Appendix C2). These methods are consistent with those suggested by Leary and Ganti (2020), but we acknowledge that other approaches could be implemented. As the exact error margins of palaeohydraulic inversion methods are unknown, we used a Monte Carlo uncertainty propagation method to estimate uncertainty, which yielded 10^6 values of T_t per cross-set (Appendix C2). From these estimates we extracted median T_t, the 25–75 percentile range of T_t, and the 10–90 percentile range of T_t. For each cross-set, we suggest that the 10–90 percentile range of T_t offers a plausible minimum and maximum value for mean T_t, and that the 25–75 percentile range of T_t offers the bounds in which the true value of mean T_t is most likely to occur.

Reconstruction of T_t included reconstruction of h_d from h_{xs}, which requires a priori knowledge of the bedform preservation ratio (h_{xs}/h_d), which itself is a function of whether bedforms were preserved in steady-state or disequilibrium conditions. To evaluate a maximum T_t value, we used the relation of Leclair and Bridge (2001), in which $h_{xs}/h_d \sim 0.3$, and which assumes steady-state preservation under low bedform climb angle. We then assessed the sensitivity of T_t to h_{xs}/h_d by repeating the methodology outlined above for h_{xs}/h_d values from 0 to 1. In the absence of preserved formsets that reflect $h_{xs}/h_d \geq 1.0$ (Reesink et al., 2015), enhanced bedform preservation is characterized by $0.3 < h_{xs}/h_d \leq 0.7$ (Appendix C; Jerolmack & Mohrig, 2005; Reesink et al., 2015; Ganti et al., 2020; Leary & Ganti, 2020). For the sensitivity analyses, we used the h_{xs} and D_{50} of each measured cross-set and calculated the overall mean h_{xs} and mean D_{50} for the Blackhawk Formation, Castlegate Sandstone and Ferron Sandstone, respectively.

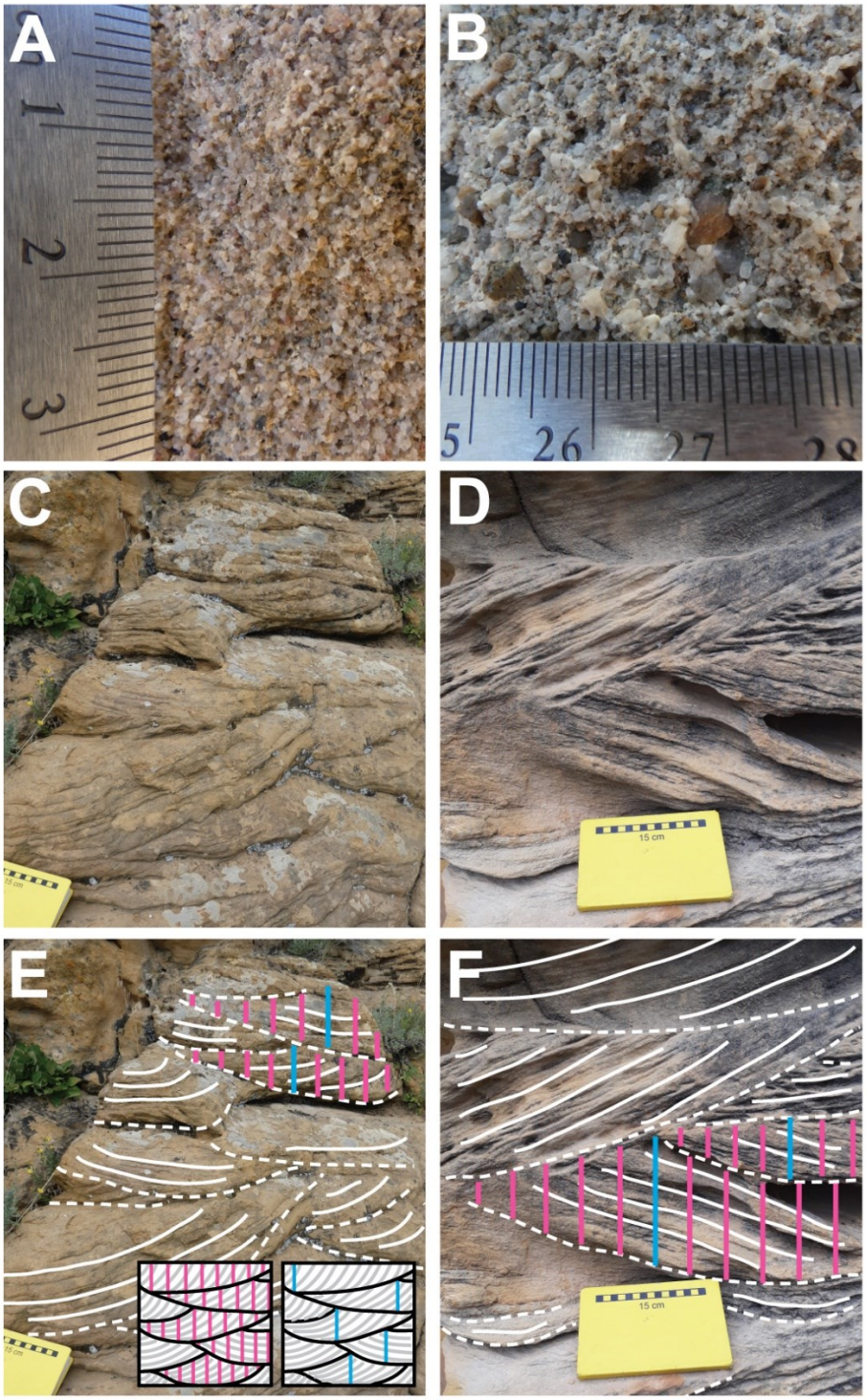

Figure 4.3 | Field methods. **A,B**) For each measured cross-set, grain-size was assigned using the Wentworth (1922) classification. **C,D**) Examples of cross-sets from which distributions of cross-set thicknesses were measured. **E,F**) Interpreted versions of the images in **C,D**. Dashed white lines indicate bounding surfaces between cross-sets and solid white lines indicate individual foresets within cross-sets. To exemplify how cross-sets were measured, pink vertical lines indicate the regular spacing within individual cross-sets at which thicknesses were measured, and blue vertical lines indicate where maximum cross-set thicknesses would have been measured for a sample of cross-sets within co-sets at each locality. Insets in **E** are schematic representations of these two methods of data collection from cross-sets using pink and blue lines, respectively. Figure adapted from Chapter 3 (Lyster et al., 2021).

4.4 Results

4.4.1 Cross-set geometries

We present results aggregated at the formation scale, with no spatial or temporal reference frame, as ancillary field observations suggest there is little variation between field sites (see Appendix C and Chapter 3 (Lyster et al., 2021)). We measured >400 individual dune-scale cross-sets of the Blackhawk Formation (n = 81), Castlegate Sandstone (n = 146) and Ferron Sandstone (n = 190) (Figure 4.4), with ~5–15 thickness measurements per cross-set, totalling >3800 measurements. For each cross-set we recorded grain-size, which is reported in the Appendix C, and we calculated the mean thickness and the maximum thickness. Distributions of mean cross-set thicknesses are similar for the Blackhawk Formation and Castlegate Sandstone (two-sample t-test; p = 0.067; test statistic = −1.838, degrees of freedom = 225); distributions have median values of ~0.13–0.14 m and 10–90 percentile ranges of 0.10–0.18 m. Distributions of maximum cross-set thicknesses for the Blackhawk Formation and Castlegate Sandstone generally have medians of 0.17–0.18 m and 10–90 percentile ranges of 0.13–0.27 m (Figure 4.4a,b). Whereas for the Ferron Sandstone, cross-sets are larger with broader percentile ranges. The distribution of mean cross-set thicknesses has a median of 0.15 m and a 10–90 percentile range of 0.08–0.25 m, and the distribution of maximum cross-set thicknesses has a median of 0.22 m and a 10–90 percentile range of 0.12–0.45 m (Figure 4.4c).

We also measured maximum thicknesses of >3000 dune-scale cross-sets across the Blackhawk Formation (801 measurements across 26 samples), Castlegate Sandstone (1015 measurements across 27 samples) and Ferron Sandstone (1257 measurements across 21 samples), with between 25–75 measurements per sample (Figure 4.5). For each formation, distributions of maximum thicknesses of cross-sets have median values of ~0.20 m (Figure 4.5); these values are consistent with maximum values extracted from individually measured cross-sets (Figure 4.4). For the Blackhawk Formation and Castlegate Sandstone, 90% of maximum cross-set thicknesses are between ~0.15–0.30 m, and the upper 10% of maximum cross-set thicknesses are markedly larger (≤0.50–0.60 m) (Figure 4.5a,c). Meanwhile, for the Ferron Sandstone, 90% of maximum cross-set thicknesses are between ~0.15–0.35 m and the upper 10% of maximum cross-set thicknesses are also markedly larger (≤ 0.70 m) (Figure 4.5e). These distributions of maximum cross-set thicknesses across all cross-set samples are generally mirrored in individual cross-set samples (Figure 4.5b,d,f), with median values of ~0.20 m, suggesting they are not from a limited subset of locations. Most samples of maximum cross-set thicknesses demonstrate positively-skewed, long-tailed distributions wherein relatively few large cross-sets exist among abundant smaller cross-sets (Fig 5b,d,f). The kurtosis of distributions varies for each formation, such that distributions in the Castlegate Sandstone and Ferron Sandstone are more long-tailed than in the Blackhawk Formation (Fig 5b,d,f).

Our data show that *CV* values of cross-set thicknesses are significantly lower than the expected steady-state values of 0.88 (Figure 4.6). We found low *CV* of thicknesses within individual cross-sets ($CV(h_{xs})$), as

well as low *CV* of thicknesses for a sample of measured cross-sets within related co-sets ($CV(h_p)$) (Figure 4.6). In the Blackhawk Formation and Castlegate Sandstone, median $CV(h_{xs})$ is 0.3 with a 25–75 percentile range of ~0.25–0.38, and maximum $CV(h_{xs})$ extends to 0.45–0.55 (Figure 4.6a,b). The Ferron Sandstone $CV(h_{xs})$ values are also low (relative to steady-state) but are higher than in the Blackhawk–Castlegate succession. For the Ferron Sandstone, median $CV(h_{xs})$ is 0.4 with a broader 25–75 percentile range of ~0.3–0.5, and maximum $CV(h_{xs})$ extends to 0.6–0.75 (Figure 4.6c). We found that none of the measured $CV(h_{xs})$ values were consistent with the proposed empirical range of 0.88 ± 0.30 for steady-state preservation (Bridge, 1997) in the Blackhawk–Castlegate succession; however, 6% of the measurements were within this range for the Ferron Sandstone. For $CV(h_p)$, recovered values are even lower. In the Blackhawk Formation and Castlegate Sandstone median $CV(h_p)$ is 0.2, with 25–75 percentile ranges of ~0.15–0.25 (Figure 4.6a,b), and in the Ferron Sandstone median $CV(h_p)$ is 0.3, with a 25–75 percentile range of ~0.25–0.35 (Figure 4.6c).

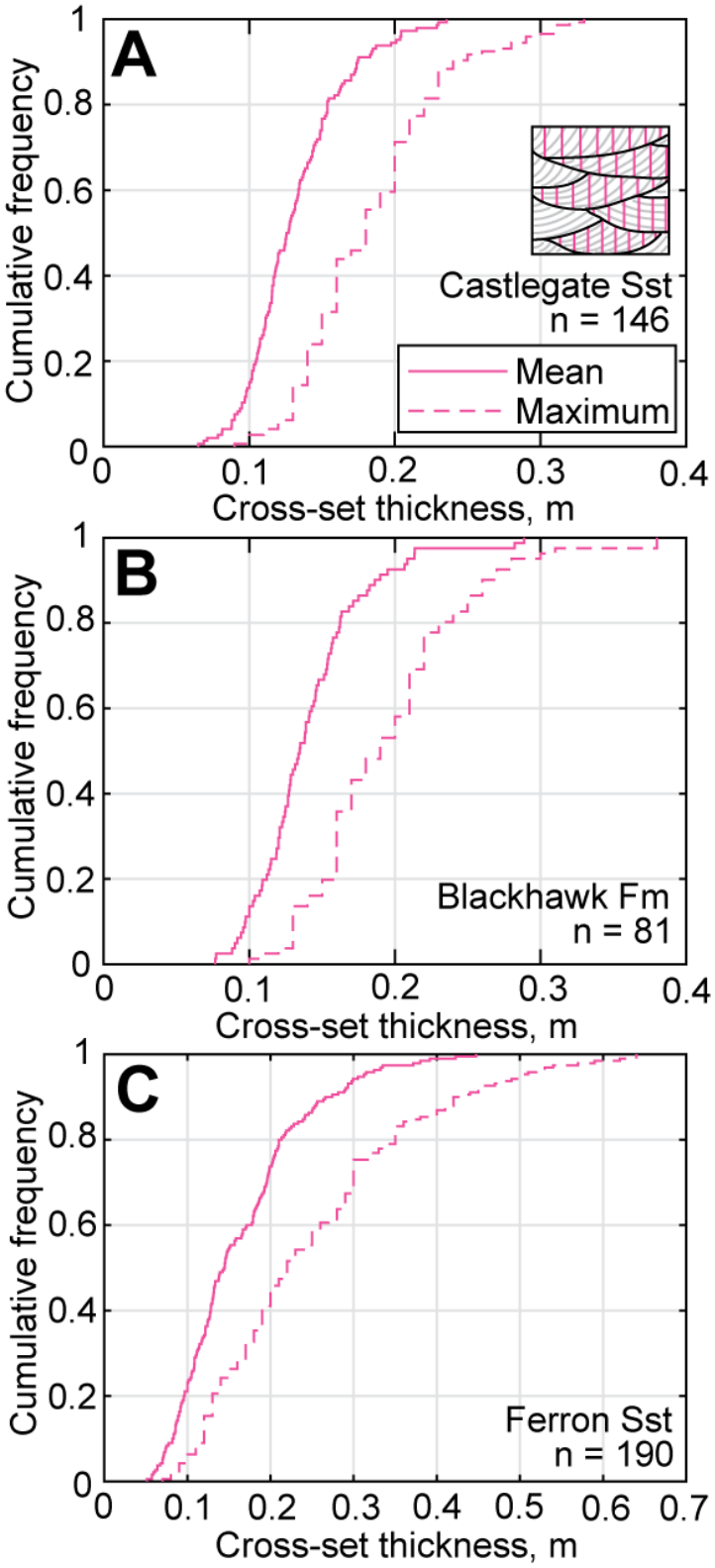

Figure 4.4 | The cumulative frequency of the mean, median and maximum cross-set thickness for (**A**) the Castlegate Sandstone, (**B**) the Blackhawk Formation, and (**C**) the Ferron Sandstone. The solid pink line indicates the measured mean and the dashed pink line indicates the measured maximum. n indicates the number of cross-sets in which thickness distributions were measured, and therefore the number of cross-sets from which a mean and maximum were subsequently extracted. The inset in **A** is a schematic representation of how thickness distributions were measured within each cross-set.

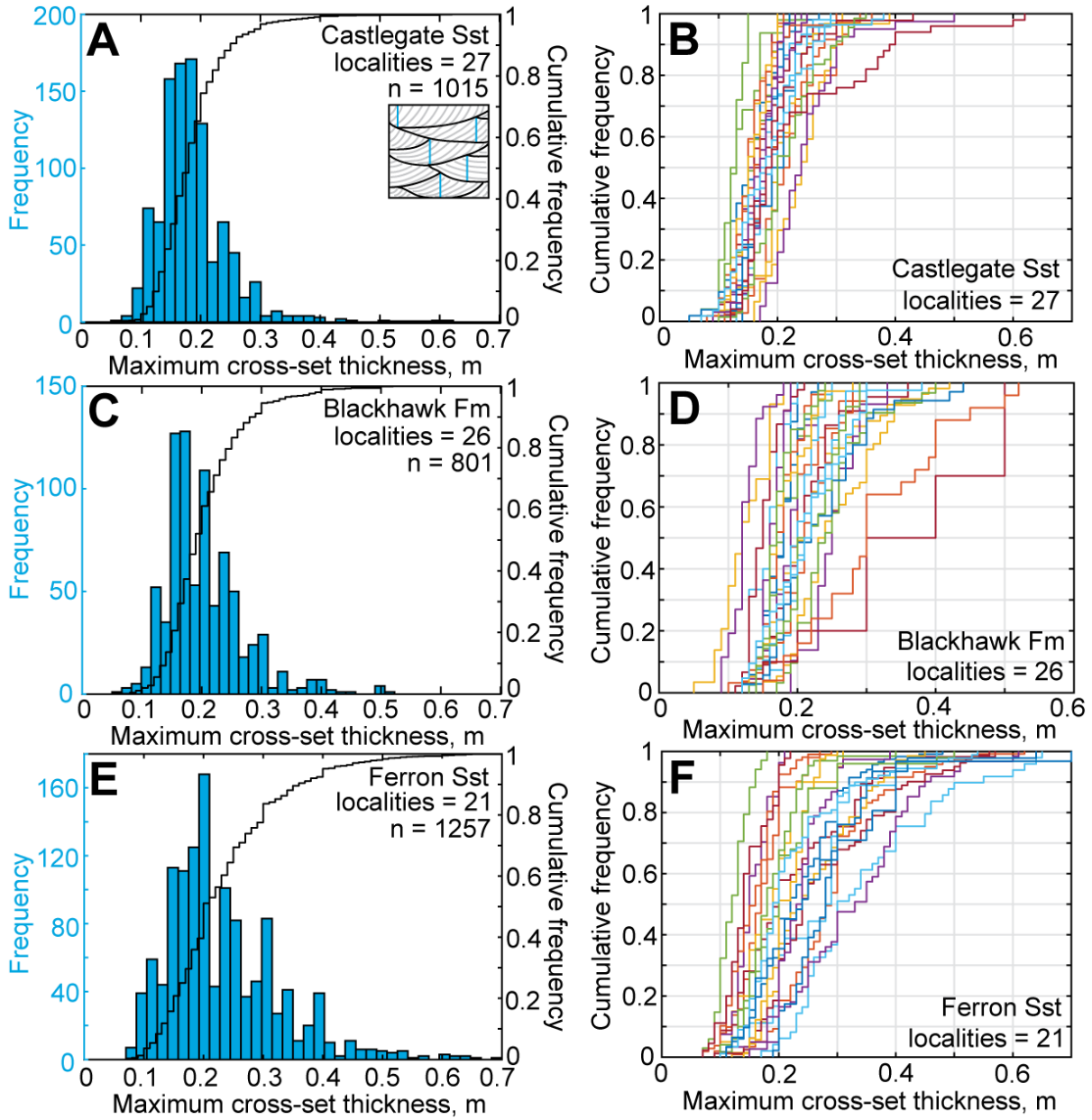

Figure 4.5 | A) The frequency (left y axis; blue) and cumulative frequency (right y axis; black) of maximum cross-set thicknesses measured across the Castlegate Sandstone. n indicates the total number of cross-sets measured for the entire formation, and the number of localities refers to the field sites across which these measurements were made. Measurements at each locality were for a sample of related cross-sets within cosets, and typically comprised ~25–75 measurements. **B**) The cumulative frequency of maximum cross-set thicknesses for each locality within the Castlegate Sandstone. **C**) The frequency and cumulative frequency of maximum cross-set thicknesses measured across the Blackhawk Formation. **D**) The cumulative frequency of maximum cross-set thicknesses for each locality within the Blackhawk Formation. **E**) The frequency and cumulative frequency of maximum cross-set thicknesses measured across the Ferron Sandstone. **F**) The cumulative frequency of maximum cross-set thicknesses for each locality within the Ferron Sandstone. The inset in **A** is a schematic representation of how maximum thicknesses were measured across samples of cross-sets.

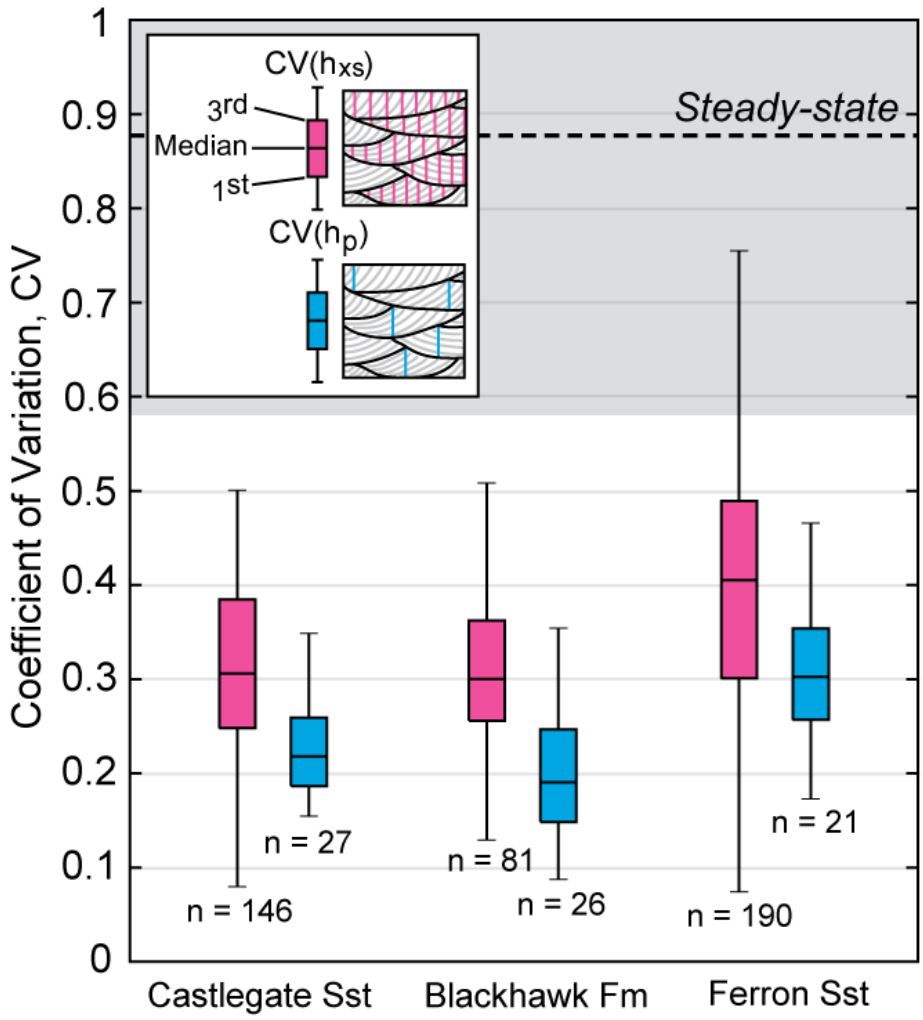

Figure 4.6 | The coefficient of variation, *CV*, of cross-set thicknesses measured in the Castlegate Sandstone, Blackhawk Formation, and Ferron Sandstone. Pink boxes indicate *CV*s of thickness distributions within individually measured cross-sets ($CV(h_{xs})$), with n indicating the number of individually measured cross-sets. The blue boxes indicate *CV*s of thickness distributions across a sample of (related) cross-sets ($CV(h_p)$), with n indicating the number of field localities at which a sample of cross-set thicknesses was measured. At each locality, the sample of measured cross-sets typically included ~25–75 cross-sets. Insets within the key demonstrate, schematically, how thicknesses would have been measured for both $CV(h_{xs})$ and $CV(h_p)$ respectively (see Section 4.3). The central mark of each box indicates the median estimate, and the bottom and top edges of each box indicate the 1st and 3rd quartiles (or 25th and 75th percentiles), respectively. The whiskers extend to the most extreme values of *CV* that are not considered to be outliers. The dashed black line indicates the theoretical steady-state *CV* of 0.88, following Paola & Borgman (1991), and the grey shaded region indicates the empirical steady-state *CV* of 0.88±0.30, following Bridge (1997).

4.4.2 Maximum bedform turnover timescales

We first present results for reconstructed T_t values for each formation using a bedform preservation ratio of 0.3, and then explore the sensitivity of T_t to $h_{xs}/h_d > 0.3$ which is expected for the preservation of bedforms under high angles of local bedform climb. The geometries and grain-sizes of measured cross-sets imply that T_t values typically span 1–10 days, with a median value of 2–4 days (Figure 4.7). The overall distributions of T_t vary between the geologic formations (Figure 4.7). For the Castlegate Sandstone median T_t is 2.5–3 days, with a 10–90 percentile range of 1–7 days (Figure 4.7a). For the Blackhawk Formation, values are marginally higher with a median T_t of 3–3.5 days, and a 10–90 percentile range of 1.5–8 days (Figure 4.7b). While the Ferron Sandstone has a similar median T_t of 3–3.5 days, it has a much broader 10–90 percentile range spanning <1–15 days (Figure 4.7c).

We recovered 10^6 values of T_t for each cross-set using a Monte Carlo approach (see Section 4.3 and Appendix C2) and the results described above present the cumulative distribution function (CDF) of median T_t values for each cross-set (Figure 4.7). We also computed the CDFs for the 10th, 25th, 75th and 90th percentiles of T_t values of each cross-set to highlight the plausible range of values that are consistent with field observations. These CDFs demonstrate that, despite uncertainty in T_t of up to one order of magnitude, the majority of possible T_t values are between 1 and 10 days (Figure 4.7). These T_t values suggest that floods with typical recessions >10 days would have fully equilibrated bedforms, similar to observations in relatively shallow modern rivers (Leary & Ganti, 2020). Further, the estimated maximum T_t of 2–4 days, with an overall span of 1–10 days (Figure 4.7) for dune-scale cross-strata in the Blackhawk-Castlegate succession and the Ferron sandstone are consistent with dune migration in modern natural rivers (e.g., Hajek & Straub, 2017; Leary & Ganti, 2020).

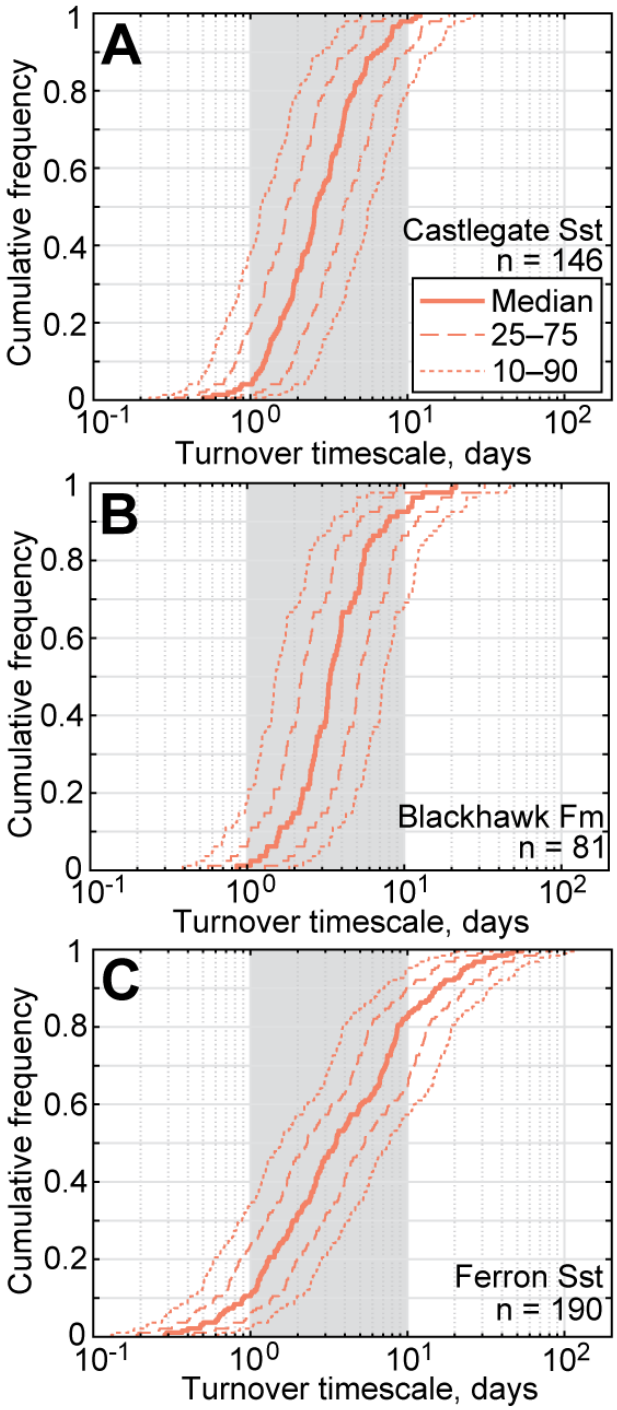

Figure 4.7 | The cumulative frequency of estimated turnover timescales, T_t, calculated for (**A**) the Castlegate Sandstone, (**B**) the Blackhawk Formation, and (**C**) the Ferron Sandstone (see Appendix C2). T_t was calculated for each cross-set from which a cross-set thickness distribution was measured, using the mean thickness and the measured grain-size (Figure 4.3; see Section 4.3). n indicates the number of T_t values that were calculated (equal to the number of measured cross-set thickness distributions). The solid orange line indicates the median T_t reconstructed for each cross-set, the dashed orange lines indicate the 25th–75th percentile range of T_t values reconstructed for each cross-set, and the dotted orange lines indicate the 10th–90th percentile range of T_t values reconstructed for each cross-set, which we offer as plausible spreads of values for mean T_t (see Appendix C2). Grey shaded region indicates T_t values of 1–10 days; for the Castlegate Sandstone and Blackhawk Formation, ~90–95% of median T_t values fall within this range and, for the Ferron Sandstone, ~70% of median T_t values fall within this range.

4.4.3 Sensitivity of bedform turnover timescales to bedform preservation ratio

To assess the sensitivity of T_t to h_{xs}/h_d, we systematically varied h_{xs}/h_d for each formation from 0 to 1 (Figure 4.8), where the former indicates no preservation and the latter implies complete preservation of formsets. An increase in h_{xs}/h_d corresponds analytically with a decrease in T_t (see Appendix C2). For example, increasing h_{xs}/h_d by a factor of 2, from 0.3 to 0.6, reduces T_t by a factor of 5–6 (Figure 4.8). Compared to results for h_{xs}/h_d=~0.3, the median T_t values for the Castlegate Sandstone and the Blackhawk Formation are smaller by a factor of 5, with median T_t of 0.7 days (~17 hours) and 1 day, respectively (Figs. 8a, b). For the Ferron Sandstone, h_{xs}/h_d=0.6 reduces the median T_t by a factor of 6 to ~1 day, when compared to h_{xs}/h_d=~0.3 (Figure 4.8c). In all cases, extreme dune preservation with h_{xs}/h_d=1 yielded T_t <0.1 days, and extremely low values of h_{xs}/h_d << 0.3 yielded unrealistic T_t values as high as 10^5 days (Figure 4.8). Experimental bedform preservation under steady and unsteady flows indicates that the h_{xs}/h_d may likely span 0.3 and 0.7 (grey bars, Figure 4.8; Appendix C) in the absence of evidence for formset preservation (Leary & Ganti, 2020).

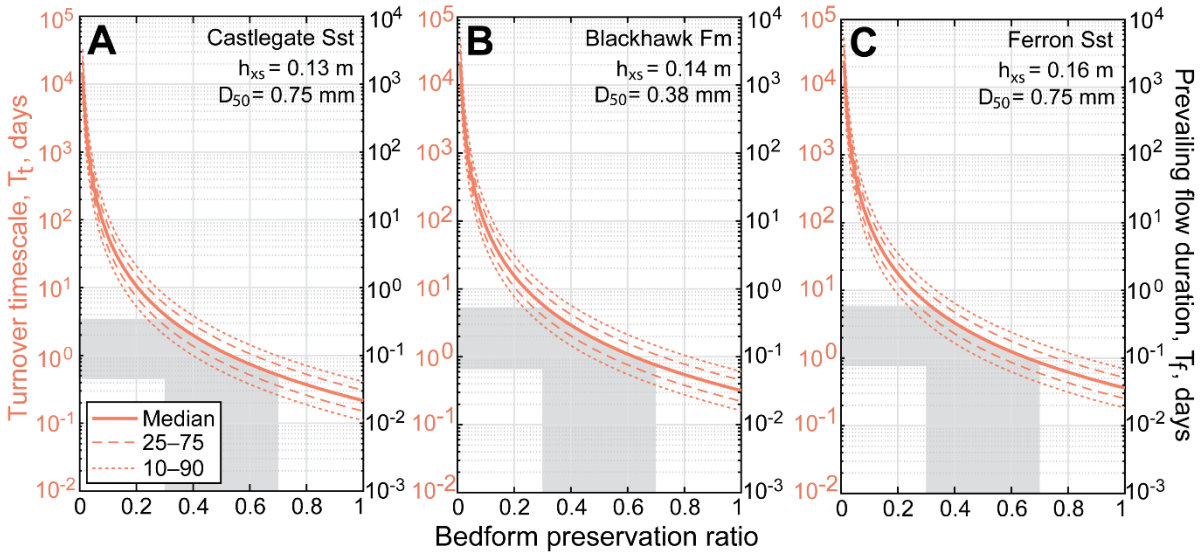

Figure 4.8 | Turnover timescales, T_t, reconstructed for the (**A**) Castlegate Sandstone, (**B**) Blackhawk Formation, and (**C**) Ferron Sandstone using a range of preservation ratios. For these purposes, the mean cross-set thickness (h_{xs}) and median grain-size (D_{50}) for each geologic formation have been used (i.e., the mean and median across all measured cross-set distributions). The solid orange line indicates the median T_t reconstructed for each bedform preservation ratio, the dashed orange lines indicate the 25th–75th percentile range of T_t values reconstructed for each bedform preservation ratio, and the dotted orange lines indicate the 10th–90th percentile range of T_t values reconstructed for each bedform preservation ratio, which we offer as plausible spreads of values for mean T_t (see Appendix C2). The grey region highlights the range of median T_t values associated with a plausible range of bedform preservation ratios; steady-state bedform preservation ratios are ~0.3, and Leary & Ganti (2020) documented that higher bedform preservation ratios may extend up to ~0.7 during flash floods. On the right y axis, we show reconstructed prevailing flow durations, T_f, for the scenario in which T_f is a factor of 10 smaller than the reconstructed bedform turnover timescale.

4.5 Discussion

From >400 individually measured dune-scale cross-sets (n=5–15 measurements per cross-set) across the three geologic formations, our results indicated that estimated $CV(h_{xs})$ was always lower than 0.88 and ranged from ~0.25–0.5 (Figure 4.6). Across these formations, only 3% of the estimated $CV(h_{xs})$ were consistent with the empirical range of 0.88±0.30 expected for bedform preservation under steady-state conditions (Bridge, 1997). Low $CV(h_{xs})$ is inconsistent with steady-state preservation of bedforms and does not support generation of cross-sets by random variability in scour depths through time (Paola & Borgman, 1991; Leclair & Bridge, 2001; Leclair, 2002; Jerolmack & Mohrig, 2005). Instead, our observations provide evidence for enhanced bedform preservation driven by localized increase in sedimentation rates relative to the bedform migration rates (Jerolmack & Mohrig, 2005; Ganti et al., 2020; Leary & Ganti, 2020), and suggest that river dune deposits of the Blackhawk Formation, Castlegate Sandstone, and Ferron Sandstone are dominated by bedform disequilibrium dynamics. Below we discuss the implications of these observations under the flood and hierarchy hypotheses and delineate potential approaches to disentangle their relative roles in ancient fluvial systems.

4.5.1 Implications of the flood hypothesis for bedform preservation

Using physical experiments, Leary and Ganti (2020) showed that, where bedform disequilibrium dynamics are only controlled by formative flow variability, low $CV(h_{xs})$ indicates a scenario in which the formative flow duration (T_f), i.e., the flood recession, is significantly less than the bedform turnover timescale (T_t). Bedform disequilibrium dynamics associated with formative flow variability typically manifest in rivers with flashy flood hydrographs, in which river discharge is characterized by floods with a short flood recession period relative to T_t (Leary & Ganti, 2020) — the rapid decline in water discharge following peak flood minimizes the time available for bedform reworking and enhances bedform preservation (Leary & Ganti, 2020). Under the flood hypothesis, the documented low $CV(h_{xs})$ is consistent with T_f values that are a factor of 10 smaller than T_t (assuming the ratio of T_f to T_t is ~0.1; c.f. Leary & Ganti, 2020). As the maximum T_t values fall between 1–10 days for our field data, the estimated $CV(h_{xs})$ indicates typical T_f values spanning 0.1–1 day (2.4–24 hours) for h_{xs}/h_d=~0.3. The range of plausible T_f values consistent with experimentally observed bedform preservation ratios and field-estimated $CV(h_{xs})$ is on the order of 0.1 days for all the geologic formations considered here (Figure 4.8).

Under the flood hypothesis, our field data consistently indicate that flood recessions did not exceed a few hours to a day for these Late Cretaceous fluvial systems. Given the typical shape of flashy flood hydrographs, we also anticipate that total flood durations did not exceed a few hours to a few days. Our estimated flood durations are plausible and consistent with recent (decadal-scale) observations of modern rivers in sub-tropical and/or mid-latitude regions (e.g., Serinaldi et al., 2018). Moreover, compilations of global flood data indicate that, for flood durations on the order of hours to days, the main causes are: heavy rain, brief torrential rain, tropical storms, and extra-tropical storms (Serinaldi et al., 2018). These flood

durations, and associated causes, are typical of perennial discharge regimes. While the Blackhawk Formation, Castlegate Sandstone and Ferron Sandstone have not been explicitly studied using variable discharge facies models, existing facies analyses of these formations have typically described sedimentary and architectural structures associated with perennial rivers (see review by Plink-Björklund, 2015). These include abundant Froude subcritical structures (i.e., cross-sets from which we collected data; Figure 4.3) and well-developed macroforms (i.e., bars and accretion sets) (Cotter, 1971; Miall, 1994; Chidsey et al., 2004; Adams & Bhattacharya, 2005; Hampson et al., 2013; Flood & Hampson, 2014; Chamberlin & Hajek, 2019).

Independent modelling and proxy studies of palaeoclimate for the Late Cretaceous of central Utah suggest the region was subject to a sub-tropical/monsoonal climate with monsoonal precipitation and frequent seasonal flooding in low-lying alluvial plains (e.g., Fricke et al., 2010; Sewall & Fricke, 2013). However, floods caused by monsoonal rains typically have long durations spanning ~5–25 days (Serinaldi et al., 2018). Additionally, an abundance of features associated with monsoonal systems, e.g., in-channel mud layers, abundant soft-sediment deformation, soft-sediment clast conglomerates (see review by Plink-Björklund, 2015), have not been reported in the literature for these formations or observed at our field localities. Given that our reconstructed flood durations and existing facies models indicate perennial discharge regimes, the flood hypothesis indicates that these river dune deposits could record bedform adjustment to flooding associated with storm events as opposed to sustained monsoonal flooding.

4.5.2 Implications of the hierarchy hypothesis for bedform preservation

Under the alternative hierarchy hypothesis, enhanced bedform preservation is facilitated by self-organization of fluvial systems into a series of hierarchical elements (Ganti et al., 2020), where the nature of preservation of topography within a given hierarchical level is solely controlled by the next level in the morphodynamic hierarchy. The presence of bars — the higher-order hierarchical elements of dunes — will locally enhance preservation of river dunes because the bars both provide accommodation for bedforms and increase bedform climb angles (Reesink et al., 2015; Ganti et al., 2020). Cardenas et al. (2020) observed low $CV(h_{xs})$ for dune-scale cross-strata on the stoss and lee slopes of point bar and free bar deposits, when compared to dune-scale cross-strata in thalweg deposits of the Cretaceous Cedar Mountain Formation, Utah, which is consistent with the hierarchy hypothesis for bedform preservation. Numerical models indicate that observed low $CV(h_{xs})$ values are associated with rapid sedimentation rates relative to bedform migration rates such that the bedform climb angle is of the order of 10^{-2} to 10^{-1} (Jerolmack & Mohrig, 2005). Given that the local angle of climb for bedforms is influenced by the relative rates of dune migration to bar migration (Ganti et al., 2020), these results suggest low $CV(h_{xs})$ values measured in the field are consistent with timescales of bar migration on the order of days to months.

The nature of stratigraphic architecture, particularly of barform deposits, is well-documented for the Blackhawk Formation, Castlegate Sandstone and Ferron Sandstone (Cotter, 1971; Miall, 1993, 1994;

Chidsey et al., 2004; Adams & Bhattacharya, 2005; Hampson et al., 2013; Flood & Hampson, 2014; Chamberlin & Hajek, 2019; Chapter 3 (Lyster et al., 2021)). The Castlegate Sandstone comprises amalgamated fluvial channel-belt deposits which, architecturally, are dominated by barforms (e.g., mid-channel bars) (Miall, 1993, 1994; Chamberlin & Hajek, 2019). Therefore, dune-scale cross-sets that we measured in the Castlegate Sandstone likely preserve dunes that were influenced by bar migration, and it is possible that low $CV(h_{xs})$ values observed in these cross-sets reflect bedform disequilibrium dynamics associated with the hierarchy hypothesis, especially given that unit bar migration rates typical of braided rivers are sometimes comparable to dune migration rates (Strick et al., 2019). Conversely, fluvial strata of the Blackhawk Formation and Ferron Sandstone comprise major channelized sandstone bodies (Cotter, 1971; Chidsey et al., 2004; Adams & Bhattacharya, 2005; Hampson et al., 2013; Flood & Hampson, 2014) which, while abundant in barforms (e.g., laterally accreted point bar deposits; Figure 4.2f), also likely preserve a much larger proportion of channel deposits that are devoid of barform architecture and which may reflect thalweg deposits. Cardenas et al. (2020) hypothesized that thalweg strata represent aggradation in channel beds during the final flood event prior to channel avulsion. We therefore consider that enhanced bedform preservation in thalweg deposits of the Blackhawk Formation and Ferron Sandstone is less likely to reflect bedform preservation in the presence of rapid bar migration and, instead, is more likely to reflect formative flow variability.

4.5.3 Detangling flood versus hierarchy controls on bedform preservation

While both the flood hypothesis and the hierarchy hypothesis explain the observed dominance of enhanced bedform preservation, disentangling their relative roles in controlling bedform preservation is currently non-trivial. We hypothesize that spatially contextualizing the observed deposits may be critical for evaluating the controls on bedform preservation. For example, it is likely that dunes preserved in channel-thalweg deposits of single-thread rivers are not influenced by the presence of bars and, therefore, may reflect the formative flood variability. This scenario may be similar to physical experiments that do not exhibit the multiple morphodynamic hierarchical levels that typify natural rivers. We hypothesise that, where low $CV(h_{xs})$ values are observed in dune-scale cross-sets associated with thalweg deposits, we can use estimated bedform turnover timescales to constrain formative flow durations. Similarly, field observations indicate that dunes preserved in the presence of bars are likely to be better preserved than expected under steady-state conditions (Reesink et al., 2015; Cardenas et al., 2020). In this scenario, $CV(h_{xs})$ may yield insight into the relative rates at which bedforms and barforms migrated in ancient fluvial systems.

Together, single-thread river deposits may display a larger range of $CV(h_{xs})$ that reflects both formative flow variability and the relative kinematic rates of evolution of successive hierarchical levels in the morphodynamic hierarchy. In contrast, braided rivers are characterized by relatively rapid migration of unit bars and free bars in the presence of river dunes (e.g., Strick et al., 2019) and detangling the role of morphodynamic hierarchy and flood variability may be more difficult. Our results are consistent with this hypothesis as we observe a larger range of $CV(h_{xs})$ for single-thread river deposits of the Ferron Sandstone

compared to the predominantly braided river deposits of the Castlegate Sandstone (Figure 4.6). Nonetheless, this work provides a basis for further testing the roles of flow variability and morphodynamic hierarchy on the preservation of bedform dynamics, including other causes of non-uniform flow such as channel abandonment and backwater hydraulics (e.g., Wu et al., 2020).

In terms of cross-set geometries, a promising avenue to decipher the dominant control on bedform disequilibrium dynamics is to compare population statistics of related cross-sets, measured in the field, with those from experimental observations. For instance, Leary and Ganti (2020) showed that, in flashy flood hydrographs, the rapid decline of water discharge associated with short waning-flow durations enhances preservation of relatively larger, peak-flood equilibrated, dunes (Leary & Ganti, 2020). In this scenario, we expect maximum cross-set thicknesses to have a positively skewed long-tailed distribution with large cross-sets interspersed with relatively smaller cross-sets (Leary & Ganti, 2020). Whereas bedform preservation in steady-state conditions, or under a broad flood hydrograph, will likely result in maximum cross-set thicknesses that have a short-tailed distribution, with a much higher frequency of smaller cross-sets, as longer waning-flow durations enable reworking of larger dunes such that the preservation potential of peak-flood equilibrated dunes is low (Leclair, 2011; Leary & Ganti, 2020). Across our measured samples, distributions of maximum cross-set thicknesses are consistent with bedform preservation under the flood hypothesis; most samples have long-tailed, positively skewed distributions (Figures 4.5b,d,f). Based on these considerations, we judge it plausible that fluvial stratigraphy in the Blackhawk Formation and Ferron Sandstone may record bedform disequilibrium dynamics driven by formative flow variability, associated with the magnitudes and timescales of individual discharge events on the timescale of hours to days. Future experimental and modelling work should investigate whether and how bedform preservation ratios and the statistical nature of preserved cross-sets differs between systems in which bedform disequilibrium dynamics are driven by flashy flood hydrographs versus coevolution of dunes and bars, respectively. We advocate that this is the next step in determining the extent to which discharge variability can be quantitatively reconstructed from stratigraphic observations.

Ultimately, despite sampling a variety of fluvial planform styles across large geographic regions, our results indicate that measured dune-scale cross-sets do not demonstrate the geometries expected for bedform preservation under steady-state conditions, which routinely underpin palaeohydraulic investigations of ancient fluvial systems. This indicates that application of bedform preservation ratios of ~0.3 to fluvial strata may result in overestimation of true palaeoflow depths (c.f. Leclair & Bridge, 2001) and consequently underestimate palaeoslopes. We argue that systematic measurements of cross-set geometries and, where possible, bedform preservation ratios should be a routine tool to facilitate and contextualize palaeohydraulic reconstructions, and to test for the presence of bedform disequilibrium dynamics.

4.6 Conclusions

We made systematic measurements of dune-scale cross-set geometries and grain-sizes in fluvial strata of three Upper Cretaceous geologic formations in central Utah, USA: the Blackhawk Formation, Castlegate Sandstone, and Ferron Sandstone. Across all three formations, we documented consistently low $CV(h_{xs})$ in preserved cross-set thicknesses of 0.25–0.5. These field observations are inconsistent with the steady-state bedform preservation model that assumes cross-sets are generated by random variability in scour depth with time (Paola & Borgman, 1991; Leclair & Bridge, 2001). Instead, our observations add to the growing recognition that bedform preservation is dominated by disequilibrium dynamics (Reesink et al., 2015; Ganti et al., 2020; Leary & Ganti, 2020), resulting in higher bedform preservation ratios and the deposition of cross-sets which preserve a relatively narrow distribution of thicknesses ($CV(h_{xs})<<0.88$).

We considered two independent hypotheses that lead to enhanced bedform preservation in disequilibrium conditions. Under the flood hypothesis, our data indicate that the flood durations that typify these deposits likely ranged from hours to days, which are reflective of heavy rain and tropical storms in these ancient fluvial landscapes. Under the hierarchy hypothesis, the observed low $CV(h_{xs})$ is consistent with bedform deposits preserved with rapidly evolving bars whose timescale of migration likely spans days to months. Detangling the flood versus hierarchy controls on bedform preservation may be possible through the spatial contextualization of preserved deposits of single-thread rivers, with flow variability potentially the dominant control on the nature of bedform preservation in channel-thalweg deposits, such as those observed in the Ferron Sandstone and Blackhawk Formation. However, detangling these relative controls may be difficult in the deposits of braided rivers, such as the Castlegate Sandstone, which are characterized by migration of unit bars and braid bars that can lead to the enhanced bedform preservation.

Where low $CV(h_{xs})$ reflects enhanced bedform preservation associated with formative flow variability, the approaches presented in this paper have significant implications for investigating discharge variability in the geologic past, particularly the magnitudes, transport capacities, and durations of individual flood events generated during short-period climatic perturbations. Meanwhile, where low $CV(h_{xs})$ reflects enhanced bedform preservation associated with the presence of a morphodynamic hierarchy, these results have implications for evaluating the nature of interactions between dunes, bars, channel migration and channel avulsion in palaeo-channel networks. We advocate that quantifying cross-set geometries should become a standard approach in future studies to improve and contextualize palaeohydrological reconstructions from ancient fluvial deposits.

CHAPTER 5: The problem of palaeo-planforms[1]

ABSTRACT

Reconstructing river planform is crucial to understand ancient fluvial systems on Earth and other planets. Palaeo-planform is typically interpreted from qualitative facies observations of fluvial strata, but these can be inconsistent with quantitative approaches. Here we test three hydraulic planform predictors in Upper Cretaceous fluvial strata (Utah, USA) where there is a facies-derived consensus on palaeo-planform. However, results of each predictor cannot be reconciled with facies observations nor with each other. We find the well-known predictor of Parker (1976) is analytically best suited for geologic application but favours single-thread planforms. Given this predictor was originally tested using just 53 data points from natural rivers, we compile a new dataset of hydraulic geometries in natural rivers (n=1688), which span >550 globally widespread, sand- and gravel-bed rivers from various climate and vegetative regimes. We find the Parker (1976) criteria misclassify 65% of multi-thread rivers, and we show that depth/width (H/W) ratios alone are sufficient to discriminate single-thread ($H/W > 0.02$) and multi-thread ($H/W < 0.02$) rivers, suggesting that bank cohesion and stability are critical determinants of planform. However, we find that slope/Froude (S/Fr) ratios are useful to discriminate process in multi-thread rivers, i.e., whether generation of new threads is avulsion-dominated (anastomosing) or bifurcation-dominated (braided). Multi-thread rivers are likely to be anastomosing when $S/Fr < 0.003$ (shallower slopes) and braided when $S/Fr > 0.003$ (steeper slopes). Our new criteria successfully discriminate planform in modern rivers and our geologic examples, and offer an effective approach to predict planform in the geologic past.

5.1 Introduction

River planforms constitute a fundamental physical element of fluvial landscapes and reflect the quasi-equilibrium form of channels in response to water and sediment discharges. In ancient fluvial systems, their reconstruction is crucial to determine river response to climate and land-cover change (Gibling & Davies, 2012; Gibling et al., 2014; Colombera et al., 2017; Ielpi & Lapôtre, 2019a, 2020); water, sediment and biogeochemical fluxes (Ielpi & Lapôtre, 2020; Chapter 3 (Lyster et al., 2021)); and pre-vegetation landscape dynamics on Earth and other planets (Ielpi & Rainbird, 2016; Ielpi et al., 2018; Ganti et al., 2019; Ielpi & Lapôtre, 2019b; Lapôtre et al., 2019; Lapôtre & Ielpi, 2020). In fluvial strata, facies and architectural analyses provide qualitative insights into palaeo-planform (Miall, 1993, 1994; Adams & Bhattacharya, 2005; Hampson et al., 2013), however quantitative planform predictors are an important complement to these approaches. They are particularly important where preservation of fluvial architecture is limited by, e.g., discharge variability or channel reworking (Fielding et al., 2018; Chamberlin & Hajek, 2019; Herbert et al., 2020), where palaeohydraulic calculations are required (Chapter 3 (Lyster et. al., 2021)), and where facies interpretations may be equivocal. Recent debates about the implication of "sheet-braided" facies models

[1] A revised version of this chapter has been accepted for publication in ***Geology***

for pre-vegetation rivers underscore this latter issue (Gibling & Davies, 2012; Gibling et al., 2014; Ielpi & Rainbird, 2016; Ganti et al., 2019; Ielpi & Lapôtre, 2019a).

Planform predictors include empirically derived relations (e.g., van den Berg, 1995) and theoretical approaches, where the origins of meandering and braiding are predicted by mathematical models of channel stability and bar formation (e.g., Parker, 1976; Crosato & Mosselman, 2009). However, insights from these predictors can be inconsistent with stratigraphic observations (Ganti et al., 2019; Chapter 3 (Lyster et al., 2021)). Further, the discriminatory power of these predictors for geologic use is unclear because: (1) they are tested on modern datasets that lack of natural river data (relative to experimental and manmade channels) and which are bias toward North American and gravel-bed rivers; (2) they often discriminate only single- and multi-thread rivers, neglecting to differentiate anastomosing and braided multi-thread rivers (Schumm, 1985; Church, 2006; Church & Ferguson, 2015).

Here we assessed how three planform predictors perform, when applied to fluvial strata with consensus facies-derived interpretations of planform, to establish which approach is most suitable for geologic application. We then compiled a new dataset of hydraulic geometries in natural rivers and used these data to propose new criteria for palaeo-planform prediction.

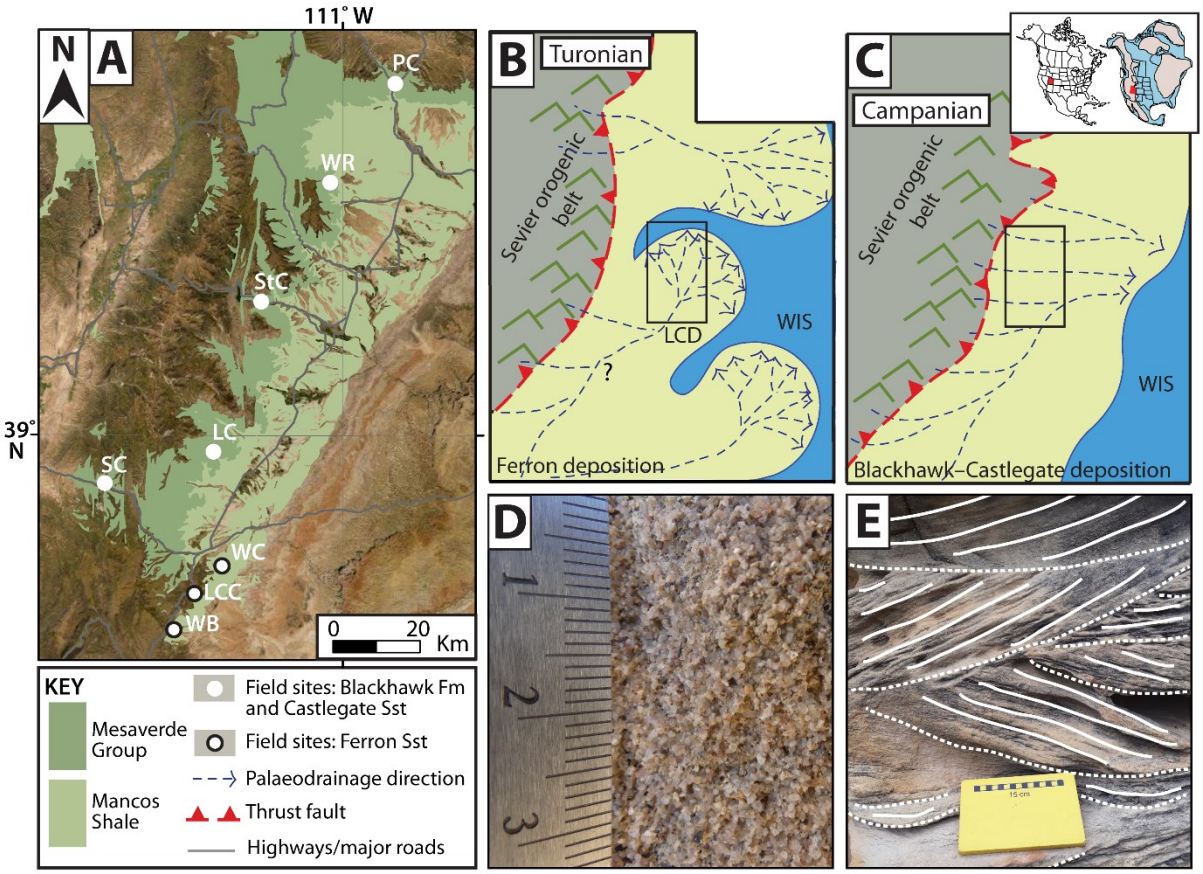

Figure 5.1 | A) Field sites in central Utah, USA: Last Chance Creek (LCC); Link Canyon (LC); Price Canyon (PC); Salina Canyon (SC); Straight Canyon (StC); Wattis Road (WR); Willow Basin (WB); Willow Creek (WC). **B, C)** Palaeogeography of Utah in the **(B)** Turonian and **(C)** Campanian. Black boxes indicate the position of **A**. Inset indicates the position of Utah (red) relative to modern (left) and Late Cretaceous (right) North America. For each cross-set we measured the **(D)** median grain-size and **(E)** mean cross-set thickness. Dotted and solid white lines indicate bounding surfaces and individual foresets, respectively. LCD = Last Chance delta; WIS = Western Interior Seaway.

5.2 Methods

5.2.1 Palaeo-planform reconstruction

We focused on three Upper Cretaceous geologic formations, Utah, USA (Figure 5.1a), where distinct planforms have been interpreted from detailed facies and architectural analyses: the Ferron Sandstone preserves meandering trunk channels (Cotter, 1971; Chidsey et al., 2004) (Figure 5.1b); the Blackhawk Formation preserves single- and multi-thread channels (Adams & Bhattacharya, 2005; Hampson et al., 2013) (Figure 5.1c); and the Castlegate Sandstone preserves mostly braided channels (Miall, 1993, 1994) (Figure 5.1c).

For individual cross-sets in the Blackhawk Formation (n=81), Castlegate Sandstone (n=146) and Ferron Sandstone (n=190), we determined mean cross-set thickness, h_{xs}, and median grain-size, D_{50} (Figure 5.1d,e), and used a well-established quantitative framework (c.f. Chapter 3 (Lyster et al., 2021); Supplementary Methods) to reconstruct flow depth, H, slope, S, flow velocity, U, and Froude number, Fr. We also require the wetted channel width, W, which is difficult to constrain from geologic outcrop. To address this, we: (1) implemented plausible lower and upper estimates of W (W_{min} and W_{max}) based on published constraints; and (2) evaluated the sensitivity of each predictor to channel aspect ratio (H/W) for a given h_{xs} and D_{50}, using a Monte Carlo method to estimate uncertainty (Supplementary Methods).

For each cross-set we used three predictors to reconstruct planform (Table 5.1). First, we used the predictor of Parker (1976) (PK) where ϵ is a planform parameter, and where $\epsilon < 1$ for single-thread rivers, $\epsilon > 1$ for multi-thread rivers with 1–10 threads, and $\epsilon > 10$ for multi-thread rivers with >10 threads (Table 5.1; Equation 5.1). Second, we used the predictor of Crosato and Mosselman (2009) (C&M) to estimate the bar mode, m, of rivers, where $m \leq 1.5$ for single-thread rivers, $m \geq 2.5$ for multi-thread rivers, and $1.5 < m < 2.5$ for transitional rivers (Table 5.1; Equation 5.2). Third, we used the predictor of van den Berg (1995) (VdB) to estimate a potential specific stream power parameter, ω, to discriminate single- and multi-thread rivers (Table 5.1; Equation 5.3).

5.2.2 Validating planform predictors

We compiled a dataset of hydraulic geometries in natural rivers. We focused data collection on rivers that are appropriate modern analogues for rivers in the rock record, and we worked to include sand- and gravel-bed rivers that are globally widespread and from various climate and vegetative regimes (Supplementary Methods). We included rivers with reported values of W, H, S, U, and discharge (Q); we calculated Fr (Supplementary Methods). Our dataset contains 1688 data points for >550 rivers from 87 sources, with 758 observations of multi-thread rivers, including braided (n=402), anastomosing (n=124) and transitional (n=232) planforms, and 930 observations of single-thread rivers. With these data we evaluated the efficacy of existing single- to multi-thread thresholds, and we analysed data distributions to propose new thresholds which honour both modern and stratigraphic observations.

Table 5.1 | Planforms reconstructed for the Blackhawk Formation, Castlegate Sandstone and Ferron Sandstone

Planform predictor*		**Equation 5.1**		**Equation 5.2**			**Equation 5.3**	
		Parker (1976)		Crosato & Mosselman (2009)			Van den Berg (1995)	
		$\epsilon = \frac{S}{Fr}\frac{H}{W}$		$m^2 = 0.17g\frac{b-3}{\sqrt{RD_{50}}}\frac{W^3S}{CQ}$			$\omega = 2.1\,S\sqrt{Q}$	
Planform reconstructed		Single-thread	Multi-thread	Single-thread	Transi-tional	Multi-thread	Single-thread	Multi-thread
Blackhawk Formation	W_{min}†	100%§	0%	0%	2%	98%	95%	5%
	W_{max}‡	91%	9%	0%	0%	100%	9%	91%
Castlegate Sandstone	W_{min}	100%	0%	0%	0%	100%	100%	0%
	W_{max}	87%	13%	0%	0%	100%	64%	36%
Ferron Sandstone	W_{min}	100%	0%	7%	31.5%	61.5%	99%	1%
	W_{max}	100%	0%	1%	10%	89%	94%	6%

*Listed variables are as follows: ϵ = planform parameter; S = slope; H = flow depth; Fr = Froude number; W = channel width; m = bar mode; g = acceleration due to gravity; b = degree of nonlinearity of the dependence of sediment transport on flow velocity, assumed to be 4 in sand-bed rivers; R = submerged specific density of sediment; D_{50} = median grain-size; C = Chézy friction coefficient; Q = total water discharge (see Supplementary Methods)

†Planforms reconstructed using a minimum plausible channel width, W_{min} (see Figure 5.2 and Supplementary Methods)

‡Planforms reconstructed using a maximum plausible channel width, W_{max} (see Figure 5.2 and Supplementary Methods)

5.3 Results

5.3.1 Palaeo-planform reconstruction

For each formation, we present the planforms implied using W_{min} and W_{max} (Figure 5.2; Table 5.1). We find the PK predictor strongly favours single-thread planforms, even for maximum plausible widths (Figure 5.2a–c), which is inconsistent with observations of multi-thread Blackhawk and Castlegate channels. Meanwhile, C&M strongly favours multi-thread planforms (Figure 5.2e–g), which is inconsistent with observations of single-thread Blackhawk and Ferron channels, and VdB mostly favours single-thread planforms (Figure 5.2i–j) which, again, is inconsistent with multi-thread Blackhawk and Castlegate channels. Ultimately, the predictors are inconsistent with one another, and no predictor is consistent with stratigraphic consensus for all three geologic examples. We also evaluated the sensitivity of each predictor to H/W (Figure 5.2d,h,l) and, despite identical data inputs for h_{xs} and D_{50}, we find that threshold H/W between multi- and single-thread rivers is markedly different for each predictor (PK ~0.002, C&M ~0.03, VdB ~0.005). In particular, we highlight an order of magnitude difference in threshold H/W between PK and C&M (Figure 5.2d,h).

For geologic applications, the PK predictor is analytically most appropriate because the threshold between multi- and single-thread rivers is dependent on H/W (Figure 5.2d), whereas in C&M and VdB the threshold is independent of H/W and implicitly assumes that H/W is known (Figure 5.2h,l). This is not an issue in modern systems where H/W is known but is vital in geologic applications where W is uncertain. Moreover, PK requires the fewest assumptions and does not impart additional uncertainty in W to the y-axis, unlike C&M and VdB (Figure 5.2d,h,l; Table 5.1; Equations 5.1–5.3). However, PK favours single-thread classifications, and we therefore evaluated this predictor with our new dataset.

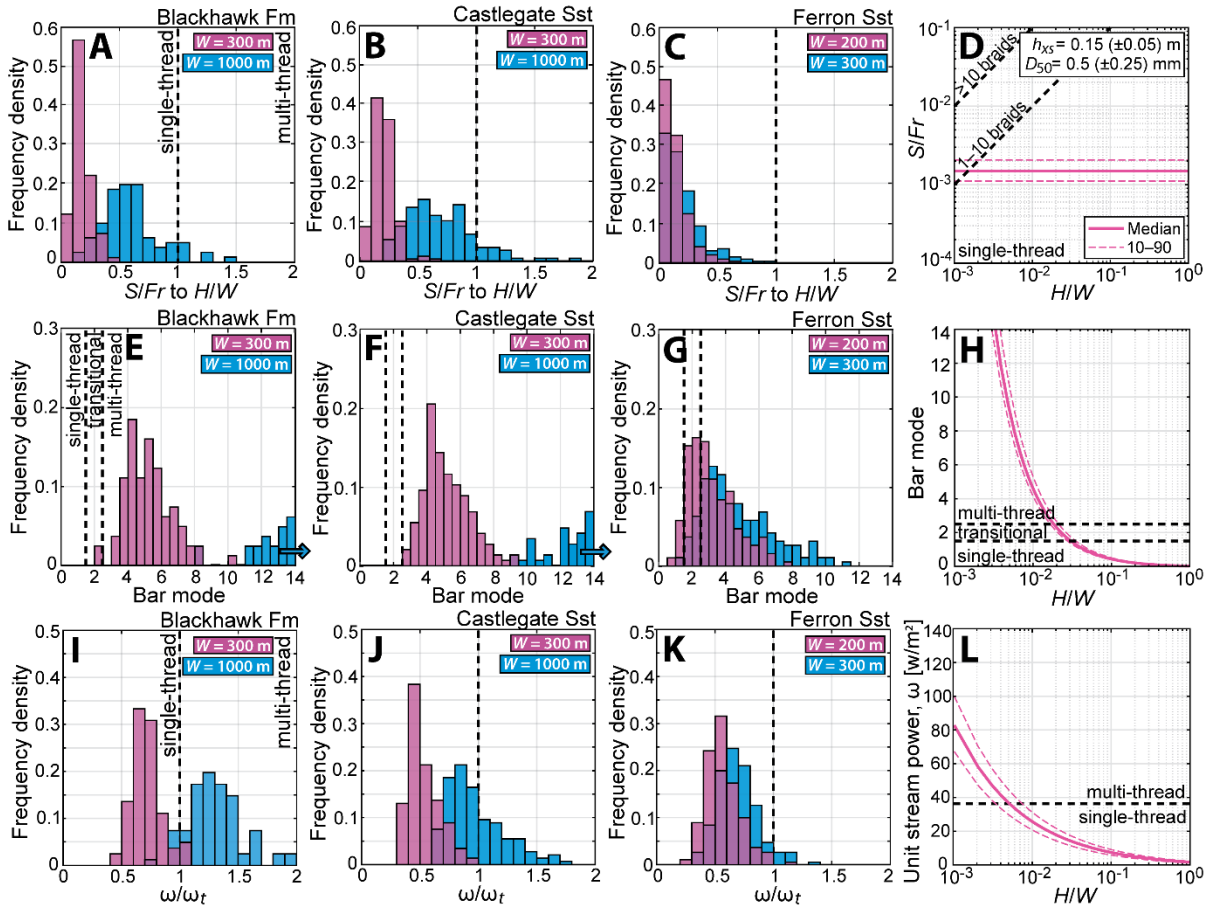

Figure 5.2 | Planforms reconstructed for cross-sets in each formation, assuming plausible endmember widths (pink and blue boxes). Planforms reconstructed using Parker's (1976) approach (PK) for the **(A)** Blackhawk Formation, **(B)** Castlegate Sandstone and **(C)** Ferron Sandstone. **D)** Sensitivity of PK to depth/width (*H*/*W*). Planforms reconstructed using Crosato & Mosselman's (2009) approach (C&M) for the **(E)** Blackhawk Formation, **(F)** Castlegate Sandstone and **(G)** Ferron Sandstone. **H)** Sensitivity of C&M to *H*/*W*. Planforms reconstructed using van den Berg's (1995) approach (VdB) for the **(I)** Blackhawk Formation, **(J)** Castlegate Sandstone and **(K)** Ferron Sandstone. **L)** Sensitivity of VdB to *H*/*W*. See **D** for the mean and standard deviation of cross-set height, h_{xs}, and grain-size, D_{50}, used to evaluate sensitivity. *S*/*Fr* = slope/Froude; ω/ω_t = potential specific stream power/threshold stream power.

5.3.2 Validating planform predictors

In our dataset, the PK predictor correctly predicts planform in 93% of single-thread rivers, but only 35% of multi-thread rivers (Figure 5.3a), which indicates that the existing PK calibration requires improvement. Significantly, for single- and multi-thread rivers, our data show that H/W distributions are statistically distinct whereas S/Fr distributions have similar medians and interquartile ranges. Consequently, we find a simple H/W threshold can effectively discriminate single-thread ($H/W > 0.02$) and multi-thread ($H/W < 0.02$) rivers (Figure 5.3a). This threshold correctly predicts planform in 82% of single-thread rivers (90% predicted by $H/W > 0.014$) and 84% of multi-thread rivers (90% predicted by $H/W < 0.027$) (Figure 5.3a).

Existing planform predictors do not discriminate multi-thread planform styles, i.e., braiding and anastomosing, however our dataset enables this. We find that braided and anastomosing rivers have similar median H/W but distinct S/Fr distributions (Figure 3b). In braided rivers S/Fr spans ~0.001−0.1, whereas in anastomosing rivers S/Fr spans ~0.0001−0.001 (Figure 5.3b). In transitional rivers S/Fr values of ~0.001−0.01 overlap with braided and anastomosing rivers, which we expect as these data may reflect meandering–anastomosing or sinuous–braided transitions. Of multi-thread rivers, the PK predictor correctly predicts planform in 47% of braided rivers, but only 5% of anastomosing rivers. Again, we find that a simple threshold can discriminate braided ($S/Fr > 0.003$) and anastomosing ($S/Fr < 0.003$) rivers, which correctly predicts planform in 84% of braided rivers (90% predicted by $S/Fr > 0.002$) and 85% of anastomosing rivers (90% predicted by $S/Fr < 0.0034$) (Figure 5.3b).

Using these thresholds together, i.e., $H/W < 0.02$ and $S/Fr < 0.003$ for anastomosing rivers, $H/W < 0.02$ and $S/Fr > 0.003$ for braided rivers, and $H/W > 0.02$ for single-thread rivers, we correctly predict 70% of anastomosing rivers, 65% of braided rivers, and 82% of single-thread rivers in our dataset. Applying these criteria to our geologic data, Ferron rivers plot as single-thread (triangle, Figure 5.3b), consistent with stratigraphic interpretations (Cotter, 1971; Chidsey et al., 2004), and Blackhawk and Castlegate rivers plot as anastomosing (squares, Figure 5.3b), consistent with stratigraphic interpretations of multi-thread rivers with sand beds, high suspended sediment loads, and a propensity to avulsion (e.g., Miall, 1993, 1994; Chamberlin & Hajek, 2019; Chapter 3 (Lyster et al., 2021)). Depending on the assumed W, Blackhawk channels plot near the single-thread transition, consistent with observations of single-thread Blackhawk channels (Hampson et al., 2013).

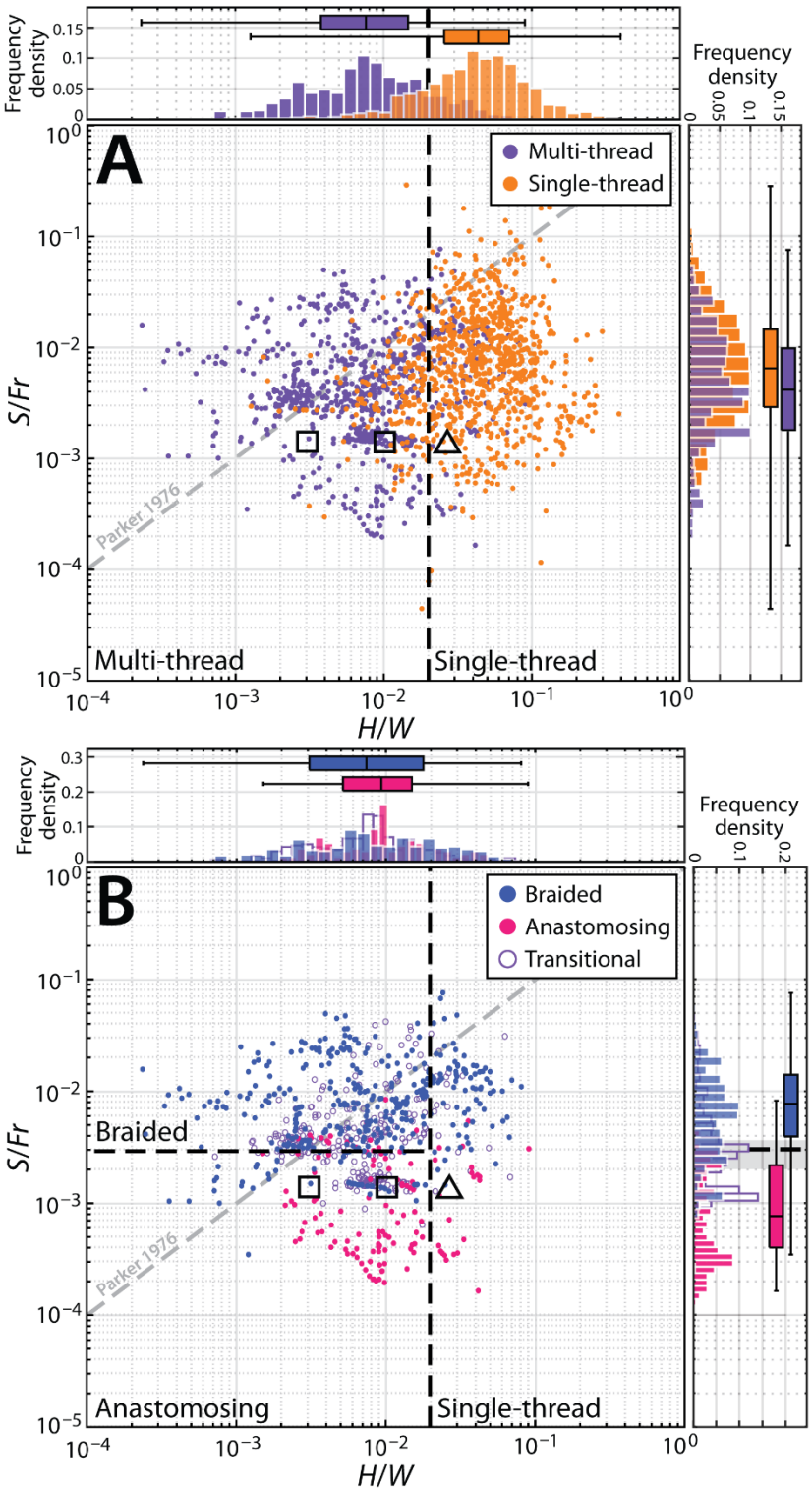

Figure 5.3 | Observations of: **(A)** single- and multi-thread rivers; **(B)** braided, anastomosing and transitional multi-thread rivers. X-axis histograms indicate frequency densities of depth/width ratios (H/W). X-axis box plots indicate median H/W (box central marks), the 25–75 percentile range of H/W (box edges) and minimum–maximum H/W (whiskers). Y-axis histograms and box plots depict the same but for slope/Froude ratios (S/Fr). Grey dashed lines indicate the single- to multi-thread threshold defined by Parker (1976). Black dashed lines indicate the thresholds defined in this study. Squares indicate where Blackhawk and Castlegate channels plot (assuming W = 1000 m or 300 m (interchangeable)) and triangles indicate where Ferron channels plot (assuming W = 250 m).

5.4 Discussion and conclusions

For geologic applications, we show that existing planform predictors disagree with each other and with facies interpretations. While the PK approach is most suitable for palaeo-planform prediction, the current PK predictor favours single-thread classifications (Figure 5.2a−d) and incorrectly classifies 2/3 of modern multi-thread rivers in our dataset (Figure 5.3a). We note that the theory used to derive the PK predictor (and C&M) assumes straight channels with rectangular cross-sections and non-erodible banks. Consequently, theory-based predictors may not capture the wide variability of natural rivers, minimizing the potential importance of factors beyond this geometry. Moreover, the original dataset used to validate the PK predictor was small and heavily relied on experimental and manmade channels. In our new, larger dataset, H/W is the most important discriminator of planform, rather than S/Fr, with $H/W > 0.02$ in single-thread rivers and $H/W < 0.02$ in multi-thread rivers (Figure 5.3a). We hypothesise that the apparent connection between H/W and planform may indicate that bank cohesion and erodibility are critical determinants of planform (Lapôtre et al., 2019; Dunne & Jerolmack, 2020) as opposed to channel slope.

While our data show that S/Fr cannot discriminate single- and multi-thread planforms, we find that S/Fr is important for discriminating multi-thread planform style. In multi-thread rivers, new threads may have multiple origins, including avulsion in anastomosing rivers and bifurcation in braided rivers (Jerolmack & Mohrig, 2007; Kleinhans et al., 2013; Carling et al., 2014). Our data suggest that S/Fr may capture a slope-controlled process transition — we show that multi-thread rivers are likely to be anastomosing when $S/Fr < 0.003$ (relatively shallow slopes) and braided when $S/Fr > 0.003$ (steep slopes) (Figure 5.3b). These new thresholds are easy to apply to geologic data, where palaeoslope can be reconstructed (e.g., Trampush et al., 2014), and are a better fit to modern and stratigraphic observations of multi-thread rivers.

Going forward, palaeo-planform prediction remains limited by uncertainties in channel aspect ratios. While H can be estimated and validated from geologic outcrop (e.g., Chapter 3 (Lyster et al., 2021)), it remains difficult to constrain W. New approaches to estimate W are promising (e.g., Greenberg et al., 2021), however uncertainties associated with the number of active threads in rivers remain. For palaeo-planform prediction, we advise that our criteria are implemented for a range of plausible widths. Moreover, while our criteria resolve inconsistencies between facies interpretations and planform predictors, we stress the importance of coupling these approaches. For the Blackhawk Formation and Castlegate Sandstone, reconstructed planforms and hydraulic geometries are broadly similar (Figure 5.2), however their stratigraphic architectures are distinct. Therefore, understanding the kinematic and stratigraphic controls on the geologic preservation of planforms, as opposed to their geomorphic equivalents, is now a pressing research need.

Where hydraulic geometries can be reconstructed from fluvial strata, our new criteria provide a simple and effective way to predict palaeo-planform. These criteria will enhance the fidelity of water, sediment, and biogeochemical flux reconstructions, and offer new insights into channel-forming processes and landscape

evolution in the geologic past. Our criteria will be particularly useful where outcrop is limited or facies interpretations are equivocal, such as unvegetated fluvial systems of early Earth and Mars.

CHAPTER 6: Discussion

6.1 General synthesis

In this thesis I sought to develop new methods and frameworks to quantify the dynamics and behaviour of ancient fluvial systems. To achieve this I exploited novel datasets, including palaeo-digital elevation models (palaeoDEMs) and general circulation model (GCM) outputs, and I compiled my own datasets, including stratigraphic observations of fluvial strata (primary data from field data collection) and modern river observations (secondary data from literature). With these datasets, I exemplified a new approach to reconstruct water and suspended sediment discharges in ancient fluvial systems (Chapter 2) and I developed new frameworks and methods to reconstruct river morphologies and hydrodynamics (Chapters 3, 4), including river planform (Chapter 5). Collectively, the work presented in this thesis satisfies the Aims and Objectives outlined in the Introduction (***Section 1.4***).

Aim 1 of this thesis was to develop a novel approach to reconstruct water and sediment discharges in ancient fluvial systems. I addressed this aim in Chapter 2 where I used palaeoDEMs, geographic information systems (GIS) techniques, and spatial statistics to reconstruct palaeocatchments and extract their geometries (Objective 1.1), and where I used GCM outputs and spatial statistics to extract catchment-averaged climate, i.e., temperatures, precipitation, and water discharges (Objective 1.2). I then used the BQART model of Syvitski and Milliman (2007) to reconstruct mean annual suspended sediment discharges in palaeocatchments (Objective 1.3) and, as a by-product of these results, I was additionally able to reconstruct catchment-averaged erosion rates. I demonstrated this approach for the Cenomanian and Turonian North American continent (Figure 2.8) and showed how it can be used to explore spatiotemporal trends in the movement of water and sediment across Earth's surface in the geological past. I predicted that the Late Cretaceous North American continent exported twice as much sediment to oceans than the modern North American continent and, further, that this sediment was exported from half of the land (i.e., sediment yields were four times greater). Moreover, within the North American continent I predicted that sediment supply was highly variable in space, spanning seven orders of magnitude in units of m^3/yr (Figure 2.8). For example, I predicted that the western margin of the Western Interior Seaway (WIS) contributed approximately three times more sediment to the WIS than the eastern margin, and that the eastern margin was only an important source of sediment in low latitude catchments draining the Appalachians southwest towards the Gulf of Mexico (Figure 2.8). These spatial variations offer new insights into the relative roles of the active continental margin (western WIS margin) and stable continental craton (eastern WIS margin) in the evolution of Western Interior foreland basin during the Cretaceous.

Importantly, to validate my palaeoDEM–GCM–BQART approach, I corroborated estimates of suspended sediment discharges with estimates derived using independent approaches, and I evaluated the univariate and multivariate sensitivity of the approach to uncertainty (Objective 1.4; Figure 2.7). My estimates of

suspended sediment discharges were in good agreement with the published estimates of Lin and Bhattacharya (2017) and Sharma et al. (2017), and evaluation of univariate and multivariate sensitivity highlighted that this new palaeoDEM–GCM–BQART approach can successfully recover first order approximations of suspended sediment discharges in the geological past.

The overarching goal of this thesis is to improve our ability to quantify the dynamics and behaviour of ancient fluvial systems and, using my new palaeoDEM–GCM–BQART approach, I argue that we should now be able to gain continental-scale insights into the behaviours of ancient fluvial systems where palaeogeographies and climate model outputs exist, or where they can be produced. Using this approach, we can now predict water discharges, sediment discharges, and catchment-averaged erosion rates in palaeocatchments with limited outcrop preservation. Beyond these constraints, my palaeoDEM–GCM–BQART approach also enables us to: (1) extract information pertaining to the sizes, configurations, and distributions of palaeocatchments (Appendix Figure A1); (2) identify the loci of water and sediment supply to oceans (Figures 2.3, 2.10); and, more generally, (3) understand the movement of water and sediment across Earth's surface in palaeoclimates characterized by elevated atmospheric CO_2 concentrations (see Wang et al., 2014). The palaeoDEM–GCM–BQART approach therefore provides insights that can be used to explore the dynamics and evolution of ancient fluvial systems at large spatial and temporal scales, and which are particularly useful where the rock record is limited and/or absent.

Having developed a new approach to investigate ancient fluvial systems at continental scales, I moved focus to investigate river dynamics at regional-, catchment-, and channel reach-scales. Insights into the morphology and behaviour of ancient fluvial systems at smaller spatial scales are crucial complements to continental-scale insights. For instance, constraints on river morphologies and hydrodynamics can be used to reconstruct water and sediment discharges using a fulcrum-style approach (c.f. Holbrook & Wanas, 2014), and these estimates can be used to corroborate estimates of water and sediment discharges derived from continental-scale approaches (i.e., the palaeoDEM–GCM–BQART approach in Chapter 2). In addition, insights into the behaviour of fluvial systems at smaller spatial scales can be used to explain observed trends and/or variability in the behaviour of fluvial systems at continental-scales.

Given the importance of investigating ancient fluvial systems at regional-, catchment-, and channel-reach scales, Aim 2 of this thesis was to develop quantitative frameworks and methods to reconstruct river morphologies, hydrodynamics, and morphodynamics from fluvial strata. I addressed this aim in Chapters 3 and 4 using detailed field measurements of grain-sizes, cross-set geometries, maximum cross-set thicknesses, architectural element dimensions, and more, which I collected from fluvial strata of the Upper Cretaceous Ferron Sandstone, Blackhawk Formation, Castlegate Sandstone, and Price River Formation in central Utah, USA (Objective 2.1).

In Chapter 3, I directly addressed Aim 2 and presented a quantitative framework to reconstruct river morphologies, hydrodynamics and morphodynamics from detailed field measurements of fluvial strata. This framework incorporated a variety of empirically, theoretically, and experimentally derived relations

(including Parker, 1976; Paola & Borgman, 1991; Dade & Friend, 1998; Leclair & Bridge, 2001; Ferguson & Church, 2004; Trampush et al., 2014) (Objective 2.2), and a Monte Carlo uncertainty propagation method (Objective 2.4). I exemplified this new framework for the Blackhawk Formation, Castlegate Sandstone, and Price River Formation, central Utah, USA; reconstructed parameters included: dune heights, flow depths, slopes, alluvial relief, flow velocities, unit water discharges, sediment transport modes, and planform morphologies (Figures 3.6–3.13). In principle, these reconstructions are point reconstructions (i.e., they are for a particular point in space and time) and therefore reflect local instantaneous conditions in individual channel reaches. To implement this framework at catchment scales, I visited multiple field sites for the same fluvial system (upstream to downstream, as informed by detrital zircon (DZ) analysis and palaeoflow measurements) and, to implement this framework at regional scales, I visited field sites for a number of adjacent fluvial systems (as informed by DZ analysis and theory of catchment outlet spacing). In total, I reconstructed spatial trends in river morphologies, hydrodynamics and morphodynamics across five parallel fluvial systems, two of which included upstream to downstream transects (Figure 3.1). Moreover, I reconstructed temporal trends across seven stratigraphic intervals through Blackhawk, Castlegate, and Price River deposition (Figure 3.2). Importantly, implementing this framework at catchment- and regional-scales is a useful complement to the space- and time-averaged approach that I presented in Chapter 2.

This framework enabled me to gain new insights into the evolution of Blackhawk, Castlegate, and Price River rivers at million to multi-million-year timescales. The most prominent trend that I reconstructed was an up to four-fold increase in slope at the Blackhawk–Castlegate transition (Figure 3.8). Coeval to this increase I observed no change in unit water discharges (Figure 3.10) which argues against a climatically driven slope increase (assuming channel widths did not decrease) and points to a tectonically driven slope increase. Importantly, reconstruction of a regional slope increase at the Blackhawk–Castlegate transition occurred *within* the Campanian stage of the Late Cretaceous. However, field investigation could instead focus on two formations that straddle a stage boundary, such as the Cenomanian and Turonian stages. In this scenario, results using this framework would complement results for the Cenomanian and Turonian stages using the palaeoDEM–GCM–BQART approach (i.e., the results of Chapter 2). The palaeoDEM–GCM–BQART uses stage-specific palaeoDEMs and therefore tracks changes in fluvial behaviour between stages. Insights gained from fluvial strata at regional scales, particularly from strata which straddle stage boundaries, can offer further insights and possibly explain trends that have been observed at continental-scales using an approach such as the palaeoDEM–GCM–BQART approach. Another means by which this framework can complement the palaeoDEM–GCM–BQART approach is by comparison of sediment discharge estimates. In Chapter 3 I constrained the morphologies and hydrodynamics of Blackhawk and Castlegate rivers. In principle, I can now use these constraints to reconstruct sediment discharges using a fulcrum-style approach (c.f. Holbrook & Wanas, 2014), similar to the method used to reconstruct sediment discharges in the case studies presented in Chapter 2 (Lin & Bhattacharya, 2017; Sharma et al., 2017). With estimates of sediment discharges in Blackhawk and Castlegate rivers derived using a fulcrum-style approach,

I could validate estimates of sediment discharges that were instead derived using the palaeoDEM–GCM–BQART approach — I return to this research opportunity in ***Section 6.3***.

Effective estimation of uncertainty is important in quantitative sedimentology. To account for uncertainties of the framework that I present in Chapter 3, and to therefore evaluate its efficacy, I incorporated a Monte Carlo uncertainty propagation method (Objectives 2.4 and 2.5). Further, I contrasted different methods of reconstructing the same parameter, e.g., I used a Shields stress inversion and the method of Trampush et al. (2014) to reconstruct slope (Equations 3.3 and 3.4), and I also contrasted estimates of flow depth using the method of Bradley and Venditti (2017) (Equation 3.2) with independent flow depth proxies (Objective 2.5). In evaluating the efficacy of my new framework, two key observations arose which provided additional motivation to the work presented in subsequent research chapters (Chapters 4 and 5).

The first key observation arose when contrasting reconstructed flow depths with independent flow depth proxies — agreement between these values is good and highlights that bedform-scale approaches to flow depth reconstructions are useful, particularly where barforms are poorly preserved, and/or when using core data. Interestingly, this reconstruction method assumed steady-state conditions (Paola & Borgman, 1991; Leclair & Bridge, 2001), and agreement between reconstructed flow depths and independent proxies might therefore suggest that steady-state assumptions were appropriate and that Blackhawk and Castlegate rivers flowed at steady-state. However, when analysing field measurements of cross-sets, I noticed that cross-set geometries were not consistent with the geometries we expect for preservation in steady-state conditions (Paola & Borgman, 1991; Bridge, 1997; Leclair & Bridge, 2001; Leclair, 2002; Jerolmack & Mohrig, 2005). Instead, cross-set geometries were consistent with the geometries we expect for preservation in non-steady state conditions (Jerolmack & Mohrig, 2005; Reesink et al., 2015; Ganti et al., 2020; Leary & Ganti, 2020). This observation was a major motivation for work presented in Chapter 4. The second key observation was that quantitative reconstructions of river planform, which I derived using the stability criterion of Parker (1976), were inconsistent with stratigraphic interpretations of planform. Not only did I observe this inconsistency, but this inconsistency has also been reported for other formations (Ganti et al., 2019) and provided additional motivation to work presented in Chapter 5.

I further addressed Aim 2 in Chapter 4. Theoretically derived approaches to reconstruct the morphologies of ancient rivers typically assume that bedform preservation occurred in steady-state flow conditions (e.g., Paola & Borgman, 1991; Leclair, 2002). However, this assumption may be unreasonable as, strictly defined, steady-state conditions are commonly violated in natural systems when discharge is variable (Fielding et al., 2018; Herbert et al., 2020) or under relatively constant discharge conditions in which spontaneously developed features such as bars establish locally variable flow conditions that change as bars shift and channels migrate (Ganti et al., 2020; Wysocki & Hajek, 2021). Chapter 4 was primarily motivated by observations in literature that non-steady conditions directly influence bedform preservation (Ten Brinke et al., 1999; Jerolmack & Mohrig, 2005; Reesink & Bridge, 2007; Reesink & Bridge, 2009; Reesink et al.,

2015; Fielding et al., 2018; Herbert et al., 2020; Leary & Ganti, 2020), but was additionally motivated by the field observations that I made in Chapter 3.

In Chapter 4 I therefore investigated whether steady-state assumptions are appropriate for investigation of ancient fluvial systems (Objective 2.3) and, for the Blackhawk Formation, Castlegate Sandstone, and, additionally, the Ferron Sandstone, I documented unambiguous evidence for enhanced bedform preservation in non-steady, or disequilibrium, conditions (Figure 4.6). This information is crucial because, along with other palaeohydrological studies (e.g., Holbrook & Wanas, 2014; Ganti et al., 2019; Wang et al., 2020), the framework that I presented in Chapter 3 used steady-state assumptions to estimate bedform size and flow depth.

With evidence of enhanced bedform preservation in disequilibrium conditions, I explored whether it is possible to extract quantitative information pertaining to the nature of these disequilibrium conditions (i.e., constraints on flow variability and/or relative rates of bedform and barform migration) from these fluvial strata (Objective 2.2). However, we currently have no method of distinguishing whether enhanced bedform preservation in disequilibrium conditions is the result of flow variability (Leary & Ganti, 2020) or concurrent migration of dunes and bars, i.e., the presence of a morphodynamics hierarchy (Ganti et al., 2020). Therefore, I calculated bedform turnover timescales to contextualise the implications of both scenarios, respectively (Figure 4.7). Assuming that enhanced bedform preservation was controlled by flow variability, I estimated flood durations of order a few hours to a few days (Figure 4.8), which is consistent with flooding generated by torrential rains and storms in perennial discharge regimes (Serinaldi et al., 2018). Moreover, my interpretation of perennial fluvial systems is consistent with published facies analyses of these systems, which describe sedimentary and architectural structures typically associated with perennial discharge regimes (see review by Plink-Björklund, 2015). Whereas, if enhanced bedform preservation was controlled by the concurrent migration of dunes and bars, then I anticipated that bar migration rates must approach the rates of dune migration, such that dunes have high angles of climb.

Going forward, future work must aim to disentangle the relative roles of flow variability and morphodynamic hierarchy on enhanced bedform preservation, so that we can isolate and extract meaningful constraints on flow variability from fluvial strata. I revisit this topic in ***Section 6.4*** where I outline how future work can directly tackle this research challenge. In addition, future work must consider the implication of enhanced bedform preservation on palaeohydraulic reconstructions. In steady-state conditions we expect bedform preservation ratios of ~0.3 whereas, in disequilibrium conditions, bedform preservation ratios may reach 0.7 (Leary & Ganti, 2020). Higher bedform preservation ratios have implications for the framework that I presented in Chapter 3, as they imply that the model parameter in Equation 3.1 is incorrect and overpredicts dune heights — I return to these implications in ***Section 6.2***.

Finally, Aim 3 of this thesis was to develop a new approach to reconstruct planform morphology in ancient fluvial systems and I addressed this aim in Chapter 5. This aim was primarily motivated by the importance of planform reconstruction for the investigation of ancient rivers — constraints on the number of active

threads in ancient rivers are crucial to reconstruct total volumetric water and sediment discharges. However, Aim 3 was additionally motivated by observations made in Chapter 3, and by Ganti et al. (2019), that quantitative reconstructions of planform using the theoretically derived planform stability criterion of Parker (1976) imply planforms that are inconsistent with facies-based interpretations of planform. This raises questions as to the efficacy of quantitative planform predictors, which has implications for their use where the rock record is limited, or where facies interpretations are equivocal (Davies & Gibling, 2010, 2011; Ielpi & Rainbird, 2016; Ielpi et al., 2018; McMahon & Davies, 2018; Ganti et al., 2019). In Chapter 4, further motivation was provided. Here I hypothesized that thalweg deposits of single-thread rivers preserve bedform disequilibrium dynamics controlled by flow variability, and that thalweg deposits of single-thread rivers may therefore offer the best chance to quantify flow variability from fluvial strata. Whereas in multi-thread rivers I hypothesized that enhanced bedform preservation is likely to be controlled by hierarchy. Future work to test this hypothesis in fluvial strata will therefore require knowledge of planform; we expect the distributions of different hierarchical elements to vary between rivers characterized by different planforms, and we therefore might expect the role of flow variability on enhanced bedform preservation to vary between rivers characterized by different planforms.

To address Aim 3, as well as observations made in Chapters 3 and 4 and by Ganti et al. (2019), I evaluated three well-known, and widely used, quantitative planform predictors (Parker, 1976; van den Berg, 1995; Crosato & Mosselman, 2009) (Objective 3.1). I applied these predictors to field measurements of the Ferron Sandstone, Blackhawk Formation, and Castlegate Sandstone, each of which has a consensus facies interpretation of planform, and I found that the results of each predictor are inconsistent with each other and with stratigraphic consensus for all three formations (Objective 3.1). As planform predictors are typically tested using few observations of hydraulic geometries in natural rivers (e.g., n = 53 in Parker (1976)), I compiled a large database of hydraulic geometries in natural rivers (n = 1688; Objective 3.2). I then used this new dataset to evaluate the efficacy of the existing Parker (1976) stability criterion, and I established new criteria for palaeo-planform prediction, including confidence intervals, which honour both modern rivers and the three geologic examples (Objectives 3.3 and 3.4).

Significantly, in compiling hydraulic geometries of natural rivers, I found that channel aspect ratio is the most important discriminator of single-thread and multi-thread planforms, and that slope is relatively unimportant (Figure 5.3). This contradicts the use of planform predictors in which slope is an important discriminant of single-thread and multi-thread planforms (Leopold & Wolman, 1957; Parker, 1976; Eaton et al., 2010). Steep slopes are traditionally perceived as conditions conducive to the development of braiding (Knighton, 1998) and, because existing planform predictors are usually tested using relatively few data from natural rivers (compared to data from manmade channels and flume experiments), the importance of slope may have been overstated. My new database suggests that channel aspect ratios are the best discriminant of single-thread and multi-thread planforms, which points to the possibility that bank stability and cohesion are critical determinants of planform, and is in line with vast recent work to investigate the important role

of bank stability and cohesion on setting channel widths and lateral mobility in modern rivers (Ielpi & Lapôtre, 2019b; Lapôtre et al., 2019; Dunne & Jerolmack, 2020; Ielpi & Lapôtre, 2020).

While slope may not be useful for discriminating multi-thread rivers, I found that slope may instead capture a process-controlled transition between braided and anastomosing multi-thread rivers. Existing planform predictors typically only discriminate single-thread and multi-thread rivers, which is a limitation because planform morphology exists on a spectrum with multiple dimensions; the endmembers of multi-thread rivers are braided and anastomosing multi-thread rivers, whereas the endmembers of single-thread rivers are meandering and sinuous/straight single-thread rivers. The exact nature of single-thread and multi-thread planforms varies as a function of multiple parameters (Schumm, 1963; Church & Rood, 1983; Schumm, 1985; Grant et al., 1990; Nanson & Knighton, 1996; Makaske, 2001; Church, 2006; Ashmore, 2013; Carling et al., 2014; Church & Ferguson, 2015). It is therefore important that planform predictors can discriminate these planform styles so that, when applied to fluvial strata, we can gain new insights into process in ancient fluvial systems, such as thread stability, dominant sediment transport mode, mechanism of thread generation, whether planform is the same at high and low flows, and more (Jerolmack & Mohrig, 2007; Kleinhans et al., 2013; Carling et al., 2014). The dataset I presented in Chapter 5 indicated that slope is useful to discriminate braided and anastomosing rivers and I presented a new threshold to discriminate these planform styles, which is simple and straightforward to apply to fluvial strata.

Together, my new thresholds advance on existing planform predictors, not only in their ability to discriminate planform style (i.e., braided *versus* anastomosing), but also in the fact they are underpinned by a comprehensive dataset of hydraulic geometries in natural rivers, which avoids the limitations and biases associated with previous datasets used to develop and/or test planform predictors (Parker, 1976; van den Berg, 1995; Crosato & Mosselman, 2009).

As a whole, the four research chapters in this thesis present new approaches and frameworks that enable us to gain sophisticated and quantitative insights into the dynamics and behaviour of ancient fluvial systems. These insights reflect allogenic forcing, including river behaviour as a function of tectonic boundary conditions (Chapters 2 and 3) and climatic boundary conditions (Chapters 2, 3 and 4), as well as autogenic forcing, including the geomorphic self-organization of rivers (Chapter 4) and river morphodynamics associated with planform and planform stability (Chapters 4 and 5). Importantly, the work presented in each of these research chapters complements one another and, further, opens doors to a number of new research trajectories — I will discuss the complementary nature of this work, as well as current/ongoing and future research trajectories for the remainder of Chapter 6.

6.2 Cross-cutting themes

The four research chapters in this thesis can be read as standalone studies but, together, they address the behaviour of ancient fluvial systems from different perspectives and at a range of scales. There are a series of themes which are common to some, if not all, chapters, and here I discuss a selection of these in detail.

6.2.1 Importance of spatial and temporal scales

In this thesis I present new methods and frameworks to quantify the dynamics and behaviour of ancient fluvial systems. These methods and frameworks tackle river behaviour at a variety of spatial and temporal scales, which is important for a number of reasons.

Rivers respond to different forcings on different timescales, and these timescales can dictate the propagation of environmental signals and their subsequent preservation in the rock record (Castelltort & Van Den Driessche, 2003; Romans et al., 2016). Consequently, different methods are typically used to investigate river behaviour at different timescales. For example, to generate catchment-averaged erosion rates using geochronology, cosmogenic radionuclide analysis is suitable at intermediate timescales of 10^2–10^6 yrs (von Blanckenburg, 2005) and U–Pb dating is suitable at geologically long timescales of $\geq 10^7$ yrs (Reiners et al., 2003; Painter et al., 2014). Further, different methods recover results at different timescales, e.g., reconstruction of instantaneous bankfull sediment discharges *versus* mean annual sediment discharges. Likewise, various methods are typically used to investigate river behaviour at different spatial scales, including continental-, regional-, catchment-, and reach-scales. Further, these methods may recover results associated with different spatial scales, and some methods even recover results for a different spatial scale than that of the input data. To reuse the example of cosmogenic radionuclide analysis, samples from a trunk channel reach (small spatial scale) are often used to infer an erosion rate for the entire catchment (large spatial scale) (e.g., von Blanckenburg, 2005; Wittmann et al., 2007; Hidy et al., 2014).

Methods to investigate ancient rivers can therefore offer insights at a variety of spatial and temporal scales. In general, field-based grain-scale stratigraphic approaches usually recover instantaneous bankfull conditions at channel reach and catchment scales (Holbrook & Wanas, 2014; Lin & Bhattacharya, 2017; Sharma et al., 2017; Ganti et al., 2019; Brewer et al., 2020). Whereas modelling methods tend to focus on regional and continental scales, and typically recover mean annual conditions, or even mean conditions on longer million-year timescales (Stephenson et al., 2014; Watkins, Whittaker, Bell, et al., 2018; Fernandes et al., 2019; Brewer et al., 2020; Chapter 2 (Lyster et al., 2020)). Importantly, there is no one-size-fits-all approach to investigate river behaviour at different spatial and temporal scales, which highlights the importance of using multiple approaches as complements to one another. Further, use of multiple approaches is important because different methods are subject to different limitations which are often related to the spatial or temporal scale of investigation. In this thesis, the methods and frameworks that I presented encompass a range of spatial and temporal scales of study areas, input data, results, and the associated allogenic and autogenic forcing mechanisms.

As discussed in ***Section 6.1***, field measurements from individual field sites are often used to make point reconstructions of river morphologies and hydrodynamics in ancient fluvial systems (e.g., Holbrook & Wanas, 2014; Lin & Bhattacharya, 2017; Sharma et al., 2017; Brewer et al., 2020). These insights are all useful, however they merely provide a snapshot into ancient fluvial systems at a particular moment in space and time. Relatively few studies have incorporated a spatial and/or temporal element of investigation. For example, Ganti et al. (2019) incorporated a temporal element by reconstructing morphologies and hydrodynamics from fluvial strata for different members of the Torridonian Group, Scotland. Meanwhile, Chen et al., (2018) incorporated a temporal element by documenting the response of grain-size and channel morphologies to the Paleocene–Eocene Thermal Maximum in the Tremp Group, Spain. While incorporation of a temporal element is possible, it is seldom done. Therefore, in this thesis, I was particularly motivated to use the framework that I presented in Chapter 3 to reconstruct high resolution spatial and temporal trends in river morphologies and hydrodynamics, which enables sophisticated insights into the long-term evolution of ancient rivers, particularly in response to tectonic and climatic forcing. To achieve this, in Chapter 3 I subdivided the Blackhawk Formation and Castlegate Sandstone into lower, middle, and upper stratigraphic intervals (Figure 3.2). Further, I traced individual palaeorivers associated with these formations from upstream to downstream and included multiple parallel palaeorivers (Figure 3.1). This high spatial and temporal resolution was facilitated by exceptional outcrop preservation across the entire region and, more importantly, by extensive work to reconstruct palaeodrainage networks (Bartschi et al., 2018; Pettit et al., 2019) and to regionally correlate up-dip proximal strata with down-dip distal strata (Robinson & Slingerland, 1998; Aschoff & Steel, 2011a, 2011b) (Figure 3.2).

Having successfully used this new framework to reconstruct high resolution spatial and temporal trends in river morphologies and hydrodynamics, I noticed that application of this framework in the exact same manner, but to different fluvial strata, can result in insights at different spatial scales. This occurs simply due to the planform of ancient fluvial systems, and due to the position of field sites within palaeocatchments. In Chapter 3 I investigated the Blackhawk Formation and Castlegate Sandstone. Importantly, the Blackhawk Formation preserves both single-thread and multi-thread channels, and the Castlegate Sandstone preserves mostly braided fluvial systems. My field sites therefore encompassed multiple parallel threads and channels and, further, these field sites were sufficiently up-dip of the palaeoshoreline such that these channels were predicted to coalesce downstream (Lawton, 1983, 1986; Miall, 1994; Miall & Arush, 2001; Bartschi et al., 2018; Pettit et al., 2019). Whereas in Chapters 4 and 5 I additionally investigated the Ferron Sandstone, which preserves major meandering trunk channels that fed a series of deltas. My field sites were focused on the deposits of trunk channels that drained to one particular delta, and were sufficiently close to the palaeoshoreline, such that downstream confluences are not predicted (Cotter, 1971, 1975a, 1975b, 1976). In this thesis, the nature of my field sites provides insights into ancient fluvial systems at reach scales. However, for the Ferron Sandstone, my field sites enable additional insights at catchment scales because a mass balance assumption can be made for major trunk channels of single-thread rivers. With the potential to use reach-scale field measurements of the Ferron

Sandstone to make inference of the entire catchment, I return to this opportunity in ***Section 6.3***. Whereas for the Blackhawk Formation and Castlegate Sandstone, the same mass balance assumption cannot be made due to the nature of ancient river planforms, and due to the anticipated presence of downstream confluences. Instead, field measurements of the Blackhawk Formation and Castlegate Sandstone solely provide reach scale insights (which, where multi-thread, are specifically thread scale insights). To use these measurements to gain catchment scale insights, it is important to incorporate multiple field sites spanning upstream to downstream. These observations and examples highlight how spatial (and temporal) scales must be considered on a case-by-case bases for the investigation of individual ancient fluvial systems to maximise our ability to interpret fluvial strata.

6.2.2 Quantitative palaeohydrology versus qualitative palaeohydrology

In developing quantitative methods and frameworks to investigate ancient fluvial systems, it is important to evaluate their efficacy. Therefore, a prominent theme in this thesis was the reconciliation of quantitative and qualitative insights from fluvial strata. It is important that quantitative and qualitative approaches produce results that are consistent with one another, because (1) in certain situations the nature of preserved fluvial strata may limit our ability to implement multiple approaches, and (2) where insights can be reconciled with one another, the respective insights offer useful complements to one another.

To offer an example of the complementary nature of quantitative and qualitative insights, consider fluvial strata that preserve major meandering rivers. Qualitative approaches to investigate river planform from these strata may include facies mapping of architectural elements to reconstruct reach-scale palaeogeography. These observations provide qualitative insights into planform evolution, including channel sinuosity and the nature of meander-bend transformations, e.g., expansional *versus* translational meander bends (Ghinassi et al., 2014; Ielpi & Ghinassi, 2014; Ghinassi & Ielpi, 2015; Ghinassi et al., 2016). These insights can then be supplemented by quantitative insights, such as insights into channel sinuosity using structural measurements to calculate flow divergence between bar accretion surfaces and local dune migration (Ghinassi et al., 2021). Further, quantitative insights from reconstruction of river morphologies and hydrodynamics (Chapters 3 and 4) and planform stability fields (Chapter 5) can offer precise insights into the boundary conditions associated with the observed river planform and, therefore, the magnitude of boundary condition change that would result in a major river planform change. These insights, combined, offer a complete and holistic picture of planform and planform evolution from the studied fluvial strata.

In this thesis I have highlighted consistencies, and resolved inconsistencies, between various quantitative and qualitative methods. However, some limitations remain. With motivation to maximise the complementary nature of quantitative and qualitative methods, I now highlight two key areas where I found consistency between quantitative and qualitative methods, or resolved inconsistency, but where discrepancy remains. I discuss these two areas to highlight progress, but also to consider future research needs.

Quantitative and qualitative interpretation of river planform

Having highlighted the complementary benefits of quantitative and qualitative insights into river planform, and having discussed that Chapter 5 was partially motivated by observed inconsistencies between quantitative planform prediction and qualitative planform interpretation, a major success in this thesis has been the development of new planform stability criteria which, when applied to geological examples, honour stratigraphic interpretations (Chapter 5).

In Chapter 5 I showed that the quantitative planform predictor of Parker (1976), when applied to field measurements of fluvial strata in the Blackhawk Formation, Castlegate Sandstone, and Ferron Sandstone, favours the prediction of single-thread planforms. In detail, the predictor of Parker (1976) consistently favours single-thread planforms when implementing both a minimum plausible palaeochannel width, W_{min}, and a maximum plausible palaeochannel width, W_{max} (Figure 5.2). Prediction of single-thread channels using W_{min} and W_{max} is consistent with interpretation of single-thread channels in the Ferron Sandstone and Blackhawk Formation (Figure 5.2). However, prediction of single-thread channels using W_{min} and W_{max} is discrepant with interpretation of multi-thread channels in the Castlegate Sandstone, and with the presence of many wide multi-thread channels in the Blackhawk Formation (Figure 5.2).

Using the criteria that I derived and presented in Chapter 5, the implied planforms are a much better fit with stratigraphic observations. Using my new multi-thread to single-thread threshold, the Ferron Sandstone plots as single-thread for W_{min} and W_{max}, which is consistent with facies interpretations of major meandering trunk channels (Cotter, 1971, 1975a, 1976) (Figure 5.3a). Meanwhile, using W_{max}, both the Castlegate Sandstone and Blackhawk Formation plot as multi-thread, which is consistent with interpretation of predominantly braided channels in the Castlegate Sandstone (Miall, 1993, 1994; Miall & Arush, 2001), and of wide multi-thread Blackhawk channels (Adams & Bhattacharya, 2005; Hampson et al., 2013; Flood & Hampson, 2014, 2015) (Figure 5.3a). Finally, using W_{min}, both the Castlegate Sandstone and Blackhawk Formation plot as multi-thread, which is consistent with braided channels in the Castlegate Sandstone, but inconsistent with single-thread channels of the Blackhawk Formation (Figure 5.3a). However, it is important to note that, using W_{min}, the Blackhawk Formation plots near the defined multi-thread to single-thread transition (Figure 5.3a). Narrower channels of the Blackhawk Formation have depth/width (H/W) ratios of ~0.01, which is close to my multi-thread to single-thread threshold of 0.02 (with 90% of single-thread rivers can be predicted by $H/W > 0.014$). Given the width uncertainty, and the uncertainty of this new predictor, I consider it reasonable that the Blackhawk Formation plots very near the threshold given that it preserves both single-thread and multi-thread channels.

Further, using my new braided–anastomosing threshold, I find that multi-thread channels of the Blackhawk Formation and Castlegate Sandstone plot as anastomosing. This is consistent with stratigraphic observations of river stability, processes and characteristics that are typical of anastomosing multi-thread rivers (Makaske, 2001; Jerolmack & Mohrig, 2007; Eaton et al., 2010; Kleinhans et al., 2013; Carling et al.,

2014). The Blackhawk Formation and Castlegate Sandstone are interpreted to preserve relatively stable sand-bed rivers which traverse low-sloping regions, and which have high sediment supply and a propensity to generate new channels by avulsion, (Miall, 1994; Miall & Arush, 2001; Hampson et al., 2012; Flood & Hampson, 2014; Hampson, 2016; Chamberlin & Hajek, 2019; Chapter 3 (Lyster et al., 2021)). Whereas the more braided endmember of multithread rivers tends to be relatively less stable, more gravel-bedded, traverse steep-sloping regions, and generate new threads via bifurcation (Makaske, 2001; Jerolmack & Mohrig, 2007; Eaton et al., 2010; Kleinhans et al., 2013; Carling et al., 2014).

While I appear to reconcile quantitative and qualitative observations of planform in Chapter 5, one prominent discrepancy remains. In this thesis I found that field measurements of cross-sets thicknesses in the Blackhawk Formation and Castlegate Sandstone are near identical (see Figures 4.4 and 4.5, Table B3, and Appendix C4), as well as their internal geometries (Figure 4.6 and Appendix C4) and grain-sizes (Table B2 and Appendix C4). As a result, my quantitative palaeohydraulic framework implies the same flow depths, slopes, flow velocities, etc., for both formations (Figure 3.6−3.12) and, therefore, for a given width, hydraulic planform predictors imply the same planforms for both formations (Figure 3.13 and Figure 5.2). This is odd because the Blackhawk Formation and Castlegate Sandstone have entirely distinct stratigraphic architectures, leading to facies interpretations of distinct planforms, whereas quantitative predictors imply the same planforms. The reason for this discrepancy is unresolved. It could potentially be an artefact of uncertainty in palaeochannel widths — if aspect ratios were known then maybe the implied planforms would be distinct. Or, it could be that aspect ratio is a non-unique determinator of planform in some instances, and that factors such as bank vegetation and cohesion/stability are important determinants, Alternatively, it could potentially be that these ancient channels had the same planform, but that the preserved fluvial strata record kinematic differences. Nonetheless, this discrepancy highlights the importance of coupling both quantitative and qualitative insights.

Quantitative and qualitative interpretation of flow variability

In fluvial strata, flow variability is usually assessed qualitatively using well-established facies and architecture models (Plink-Björklund, 2015; Gall et al., 2017; Birgenheier et al., 2019; Wang & Plink-Björklund, 2020). In these models, different discharge regimes are characterised by potentially distinctive sedimentary structures and macroforms. For instance, fluvial strata associated with highly variable discharge systems (i.e., monsoonal/subtropical rivers) are often argued to be associated with: Froude transcritical and supercritical upper flow regime structures, high deposition rate structures, soft sediment deformation, soft sediment clast conglomerates, a lack of well-developed barforms, etc (see review by Plink-Björklund, 2015). Conversely, fluvial strata associated with less variable discharge systems (i.e., perennial rivers) are argued to be associated with: Froude subcritical flow structures, a lack of soft sediment deformation and soft sediment clast conglomerates, an abundance of well-developed barforms, etc (Plink-Björklund, 2015).

In Chapter 4, I estimated potential flood durations for ancient Blackhawk, Castlegate and Ferron rivers (assuming that flow variability was the dominant control on enhanced bedform preservation). Importantly, flood durations of order days pointed towards flooding associated with torrential rains and storms in perennial discharge regimes. While fluvial strata of the Blackhawk Formation, Castlegate Sandstone, and Ferron Sandstone have not explicitly been studied using variable discharge facies models, published facies analyses typically describe sedimentary structures associated with perennial discharge regimes. It therefore appears that these quantitative and qualitative insights are consistent with one another.

However, while qualitative insights from variable discharge facies models appear to be consistent with quantitative insights, and therefore useful for discriminating monsoonal/subtropical and perennial systems from fluvial strata, their applicability is uncertain. These models typically assume that deposits of monsoonal/subtropical rivers are dominated by transcritical and supercritical flow structures, however it is difficult to produce Froude numbers >1 in flow depths greater than a few metres. This raises questions as to the applicability of these models to fluvial deposits of large lowland rivers. Using field data and the framework that I presented in Chapter 3, I can explicitly demonstrate this issue and its implications.

For down-dip localities (i.e., lowland river reaches) in the Castlegate Sandstone, I reconstructed palaeoflow depths of 2–4 metres (Figure 3.6) and I validated these estimates using independent proxies. Using Equation 3.11, I would require flow velocities of 4.5–6.5 m/s (and above) to produce Froude numbers of 1 (and above), which are exceedingly large compared to reconstructed flow velocities of just under 1 m/s (Figure 3.10). In addition, mean flow velocities of global rivers are ~1 m/s, as observed in the dataset I compiled and presented in Chapter 5 (Appendix D). Further, using Equation 3.7, flow velocities of 4.5–6.5 m/s (and above) would require much steeper slopes, which would be inconsistent with these field localities representing lowland reaches of ancient Castlegate channels. Conversely, using Equation 3.11, but instead using flow velocities of just under 1 m/s, I would require palaeoflow depths of 0.1 m (and below) to produce Froude numbers of 1 (and above). These palaeoflow depth values are implausible as they are inconsistent with barform heights and, importantly, are smaller than cross-set thicknesses measured in the field (Figure 3.5). This exercise, when applied to Blackhawk Formation and Ferron Sandstone (using field data and results in Chapters 3 and 4) similarly demonstrates that implausibly high flow velocities (and therefore slopes) or implausibly small palaeoflow depths, are necessary to produce transcritical and supercritical flow conditions in lowland rivers. These observations suggest that variable discharge facies models may not be applicable to large lowland rivers because, in practice, it is difficult to produce transcritical and supercritical flow and, therefore, the associated sedimentary structures in fluvial strata that would be consistent with highly variable discharge systems. This makes it difficult to consider discharge regimes in Blackhawk, Castlegate and Ferron channels using insights from variable discharge facies models.

6.2.3 Errors and uncertainties of quantitative reconstruction methods

Beyond striving to reconcile discrepancies between quantitative and qualitative insights into ancient fluvial systems, another prominent theme in this thesis has been more formal consideration of error and

uncertainty associated with quantitative insights. Aims 1, 2 and 3 in this thesis all focused on developing methods and frameworks to quantify river dynamics and behaviour in ancient fluvial systems. In detail, crucial objectives associated with Aims 1, 2 and 3 were to evaluate the efficacy of these new approaches (Objectives 1.4, 2.5, and 3.4) and, further, a crucial objective of Aim 2 was to incorporate error analysis into my new framework to reconstruct river morphologies and hydrodynamics (Objective 2.4), which I implemented in Chapters 3, 4, and 5.

The only existing "framework" to reconstruct morphologies and hydrodynamics of ancient fluvial systems is the fulcrum approach of Holbrook and Wanas (2014). In this framework, the sources of errors and uncertainties are discussed in detail, and their magnitude is described as limiting resolution to between a factor of two and one order of magnitude, however the estimated error margins are not incorporated into the results. In this thesis, I carefully incorporate error and uncertainty analysis into my framework to reconstruct river morphologies and hydrodynamics. In doing so, this enables us to gauge how far predicted river morphologies and hydrodynamics might be from real river morphologies and hydrodynamics (Figure 6.1). Further, incorporating error and uncertainty analysis maximises our ability to identify statistically significant trends in morphologic and hydrodynamic properties in space and time. To incorporate error and uncertainty, I implemented a Monte Carlo uncertainty propagation method. This method is outlined in detail in Chapters 3, 4, and 5, and in their respective appendices. To synthesise this method, for each step in my quantitative framework I took the uncertainty bounds associated with the model parameter (usually the mean ± 1 standard deviation, but in one instance the median of the model parameter and the 1st and 3rd quartiles of the model parameter), and I randomly sampled 10^6 model parameters between the defined bounds. For each step in the methodology, I used these 10^6 samples of the model parameter to generate 10^6 values for the model result. These values were then propagated forwards, through each model, and resulted in 10^6 values for the mean value of each reconstructed parameter. I offered these values as plausible spreads of values for the mean, and from these values I extracted the median value, as well as the 10th and 90th percentiles and/or the 25th and 75th percentiles.

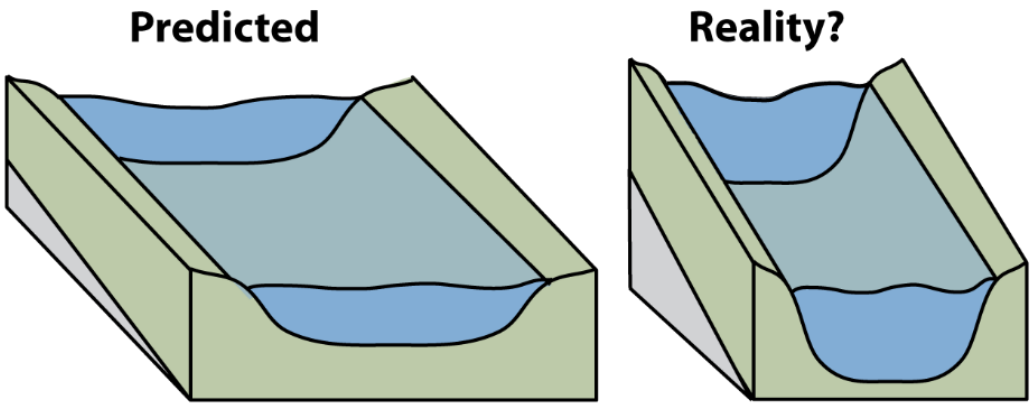

Figure 6.1 | A schematic showing how the predicted morphology (left) of an ancient river might differ from the true morphology (right) due to the errors and uncertainties associated with reconstruction methods.

Of all the sources of error and uncertainty that I encountered in this thesis, I consider two sources to be the largest and most significant. First, I consider uncertainty in palaeochannel width, *W*, to be the largest source of error in point reconstructions of river hydrodynamics. While it is possible to reconstruct various morphologic and hydrodynamic properties without *W*, constraints on *W* are crucial to reconstruct total water and sediment discharges. Uncertainty in the value of *W* can invoke significant uncertainty in total water and sediment discharges, which limits our ability to interpret whether reconstructed and/or observed changes to total water and sediment discharges are the result of changes to tectonic and/or climatic boundary conditions (see discussion of the Blackhawk−Castlegate transition in Chapter 3). For example, in a channel with a mean depth of 5 m, and a mean flow velocity of 1 m/s, the mean water discharge per unit width is 5 m^2/s. If *W* is 500 m then the total water discharge is 2500 m^3/s, whereas if *W* is 800 m then total water discharge is 4000 m^3/s — it is important to note that uncertainty in *W* of order hundreds of metres is completely plausible when inferring *W* from fluvial strata. For instance, widths of channelized sand bodies offer absolute maximum values of *W* and we expect true values of *W* to be smaller (Hampson et al., 2012; Flood & Hampson, 2014, 2015) — the amount by which the true value of *W* will be smaller will depend on the number of active threads and the lateral mobility of threads. Going forward, we urgently require an improved ability to constrain *W* from fluvial strata. Fortunately, various new approaches are emerging to reconstruct *W* from point bar widths (Greenberg et al., 2021), and future work must aim to test and implement these new approaches.

Second, beyond point reconstructions of river hydrodynamics (i.e., instantaneous bankfull water and sediment discharges), I consider the largest source of error at longer timescales (i.e., mean annual water and sediment discharges) to be uncertainty in flow variability and sediment transport intermittency. On top of uncertainty associated with *W*, estimates of mean annual water and sediment discharges are also subject to uncertainty regarding the assumption of interannual flow variability and sediment transport intermittency. This assumption is used to upscale instantaneous bankfull water and sediment discharges to mean annual water and sediment discharges. Not only does this determine the order of magnitude of reconstructed mean annual water and sediment discharges, but uncertainty can result in values that span several orders of magnitudes. Going forwards, we require novel methods to gauge flow variability and sediment transport intermittency in ancient fluvial systems and, in ***Section 6.4***, I highlight potential research avenues to directly tackle this issue.

6.2.4 Steady-state versus non-steady state

Steady-state models of bedform preservation are widely used in field-scale palaeohydrological studies (Holbrook & Wanas, 2014; Lin & Bhattacharya, 2017; Sharma et al., 2017; Ganti et al., 2019; Brewer et al., 2020; Wang et al., 2020). Importantly, in Chapter 3 I used a steady-state model to reconstruct bedform heights from preserved cross-set thicknesses (e.g., Paola & Borgman, 1991; Leclair, 2002), which assumed the bedform preservation ratio is a near-constant value of ~0.3 (Paola & Borgman, 1991; Leclair & Bridge, 2001; Leclair, 2002; Jerolmack & Mohrig, 2005). This steady-state assumption therefore fed into the

framework that I presented in Chapter 3 to reconstruct river morphologies, hydrodynamics, and morphodynamics from fluvial strata.

To check whether steady-state assumptions were appropriate in this framework, I would have ideally contrasted reconstructed values of bedform heights with independent proxies for bedform heights — however such a proxy does not exist. Instead, I contrasted reconstructed palaeoflow depths with independent palaeoflow depth proxies, e.g., barform heights (c.f. Hajek & Heller, 2012). If palaeoflow depths reconstructed from mean cross-set thicknesses, using steady-state assumptions, agree with independent palaeoflow depth proxies, then the palaeohydrological method can be interpreted to produce good results. However, I note that this approach also requires us to assume the relationship between dune heights and flow depths.

In central Utah, barforms preserved in the Blackhawk Formation and Castlegate Sandstone are well-documented (Adams & Bhattacharya, 2005; Lynds & Hajek, 2006; McLaurin & Steel, 2007; Hajek & Heller, 2012; Chamberlin & Hajek, 2019) and, where fully preserved, are a direct proxy for palaeoflow depths (Bridge & Tye, 2000; Hajek & Heller, 2012). In Chapter 3, I found good agreement between reconstructed palaeoflow depths and barform heights (***Section 3.4.1***). I reconstructed median palaeoflow depths of 2−4 m for the Castlegate Sandstone, which agree with mean barform heights of 2.6 m, 3.6 m, and 3.9 m reported by Chamberlin and Hajek (2019) for various localities. Further, I reconstructed a range of palaeoflow depths spanning 1–7 m, which similarly agree with barform heights spanning 1–8 m reported by Lynds and Hajek (2006) and McLaurin and Steel (2007). The agreement between reconstructed palaeoflow depths and preserved barform heights implies that steady-state assumptions produce plausible results and might suggest that bedforms were preserved in steady-state conditions with bedform preservation ratios of ~0.3. However, these observations are at odds with increasing evidence for bedform preservation in non-steady state conditions (Reesink et al., 2015; Ganti et al., 2020; Leary & Ganti, 2020), which has been supported by limited field observations (Jerolmack & Mohrig, 2005; Colombera et al., 2017; Cardenas et al., 2020; Wang et al., 2020). Further, when I analysed field measurements of cross-sets, I found that cross-set geometries were inconsistent with the geometries we expect for preservation in steady-state conditions (Paola & Borgman, 1991; Bridge, 1997; Leclair & Bridge, 2001; Leclair, 2002; Jerolmack & Mohrig, 2005) and, instead, were consistent with the geometries we expect for preservation in non-steady state conditions (Jerolmack & Mohrig, 2005; Reesink et al., 2015; Ganti et al., 2020; Leary & Ganti, 2020). So, while flow depths reconstructed using steady-state assumptions produced good results, preserved cross-set geometries did not support the notion of bedform preservation under steady-state conditions, and this discrepancy motivated the work that I presented in Chapter 4.

In Chapter 4, I presented direct evidence for bedform preservation in disequilibrium conditions for the Blackhawk Formation and Castlegate Sandstone (and, additionally, the Ferron Sandstone). In steady-state conditions, bedform preservation ratios are ~0.3 and the CV of cross-set thicknesses is equal to 0.88 (Figure 6.2). Whereas in non-steady state, or disequilibrium conditions, bedform preservation ratios are higher than

0.3 (<0.7) and CV << 0.88 (Jerolmack & Mohrig, 2005; Reesink et al., 2015; Leary & Ganti, 2020) (Figure 6.2). For the Blackhawk, Castlegate and Ferron, I found that CV of cross-set thicknesses was always lower than 0.88 and ranged from ~0.25–0.5 — only 3% of estimated CV values were consistent with the empirical range of CV = 0.88±0.30 expected for bedform preservation in steady-state conditions (Bridge, 1997) (Figure 4.6). Observations of low CV point to enhanced bedform preservation in disequilibrium conditions, with bedform preservation ratios higher than 0.3.

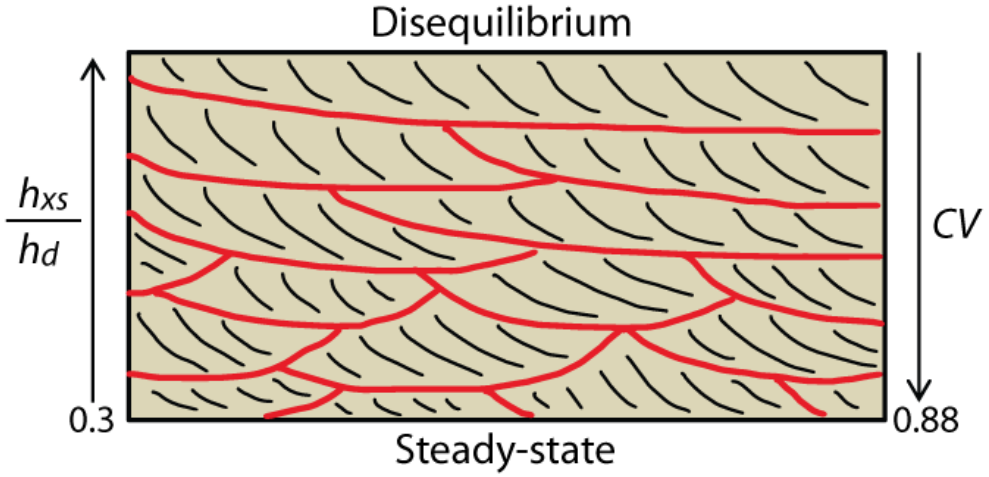

Figure 6.2 | Schematic illustrating the nature of preserved cross-set geometries when bedform preservation occurs in steady-state *versus* disequilibrium conditions. In steady-state conditions, the bedform preservation ratio, h_{xs}/h_d, is 0.3, and is larger in disequilibrium conditions. Meanwhile in steady-state conditions, the coefficient of variation, CV, of preserved cross-set thicknesses is 0.88, and is smaller in disequilibrium conditions. Red solid lines indicate bounding surfaces between cross-sets. Black solid lines indicate individual cross-strata.

Analytically, bedform preservation ratios higher than 0.3 result in the reconstruction of smaller dune heights and smaller flow depths (see Equations 3.1 and 3.2; Figure 6.3). This is a concern for palaeohydrological reconstructions because smaller dune heights and flow depths have implications for subequent reconstructions of slopes, flow velocities, and bedform turnover timescales, as I demonstrated in Chapter 4 (Figure 4.8). In theory, it might be true that dune heights and flow depths were smaller. However, in Chapter 3 I independently constrained flow depths using bar beights (Appendices B and C) and found that, in general, median flow depths reconstructed using steady-state assumptions were the same as mean flow depths implied using mean bar heights (Figure 6.3c). If I had implemented a higher bedform preservation ratio, I would have recovered smaller flow depths that disagreed with mean flow depths implied using mean bar heights. The only way to explain this observation, analytically, is to say that the issue must lie in the relationship between dune height and flow depth.

Flow depths generally scale with dune height, however the exact nature of this relationship is not fully-understood (Bradley & Venditti, 2017; Bradley & Venditti, 2019b, 2019a). Further, it is widely observed

that dunes in a channel reach can have a wide range of heights for the same flow depth (Bradley & Venditti, 2017). In this thesis, the dune–depth scaling relation that I implemented throughout was the non-parametric relation of Bradley and Venditti (2017). I note that various other scaling relations exist, many of which incorporate additional parameters such as shear stress, grain-size, transport stage (e.g., ratio of shear velocity to settling velocity), and Froude number (Yalin, 1964; Gill, 1971; Allen, 1978; van Rijn, 1984a; Julien & Klaassen, 1995; Karim, 1995, 1999), however incorporation of additional parameters does not improve their predictability power (Bradley & Venditti, 2017). In the relation of Bradley and Venditti (2017), median flow depth is approximated as 6.7 times the dune height, and the 1st and 3rd quartiles of flow depth are approximated as 4.4 and 10.1 times the dune height, respectively (Figure 6.3a,b). With unambiguous evidence of enhanced bedform preservation implying smaller dunes, but with bar heights that exceed the flow depths implied using these small dunes and the median relation of Bradley and Venditti (2017), we must conclude that, in these systems, flow depths were large relative to the small dunes. In other words, we may have over-predicted the dune height in Chapter 3, but under-predicted the flow depth relative to the dune by a similar factor (compare Figure 6.3a and b, given the known bar height in Figure 6.3c).

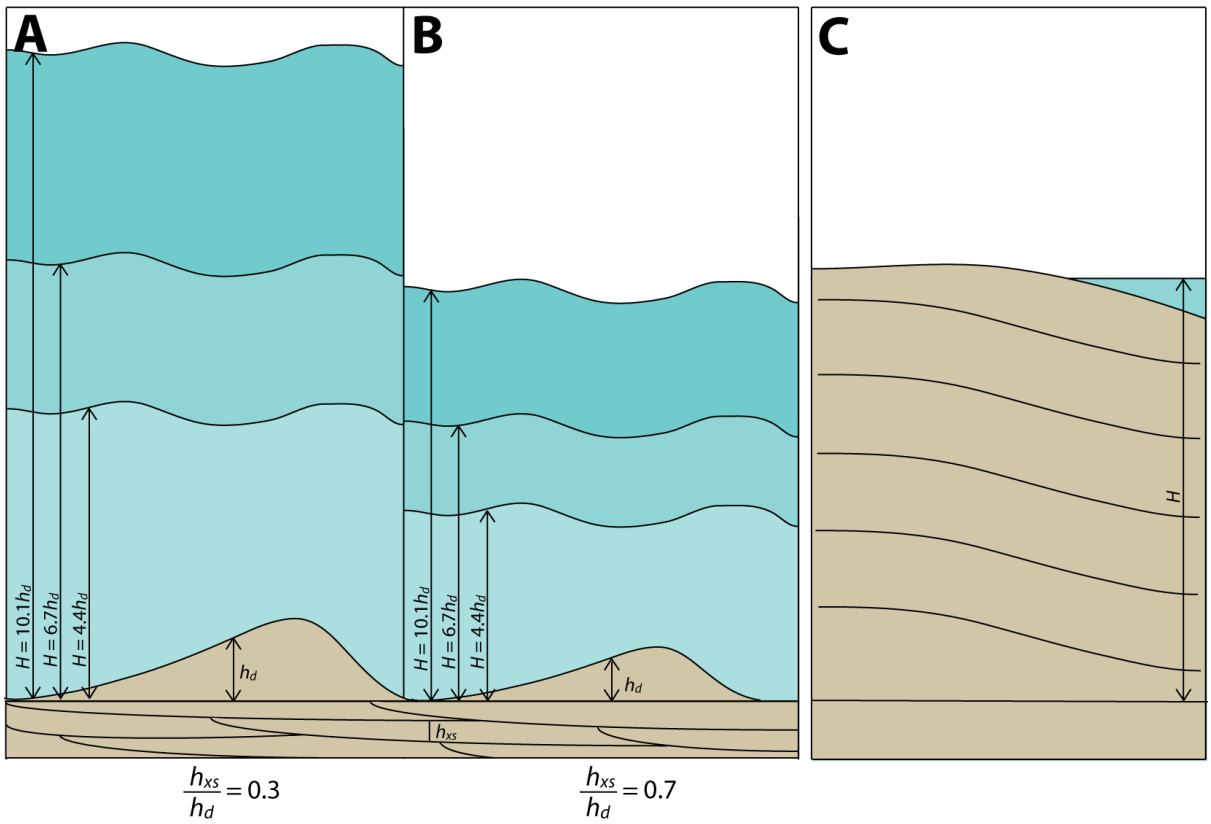

Figure 6.3 | A schematic showing the implications of bedform preservation ratios, h_{xs}/h_d, which is defined as the ratio of the average preserved cross-set thicknesses, h_{xs}, to the average original bedform height, h_d, on palaeohydraulic reconstructions. **A**) Scenario in which h_{xs}/h_d = 0.3, with the 1st, 2nd, and 3rd quartiles of palaeoflow depth, H, calculated as H=4.4h_d, H=6.7h_d, and H=10.1h_d, respectively. **B**) Scenario in which h_{xs}/h_d = 0.7, with the 1st, 2nd, and 3rd quartiles of H calculated as H=4.4h_d, H=6.7h_d, and H=10.1h_d, respectively. **C**) Fully preserved barform, where mean barform height is a proxy for H.

One simple physical explanation for this observation could be the apparent scaling break in dune height that occurs at flow depths of 2.5 m. Bradley and Venditti (2017) proposed that, at flow depths < 2.5 m, dunes are larger relative to the flow depth whereas, at flow depths > 2.5, dunes are smaller relative to the flow depth. This scale break emerges due to a change in dune morphology between shallower flows (strongly asymmetric; higher lee slope angles) and deeper flows (more symmetric; lower lee slope angles) (Bradley & Venditti, 2017). Bradley and Venditti (2017) provided an alternative relation for flow depths > 2.5 m, where median flow depth is approximated as 7.7 times the dune height, and the 1st and 3rd quartiles of flow depth are approximated as 6.1 and 11.8 times the dune height, respectively. To try and reconcile the disparity between smaller implied dunes and larger flow depths, I revisted my field data to explore the implications of using a higher bedform preservation ratio (e.g., 0.6) and the Bradley and Venditti (2017) relation for flow depths > 2.5 m.

To exemplify this for the Ferron Sandstone, in Appendix C I documented mean bar heights of 4.7 m, which have an interquartile range of 2.9–6.5 m and minimum–maximum values of 1.1–10 m. Further, published constraints on point bar heights and maximum thicknesses of channel-fill deposits are ~9 m (Cotter, 1971; Gardner et al., 2004; Garrison & Bergh, 2004). Meanwhile, I documented median cross-set thicknesses of 0.15 m. Assuming a bedform preservation ratio of 0.3, and using the universal relation of Bradley and Venditti (2017), I reconstructed an interquartile range of flow depths of 2.2–5.1 m, which agrees with my documented interquartile range of bar heights. If I then assume a bedform preservation ratio of 0.6, but still use the universal relation of Bradley and Venditti (2017), then I reconstruct an interquartile range of 1.1–2.5 m, which is small relative to mean bar heights. Whereas, when I assume a bedform preservation ratio of 0.6, but newly implement the relation of Bradley and Venditti (2017) for flow depths > 2.5 m, I reconstruct an interquartile range of 1.5–3 m, which is still small relative to mean bar heights. It is important to note that this interquartile range is a factor of 2 smaller than the interquartile range of documented bar heights (2.9–6.5 m). Ultimately, despite accounting for an apparent scaling break in dune–depth relations, I still find disparity between smaller dunes and larger flow depths.

Interestingly, the observation that flow depths were large relative to dune heights in ancient Ferron channels might attest to enhanced bedform preservation controlled by flow variability. This may, therefore, offer a potential route to disentangle the competing roles of flow variability and morphodynamic hiearchy on enhanced bedform preservation in disequilibrium conditions which, in Chapter 4, I stressed was a crucial research need. With regards to how this observation might attest to preservation controlled by flow variability, one simple reason is that in bankfull/flood conditions we expect flow depths to be large relative to mean flow depths. A more significant reason is that, with smaller dunes, we can assume that dune turnover timescales were smaller (Figure 4.8). If enhanced preservation of these smaller dunes was controlled by morphodynamic hiearchy, in detail the concurrent migration of dunes and bars, then bars must have been migrating at relatively rapid rates, possibly implausible rates. One explanation for this could

be that smaller dunes were simply migrating over larger dunes, however, this is something that can be observed in preserved fluvial strata, and which was not observed.

While evidence of enhanced bedform preservation may initially seem problematic — given that uncertainty in true bedform preservation ratios has analytical implications for reconstructing river morphologies and hydrodynamics — it is possible to avoid this issue by independently constraining palaeoflow depths from bar heights. In fact I argue that addressing this "problem" has the potential to provide us with more information pertaining the dynamics of the fluvial system in question and, in the future, may potentially shed light on the prevailing flow conditions at the time of preservation.

6.2.5 Multiple approaches to water and sediment discharge reconstruction

The final cross-cutting theme that I will discuss in this thesis is the comparison of different approaches to reconstruct water and sediment discharges. Previously, I discussed the importance of comparing quantitative insights with qualitative insights, however it is also extremely important to compare quantitative insights with other quantitative insights. In particular, comparison with other quantitative insights that have been derived using alternative approaches that depend on different parameters, and which therefore have different uncertainties and limitations.

There are multiple approaches to reconstruct sediment discharges, and each approach comes with its own uncertainties and limitations. Reconciling these approaches is important to maximise understanding of how sediment was routed across Earth's surface in the geological past. In this section, I specifically focus on reconciling two approaches to reconstruct sediment discharge. In Chapter 2 I presented the palaeoDEM–GCM–BQART approach to reconstruct suspended sediment discharges and, given the importance of comparing estimates with estimates derived using alternative approaches, I sought out published constraints on sediment discharges for the same study area and period — the Cenomanian and Turonian North American continent. I corroborated estimates of suspended sediment discharges using the palaeoDEM–GCM–BQART approach with published estimates by Lin and Bhattacharya (2017) and Sharma et al. (2017) (Figure 2.7), which were derived using the fulcrum approach of Holbrook and Wanas (2014). In ancient fluvial systems, the fulcrum approach has been frequently used to estimate Q_S (Holbrook & Wanas, 2014; Lin & Bhattacharya, 2017; Sharma et al., 2017; Brewer et al., 2020), and estimates of Q_S have been corroborated with estimates derived using BQART, and vice versa (Lin & Bhattacharya, 2017; Brewer et al., 2020; Chapter 2 (Lyster et al., 2020)).

The fulcrum approach uses various empirical, theoretical, and experimental relations to reconstruct bedload discharges and suspended sediment discharges in ancient rivers from fluvial strata and, to do so, the fulcrum approach first requires reconstruction of the river morphologies and hydrodynamics — the precise methods that this thesis explores. Aim 2 of this thesis was to develop a quantitative framework to reconstruct river morphologies and hydrodynamics from fluvial strata and I addressed this aim in Chapter 3. Importantly, in ***Section 6.1*** I highlighted that, in principle, I can now use the framework that I presented in Chapter 3, and

field measurements presented in Chapters 3–5, to reconstruct suspended sediment discharges via a fulcrum-style approach. I also highlighted that these estimates of suspended sediment discharges could be used to further corroborate estimates that I derived in Chapter 2 using my palaeoDEM–GCM–BQART.

The fulcrum approach uses channel-fill palaeohydraulics to reconstruct water discharge, Q_w, bedload discharge, Q_b, and suspended sediment discharge, Q_S, in ancient rivers (Holbrook & Wanas, 2014). It requires field measurements of grain-size and bankfull channel dimensions, and implements various flow transport equations, to calculate the instantaneous bankfull Q_w, Q_b, and Q_S at a channel cross-section. These values are then projected across a given duration of time using a flood hydrograph to calculate mean annual Q_w, Q_b, and Q_S (Holbrook & Wanas, 2014). A key assumption in the fulcrum approach is that the total volume of sediment passing through a channel cross-section is equal to the volume of sediment contributed by the erosional source region and the volume of sediment delivered to the depositional sink region (Holbrook & Wanas, 2014). This mass balance assumption is crucial as preservation potential is not uniform in catchments; erosional source regions are inherently not preserved and, therefore, investigation of palaeocatchments often relies on interpretation of preserved depositional stratigraphy to make inference of the entire system (Romans & Graham, 2013; Romans et al., 2016). Therefore, application of the fulcrum approach to ancient fluvial systems ideally requires preservation of the major trunk channel in a single thread river — application to a multi-thread river would require knowledge of the number of active threads, and preservation of all active threads, which is unlikely.

In principle, using the framework I presented in Chapter 3, and field measurements for the Ferron Sandstone that I presented in Chapters 4 and 5 (which preserves trunk channels of single-thread rivers), I can use the fulcrum approach to reconstruct mean annual Q_w, Q_b, and Q_S, and I can compare these estimates with those derived in Chapter 2 using the palaeoDEM−GCM−BQART approach. However, it would not be appropriate to use the fulcrum approach to calculate Q_w, Q_b, and Q_S for the Blackhawk Formation and Castlegate Sandstone because (1) these strata preserve both single-thread and multi-thread rivers, and (2) field sites were sufficiently upstream. For these formations and field sites it is therefore difficult to justify a mass balance assumption.

With the possibility of using the fulcrum approach to reconstruct Q_w, Q_b, and Q_S in trunk channels draining to the Ferron Last Chance delta (note that Sharma et al. (2017) reconstructed Q_w, Q_b, and Q_S in trunk channels draining to the neighbouring Ferron Notom delta), I began to consider the errors and uncertainties of the fulcrum approach. Holbrook and Wanas (2014) reported that estimates of Q_w, Q_b, and Q_S derived using the fulcrum approach are first-order approximations, which limits accuracy to one order of magnitude, but that this error can largely be reduced by targeted efforts to constrain the input parameters in individual studies. Given the errors and uncertainties, I was motivated to carefully analyse the fulcrum methodology. In doing so, I have identified a number of analytical limitations which can be minimised by revising the fulcrum methodology, and which brings me to my current and ongoing work.

6.3 Current and ongoing work

In the previous section I discussed a number of cross-cutting themes in which I highlighted a number of limitations and unknowns associated with quantitative approaches to investigate ancient fluvial systems. These limitations and unknowns presented obstacles to my work and have motivated my current and ongoing work. In this section I outline some of my current and ongoing work, which follows on directly from my previous discussion of the fulcrum approach, and I offer preliminary insights and results from this work. In the subsequent section, ***Section 6.4***, I outline two future research directions that are linked with this current and ongoing work, but which also aim to tackle some of the other limitations and unknowns in this thesis that I raised when discussing cross-cutting themes in ***Section 6.2***.

6.3.1 A revised fulcrum approach to reconstruct sediment discharges in ancient fluvial systems

I have recently been investigating the fulcrum approach to minimise limitations and maximise its potential for stratigraphic application. In doing so, a number of analytical limitations have become apparent, most of which are relatively straightforward to address. However, one major limitation has become apparent, which has not previously been discussed in literature. While it is usually said that estimates of Q_S derived from the fulcrum approach are suspended sediment discharges (Holbrook & Wanas, 2014; Lin & Bhattacharya, 2017; Sharma et al., 2017; Brewer et al., 2020), my detailed analysis of the methodology reveals that the fulcrum approach in fact recovers estimates of the suspended portion of the bed material load, i.e., the fraction of the suspended sediment load that interacts with the bed. It does not calculate the portion of the suspended sediment load that never interacts with the bed. This raises questions as to whether it is appropriate to compare estimates of Q_S derived using BQART with "suspended" sediment discharges derived using the fulcrum approach. Given published constraints on ratios of bedload to suspended load in sand-bed rivers (Cantalice et al., 2013; Ashley et al., 2020), we should anticipate that the suspended fraction of the bed material load is significantly smaller than suspended sediment load. It is therefore problematic that estimates of "suspended" sediment discharges derived using the fulcrum approach agree with, or even exceed, estimates derived using alternative reconstruction methods (Lin & Bhattacharya, 2017; Brewer et al., 2020; Chapter 2 (Lyster et al., 2020)).

The existing fulcrum approach is outlined in detail by Holbrook and Wanas (2014), Lin and Bhattacharya (2017), and Sharma et al. (2017). Within the existing fulcrum approach, the methodology of van Rijn (1984b) is used to estimate sediment discharges, which is also outlined in the aforementioned work, however more detailed information can be found in the original work of van Rijn (1984b). I have been revising this original fulcrum approach to minimise analytical limitations and, further, I have been applying this revised methodology to field data that I presented in this thesis. I outline this revised methodology below, which follows the original order of Holbrook and Wanas (2014), and I highlight where, and why, I have made amendments. Then, I discuss preliminary results from application of this revised methodology to field data.

(1) Calculate **original bedform height, h_d,** from mean cross-set thickness, h_{xs}, following Leclair and Bridge (2001) as:

$$h_d = 2.9(\pm 0.7)h_{xs},$$

or, where there is evidence of enhanced bedform preservation, calculate h_d assuming a plausible higher value for the bedform preservation ratio.

(2) Calculate median **formative flow depth, H,** using the relation of Bradley and Venditti (2017), where

$$H = 6.7h_d,$$

and where the first and third quartiles of H are given by $H = 4.4h_d$ and $H = 10.1h_d$, respectively. Or, where possible, skip Step 2 and instead use independent proxies of H, e.g., bar clinoform heights.

(3) Calculate the **particle Reynold's number, Re_p,** as

$$Re_p = \frac{\sqrt{RgD_{50}}D_{50}}{\nu}.$$

where R is the submerged specific gravity of sediment in water (1.65 for quartz), g is acceleration due to gravity (9.81 m/s^2), and ν is the kinematic viscosity of water (1×10^{-6} m^2/s for water at 20°C).

(4) Calculate **palaeoslope, S,** using the method of Trampush et al. (2014), where

$$\log S = \alpha_0 + \alpha_1 \log D_{50} + a_2 \log H,$$

and where the constants are given by $a_0 = -2.08\pm0.036$, $a_1 = 0.254\pm0.016$, and $a_2 = -1.09\pm0.044$. A Shields stress inversion can alternatively be used to calculate S, however I advise using the Trampush et al. (2014) palaeoslope approach for consistency with the bedload relation that is later implemented.

(5) Calculate the **grain roughness height, k_s,** as

$$k_s \cong n_k D_{90},$$

where n_k is a dimensionless number between 1.5 and 3. I recommend assuming $n_k = 3$, following Wright and Parker (2004) and van Rijn (1984b).

(6) Calculate **flow velocity, U,** using a dimensionless Chézy friction coefficient, C_z, and/or a dimensionless bed resistance coefficient, C_f, which are given as:

$$C_z \equiv \frac{U}{u_*} = C_f^{-\frac{1}{2}},$$

where **u^* is bed shear velocity** ($u^* = gHS^{01/2}$). Using the Manning–Strickler formulation, C_f can be calculated as

$$C_f^{-1/2} = \alpha_r \left(\frac{H}{k_s}\right)^{\frac{1}{6}},$$

Where α_r is a dimensionless constant between 8 and 9. For sand-bed streams $\alpha_r = 8.32$ is often used, whereas for gravel-bed streams $\alpha_r = 8.1$ is often used (Wright & Parker, 2004).

The equations in Steps 5 and 6 account for hydraulic resistance, however, they all assume plane-bed transport in which all drag force exerted on the riverbed is skin friction. Drag is subdivided into skin friction, which is generated by tangential shear stress on a body, and form drag, which is generated by normal stress on a body, i.e., pressure. In the absence of bedforms, all drag exerted on a riverbed is skin friction, whereas the presence of bedforms exerts additional form drag, which reduces the ability of a flow to transport sediment. As calculated in Step 6, C_f is a skin friction predictor and assumes the absence of bedforms. In fulcrum-style sediment discharge reconstructions, use of a skin friction predictor is problematic as it acts to overestimate the shear stress on a riverbed and, therefore, the ability of a flow to transport sediment. In addition, use of a skin friction predictor that assumes the absence of bedforms is directly in conflict with the use of cross-set thicknesses to reconstruct bedform heights and flow depths.

In the presence of bedforms it is important to account for form drag. The existing fulcrum approach does not account for form drag and, therefore, application to fluvial strata has likely resulted in an overestimation of sediment transport capability and, therefore, sediment discharges (Holbrook & Wanas, 2014; Lin & Bhattacharya, 2017; Sharma et al., 2017; Brewer et al., 2020). Further, this overprediction is potentially large. Kean and Smith (2006) found that, in Lost Creek, Montana, neglecting to account for form drag (and lateral stresses) results in a 56% overestimate of water discharge. Meanwhile, Andrews (1984) observed that, in East Fork Virgin River, Utah, the skin-friction shear stress was 46% the total shear stress.

To account for form drag, I suggest using the form drag predictor of Wright and Parker (2004), which is suited to large, low-sloping sand-bed rivers, unlike previous drag form predictors (e.g., Engelund & Hansen, 1967). Moreover, the form drag predictor of Wright and Parker (2004) has been shown to perform well when compared to field observations of relatively small (Niobrara, Middle Loup), medium (Rio Grande), and large (Red, Atchafalaya, and Mississippi) sand-bed streams. Analytically, to account for form drag the form drag is effectively "removed". The flow depth of a river, H, can also be considered a composite flow depth, H_c, which is the flow depth due to both form drag and skin-friction. It is possible to calculate a skin-friction flow depth, H_{sk}, which is the flow depth due to skin friction alone, i.e., the portion of the flow depth that is unaffected by form drag. The predictor of Wright and Parker (2004) is an empirical predictor of the Shields stress due to skin friction, τ^*_{sk}; the relation predicts τ^*_{sk} as a function of τ^* and Froude number, Fr, and I outline how to implement this predictor in Step 7 below.

(7) The **Shields stress due to skin friction, τ^*_{sk},** can be predicted as

$$\tau^*_{sk} = 0.05 + 0.7(\tau^* Fr^{0.7})^{0.8}.$$

To solve for this, iterate through values of H_{sk} spanning 0 to H. For each value of H_{sk}, calculate: (1) the skin friction bed shear velocity, $u*_{sk}$, as $u*_{sk}=gH_{sk}S^{1/2}$; (2) the skin friction Shields stress, $\tau*_{sk}$, as $\tau*_{sk}=H_{sk}S/RD_{50}$; (3) a constant, T, as $T=(\tau*_{sk}-0.05/0.7)^{5/4}$; (4) the skin friction flow velocity, U_{sk}, as $U_{sk}=8.32(gH_{sk}S^{1/2})(H_{sk}/k_s)^{1/6}$; (5) the composite flow depth, H_c, as $H_c=(T(RD_{50}/S)(g^{1/2}/U_{sk})^{0.7})^{20/13}$. Iterate through values of H_{sk} until the value of H_{sk} is found such that H_c is equal to H.

(8) The grain roughness height, k_s, that has been calculated is a skin friction roughness height. Now, calculate the **composite roughness height, k_c,** following Parker (2004) as

$$k_c = \frac{11H}{e^{\kappa Cz}},$$

where κ is the von Karman constant, taken as 0.4, and where C_z is the skin friction C_z, i.e., $C_z=U_{sk}/u*$.

(9) Calculate the **sediment settling velocity, w_s,** following Ferguson and Church (2004), as

$$w_s = \frac{RgD_{50}{}^2}{C_1 v + (0.75C_2 RgD_{50}{}^3)^{0.5}},$$

where C_1 and C_2 are constants associated with grain sphericity and roundness. I suggest implementing $C_1 = 18$ and $C_2 = 1$, which Ferguson and Church (2004) proposed as intermediate values between smooth spheres ($C_1 = 18$ and $C_2 = 0.4$) and angular natural grains ($C_1 = 24$ and $C_2 = 1.2$). In the existing fulcrum approach, w_s, is calculated using the relation of van Rijn (1984b), however this relation is restricted to grain-sizes between 0.1 and 1 mm. I therefore recommend the approach of Ferguson and Church (2004) which is applicable and effective for the full range of grain-sizes.

(10) Calculate the **Rouse number, Z,** to determine the dominant mode of sediment transport, as,

$$Z = \frac{w_s}{\beta \kappa u_*}$$

where β is a constant that correlates eddy viscosity to eddy diffusivity, typically taken as 1. With Z, dominant mode of sediment transport is typically wash load for $Z < 0.8$, 100% suspended load for $0.8 < Z < 1.2$, 50% suspended load (i.e., mixed load) for $1.2 < Z < 2.5$, and bedload for $Z > 2.5$.

Several relations have been proposed to calculate the **entrainment, E,** of uniform material (see review by García and Parker, 1991), which is effectively the concentration of suspended sediment at the **reference height/level, a**. In the existing fulcrum approach, a range of entrainment relations are presented and implemented (van Rijn, 1984b; García & Parker, 1991; Wright & Parker, 2004). I suggest using the relation of Wright and Parker (2004), which best suits larger, low-sloping sand-bed rivers, and which is an adaptation of the relation of García and Parker (1991) which best suits small to medium sand-bed rivers.

(11) Using the value of H_{sk} that resulted in $H_c = H$, calculate entrainment as

$$E = \frac{AZ_u^5}{1+\frac{A}{0.3}Z_u^5}, \qquad Z_u = \frac{u_{*sk}}{w_s} Re_p^{0.6} S^{0.7},$$

where $A = 5.7\times10^{-7}$.

(12) Compute the **Rouse–Vanoni profile for suspended sediment** as

$$\mathrm{I} = \int_{\varsigma b}^{1} \left[\frac{(1-\varsigma)/\varsigma}{(1-\varsigma_b)/\varsigma_b}\right]^Z \ln\left(30\frac{H}{k_c}\varsigma\right) d\varsigma,$$

where b is a a/H, and where $a = 0.05H$, so b=0.05.

(13) Finally, calculate the **suspended bed material load, *Qs*,** in units of m²/s as

$$Qs = \frac{u_* EH}{\kappa}\mathrm{I}.$$

This framework recovers an instantaneous bankfull discharge of the suspended bed material load, i.e., the portion of the bed material load that is intermittently suspended in the water column. It is inappropriate to refer to this value as a suspended sediment discharge. At present, the suspended bed material load has been reconstructed per unit width. To calculate the total suspended bed material load, this value must be multiplied by the channel width, which can be difficult to measure in fluvial strata. Implementing an appropriate channel width will determine the order of magnitude of results, and uncertainty in channel widths may therefore result in uncertainties of results spanning several orders of magnitude. To minimize this, I suggest that application of this revised fulcrum approach to fluvial strata is restricted to single-thread rivers, or single-thread reaches in multi-thread rivers. If applied to multi-thread rivers, not only is there uncertainty in thread width, but there is additional uncertainty as to the number of active threads.

With the total suspended bed material load, we can calculate the total bedload and sum these together to recover the total bed material load. Various relations exist to predict bedload in gravel-bed (Meyer-Peter & Müller, 1948; Einstein, 1950; Wong & Parker, 2006) and sand-bed rivers (Ashida & Michiue, 1972; Engelund & Fredsøe, 1976; Wilcock & Crowe, 2003). These are grain-scale approaches, and most calculate bedload as a function of Shields stress and/or critical Shields stress. Importantly, these bedload transport relations also assume plane-bed transport. As such, I suggest implementing the bedload transport relation of Mahon and McElroy (2018), which is a bedform-scale approach (see Appendix C). Summing the total bedload and the total suspended bed material load results in an estimate of the instantaneous total bed material load, Q_{bm}, in units of m³/s.

6.3.2 Application of the revised fulcrum approach to the Ferron Sandstone, Utah, USA

Having revised the fulcrum methodology, I have also exemplified the revised methodology using existing field measurements of the Turonian Ferron Sandstone — these field data are presented in Chapters 4 and

5. Importantly, in exemplifying the revised methodology, I also discuss more appropriate ways to compare estimates of Q_{bm} with estimates of Q_S derived from alternative reconstruction methods.

The Ferron Sandstone comprises three deltaic clastic wedges, known as the Last Chance, Notom, and Vernal deltaic complexes (Cotter, 1975a, 1975b, 1976; Chidsey et al., 2004) which were fed by rivers that drained the Sevier orogenic front toward the WIS, and which may have also featured an additional/intermittent longitudinal component of drainage from the south-southwest (Kynaston, 2019) (Figures 4.1 and 5.1). In Chapters 4 and 5 I presented field data for the Ferron Sandstone, which I collected from outcrops that preserve terrestrial fluvial facies (c.f. Chapters 4 and 5 and Appendix C), and which preserve major meandering trunk channels that delivered sediment to the Last Chance delta (Cotter, 1971; Chidsey et al., 2004). This field site is an ideal location to exemplify my revised fulcrum approach because: (1) it preserves major trunk channels and it is therefore reasonable to assume mass balance; (2) Sharma et al. (2017) used the original fulcrum approach to estimate sediment discharges in major trunk channels draining to the neighbouring Notom delta, and I can therefore compare my results with their results; and (3) I can compare estimates of Q_{bm} for Ferron trunk channels with estimates of Q_S that I presented in Chapter 2 for Ferron palaeocatchments.

My field measurements for trunk channel deposits of the Last Chance Ferron Sandstone include the geometries and grain-sizes of 190 individual cross-sets. For each individual cross-set and its respective grain-size, I used the bedform migration method of Mahon and McElroy (2018) to estimate bedload discharges, and I then implemented my revised fulcrum methodology, as outlined in the previous section, to reconstruct the suspended fraction of the bed material load. Then, I summed these constraints together, for each individual cross-set, to recover estimates of Q_{bm}.

To implement my revised fulcrum methodology, the two major "unknown" parameters that I needed to assign were channel width and sediment transport intermittency. For channel width, I did not estimate this using empirical scaling relations, instead I used published constraints which are relatively robust for this field area. For Last Chance Ferron trunk channels, Bhattacharya and Tye (2004) reported valley-scale channels with widths of 250 m. In addition, Garrison and Bergh (2004) also reported average channel widths of 250 m, and found no evidence to suggest that channel widths exceeded a few hundred metres, and also reported that measured channel-belt widths did not exceed 2 km. To allow for uncertainty in channel width, I implemented my revised fulcrum methodology for each individual cross-set using both a minimum plausible channel width, W_{min}, of 200 m, and a maximum plausible channel width, W_{max}, of 300 m. This is the same protocol, and the same values of W_{min} and W_{max}, that I implemented in Chapter 5 to evaluate the efficacy of quantitative planform predictors when applied to the Ferron Sandstone. Meanwhile, for sediment transport intermittency, I also did not estimate this using an empirical scaling relation (e.g., Meybeck et al., 2003). Constraining sediment transport intermittency is a major outstanding research challenge (see ***Section 6.4***; ***Proposal 2***) and, for now, I simply estimated total bedload discharges using a spread of potential intermittency factors. Further, instead of presenting these intermittency factors as ratios,

I present them as the length of time in a year that sediment transport is sustained for. For example, an intermittency factor of 0.019 equates to sediment transport being sustained for 1 week per year. Here, I assume intermittency factors that equate to 1 day, 1 week, 2 weeks, 1 month, 2 months, and 3 months of sustained sediment transport each year (Figure 6.4).

To discuss my preliminary results, the most important observation is that accounting for form drag results in an order of magnitude decrease in the implied Q_{bm} (Figure 6.4). Without accounting for form drag, and assuming that sediment transport is sustained anywhere from 1 week per year to 3 months per year, estimates of Q_{bm} broadly span 10^6-10^7 m^3/yr for channel widths of 200 m and 300 m (Figure 6.4a,c). These values are too large, relative to estimates of Q_S derived using the palaeoDEM–GCM–BQART in Chapter 2 (Figure 6.4; dashed grey lines), and they imply ratios of bedload to suspended load transport that are implausibly high for sand-bed rivers. Whereas, when form drag is accounted for, and assuming that sediment transport is sustained anywhere from 1 week per year to 3 months per year, estimates of Q_{bm} broadly span 10^5-10^6 m^3/yr for channel widths of 200 m and 300 m (Figure 6.4b,d). These values of Q_{bm}, relative to estimates of Q_S presented in Chapter 2 (Figure 6.4; dashed grey lines), imply ratios of bedload to suspended load transport that are more plausible for sand-bed rivers.

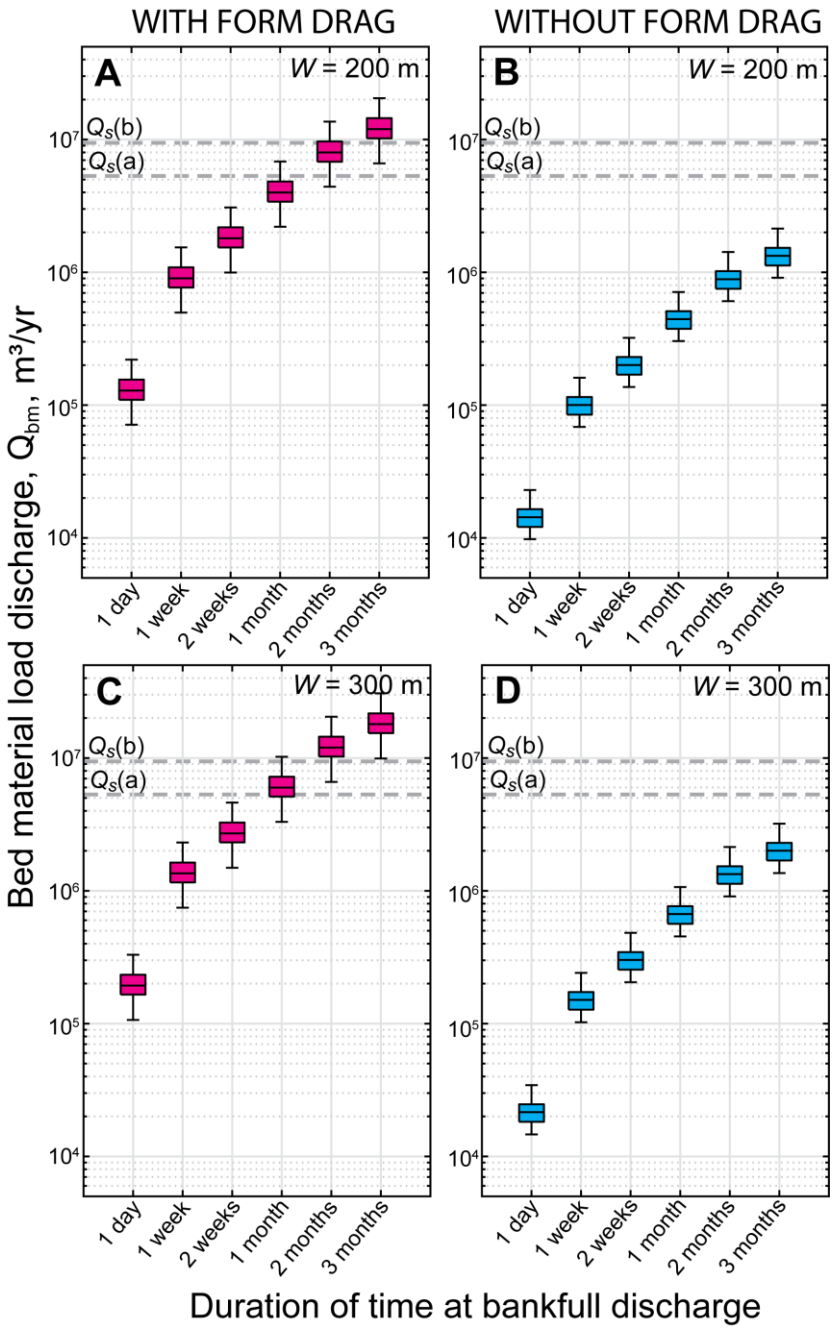

Figure 6.4 | Estimates of total bed material load discharge, *Qbm*, in units of m^3/yr, in Ferron Sandstone trunk channels, assuming that the instantaneous bankfull bedload discharge is sustained for a period of 1 day, 1 week, 2 weeks, 1 month, 2 months, and 3 months in a year (see x axes). **A**) Estimates of *Qbm*, assuming a channel width, *W*, of 200 m, without form drag removed. **B**) Estimates of *Qbm*, assuming *W* = 200 m, with form drag removed. **C**) Estimates of *Qbm*, assuming *W* = 300 m, without form drag removed. **D**) Estimates of *Qbm*, assuming *W* = 300 m, with form drag removed. In each figure part, the central mark of each box indicates the median estimate, the bottom and top edges of each box indicate the 1st and 3rd quartiles (or 25th and 75th percentiles), respectively, and the whiskers extend to the most extreme estimates that are not considered to be outliers. Further, each figure part includes dashed grey lines to indicate estimates of mean annual suspended sediment discharges, *Qs*, that I calculated and presented in Chapter 2 for the Turonian Ferron Sandstone. The dashed grey line labelled *Qs*(a) refers to the value of *Qs* reconstructed for catchment F2 in Chapter 2 (see Figure 2.7, parts G and H), and *Qs*(b) refers to the value of *Qs* reconstructed for catchment F1 in Chapter 2 (see Figure 2.7, parts E and F).

For the Ferron Notom delta, which neighboured the Ferron Last Chance delta, Sharma et al. (2017) predicted a mean annual suspended sediment discharge of between 1.5−4.4 $\times 10^6$ m^3, a mean annual bedload discharge of 1.4−3.0 $\times 10^5$ m^3 and, therefore, a total mean annual sediment discharge of 1.7−4.7 $\times 10^6$ m^3. However, we now know that the authors' estimation of mean annual suspended sediment discharge is, in fact, an estimate of the mean annual suspended fraction of the bed material load. Instead of a mean annual sediment discharge of 1.7−4.7 $\times 10^6$ m^3, the authors have estimated a mean annual bed material load of 1.7−4.7 $\times 10^6$ m^3. If my estimates of mean annual Q_S for the Ferron, derived using the palaeoDEM–GCM–BQART approach, are true (5.2 and 10.7 $\times 10^6$ m^3/yr), this would imply ratios of bedload to suspended load that have a lower value between 0.16−0.33 and an upper value of 0.44−0.9. These ratios are very high for sand-bed rivers, compared to documented ratios of bedload to suspended load in sandbed rivers of order 0.05 (Cantalice et al., 2013; Ashley et al., 2020). These implausibly high ratios likely result from the analytical limitations of the original fulcrum approach, but also because estimates made by Sharma et al. (2017) used an assumption of sediment transport intermittency. Whereas, using my revised fulcrum methodology, I can compare these new estimates of Q_{bm} with my estimates of mean annual Q_S for the Ferron, derived using the palaeoDEM–GCM–BQART approach in Chapter 2. Here, for a range of plausible intermittencies (1 week to 3 months), and for endmember channel widths, my results imply ratios of bedload to suspended load that have lower values of ~0.01−0.018 and upper values of ~0.18−0.35. These values are much more plausible for natural sand-bed rivers (Cantalice et al., 2013; Ashley et al., 2020).

6.4 Future work

In this thesis I developed new approaches which advance our ability to quantify the dynamics and behaviour of ancient fluvial systems. Importantly, I have identified a number of future research avenues which directly build on this work, and which are important next steps to further advance our understanding. These research avenues centre around temporal scales of investigation. In Chapter 2, I developed an approach to reconstruct mean annual Q_w and Q_s in units of m^3/yr, whereas in Chapter 3 I developed a framework to quantify hydrodynamic parameters from fluvial strata, which recovered instantaneous bankfull Q_w in units of m^3/s and, as I presented in ***Section 6.3***, instantaneous bankfull Q_{bm} in units of m^3/s. Throughout ***Sections 6.1 and 6.2***, I discussed that a major outstanding challenge in the investigation of ancient fluvial systems is to reconcile different timescales of investigation. This is crucial to facilitate comparison of constraints and insights gained from different approaches.

In particular we require a better understanding of flow variability (particularly seasonal–interannual flow variability associated with the shape of river hydrographs) and sediment transport intermittency to accurately constrain palaeo-water and sediment discharges, and therefore enhance our understanding of the movement of water and sediment, and biogeochemical cycling, across Earth's surface in the geological past. Not only are seasonal–interannual flow variability and sediment transport intermittency important to reconcile temporal scales of investigation, but they are also important for investigating fluvial response to climatic perturbations in the geological past. A change, or no change, in mean annual water and sediment discharges does not necessarily equate to a change, or no change, in the interannual variability of water and sediment discharges. I argue that that future research must develop and test new approaches to constrain flow variability and sediment transport intermittency in ancient fluvial systems. In this section I outline three research proposals which directly tackle this goal.

Proposal 1: Solving the flow variability puzzle

In Chapter 4 I used cross-set geometries to provide direct evidence for enhanced bedform preservation in disequilibrium conditions. However, enhanced bedform preservation in disequilibrium conditions may result from flow variability (Leary & Ganti, 2020) and/or concurrent migration of dunes and bars, i.e., the presence of a morphodynamic hierarchy (Ganti et al., 2020). While we can use bedform turnover timescales to contextualise the implications of these respective controls, we currently have no method to distinguish the dominant control. The inability to disentangle these competing controls is a crucial obstacle to quantifying flow variability from fluvial strata.

However, the work that I presented in Chapter 4 is optimistic and highlights the potential to isolate the signal of flow variability by spatially contextualising field measurements according to facies e.g., point bar deposits versus channel floor/thalweg deposits. In Chapter 4 I hypothesised that the relative role of flow variability and morphodynamic hierarchy on enhanced bedform preservation is likely to vary spatially in rivers. For instance, cross-sets associated with point bar or mid-channel bar deposits are likely to reflect

enhanced bedform preservation due to concurrent dune and bar migration, whereas cross-sets associated with channel floor or thalweg deposits are less likely to be influenced by bar migration and are more likely to be influenced by flow variability. These insights suggest that thalweg deposits in fluvial are likely to provide a record of bedform disequilibrium dynamics controlled by flow variability.

To tackle this problem, we require knowledge of how flow variability is preserved in point bar deposits and channel floor/thalweg deposits — I suggest future work should directly test the hypothesis that thalweg deposits in rivers preserve bedform disequilibrium dynamics associated with flow variability. This hypothesis could be tested experimentally, via flume experiments. However, it can be difficult to impose multiple levels of hierarchy in flume experiments. Further, the spatiotemporal scales associated with experimental observations are difficult to compare with the spatiotemporal scales associated with the evolution of fluvial systems on geological timescales. To help bridge the gap between experimental observations and stratigraphic observations, I propose testing this hypothesis by investigating fluvial deposits of modern rivers. With detailed understanding as to how flow variability is preserved in modern fluvial deposits, at catchment scales, this will advance our ability to understand, and quantify, signals of flow variability in fluvial strata.

I suggest testing this hypothesis in modern dryland rivers, which are conducive to field investigation (e.g., Ielpi, 2018; Ielpi & Lapôtre, 2019b, 2019a; Lapôtre et al., 2019; Ielpi et al., 2020). Modern dryland rivers are usually ephemeral, which enables detailed investigation of bank, bed, and subsurface sediments, and are usually associated with flashy flood hydrographs, which means that their deposits are likely to reflect flood conditions. Further, modern dryland rivers often occur in remote locations where their banks and floodplains are less likely to be influenced by anthropogenic activity, e.g., presence of infrastructure. One potential field site is the McLeod Springs Wash in the Toiyabe Basin, Nevada, USA, which is an ephemeral dryland river subject to a flashy flood hydrograph. Moreover, McLeod Springs Wash is accessible and well-studied; previous work includes detailed geomorphic mapping of McLeod Springs Wash to distinguish trunk channels, including floodwater marks and flood distributary channels (Ielpi & Lapôtre, 2019a).

In detail, I propose to define river a number of cross-sections across McLeod Springs Wash, across both meander bend reaches and relatively straight reaches. For each cross-section, I would measure channel hydraulic geometries (width, mean depth, maximum depth, bed slope, cross-sectional area) and grain-sizes of bed material. Then, I would dig a series of trenches on the riverbed, orientated parallel to the flow direction, to provide a flow-parallel view of cross-sets preserved in sub-surface deposits (Figure 6.5). Meander bend cross-sections would span point bar to thalweg deposits, whereas cross-sections in relatively straight reaches would span bank to bank. Within each trench, I would implement the same measurement strategy as Chapter 4. I would measure the distributions of thicknesses within individual cross-sets, and I would determine the median grain-size of each measured cross-set. Moreover, I would measure the distributions of maximum thicknesses of cross-sets exposed in the subsurface.

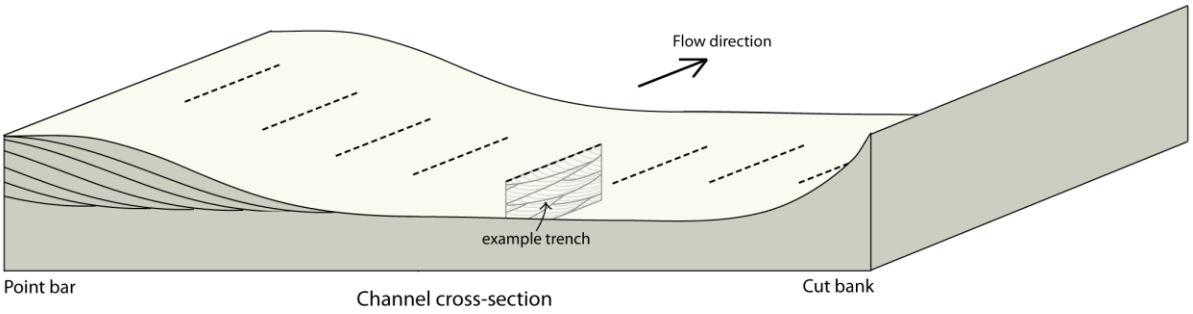

Figure 6.5 | Schematic cross-section of a dryland river channel. Dashed black lines indicate potential locations and orientations of trenches, and the example trench shows subsurface deposits that would be visible in each trench, and which we would measure.

With these field data, I would use the hydraulic geometries and grain-sizes measured for channel cross-section to estimate flow velocities, instantaneous bankfull water discharges, and more, using hydraulic equations that are routinely implemented for geological applications, i.e., using the framework that I presented in Chapter 3. Then, I would use field measurements of cross-set geometries in trenches, and the methodology that I presented in Chapter 4, to determine whether bedforms were preserved in equilibrium or disequilibrium conditions, and I would calculate the bedform turnover timescales associated with individual cross-sets. With knowledge of whether bedforms were preserved in equilibrium or disequilibrium conditions, I would estimate formative flow durations relative to bedform turnover timescales, and I would use estimated flow velocities and bankfull water discharges to estimate total flood discharges. If the hypothesis is correct, then estimates flow velocities, bankfull water discharges, and total flood discharges estimated using field measurement of cross-sets in thalweg deposits should be consistent with stream gauge data. Further, if the hypothesis is correct, this would mean that we can theoretically use evidence of disequilibrium dynamics in thalweg facies of preserved fluvial strata, and the outlined methods, to quantify flow variability. Given investigation of a modern dryland river, we can use these methods to explore flow variability in pre-vegetation fluvial strata and, potentially, flow variability on other planets.

Proposal 2: Solving the sediment transport intermittency puzzle

With interest in flow variability in ancient fluvial systems, another useful parameter to constrain is sediment transport intermittency, which offers insights into the timespans over which fluvial systems redistribute sediment, or the timespans over which geomorphic work occurs. The intermittency factor of a river can be calculated, and can be defined as the fraction of the total time that a river could transport the same amount of water or sediment at bankfull conditions, as it transports during the real hydrograph (Paola et al., 1992) — this inherently assumes that bankfull conditions do all geomorphic work (Wolman & Miller, 1960).

In rivers, it is possible to calculate intermittency factors for both flow intermittency (i.e., flow variability) and sediment transport intermittency. However, it is important to make the distinction between these as sediment transport intermittency is not necessarily a proxy for flow intermittency. While one river may

transport its entire annual sediment load during bankfull conditions associated with flood events, another river may transport sediment all year around at both high and low flow conditions. Therefore, sediment transport intermittency is only useful as a proxy for flow intermittency in rivers that transport their entire sediment load during bankfull/flood events which, practically, limits application. Nonetheless, constraints on sediment transport intermittency are useful complements to constraints on flow intermittency and are hugely informative themselves. In fluvial systems with high erosional thresholds, the annual sediment budget may be determined by the frequency of threshold-surpassing storm events. In these systems, small changes to sediment transport intermittency could be driven by, e.g., enhanced storminess, and result in major changes to the annual sediment budget. Therefore, constraints on sediment transport intermittency also encode detailed information regarding fluvial response to climatic perturbation.

Future work should aim to constrain sediment transport intermittency in ancient fluvial systems. Intermittency factors have been documented for a number of modern rivers (e.g., Meybeck et al., 2003; Sklar & Dietrich, 2004; Wright & Parker, 2005; Czuba & Foufoula-Georgiou, 2014; Hayden, Lamb, & McElroy, 2021). In some instances, intermittency has been correlated with parameters such as catchment area (Meybeck et al., 2003), and these observations have been used to predict intermittency in ancient systems (Holbrook & Wanas, 2014; Lin & Bhattacharya, 2017; Sharma et al., 2017; Brewer et al., 2020). However, as previously discussed, the predictability power of this relation is poor (see Figure 7 in Meybeck et al., 2003).

Alternatively, stratigraphic approaches can be used to constrain intermittency in ancient fluvial systems. These approaches include using estimates of sediment discharges and depositional sediment volumes to calculate the minimum time required to accumulate the sediment volume (Moore et al., 2003; Jerolmack et al., 2004; Bhattacharya et al., 2005; Kleinhans, 2005; Metz et al., 2009). Where depositional sediment volumes have been age-constrained, or where the approximate timespan of deposition is known, an intermittency factor can then be calculated (Buhler et al., 2014; Lapôtre & Ielpi, 2020; Hayden, Lamb, & McElroy, 2021; Hayden, Lamb, Myrow, et al., 2021). This approach is frequently used to investigate ancient fluvial systems on Mars, but lesser so on Earth. Another stratigraphic approach can be implemented where annual Q_S is known. This approach involves calculating instantaneous Q_b or Q_{bm} from fluvial strata and, assuming that bankfull conditions move bedload, calculating the length of time bankfull conditions must be sustained to transport the annual bedload budget (Watkins, Whittaker, Ganti, et al., 2018; Watkins, 2019). However, this approach requires an assumption to be made about the ratio of bedload to suspended load.

With limited previous work in this area, I propose to develop and test these approaches to constrain sediment transport intermittency in ancient fluvial systems. Moreover, I would test these approaches for the Turonian Last Chance Ferron Sandstone, which is an ideal candidate for investigation of sediment transport intermittency for a number of reasons:

(1) Terrestrial fluvial strata of the Last Chance Ferron Sandstone preserve major meandering trunk channels; it is therefore reasonable to make a mass-balance assumption which is crucial for the comparison of sediment discharges with preserved depositional volumes.
(2) Stratigraphic thicknesses are well-documented, and the depositional area of the Last Chance deltas is somewhat constrained (Bhattacharya & Tye, 2004; Gardner et al., 2004; Ryer & Anderson, 2004).
(3) The Last Chance delta has been age-constrained using the biostratigraphic correlation charts of Molenaar and Cobban (1991) and Kauffman et al. (1993), and the correlation charts of Gardner (1995) and Shanley and McCabe (1995). These charts were compiled and adapted by Garrison and Bergh (2004), and calibrated using $^{40}Ar/^{39}Ar$ isotopic data by Obradovich (1993). The Last Chance delta was deposited over a period of 1.7 million years, between 90.3−88.6 Ma (Garrison & Bergh, 2004).
(4) Palaeo-channel widths of Ferron trunk channels are well-constrained (relative to the Blackhawk Formation and Castlegate Sandstone), with average channel widths of 250 m (Bhattacharya & Tye, 2004; Chidsey et al., 2004; Garrison & Bergh, 2004). This facilitates reconstruction of total palaeo-water and sediment discharges.

In detail, I would implement two approaches to investigate sediment transport intermittency. Approach 1 would be entirely stratigraphic, using field measurements and stratigraphic observations, and Approach 2 would combine field measurements and GCM/palaeoDEM model constraints. Importantly, these two approaches would both use the datasets, methods, and results presented in this thesis.

For Approach 1, I would use field measurements of the Ferron Sandstone presented in Chapter 4, and the framework presented in Chapter 3, to reconstruct morphologies and hydrodynamics of ancient Ferron trunk channels. I would then use the revised fulcrum methodology, outlined and exemplified in ***Section 6.3***, to reconstruct instantaneous bankfull Q_{bm} in trunk channels (i.e., the bedload plus the suspended fraction of the bed material load). Using these estimates of Q_{bm} (in units of m^3/s), and an estimate of the depositional volume in the Ferron Last Chance delta (in units of m^3; derived using constraints on stratigraphic thickness and approximate delta plan view area), I would calculate the sediment accumulation rate (in units of m/s) and, subsequently, the minimum time required to accumulate the observed stratigraphic thickness. Finally, I would calculate the intermittency factor by calculating the minimum time required as a fraction of the total depositional age (1.7 million years).

For Approach 2, I would use estimates of Q_S for the Ferron Sandstone, derived using the palaeoDEM–GCM–BQART approach that I presented in Chapter 2, and plausible estimates for the ratio of bedload to suspended load in sand-bed rivers (Cantalice et al., 2013; Ashley et al., 2020). With these constraints, I would use the same estimates of Q_{bm}, as in Approach 1, to calculate the length of time that bankfull conditions must have been sustained to transport enough bedload to satisfy the assumed ratio of bedload to suspended load.

In implementing these suggested approaches, we can gain new insights into the likely values of sediment transport intermittency in ancient fluvial systems, and these insights can be contrasted and/or corroborated

with one another. These insights will not only help to constrain timespans of fluvial activity in the geological past, but will also have implications for constraining timespans of fluvial activity on other planets.

Proposal 3: Using extreme GCM results to solve the flow variability and sediment transport intermittency puzzles

One final, prominent, research opportunity has arisen based on my research, and involves the use of "extreme" climate variables from GCM outputs to further tackle both the flow variability and sediment transport intermittency puzzles. In Chapter 2 I used GCM outputs to develop the palaeoDEM–GCM–BQART approach, and the specific climate variables that I used from GCM outputs were mean annual climate variables. However, GCMs are routinely used to model "extreme" climate variables, such as mean precipitation rates and maximum precipitation rates for individual seasons — this modelling work is motivated by interest in the evolution and sensitivity of monsoonal climates (Abe et al., 2003; Kitoh et al., 2010; Marzocchi et al., 2015; Farnsworth et al., 2019).

In Proposal 1 I suggested one possible approach to explore flow variability in ancient fluvial systems. Here, I can suggest a second approach that utilizes extreme climate variables. While constraints from GCM outputs are tentative, the methodology that I presented in Chapter 2 could be used to extract catchment water discharges using both "extreme" climate variables (as a proxy for flood conditions) and mean annual climate variables. This would recover estimates of peak flood discharges in catchments, as well as mean discharges in catchments. These estimates could then be contrasted to gain insights into flow variability — we expect that the ratio of peak flood discharge to mean discharge is much larger in monsoonal/subtropical systems than in perennial systems.

Further, in Proposal 2 I suggested two possible approaches to constrain sediment transport intermittency in ancient fluvial systems. The first approach was a stratigraphic approach, whereas the second approach involved the use of mean annual Q_S that I estimated using the palaeoDEM–GCM–BQART approach and presented in Chapter 2. Following this, I can suggest a third approach to constrain sediment transport intermittency, which involves using both mean climate variables and extreme climate variables from GCMs to model both mean and extreme sediment discharges.

In Chapter 2 I used mean climate variables from HadCM3L GCM outputs, and the palaeoDEM–GCM–BQART approach, to reconstruct mean annual Q_S in palaeo-catchments. To estimate sediment transport intermittency, I would repeat this methodology using "extreme" climate variables (as a proxy for flood conditions). Using extreme climate variables, e.g., the mean precipitation rate of the wettest season in a year, I would similarly reconstruct Q_S, and I would contrast these estimates of Q_S for bankfull/flood conditions with mean annual Q_S.

CHAPTER 7: Conclusions

In this thesis I developed new methods and frameworks to quantify the dynamics and behaviour of ancient fluvial systems. These new approaches tackle multiple spatial and temporal scales of investigation, and I exemplified these approaches for ancient fluvial systems in the Late Cretaceous North American continent. Based on the results and discussion of my research chapters, as well as discussion of my current and ongoing research, I present a number of conclusions. These are separated into those associated with methods to investigate the dynamics of ancient fluvial systems and those associated with the dynamics of ancient fluvial systems in the Late Cretaceous North American continent.

Methods to investigate the dynamics of ancient fluvial systems

1. **Palaeo-digital elevation models (palaeoDEMs), general circulation model (GCM) results, and the BQART suspended sediment discharge model can be successfully used to make first-order estimates of water and sediment discharges in ancient fluvial systems.**
    - Geographic information systems (GIS) techniques can be used to reconstruct palaeocatchments from palaeoDEMs, which are increasingly being made available by universities and commercial providers. Using palaeoDEMs of the Cenomanian and Turonian North American continent, provided by *Getech Group Plc.*, reconstructed palaeocatchments are reasonable compared to published palaeogeographies. Further, reconstructed palaeocatchment configurations provide insights into the loci of freshwater and sediment supply to oceans.
    - GCM results can be used to extract catchment-averaged climate variables in palaeocatchments. Catchment-averaged climate variables include mean annual precipitation which, if a rainfall−runoff ratio is assumed, can be used to estimate mean annual water discharges. Alternatively, if a rainfall−runoff ratio is not assumed (i.e., a value of 1 is implemented), then mean annual precipitation can be used to estimate maximum annual water discharges.
    - With constraints on palaeocatchment geometries and catchment-averaged climate variables, the BQART model can be used to reconstruct suspended sediment discharges in palaeocatchments.
    - Estimates of suspended sediment discharges are the same order of magnitude as, and are either consistent with, or within a factor of two to three of, published estimates of suspended sediment discharges in two case studies. When allowing large uncertainties (≤50%/±5°C) on BQART input parameters, estimates of suspended sediment discharges are still the same order of magnitude, and within a factor of four to seven of, published estimates.
2. **Quantitative palaeohydraulic methods can be successfully applied to preserved fluvial strata to reconstruct the dynamics and behaviour of ancient fluvial systems in space and time.**
    - Measurements of cross-set geometries and grain-size in channel-fill fluvial strata can be used to reconstruct various morphologic properties (e.g., dune heights, flow depths, slopes),

morphodynamic properties (e.g., bedform turnover timescales), hydrodynamic properties (e.g., flow velocities, unit water discharges), and sediment transport properties (e.g., dominant sediment transport modes, unit bedload discharges, unit bed material load discharges). Where channel widths are known, the same field measurements can also be used to reconstruct total water discharges, total bedload discharges, and total bed material load discharges.

- Where channel widths are known, or where they can be constrained, planform morphology can be reconstructed using channel aspect ratios. At depth/width ratios greater than 0.02 (or width/depth ratios smaller than 50), rivers are likely to have a single-thread planform type. Whereas at depth/width ratios smaller than 0.02 (or width/depth ratios larger than 50), rivers are likely to have a multi-thread planform type.
- In multi-thread rivers, slope/Froude ratios can be used to inform whether rivers were braided or anastomosing. At slope/Froude ratios greater than 0.003, rivers are likely to be braided. Whereas as slope/Froude ratios smaller than 0.003, rivers are likely to be anastomosing.

3. **Bedform disequilibrium dynamics are prevalent in preserved fluvial strata and this has implications for the application of quantitative palaeohydraulic methods to preserved fluvial strata.**
    - Palaeohydraulic reconstructions from fluvial strata typically assume that bedform preservation occurred in steady-state conditions. However, preserved dune-scale cross-sets in fluvial strata of the Upper Cretaceous Ferron Sandstone, Blackhawk Formation, and Castlegate Sandstone, central Utah, USA, provide unambiguous evidence of enhanced bedform preservation in non-steady, or disequilibrium conditions. This highlights the potential ubiquity of bedform disequilibrium dynamics in fluvial strata beyond the three formations considered in this thesis.
    - Two competing controls lead to enhanced bedform preservation in disequilibrium conditions, the effect of formative flow variability on dune migration and preservation (*flood hypothesis*) and the effect of concurrent bar and dune migration on preservation (*hierarchy hypothesis*).
    - If enhanced bedform preservation is explained by the flood hypothesis, then flood recessions are anticipated to shorter than bedform turnover timescales and would have been of order a few hours to a few days. Flood recessions of a few hours to a few days are consistent with total flood durations of order days, depending on the shape of individual flood hydrographs.
    - If enhanced bedform preservation is explained by the hierarchy hypothesis, then rates of bar migration are anticipated to be relatively rapid, with bars migrating on timescales that approach bedform turnover timescales, i.e., the rates of dune migration.
    - To isolate the role of formative flow variability on enhanced bedform preservation, i.e., to identify enhanced bedform preservation that is consistent with the flood hypothesis, future work should test the hypothesis that channel floor or thalweg deposits preferentially preserve evidence of enhanced bedform preservation driven by formative flow variability.

- Where evidence of bedform disequilibrium dynamics in dune-scale cross-strata can be directly attributed to the control of formative flow variability, then quantitative constraints on flood recession durations and, therefore, total flood durations can be inferred from fluvial strata. Using the framework presented in Chapter 3, estimates of flood durations using the approach presented in Chapter 4, and the revised fulcrum methodology presented in Chapter 6, it is possible to predict total flood discharges and flood sediment transport capacities.
- Where there is evidence of enhanced bedform preservation in disequilibrium conditions, use of steady-state assumptions to reconstruct original dune heights and formative flow depths should be treated with caution. Instead, I recommend that original dune heights should be reconstructed using a range of bedform preservation ratios higher than 0.3 (i.e., the steady-state condition), and flow depths should be independently constrained using measurements of palaeoflow depth proxies such as bar clinoform heights.

Dynamics of ancient fluvial systems in the Late Cretaceous North American continent

4. **Rivers in the Late Cretaceous North American continent exported more sediment to oceans than the modern North American continent**
    - Total continental suspended sediment discharges were a factor of two bigger in the Cenomanian (3.4 GT/yr) and Turonian (3.2 GT/yr) North American continent than in the Holocene pre-anthropogenic (1.7 GT/yr) North American continent.
    - The total continental suspended sediment load in the Cenomanian and Turonian North American continent was exported from approximately half the landmass, meaning that suspended sediment yields were a factor of four bigger in the Cenomanian and Turonian North American continent than in the Holocene pre-anthropogenic North American continent.
5. **Sediment export from rivers in the Late Cretaceous North American continent can be linked with tectonic and climatic forcing.**
    - Suspended sediment discharges were highly variable across the Cenomanian and Turonian North American continent, spanning seven orders of magnitude (in units of m^3/yr).
    - Spatial variability in suspended sediment discharges in the Late Cretaceous North American continent can be linked with tectonic forcing. The western margin of the Western Interior Seaway (WIS), which is associated with the active Sevier fold-and-thrust belt, may have contributed three times more suspended sediment to the WIS than the eastern margin of the WIS, which is associated with the stable continental craton.
    - Spatial variability in suspended sediment discharges in the Late Cretaceous North American continent can also be linked with climatic forcing. Suspended sediment discharges are lowest at high-latitudes, where mean annual temperature and mean annual precipitation are lowest.

Suspended sediment discharges increase towards, and peak, at mid-latitudes, where both mean annual temperature and mean annual precipitation are higher. Suspended sediment discharges decrease slightly towards low latitudes, where mean annual precipitation is highest, but where mean annual precipitation is lower (than at mid-latitudes).

6. **The dynamics and behaviour of rivers in the Late Cretaceous North American continent can be linked with tectonic and climatic forcing.**
    - An up to four-fold increase in slopes at the transition between the Campanian Blackhawk Formation and Castlegate Sandstone, central Utah, USA, reflects river response to tectonic forcing associated with uplift in the Sevier hinterland. This slope increase is unlikely to reflect climatic forcing, unless a decrease in channel width is inferred at the Blackhawk−Castlegate transition, which is unlikely.
    - Evidence of bedform disequilibrium dynamics in dune-scale cross-strata of the Turonian Ferron Sandstone, and Campanian Blackhawk Formation and Castlegate Sandstone, central Utah, USA, potentially preserve a record of formative flow variability. If true, these cross-strata imply flood recession durations of order hours to a few days and, therefore, total flood durations of order a few days. These total flood durations are consistent with flood durations associated with the causes of flooding in perennial discharge regimes.
7. **Upper Cretaceous fluvial strata in the Late Cretaceous North American continent provide evidence of both stability and instability in ancient rivers.**
    - Multi-thread rivers of the Campanian Blackhawk Formation and Castlegate Sandstone, central Utah, USA, were characterised by anastomosing multi-thread planforms. Reconstruction of anastomosing planforms is consistent with modern anastomosing rivers, which are typically characterised by high suspended sediment supply, sand-beds, and relative stability (compared to braided multi-thread rivers). Anastomosing planforms in Blackhawk and Castlegate multi-thread channels point to large, low-sloping, and stable fluvial systems, in which mid-channel bars formed permanent islands that likely didn't flood in bankfull/flood conditions.
    - While anastomosing planforms implying relative stability of multi-thread Blackhawk and Castlegate channels, evidence of bedform disequilibrium dynamics in dune-scale cross-strata implies the prevalence of non-steady flow conditions and, therefore, instability at channel reach scales.
    - Evidence of bedform disequilibrium dynamics in fluvial strata of single-thread Blackhawk and Ferron channels also implies the prevalence of non-steady flow conditions and, therefore, instability at channel reach scales.

BIBLIOGRAPHY

Abe, M., Kitoh, A., & Yasunari, T. (2003). An evolution of the Asian Summer Monsoon associated with mountain uplift; Simulation with the MRI Atmosphere-Ocean Coupled GCM. *Journal of the Meteorological Society of Japan. Ser. II*, *81*(5), 909-933. DOI:10.2151/jmsj.81.909

Adam, J. C., Clark, E. A., Lettenmaier, D. P., & Wood, E. F. (2006). Correction of global precipitation products for orographic effects. *Journal of Climate*, *19*, 15-38. DOI:10.1175/JCLI3604.1

Adams, M. M., & Bhattacharya, J. P. (2005). No change in fluvial style across a sequence boundary, Cretaceous Blackhawk and Castlegate formations of central Utah, U.S.A. *Journal of Sedimentary Research*, *75*(6), 1038-1051. DOI:10.2110/jsr.2005.080

Adams, R. L., & Carr, J. P. (2010). Regional depositional systems of the Woodbine, Eagle Ford, and Tuscaloosa of the U.S. Gulf Coast. *Gulf Coast Association of Geological Societies Transactions*, *60*, 3-27.

Allen, J. R. L. (1978). Computational models for dune time-lag: calculations using Stein's rule for dune height. *Sedimentary Geology*, *20*, 165-216. DOI:DOI:10.1016/0037-0738(78)90054-4

Allen, J. R. L. (1982a). *Sedimentary Structures; Their Character and Physical Basis. Volume I* (Vol. 30). Elsevier.

Allen, J. R. L. (1982b). *Sedimentary Structures; Their Character and Physical Basis. Volume II* (Vol. 30). Elsevier.

Allen, P. A. (2008a). From landscapes into geological history. *Nature*, *451*, 274-276. DOI:10.1038/nature06586

Allen, P. A. (2008b). Time scales of tectonic landscapes and their sediment routing systems. *Geological Society, London, Special Publications*, *296*(1), 7-28. DOI:10.1144/sp296.2

Allen, P. A. (2017). *Sediment Routing Systems: The Fate of Sediment from Source to Sink*. Cambridge University Press. DOI:DOI: 10.1017/9781316135754

Allen, P. A., Armitage, J. J., Carter, A., Duller, R. A., Michael, N. A., Sinclair, H. D., Whitchurch, A. L., & Whittaker, A. C. (2013). The *Qs* problem: Sediment volumetric balance of proximal foreland basin systems. *Sedimentology*, *60*(1), 102-130. DOI:10.1111/sed.12015

Allmendinger, R. W. (1992). Fold and thrust tectonics of the western United States exclusive of the accreted terranes. In B. C. Burchfiel, P. W. Lipman, & M. L. Zoback (Eds.), *The Cordilleran Orogen*. Geological Society of America. DOI:10.1130/DNAG-GNA-G3.583

Amiot, R., Lécuyer, C., Buffetaut, E., Fluteau, F., Legendre, S., & Martineau, F. (2004). Latitudinal temperature gradient during the Cretaceous Upper Campanian–Middle Maastrichtian: $\delta^{18}O$ record of continental vertebrates. *Earth and Planetary Science Letters*, *226*(1-2), 255-272. DOI:10.1016/j.epsl.2004.07.015

Anderson, P. B., & Ryer, T. A. (2004). Regional Stratigraphy of the Ferron Sandstone. In T. C. Chidsey, Jr., R. D. Adams, & T. H. Morris (Eds.), *Regional to Wellbore Analog for Fluvial-Deltaic Reservoir Modeling: The Ferron Sandstone of Utah* (Vol. 50). American Association of Petroleum Geologists. DOI:10.1306/St50983

Andrews, E. D. (1984). Bed-material entrainment and hydraulic geometry of gravel-bed rivers in Colorado. *GSA Bulletin*, *95*(3), 371-378. DOI:10.1130/0016-7606(1984)95<371:BEAHGO>2.0.CO;2

Armitage, J. J., Duller, R. A., Whittaker, A. C., & Allen, P. A. (2011). Transformation of tectonic and climatic signals from source to sedimentary archive. *Nature Geoscience*, *4*(4), 231-235. DOI:10.1038/ngeo1087

Armstrong, H. A., Wagner, T., Herringshaw, L. G., Farnsworth, A. J., Lunt, D. J., Harland, M., Imber, J., Loptson, C., & Atar, E. F. L. (2016). Hadley circulation and precipitation changes controlling black shale deposition in the Late Jurassic Boreal Seaway. *Paleoceanography*, *31*(8), 1041-1053. DOI:10.1002/2015PA002911

Armstrong, R. L. (1968). Sevier Orogenic Belt in Nevada and Utah. *GSA Bulletin*, *79*(4), 429-458. DOI:10.1130/0016-7606(1968)79[429:SOBINA]2.0.CO;2

Aschoff, J., & Steel, R. (2011a). Anomalous clastic wedge development during the Sevier-Laramide transition, North American Cordilleran foreland basin, USA. *GSA Bulletin*, *123*(9-10), 1822-1835. DOI:10.1130/B30248.1

Aschoff, J., & Steel, R. (2011b). Anatomy and development of a low-accommodation clastic wedge, upper Cretaceous, Cordilleran Foreland Basin, USA. *Sedimentary Geology*, *236*(1), 1-24. DOI:10.1016/j.sedgeo.2010.10.006

Ashida, K., & Michiue, M. (1972). Study on hydraulic resistance and bed-load transport rate in alluvial streams. *Proceedings of the Japan Society of Civil Engineers*, *1972*(206), 59-69. DOI:10.2208/jscej1969.1972.206_59

Ashley, T. C., McElroy, B., Buscombe, D., Grams, P. E., & Kaplinski, M. (2020). Estimating Bedload From Suspended Load and Water Discharge in Sand Bed Rivers [DOI:10.1029/2019WR025883]. *Water Resources Research*, *56*(2), e2019WR025883. DOI:DOI:10.1029/2019WR025883

Ashmore, P. (2013). Morphology and Dynamics of Braided Rivers. *Treatise on Geomorphology*, *9*, 289-312. DOI:10.1016/B978-0-12-374739-6.00242-6

Barrell, J. (1917) Rhythms and the measurements of geologic time. *GSA Bulletin*, 28, 745–904.

Barron, E. J. (1983). A warm, equable Cretaceous: The nature of the problem. *Earth-Science Reviews*, *19*(4), 305-338. DOI:10.1016/0012-8252(83)90001-6

Barron, E. J., Fawcett, P. J., Pollard, D., & Thompson, S. (1993). Model simulations of Cretaceous climates: the role of geography and carbon dioxide [10.1098/rstb.1993.0116]. *Philosophical Transactions of the Royal Society B: Biological Sciences*, *341*(1297), 307-316. DOI:10.1098/rstb.1993.0116

Barron, E. J., Hay, W. W., & Thompson, S. (1989). The hydrologic cycle: A major variable during earth history. *Global and Planetary Change*, 1(3), 157-174. DOI:DOI:10.1016/0921-8181(89)90001-5

Bartschi, N. C., Saylor, J. E., Lapen, T. J., Blum, M. D., Pettit, B. S., & Andrea, R. A. (2018). Tectonic controls on Late Cretaceous sediment provenance and stratigraphic architecture in the Book Cliffs, Utah. *GSA Bulletin*, *130*(11-12), 1763-1781. DOI:10.1130/B31927.1

Beck, H. J., & Birch, G. F. (2012). Metals, nutrients and total suspended solids discharged during different flow conditions in highly urbanised catchments. *Environmental Monitoring and Assessment*, 184(2), 637-653. DOI:10.1007/s10661-011-1992-z

Benyon, C., Leier, A., Leckie, D. A., Webb, A., Hubbard, S. M., & Gehrels, G. (2014). Provenance of the Cretaceous Athabasca Oil Sands, Canada: Implications for continental-scale sediment transport. *Journal of Sedimentary Research*, *84*(2), 136-143. DOI:10.2110/jsr.2014.16

Bernard, C. Y., Dürr, H. H., Heinze, C., Segschneider, J., & Maier-Reimer, E. (2011). Contribution of riverine nutrients to the silicon biogeochemistry of the global ocean – a model study. *Biogeosciences*, *8*(3), 551-564. DOI:10.5194/bg-8-551-2011

Berner, R. A. (1994). Geocarb III: A Revised Model of Atmospheric CO2 over Phanerozoic Time. *American Journal of Science*, 301, 182-204.

Bertrand-Krajewski, J.-L., Chebbo, G., & Saget, A. (1998). Distribution of pollutant mass vs volume in stormwater discharges and the first flush phenomenon. *Water Research*, 32(8), 2341-2356. DOI:10.1016/S0043-1354(97)00420-X

Best, J. (2005). The fluid dynamics of river dunes: A review and some future research directions. *Journal of Geophysical Research: Earth Surface*, 110(F4). doi:10.1029/2004JF000218

Beusen, A. H. W., Bouwman, A. F., Dürr, H. H., Dekkers, A. L. M., & Hartmann, J. (2009). Global patterns of dissolved silica export to the coastal zone: Results from a spatially explicit global model. *Global Biogeochemical Cycles*, *23*(4), GB0A02. DOI:10.1029/2008GB003281

Bhattacharya, J., & Tye, B. (2004). Searching for modern Ferron analogs and application to subsurface interpretation. In T. C. Chidsey Jr., R. D. Adams, & T. H. Morris (Eds.), *Regional to Wellbore Analog for Fluvial-Deltaic Reservoir Modeling: The Ferron Sandstone of Utah* (Vol. 50, pp. 39-57). AAPG Studies in Geology. DOI:10.1306/St50983

Bhattacharya, J. P., Copeland, P., Lawton, T. F., & Holbrook, J. (2016). Estimation of source area, river paleo-discharge, paleoslope, and sediment budgets of linked deep-time depositional systems and implications for hydrocarbon potential. *Earth-Science Reviews*, *153*, 77-110. DOI:10.1016/j.earscirev.2015.10.013

Bhattacharya, J. P., Payenberg, T. H. D., Lang, S. C., & Bourke, M. (2005). Dynamic river channels suggest a long-lived Noachian crater lake on Mars [DOI:10.1029/2005GL022747]. *Geophysical Research Letters*, *32*(10). DOI:10.1029/2005GL022747

Bhattacharyya, P., Bhattacharya, J. P., & Khan, S. D. (2015). Paleo-channel reconstruction and grain size variability in fluvial deposits, Ferron Sandstone, Notom Delta, Hanksville, Utah. *Sedimentary Geology*, *325*, 17-25. DOI:10.1016/j.sedgeo.2015.05.001

Birgenheier, L. P., Berg, M. D. V., Plink-Björklund, P., Gall, R. D., Rosencrans, E., Rosenberg, M. J., Toms, L. C., & Morris, J. (2019). Climate impact on fluvial-lake system evolution, Eocene Green River Formation, Uinta Basin, Utah, USA. *GSA Bulletin*, *132*(3-4), 562-587. DOI:10.1130/B31808.1

Blair, N. E., Leithold, E. L., & Aller, R. C. (2004). From bedrock to burial: the evolution of particulate organic carbon across coupled watershed-continental margin systems. *Marine Chemistry*, *92*(1), 141-156. DOI:10.1016/j.marchem.2004.06.023

Blair, N. E., Leithold, E. L., Ford, S. T., Peeler, K. A., Holmes, J. C., & Perkey, D. W. (2003). The persistence of memory: the fate of ancient sedimentary organic carbon in a modern sedimentary system. *Geochimica et Cosmochimica Acta*, 67(1), 63-73. DOI:10.1016/S0016-7037(02)01043-8

Blum, M., & Pecha, M. (2014). Mid-Cretaceous to Paleocene North American drainage reorganization from detrital zircons. *Geology*, *42*, 607-610. DOI:10.1130/G35513.1

Blum, M. D., Milliken, K. T., Pecha, M. A., Snedden, J. W., Frederick, B. C., & Galloway, W. E. (2017). Detrital-zircon records of Cenomanian, Paleocene, and Oligocene Gulf of Mexico drainage integration and sediment routing: Implications for scales of basin-floor fans. *Geosphere*, *13*(6), 2169–2205. DOI:10.1130/GES01410.1

Bonne, K. P. M. (2014). Reconstruction of the evolution of the Niger River and implications for sediment supply to the Equatorial Atlantic margin of Africa during the Cretaceous and the Cenozoic. *Geological Society, London, Special Publications*, *386*(1), 327-349. DOI:10.1144/sp386.20

Boulton, S. J., & Whittaker, A. C. (2009). Quantifying the slip rates, spatial distribution and evolution of active normal faults from geomorphic analysis: Field examples from an oblique-extensional graben, southern Turkey. *Geomorphology*, *104*(3), 299-316. DOI:10.1016/j.geomorph.2008.09.007

Bradley, R. W., & Venditti, J. G. (2017). Reevaluating dune scaling relations. *Earth-Science Reviews*, *165*, 356-376. DOI:10.1016/j.earscirev.2016.11.004

Bradley, R. W., & Venditti, J. G. (2019a). The Growth of Dunes in Rivers [DOI:10.1029/2018JF004835]. *Journal of Geophysical Research: Earth Surface*, *124*(2), 548-566. DOI:DOI:10.1029/2018JF004835

Bradley, R. W., & Venditti, J. G. (2019b). Transport Scaling of Dune Dimensions in Shallow Flows [DOI:10.1029/2018JF004832]. *Journal of Geophysical Research: Earth Surface*, *124*(2), 526-547. DOI:DOI:10.1029/2018JF004832

Brenner, R. L., Ludvigson, G. A., Witzke, B. L., Phillips, P. L., White, T. S., Ufnar, D. F., González, L. A., Joeckel, R. M., Goettemoeller, A., & Shirk, B. R. (2003). Aggradation of gravels in tidally influenced fluvial systems: upper Albian (Lower Cretaceous) on the cratonic margin of the North American Western Interior foreland basin. *Cretaceous Research*, *24*(4), 439-448. DOI:10.1016/s0195-6671(03)00054-5

Brewer, C. J., Hampson, G. J., Whittaker, A. C., Roberts, G. G., & Watkins, S. E. (2020). Comparison of methods to estimate sediment flux in ancient sediment routing systems. *Earth-Science Reviews*, *207*, 103217. DOI:10.1016/j.earscirev.2020.103217

Bridge, J. S. (1997). Thickness of sets of cross strata and planar strata as a function of formative bed-wave geometry and migration, and aggradation rate. *Geology*, *25*(11), 971-974. DOI:10.1130/0091-7613(1997)025<0971:TOSOCS>2.3.CO;2

Bridge, J. S., & Mackey, S. D. (1993). A revised alluvial stratigraphy model. In M. Marzo & C. Puigdefábregas (Eds.), *Alluvial Sedimentation* (pp. 317-336). Wiley-Blackwell. DOI:10.1002/9781444303995.ch22

Bridge, J. S., & Tye, B. (2000). Interpreting the dimensions of ancient fluvial channel bars, channels, and channel belts from wireline-logs and cores. *AAPG Bulletin*, *84*(8), 1205-1228. DOI:10.1306/A9673C84-1738-11D7-8645000102C1865D

Brooke, S. A. S., Whittaker, A., Armitage, J. J., D'Arcy, M., & Watkins, S. E. (2018). Quantifying sediment transport dynamics on alluvial fans from spatial and temporal changes in grain size, Death Valley, California. *Journal of Geophysical Research: Earth Surface*, *123*, 2039-2067.

Bruhn, R. L., Picard, M. D., & Isby, J. S. (1986). Tectonics and Sedimentology of Uinta Arch, Western Uinta Mountains, and Uinta Basin. In J. A. Peterson (Ed.), *Paleotectonics and sedimentation in the Rocky Mountain Region, United States* (Vol. 41). American Association of Petroleum Geologists. DOI:10.1306/M41456C16

Bryant, B., & Nichols, D. J. (1988). Late Mesozoic and early Tertiary reactivation of an ancient crustal boundary along the Uinta trend and its interaction with the Sevier orogenic belt. In C. J. Schmidt & W. J. Perry, Jr. (Eds.), *Interaction of the Rocky Mountain Foreland and the Cordilleran Thrust Belt* (Vol. 171). Geological Society of America. DOI:10.1130/MEM171-p411

Buhler, P. B., Fassett, C. I., Head, J. W., & Lamb, M. P. (2014). Timescales of fluvial activity and intermittency in Milna Crater, Mars. *Icarus*, *241*, 130-147. DOI:10.1016/j.icarus.2014.06.028

Burgener, L., Hyland, E., Huntington, K. W., Kelson, J. R., & Sewall, J. O. (2019). Revisiting the equable climate problem during the Late Cretaceous greenhouse using paleosol carbonate clumped isotope temperatures from the Campanian of the Western Interior Basin, USA. *Palaeogeography, Palaeoclimatology, Palaeoecology*, 516, 244-267. DOI:10.1016/j.palaeo.2018.12.004

Burns, C. E., Mountney, N. P., Hodgson, D. M., & Colombera, L. (2017). Anatomy and dimensions of fluvial crevasse-splay deposits: Examples from the Cretaceous Castlegate Sandstone and Neslen Formation, Utah, U.S.A. *Sedimentary Geology*, 351, 21-35. DOI:10.1016/j.sedgeo.2017.02.003

Caldeira, K., & Rampino, M. R. (1991). The Mid-Cretaceous Super Plume, carbon dioxide, and global warming. *Geophysical Research Letters*, 18(6), 987-990. DOI:DOI:10.1029/91GL01237

Cantalice, J. R. B., Cunha Filho, M., Stosic, B. D., Piscoya, V. C., Guerra, S. M. S., & Singh, V. P. (2013). Relationship between bedload and suspended sediment in the sand-bed Exu River, in the semi-arid region of Brazil. *Hydrological Sciences Journal*, *58*(8), 1789-1802. DOI:10.1080/02626667.2013.839875

Cardenas, B. T., Mohrig, D., & Goudge, T. A. (2017). Fluvial stratigraphy of valley fills at Aeolis Dorsa, Mars: Evidence for base-level fluctuations controlled by a downstream water body. *GSA Bulletin*, 130(3-4), 484-498. DOI:10.1130/B31567.1

Cardenas, B. T., Mohrig, D., Goudge, T. A., Hughes, C. M., Levy, J. S., Swanson, T., Mason, J., & Zhao, F. (2020). The anatomy of exhumed river-channel belts: Bedform to belt-scale river kinematics of the Ruby Ranch Member, Cretaceous Cedar Mountain Formation, Utah, USA [10.1111/sed.12765]. *Sedimentology*, *67*(7), 3655-3682. DOI:10.1111/sed.12765

Carling, P., Jansen, J., & Meshkova, L. (2014). Multichannel rivers: Their definition and classification. *Earth Surface Processes and Landforms*, *39*. DOI:10.1002/esp.3419

Carling, P. A. (1999). Subaqueous gravel dunes. *Journal of Sedimentary Research*, *69*(3), 534-545. DOI:10.2110/jsr.69.534

Carlston, C. W. (1969). Longitudinal slope characteristics of rivers of the midcontinent and the Atlantic east gulf slopes. *International Association of Scientific Hydrology - Bulletin*, *14*(4), 21-31. DOI:10.1080/02626666909493751

Carvajal, C., & Steel, R. (2012). Source-to-sink sediment volumes within a tectono-stratigraphic model for a Laramide shelf-to-deep-water basin: methods and results. In C. Busby & A. Azor (Eds.), *Tectonics of Sedimentary Basins: Recent Advances* (pp. 131-151). Blackwell Publishing Ltd. DOI:10.1002/9781444347166.ch7

Castelltort, S., Goren, L., Willett, S. D., Champagnac, J.-D., Herman, F., & Braun, J. (2012). River drainage patterns in the New Zealand Alps primarily controlled by plate tectonic strain. *Nature Geoscience*, *5*(10), 744-748. DOI:10.1038/ngeo1582

Castelltort, S., Simpson, G., & Darrioulat, A. (2009). Slope-control on the aspect ratio of river basins. *Terra Nova*, *21*(4), 265-270. DOI:10.1111/j.1365-3121.2009.00880.x

Castelltort, S., & Van Den Driessche, J. (2003). How plausible are high-frequency sediment supply-driven cycles in the stratigraphic record? *Sedimentary Geology*, *157*(1), 3-13. DOI:10.1016/S0037-0738(03)00066-6

Castelltort, S., Whittaker, A., & Vergés, J. (2015). Tectonics, sedimentation and surface processes: from the erosional engine to basin deposition. *Earth Surface Processes and Landforms*, 40(13), 1839-1846. DOI:10.1002/esp.3769

Cederbom, C. E., van der Beek, P., Schlunegger, F., Sinclair, H. D., & Oncken, O. (2011). Rapid extensive erosion of the North Alpine foreland basin at 5-4 Ma. *Basin Research*, *23*(5), 528-550. DOI:10.1111/j.1365-2117.2011.00501.x

Chamberlain, C. P., & Poage, M. A. (2000). Reconstructing the paleotopography of mountain belts from the isotopic composition of authigenic minerals. *Geology 28*, 115-118. DOI:10.1130/0091-7613(2000)28<115:RTPOMB>2.0.CO;2

Chamberlin, E. P., & Hajek, E. A. (2015). Interpreting Paleo-Avulsion Dynamics from Multistory Sand Bodies. *Journal of Sedimentary Research*, 85(2), 82-94. DOI:10.2110/jsr.2015.09

Chamberlin, E. P., & Hajek, E. A. (2019). Using bar preservation to constrain reworking in channel-dominated fluvial stratigraphy. *Geology*, *47*(6), 531-534. DOI:10.1130/G46046.1

Champagnac, J.-D., Molnar, P., Sue, C., & Herman, F. (2012). Tectonics, climate, and mountain topography. *Journal of Geophysical Research: Solid Earth*, *117*(B2). DOI:10.1029/2011JB008348

Chase, C. G., Gregory-Wodzicki, K. M., Parrish, J. T., & DeCelles, P. G. (1998). Topographic history of the Western Cordillera of North America and controls on climate. In T. J. Crowley & K. Burke (Eds.), *Tectonic Boundary Conditions for Climate Reconstructions* (Vol. 39, pp. 73-99). Oxford Monographs on Geology and Geophysics.

Chen, C., Guerit, L., Foreman, B. Z., Hassenruck-Gudipati, H. J., Adatte, T., Honegger, L., Perret, M., Sluijs, A., & Castelltort, S. (2018). Estimating regional flood discharge during Palaeocene-Eocene global warming. *Scientific Reports*, *8*(1), 13391. DOI:10.1038/s41598-018-31076-3

Chen, D., Yu, M., Li, L., Liu, Y., & Deng, C. (2020). Effective discharge variability for suspended sediment transport in the middle Yangtze River. *Arabian Journal of Geosciences*, 13(14), 596. DOI:10.1007/s12517-020-05587-1

Chiarenza, A. A., Mannion, P. D., Lunt, D. J., Farnsworth, A., Jones, L. A., Kelland, S.-J., & Allison, P. A. (2019). Ecological niche modelling does not support climatically-driven dinosaur diversity decline before the Cretaceous/Paleogene mass extinction. *Nature Communications*, *10*(1), 1091. DOI:10.1038/s41467-019-08997-2

Chidsey, T. C., Adams, R. D., & Morris, T. H. (2004). *Regional to Wellbore Analog for Fluvial-Deltaic Reservoir Modeling: The Ferron Sandstone of Utah* (Vol. 50). DOI:10.1306/St50983

Chitale, S. V. (1970). River Channel Patterns. *Journal of Hydraulic Division American Society Civil Engineering*, *96*, 201-221.

Chumakov, N. M., Zharkov, M. A., Herman, A. B., Doludenko, M. P., Kalandadze, N. N., Lebedev, E. A., Ponomarenko, A. G., & Rautian, A. S. (1995). Climate belts of the mid-Cretaceous time. *Stratigraphy and Geological Correlation*, *3*, 42-63.

Church, M. (2006). Bed material transport and the morphology of alluvial river channels. *Annual Review of Earth and Planetary Sciences*, *34*(1), 325-354. DOI:10.1146/annurev.earth.33.092203.122721

Church, M., & Ferguson, R. I. (2015). Morphodynamics: Rivers beyond steady state. *Water Resources Research*, *51*(4), 1883-1897. DOI:10.1002/2014WR016862

Church, M., & Rood, K. (1983). *Catalogue of Alluvial River Channel Regime Data* (Vol. 99). University of British Columbia.

Cobban, W. A., McKinney, K. C., Obradovich, J. D., & Walasczyk, I. (2006). A USGS zonal table for the Upper Cretaceous Middle Cenomanian–Maastrichtian of the Western Interior of the United States based on Ammonites, Inoceramids, and radiometric ages: U.S. Geological Survey, Open-File Report 2006-1250. 1-46.

Cohen, S., Kettner, A. J., Syvitski, J. P. M., & Fekete, B. M. (2013). WBMsed, a distributed global-scale riverine sediment flux model: Model description and validation. *Computers & Geosciences*, *53*(Supplement C), 80-93. DOI:10.1016/j.cageo.2011.08.011

Colombera, L., Arévalo, O. J., & Mountney, N. P. (2017). Fluvial-system response to climate change: The Paleocene-Eocene Tremp Group, Pyrenees, Spain. *Global and Planetary Change*, *157*, 1-17. DOI:10.1016/j.gloplacha.2017.08.011

Constenius, K., Esser, R., & Layer, P. (2003). Extensional collapse of the Charleston-Nebo salient and its relationship to space-time variations in Cordilleran orogenic belt tectonism and continental stratigraphy.

Cenozoic systems of the Rocky Mountain region, Raynolds, R.G. and Flores, R. M., eds.,Rocky Mountain Section, Society of Economic Paleontologists and Mineralogists, 303-353.

Cotter, E. (1971). Paleoflow characteristics of a late Cretaceous river in Utah from analysis of sedimentary structures in the Ferron sandstone. *Journal of Sedimentary Research 41*, 129–138. DOI:10.1306/74D72202-2B21-11D7-8648000102C1865D

Cotter, E. (1975a). Deltaic deposits in the Upper Cretaceous Ferron Sandstone, Utah. In M. L. Broussard (Ed.), *Deltas: Models for Exploration* (pp. 471-484). Houston Geological Society.

Cotter, E. (1975b). Late Cretaceous sedimentation in a low-energy coastal zone; the Ferron Sandstone of Utah. *Journal of Sedimentary Research*, *45*(3), 669-685. DOI:10.1306/212F6E0B-2B24-11D7-8648000102C1865D

Cotter, E. (1976). The role of deltas in the evolution of the Ferron Sandstone and its coals. *Brigham Young University Geology Studies*, *22*, 15-41.

Cox, P. (2001). Description of the "TRIFFID" dynamic global vegetation model. *Hadley Centre technical note*, *24*, 1-16.

Cox, P. M., Betts, R. A., Bunton, C. B., Essery, R. L. H., Rowntree, P. R., & Smith, J. (1999). The impact of new land surface physics on the GCM simulation of climate and climate sensitivity. *Climate Dynamics*, *15*(3), 183-203. DOI:10.1007/s003820050276

Craggs, H. J., Valdes, P. J., & Widdowson, M. (2012). Climate model predictions for the latest Cretaceous: An evaluation using climatically sensitive sediments as proxy indicators. *Palaeogeography, Palaeoclimatology, Palaeoecology*, *315-316*(Supplement C), 12-23. DOI:10.1016/j.palaeo.2011.11.004

Crosato, A., & Mosselman, E. (2009). Simple physics-based predictor for the number of river bars and the transition between meandering and braiding. *Water Resources Research*, *45*(3). DOI:10.1029/2008WR007242

Cross, T. A. (1986). Tectonic controls of foreland basin subsidence and Laramide style deformation, western United States. In P. A. Allen & P. Homewood (Eds.), *Foreland Basins* (Vol. 8, pp. 15-39). International Association of Sedimentologists Special Publication.

Crowley, T. J., Hyde, W. T., & Short, D. A. (1989). Seasonal cycle variations on the supercontinent of Pangaea. *Geology*, *17*(5), 457-460. DOI:10.1130/0091-7613(1989)017<0457:SCVOTS>2.3.CO;2

Crowley, T. J., Mengel, J. G., & Short, D. A. (1987). Gondwanaland's seasonal cycle. *Nature*, *329*, 803-807. DOI:10.1038/329803a0

Czuba, J. A., & Foufoula-Georgiou, E. (2014). A network-based framework for identifying potential synchronizations and amplifications of sediment delivery in river basins [DOI:10.1002/2013WR014227]. *Water Resources Research*, *50*(5), 3826-3851. DOI:10.1002/2013WR014227

D'Arcy, M., & Whittaker, A. C. (2014). Geomorphic constraints on landscape sensitivity to climate in tectonically active areas. *Geomorphology*, *204*, 366-381. DOI:10.1016/j.geomorph.2013.08.019

D'Arcy, M., Whittaker, A. C., & Roda-Boluda, D. C. (2017). Measuring alluvial fan sensitivity to past climate changes using a self-similarity approach to grain-size fining, Death Valley, California. *Sedimentology*, *64*(2), 388-424. DOI:10.1111/sed.12308

Dade, W. B., & Friend, P. F. (1998). Grain size, sediment transport regime, and channel slope in alluvial rivers. *The Journal of Geology*, *106*(6), 661-676. DOI:10.1086/516052

Davies, N. S., & Gibling, M. R. (2010). Paleozoic vegetation and the Siluro-Devonian rise of fluvial lateral accretion sets. *Geology*, *38*(1), 51-54. DOI:10.1130/G30443.1

Davies, N. S., & Gibling, M. R. (2011). Evolution of fixed-channel alluvial plains in response to Carboniferous vegetation. *Nature Geoscience*, *4*(9), 629-633. DOI:10.1038/ngeo1237

Davis, J. M., Balme, M., Grindrod, P. M., Williams, R. M. E., & Gupta, S. (2016). Extensive Noachian fluvial systems in Arabia Terra: Implications for early Martian climate. *Geology*, 44(10), 847-850. DOI:10.1130/G38247.1

DeCelles, P. G. (1994). Late Cretaceous–Paleocene synorogenic sedimentation and kinematic history of the Sevier thrust belt, northeast Utah and southwest Wyoming. *GSA Bulletin*, *106*, 32-56. DOI:10.1130/0016-7606(1994)106<0032:LCPSSA>2.3.CO;2

DeCelles, P. G. (2004). Late Jurassic to Eocene evolution of the Cordilleran thrust belt and foreland basin system, western U.S.A. *American Journal of Science*, *304*. DOI:10.2475/ajs.304.2.105

DeCelles, P. G., & Coogan, J. C. (2006). Regional structure and kinematic history of the Sevier fold-and-thrust belt, central Utah. *GSA Bulletin*, *118*(7/8), 841-864. DOI:10.1130/B25759.1

DeConto, R. M., Hay, W. W., Thompson, S. L., & Bergengren, J. (1999). Late Cretaceous climate and vegetation interactions: Cold continental interior paradox. In E. Barrera & C. C. Johnson (Eds.), *Evolution of the Cretaceous Ocean-Climate System* (Vol. 332, pp. 0). Geological Society of America. DOI:10.1130/0-8137-2332-9.391

Dee, D. P., Uppala, S. M., Simmons, A. J., Berrisford, P., Poli, P., Kobayashi, S., Andrae, U., Balmaseda, M. A., Balsamo, G., Bauer, P., Bechtold, P., Beljaars, A. C. M., van de Berg, L., Bidlot, J., Bormann, N., Delsol, C., Dragani, R., Fuentes, M., Geer, A. J., . . . Vitart, F. (2011). The ERA-Interim reanalysis: configuration and performance of the data assimilation system. *Quarterly Journal of the Royal Meteorological Society,* 137(656), 553-597. DOI:10.1002/qj.828

DiBiase, R. A., & Whipple, K. X. (2011). The influence of erosion thresholds and runoff variability on the relationships among topography, climate, and erosion rate. *Journal of Geophysical Research: Earth Surface*, *116*(F4). DOI:10.1029/2011JF002095

DiBiase, R. A., Whipple, K. X., Heimsath, A. M., & Ouimet, W. B. (2010). Landscape form and millennial erosion rates in the San Gabriel Mountains, CA. *Earth and Planetary Science Letters*, *289*(1), 134-144. DOI:10.1016/j.epsl.2009.10.036

Duller, R. A., Armitage, J. J., Manners, H. R., Grimes, S., & Jones, T. D. (2019). Delayed sedimentary response to abrupt climate change at the Paleocene-Eocene boundary, northern Spain. *Geology*, *47*(2), 159-162. DOI:10.1130/G45631.1

Duller, R. A., Whittaker, A. C., Fedele, J. J., Whitchurch, A. L., Springett, J., Smithells, R., Fordyce, S., & Allen, P. A. (2010). From grain size to tectonics. *Journal of Geophysical Research: Earth Surface*, *115*(F3), F03022. DOI:10.1029/2009JF001495

Dunne, K. B. J., & Jerolmack, D. J. (2020). What sets river width? *Science Advances*, *6*(41), eabc1505. DOI:10.1126/sciadv.abc1505

Dürr, H. H., Meybeck, M., Hartmann, J., Laruelle, G. G., & Roubeix, V. (2011). Global spatial distribution of natural riverine silica inputs to the coastal zone. *Biogeosciences*, *8*(3), 597-620. DOI:10.5194/bg-8-597-2011

Eaton, B., Millar, R., & Davidson, S. (2010). Channel Patterns: Braided, Anabranching, and Single-Thread. *Geomorphology*, *120*, 353-364. DOI:10.1016/j.geomorph.2010.04.010

Edgar, L. A., Gupta, S., Rubin, D. M., Lewis, K. W., Kocurek, G. A., Anderson, R. B., Bell Iii, J. F., Dromart, G., Edgett, K. S., Grotzinger, J. P., Hardgrove, C., Kah, L. C., Leveille, R., Malin, M. C., Mangold, N., Milliken, R. E., Minitti, M., Palucis, M., Rice, M., . . . Williams, A. J. (2018). Shaler: in situ analysis of a fluvial sedimentary deposit on Mars. *Sedimentology*, 65(1), 96-122. doi:10.1111/sed.12370

Eide, C. H., Müller, R., & Helland-Hansen, W. (2018). Using climate to relate water discharge and area in modern and ancient catchments. *Sedimentology*, *65*(4), 1378-1389. DOI:10.1111/sed.12426

Einstein, H. A. (1950). The Bed-Load Function for Sediment Transportation in Open Channel Flows. *Technical Bulletin 1026, United States Department of Agriculture, Economic Research Service* DOI:10.22004/ag.econ.156389

Engelund, F., & Fredsøe, J. (1976). A Sediment Transport Model for Straight Alluvial Channels. *Hydrology Research*, *7*(5), 293-306. DOI:10.2166/nh.1976.0019

Engelund, F., & Hansen, E. (1967). *A Monograph on Sediment Transport in Alluvial Streams*. Technisk Vorlag.

Eo, S., Hong, S. H., Song, Y. K., Han, G. M., & Shim, W. J. (2019). Spatiotemporal distribution and annual load of microplastics in the Nakdong River, South Korea. *Water Research*, 160, 228-237. DOI:10.1016/j.watres.2019.05.053

Esposito, C. R., Di Leonardo, D., Harlan, M., & Straub, K. M. (2018). Sediment storage partitioning in alluvial stratigraphy: The influence of discharge variability. *Journal of Sedimentary Research*, 88(6), 717-726. DOI:10.2110/jsr.2018.36

Farnsworth, A., Lunt, D. J., O'Brien, C., Foster, G. L., Inglis, G. N., Markwick, P., Pancost, R. D., & Robinson, S. A. (2019a). Climate sensitivity on geological timescales controlled by non-linear feedbacks and ocean circulation. *Geophysical Research Letters*, *0*(ja). DOI:10.1029/2019GL083574

Farnsworth, A., Lunt, D. J., Robinson, S. A., Valdes, P. J., Roberts, W. H. G., Clift, P. D., Markwick, P., Su, T., Wrobel, N., Bragg, F., Kelland, S.-J., & Pancost, R. D. (2019b). Past East Asian monsoon evolution controlled by paleogeography, not CO_2. *Science Advances*, *5*(10), eaax1697. DOI:10.1126/sciadv.aax1697

Fedele, J. J., & Paola, C. (2007). Similarity solutions for fluvial sediment fining by selective deposition. *Journal of Geophysical Research: Earth Surface*, *112*(F2), F02038. DOI:10.1029/2005JF000409

Ferguson, R. I., & Church, M. (2004). A simple universal equation for grain settling velocity. *Journal of Sedimentary Research*, *74*(6), 933-937. DOI:10.1306/051204740933

Fernandes, V. M., Roberts, G. G., White, N., & Whittaker, A. C. (2019). Continental-Scale Landscape Evolution: A History of North American Topography. *Journal of Geophysical Research: Earth Surface*, *124*(11), 2689-2722. DOI:10.1029/2018JF004979

Fielding, C. R., Alexander, J., & Allen, J. P. (2018). The role of discharge variability in the formation and preservation of alluvial sediment bodies. *Sedimentary Geology*, *365*, 1-20. DOI:10.1016/j.sedgeo.2017.12.022

Fielding, C. R., Allen, J. P., Alexander, J., & Gibling, M. R. (2009). Facies model for fluvial systems in the seasonal tropics and subtropics. *Geology*, 37(7), 623-626. DOI:10.1130/G25727A.1

Finzel, E. S. (2014). Detrital zircons from Cretaceous midcontinent strata reveal an Appalachian Mountains–Cordilleran foreland basin connection. *Lithosphere*, *6*(5), 378-382. DOI:10.1130/L400.1

Flint, J. J. (1974). Stream gradient as a function of order, magnitude, and discharge. *Water Resources Research*, *10*(5), 969-973. DOI:10.1029/WR010i005p00969

Flood, Y. S., & Hampson, G. J. (2014). Facies and architectural analysis to interpret avulsion style and variability: Upper Cretaceous Blackhawk Formation, Wasatch Plateau, central Utah, U.S.A. *Journal of Sedimentary Research*, *84*(9), 743-762. DOI:10.2110/jsr.2014.59

Flood, Y. S., & Hampson, G. J. (2015). Quantitative analysis of the dimensions and distribution of channelized fluvial sandbodies within a large outcrop dataset: Upper Cretaceous Blackhawk Formation, Wasatch Plateau, central Utah, U.S.A. *Journal of Sedimentary Research*, *85*(4), 315-336. DOI:10.2110/jsr.2015.25

Foreman, B. Z. (2014). Climate-driven generation of a fluvial sheet sand body at the Paleocene–Eocene boundary in northwest Wyoming (USA). *Basin Research*, *26*, 225-241. DOI:10.1111/bre.12027

Foreman, B. Z., Heller, P. L., & Clementz, M. T. (2012). Fluvial response to abrupt global warming at the Palaeocene/Eocene boundary. *Nature*, *491*, 92-95. DOI:10.1038/nature11513

Foreman, B. Z., Roberts, E. M., Tapanila, L., Ratigan, D., & Sullivan, P. (2015). Stable isotopic insights into paleoclimatic conditions and alluvial depositional processes in the Kaiparowits Formation (Campanian, south-central Utah, U.S.A.). *Cretaceous Research*, *56*, 180-192. DOI:10.1016/j.cretres.2015.05.001

Foster, G. L., Royer, D. L., & Lunt, D. J. (2017). Future climate forcing potentially without precedent in the last 420 million years [Article]. *Nature Communications*, *8*, 14845. DOI:10.1038/ncomms14845

Fouch, T. D., Lawton, T. F., Nichols, D. J., Cashion, W. B., & Cobban, W. A. (1983). Patterns and timing of synorogenic sedimentation in Upper Cretaceous rocks of central and northeast Utah. In M. W. Reynolds & E. D. Dolly (Eds.), *Mesozoic Paleogeography of West-Central United States* (pp. 305-336). SEPM Rocky Mountain Section.

Frakes, L. A., & Francis, J. E. (1988). A guide to Phanerozoic cold polar climates from high-latitude ice-rafting in the Cretaceous. *Nature*, 333(6173), 547-549. DOI:10.1038/333547a0

Francis, J. E., & Poole, I. (2002). Cretaceous and early Tertiary climates of Antarctica: evidence from fossil wood. *Palaeogeography, Palaeoclimatology, Palaeoecology*, *182*, 47-64. DOI:10.1016/S0031-0182(01)00452-7

Fredsøe, J. (1978). Meandering and braiding of rivers. *Journal of Fluid Mechanics*, 84(4), 609-624. doi:10.1017/S0022112078000373

Fricke, H. C., Foreman, B. Z., & Sewall, J. O. (2010). Integrated climate model-oxygen isotope evidence for a North American monsoon during the Late Cretaceous. *Earth and Planetary Science Letters*, *289*(1-2), 11-21. DOI:10.1016/j.epsl.2009.10.018

Gall, R. D., Birgenheier, L. P., & Berg, M. D. V. (2017). Highly seasonal and perennial fluvial facies: Implications for climatic control on the Douglas Creek and Parachute Creek members, Green River Formation, southeastern Uinta Basin, Utah, U.S.A. *Journal of Sedimentary Research*, *87*(9), 1019-1047. DOI:10.2110/jsr.2017.54

Galloway, W. E., Whiteaker, T. L., & Ganey-Curry, P. (2011). History of Cenozoic North American drainage basin evolution, sediment yield, and accumulation in the Gulf of Mexico basin. *Geosphere*, *7*(4), 938-973. DOI:10.1130/ges00647.1

Ganti, V., Hajek, E. A., Leary, K., Straub, K. M., & Paola, C. (2020). Morphodynamic hierarchy and the fabric of the sedimentary record. *Geophysical Research Letters*, *47*(14), e2020GL087921. DOI:10.1029/2020GL087921

Ganti, V., Lamb, M. P., & Chadwick, A. J. (2019). Autogenic erosional surfaces in fluvio-deltaic stratigraphy from floods, avulsions, and backwater hydrodynamics. *Journal of Sedimentary Research*, *89*(8), 815-832. DOI:10.2110/jsr.2019.40

Ganti, V., Lamb, M. P., & McElroy, B. (2014). Quantitative bounds on morphodynamics and implications for reading the sedimentary record. *Nature Communications*, *5*(1), 3298. DOI:10.1038/ncomms4298

Ganti, V., Paola, C., & Foufoula-Georgiou, E. (2013). Kinematic controls on the geometry of the preserved cross sets. *Journal of Geophysical Research: Earth Surface*, *118*(3), 1296-1307. DOI:10.1002/jgrf.20094

Ganti, V., Whittaker, A., Lamb, M. P., & Fischer, W. W. (2019). Low-gradient, single-threaded rivers prior to greening of the continents. *Proceedings of the National Academy of Sciences*, *116*(4), 11652-11657. DOI:10.1073/pnas.1901642116

García, M., & Parker, G. (1991). Entrainment of Bed Sediment Into Suspension. *Journal of Hydraulic Engineering-asce - J HYDRAUL ENG-ASCE*, *117*. DOI:10.1061/(ASCE)0733-9429(1991)117:4(414)

Gardner, M. H. (1995). Tectonic and Eustatic Controls on the Stratal Architecture of Mid-Cretaceous Stratigraphic Sequences, Central Western Interior Foreland Basin of North America. In S. L. Dorobek & G. M. Ross (Eds.), *Stratigraphic Evolution of Foreland Basins* (Vol. 52, pp. 0). SEPM Society for Sedimentary Geology. DOI:10.2110/pec.95.52.0243

Gardner, M. H., Cross, T. A., & Levorsen, M. (2004). Stacking Patterns, Sediment Volume Partitioning, and Facies Differentiation in Shallow-Marine and Coastal-Plain Strata of the Cretaceous Ferron Sandstone, Utah. In T. C. Chidsey, Jr., R. D. Adams, & T. H. Morris (Eds.), *Regional to Wellbore Analog for Fluvial-Deltaic Reservoir Modeling: The Ferron Sandstone of Utah* (Vol. 50, pp. 0). American Association of Petroleum Geologists. DOI:10.1306/St50983

Garrison Jr, J. R. & van den Bergh, T. C. V. (2004). High-Resolution Depositional Sequence Stratigraphy of the Upper Ferron Sandstone Last Chance Delta: An Application of Coal-Zone Stratigraphy. In T. C. Chidsey, Jr., R. D. Adams, & T. H. Morris (Eds.), *Regional to Wellbore Analog for Fluvial-Deltaic Reservoir Modeling: The Ferron Sandstone of Utah* (Vol. 50). American Association of Petroleum Geologists. DOI:10.1306/St50983

Garrison Jr, J. R., van den Bergh, T. C. V., Barker, C. E., & Tabet, D. E. (1997). Depositional sequence stratigraphy and architecture of the Cretaceous Ferron Sandstone: Implications for coal and coalbed methane resources - a field excursion. In P. K. Link & B. J. Kowallis (Eds.), *Mesozoic to Recent geology of Utah, Brigham Young University Geology Studies* (Vol. 42, pp. 155-202). http://pubs.er.usgs.gov/publication/70019477

Garvin, M. G. (2008). Late quaternary geochronologic, stratigraphic, and sedimentologic framework of the Trinity River incised valley: east Texas coast. *LSU Master's Theses*, 1122.

Gaurav, K., Métivier, F., Devauchelle, O., Sinha, R., Chauvet, H., Houssais, M., & Bouquerel, H. (2015). Morphology of the Kosi megafan channels. *Earth Surface Dynamics*, 3(3), 321-331. doi:10.5194/esurf-3-321-2015

Gaurav, K., Tandon, S. K., Devauchelle, O., Sinha, R., & Métivier, F. (2017). A single width–discharge regime relationship for individual threads of braided and meandering rivers from the Himalayan Foreland. *Geomorphology*, 295, 126-133. doi:10.1016/j.geomorph.2017.07.004

Ghinassi, M., & Ielpi, A. (2015). Stratal Architecture and Morphodynamics of Downstream-Migrating Fluvial Point Bars (Jurassic Scalby Formation, U.K.). *Journal of Sedimentary Research*, *85*(9), 1123-1137. DOI:10.2110/jsr.2015.74

Ghinassi, M., Ielpi, A., Aldinucci, M., & Fustic, M. (2016). Downstream-migrating fluvial point bars in the rock record. *Sedimentary Geology*, *334*, 66-96. DOI:DOI:10.1016/j.sedgeo.2016.01.005

Ghinassi, M., Ielpi, A., Ventra, D., Martini, I., Finotello, A., & Bellizia, E. (2021). Distinguishing mid-channel and bank-attached fluvial bars by flow divergence: Implications for the interpretation of stratigraphic records. *Sedimentology*, *n/a*(n/a). DOI:10.1111/sed.12873

Ghinassi, M., Moody, J., & Martin, D. (2018). Influence of extreme and annual floods on point-bar sedimentation: Inferences from Powder River, Montana, USA. *GSA Bulletin*, 131(1-2), 71-83. doi:10.1130/B31990.1

Ghinassi, M., Nemec, W., Aldinucci, M., Nehyba, S., Özaksoy, V., & Fidolini, F. (2014). Plan-form evolution of ancient meandering rivers reconstructed from longitudinal outcrop sections. *Sedimentology*, *61*(4), 952-977. DOI:10.1111/sed.12081

Gibbard, P. L. (1988). The history of the great northwest European rivers during the past three million years. *Philosophical Transactions of the Royal Society B: Biological Sciences*, *318*(1191), 559-602. DOI:10.1098/rstb.1988.0024

Gibling, M. R., & Davies, N. S. (2012). Palaeozoic landscapes shaped by plant evolution. *Nature Geoscience*, 5(2), 99-105. doi:10.1038/ngeo1376

Gibling, M. R., Davies, N. S., Falcon-Lang, H. J., Bashforth, A. R., DiMichele, W. A., Rygel, M. C., & Ielpi, A. (2014). Palaeozoic co-evolution of rivers and vegetation: a synthesis of current knowledge. *Proceedings of the Geologists' Association*, 125(5), 524-533. doi:10.1016/j.pgeola.2013.12.003

Gilbert, G.K.. (1914) The transportation of debris by running water, based on experiments made with assistance of E.C. Murphy. *U.S. Geological Survey, Professional Paper*, 86, 263 p.

Gill, J. R., & Hail Jr, W. J. (1975). Stratigraphic sections across Upper Cretaceous Mancos Shale-Mesaverde Group boundary, eastern Utah and western Colorado [Report]. *U.S. Geological Survey Publication*, *68*. DOI:10.3133/oc68

Gill, M. A. (1971). Height of sand dunes in open channel flows. *Journal of the Hydraulics Division*, *97*(12), 2067-2074.

Goddéris, Y., Donnadieu, Y., Carretier, S., Aretz, M., Dera, G., Macouin, M., & Regard, V. (2017). Onset and ending of the late Palaeozoic ice age triggered by tectonically paced rock weathering [Article]. *Nature Geoscience*, *10*, 382. DOI:10.1038/ngeo2931

Goñi, M. A., Hatten, J. A., Wheatcroft, R. A., & Borgeld, J. C. (2013). Particulate organic matter export by two contrasting small mountainous rivers from the Pacific Northwest, U.S.A. *Journal of Geophysical Research: Biogeosciences*, 118(1), 112-134. DOI:10.1002/jgrg.20024

Gordon, C., Cooper, C., Senior, C. A., Banks, H., Gregory, J. M., Johns, T. C., Mitchell, J. F. B., & Wood, R. A. (2000). The simulation of SST, sea ice extents and ocean heat transports in a version of the Hadley Centre coupled model without flux adjustments. *Climate Dynamics*, *16*(2), 147-168. DOI:10.1007/s003820050010

Gough, D. O. (1981). Solar interior structure and luminosity variations. *Solar Physics*, *74*(1), 21-34. DOI:10.1007/BF00151270

Grant, G. E., Swanson, F. J., & Wolman, M. G. (1990). Pattern and origin of stepped-bed morphology in high-gradient streams, Western Cascades, Oregon. *GSA Bulletin*, *102*(3), 340-352. DOI:10.1130/0016-7606(1990)102<0340:PAOOSB>2.3.CO;2

Greenberg, E., Ganti, V., & Hajek, E. (2021). Quantifying bankfull flow width using preserved bar clinoforms from fluvial strata. *Geology*. DOI:10.1130/G48729.1

Greenwood, D. R., & Wing, S. L. (1995). Eocene continental climates and latitudinal temperature gradients. *Geology*, 23(11), 1044-1048. DOI:10.1130/0091-7613(1995)023<1044:ECCALT>2.3.CO;2

Hack, J. T. (1957). Studies of longitudinal stream profiles in Virigina and Maryland. *U.S. Geological Survey Professional Paper*, *294-B*, 45-97.

Hack, J. T. (1973). Stream profile analysis and stream gradient index. *US Geological Survey Journal of Research*, *1*, 421–429.

Hajek, E. A., & Edmonds, D. A. (2014). Is river avulsion style controlled by floodplain morphodynamics? *Geology*, 42(3), 199-202. DOI:10.1130/G35045.1

Hajek, E. A., & Heller, P. L. (2012). Flow-depth scaling in alluvial architecture and nonmarine sequence stratigraphy: Example from the Castlegate Sandstone, central Utah, U.S.A. *Journal of Sedimentary Research*, *82*(2), 121-130. DOI:10.2110/jsr.2012.8

Hajek, E. A., Heller, P. L., & Sheets, B. A. (2010). Significance of channel-belt clustering in alluvial basins. *Geology*, *38*(6), 535-538. DOI:10.1130/G30783.1

Hajek, E. A., & Straub, K. M. (2017). Autogenic sedimentation in clastic stratigraphy. *Annual Review of Earth and Planetary Sciences*, 45(1), 681-709. doi:10.1146/annurev-earth-063016-015935

Hajek, E. A., & Wolinsky, M. A. (2012). Simplified process modeling of river avulsion and alluvial architecture: Connecting models and field data. *Sedimentary Geology*, *257-260*, 1-30. DOI:10.1016/j.sedgeo.2011.09.005

Hallam, A. (1985). A review of Mesozoic climates. *Journal of the Geological Society*, *142*(3), 433-445. DOI:10.1144/gsjgs.142.3.0433

Hallet, B., Hunter, L., & Bogen, J. (1996). Rates of erosion and sediment evacuation by glaciers: A review of field data and their implications. *Global and Planetary Change*, *12*(1), 213-235. DOI:10.1016/0921-8181(95)00021-6

Hampson, G. J. (2010). Sediment dispersal and quantitative stratigraphic architecture across an ancient shelf. *Sedimentology*, *57*(1), 96-141. DOI:10.1111/j.1365-3091.2009.01093.x

Hampson, G. J. (2016). Towards a sequence stratigraphic solution set for autogenic processes and allogenic controls: Upper Cretaceous strata, Book Cliffs, Utah, USA [10.1144/jgs2015-136]. *Journal of the Geological Society*. http://jgs.lyellcollection.org/content/early/2016/03/10/jgs2015-136.abstract

Hampson, G. J., Duller, R. A., Petter, A. L., Robinson, R. A. J., & Allen, P. A. (2014). Mass-balance constraints on stratigraphic interpretation of linked alluvial-coastal-shelfal deposits from source to sink: example from Cretaceous Western Interior Basin, Utah and Colorado, U.S.A. *Journal of Sedimentary Research*, *84*(11), 935-960. DOI:10.2110/jsr.2014.78

Hampson, G. J., Jewell, T. O., Irfan, N., Gani, M. R., & Bracken, B. (2013). Modest change in fluvial style with varying accommodation in regressive alluvial-to-coastal-plain wedge: Upper Cretaceous Blackhawk Formation, Wasatch Plateau, central Utah, U.S.A. *Journal of Sedimentary Research*, *83*(2), 145-169. DOI:10.2110/jsr.2013.8

Hampson, G. J., Royhan Gani, M., Sahoo, H., Rittersbacher, A., Irfan, N., Ranson, A., Jewell, T. O., Gani, N. D. S., Howell, J. A., Buckley, S. J., & Bracken, B. (2012). Controls on large-scale patterns of fluvial sandbody distribution in alluvial to coastal plain strata: Upper Cretaceous Blackhawk Formation, Wasatch Plateau, Central Utah, USA. *Sedimentology*, *59*(7), 2226-2258. DOI:10.1111/j.1365-3091.2012.01342.x

Hansford, M. R., & Plink-Björklund, P. (2020). River discharge variability as the link between climate and fluvial fan formation. *Geology*. DOI:10.1130/G47471.1

Haq, B. U., Hardenbol, J. A. N., & Vail, P. R. (1987). Chronology of fluctuating sea levels since the Triassic [10.1126/science.235.4793.1156]. *Science*, *235*(4793), 1156-1167. DOI:10.1126/science.235.4793.1156

Hay, W., L. Eicher, D., & Diner, R. (1993). Physical oceanography and water masses of the Cretaceous Western Interior Seaway. In W. E. G. Caldwell & E. G. Kauffman (Eds.), *Evolution of the Western Interior Basin* (pp. 297-318). Geological Association of Canada.

Hay, W. W. (2017). Toward understanding Cretaceous climate — an updated review. *Science China Earth Sciences*, *60*(1), 5-19. DOI:10.1007/s11430-016-0095-9

Hay, W. W., DeConto, R. M., Wold, C. N., Wilson, K. M., Voigt, S., Schulz, M., Wold, A. R., Dullo, W.-C., Ronov, A. B., Balukhovsky, A. N., & Söding, E. (1999). Alternative global Cretaceous paleogeography. In E. Barrera & C. C. Johnson (Eds.), *Evolution of the Cretaceous Ocean-Climate System*. Geological Society of America. DOI:10.1130/0-8137-2332-9.1

Hay, W. W., & Floegel, S. (2012). New thoughts about the Cretaceous climate and oceans. *Earth-Science Reviews*, *115*(4), 262-272. DOI:10.1016/j.earscirev.2012.09.008

Hayden, A. T., Lamb, M. P., Fischer, W. W., Ewing, R. C., McElroy, B. J., & Williams, R. M. E. (2019). Formation of sinuous ridges by inversion of river-channel belts in Utah, USA, with implications for Mars. *Icarus*, *332*, 92-110. DOI:10.1016/j.icarus.2019.04.019

Hayden, A. T., Lamb, M. P., & McElroy, B. J. (2021). Constraining the timespan of fluvial activity from the intermittency of sediment transport on Earth and Mars [DOI:10.1029/2021GL092598]. *Geophysical Research Letters*, *n/a*(n/a), e2021GL092598. DOI:10.1029/2021GL092598

Hayden, A. T., Lamb, M. P., Myrow, P. M., Mohrig, D., Williams, R. M. E., Cuevas Martínez, J. L., Cardenas, B. T., Findlay, C. P., Ewing, R. C., & McElroy, B. J. (2021). The Oligocene-Miocene Guadalope-Matarranya Fan, Spain, as an Analog for Long-Lived, Ridge-Bearing Megafans on Mars [DOI:10.1029/2021JE006993]. *Journal of Geophysical Research: Planets*, *126*(12), e2021JE006993. DOI:DOI:10.1029/2021JE006993

Helland-Hansen, W., Sømme, T., Martinsen, O. J., Lunt, I., & Thurmond, J. (2016). Deciphering Earth's natural hourglasses: perspectives on source-to-sink analysis. *Journal of Sedimentary Research*, *86*, 1008-1033. DOI:10.2110/jsr.2016.56

Herbert, C. M., Alexander, J., Amos, K. J., & Fielding, C. R. (2020). Unit bar architecture in a highly-variable fluvial discharge regime: Examples from the Burdekin River, Australia. *Sedimentology*, *67*(1), 576-605. DOI:10.1111/sed.12655

Hettinger, R. D., & Kirschbaum, M. A. (2002). Stratigraphy of the Upper Cretaceous Mancos Shale (upper part) and Mesaverde Group in the southern part of the Uinta and Piceance basins, Utah and Colorado [Report]. *USGS Geologic Investigation Series: IMAP*, *2764*, 21. DOI:10.3133/i2764

Hidy, A. J., Gosse, J. C., Blum, M. D., & Gibling, M. R. (2014). Glacial–interglacial variation in denudation rates from interior Texas, USA, established with cosmogenic nuclides. *Earth and Planetary Science Letters*, *390*, 209-221. DOI:10.1016/j.epsl.2014.01.011

Hijmans, R. J., Cameron, S. E., Parra, J. L., Jones, P. G., & Jarvis, A. (2005). Very high resolution interpolated climate surfaces for global land areas. *International Journal of Climatology*, *25*(15), 1965-1978. DOI:10.1002/joc.1276

Hilton, R. G., Galy, A., Hovius, N., Chen, M.-C., Horng, M.-J., & Chen, H. (2008). Tropical-cyclone-driven erosion of the terrestrial biosphere from mountains. *Nature Geoscience*, 1(11), 759-762. DOI:10.1038/ngeo333

Hinderer, M. (2012). From gullies to mountain belts: A review of sediment budgets at various scales. *Sedimentary Geology*, 280, 21-59. DOI:10.1016/j.sedgeo.2012.03.009

Hitchcock, J. N. (2020). Storm events as key moments of microplastic contamination in aquatic ecosystems. *Science of The Total Environment*, 734, 139436. DOI:10.1016/j.scitotenv.2020.139436

Holbrook, J., & Wanas, H. (2014). A fulcrum approach to assessing source-to-sink mass balance using channel paleohydrologic paramaters derivable from common fluvial data sets with an example from the Cretaceous of Egypt. *Journal of Sedimentary Research*, *84*(5), 349-372. DOI:10.2110/jsr.2014.29

Horton, B., Parra, M., Saylor, J., Nie, J., Mora, A., Torres, V., Stockli, D., & Strecker, M. (2010). Resolving uplift of the Northern Andes using detrital zircon age signatures. *GSA Today*, *20*, 4-9. DOI:10.1130/GSATG76A.1

Horton, B., Saylor, J., Nie, J., Mora, A., Parra, M., Reyes-Harker, A., & Stockli, D. (2010). Linking sedimentation in the northern Andes to basement configuration, Mesozoic extension, and Cenozoic shortening: Evidence from detrital zircon U-Pb ages, Eastern Cordillera, Colombia. *GSA Bulletin*, *122*, 1423-1442. DOI:10.1130/B30118.1

Horton, B. K., Constenius, K. N., & DeCelles, P. G. (2004). Tectonic control on coarse-grained foreland-basin sequences: An example from the Cordilleran foreland basin, Utah. *Geology*, *32*(7), 637-640. DOI:10.1130/G20407.1

Hovius, N. (1996). Regular spacing of drainage outlets from linear mountain belts. *Basin Research*, *8*(1), 29-44. DOI:10.1111/j.1365-2117.1996.tb00113.x

Howard, A. D. (1965) Geomorphological systems: equilibrium and dynamics. *American Journal of Science*, 263, 302–312

Howell, J., Vassel, Å., & Aune, T. (2008). Modelling of dipping clinoform barriers within deltaic outcrop analogues from the Cretaceous Western Interior Basin, USA. *Geological Society, London, Special Publications*, *309*(1), 99-121 DOI: 10.1144/SP309.8

Hunter, S. J., Haywood, A. M., Valdes, P. J., Francis, J. E., & Pound, M. J. (2013). Modelling equable climates of the Late Cretaceous: Can new boundary conditions resolve data–model discrepancies? *Palaeogeography, Palaeoclimatology, Palaeoecology*, *392*, 41-51. DOI:10.1016/j.palaeo.2013.08.009

Hunter, S. J., Valdes, P. J., Haywood, A. M., & Markwick, P. J. (2008). Modelling Maastrichtian climate: investigating the role of geography, atmospheric CO2 and vegetation. *Climate of the Past Discussions*, *4*, 981–1019. DOI:10.5194/cpd-4-981-2008

Huyghe, D., Castelltort, S., Mouthereau, F., Serra-Kiel, J., Filleaudeau, P.-Y., Emmanuel, L., Berthier, B., & Renard, M. (2012). Large scale facies change in the middle Eocene South-Pyrenean foreland basin: The role of tectonics and prelude to Cenozoic ice-ages. *Sedimentary Geology*, 253-254, 25-46. DOI:10.1016/j.sedgeo.2012.01.004

Ielpi, A. (2018). Morphodynamics of meandering streams devoid of plant life: Amargosa River, Death Valley, California. *GSA Bulletin*, *131*(5-6), 782-802. DOI:10.1130/B31960.1

Ielpi, A., Fralick, P., Ventra, D., Ghinassi, M., Lebeau, L. E., Marconato, A., Meek, R., & Rainbird, R. H. (2018). Fluvial floodplains prior to greening of the continents: Stratigraphic record, geodynamic setting, and modern analogues. *Sedimentary Geology*, *372*, 140-172. DOI:10.1016/j.sedgeo.2018.05.009

Ielpi, A., & Ghinassi, M. (2014). Planform architecture, stratigraphic signature and morphodynamics of an exhumed Jurassic meander plain (Scalby Formation, Yorkshire, UK). *Sedimentology*, *61*(7), 1923-1960. DOI:10.1111/sed.12122

Ielpi, A., Ghinassi, M., Rainbird, R. H., & Ventra, D. (2018). Planform sinuosity of Proterozoic rivers: A craton to channel-reach perspective. *International Association of Sedimentology Special Publication, 48*, 81-118. doi:10.1002/9781119424437.ch4

Ielpi, A., & Lapôtre, M. G. A. (2019a). Barren meandering streams in the modern Toiyabe Basin of Nevada, U.S.A., and their relevance to the study of the pre-vegetation rock record. *Journal of Sedimentary Research*, *89*(5), 399-415. DOI:10.2110/jsr.2019.25

Ielpi, A., & Lapôtre, M. G. A. (2019b). Biotic forcing militates against river meandering in the modern Bonneville Basin of Utah. *Sedimentology*, *66*(5), 1896-1929. DOI:10.1111/sed.12562

Ielpi, A., & Lapôtre, M. G. A. (2020). A tenfold slowdown in river meander migration driven by plant life. *Nature Geoscience*, *13*(1), 82-86. DOI:10.1038/s41561-019-0491-7

Ielpi, A., Lapôtre, M. G. A., Finotello, A., Ghinassi, M., & D'Alpaos, A. (2020). Channel mobility drives a diverse stratigraphic architecture in the dryland Mojave River (California, USA). *Earth Surface Processes and Landforms*, *45*(8), 1717-1731. DOI:10.1002/esp.4841

Ielpi, A., & Rainbird, R. H. (2016). Reappraisal of Precambrian sheet-braided rivers: Evidence for 1·9 Ga deep-channelled drainage. *Sedimentology*, *63*(6), 1550-1581. DOI:10.1111/sed.12273

IPCC. (2014). Climate Change 2014: Synthesis Report. Contribution of Working Groups I, II and III to the Fifth Assessment Report of the Intergovernmental Panel on Climate Change. [Core Writing Team, R. K. Pachauri and L. A. Meyer (eds)], 151.

Jensen, M. A., & Pedersen, G. K. (2010). Architecture of vertically stacked fluvial deposits, Atane Formation, Cretaceous, Nuussuaq, central West Greenland. *Sedimentology*, *57*, 1280-1314. DOI:10.1111/j.1365-3091.2010.01146.x

Jerolmack, D. J., & Mohrig, D. (2005). Frozen dynamics of migrating bedforms. *Geology*, *33*(1), 57-60. DOI:10.1130/G20897.1

Jerolmack, D. J., & Mohrig, D. (2007). Conditions for branching in depositional rivers. *Geology*, *35*(5), 463-466. DOI:10.1130/G23308A.1

Jerolmack, D. J., Mohrig, D., Zuber, M. T., & Byrne, S. (2004). A minimum time for the formation of Holden Northeast fan, Mars. *Geophysical Research Letters*, *31*(21). DOI:10.1029/2004GL021326

Jerolmack, D. J., & Paola, C. (2010). Shredding of environmental signals by sediment transport. *Geophysical Research Letters*, *37*(19), 1-5. DOI:10.1029/2010gl044638

Jerolmack, D. J., & Sadler, P. (2007). Transience and persistence in the depositional record of continental margins. *Journal of Geophysical Research: Earth Surface*, *112*(F3). DOI:10.1029/2006JF000555

Jinnah, Z. A., Roberts, E. M., Deino, A. L., Larsen, J. S., Link, P. K., & Fanning, C. M. (2009). New ^{40}Ar-^{39}Ar and detrital zircon U-Pb ages for the Upper Cretaceous Wahweap and Kaiparowits formations on the Kaiparowits Plateau, Utah: Implications for regional correlation, provenance, and biostratigraphy. *Cretaceous Research*, *30*(2), 287-299. DOI:10.1016/j.cretres.2008.07.012

Jones, H. L., & Hajek, E. A. (2007). Characterizing avulsion stratigraphy in ancient alluvial deposits. *Sedimentary Geology*, 202(1), 124-137. DOI:10.1016/j.sedgeo.2007.02.003

Jordan, T. E. (1981). Thrust loads and foreland basin evolution, Cretaceous, western United States. *AAPG Bulletin*, *65*(12), 2506-2520.

Julien, P. Y., & Klaassen, G. J. (1995). Sand-Dune Geometry of Large Rivers during Floods. *Journal of Hydraulic Engineering*, *121*(9), 657-663. DOI:10.1061/(ASCE)0733-9429(1995)121:9(657)

Karim, F. (1995). Bed Configuration and Hydraulic Resistance in Alluvial-Channel Flows. *Journal of Hydraulic Engineering*, *121*(1), 15-25. DOI:10.1061/(ASCE)0733-9429(1995)121:1(15)

Karim, F. (1999). Bed-Form Geometry in Sand-Bed Flows. *Journal of Hydraulic Engineering*, *125*(12), 1253-1261. DOI:10.1061/(ASCE)0733-9429(1999)125:12(1253)

Kauffman, E., Sageman, B., Kirkland, J., Elder, W., Harries, P., & Villamil, T. (1993). Molluscan biostratigraphy of the Cretaceous Western Interior Basin, North America. In (Vol. 39, pp. 397-434).

Kauffman, E. G. (1977). Geological and biological overview: Western Interior Basin In E. G. Kauffman (Ed.), *Cretaceous facies, faunas, and paleoenvironments across the Western Interior Basin* (pp. 75-99). Rocky Mountain Association of Geologists.

Kauffman, E. G., & Caldwell, W. (1993). The Western Interior Basin in space and time. In E. G. Kauffman & W. Caldwell (Eds.), *Evolution of the Western Interior Basin: Geological Association of Canada, Special Paper 39* (pp. 1-30).

Kean, J. W., & Smith, J. D. (2006). Form drag in rivers due to small-scale natural topographic features: 1. Regular sequences [DOI:10.1029/2006JF000467]. *Journal of Geophysical Research: Earth Surface*, *111*(F4). DOI:DOI:10.1029/2006JF000467

Kent, D. V., & Muttoni, G. (2013). Modulation of Late Cretaceous and Cenozoic climate by variable drawdown of atmospheric pCO_2 from weathering of basaltic provinces on continents drifting through the equatorial humid belt. *Climate of the Past*, *9*(2), 525-546. DOI:10.5194/cp-9-525-2013

Kimmerle, S., & Bhattacharya, J. P. (2018). Facies, backwater limits, and paleohydraulic analysis of rivers in a forced-regressive, compound incised valley, Cretaceous Ferron Sandstone, Utah, U.S.A. *Journal of Sedimentary Research*, *88*(2), 177-200. DOI:10.2110/jsr.2018.5

Kirby, E., & Whipple, K. (2001). Quantifying differential rock-uplift rates via stream profile analysis. *Geology*, *29*(5), 415-418. DOI:10.1130/0091-7613(2001)029<0415:QDRURV>2.0.CO;2

Kirby, E., & Whipple, K. X. (2012). Expression of active tectonics in erosional landscapes. *Journal of Structural Geology*, *44*, 54-75. DOI:10.1016/j.jsg.2012.07.009

Kirby, E., Whipple, K. X., Tang, W., & Chen, Z. (2003). Distribution of active rock uplift along the eastern margin of the Tibetan Plateau: Inferences from bedrock channel longitudinal profiles. *Journal of Geophysical Research: Solid Earth*, *108*(B4). DOI:10.1029/2001JB000861

Kitoh, A., Motoi, T., & Arakawa, O. (2010). Climate modelling study on mountain uplift and Asian monsoon evolution. *Geological Society, London, Special Publications*, *342*(1), 293. DOI:10.1144/SP342.17

Kleinhans, M. G. (2005). Flow discharge and sediment transport models for estimating a minimum timescale of hydrological activity and channel and delta formation on Mars [DOI:10.1029/2005JE002521]. *Journal of Geophysical Research: Planets*, *110*(E12). DOI:10.1029/2005JE002521

Kleinhans, M. G., Ferguson, R. I., Lane, S. N., & Hardy, R. J. (2013). Splitting rivers at their seams: bifurcations and avulsion [DOI:10.1002/esp.3268]. *Earth Surface Processes and Landforms*, *38*(1), 47-61. DOI:DOI:10.1002/esp.3268

Knighton, D. (1998). *Fluvial Forms and Processes: A New Perspective*. Arnold.

Krause, F., Deutsch, K. B., Joiner, S. D., Barclay, J., Hall, R. L., & Hills, L. V. (1994). Cretaceous Cardium Formation of the Western Canada sedimentary basin. In G. D. Mossop & I. Shetson (Eds.), *Geological Atlas of the Western Canada Sedimentary Basin. Canadian Society of Petroleum Geologists and Alberta Research Council* (pp. 485-511).

Kutzbach, J., Prell, W., & Ruddiman, W. (1993). Sensitivity of Eurasian climate to surface uplift of the Tibetan Plateau. *The Journal of Geology*, *101*(2), 177-190. DOI:10.1086/648215

Kynaston, D. (2019). *Stratigraphy, provenance, timing and control of incised valleys in the Ferron Sandstone* McMaster University]. http://hdl.handle.net/11375/25035

Lamb, M. P., Grotzinger, J. P., Southard, J. B., & Tosca, N. J. (2012). Were aqueous ripples on Mars formed by flowing brines? In J. P. Grotzinger & R. E. Milliken (Eds.), *Sedimentary Geology of Mars* (Vol. 102). SEPM Society for Sedimentary Geology. DOI:10.2110/pec.12.102.0139

Lapôtre, M. G. A., & Ielpi, A. (2020). The pace of fluvial meanders on Mars and implications for the western delta deposits of Jezero Crater. *AGU Advances*, *1*(2), e2019AV000141. DOI:10.1029/2019AV000141

Lapôtre, M. G. A., Ielpi, A., Lamb, M. P., Williams, R. M. E., & Knoll, A. H. (2019). Model for the formation of single-thread rivers in barren landscapes and implications for pre-Silurian and Martian fluvial deposits. *Journal of Geophysical Research: Earth Surface*, *124*(12), 2757-2777. DOI:10.1029/2019JF005156

Lawton, T. F. (1982). Lithofacies correlations within the Upper Cretaceous Indianola Group, central Utah. *Utah Geological Association Publication*, *10*, 199-213.

Lawton, T. F. (1983). Late Cretaceous fluvial systems and the age of foreland uplifts in central Utah. In J. D. Lowell (Ed.), *Rocky Mountain Foreland Basins and Uplifts* (pp. 181-199). Rocky Mountain Association of Geologists.

Lawton, T. F. (1986a). Compositional trends within a clastic wedge adjacent to a fold-thrust belt: Indianola Group, central Utah, USA. In P. A. Allen & P. Homewood (Eds.), *Foreland Basins* (pp. 411-423). Blackwell. DOI:10.1002/9781444303810.ch22

Lawton, T. F. (1986b). Fluvial Systems of the Upper Cretaceous Mesaverde Group and Paleocene North Horn Formation, Central Utah: A Record of Transition from Thin-Skinned to Thick-Skinned Deformation in the Foreland Region. In J. A. Peterson (Ed.), *Paleotectonics and sedimentation in the Rocky Mountain Region, United States* (Vol. 41). American Association of Petroleum Geologists. DOI:10.1306/M41456C20

Lawton, T. F., Pollock, S. L., & Robinson, R. A. J. (2003). Integrating sandstone petrology and nonmarine sequence stratigraphy: application to the Late Cretaceous fluvial systems of southwestern Utah, USA. *Journal of Sedimentary Research*, *73*, 398-406.

Leary, K. C. P., & Ganti, V. (2020). Preserved fluvial cross strata record bedform disequilibrium dynamics. *Geophysical Research Letters*, *47*(2), e2019GL085910. DOI:10.1029/2019GL085910

Leclair, S. F. (2002). Preservation of cross-strata due to the migration of subaqueous dunes: an experimental investigation. *Sedimentology*, *49*(6), 1157-1180. DOI:10.1046/j.1365-3091.2002.00482.x

Leclair, S. F. (2011). Interpreting Fluvial Hydromorphology from the Rock Record: Large-River Peak Flows Leave No Clear Signature. In S. K. Davidson, S. Leleu, & C. P. North (Eds.), *From River to Rock Record: The preservation of fluvial sediments and their subsequent interpretation* (Vol. 97, pp. 0): SEPM Society for Sedimentary Geology. doi:10.2110/sepmsp.097.113

Leclair, S. F., & Bridge, J. S. (2001). Quantitative interpretation of sedimentary structures formed by river dunes. *Journal of Sedimentary Research*, *71*(5), 713-716. DOI:1527-1404/01/071-713/$03.00

Leier, A. L., DeCelles, P. G., & Pelletier, J. D. (2005). Mountains, monsoons, and megafans. *Geology*, 33(4), 289-292. DOI:10.1130/G21228.1

Leithold, E. L., Blair, N. E., & Wegmann, K. W. (2016). Source-to-sink sedimentary systems and global carbon burial: A river runs through it. *Earth-Science Reviews*, *153*, 30-42. DOI:10.1016/j.earscirev.2015.10.011

Leopold, L. B., & Maddock Jr, T. (1953). The hydraulic geometry of stream channels and some physiographic implications [Report]. *USGS Professional Paper*, *252*, 64. DOI:10.3133/pp252

Leopold, L. B., & Wolman, M. G. (1957). River channel patterns: Braided, meandering, and straight [Report]. *USGS Professional Paper*, *282B*, 50. DOI:10.3133/pp282B

Lericolais, G., Auffret, J. P., & Bourillet, J. F. (2003). The Quaternary Channel River: seismic stratigraphy of its palaeo-valleys and deeps. *Journal of Quaternary Science*, *18*, 245-260. DOI:10.1002/jqs.759

Li, Y., Bhattacharya, J. P., Ahmed, S., & Garza, D. (2018). Re-evaluating the paleogeography of the river-dominated and wave-influenced Ferron Notom Delta, Southern Central Utah: an integration of detailed facies-architecture and paleocurrent analysis. *Journal of Sedimentary Research*, *88*(2), 214-240. DOI:10.2110/jsr.2018.9

Lin, W., & Bhattacharya, J. P. (2017). Estimation of source-to-sink mass balance by a fulcrum approach using channel paleohydrologic parameters of the Cretaceous Dunvegan Formation, Canada. *Journal of Sedimentary Research*, *87*(1), 97-116. DOI:10.2110/jsr.2017.1

Litty, C., & Schlunegger, F. (2017). Controls on pebbles' size and shape in streams of the Swiss Alps. *The Journal of Geology*, *125*(1), 101-112. DOI:10.1086/689183

Litty, C., Schlunegger, F., & Viveen, W. (2017). Possible threshold controls on sediment grain properties of Peruvian coastal river basins. *Earth Surf. Dynam.*, *5*(3), 571-583. DOI:10.5194/esurf-5-571-2017

Liu, S., & Nummedal, D. (2004). Late Cretaceous subsidence in Wyoming: Quantifying the dynamic component. *Geology*, *32*(5), 397-400. DOI:10.1130/G20318.1

Liu, S., Nummedal, D., & Gurnis, M. (2014). Dynamic versus flexural controls of Late Cretaceous Western Interior Basin, USA. *Earth and Planetary Science Letters*, *389*, 221-229. DOI:10.1016/j.epsl.2014.01.006

Liu, S., Nummedal, D., & Liu, L. (2011). Migration of dynamic subsidence across the Late Cretaceous United States Western Interior Basin in response to Farallon plate subduction. *Geology*, *39*(6), 555-558. DOI:10.1130/G31692.1

Lunt, D., Farnsworth, A., Loptson, C., Foster, G., Markwick, P., O'Brien, C., Pancost, R. D., Robinson, S. A., & Wrobel, N. (2016). Palaeogeographic controls on climate and proxy interpretation. *Climate of the Past*, *12*, 1181-1198. DOI:10.5194/cpd-11-5683-2015

Lunt, D. J., Ross, I., Hopley, P. J., & Valdes, P. J. (2007). Modelling Late Oligocene C4 grasses and climate. *Palaeogeography, Palaeoclimatology, Palaeoecology*, *251*(2), 239-253. DOI:10.1016/j.palaeo.2007.04.004

Lynds, R., & Hajek, E. (2006). Conceptual model for predicting mudstone dimensions in sandy braided-river reservoirs. *AAPG Bulletin*, *90*(8), 1273-1288. DOI:10.1306/03080605051

Lyster, S. J., Whittaker, A. C., Allison, P. A., Lunt, D. J., & Farnsworth, A. (2020). Predicting sediment discharges and erosion rates in deep time—examples from the late Cretaceous North American continent. *Basin Research*, 1-27. DOI:10.1111/bre.12442

Lyster, S. J., Whittaker, A. C., Hajek, E. A., and Ganti, V. (2022) Field evidence for disequilibrium dynamics in preserved fluvial cross-strata: A record of discharge variability or morphodynamic hierarchy? Earth and Planetary Science Letters, 579, 117355, DOI: 10.1016/j.epsl.2021.117355

Lyster, S. J., Whittaker, A. C., Hampson, G. J., Hajek, E. A., Allison, P. A., & Lathrop, B. A. (2021). Reconstructing the morphologies and hydrodynamics of ancient rivers from source to sink: Cretaceous Western Interior Basin, Utah, USA. *Sedimentology*. DOI:10.1111/sed.12877

Macdonald, F. A., Swanson-Hysell, N. L., Park, Y., Lisiecki, L., & Jagoutz, O. (2019). Arc-continent collisions in the tropics set Earth's climate state. *Science*, *364*(6436), 181. DOI:10.1126/science.aav5300

Mack, G. H., & James, W. C. (1994). Paleoclimate and the global distribution of paleosols. *The Journal of Geology*, 102(3), 360-366. DOI:10.1086/629677

Mahon, R. C., & McElroy, B. (2018). Indirect estimation of bedload flux from modern sand-bed rivers and ancient fluvial strata. *Geology*, *46*(7), 579-582. DOI:10.1130/G40161.1

Makaske, B. (2001). Anastomosing rivers: a review of their classification, origin and sedimentary products. *Earth-Science Reviews*, *53*(3), 149-196. DOI:10.1016/S0012-8252(00)00038-6

Manger, G. E. (1963). Porosity and bulk density of sedimentary rocks [Report]. *Geological Survey Bulletin*, *1144-E*.

Markwick, P. J. (2018). Palaeogeography in exploration. *Geological Magazine*, *156*, 366-407. DOI:10.1017/S0016756818000468

Markwick, P. J., & Valdes, P. J. (2004). Palaeo-digital elevation models for use as boundary conditions in coupled ocean–atmosphere GCM experiments: a Maastrichtian (late Cretaceous) example. *Palaeogeography, Palaeoclimatology, Palaeoecology*, *213*(1-2), 37-63. DOI:10.1016/j.palaeo.2004.06.015

Martin, R. L., & Jerolmack, D. J. (2013). Origin of hysteresis in bed form response to unsteady flows. *Water Resources Research*, 49(3), 1314-1333. doi:10.1002/wrcr.20093

Marzocchi, A., Lunt, D. J., Flecker, R., Bradshaw, C. D., Farnsworth, A., & Hilgen, F. J. (2015). Orbital control on late Miocene climate and the North African monsoon: insight from an ensemble of sub-precessional simulations. *Clim. Past*, *11*(10), 1271-1295. DOI:10.5194/cp-11-1271-2015

Matthews, R. K., & Poore, R. Z. (1980). Tertiary δ180 record and glacio-eustatic sea-level fluctuations. *Geology*, 8, 501-504.

McLaurin, B. T., & Steel, R. J. (2007). Architecture and origin of an amalgamated fluvial sheet sand, lower Castlegate Formation, Book Cliffs, Utah. *Sedimentary Geology*, *197*(3), 291-311. DOI:10.1016/j.sedgeo.2006.10.005

McMahon, W. J., & Davies, N. S. (2018). The shortage of geological evidence for pre-vegetation meandering rivers. *Fluvial Meanders and Their Sedimentary Products in the Rock Record*, 119-148. DOI:10.1002/9781119424437.ch5 (Wiley Online Books)

Meade, R. H. (1972). Transport and deposition of sediments in estuaries. In B. C. Nelson (Ed.), *Environmental Framework of Coastal Plain Estuaries* (Vol. Memoir 133, pp. 91-120). Geological Society of America.

Meade, R. H. (1982). Sources, sinks, and storage of river sediment in the Atlantic drainage of the United States. *The Journal of Geology*, 90, 235-252.

Metz, J. M., Grotzinger, J. P., Mohrig, D., Milliken, R., Prather, B., Pirmez, C., McEwen, A. S., & Weitz, C. M. (2009). Sublacustrine depositional fans in southwest Melas Chasma. *Journal of Geophysical Research: Planets*, *114*(E10). DOI:10.1029/2009JE003365

Meybeck, M., Laroche, L., Dürr, H. H., & Syvitski, J. P. M. (2003). Global variability of daily total suspended solids and their fluxes in rivers. *Global and Planetary Change*, *39*(1), 65-93. DOI:10.1016/S0921-8181(03)00018-3

Meyer-Peter, E., & Müller, R. D. (1948). Formulas for Bed-Load Transport. Proceedings, 2nd Congress, International Association of Hydraulic Research, Stockholm.

Miall, A. D. (1993). The architecture of fluvial-deltaic sequences in the Upper Mesaverde Group (Upper Cretaceous), Book Cliffs, Utah. In J. L. Best & C. S. Bristow (Eds.), *Braided Rivers* (Vol. 75, pp. 305-332). DOI:10.1144/GSL.SP.1993.075.01.19

Miall, A. D. (1994). Reconstructing fluvial macroform architecture from two-dimensional outcrops; examples from the Castlegate Sandstone, Book Cliffs, Utah. *Journal of Sedimentary Research*, *64*(2b), 146-158. DOI:10.1306/D4267F78-2B26-11D7-8648000102C1865D

Miall, A. D., & Arush, M. (2001). The Castlegate Sandstone of the Book Cliffs, Utah: Sequence stratigraphy, paleogeography, and tectonic controls. *Journal of Sedimentary Research*, *71*(4), 537-548. DOI:10.1306/103000710537

Miall, A. D., Catuneanu, O., Vakarelov, B. K., & Post, R. (2008). The Western Interior Basin. In A. D. Miall (Ed.), *Sedimentary Basins of the World* (Vol. 5, pp. 329-362). Elsevier. DOI:10.1016/S1874-5997(08)00009-9

Michael, N. A., Whittaker, A. C., Carter, A., & Allen, P. A. (2014). Volumetric budget and grain-size fractionation of a geological sediment routing system: Eocene Escanilla Formation, south-central Pyrenees. *GSA Bulletin*, *126*(3-4), 585-599. DOI:10.1130/B30954.1

Miller, I. M., Johnson, K., Kline, D. E., Nichols, D. J., & Barclay, R. (2013). A Late Campanian Flora from the Kaiparowits Formation, southern Utah, and a brief overview of the widely sampled but little-known Campanian vegetation of the Western Interior of North America. *At the Top of the Grand Staircase: The Late Cretaceous of southern Utah*, 107-131.

Miller, K. G., Barrera, E., Olsson, R. K., Sugarman, P. J., & Savin, S. M. (1999). Does ice drive early Maastrichtian eustasy? *Geology*, *27*(9), 783-786. DOI:10.1130/0091-7613(1999)027<0783:DIDEME>2.3.CO;2

Miller, K. G., Sugarman, P. J., Browning, J. V., Kominz, M. A., Hernández, J. C., Olsson, R. K., Wright, J. D., Feigenson, M. D., & Van Sickel, W. (2003). Late Cretaceous chronology of large, rapid sea-level changes: Glacioeustasy during the greenhouse world. *Geology*, *31*(7), 585-588. DOI:10.1130/0091-7613(2003)031<0585:LCCOLR>2.0.CO;2

Milliman, J. D., & Farnsworth, K. L. (2013). *River Discharge to the Coastal Ocean: A Global Synthesis*. Cambridge University Press.

Mohrig, D., Heller, P., Paola, C., & Lyons, W. (2000). Interpreting avulsion process from ancient alluvial sequences: Guadalope-Matarranya system (Northern Spain) and Wasatch formation (Western Colorado). *Geological Society of America Bulletin*, 112. DOI:10.1130/0016-7606(2000)112<1787:IAPFAA>2.0.CO;2

Molenaar, C. M., & Cobban, W. A. (1991). Middle Cretaceous stratigraphy on the south side of the Uinta Basin, east-central Utah. In T. C. Chidsey Jr (Ed.), *Geology of east-central Utah* (Vol. 19, pp. 29-43). Utah Geological Association.

Montero, J. M., Colombera, L., Yan, N., & Mountney, N. P. (2021). A workflow for modelling fluvial meander-belt successions: Combining forward stratigraphic modelling and multi-point geostatistics. *Journal of Petroleum Science and Engineering*, 201, 108411. DOI:10.1016/j.petrol.2021.108411

Molnar, P., & England, P. (1990). Late Cenozoic uplift of mountain ranges and global climate change: chicken or egg? *Nature*, *346*, 29-23. DOI:10.1038/346029a0

Moore, J. M., Howard, A. D., Dietrich, W. E., & Schenk, P. M. (2003). Martian Layered Fluvial Deposits: Implications for Noachian Climate Scenarios. *Geophysical Research Letters*, *30*(24). DOI:10.1029/2003GL019002

Myrow, P. M., Jerolmack, D. J., & Perron, J. T. (2018). Bedform disequilibrium. *Journal of Sedimentary Research*, 88(9), 1096-1113. doi:10.2110/jsr.2018.55

Nanson, G. C., & Huang, H. Q. (2017). Self-adjustment in rivers: Evidence for least action as the primary control of alluvial-channel form and process. Earth Surface Processes and Landforms, 42(4), 575-594. doi:10.1002/esp.3999

Nanson, G. C., & Knighton, A. D. (1996). Anabranching rivers: Their cause, character and classification. *Earth Surface Processes and Landforms*, *21*(3), 217-239. DOI:10.1002/(SICI)1096-9837(199603)21:3<217::AID-ESP611>3.0.CO;2-U

Nyberg, B., & Howell, J. A. (2015). Is the present the key to the past? A global characterization of modern sedimentary basins. *Geology*, 43(7), 643-646. doi:10.1130/G36669.1

Obradovich, J. D. (1993). A Cretaceous time scale. In W. E. G. Caldwell & E. Kauffman (Eds.), *Evolution of the Western Interior Basin* (Vol. Special Paper 39, pp. 379-396). Geological Association of Canada.

Otto-Bliesner, B. L., Brady, E. C., & Shields, C. (2002). Late Cretaceous ocean: Coupled simulations with the National Center for Atmospheric Research Climate System Model. *Journal of Geophysical Research: Atmospheres*, *107*(D2), 4019. DOI:10.1029/2001JD000821

Otto-Bliesner, B. L., & Houghton, D. D. (1986). Sensitivity of the seasonal climate of a general circulation model to ocean surface conditions and solar forcing. *Journal of Geophysical Research*, *91*, 6682-6694. DOI:10.1029/JD091iD06p06682

Owen, A., Jupp, P., Nichols, G., Hartley, A., Weissmann, G., & Sadykova, D. (2015). Statistical estimation of the position of an apex: Application to the geological record. *Journal of Sedimentary Research*, *85*, 142-152. DOI:10.2110/jsr.2015.16

Painter, C. S., Carrapa, B., DeCelles, P. G., Gehrels, G. E., & Thomson, S. N. (2014). Exhumation of the North American Cordillera revealed by multi-dating of Upper Jurassic–Upper Cretaceous foreland basin deposits. *GSA Bulletin*, *126*(11/12), 1439-1464. DOI:10.1130/B30999.1

Pang, M., & Nummedal, D. (1995). Flexural subsidence and basement tectonics of the Cretaceous Western Interior basin, United States. *Geology*, *23*(2), 173-176. DOI:10.1130/0091-7613(1995)023<0173:FSABTO>2.3.CO;2

Paola, C., & Borgman, L. (1991). Reconstructing random topography from preserved stratification. *Sedimentology*, *38*(4), 553-565. DOI:10.1111/j.1365-3091.1991.tb01008.x

Paola, C., Ganti, V., Mohrig, D., Runkel, A. C., & Straub, K. M. (2018). Time not our time: Physical controls on the preservation and measurement of geologic time. *Annual Review of Earth and Planetary Sciences*, 46(1), 409-438. doi:10.1146/annurev-earth-082517-010129

Paola, C., Heller, P., & Angevine, C. (1992). The large-scale dynamics of grain-size variation in alluvial basins, 1: Theory. *Basin Research*, *4*(2), 73-90. DOI:10.1111/j.1365-2117.1992.tb00145.x

Parker, G. (1976). On the cause and characteristic scales of meandering and braiding in rivers. *Journal of Fluid Mechanics*, *76*(3), 457-480. DOI:10.1017/S0022112076000748

Parker, G. (2004). *1D Sediment Transport Morphodynamics with Applications to Rivers and Turbidity Currents*.

Parker, G., Wilcock, P. R., Paola, C., Dietrich, W. E., & Pitlick, J. (2007). Physical basis for quasi-universal relations describing bankfull hydraulic geometry of single-thread gravel bed rivers. *Journal of Geophysical Research: Earth Surface,* 112(F4). doi:10.1029/2006JF000549

Parker, L. R. (1976b). The paleoecology of the fluvial coal-forming swamps and associated floodplain environments in the Blackhawk Formation (Upper Cretaceous) of central Utah. *Brigham Young University, Geological Studies*, *22*, 99-116.

Parsons, A. J., Michael, N. A., Whittaker, A. C., Duller, R. A., & Allen, P. A. (2012). Grain-size trends reveal the late orogenic tectonic and erosional history of the south–central Pyrenees, Spain. *Journal of the Geological Society*, 169(2), 111. http://jgs.lyellcollection.org/content/169/2/111.abstract

Paul, J. D., Roberts, G. G., & White, N. (2014). The African landscape through space and time. *Tectonics*, *33*(6), 898-935. DOI:10.1002/2013TC003479

Pavlov, V. K., & Pfirman, S. L. (1995). Hydrographic structure and variability of the Kara Sea: Implications for pollutant distribution. *Deep Sea Research Part II: Topical Studies in Oceanography*, 42(6), 1369-1390. DOI:10.1016/0967-0645(95)00046-1

Pedersen, G. K., & Pulvertaft, T. C. R. (1992). The nonmarine Cretaceous of the West Greenland Basin, onshore West Greenland. *Cretaceous Research*, *13*(3), 263-272. DOI:10.1016/0195-6671(92)90002-8

Pederson, J. L., & Tressler, C. (2012). Colorado River long-profile metrics, knickzones and their meaning. *Earth and Planetary Science Letters*, *345-348*, 171-179. DOI:10.1016/j.epsl.2012.06.047

Pelletier, J. D. (2012). A spatially distributed model for the long-term suspended sediment discharge and delivery ratio of drainage basins. *Journal of Geophysical Research: Earth Surface*, *117*(F2), 1-15. DOI:10.1029/2011JF002129

Perry, G. D., Duffy, P. B., & Miller, N. L. (1996). An extended data set of river discharges for validation of general circulation models. *Journal of Geophysical Research: Atmospheres*, *101*(D16), 21339-21349. DOI:10.1029/96JD00932

Petter, A. L., Steel, R. J., Mohrig, D., Kim, W., & Carvajal, C. (2013). Estimation of the paleoflux of terrestrial-derived solids across ancient basin margins using the stratigraphic record. *GSA Bulletin*, *125*, 578-593. DOI:10.1130/B30603.1

Pettit, B. S., Blum, M., Pecha, M., McLean, N., Bartschi, N. C., & Saylor, J. E. (2019). Detrital-zircon U-Pb paleodrainage reconstruction and geochronology of the Campanian Blackhawk–Castlegate succession, Wasatch Plateau and Book Cliffs, Utah, U.S.A. *Journal of Sedimentary Research*, *89*(4), 273-292. DOI:10.2110/jsr.2019.18

Plink-Björklund, P. (2015). Morphodynamics of rivers strongly affected by monsoon precipitation: Review of depositional style and forcing factors. *Sedimentary Geology*, *323*, 110-147. DOI:10.1016/j.sedgeo.2015.04.004

Plint, A. G. (2002). Paleovalley systems in the Upper Cretaceous Dunvegan Formation, Alberta and British Columbia. *Bulletin of Canadian Petroleum Geology*, *50*(2), 277-296. DOI:10.2113/50.2.277

Plint, A. G., & Wadsworth, J. A. (2003). Sedimentology and palaeogeomorphology of four large valley systems incising delta plains, western Canada Foreland Basin: implications for mid-Cretaceous sea-level changes. *Sedimentology*, *50*(6), 1147-1186. DOI:10.1111/j.1365-3091.2003.00599.x

Plint, A. G., & Wadsworth, J. A. (2006). Delta-plain paleodrainage patterns reflect small-scale fault movement and subtle forebulge uplift: Upper Cretaceous Dunvegan Formation, Western Canada Foreland Basin. In R. W. Dalrymple, D. A. Leckie, & R. W. Tillman (Eds.), *Incised Valleys in Time and Space* (Vol. 85, pp. 0). SEPM Society for Sedimentary Geology. DOI:10.2110/pec.06.85.0219

Poag, C. W., & Sevon, W. D. (1989). A record of Appalachian denudation in postrift Mesozoic and Cenozoic sedimentary deposits of the U.S. Middle Atlantic continental margin. *Geomorphology*, 2(1-3), 119-157. DOI:10.1016/0169-555X(89)90009-3

Poole, I., Cantrill, D., & Utescher, T. (2005). A multi-proxy approach to determine Antarctic terrestrial palaeoclimate during the Late Cretaceous and Early Tertiary. *Palaeogeography, Palaeoclimatology, Palaeoecology*, *222*(1), 95-121. DOI:10.1016/j.palaeo.2005.03.011

Pope, V. D., Gallani, M. L., Rowntree, P. R., & Stratton, R. A. (2000). The impact of new physical parametrizations in the Hadley Centre climate model: HadAM3. *Climate Dynamics*, *16*(2), 123-146. DOI:10.1007/s003820050009

Primm, J. W., Johnson, C. L., & Stearns, M. (2018). Basin-axial progradation of a sediment supply driven distributive fluvial system in the Late Cretaceous southern Utah foreland. *Basin Research*, *30*(2), 249-278. DOI:10.1111/bre.12252

Reesink, A. J. H., & Bridge, J. S. (2007). Influence of superimposed bedforms and flow unsteadiness on formation of cross strata in dunes and unit bars. *Sedimentary Geology*, *202*(1), 281-296. DOI:10.1016/j.sedgeo.2007.02.005

Reesink, A. J. H., & Bridge, J. S. (2009). Influence of bedform superimposition and flow unsteadiness on the formation of cross strata in dunes and unit bars — Part 2, further experiments. *Sedimentary Geology*, *222*(3), 274-300. DOI:10.1016/j.sedgeo.2009.09.014

Reesink, A. J. H., Van den Berg, J. H., Parsons, D. R., Amsler, M. L., Best, J. L., Hardy, R. J., Orfeo, O., & Szupiany, R. N. (2015). Extremes in dune preservation: Controls on the completeness of fluvial deposits. *Earth-Science Reviews*, *150*, 652-665. DOI:10.1016/j.earscirev.2015.09.008

Reiners, P. W., Ehlers, T. A., Mitchell, S. G., & Montgomery, D. R. (2003). Coupled spatial variations in precipitation and long-term erosion rates across the Washington Cascades. *Nature*, *426*(6967), 645-647. DOI:10.1038/nature02111

Retallack, G. J. (1997). *A colour guide to paleosols*. Wiley

Rittersbacher, A., Howell, J. A., & Buckley, S. J. (2014). Analysis of fluvial architecture in the Blackhawk Formation, Wasatch Plateau, Utah, U.S.A., using large 3D photorealistic models. *Journal of Sedimentary Research*, *84*(2), 72-87. DOI:10.2110/jsr.2014.12

Rivera-Hernández, F., Sumner, D. Y., Mangold, N., Banham, S. G., Edgett, K. S., Fedo, C. M., Gupta, S., Gwizd, S., Heydari, E., Maurice, S., Nachon, M., Newsom, H., Schieber, J., Stack-Morgan, K., Stein, N., & Wiens, R. C. (2020). Grain Size Variations in the Murray Formation: Stratigraphic Evidence for Changing Depositional Environments in Gale Crater, Mars. *Journal of Geophysical Research: Planets*, 125(2), e2019JE006230. DOI:10.1029/2019JE006230

Roberts, E. M. (2007). Facies architecture and depositional environments of the Upper Cretaceous Kaiparowits Formation, southern Utah. *Sedimentary Geology*, *197*(3), 207-233. DOI:10.1016/j.sedgeo.2006.10.001

Roberts, E. M., Tapanila, L., & Mijal, B. (2008). Taphonomy and sedimentology of storm-generated continental shell beds: A case example from the Cretaceous Western Interior Basin. *The Journal of Geology*, *116*(5), 462-479. DOI:10.1086/590134

Roberts, G. G., White, N., & Lodhia, B. H. (2019). The generation and scaling of longitudinal river profiles [DOI:10.1029/2018JF004796]. *Journal of Geophysical Research: Earth Surface*, *124*(1), 137-153. DOI:10.1029/2018JF004796

Roberts, G. G., White, N. J., Martin-Brandis, G. L., & Crosby, A. G. (2012). An uplift history of the Colorado Plateau and its surroundings from inverse modeling of longitudinal river profiles. *Tectonics*, *31*(4). DOI:10.1029/2012TC003107

Roberts, L. N. R., & Kirschbaum, M. A. (1995). Paleogeography and the Late Cretaceous of the Western Interior of middle North America: coal distribution and sediment accumulation [Report]. *U.S. Geological Survey Professional Paper*, *1561*, 1-65. DOI:10.3133/pp1561

Robinson, R. A. J., & Slingerland, R. L. (1998). Grain-size trends, basin subsidence and sediment supply in the Campanian Castlegate Sandstone and equivalent conglomerates of Central Utah. *Basin Research*, *10*, 109-127.

Romans, B. W., Castelltort, S., Covault, J. A., Fildani, A., & Walsh, J. P. (2016). Environmental signal propagation in sedimentary systems across timescales. *Earth-Science Reviews*, *153*, 7-29. DOI:10.1016/j.earscirev.2015.07.012

Romans, B. W., & Graham, S. A. (2013). A deep-time perspective of land-ocean linkages in the sedimentary record. *Annual Review of Marine Science*, *5*, 69-94. DOI:10.1146/annurev-marine-121211-172426

Rosgen, D. L. (1994). A classification of natural rivers. *CATENA*, 22(3), 169-199. doi:10.1016/0341-8162(94)90001-9

Rowley, D. B., & Currie, B. S. (2006). Palaeo-altimetry of the late Eocene to Miocene Lunpola basin, central Tibet [Article]. *Nature*, *439*, 677-681. DOI:10.1038/nature04506

Rowley, D. B., & Garzione, C. N. (2007). Stable isotope-based paleoaltimetry. *Annual Review of Earth and Planetary Sciences*, *35*(1), 463-508. DOI:10.1146/annurev.earth.35.031306.140155

Rowley, D. B., Pierrehumbert, R. T., & Currie, B. S. (2001). A new approach to stable isotope-based paleoaltimetry: implications for paleoaltimetry and paleohypsometry of the High Himalaya since the Late Miocene. *Earth and Planetary Science Letters*, *188*(1), 253-268. DOI:10.1016/S0012-821X(01)00324-7

Rudge, J. F., Roberts, G. G., White, N. J., & Richardson, C. N. (2015). Uplift histories of Africa and Australia from linear inverse modeling of drainage inventories. *Journal of Geophysical Research: Earth Surface*, *120*(5), 894-914. DOI:10.1002/2014JF003297

Ryer, T. A., & Anderson, P. B. (2004). Facies of the Ferron Sandstone, East-Central Utah. In T. C. Chidsey, Jr., R. D. Adams, & T. H. Morris (Eds.), *Regional to Wellbore Analog for Fluvial-Deltaic Reservoir Modeling: The Ferron Sandstone of Utah* (Vol. 50, pp. 0). American Association of Petroleum Geologists. DOI:10.1306/St50983

Sadler, P. M. (1981). Sediment accumulation rates and the completeness of stratigraphic sections. *The Journal of Geology*, *89*, 569-584. DOI:10.1086/628623

Savin, S. M., Douglas, R. G., & Stehli, F. G. (1975). Tertiary marine paleotemperatures. *GSA Bulletin*, *86*(11), 1499-1510. DOI:10.1130/0016-7606(1975)86<1499:TMP>2.0.CO;2

Schlunegger, F., & Hinderer, M. (2003). Pleistocene/Holocene climate change, re-establishment of fluvial drainage network and increase in relief in the Swiss Alps. *Terra Nova*, *15*(2), 88-95. DOI:10.1046/j.1365-3121.2003.00469.x

Schulze, K., Hunger, M., & Döll, P. (2005). Simulating river flow velocity on global scale. *Advances in Geosciences*, *5*, 133-136.

Schumm, S. A. (1963). A tentative classification of alluvial river channels. *U.S. Geological Survey Circular*, *477*, 10 p.

Schumm, S. A. (1968). River adjustment to altered hydrologic regimen - Murrumbidgee River and paleochannels, Australia. *U.S. Geological Survey Professional Paper*, *598*, 65. DOI:10.3133/pp598

Schumm, S. A. (1977). *The Fluvial System*. John Wiley & Sons.

Schumm, S. A. (1985). Patterns of alluvial rivers. *Annual Review of Earth and Planetary Sciences*, *13*(1), 5-27. DOI:10.1146/annurev.ea.13.050185.000253

Sellwood, B. W., Price, G. D., Shackleton, N. J., Francis, J., Allen, J. R. L., Hoskins, B. J., Sellwood, B. W., Spicer, R. A., & Valdes, P. J. (1993). Sedimentary facies as indicators of Mesozoic palaeoclimate. *Philosophical Transactions of the Royal Society of London. Series B: Biological Sciences*, 341(1297), 225-233. DOI:10.1098/rstb.1993.0107

Serinaldi, F., Loecker, F., Kilsby, C. G., & Bast, H. (2018). Flood propagation and duration in large river basins: a data-driven analysis for reinsurance purposes. *Natural Hazards*, *94*(1), 71-92. DOI:10.1007/s11069-018-3374-0

Sewall, J. O., & Fricke, H. C. (2013). Andean-scale highlands in the Late Cretaceous Cordillera of the North American western margin. *Earth and Planetary Science Letters*, *362*, 88-98. DOI:10.1016/j.epsl.2012.12.002

Seymour, D. L., & Fielding, C. R. (2013). High resolution correlation of the Upper Cretaceous stratigraphy between the Book Cliffs and the western Henry Mountains syncline, Utah, U.S.A. *Journal of Sedimentary Research*, *83*(6), 475-494. DOI:10.2110/jsr.2013.37

Shackleton, N. J., & Kennett, J. P. (1975). Paleotemperature history of the Cenozoic and the initiation of Antarctic glaciation: oxygen and carbon isotope analyses in DSDP Sites 277, 279, and 281. *Initial reports of the Deep Sea Drilling Project 29*, 743-755. DOI:10.2973/dsdp.proc.29.1975

Shanley, K. W., & McCabe, P. J. (1995). Sequence Stratigraphy of Turonian–Santonian Strata, Kaiparowits Plateau, Southern Utah, U.S.A.: Implications for Regional Correlation and Foreland Basin Evolution. In J. C. V. Wagoner & G. T. Bertram (Eds.), *Sequence Stratigraphy of Foreland Basin Deposits: Outcrop and Subsurface Examples from the Cretaceous of North America* (Vol. 64, pp. 0). American Association of Petroleum Geologists. DOI:10.1306/M64594C6

Sharma, S., Bhattacharya, J. P., & Richards, B. (2017). Source-to-sink sediment budget analysis of the Cretaceous Ferron Sandstone, Utah, U.S.A., using the fulcrum approach. *Journal of Sedimentary Research*, *87*(6), 594-608. DOI:10.2110/jsr.2017.23

Skelton, P. W., Spicer, R. A., Kelley, S. P., & Gilmour, I. (2003). *The Cretaceous World*. Cambridge University Press.

Sklar, L. S., & Dietrich, W. E. (2004). A mechanistic model for river incision into bedrock by saltating bed load. *Water Resources Research*, *40*(6). DOI:10.1029/2003WR002496

Sloss, L. L. (1988) Forty years of sequence stratigraphy. *GSA Bulletin*, 100, 1661–1665.

Smith, N. D., Cross, T. A., Dufficy, J. P., & Clough, S. R. (1989). Anatomy of an avulsion. *Sedimentology*, 36(1), 1-23. DOI:10.1111/j.1365-3091.1989.tb00817.x

Snell, K. E., Koch, P. L., Druschke, P., Foreman, B. Z., & Eiler, J. M. (2014). High elevation of the 'Nevadaplano' during the Late Cretaceous. *Earth and Planetary Science Letters*, 386, 52-63. DOI:10.1016/j.epsl.2013.10.046

Snieder, S., Griffiths, C. M., Owen, A., Hartley, A. J., & Howell, J. A. (2021). Stratigraphic forward modelling of distributive fluvial systems based on the Huesca System, Ebro Basin, northern Spain. *Basin Research*, 33(6), 3137-3158. DOI:10.1111/bre.12597

Sømme, T. O., Helland-Hansen, W., Martinsen, O. J., & Thurmond, J. B. (2009). Relationships between morphological and sedimentological parameters in source-to-sink systems: a basis for predicting semi-quantitative characteristics in subsurface systems. *Basin Research*, *21*(4), 361-387. DOI:10.1111/j.1365-2117.2009.00397.x

Sømme, T. O., Martinsen, O. J., & Lunt, I. (2013). Linking offshore stratigraphy to onshore paleotopography: The Late Jurassic–Paleocene evolution of the south Norwegian margin. *GSA Bulletin*, *125*(7-8), 1164-1186. DOI:10.1130/B30747.1

Sømme, T. O., Piper, D. J. W., Deptuck, M. E., & Helland-Hansen, W. (2011). Linking onshore–offshore sediment dispersal in the Golo source-to-sink system (Corsica, France) during the late Quaternary. *Journal of Sedimentary Research*, *81*(2), 118-137. DOI:10.2110/jsr.2011.11

Soria-Jáuregui, Á., Jiménez-Cantizano, F., & Antón, L. (2019). Geomorphic and tectonic implications of the endorheic to exorheic transition of the Ebro River system in northeast Iberia. *Quaternary Research*, *91*(2), 472-492. DOI:10.1017/qua.2018.87

Spencer, C. J., Prave, A. R., Cawood, P. A., & Roberts, N. M. W. (2014). Detrital zircon geochronology of the Grenville/Llano foreland and basal Sauk Sequence in west Texas, USA. *GSA Bulletin*, *126*(7-8), 1117-1128. DOI:10.1130/B30884.1

Spicer, R., Ahlberg, A., Herman, A., Hofmann, C.-C., Raikevich, M., Valdes, P., & Markwick, P. J. (2008). The Late Cretaceous continental interior of Siberia: A challenge for climate models. *Earth and Planetary Science Letters*, *267*, 228-235. DOI:10.1016/j.epsl.2007.11.049

Spieker, E. M. (1946). Late Mesozoic and early Cenozoic history of central Utah [Report]. *U.S. Geological Survey Professional Paper*, *205D*. DOI:10.3133/pp205D

Stephenson, S. N., Roberts, G. G., Hoggard, M. J., & Whittaker, A. C. (2014). A Cenozoic uplift history of Mexico and its surroundings from longitudinal river profiles. *Geochemistry, Geophysics, Geosystems*, *15*(12), 4734-4758. DOI:10.1002/2014GC005425

Stepinski, T. F., & Coradetti, S. (2004). Comparing morphologies of drainage basins on Mars and Earth using integral-geometry and neural maps. *Geophysical Research Letters*, 31(15). DOI:10.1029/2004GL020359

Stoll, H. M., & Schrag, D. P. (2000). High-resolution stable isotope records from the Upper Cretaceous rocks of Italy and Spain: Glacial episodes in a greenhouse planet? *GSA Bulletin*, *112*(2), 308-319. DOI:10.1130/0016-7606(2000)112<308:HSIRFT>2.0.CO;2

Strahler, A. N. (1957). Quantitative analysis of watershed geomorphology. *Eos, Transactions American Geophysical Union*, *38*(6), 913-920. DOI:10.1029/TR038i006p00913

Straub, K. M., Duller, R. A., Foreman, B. Z., & Hajek, E. A. (2020). Buffered, incomplete, and shredded: The challenges of reading an imperfect stratigraphic record. *Journal of Geophysical Research: Earth Surface*, *125*(3), e2019JF005079. DOI:10.1029/2019JF005079

Strick, R. J. P., Ashworth, P. J., Sambrook Smith, G. H., Nicholas, A. P., Best, J. L., Lane, S. N., . . . Dale, J. (2019). Quantification of bedform dynamics and bedload sediment flux in sandy braided rivers from airborne and satellite imagery. *Earth Surface Processes and Landforms*, 44(4), 953-972. doi:10.1002/esp.4558

Stucky de Quay, G., Kite, E. S., & Mayer, D. P. (2019). Prolonged fluvial activity from channel-fan systems on Mars. *Journal of Geophysical Research: Planets*, *124*(11), 3119-3139. DOI:10.1029/2019JE006167

Syvitski, J. P., & Kettner, A. (2011). Sediment flux and the Anthropocene. *Philosophical Transactions of the Royal Society A: Mathematical, Physical and Engineering Sciences*, *369*(1938), 957-975. DOI:10.1098/rsta.2010.0329

Syvitski, J. P., Vörösmarty, C. J., Kettner, A. J., & Green, P. (2005). Impact of humans on the flux of terrestrial sediment to the global coastal ocean. *Science*, *308*(5720), 376-380. DOI:10.1126/science.1109454

Syvitski, J. P. M., & Milliman, J. D. (2007). Geology, geography, and humans battle for dominance over the delivery of fluvial sediment to the coastal ocean. *The Journal of Geology*, *115*(1), 1-19. DOI:10.1086/509246

Syvitski, J. P. M., & Saito, Y. (2007). Morphodynamics of deltas under the influence of humans. *Global and Planetary Change*, *57*(3-4), 261-282. DOI:10.1016/j.gloplacha.2006.12.001

Szwarc, T. S., Johnson, C. L., Stright, L. E., & McFarlane, C. M. (2015). Interactions between axial and transverse drainage systems in the Late Cretaceous Cordilleran foreland basin: Evidence from detrital zircons in the Straight Cliffs Formation, southern Utah, USA. *GSA Bulletin*, *127*(3-4), 372-392. DOI:10.1130/B31039.1

Tabor, C. R., Poulsen, C. J., Lunt, D. J., Rosenbloom, N. A., Otto-Bliesner, B. L., Markwick, P. J., Brady, E. C., Farnsworth, A., & Feng, R. (2016). The cause of Late Cretaceous cooling: A multimodel-proxy comparison. *Geology*, *44*(11), 963-966. DOI:10.1130/g38363.1

Tarduno, J. A., Brinkman, D. B., Renne, P. R., Cottrell, R. D., Scher, H., & Castillo, P. (1998). Evidence for extreme climatic warmth from Late Cretaceous Arctic vertebrates. *Science*, 282(5397), 2241-2243. DOI: 10.1126/science.282.5397.2241

Ten Brinke, W. B. M., Wilbers, A. W. E., & Wesseling, C. (1999). Dune Growth, Decay and Migration Rates during a Large-Magnitude Flood at a Sand and Mixed Sand–Gravel Bed in the Dutch Rhine River System. In N. D. Smith & J. Rogers (Eds.), *Fluvial Sedimentology VI* (pp. 15-32). DOI:10.1002/9781444304213.ch2

Tindall, J., Flecker, R., Valdes, P., Schmidt, D. N., Markwick, P., & Harris, J. (2010). Modelling the oxygen isotope distribution of ancient seawater using a coupled ocean–atmosphere GCM: Implications for reconstructing early Eocene climate. *Earth and Planetary Science Letters*, *292*(3-4), 265-273. DOI:10.1016/j.epsl.2009.12.049

Tinker, J., de Wit, M., & Brown, R. (2008). Mesozoic exhumation of the southern Cape, South Africa, quantified using apatite fission track thermochronology. *Tectonophysics*, *455*(1-4), 77-93. DOI:10.1016/j.tecto.2007.10.009

Torsvik, T. H., Müller, R. D., Van der Voo, R., Steinberger, B., & Gaina, C. (2008). Global plate motion frames: toward a unified model. *Reviews of Geophysics*, *46*(3), RG3004. DOI:10.1029/2007RG000227

Trampush, S. M., Huzurbazar, S., & McElroy, B. (2014). Empirical assessment of theory for bankfull characteristics of alluvial channels. *Water Resources Research*, *50*(12), 9211-9220. DOI:10.1002/2014WR015597

Trower, E. J., Ganti, V., Fischer, W. W., & Lamb, M. P. (2018). Erosional surfaces in the Upper Cretaceous Castlegate Sandstone (Utah, USA): Sequence boundaries or autogenic scour from backwater hydrodynamics? *Geology*, *46*(8), 707-710. DOI:10.1130/G40273.1

Tucker, G. E., & Whipple, K. X. (2002). Topographic outcomes predicted by stream erosion models: Sensitivity analysis and intermodel comparison. *Journal of Geophysical Research: Solid Earth*, *107*(B9), ETG 1-1-ETG 1-16. DOI:10.1029/2001JB000162

Turowski, J. M., Rickenmann, D., & Dadson, S. J. (2010). The partitioning of the total sediment load of a river into suspended load and bedload: a review of empirical data. *Sedimentology*, *57*(4), 1126-1146. DOI:10.1111/j.1365-3091.2009.01140.x

Upchurch Jr., G. R., Kiehl, J., Shields, C., Scherer, J., & Scotese, C. (2015). Latitudinal temperature gradients and high-latitude temperatures during the latest Cretaceous: Congruence of geologic data and climate models. *Geology*, *43*(8), 683-686. DOI:10.1130/g36802.1

Valdes, P. J., Armstrong, E., Badger, M. P. S., Bradshaw, C. D., Bragg, F., Crucifix, M., Davies-Barnard, T., Day, J. J., Farnsworth, A., Gordon, C., Hopcroft, P. O., Kennedy, A. T., Lord, N. S., Lunt, D. J., Marzocchi, A., Parry, L. M., Pope, V., Roberts, W. H. G., Stone, E. J., . . . Williams, J. H. T. (2017). The BRIDGE HadCM3 family of climate models: HadCM3@Bristol v1.0. *Geoscientific Model Development*, *10*(10), 3715-3743. DOI:10.5194/gmd-10-3715-2017

Valora, P. M. (2010). *Late Cretaceous to Paleocene Tectono-Stratigraphic Evolution of the Southern Part of the Provo Salient, Sevier Fold-Thrust Belt, Central Utah: New Insights from Geologic Mapping, Growth-Strata Analysis and Structural Modeling in the Thistle, UT 7.5' Quadrangle* [M.S. thesis, Colorado School of Mines]. Golden, Colorado.

van den Berg, J. H. (1995). Prediction of alluvial channel pattern of perennial rivers. *Geomorphology*, *12*(4), 259-279. DOI:10.1016/0169-555X(95)00014-V

van Rijn, L. C. (1984a). Sediment transport III: bedforms and alluvial roughness. *Journal of Hydraulic Engineering*, *110*(12), 1733-1754. DOI:10.1061/(ASCE)0733-9429(1984)110:12(1733)

van Rijn, L. C. (1984b). Sediment transport, part II: Suspended load transport. *Journal of Hydraulic Engineering*, *110*(11), 1613-1641. DOI:10.1061/(ASCE)0733-9429(1984)110:11(1613)

van Wagoner, J. C. (1995). Sequence Stratigraphy and Marine to Nonmarine Facies Architecture of Foreland Basin Strata, Book Cliffs, Utah, U.S.A. In J. C. van Wagoner & G. T. Bertram (Eds.), *Sequence Stratigraphy of Foreland Basin Deposits: Outcrop and Subsurface Examples from the Cretaceous of North America* (Vol. 64). American Association of Petroleum Geologists. DOI:10.1306/M64594C7

Vernon, A. J., van der Beek, P. A., Sinclair, H. D., & Rahn, M. K. (2008). Increase in late Neogene denudation of the European Alps confirmed by analysis of a fission-track thermochronology database. *Earth and Planetary Science Letters*, *270*(3-4), 316-329. DOI:10.1016/j.epsl.2008.03.053

von Blanckenburg, F. (2005). The control mechanisms of erosion and weathering at basin scale from cosmogenic nuclides in river sediment. *Earth and Planetary Science Letters*, *237*(3-4), 462-479. DOI:10.1016/j.epsl.2005.06.030

Wade, D. C., Abraham, N. L., Farnsworth, A., Valdes, P. J., Bragg, F., & Archibald, A. T. (2019). Simulating the climate response to atmospheric oxygen variability in the Phanerozoic: a focus on the Holocene, Cretaceous and Permian. *Climate of the Past*, 15(4), 1463-1483. DOI:10.5194/cp-15-1463-2019

Walford, H., White, N., & Sydow, J. (2005). Solid sediment load history of the Zambezi Delta. *Earth and Planetary Science Letters*, *238*(1-2), 49-63. DOI:10.1016/j.epsl.2005.07.014

Wang, J., & Plink-Björklund, P. (2020). Variable-discharge-river macroforms in the Sunnyside Delta Interval of the Eocene Green River Formation, Uinta Basin, USA. *Sedimentology*, *67*(4), 1914-1950. DOI:10.1111/sed.12688

Wang, R., Colombera, L., & Mountney, N. P. (2020). Palaeohydrological characteristics and palaeogeographic reconstructions of incised-valley-fill systems: Insights from the Namurian successions of the United Kingdom and Ireland. *Sedimentology*, *67*(7), 3844-3873. DOI:10.1111/sed.12773

Wang, Y., Huang, C.-m., Sun, B., Quan, C., Wu, J., & Lin, Z. (2014). Paleo-CO_2 variation trends and the Cretaceous greenhouse climate. *Earth-Science Reviews*, *129*, 136–147. DOI:10.1016/j.earscirev.2013.11.001

Watkins, S. E. (2019). *Linking source and sink in an active rift: quantifying controls on sediment export and depositional stratigraphy in the Gulf of Corinth, central Greece* Imperial College London].

Watkins, S. E., Whittaker, A., Ganti, V., Bell, R., Brooke, S., Gawthorpe, R., & McNeill, L. (2018). Quantifying sediment dynamics and intermittency of gravel bed rivers; examples from the Gulf of Corinth. *EGU General Assembly Conference Abstracts*, 19573. https://ui.adsabs.harvard.edu/abs/2018EGUGA..2019573W

Watkins, S. E., Whittaker, A. C., Bell, R. E., Brooke, S. A. S., Ganti, V., Gawthorpe, R. L., McNeill, L. C., & Nixon, C. W. (2020). Straight from the source's mouth: Controls on field-constrained sediment export across the entire active Corinth Rift, central Greece. *Basin Research*, *n/a*(n/a). DOI:10.1111/bre.12444

Watkins, S. E., Whittaker, A. C., Bell, R. E., McNeill, L. C., Gawthorpe, R. L., Brooke, S. A. S., & Nixon, C. W. (2018). Are landscapes buffered to high-frequency climate change? A comparison of sediment fluxes and depositional volumes in the Corinth Rift, central Greece, over the past 130 k.y. *GSA Bulletin*, *131*, 372-388. DOI:10.1130/B31953.1

Weissmann, G. S., Hartley, A. J., Scuderi, L. A., Nichols, G. J., Owen, A., Wright, S., . . . Anaya, F. M. L. (2015). Fluvial geomorphic elements in modern sedimentary basins and their potential preservation in the rock record: A review. *Geomorphology*, 250, 187-219. doi:10.1016/j.geomorph.2015.09.005

Wentworth, C. K. (1922). A scale of grade and class terms for clastic sediments. *The Journal of Geology*, 30(5), 377-392. doi:10.1086/622910

Wheeler, H. E. (1964) Base level, lithosphere surface, and time-stratigraphy. *GSA Bulletin*, 75, 599–610.

Whipple, K., & Meade, B. (2006). Orogen response to changes in climatic and tectonic forcing. *Earth and Planetary Science Letters*, *243*(1-2), 218-228. DOI:10.1016/j.epsl.2005.12.022

Whipple, K. X. (2004). Bedrock rivers and the geomorphology record of active orogens. *Annual Review of Earth and Planetary Sciences*, *32*(1), 151-185. DOI:10.1146/annurev.earth.32.101802.120356

Whipple, K. X. (2009). The influence of climate on the tectonic evolution of mountain belts. *Nature Geoscience*, *2*(2), 97-104. DOI:10.1038/ngeo413

Whitchurch, A., Carter, A., Sinclair, H., Duller, R., Whittaker, A., & Allen, P. (2011). Sediment routing system evolution within a diachronously uplifting orogen: Insights from detrital zircon thermochronological analyses from the South-Central Pyrenees. *American Journal of Science*, *311*, 442-482. DOI:10.2475/05.2011.03]

White, T., González, L., Ludvigson, G., & Poulsen, C. (2001). Middle Cretaceous greenhouse hydrologic cycle of North America. *Geology*, *29*(4), 363-366. DOI:10.1130/0091-7613(2001)029<0363:MCGHCO>2.0.CO;2

Whittaker, A. C. (2012). How do landscapes record tectonics and climate? *Lithosphere*, *4*(2), 160-164. DOI:10.1130/rf.l003.1

Whittaker, A. C., Attal, M., & Allen, P. A. (2010). Characterising the origin, nature and fate of sediment exported from catchments perturbed by active tectonics. *Basin Research*, *22*(6), 809-828. DOI:10.1111/j.1365-2117.2009.00447.x

Whittaker, A. C., Duller, R. A., Springett, J., Smithells, R. A., Whitchurch, A. L., & Allen, P. A. (2011). Decoding downstream trends in stratigraphic grain size as a function of tectonic subsidence and sediment supply. *GSA Bulletin*, *123*(7-8), 1363-1382. DOI:10.1130/B30351.1

Wilcock, P. R., & Crowe, J. C. (2003). Surface-based Transport Model for Mixed-Size Sediment. *Journal of Hydraulic Engineering*, *129*(2), 120-128. DOI:10.1061/(ASCE)0733-9429(2003)129:2(120)

Willett, S. D. (1999). Orogeny and orography: The effects of erosion on the structure of mountain belts. *Journal of Geophysical Research: Solid Earth*, *104*(B12), 28957-28981. DOI:10.1029/1999jb900248

Wilson, J. T. (1966). Did the Atlantic close and then re-open? *Nature*, *211*, 676-681. DOI:10.1038/211676a0

Wittmann, H., von Blanckenburg, F., Kruesmann, T., Norton, K. P., & Kubik, P. W. (2007). Relation between rock uplift and denudation from cosmogenic nuclides in river sediment in the Central Alps of Switzerland. *Journal of Geophysical Research: Earth Surface*, *112*(F4), n/a-n/a. DOI:10.1029/2006JF000729

Witzke, B. J., & Ludvigson, G. A. (1994). The Dakota Formation in Iowa and the type area. In G. W. Shurr, G. A. Ludvigson, & R. H. Hammond (Eds.), *Perspectives on the Eastern Margin of the Cretaceous Western Interior Basin* (Vol. 287). The Geological Society of America. DOI:10.1130/SPE287

Witzke, B. J., Ludvigson, G. A., Poppe, J. R., & Ravn, R. L. (1983). Cretaceous paleogeography along the eastern margin of the Western Interior Seaway, Iowa, southern Minnesota, and eastern Nebraska and South Dakota. *Mesozoic Paleogeography of the West-Central United States: Rocky Mountain Symposium*, *2*, 225-252.

Wobus, C., Whipple, K. X., Kirby, E., Snyder, N., Johnson, J., Spyropolou, K., Crosby, B., & Sheehan, D. (2006). Tectonics from topography: Procedures, promise, and pitfalls. In S. D. Willett, N. Hovius, M. T. Brandon, & D. M. Fisher (Eds.), *Tectonics, Climate, and Landscape Evolution*. Geological Society of America. DOI:10.1130/2006.2398(04)

Wobus, C. W., Tucker, G. E., & Anderson, R. S. (2010). Does climate change create distinctive patterns of landscape incision? *Journal of Geophysical Research: Earth Surface*, *115*(F4). DOI:10.1029/2009JF001562

Wolfe, J. A. (1993). *A method of obtaining climatic parameters from leaf assemblages* [Report](2040). (Bulletin, Issue. G. P. O. U.S & U. M. D. For sale by. http://pubs.er.usgs.gov/publication/b2040

Wolfe, J. A., & Upchurch Jr., G. R. (1987). North American nonmarine climates and vegetation during the Late Cretaceous. *Palaeogeography, Palaeoclimatology, Palaeoecology*, *61*(Supplement C), 33-77. DOI:10.1016/0031-0182(87)90040-X

Wolman, M. G. (1954). A method of sampling coarse river-bed material. *Eos Transactions American Geophysical Union*, *35*(6), 951-956. DOI:10.1029/TR035i006p00951

Wolman, M. G., & Miller, J. P. (1960). Magnitude and Frequency of Forces in Geomorphic Processes. *The Journal of Geology*, *68*(1), 54-74. DOI:10.1086/626637

Wong, M., & Parker, G. (2006). Reanalysis and Correction of Bed-Load Relation of Meyer-Peter and Müller Using Their Own Database. *Journal of Hydraulic Engineering*, *132*(11), 1159-1168. DOI:10.1061/(ASCE)0733-9429(2006)132:11(1159)

Wright, S., & Parker, G. (2004). Flow resistance and suspended load in sand-bed rivers: Simplified stratification model. *Journal of Hydraulic Engineering*, *130*(8), 796-805. DOI:10.1061/(ASCE)0733-9429(2004)130:8(796)

Wright, S., & Parker, G. (2005). Modeling downstream fining in sand-bed rivers. I: formulation. *Journal of Hydraulic Research*, *43*(6), 613-620. DOI:10.1080/00221680509500381

Wu, C., Nittrouer, J. A., Swanson, T., Ma, H., Barefoot, E., Best, J., & Allison, M. (2020). Dune-scale cross-strata across the fluvial-deltaic backwater regime: Preservation potential of an autogenic stratigraphic signature. *Geology*, 48(12), 1144-1148. doi:10.1130/G47601.1

Wysocki, N., & Hajek, E. A. (2021). Mud in sandy riverbed deposits as a proxy for ancient fine-sediment supply. *Geology*. DOI:10.1130/G48251.1

Yalin, M. S. (1964). Geometrical properties of sand waves. *Journal of the Hydraulics Division*, *90*(5), 105-119.

Yan, N., Colombera, L., & Mountney, N. P. (2021). Controls on fluvial meander-belt thickness and sand distribution: Insights from forward stratigraphic modelling. *Sedimentology*, 68(5), 1831-1860. DOI:10.1111/sed.12830

Yoshida, S., Willis, A., & Miall, A. D. (1996). Tectonic control of nested sequence architecture in the Castlegate Sandstone (Upper Cretaceous), Book Cliffs, Utah. *Journal of Sedimentary Research*, *66*(4), 737-748.

Zachos, J. C., Dickens, G. R., & Zeebe, R. E. (2008). An early Cenozoic perspective on greenhouse warming and carbon-cycle dynamics. *Nature*, *451*, 279-283. DOI:10.1038/nature06588

Zhang, J., Covault, J., Pyrcz, M., Sharman, G., Carvajal, C., & Milliken, K. (2018). Quantifying sediment supply to continental margins: Application to the Paleogene Wilcox Group, Gulf of Mexico. *AAPG Bulletin*, *102*(9), 1685-1702. DOI:10.1306/01081817308

Zhisheng, A., Kutzbach, J. E., Prell, W. L., & Porter, S. C. (2001). Evolution of Asian monsoons and phased uplift of the Himalaya–Tibetan plateau since Late Miocene times. *Nature*, *411*(6833), 62-66. DOI:10.1038/35075035

Ziegler, A. M., Rowley, D. B., Lottes, A. L., Sahagian, D. L., Hulver, M. L., & Gierlowski, T. C. (1985). Paleogeographic interpretation: With an example from the mid-Cretaceous. *Annual Review of Earth and Planetary Sciences*, *13*(1), 385-428. DOI:10.1146/annurev.ea.13.050185.002125

APPENDIX A: *Supplement to* Predicting sediment discharges and erosion rates in deep time — examples from the late Cretaceous North American continent[1]

Contents:

[1] A version of this appendix is published in ***Basin Research*** as Supplementary Information to:

Lyster, S. J., Whittaker, A. C., Allison, P. A., Lunt, D. J. and Farnsworth, A. (2020) Predicting sediment discharges and erosion rates in deep time—examples from the late Cretaceous North American continent. ***Basin Research***, 32, 1547– 1573, doi:10.1111/bre.12442

A1 HadCM3L general circulation model (GCM) boundary conditions and extended literature

Cenomanian and Turonian palaeoclimate data are derived from the HadCM3L general circulation model (GCM) and are identical to those presented and described in Farnsworth et al. (2019a), with atmospheric CO_2 set at 1120 ppmv (×4 preindustrial atmospheric CO_2). The model used is very similar to the HadCM3BLM2.1aD model that was described and evaluated under modern climate configuration in Valdes et al. (2017), except that it includes a modification to the ozone profile to ensure that the model does not develop a runaway warming at ×4 preindustrial atmospheric CO_2, as discussed by Lunt et al. (2016).

Various boundary conditions are implemented in the HadCM3L model from which our climate data are derived. Palaeo-digital elevation models (palaeoDEMs) are used as geographic boundary conditions (of importance are the land–sea mask, topography and bathymetry), however land coverage is not prescribed, because this is calculated by separate models (MOSES 2 and TRIFFID) which are coupled to HadCM3L (Cox et al., 1999; Cox, 2001). Atmospheric CO_2 concentrations are set to 1120 ppmv for all Cretaceous time slices, which is 4× preindustrial concentrations (280 ppmv) and considered to reflect Cretaceous proxy-reconstructed averages (Wang et al., 2014), which are commonly derived from stomatal indices and pedogenic carbonates. For other important greenhouse gases, preindustrial levels are used owing to lack of geological proxies; atmospheric concentrations of methane and nitrous oxide are set to 760 ppbv and 270 ppbv, respectively, for all Cretaceous time slices. Orbital configuration is set to present-day values, with an eccentricity of 0.0167 and an obliquity of 23.4°. Total solar irradiance, or solar intensity, is reduced to account for a dimmer, younger Cretaceous sun, and is calculated in accordance with Gough (1981). Cenomanian and Turonian solar constants are set as 1353.90 W/m^2 and 1354.49 W/m^2, respectively (Lunt et al., 2016). HadCM3L simulations are run for 10,422 years; this is essential for deep-time modelling work where the initial condition may be far from the final equilibrium state. Results are derived from the final 50 years of simulations. For a full description of boundary conditions, assumptions and experimental design associated with the use of HadCM3L in pre-Quaternary palaeoclimate modelling, refer to Lunt et al. (2016), and for more detail on boundary conditions and experimental design associated with our specific HadCM3L data, refer to Farnsworth et al. (2019a).

There are various challenges with using HadCM3L GCM data in palaeo-sediment routing system analysis for the late Cretaceous, which is the period of interest in this study. GCM predictions of late Cretaceous climate have been evaluated using both marine and terrestrial proxy climate records and, while sea surface temperatures (SSTs) generally agree between models and proxies at tropical and mid-latitudes, there remain inconsistencies between terrestrial surface temperature models and proxies (Spicer et al., 2008; Upchurch Jr. et al., 2015; Tabor et al., 2016). Of particular relevance in this study, GCMs display a cold bias in northern high latitudes and continental interiors, including the Western Interior Seaway (WIS) (Barron et al., 1993; Otto-Bliesner et al., 2002; Craggs et al., 2012; Upchurch Jr. et al., 2015). Terrestrial surface temperature proxies include leaf physiognomy (e.g., the Climate Leaf Analysis Multivariate Program (CLAMP) (Wolfe,

1993)), the anatomy of fossil angiosperm wood (Francis & Poole, 2002; Poole et al., 2005), the $\delta^{18}O$ record of terrestrial vertebrate teeth (Amiot et al., 2004), and distributions of climatically sensitive sediments (Craggs et al., 2012). While discrepancies between models and proxies remain unresolved, Tabor et al. (2016) discussed that it may be inappropriate to validate GCM data with terrestrial proxies owing to the wide interannual range in terrestrial surface temperatures, as well as spatial heterogeneity that arises from local topography which is not captured in GCMs such as HadCM3L due to spatial resolution. Regardless, caution must be maintained when interpreting results of pre-Quaternary GCM experiments.

In this study, there are two main sources of error in HadCM3L model simulations, and therefore in the catchment-averaged palaeoclimate values that we derive. Firstly, there are errors with the model itself. The magnitude of these errors can be estimated by assessing the model's ability to represent modern climate, when configured with well-known modern boundary conditions (including atmospheric CO_2 and a digital elevation model (DEM)). Such a model–data comparison under modern conditions was carried out by Valdes et al. (2017). As an example, their Figure 4b shows the difference between model-simulated mean annual precipitation and observations of modern mean annual precipitation. As discussed in Valdes et al. (2017), the model has similar biases to many other models in that it overestimates precipitation in regions of topography — this is evident around the Himalayas and Tibet, and the Rockies and Andes. However, some of this error is related to negative biases in gauge stations (Adam et al., 2006). Overall, the percentage error in mean annual precipitation in North America compares favourably with other regions (Valdes et al., 2017), and we also note that our approach is least sensitive to uncertainty in catchment-averaged mean annual precipitation values (see Section 2.4.3 in Chapter 2). The second source of error is in the boundary conditions in the model. For modern climates these are known very well, but for palaeoclimates there are substantial uncertainties. For the geologic timescales addressed here (10^6–10^8 yrs), the primary uncertainties in boundary conditions are associated with the prescribed atmospheric CO_2 concentration and the DEM (i.e., the palaeoDEM). The magnitude of uncertainty associated with the DEM can be qualitatively assessed by comparing Figure 2.2c with 2.2d (Chapter 2), which shows the changes associated with a Cenomanian palaeoDEM compared with a Turonian palaeoDEM. The uncertainty associated with atmospheric CO_2 is harder to assess with only one atmospheric CO_2 concentration prescribed in the simulations presented here, but recent work by Farnsworth et al. (2019b) indicates that, in southeast Asia, palaeogeography has a much stronger control on precipitation than atmospheric CO_2.

A2 Reconstructing palaeocatchment data from palaeo-digital elevation models (palaeoDEMs) and HadCM3L general circulation model (GCM) data

PalaeoDEMs have a spatial resolution of 0.1°, whereas HadCM3L data have a spatial resolution of 2.5° latitude × 3.75° longitude. HadCM3L data are resampled to 0.1° using a bilinear resampling technique, which is suitable for continuous data. Both palaeoDEMs and HadCM3L data are in World Geodetic System (WGS) 1984 and must be projected to an equal area coordinate system to reconstruct palaeocatchment geometries. Here we use the Albers equal area conic projection for analyses, which is favoured for the North American continent by the United States Geological Survey (USGS), as distortion between two standard parallels is minimal. PalaeoDEMs possess analytically-derived sinks (see Markwick & Valdes, 2004) and are filled to create a hydrologically consistent surface prior to analysis. No threshold is applied when filling sinks — instead we use the Sink tool and construct elevation profiles to individually evaluate sinks that may not be analytically derived; in this study we determined that one sink was not analytically derived and filled this based on lack of support in literature for an intramontane basin of the size in question.

In the ArcGIS 10.5.1 hydrology toolbox, the Basin and Watershed tools may be independently used to delineate catchments. The Basin tool delineates catchments based on topographic highs in palaeoDEMs, whereas the Watershed tool delineates catchments based on the pixels that contribute to each catchment outflow point, or pour point. We use the Basins tool, which is preferred where catchment outflow points are not known, or where the study area is large. To reconstruct palaeocatchments, we create a flow direction network using a D8 algorithm and then use the Basins tool. Once palaeocatchments have been reconstructed, zonal statistics functions are used to extract catchment area and catchment maximum relief. We also use the hydrological toolbox to generate a stream network.

Once palaeocatchments have been reconstructed, some must be manually adjusted to mitigate processing errors associated with the Basins tool subdividing some palaeocatchments into a series of single-pixel catchments. At this point, palaeocatchments with no relief and/or drainage areas less than 500 km^2 are omitted; interpolation between base contours (maximum elevation, contemporary base level and minimum elevation) in palaeoDEM construction results in large low-lying areas that preserve no relief. Our investigations are therefore focused on palaeocatchments with drainage areas ≥500 km^2 (Figure A1). Palaeocatchments are then integrated with HadCM3L data and catchment-averaged palaeoclimate is reconstructed using zonal statistics functions.

We also reconstruct broad palaeodrainage networks as a visual aid, which is useful for comparison with published palaeogeographic reconstructions of ancient source-to-sink systems. The flow direction network is used to generate a flow accumulation network, and we then define a minimum threshold of 10 pixels (~1210 km^2) to generate a stream (so, not for every catchment), with stream order defined using the Strahler (1957) method.

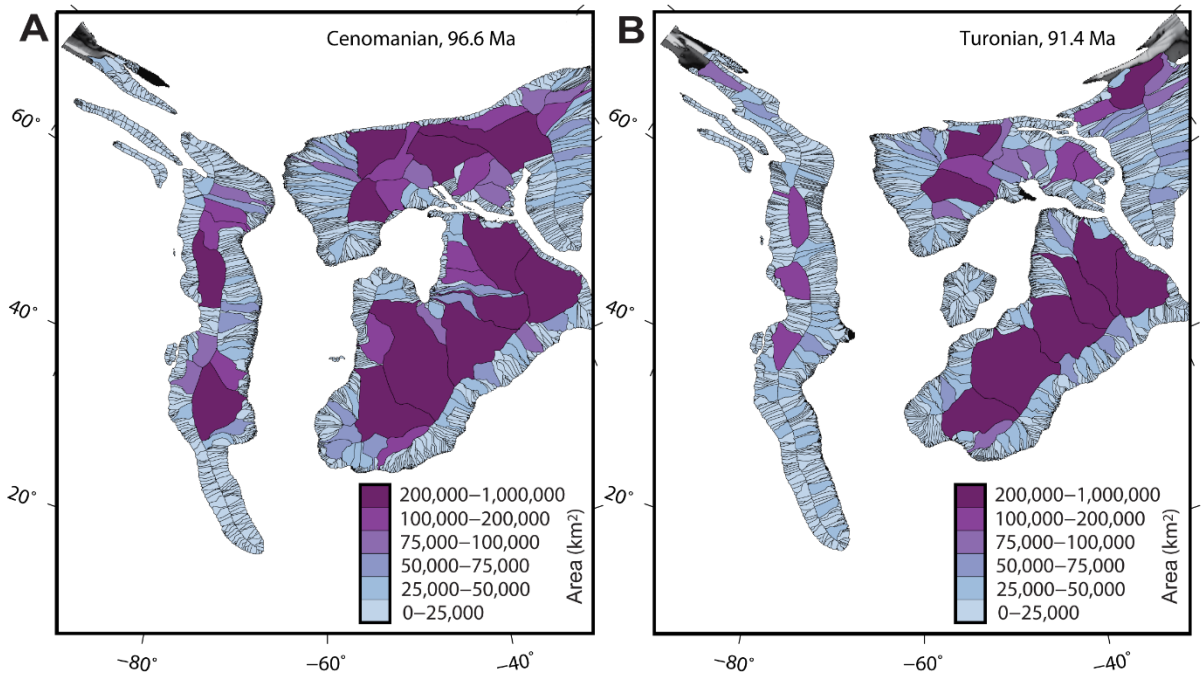

Figure A1 | Reconstructed palaeocatchments for the Cenomanian (part **A**) and Turonian (part **B**) North American continent. Palaeocatchments are colour coded by size to depict the spread of small–large palaeocatchments across the continent.

A3 Use of subsurface and surface runoff data to estimate water discharges (Q) and suspended sediment discharges (*Qs*)

Mean annual subsurface and surface runoff data are available from HadCM3L (Figure A2). However, we used mean annual precipitation to estimate water discharge, Q, at continental scales to minimise the assumptions in our BQART approach, as runoff constraints incorporate a number of further assumptions. Nevertheless, we tested the sensitivity of using mean subsurface and surface runoff data from the HadCM3L GCM to estimate Q, and subsequently suspended sediment discharge, *Qs*, as opposed to using mean annual precipitation to obtain a maximum estimate of Q. We found that using combined subsurface and surface runoff data to estimate water discharge reduces the total modelled continental *Qs* by 30% and 35%, and reduces median *Qs* by 28% and 26%, in the Cenomanian and Turonian, respectively (Figure A3; Table A1). This discrepancy is expected, as our estimates of Q are maximum estimates.

In detail, using subsurface and surface runoff to estimate water discharge reduces the 25th percentile of Q by 56% and 54% in the Cenomanian and Turonian, respectively, reduces the median by 50% and 45%, and reduces the 75th percentile by 37% and 34% (Figure A3; Table A1). These differences may seem large, however in the main text we show through univariate sensitivity that BQART-derived estimates of *Qs* are least sensitive to uncertainties associated with the data set used to estimate Q (Figure 2.7 in Chapter 2). This is also expected analytically, as shown in BQART (Equations 2.1a and 2.1b in Chapter 2). Subsequently, using subsurface and surface runoff to estimate *Qs* reduces the 25th percentile of *Qs* by 30% and 23% in the Cenomanian and Turonian, respectively, reduces the median by 28% and 26%, and reduces the 75th percentile by 11% and 18% (Figure A3; Table A1). This difference is expected, and through examination of univariate sensitivity (Figure 2.7 in Chapter 2), we show that these sorts of error margins on the data set used to estimate Q do not affect the consistency of *Qs* estimates with published *Qs* estimates.

Moreover, using subsurface and surface runoff data to estimate Q has little effect on the spatial distribution of magnitudes of *Qs*, except for at low latitudes (20–30°N) where subsurface and surface runoff estimates recover *Qs* estimates that are lower than *Qs* estimates recovered using mean annual precipitation (Figure 2.8 in Chapter 2 and Figure A4).

Going forward, we consider that subsurface and surface runoff constraints from HadCM3L could be used to estimate Q at catchment scales where runoff estimates can be corroborated by geological indicators (refer to Eide et al. (2018) for discussion of runoff in the geologic past and geological indicators indicative of arid, semi-arid, humid and wet catchments) and where contemporary bedrock lithology is known.

Table A1 | The 25th, 50th and 75th percentiles of water discharge, Q, and suspended sediment discharge, *Qs*, estimates for catchments in the Cenomanian and Turonian North American continent, using different HadCM3L general circulation model (GCM) data sets (precipitation or combined subsurface and surface runoff) to estimate water discharge.

		Water discharge, Q, m^3/s			**Suspended sediment discharge, *Qs*, m^3/yr**		
		25th	50th	75th	25th	50th	75th
Cenomanian	Precipitation	32	72	220	9,220	88,300	691,000
	Runoff	14	36	138	6,450	63,400	615,000
Turonian	Precipitation	35	85	238	9,490	91,800	549,000
	Runoff	16	47	156	7,270	68,000	449,000

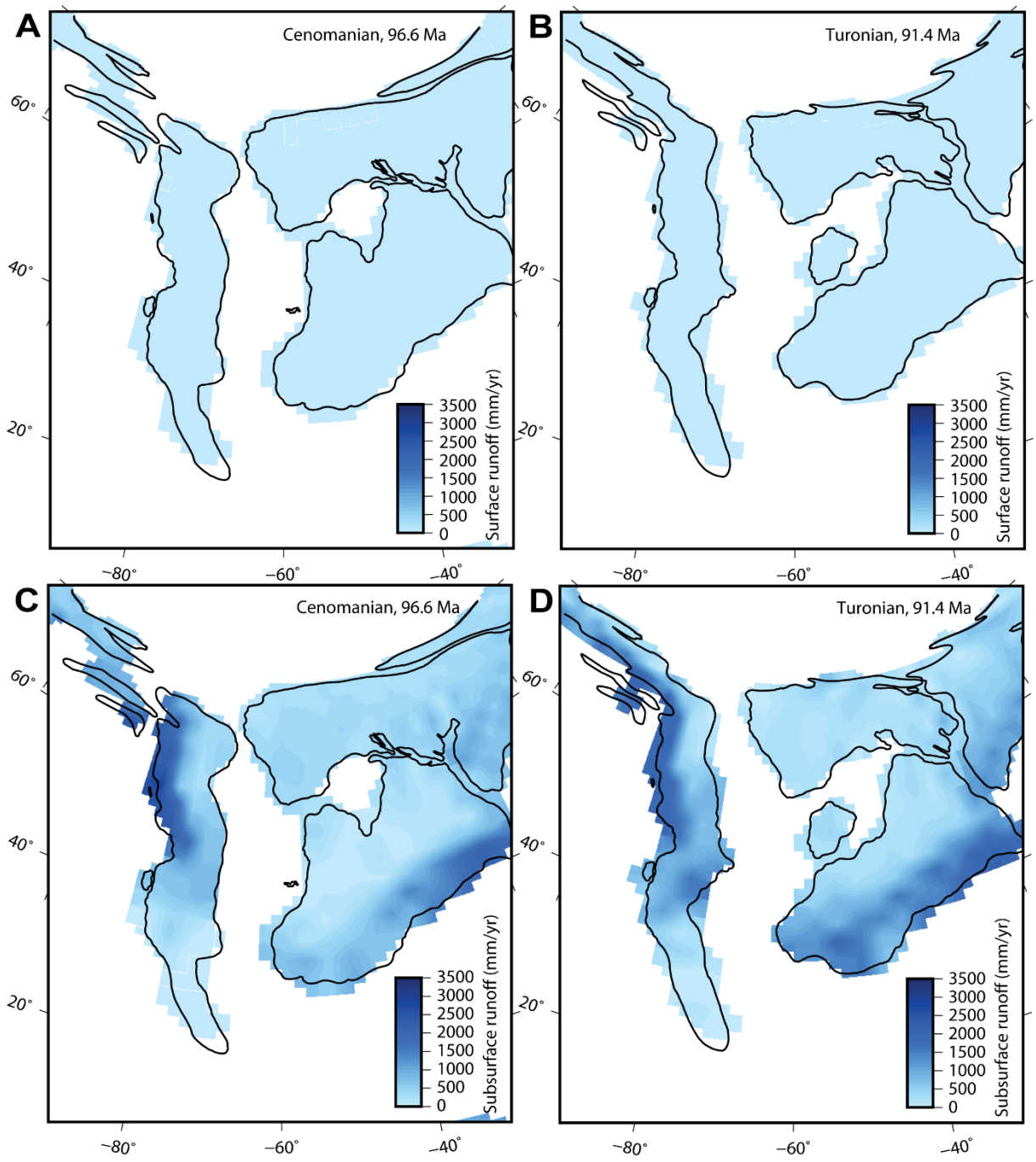

Figure A2 | Runoff data from the HadCM3L general circulation model (GCM), which include mean annual surface runoff for the Cenomanian (part **A**) and Turonian (part **B**) North American continent, and mean annual subsurface runoff for the Cenomanian (part **C**) and Turonian (part **D**) North American continent. Solid black lines illustrate (highstand) palaeoshorelines of palaeo-digital elevation models (palaeoDEMs).

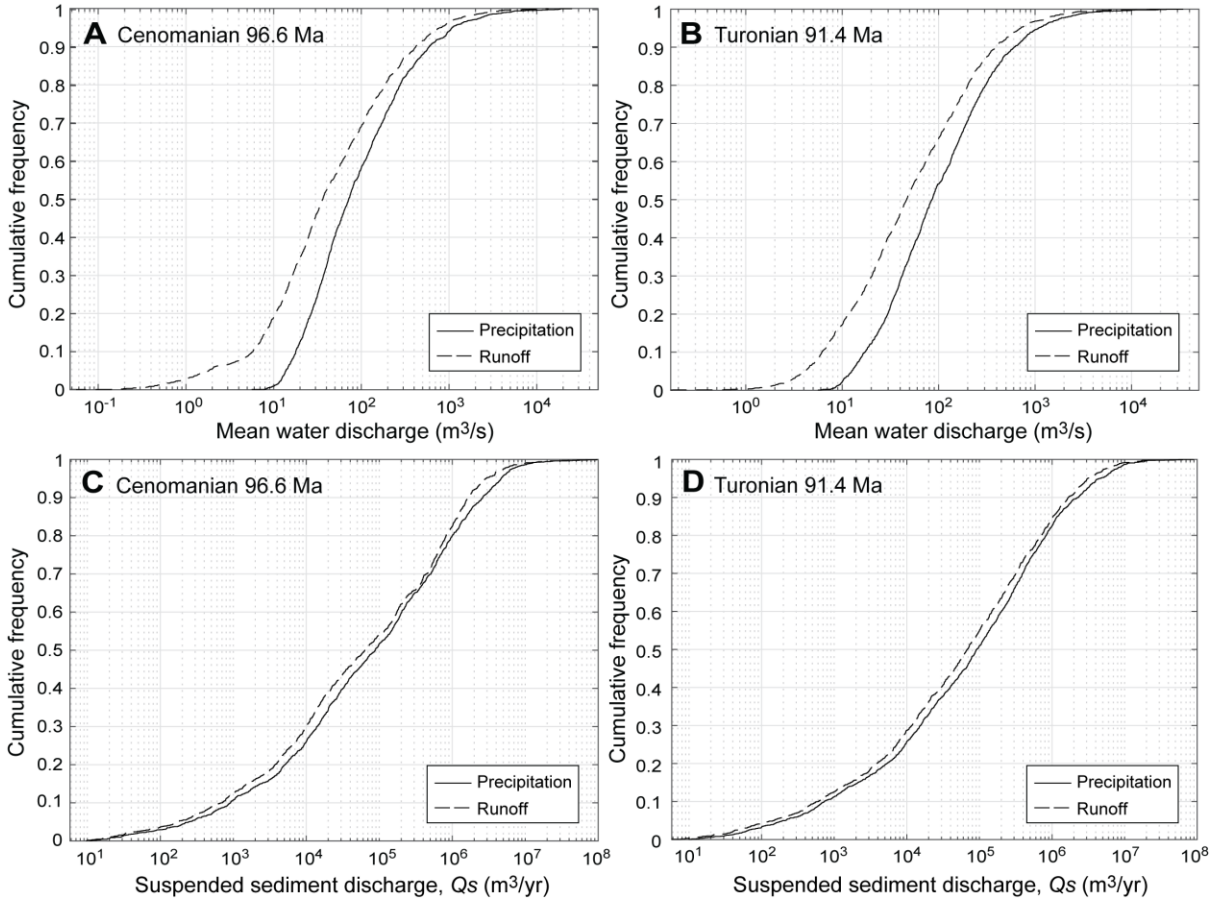

Figure A3 | Cumulative frequencies of catchments relative to their mean water discharge, Q (Cenomanian, part **A**; Turonian, part **B**), and mean annual suspended sediment discharge, *Qs* (Cenomanian, part **C**; Turonian, part **D**), when using different HadCM3L general circulation model (GCM) data sets (precipitation or combined subsurface and surface runoff) to estimate water discharge.

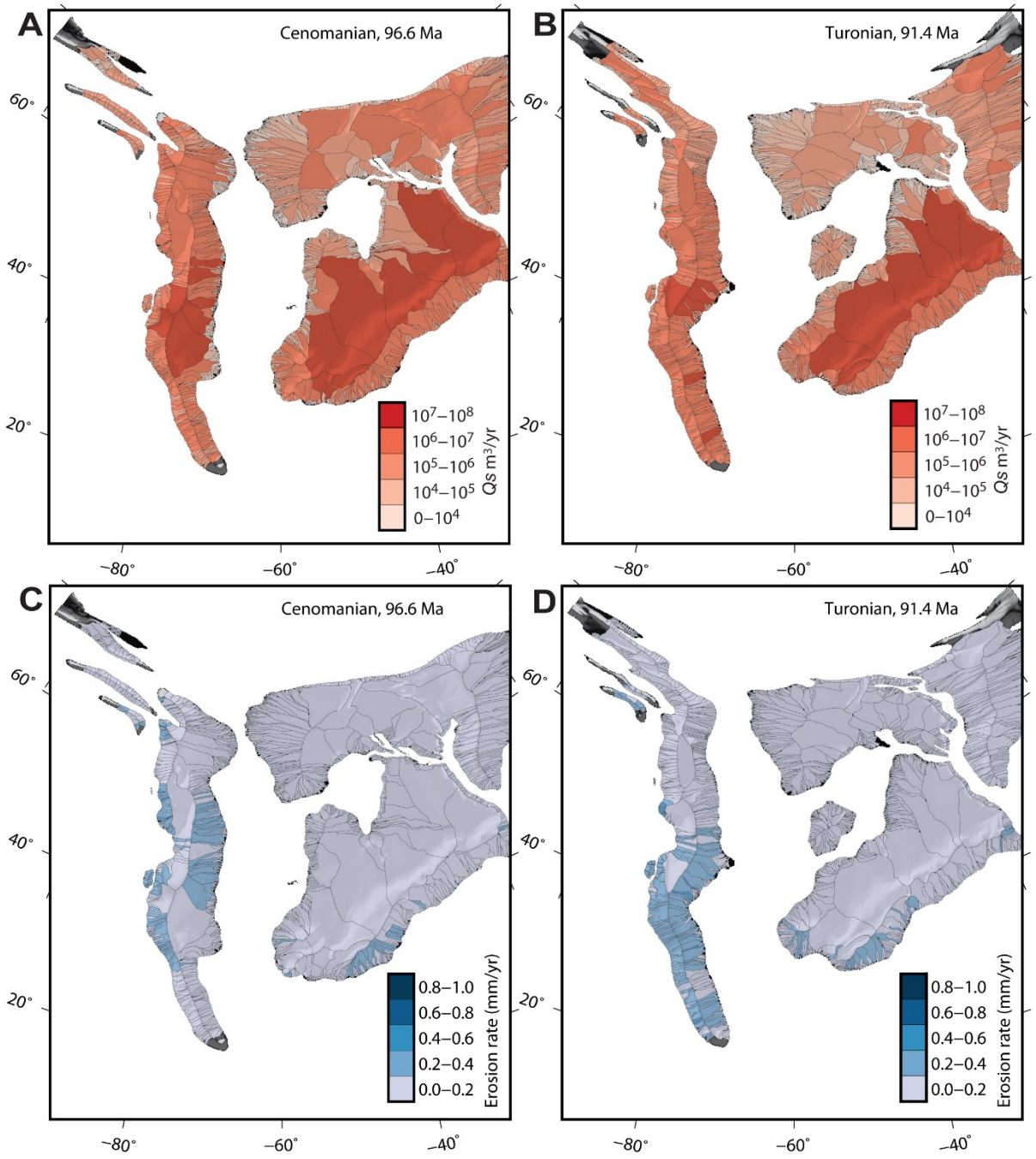

Figure A4 | Spatial distributions of suspended sediment discharges (*Qs*) that result when subsurface and surface runoff data are used to estimate water discharge for the Cenomanian (part **A**) and Turonian (part **B**) North American continent, as well as spatial distributions of catchment-averaged erosion rates for the Cenomanian (part **C**) and Turonian (part **D**) North American continent. *Qs* values are grouped by orders of magnitude whereas catchment-averaged erosion rates are grouped by equal intervals (see colour ramps). Further, *Qs* values and catchment-averaged erosion rates overlay palaeo-digital elevation model (palaeoDEM) hillshades for comparison with palaeotopography.

A4 Additional data table

Table A2 | The 25th, 50th and 75th percentiles of drainage area, maximum relief, mean annual temperature and mean annual temperature in Cenomanian North American palaeocatchments, Turonian North American palaeocatchments, and modern North American catchments, derived from smoothed ASTER and GTOPO30 digital elevation models. Note that data sets exclude Greenland.

	Drainage area (km2)			**Maximum relief (m)**			**Mean annual temperature (°C)**			**Mean annual precipitation (mm/yr)**		
	25th	50th	75th	25th	50th	75th	25th	50th	75th	25th	50th	75th
Cenomanian	1,240	2,560	6,350	59	388	2,280	5.9	11.5	19.2	617	771	1,190
Turonian	1,360	2,750	6,430	74	619	2,270	2.2	9.1	17.5	572	818	1,470
ASTER DEM	926	1,680	4,020	153	337	684	−11.3	1.8	16.3	227	687	1,260
GTOPO30 DEM	886	1,570	3,300	172	382	790	−13.7	0.0	11.6	184	602	1,230

APPENDIX B: *Supplement to* Reconstructing the morphologies and hydrodynamics of ancient rivers from source to sink: Cretaceous Western Interior Basin, Utah, USA[1]

Contents:

[1] A version of this appendix is published in ***Sedimentology*** as Supplementary Information to:

Lyster, S. J., Whittaker, A. C., Hampson, G. J., Hajek, E. A., Allison, P. A., and Lathrop, B. A. (2021) Reconstructing the morphologies and hydrodynamics of ancient rivers from source to sink: Cretaceous Western Interior Basin, Utah, USA. ***Sedimentology***, 68, 2854–2886, doi:10.1111/sed.12877

B1 Variables list

Here we present a list of all variables assigned and used in this study (see Methods section in Chapter 3):

A_x Upstream catchment area [m^2]

C_1 Constant in Equation 3.9 in Chapter 3 associated with grain sphericity and roundness [-]

C_2 Constant in Equation 3.9 in Chapter 3 associated with grain sphericity and roundness [-]

c_H Hack coefficient [-]

D_x *x*th percentile of the grain size distribution [m]

Fr Froude number [-]

g Acceleration due to gravity [m/s^2]

H Median formative flow depth [m]

h Hack exponent [m]

h_d Mean original bedform (i.e., dune) height [m]

h_{xs} Mean cross-set height [m]

k Erodibility constant [-]

k_s Steepness index [$m^{0.8}$ or m^1 or $m^{1.2}$]

L_x Upstream catchment length [m]

n Manning's constant [$s/m^{1/3}$]

Q Water discharge [m^2/s or m^3/s]

R Dimensionless submerged specific gravity of sediment in water [-]

Re_p Particle Reynold's number [-]

S Slope [-]

U Flow velocity [m/s]

u_* Bed shear velocity [m/s]

v Kinematic viscosity of water [m^2/s]

W Channel width [m]

w_s Sediment settling velocity [m/s]

Z Rouse number [-]

$\alpha 0$ Constant in Equation 3.4 in Chapter 3 [-]

$\alpha 1$ Constant in Equation 3.4 in Chapter 3 [-]

$\alpha 2$ Constant in Equation 3.4 in Chapter 3 [-]

β Eddy viscosity and diffusivity constant [-]

θ Concavity index [-]

$\varkappa$ von Karman constant [-]

λ Bedform wavelength [m]

ϱ Fluid density [kg/m^3]

τ^* Dimensionless bed shear stress, Shields stress [-]

τ_b Bed shear stress [$kg/m/s^2$]

B2 Field localities

Palaeohydrological data were collected at each field site, as described in the Methods in Chapter 3. These data centred on grain-size and cross-set measurements, but additionally included measurement of channel geometries and palaeocurrent indicators.

Field localities were grouped spatially, typically by the canyon in which they were located. From north-northeast to south-southwest, localities were grouped into five field areas along a depositional strike transect: Price Canyon, Wattis Road, Straight Canyon (including Joe's Valley Reservoir), Link Canyon and Salina Canyon (Figure B1; reproduced from Figure 3.1 in Chapter 3). These five field areas represent five parallel transverse fluvial systems draining the Sevier orogenic front. Further data were collected along 2 proximal to distal transects, to encompass an upstream to downstream element for 2 of these palaeorivers (Figure B1). The northern proximal–distal transect included field localities that were grouped as Dry Hollow, Lake Fork, Bear Canyon, and terminating at Price Canyon. Meanwhile, the southern proximal–distal transect included field localities that were grouped as Mellor Canyon, Sixmile Canyon, and terminating at Straight Canyon. These transects are in line with those implemented in previous work, both along-strike (Hampson et al., 2012; Hampson et al., 2013; Flood & Hampson, 2014, 2015; Chamberlin & Hajek, 2019) and proximal to distal (Robinson & Slingerland, 1998; Horton et al., 2004; Aschoff & Steel, 2011a, 2011b).

For each field area, localities were typically within 5 km of one another. There exist a few exceptions to this, in which localities were slightly more spread out (<10 km). These field areas were characterised by post-depositional extensional faulting and so we encompassed localities that were either along-depositional strike, or further downstream on downthrown fault blocks — when restored, it is anticipated that these field localities would have been in close proximity. All field localities are detailed in Table B1 and have been subdivided by both field area and stratigraphic interval. It is important to note that some field localities are duplicated across stratigraphic intervals — this is where data have been time-averaged across stratigraphic intervals.

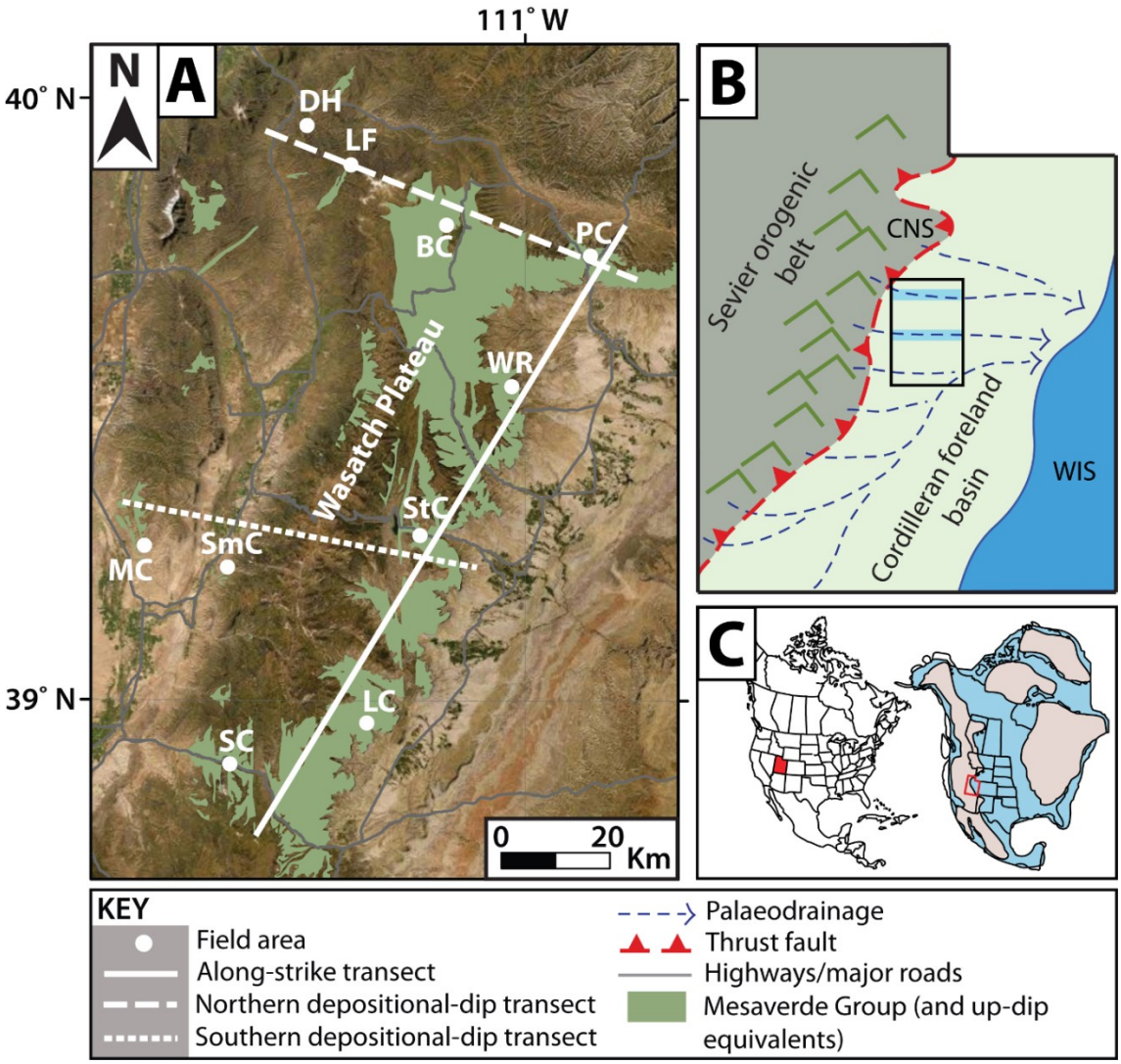

Figure B1 | Study area showing key localities mentioned in the supplement, reproduced from Figure 3.1 in Chapter 3. Part **A**) Field areas in central Utah, USA, which include Bear Canyon (BC), Dry Hollow (DH), Lake Fork (LF), Link Canyon (LC), Mellor Canyon (MC), Price Canyon (PC), Salina Canyon (SC), Sixmile Canyon (SmC), Straight Canyon (StC), and Wattis Road (WR). The solid white line indicates the along-depositional-strike transect defined in this study, the dashed white line indicates the northern proximal–distal transect defined in this study, and the dotted white line indicates the southern proximal–distal transect defined in this study. Part **B**) A conceptual diagram of Utah palaeogeography and palaeodrainage in the Campanian (Late Cretaceous). Likely configurations of drainage toward the Western Interior Seaway (WIS) are indicated by dashed blue lines. CNS = Charleston–Nebo Salient. The black outlined box indicates the study area (i.e., part **A**), and the two highlighted drainage routes (shaded blue) represent the northern and southern proximal–distal transects defined in this study (see Part **A**). Part **C**) The location of Utah relative to the modern North American continent (left) and the Late Cretaceous North American continent (right), which features the Western Interior Seaway (blue). Utah is highlighted as a red box.

Table B1 | Field localities visited in this study, for each field area (e.g., Price Canyon, Wattis Road, etc). Field localities are further subdivided into their respective stratigraphic intervals (1–7). 1 = lower Blackhawk Formation; 2 = middle Blackhawk Formation; 3 = upper Blackhawk Formation; 4 = lower Castlegate Sandstone; 5 = middle Castlegate Sandstone; 6 = upper Castlegate Sandstone; 7 = (lowermost) Price River Formation. It is important to note that some field localities are duplicated across stratigraphic intervals — this is where data have been time-averaged across stratigraphic intervals. Where 'N/A' is reported, this is the absence of data (typically due to lack of access or lack of outcrop).

Location and stratigraphic interval		**Field sites**	**Elevation, m (±3–4)**
Bear Canyon	Lower Blackhawk Formation (1)	N/A	N/A
	Middle Blackhawk Formation (2)	N39 49 53.4, W111 08 32.8	2383
		N39 46 59.3, W111 10 37.8	2325
	Upper Blackhawk Formation (3)	N39 47 31.9, W111 11 33.6	2347
		N39 47 57.4, W111 12 23.0	2373
		N39 48 04.1, W111 12 37.0	2416
		N39 48 00.5, W111 12 31.9	2371
	Lower Castlegate Sandstone (4)	N39 48 05.4, W111 12 27.5	2439
		N39 48 07.6, W111 12 35.6	2426
	Middle Castlegate Sandstone (5)	N39 50 18.2, W111 11 31.8	2263
		N39 50 10.4, W111 11 16.6	2261
	Upper Castlegate Sandstone (6)	N39 50 17.6, W111 11 42.6	2282
		N39 49 52.7, W111 08 30.5	2341
		N39 48 12.7, W111 12 33.3	2495
		N39 48 09.8, W111 12 30.1	2485
	Price River Formation (7)	N39 51 06.7, W111 11 01.7	2200
		N39 50 33.8, W111 11 17.0	2236
		N39 49 53.4, W111 08 32.8	2383
Dry Hollow	Lower Blackhawk Formation (1)	N/A	N/A
	Middle Blackhawk Formation (2)	N39 57 35.2, W111 28 42.6	1769
		N3957 35.2, W111 28 43.5	1773
	Upper Blackhawk Formation (3)	N39 57 35.2, W111 28 42.6	1769
		N3957 35.2, W111 28 43.5	1773
	Lower Castlegate Sandstone (4)	N39 57 34.8, W111 28 40.6	1764
	Middle Castlegate Sandstone (5)	N39 57 33.0, W111 23 38.0	1730
		N39 57 33.8, W111 28 37.8	1756
	Upper Castlegate Sandstone (6)	N39 57 33.0, W111 23 38.0	1730
		N39 57 33.8, W111 28 37.8	1756
	Price River Formation (7)	N/A	N/A
Lake Fork	Lower Blackhawk Formation (1)	N/A	N/A
	Middle Blackhawk Formation (2)	N/A	N/A
	Upper Blackhawk Formation (3)	N/A	N/A
	Lower Castlegate Sandstone (4)	N39 53 16.1, W111 23 49.5	2058
	Middle Castlegate Sandstone (5)	N39 53 36.6, W111 23 27.7	2063
		N39 53 29.7, W111 23 06.8	2115
	Upper Castlegate Sandstone (6)	N39 53 36.6, W111 23 27.7	2063
		N39 53 29.7, W111 23 06.8	2115
	Price River Formation (7)	N39 53 23.0, W111 22 59.1	2131

		N39 53 21.3, W111 22 57.6	2170
Link Canyon	Lower Blackhawk Formation (1)	N38 57 42.1, W111 19 57.4	2363
		N38 57 39.7, W111 19 53.9	2383
		N38 57 41.4, W111 19 53.0	2398
	Middle Blackhawk Formation (2)	N38 57 44.3, W111 19 53.8	2421
		N38 57 48.4, W111 19 53.9	2473
	Upper Blackhawk Formation (3)	N38 57 58.3, W111 19 57.3	2538
		N38 57 52.8, W111 19 55.8	2509
		N38 57 51.4, W111 19 55.0	2500
	Lower Castlegate Sandstone (4)	N38 58 05.9, W111 19 56.6	2572
	Middle Castlegate Sandstone (5)	N38 58 08.0, W111 19 55.8	2584
	Upper Castlegate Sandstone (6)	N38 58 10.6, W111 19 54.2	2600
	Price River Formation (7)	N38 58 15.8, W111 20 15.0	2643
Mellor Canyon	Lower Blackhawk Formation (1)	N39 15 07.5, W111 49 04.0	1751
		N39 15 05.2, W111 49 04.8	1732
		N39 15 03.3, W111 49 06.6	1721
		N39 15 02.3, W111 49 07.3	1715
		N39 15 00.7, W111 49 05.8	1711
		N39 15 00.0, W111 49 09.8	1701
		N39 14 59.6, W111 49 15.3	1717
		N39 14 59.8, W111 49 23.6	1691
		N39 14 58.0, W111 49 25.0	1683
	Middle Blackhawk Formation (2)	N39 15 07.5, W111 49 04.0	1751
		N39 15 05.2, W111 49 04.8	1732
		N39 15 03.3, W111 49 06.6	1721
		N39 15 02.3, W111 49 07.3	1715
		N39 15 00.7, W111 49 05.8	1711
		N39 15 00.0, W111 49 09.8	1701
		N39 14 59.6, W111 49 15.3	1717
		N39 14 59.8, W111 49 23.6	1691
		N39 14 58.0, W111 49 25.0	1683
	Upper Blackhawk Formation (3)	N39 15 07.5, W111 49 04.0	1751
		N39 15 05.2, W111 49 04.8	1732
		N39 15 03.3, W111 49 06.6	1721
		N39 15 02.3, W111 49 07.3	1715
		N39 15 00.7, W111 49 05.8	1711
		N39 15 00.0, W111 49 09.8	1701
		N39 14 59.6, W111 49 15.3	1717
		N39 14 59.8, W111 49 23.6	1691
		N39 14 58.0, W111 49 25.0	1683
	Lower Castlegate Sandstone (4)	N39 15 11.4, W111 49 00.9	1809
		N39 15 09.8, W111 49 01.6	1784
		N39 15 08.8, W111 49 01.9	1770
	Middle Castlegate Sandstone (5)	N39 15 11.4, W111 49 00.9	1809
		N39 15 09.8, W111 49 01.6	1784
		N39 15 08.8, W111 49 01.9	1770
	Upper Castlegate Sandstone (6)	N39 15 11.4, W111 49 00.9	1809
		N39 15 09.8, W111 49 01.6	1784

		N39 15 08.8, W111 49 01.9	1770
	Price River Formation (7)	N39 15 11.4, W111 49 00.9	1809
		N39 15 09.8, W111 49 01.6	1784
		N39 15 08.8, W111 49 01.9	1770
Price Canyon	Lower Blackhawk Formation (1)	N/A	N/A
	Middle Blackhawk Formation (2)	N/A	N/A
	Upper Blackhawk Formation (3)	N39 44 11.0, W110 50 47.7	1932
		N39 44 08.4, W110 50 46.9	1947
	Lower Castlegate Sandstone (4)	N39 45 05.1, W110 53 10.3	1920
		N39 44 48.5, W110 49 58.1	1969
		N39 44 52.6, W110 49 55.4	1983
	Middle Castlegate Sandstone (5)	N39 45 01.3, W110 49 43.5	2000
		N39 45 03.0, W110 49 40.6	1999
	Upper Castlegate Sandstone (6)	N39 45 10.5, W110 49 35.8	2008
		N39 45 12.0, W110 49 34.8	2003
	Price River Formation (7)	N39 46 18.3, W110 48 12.1	2115
		N39 45 58.8, W110 48 30.1	2095
		N39 45 47.1, W110 48 41.6	2044
		N39 45 32.1, W110 49 02.0	2035
Salina Canyon	Lower Blackhawk Formation (1)	N38 54 00.8, W111 39 53.8	1861
	Middle Blackhawk Formation (2)	N38 53 51.5, W111 39 02.3	1885
	Upper Blackhawk Formation (3)	N38 54 29.6, W111 41 46.8	1802
		N38 54 13.8, W111 39 05.9	1926
	Lower Castlegate Sandstone (4)	N38 54 52.9, W111 38 06.5	2036
		N38 54 52.3, W111 38 08.7	2017
	Middle Castlegate Sandstone (5)	N38 54 50.6, W111 38 18.1	2009
		N38 54 52.6, W111 38 20.2	2030
		N38 54 53.7, W111 38 ~20.2	2035
		N38 54 33.0, W111 42 32.7	1779
	Upper Castlegate Sandstone (6)	N38 54 57.1, W111 38 20.3	2076
		N38 54 59.4, W111 38 13.1	2111
	Price River Formation (7)	N38 55 04.1, W111 38 15.7	2152
Sixmile Canyon	Lower Blackhawk Formation (1)	N39 12 43.1, W111 38 55.0	1876
		N39 12 25.4, W111 39 12.5	1860
	Middle Blackhawk Formation (2)	N39 12 43.1, W111 38 55.0	1876
		N39 12 25.4, W111 39 12.5	1860
	Upper Blackhawk Formation (3)	N39 12 43.1, W111 38 55.0	1876
		N39 12 25.4, W111 39 12.5	1860
	Lower Castlegate Sandstone (4)	N39 12 51.6, W111 37 32.9	1967
		N39 12 51.6, W111 37 54.7	1931
		N39 12 44.5, W111 38 10.4	1892
		N39 12 44.9, W111 38 13.8	1923
		N39 12 49.6, W111 37 40.1	1952
	Middle Castlegate Sandstone (5)	N39 12 51.6, W111 37 32.9	1967
		N39 12 51.6, W111 37 54.7	1931
		N39 12 44.5, W111 38 10.4	1892
		N39 12 44.9, W111 38 13.8	1923
		N39 12 49.6, W111 37 40.1	1952

	Upper Castlegate Sandstone (6)	N39 12 51.6, W111 37 32.9	1967
		N39 12 51.6, W111 37 54.7	1931
		N39 12 44.5, W111 38 10.4	1892
		N39 12 44.9, W111 38 13.8	1923
		N39 12 49.6, W111 37 40.1	1952
	Price River Formation (7)	N39 12 46.4, W111 36 57.8	1995
Straight Canyon	Lower Blackhawk Formation (1)	N39 16 56.6, W111 13 58.0	2027
		N39 16 46.2, W111 13 41.9	2010
		N39 16 29.1, W111 13 11.9	1996
	Middle Blackhawk Formation (2)	N39 17 16.2, W111 14 37.5	2047
		N39 17 15.7, W111 14 30.4	2043
		N39 17 05.7, W111 14 10.5	2037
	Upper Blackhawk Formation (3)	N39 17 36.5, W111 16 16.7	2146
		N39 17 19.3, W111 16 00.0	2129
		N39 17 20.9, W111 15 19.8	2102
	Lower Castlegate Sandstone (4)	N39 17 51.9, W111 16 18.0	2161
	Middle Castlegate Sandstone (5)	N39 18 28.6, W111 16 13.2	2181
	Upper Castlegate Sandstone (6)	N39 18 55.2, W111 16 06.2	2238
	Price River Formation (7)	N/A	
Wattis Road	Lower Blackhawk Formation (1)	N39 31 45.5, W111 02 16.0	2577
	Middle Blackhawk Formation (2)	N39 31 11.9, W111 01 56.9	2692
		N39 31 19.8, W111 01 58.4	2655
	Upper Blackhawk Formation (3)	N39 31 20.7, W111 02 37.2	2798
		N39 31 14.3, W111 02 13.8	2765
	Lower Castlegate Sandstone (4)	N39 31 28.6, W111 02 44.9	2844
	Middle Castlegate Sandstone (5)	N39 31 31.7, W 111 02 50.6	2877
		N39 31 30.2, W111 02 46.4	2861
	Upper Castlegate Sandstone (6)	N39 31 33.5, W111 02 53.2	2889
	Price River Formation (7)	N/A	

B3 Regional correlation

In addition to grouping field localities in space, localities were also grouped in time. In this study 7 stratigraphic intervals were defined, which were used to reconstruct the palaeohydrological evolution of ancient rivers draining the Sevier orogenic front. These intervals are all Campanian in age, which spanned a duration of 11.5 Myr (83.6±0.2 to 72.1±0.2 Ma) in the Late Cretaceous. These 7 intervals are defined as: 1 = lower Blackhawk Formation; 2 = middle Blackhawk Formation; 3 = upper Blackhawk Formation; 4 = lower Castlegate Sandstone; 5 = middle Castlegate Sandstone; 6 = upper Castlegate Sandstone; 7 = (lowermost) Price River Formation. These intervals are referred to in the Results and in Figure 3.2 in Chapter 3. It is important to note that these stratigraphic intervals are not of equal duration — age constraints across these intervals are derived from correlation with ammonite biozones in the down-dip Mancos Shale, which have been age-constrained by radiometric dating of volcanic ash beds (Gill & Hail Jr, 1975; Fouch et al., 1983; Cobban et al., 2006) — see recent review by Seymour and Fielding (2013). The lowermost Blackhawk Formation is correlated with the *Scaphites hippocrepis II* zone (83.5±0.7–81.86±0.36 Ma), the middle Blackhawk Formation with the *Baculites obtusus* zone (80.58±0.55 Ma), and the top of the Blackhawk Formation with the *Baculites asperiformis* zone (79 Ma). The lower and middle Castlegate Sandstone are correlated with the *Baculites perplexus*, *Baculites scotti* (75.84±0.26/75.56±0.11 Ma), *Didymoceras nebrascense* and *Didymoceras stevensoni* (75.19±0.28 Ma) zones. The upper Castlegate Sandstone is correlated with the *Exiteloceras jenneyi* zone (75.08±0.11 Ma) and, finally, the Price River Formation is correlated with the *Didymoceras cheyennense* and *Baculites jenseni* zones (74.67±0.15–71.98±0.31 Ma) (Fouch et al., 1983; Cobban et al., 2006).

Distal: Eastern Wasatch Plateau

Along the eastern front of the Wasatch Plateau (Figure B1), it is straightforward to assign field localities to their appropriate stratigraphic intervals by facies associations, following extensive work that has been undertaken in this region (Lawton, 1983, 1986b; Miall, 1994; van Wagoner, 1995; Yoshida et al., 1996; Miall & Arush, 2001; Lawton et al., 2003; Adams & Bhattacharya, 2005; Hampson et al., 2012; Hampson et al., 2013; Flood & Hampson, 2014; Hampson et al., 2014; Flood & Hampson, 2015).

The lower–middle Campanian Blackhawk Formation, (Hampson, 2010; Hampson et al., 2012) represents deposition on coastal plains behind wave-dominated deltaic shorelines which, up-section, pass landward into alluvial and fluvial plains (Hampson et al., 2012; Hampson et al., 2013). The size and abundance of channelized fluvial sandstone bodies (deposited by both single- and multi-thread rivers) increase from base to top of the Blackhawk Formation (Adams & Bhattacharya, 2005; Hampson et al., 2012; Hampson et al., 2013; Flood & Hampson, 2015). The Blackhawk Formation comprises intervals 1, 2 and 3 in this study, i.e., the lower, middle, and upper Blackhawk Formation. The Blackhawk Formation is slightly challenging to subdivide into stratigraphic intervals as it is typically undifferentiated along the eastern Wasatch Plateau front (with the exception of Price Canyon) (Hampson et al., 2012; Hampson et al., 2013) — this is, in part,

because the upper half of the Blackhawk Formation lacks mappable coal zones or other stratigraphic markers along the Wasatch Plateau front (Hampson et al., 2012; Hampson et al., 2013). This study follows Flood and Hampson (2014, 2015) in subdividing the Blackhawk Formation into the lower, middle, and upper Blackhawk Formation. While these divisions may not be exact, given variation in outcrop exposure at Price Canyon, Wattis Road, Straight Canyon, Link Canyon and Salina Canyon, as well as north–south variation in stratigraphic thickness, they are appropriate for the temporal and spatial scales considered here. At Price Canyon, only the Desert Member of the Blackhawk Formation is fluvial, and so data were only collected from this member, which were then assigned to the upper Blackhawk Formation stratigraphic interval. For Wattis Road, Straight Canyon, Link Canyon, and Salina Canyon, field localities were assigned to the lower, middle and upper Blackhawk Formation, following Hampson et al. (2012); Hampson et al. (2013); Flood and Hampson (2014, 2015), based on (1) adjacency to the contact with the overlying Castlegate Sandstone or underlying Star Point Sandstone; (2) where the outcrop was positioned, stratigraphically, within the entire stratigraphic thickness of the Blackhawk Formation at the field area in question; (3) architectural and facies observations — up-section the Blackhawk Formation is more palaeo-landward and preserves an increase in the size and abundance of channelized fluvial sandstone bodies; (4) presence and abundance of coal zones, which are associated with the lower and middle Blackhawk Formation, but are most abundant in the lower Blackhawk Formation (Flood & Hampson, 2014, 2015).

The middle–upper Campanian Castlegate Sandstone is situated atop the Blackhawk Formation and is an extensive and easily recognisable cliff-forming deposit — the basal contact separates braided fluvial deposits from underlying coastal plain deposits of the Blackhawk Formation (van Wagoner, 1995; Yoshida et al., 1996). In this study the Castlegate Sandstone comprises intervals 4, 5 and 6, i.e., the lower, middle, and upper Castlegate Sandstone respectively. The lower and upper Castlegate Sandstone both comprise amalgamated braided fluvial channel-belt deposits, whereas the middle Castlegate Sandstone comprises less amalgamated, more meandering, fluvial channel-belt deposits with interbedded mudstones (Fouch et al., 1983; Lawton, 1986b; Miall, 1994; Yoshida et al., 1996; Miall & Arush, 2001).

The ledge-forming upper Campanian Price River Formation conformably overlies the Castlegate Sandstone and is interval 7 in this study. It is recognised by transition from amalgamated fluvial channel-belt deposits of the upper Castlegate Sandstone to large channelized sandstone bodies (~10–30m thick) with interbedded siltstones and mudstones — channelized sandstone bodies form ~75% of the formation (Lawton, 1983, 1986b). This transition is also recognised by a break in slope. Data were collected for channelized sandstone bodies of the lowermost Price River Formation (where accessible) atop the contact with the underlying upper Castlegate Sandstone.

Proximal: Western Wasatch Plateau

Importantly, in this study data were additionally collected along 2 proximal to distal transects, to capture upstream to downstream trends for 2 of the 5 transverse fluvial systems. This requires correlation of the 7

aforementioned stratigraphic intervals (along the eastern Wasatch Plateau front) with more proximal strata on the western and central Wasatch Plateau. Proximal field sites along the northern proximal–distal transect include Dry Hollow, Lake Fork, and Bear Canyon, meanwhile proximal field sites along the southern proximal–distal transect include Mellor Canyon and Sixmile Canyon. These proximal–distal transects follow those of Robinson and Slingerland (1998) and Horton et al. (2004). Bear Canyon can be excluded from subsequent considerations as it has been mapped using Blackhawk–Castlegate–Price River nomenclature.

At upstream field sites, on the western Wasatch Plateau, correlative strata include more proximal sediments of the Indianola Group and Price River Formation, which is now known to not be time-equivalent with the down-dip Price River Formation exposed near Price, Utah (Robinson & Slingerland, 1998; Horton et al., 2004; Aschoff & Steel, 2011a, 2011b). Here, to avoid confusion, these upstream strata are referred to as the Price River Conglomerate, following Aschoff and Steel (2011a, 2011b). It should be noted that the Price River Conglomerate has elsewhere been referred to as the Conglomerate of Thistle (Valora, 2010). The detail of upstream correlations is limited by poor exposure on the Wasatch Plateau and difficulty in dating conglomerates. Nevertheless, work by Robinson and Slingerland (1998) successfully used palynology to establish correlation of the lower Castlegate Sandstone with more proximal conglomerates exposed across a variety of localities on the Wasatch Plateau (Figure 3.2 in Chapter 3). Correlations were corroborated by field observations, e.g., correlation of a white, quartzite-dominated, cobble–boulder conglomerate in the Charleston–Nebo Salient of the Sevier thrust belt with the Castlegate–Price River succession in the Book Cliffs to the east, which can be traced in seismic reflection data (Robinson & Slingerland, 1998; Horton et al., 2004). These works were used in the field to establish correlations.

The proximal upper Sixmile Canyon Formation of the Indianola Group is predominantly characterised by synorogenic gravel–sand fluvial facies, spanning polymictic fluvial conglomerates to medium–coarse-grained sandstones (Lawton, 1982, 1986a, 1986b). The upper Sixmile Canyon Formation is time-correlative with the Blackhawk Formation (Lawton, 1982; Fouch et al., 1983; Lawton, 1986b), and therefore encompasses intervals 1, 2, and 3 in this study (Chapter 3). Meanwhile, the proximal Price River Conglomerate is characterised by quartzite-dominated synorogenic fanglomerates wherein debris flow facies interact with gravel–sand fluvial facies (Robinson & Slingerland, 1998; Aschoff & Steel, 2011a, 2011b). The Price River Conglomerate is time-correlative with the more distal lower, middle, and upper Castlegate Sandstone, and Price River Formation (Robinson & Slingerland, 1998; Horton et al., 2004), and therefore encompasses intervals 4, 5, 6 and 7 in this study (Chapter 3).

Given uncertainties in age constraints, a conservative approach to correlation is taken in this study (Chapter 3). Upstream, at Dry Hollow, Lake Fork, Mellor Canyon, and Sixmile Canyon, the upper Sixmile Canyon Formation of the Indianola Group (intervals 1–3) is time-averaged, and the entire Price River Conglomerate (intervals 4–7) is also time-averaged. It can be said that, upstream, time-averaging across intervals 1–3 and 4–7, respectively, may lead to loss of temporal signal. However, exceptions were made to time-averaging where field localities were known to be situated at the top of the upper Sixmile Canyon Formation or at

the top/base of the Price River Conglomerate. Currently, it is not possible to generate time-correlations at higher resolution. Nevertheless, the observation was made that within the upper Sixmile Canyon Formation and Price River Conglomerate, respectively, median grain-sizes and mean cross-set heights for each grain-size facies were generally similar throughout sections. The main impact of time-averaging across sections was therefore that our results do not account for how the proportions of different grain-size facies change up-section.

In the northern transect, for proximal field areas of Dry Hollow and Lake Fork, assignment of field localities to their appropriate stratigraphic intervals (as per the previous paragraph) is simple as regional mapping has differentiated the Indianola Group into its respective members, including the Sixmile Canyon Formation, and has also mapped the Price River Conglomerate (though it is mapped with its alternative name, i.e., Conglomerate of Thistle). However, in the southern transect, for proximal field areas of Mellor Canyon and Sixmile Canyon, assignment is less simple as regional mapping is older and predates recent advances in regional correlation (c.f. Robinson & Slingerland, 1998; Horton et al., 2004; Aschoff & Steel, 2011a, 2011b). In Sixmile Canyon, the Indianola Group is differentiated into its respective members. However, what would be Price River Conglomerate has here been mapped as the Price River Formation — but it is now known that the proximal Price River Formation on the western Wasatch Plateau is time-correlative with *both* the Castlegate Sandstone and Price River Formation on the eastern Wasatch Plateau (Robinson & Slingerland, 1998; Horton et al., 2004; Aschoff & Steel, 2011a, 2011b). This is taken into account accordingly and considered to be Price River Conglomerate. Secondly, in Mellor Canyon, the entire stratigraphy is undifferentiated — it is all mapped as undifferentiated Indianola Group sediments and is capped unconformably by the North Horn Formation. As such, in this study the stratigraphy in Mellor Canyon was newly logged so that stratigraphy could be appropriately assigned, (expanding on work by Robinson and Slingerland, 1998) (Figure B2). Observations of more proximal sediments in the northern proximal–distal transect (i.e., at Dry Hollow) were extrapolated to Mellor Canyon. These included observations that the Price River Conglomerate is characterised by quartzite-dominated synorogenic fanglomerates wherein debris flow facies interact with gravel–sand fluvial facies (Robinson & Slingerland, 1998; Aschoff & Steel, 2011a, 2011b), and the upper Sixmile Canyon Formation of the Indianola Group is predominantly characterised by synorogenic gravel–sand fluvial facies spanning polymictic conglomerates to medium–coarse-grained sands (Lawton, 1982, 1986a, 1986b). In logging the Mellor Canyon section, quartzite-dominated debris fanglomerates with interspersed gravel–sand channelized bodies were successfully identified, and then classified as Price River Conglomerate (Figure B2). In addition, the more polymictic fluvial conglomerates and channelized sandstone bodies, which can be likened to the upper Sixmile Canyon Formation, were also successfully identified (Figure B2). It is unclear whether logged strata encompass the entire Sixmile Canyon Formation, or just the uppermost Sixmile Canyon Formation. However, the entire Sixmile Canyon Formation at Sixmile Canyon has a stratigraphic thickness of over 1.2 km, whereas at Mellor Canyon our logging is for the uppermost 240 m of Sixmile Canyon Formation — it is therefore reasonable to assign these sediments to the upper Sixmile Canyon Formation (Figure B2).

[APPENDIX FIGURE B2 ATTACHED AT END OF APPENDIX B]

Figure B2 | Measured section through the Sixmile Canyon Formation (Indianola Group) and (extrapolated) Price River Conglomerate at Mellor Canyon.

B4 Field data

Palaeohydrologic field data collection was primarily focused on grain-size and cross-set measurements but, as mentioned, additionally included measurement of channel geometries and palaeocurrent indicators. In this section raw field data are presented for grain-size measurements (Table B2) and cross-set measurements (Table B3), as these are the data that we propagate through our quantitative palaeohydrologic framework to reconstruct various palaeohydrologic parameters (see Methods in Chapter 3). Data are tabulated and subdivided by field area and stratigraphic interval. First, extended information pertaining to grain-size data collection is presented.

Grain-Size

At each field site, the coarse-fraction (>2 mm in diameter) and sand-fraction (<2 mm in diameter) grain-size of channel-fill deposits was established (Figure 3.3a,b in Chapter 3). For coarse-fractions (>2 mm), grain-size distributions were measured via Wolman point counts (Wolman, 1954). For each count, 100 clasts were randomly selected across a 1 m^2 area of exposed outcrop (or 2 m^2, where grain-size was boulder-grade) and the long axis was measured (Figure 3.3a). The long axis was measured as opposed to the intermediate axis because: (1) it is objectively easier, and more efficient, to identify and consistently measure the long axis (Brooke et al., 2018; Watkins et al., 2020); (2) the ratio between the long and intermediate axis is broadly constant in fluvial gravels, near 0.7 (e.g., Litty & Schlunegger, 2017; Litty et al., 2017); (3) any measured axis is an apparent axis given the arbitrary orientation of the outcrop exposure, so it is therefore consistent and easiest to measure the longest observed. For sand-fractions (<2 mm), scaled photographs were instead processed in *ImageJ* software and the long axis of 50 randomly selected grains were similarly measured (Figure 3.3b) (where sand-fractions were poorly sorted 100 clasts were counted for certainty). Grain-size distributions were then used to establish the median grain size, D_{50}, and 84th percentile, D_{84}. Finally, where grain-size facies in channel-fill deposits were disparate, e.g., gravel topped with sand, data were collected for each grain-size facies and the proportions of each facies were estimated (Figure 3.3c).

To recover spatio-temporal grain-size distribution trends along several time-averaged stratigraphic intervals, it was crucial that representative time-averaged data were collected. Not only were grain-size data collected for each grain-size facies (Figure 3.3a–c), depending on overall outcrop extent Wolman point counts were also repeated and/or additional scaled photographs were taken for *ImageJ* processing at intermittent stratigraphic intervals (e.g., one count per 5–10 m of strata or per channelized body). The extent of each field site can be approximated as the extent of outcrop apparent in Figure 3.3c–h. From these data an average sand-fraction grain size and an average gravel-fraction grain size was produced for each field site. As each space–time interval includes multiple field sites, this results in multiple average sand- and gravel-fraction grain-sizes per interval, encompassing channel-fill deposits from several channelized bodies. Finally, weighted, bulk-grain size distribution was produced for each space–time interval using the gravel- vs sand-fraction weightings at each field site — each field site within a space–time interval was assigned

equal weighting. For example, say data were collected from two field sites for one space–time interval. If one of these sites was 100% sand-grade, and the second site was 80% sand-grade and 20% gravel-grade, then the bulk grain-size for that space–time interval would be calculated as follows: 50% would be the average sand-fraction grain size at Site 1, 40% would be the average sand-fraction grain-size at Site 2, and 10% would be the average gravel-fraction grain-size at Site 2.

Table B2 | Grain-size data collected and used in this study. Bulk grain-sizes include both the sand fraction grain-size and the gravel fraction grain-size, which are weighted according to their respective facies proportions. Gravel fraction grain-sizes solely represent the gravel fraction. Where 'N/A' is reported, this is the absence of data (due to lack of access) or, in the case of gravel fraction grain-sizes, absence of a gravel fraction in the exposed outcrop. D_{50} and D_{84} represent the median and 84th percentile of grain-size, respectively. Grain-size data are reported for each field location, through stratigraphic intervals 1–7: 1 = lower Blackhawk Formation; 2 = middle Blackhawk Formation; 3 = upper Blackhawk Formation; 4 = lower Castlegate Sandstone; 5 = middle Castlegate Sandstone; 6 = upper Castlegate Sandstone; 7 = (lowermost) Price River Formation.

Location and stratigraphic interval		**Bulk grain-size**		**Gravel fraction grain-size**	
		D_{50} (mm)	D_{84} (mm)	D_{50} (mm)	D_{84} (mm)
Bear Canyon	Lower Blackhawk Formation (1)	N/A	N/A	N/A	N/A
	Middle Blackhawk Formation (2)	0.24	0.38	N/A	N/A
	Upper Blackhawk Formation (3)	0.22	0.30	N/A	N/A
	Lower Castlegate Sandstone (4)	0.26	0.36	N/A	N/A
	Middle Castlegate Sandstone (5)	0.19	0.26	74.92	166.21
	Upper Castlegate Sandstone (6)	0.34	5.00	10.00	15.00
	Price River Formation (7)	0.39	3.00	10.00	20.00
Dry Hollow	Lower Blackhawk Formation (1)	N/A	N/A	N/A	N/A
	Middle Blackhawk Formation (2)	35.00	65.00	35.00	65.00
	Upper Blackhawk Formation (3)	35.00	65.00	35.00	65.00
	Lower Castlegate Sandstone (4)	65.00	126.5	65.00	126.5
	Middle Castlegate Sandstone (5)	67.00	147.5	80.00	179.00
	Upper Castlegate Sandstone (6)	67.00	147.5	80.00	179.00
	Price River Formation (7)	N/A	N/A	N/A	N/A
Lake Fork	Lower Blackhawk Formation (1)	N/A	N/A	N/A	N/A
	Middle Blackhawk Formation (2)	N/A	N/A	N/A	N/A
	Upper Blackhawk Formation (3)	N/A	N/A	N/A	N/A
	Lower Castlegate Sandstone (4)	30.00	50.00	30.00	50.00
	Middle Castlegate Sandstone (5)	30.00	60.00	30.00	63.00
	Upper Castlegate Sandstone (6)	30.00	60.00	30.00	63.00
	Price River Formation (7)	13.00	46.50	32.00	60.00
Link Canyon	Lower Blackhawk Formation (1)	0.31	0.43	N/A	N/A
	Middle Blackhawk Formation (2)	0.30	0.56	N/A	N/A
	Upper Blackhawk Formation (3)	0.27	0.40	N/A	N/A
	Lower Castlegate Sandstone (4)	0.62	1.55	5.00	9.00
	Middle Castlegate Sandstone (5)	0.27	0.42	N/A	N/A
	Upper Castlegate Sandstone (6)	0.25	0.31	N/A	N/A
	Price River Formation (7)	0.14	0.18	N/A	N/A
Mellor Canyon	Lower Blackhawk Formation (1)	10.00	30.00	20.00	36.00
	Middle Blackhawk Formation (2)	10.00	30.00	20.00	36.00
	Upper Blackhawk Formation (3)	10.00	30.00	20.00	36.00
	Lower Castlegate Sandstone (4)	24.00	52.00	34.00	65.00
	Middle Castlegate Sandstone (5)	24.00	52.00	34.00	65.00
	Upper Castlegate Sandstone (6)	24.00	52.00	34.00	65.00
	Price River Formation (7)	24.00	52.00	34.00	65.00

Price Canyon	Lower Blackhawk Formation (1)	N/A	N/A	N/A	N/A
	Middle Blackhawk Formation (2)	N/A	N/A	N/A	N/A
	Upper Blackhawk Formation (3)	0.27	0.40	N/A	N/A
	Lower Castlegate Sandstone (4)	0.18	0.25	13.00	30.00
	Middle Castlegate Sandstone (5)	0.17	0.21	N/A	N/A
	Upper Castlegate Sandstone (6)	0.26	0.39	N/A	N/A
	Price River Formation (7)	0.32	0.72	6.00	11.00
Salina Canyon	Lower Blackhawk Formation (1)	0.13	0.17	N/A	N/A
	Middle Blackhawk Formation (2)	0.49	0.67	N/A	N/A
	Upper Blackhawk Formation (3)	0.39	0.58	3.94	7.00
	Lower Castlegate Sandstone (4)	0.48	1.03	6.00	10.00
	Middle Castlegate Sandstone (5)	0.28	0.71	6.00	14.00
	Upper Castlegate Sandstone (6)	0.32	0.41	N/A	N/A
	Price River Formation (7)	0.31	0.38	N/A	N/A
Sixmile Canyon	Lower Blackhawk Formation (1)	0.29	0.68	22.00	40.00
	Middle Blackhawk Formation (2)	0.29	0.68	22.00	40.00
	Upper Blackhawk Formation (3)	0.29	0.68	22.00	40.00
	Lower Castlegate Sandstone (4)	0.81	15.00	18.00	35.00
	Middle Castlegate Sandstone (5)	0.81	15.00	18.00	35.00
	Upper Castlegate Sandstone (6)	0.81	15.00	18.00	35.00
	Price River Formation (7)	0.43	5.00	8.00	15.00
Straight Canyon	Lower Blackhawk Formation (1)	0.37	0.48	N/A	N/A
	Middle Blackhawk Formation (2)	0.24	0.32	N/A	N/A
	Upper Blackhawk Formation (3)	0.23	0.32	N/A	N/A
	Lower Castlegate Sandstone (4)	0.64	0.97	N/A	N/A
	Middle Castlegate Sandstone (5)	0.46	11.00	10.00	23.00
	Upper Castlegate Sandstone (6)	0.34	0.52	6.00	10.00
	Price River Formation (7)	N/A	N/A	N/A	N/A
Wattis Road	Lower Blackhawk Formation (1)	0.24	0.28	N/A	N/A
	Middle Blackhawk Formation (2)	0.26	0.30	N/A	N/A
	Upper Blackhawk Formation (3)	0.29	0.36	N/A	N/A
	Lower Castlegate Sandstone (4)	0.39	0.49	N/A	N/A
	Middle Castlegate Sandstone (5)	0.26	0.35	N/A	N/A
	Upper Castlegate Sandstone (6)	0.24	0.30	N/A	N/A
	Price River Formation (7)	N/A	N/A	N/A	N/A

Table B3 | Cross-set data collected and used in this study. Mean cross-set heights are estimated from mean maximum cross-set heights (see Methods). Where 'N/A' is reported, this is the absence of data (due to lack of access) or, rarely, absence of cross-sets. Cross-set data are reported for each field location, through stratigraphic intervals 1–7: 1 = lower Blackhawk Formation; 2 = middle Blackhawk Formation; 3 = upper Blackhawk Formation; 4 = lower Castlegate Sandstone; 5 = middle Castlegate Sandstone; 6 = upper Castlegate Sandstone; 7 = (lowermost) Price River Formation.

Location and stratigraphic interval		**Mean maximum cross-set height (m)**	**Predicted mean cross-set height (m)**	**Standard error on predicted mean cross-set height (m)**	**Number of cross-sets measured**
Bear Canyon	Lower Blackhawk Formation (1)	N/A	N/A	N/A	N/A
	Middle Blackhawk Formation (2)	0.19	0.13	0.0039	123
	Upper Blackhawk Formation (3)	0.11	0.08	0.0012	117
	Lower Castlegate Sandstone (4)	0.13	0.09	0.0026	47
	Middle Castlegate Sandstone (5)	0.19	0.13	0.0091	28
	Upper Castlegate Sandstone (6)	0.23	0.16	0.0046	244
	Price River Formation (7)	0.18	0.13	0.0041	105
Dry Hollow	Lower Blackhawk Formation (1)	N/A	N/A	N/A	N/A
	Middle Blackhawk Formation (2)	N/A	N/A	N/A	N/A
	Upper Blackhawk Formation (3)	N/A	N/A	N/A	N/A
	Lower Castlegate Sandstone (4)	N/A	N/A	N/A	N/A
	Middle Castlegate Sandstone (5)	N/A	N/A	N/A	N/A
	Upper Castlegate Sandstone (6)	N/A	N/A	N/A	N/A
	Price River Formation (7)	N/A	N/A	N/A	N/A
Lake Fork	Lower Blackhawk Formation (1)	N/A	N/A	N/A	N/A
	Middle Blackhawk Formation (2)	N/A	N/A	N/A	N/A
	Upper Blackhawk Formation (3)	N/A	N/A	N/A	N/A
	Lower Castlegate Sandstone (4)	0.18	0.13	0.0250	2
	Middle Castlegate Sandstone (5)	0.12	0.08	0.0090	13
	Upper Castlegate Sandstone (6)	0.12	0.08	0.0090	13
	Price River Formation (7)	0.10	0.07	0.0089	8
Link Canyon	Lower Blackhawk Formation (1)	0.19	0.13	0.0046	94
	Middle Blackhawk Formation (2)	0.21	0.15	0.0112	54
	Upper Blackhawk Formation (3)	0.24	0.17	0.0064	83
	Lower Castlegate Sandstone (4)	0.24	0.17	0.0115	50
	Middle Castlegate Sandstone (5)	0.19	0.13	0.0061	56
	Upper Castlegate Sandstone (6)	0.22	0.15	0.0046	67
	Price River Formation (7)	0.22	0.15	0.0060	26
Mellor Canyon	Lower Blackhawk Formation (1)	0.17	0.12	0.0041	206
	Middle Blackhawk Formation (2)	0.17	0.12	0.0041	206
	Upper Blackhawk Formation (3)	0.17	0.12	0.0041	206
	Lower Castlegate Sandstone (4)	0.11	0.08	0.0028	62
	Middle Castlegate Sandstone (5)	0.11	0.08	0.0028	62
	Upper Castlegate Sandstone (6)	0.11	0.08	0.0028	62
	Price River Formation (7)	0.11	0.08	0.0028	62

Price Canyon	Lower Blackhawk Formation (1)	N/A	N/A	N/A	N/A
	Middle Blackhawk Formation (2)	N/A	N/A	N/A	N/A
	Upper Blackhawk Formation (3)	0.18	0.13	0.0053	104
	Lower Castlegate Sandstone (4)	0.16	0.12	0.0032	77
	Middle Castlegate Sandstone (5)	0.16	0.12	0.0032	58
	Upper Castlegate Sandstone (6)	0.18	0.13	0.0046	62
	Price River Formation (7)	0.29	0.20	0.0056	146
Salina Canyon	Lower Blackhawk Formation (1)	0.20	0.14	0.0046	34
	Middle Blackhawk Formation (2)	0.21	0.15	0.0046	21
	Upper Blackhawk Formation (3)	0.23	0.16	0.0054	77
	Lower Castlegate Sandstone (4)	0.22	0.15	0.0056	57
	Middle Castlegate Sandstone (5)	0.18	0.12	0.0033	140
	Upper Castlegate Sandstone (6)	0.16	0.11	0.0030	106
	Price River Formation (7)	0.24	0.17	0.0072	41
Sixmile Canyon	Lower Blackhawk Formation (1)	0.35	0.25	0.0201	40
	Middle Blackhawk Formation (2)	0.35	0.25	0.0201	40
	Upper Blackhawk Formation (3)	0.35	0.25	0.0201	40
	Lower Castlegate Sandstone (4)	0.33	0.23	0.0185	76
	Middle Castlegate Sandstone (5)	0.33	0.23	0.0185	76
	Upper Castlegate Sandstone (6)	0.33	0.23	0.0185	76
	Price River Formation (7)	0.18	0.13	0.0047	37
Straight Canyon	Lower Blackhawk Formation (1)	0.25	0.18	0.0036	116
	Middle Blackhawk Formation (2)	0.20	0.14	0.0037	69
	Upper Blackhawk Formation (3)	0.19	0.13	0.0021	84
	Lower Castlegate Sandstone (4)	0.18	0.13	0.0031	52
	Middle Castlegate Sandstone (5)	0.16	0.11	0.0028	49
	Upper Castlegate Sandstone (6)	0.23	0.16	0.0037	107
	Price River Formation (7)	N/A	N/A	N/A	N/A
Wattis Road	Lower Blackhawk Formation (1)	0.17	0.12	0.0028	40
	Middle Blackhawk Formation (2)	0.18	0.12	0.0030	49
	Upper Blackhawk Formation (3)	0.18	0.12	0.0024	61
	Lower Castlegate Sandstone (4)	0.18	0.12	0.0034	33
	Middle Castlegate Sandstone (5)	0.16	0.11	0.0025	60
	Upper Castlegate Sandstone (6)	0.18	0.12	0.0037	29
	Price River Formation (7)	N/A	N/A	N/A	N/A

B5 Grain-size sample sufficiency

Ancillary data collection was conducted to test whether grain-size sample size was sufficient. These tests determined that counts of 100 and 50 clasts for coarse-fractions and sand-fractions, respectively, successfully recovered stable D_{50} estimates.

To check whether sample size in grain-size counts is sufficient, the iterative D_{50} was calculated to determine the number of counts required to produce stable estimates of D_{50} for each grain-size fraction (Figures B3, B4). D_{50} estimates were considered to be stable when the iterative D_{50} fluctuates within ~10 mm for boulder- and cobble-grade sediments, within ~2–3 mm for pebble-grade sediments and within ~0.1 mm for sand-grade sediments. Iterative estimates of D_{50} suggest that, for coarse-fractions, <80−90 clast counts are sufficient to converge towards the median (Figures B3, B4), whereas for sand-fractions, <30−40 counts are required (Figure B3). Therefore, counts of 100 and 50 for coarse-fractions and sand-fractions, respectively, should successfully recover stable D_{50} estimates. However, where sand-fractions were poorly sorted 100 clasts were counted for certainty.

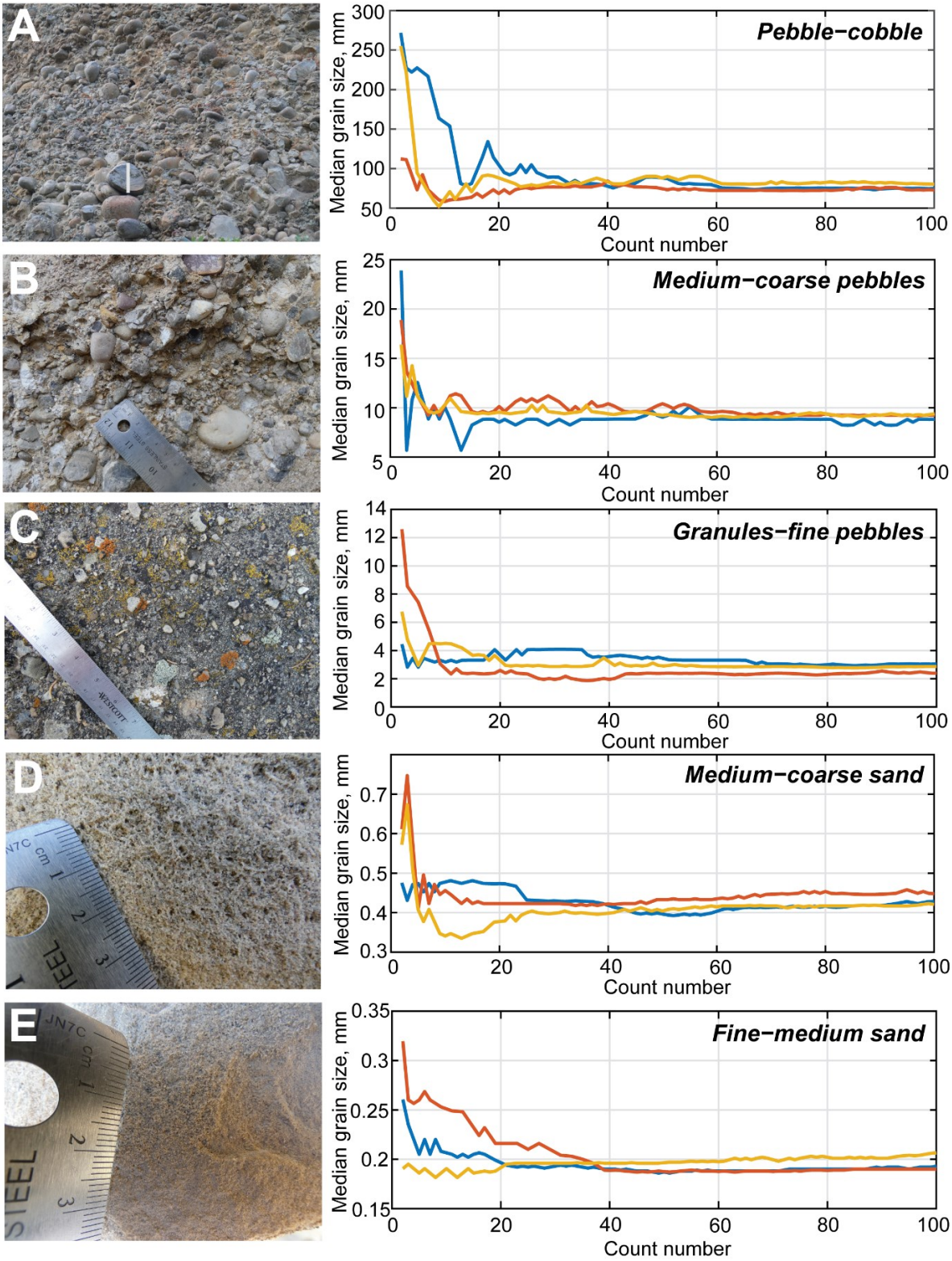

Figure B3 | The iterative convergence of median grain-size for **(A)** pebbles–cobbles, **(B)** medium–coarse pebbles, **(C)** granules–fine pebbles, **(D)** medium–coarse sand, and **(E)** fine–medium sand, as calculated from scaled photographs in *ImageJ* software. Three repeat counts were taken for each scaled photograph (red, blue and yellow solid lines). White bar in part **A** is 400 mm long.

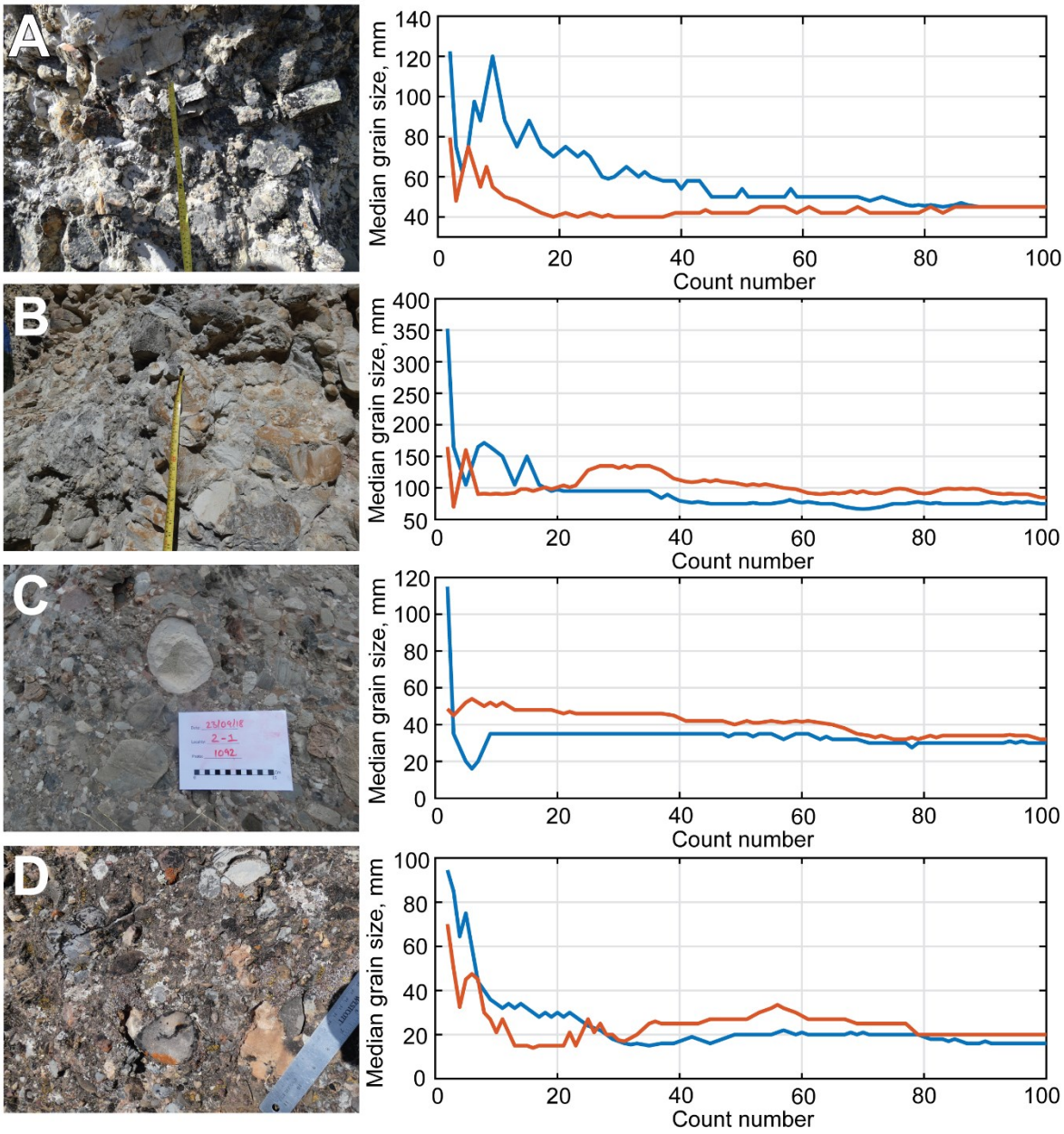

Figure B4 | The iterative convergence of median grain-size for different outcrops of gravel-grade sediments **(A–D)**, as calculated from field Wolman counts. Repeat counts were taken (red and blue solid lines.

B6 Secondary field data

As discussed in the main text, extensive work in this region has already focused on measuring geometries of architectural scale elements, which has increasingly exploited access to high-resolution imagery and three-dimensional outcrop models (Hajek & Heller, 2012; Rittersbacher et al., 2014; Flood & Hampson, 2015; Chamberlin & Hajek, 2019). These tools lend themselves to precise constraints on architectural geometries. As such, to the decision was made to primarily focus on grain-size and cross-set measurements in our field data collection, and secondary data providing constraints on architectural geometries were subsequently compiled. Specifically, data were compiled for independent indicators/proxies of palaeoflow depths (Table B4) and palaeoflow width (Table B5). The latter is particularly difficult to constrain from outcrop and, as such, indicators of palaeoflow width tend to offer apparent widths, maximum widths, or a first-order sense as to the magnitude of width. These secondary data are supplemented by some of our own field observations at each field locality, where possible (Tables B4, B5), which were measured with a Haglof Laser Geo laser range finder to a precision of ±5 cm.

Given that we implement our field data in an entirely quantitative framework, independent observations and measurements of palaeoflow depths and palaeoflow widths are useful to corroborate estimates from this study (see Results in Chapter 3). In addition, these constraints on the approximate, or order-of-magnitude, widths of these palaeorivers are further useful in probing the planform morphologies of these systems in both space and time (see Results in Chapter 3).

Table B4 | A compilation of field measurements (secondary data from published literature) for architectural scale elements, e.g., bar heights, that are commonly used as palaeoflow depth proxies. For each secondary data set we include the stratigraphic interval it would be assigned in this study (1–7) and the field location from which the data set was collected. 1 = lower Blackhawk Formation; 2 = middle Blackhawk Formation; 3 = upper Blackhawk Formation; 4 = lower Castlegate Sandstone; 5 = middle Castlegate Sandstone; 6 = upper Castlegate Sandstone; 7 = Price River Formation.

Stratigraphic interval	Location	Value (m)	Proxy	Reference
Lower Blackhawk Formation (1)	South of Straight Canyon	7	Mean apparent height of channelized fluvial sandstone bodies	Flood and Hampson (2015)
Middle Blackhawk Formation (2)	South of Straight Canyon	8	Mean apparent height of channelized fluvial sandstone bodies	Flood and Hampson (2015)
Upper Blackhawk Formation (3)	South of Straight Canyon	7, 6	Mean apparent height of channelized fluvial sandstone bodies	Flood and Hampson (2015)
Blackhawk Formation (1–3)	Link Canyon	2 to >14	Channel story height	Hampson et al. (2013)
Blackhawk Formation (1–3)	Salina Canyon	0.5–2	Fining upward bed sets	Adams and Bhattacharya (2005)
Blackhawk Formation (1–3)	Salina Canyon	1–2	Bar heights	Adams and Bhattacharya (2005)
Blackhawk Formation (1–3)	Salina Canyon	5–8	Channel-belt sandstone body heights	Adams and Bhattacharya (2005)
Lower Castlegate Sandstone (4)	Price Canyon	4.1	Mean bar height	Hajek and Heller (2012)
Lower Castlegate Sandstone (4)	Price Canyon	1.1–7.6	Bar height	McLaurin and Steel (2007)
Lower Castlegate Sandstone (4)	Price Canyon	4.1 (1.5 to >8)	Mean bar height (and range)	Lynds and Hajek (2006)
Castlegate Sandstone (4–6)	Price Canyon	2.6	Mean bar height	Chamberlin and Hajek (2019)
Castlegate Sandstone (4–6)	Straight Canyon	3.6	Mean bar height	Chamberlin and Hajek (2019)
Castlegate Sandstone (4–6)	Salina Canyon	3.9	Mean bar height	Chamberlin and Hajek (2019)
Castlegate Sandstone (4–6)	Salina Canyon	1.5–2	Bar heights	Adams and Bhattacharya (2005)

Castlegate Sandstone (4–6)	Salina Canyon	3–5	Channel story heights	Adams and Bhattacharya (2005)
Blackhawk Formation (1–3)	Bear Canyon	2.1, 2.5, 3.9, 2.3, 1.8, 3.1, 3.5, 3.6, 2.5, 1.6, 2.5, 2.3, 1.5, 2.6	Lateral accretion set heights/channelized fluvial sandstone body heights	**This study**
Blackhawk Formation (1–3)	Salina Canyon	3.5, 4.6, 2, 2.1, 2.7, 5.8, 7.5, 3.7, 5.8, 6.6, 6.7	Lateral accretion set heights/channelized fluvial sandstone body heights	**This study**
Blackhawk Formation (1–3)	Link Canyon	3, 5.1, 5.4, 4.8, 4.7, 3.5, 2.1, 3, 4.5, 3.1, 3.2, 2.2, 1.5, 2.5, 3.3, 3.8, 4.4, 4.5, 3.2	Lateral accretion set heights/channelized fluvial sandstone body heights	**This study**
Blackhawk Formation (1–3)	Price Canyon	2.4, 2.3, 1.9, 1.9, 1.7, 1.6, 1.5	Lateral accretion set heights/channelized fluvial sandstone body heights	**This study**
Blackhawk Formation (1–3)	Straight Canyon	3.5, 5, 2, 3.5, 6.7, 3, 6, 3.7	Lateral accretion set heights/channelized fluvial sandstone body heights	**This study**
Blackhawk Formation (1–3)	Wattis Road	2.2, 3.5, 2.3, 2, 2.4, 1.7	Lateral accretion set heights/channelized fluvial sandstone body heights	**This study**
Castlegate Sandstone (4–6)	Bear Canyon	4, 6.4, 2.8, 2.9, 4.7, 3.4, 2.9, 4.1, 3.2, 2.1, 2.1	Lateral accretion set heights/channelized fluvial sandstone body heights	**This study**
Castlegate Sandstone (4–6)	Price Canyon	3.4, 3, 3.5, 2, 2.2, 2.8, 3	Lateral accretion set heights/channelized fluvial sandstone body heights	**This study**
Castlegate Sandstone (4–6)	Wattis Road	3.9, 4	Lateral accretion set heights/channelized fluvial sandstone body heights	**This study**
Castlegate Sandstone (4–6)	Salina Canyon	1.6, 2.8, 2.2, 2, 3.8, 3.2, 2.3, 2.8, 1.9, 3.7, 2.4, 2.3, 2.6, 4.1	Lateral accretion set heights/channelized fluvial sandstone body heights	**This study**
Castlegate Sandstone (4–6)	Link Canyon	1.6, 3.6, 2.3, 4.3, 3.1, 3.6, 2, 3.8, 0.75, 1.1, 1.1, 1.3, 2.4, 2.5	Lateral accretion set heights/channelized fluvial sandstone body heights	**This study**

Price River Formation (1–3)	Price Canyon	7	Lateral accretion set heights/channelized fluvial sandstone body heights	**This study**
Price River Formation (7)	Bear Canyon	3.7, 2.1, 2.4, 2.15, 4.1, 5.2, 0.9, 2.2, 1.4	Lateral accretion set heights/channelized fluvial sandstone body heights	**This study**

Table B5 | A compilation of field measurements (secondary data from published literature) for architectural scale elements, e.g., sandstone bodies, that are commonly used as a proxy to infer the magnitude of channel width. For each secondary data set we include the stratigraphic interval it would be assigned in this study (1–7) and the field location from which the data set was collected. 1 = lower Blackhawk Formation; 2 = middle Blackhawk Formation; 3 = upper Blackhawk Formation; 4 = lower Castlegate Sandstone; 5 = middle Castlegate Sandstone; 6 = upper Castlegate Sandstone; 7 = (lowermost) Price River Formation.

Stratigraphic interval	Location	Value (m)	Proxy	Reference
Lower Blackhawk Formation (1)	South of Straight Canyon	350	Mean apparent width of channelized fluvial sandstone bodies	Flood and Hampson (2015)
Middle Blackhawk Formation (2)	South of Straight Canyon	370	Mean apparent width of channelized fluvial sandstone bodies	Flood and Hampson (2015)
Upper Blackhawk Formation (3)	South of Straight Canyon	420, 390	Mean apparent width of channelized fluvial sandstone bodies	Flood and Hampson (2015)
Blackhawk Formation (1–3)	Link Canyon	30 to >310	Channel story widths	Hampson et al. (2013)
Blackhawk Formation (1–3)	Link Canyon	>120 to >740	Channel belt widths	Hampson et al. (2013)
Blackhawk Formation (1–3)	Salina Canyon	8–~50	Bar widths	Adams and Bhattacharya (2005)
Lower Castlegate Sandstone (4)	Price Canyon	30, 35 (max >100)	Thalweg and bar widths	McLaurin and Steel (2007)
Castlegate Sandstone (4–6)	Price Canyon	58	Mean bar package width	Chamberlin and Hajek (2019)
Castlegate Sandstone (4–6)	Straight Canyon	180	Mean bar package width	Chamberlin and Hajek (2019)
Castlegate Sandstone (4–6)	Salina Canyon	87	Mean bar package width	Chamberlin and Hajek (2019)

B7 Goodness of fits on palaeoslope profiles inc. resolved steepness indexes

As described in the Methods, palaeorelief was reconstructed in the alluvial domain of Late Cretaceous central Utah palaeorivers. Initially, palaeoslope was reconstructed using two independent methods, a Shields stress inversion (Equation 3.3 in Chapter 3) and the approach of Trampush et al. (2014) (Equation 3.4 in Chapter 3). Palaeoslope estimates from each method were then used to estimate alluvial palaeorelief (see Methods and Results in Chapter 3). In doing so, we a non-linear least squares regression was used to derive best-fit palaeoslope profiles for the defined northern and southern transects using Equation 3.7 in Chapter 3. In doing so, three different values for the concavity index, θ, were assumed given that concavity in these ancient rivers is not known. Plausible values of 0.4, 0.5 and 0.6 were used for θ. Using the two sets of palaeoslope estimates (Equations 3.3 and 3.4) and the three different concavity values, a variety of steepness indexes, k_s (Equation 3.7 in Chapter 3), were recovered for the defined northern and southern proximal–distal transects, for each stratigraphic interval (where possible). These results are presented here; Table B6 details all k_s values recovered when reconstructing best-fit palaeoslope profiles, and also reports goodness of fit (R^2).

Table B6 | Steepness indexes, k_s, recovered for the defined northern and southern proximal–distal transects, through each stratigraphic interval (1–7), where possible. 1 =l Blackhawk Formation; 2 = middle Blackhawk Formation; 3 = upper Blackhawk Formation; 4 = lower Castlegate Sandstone; 5 = middle Castlegate Sandstone; 6 = upper Castlegate Sandstone; 7 = (lowermost) Price River Formation. k_s values are calculated using palaeoslope estimates derived from both Equations 3.3 and 3.4 in Chapter 3, and using a concavity index, θ, of either 0.4, 0.5, or 0.6. R^2 values are given for each k_s value.

Transect	**Stratigraphic interval**	**Concavity index, θ**											
		0.4				0.5				0.6			
		Shields stress inversion (Equation 3.3)		Trampush et al. 2014 (Equation 3.4)		Shields stress inversion (Equation 3.3)		Trampush et al. 2014 (Equation 3.4)		Shields stress inversion (Equation 3.3)		Trampush et al. 2014 (Equation 3.4)	
		k_s ($m^{0.8}$)	R^2	k_s ($m^{0.8}$)	R^2	k_s (m^1)	R^2	k_s (m^1)	R^2	k_s ($m^{1.2}$)	R^2	k_s ($m^{1.2}$)	R^2
Northern transect	Price River Fm (7)	18.3	0.67	12.3	0.81	34.9	0.77	23.1	0.89	64.7	0.84	42.4	0.94
	Upper Castlegate Sst (6)	16.4	0.34	10.2	0.91	22.5	0.25	14.6	0.88	30.2	0.16	20.3	0.82
	Middle Castlegate Sst (5)	16.4	0.34	10.3	0.91	22.5	0.25	14.6	0.88	30.2	0.17	20.3	0.82
	Lower Castlegate Sst (4)	14.1	0.58	9.6	0.99	19.6	0.5	13.8	0.98	26.7	0.41	19.3	0.95
	Upper Blackhawk Fm (3)	6.1	0.98	8.3	0.99	8.6	0.99	11.6	0.98	12.0	0.99	16.0	0.96
	Middle Blackhawk Fm (2)	6.1	0.96	8.1	0.98	8.6	0.99	11.4	0.99	11.9	0.99	15.8	0.99
	Lower Blackhawk Fm (1)	N/A	N/A	N/A	N/A	N/A	N/A	N/A	N/A	N/A	N/A	N/A	N/A
Southern transect	Price River Fm (7)	15.8	0.90	5.9	0.98	22.6	0.95	8.4	0.99	31.8	0.98	11.7	0.99
	Upper Castlegate Sst (6)	15.3	0.88	5.8	0.94	22.2	0.94	8.3	0.97	31.5	0.97	11.6	0.98
	Middle Castlegate Sst (5)	15.4	0.88	5.9	0.92	22.4	0.94	8.4	0.94	31.6	0.97	11.7	0.94
	Lower Castlegate Sst (4)	15.4	0.88	5.9	0.93	22.3	0.94	8.4	0.95	31.6	0.97	11.7	0.94
	Upper Blackhawk Fm (3)	3.5	0.91	3.1	0.89	5.1	0.96	4.4	0.89	7.2	0.98	6.1	0.86
	Middle Blackhawk Fm (2)	3.5	0.91	3.1	0.90	5.1	0.96	4.3	0.90	7.2	0.98	6.0	0.88
	Lower Blackhawk Fm (1)	3.5	0.90	3.0	0.91	5.1	0.95	4.3	0.92	7.2	0.98	6.0	0.91

B8 Additional results

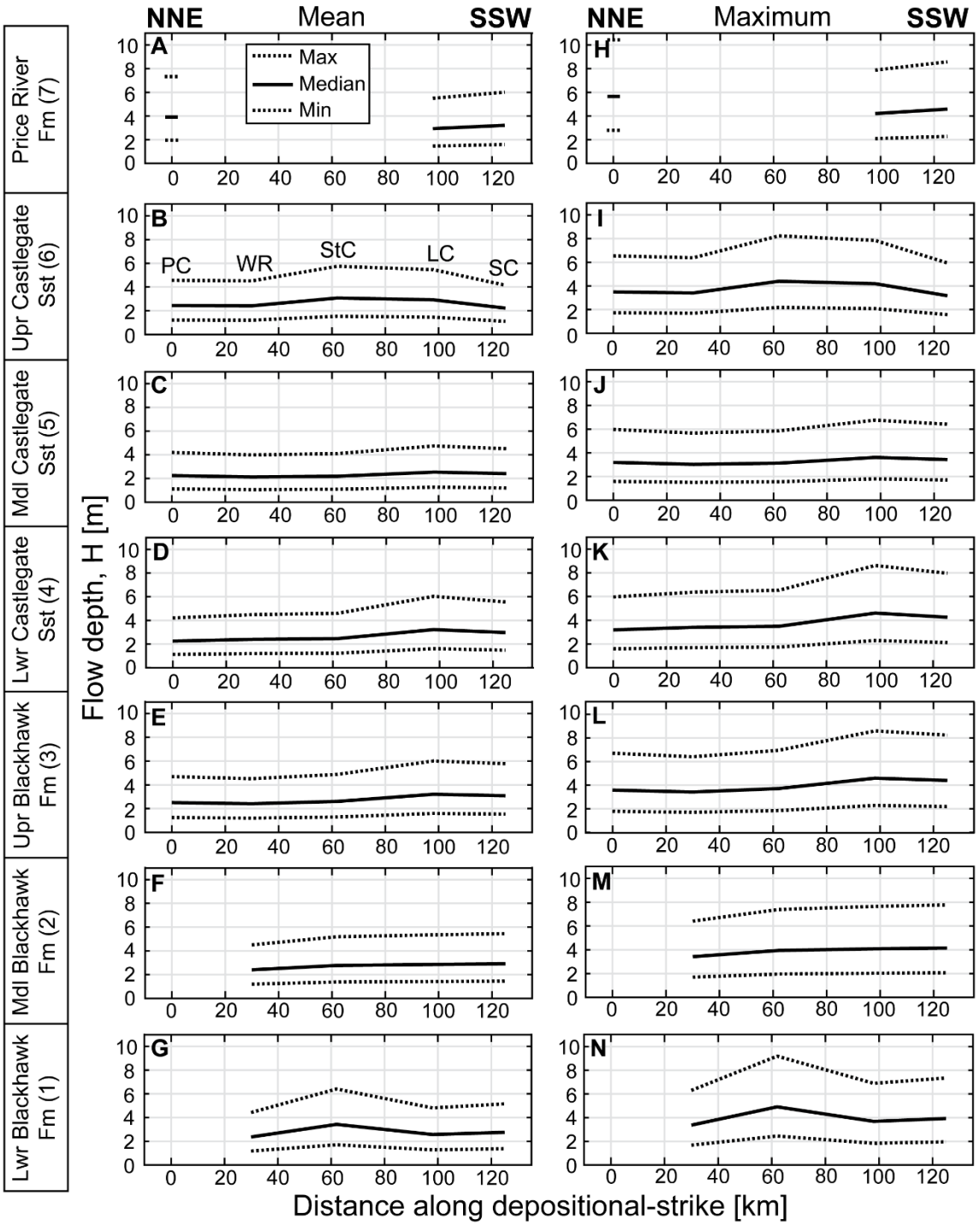

Figure B5 | Reconstructed palaeoflow depths for the 5 parallel fluvial systems, for each stratigraphic interval where possible. Parts **A–G** depict reconstructed palaeoflow depths from estimated mean cross-set heights, whereas parts **H–N** depict reconstructed palaeoflow depths from measured maximum cross-set heights. Results are presented as along-depositional strike transects from NNE (left; 0 km) to SSW (right; 125 km). Field sites span Price Canyon (PC), Wattis Road (WR), Straight Canyon (StC), Link Canyon (LC) and Salina Canyon (SC). Solid lines indicate median palaeoflow depths and dashed lines indicate plausible minimum and maximum values for median palaeoflow depths, derived from the uncertainty margins in Equation 3.2 in Chapter 3.

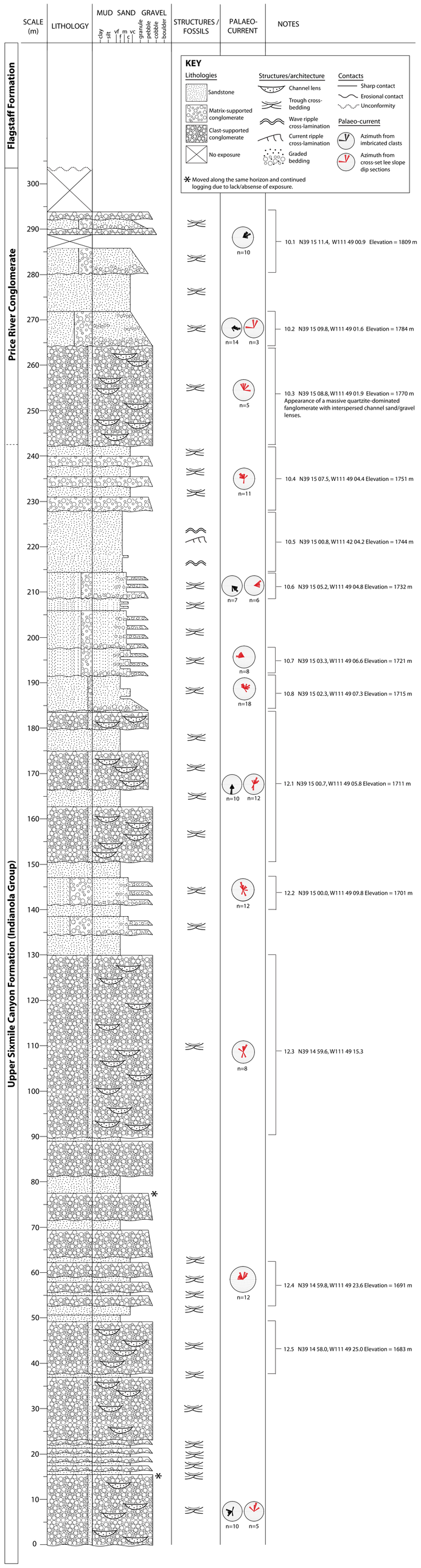
SCALE (m)
LITHOLOGY
MUD SAND GRAVEL
clay
silt
vf
f
m
c
vc
granule
pebble
cobble
boulder
STRUCTURES / FOSSILS
PALAEO-CURRENT
NOTES
KEY
Lithologies
Sandstone
Matrix-supported conglomerate
Clast-supported conglomerate
No exposure
Structures/architecture
Channel lens
Trough cross-bedding
Wave ripple cross-lamination
Current ripple cross-lamination
Graded bedding
Contacts
Sharp contact
Erosional contact
Unconformity
Palaeo-current
Azimuth from imbricated clasts
Azimuth from cross-set lee slope dip sections
* Moved along the same horizon and continued logging due to lack/absense of exposure.
Flagstaff Formation
Price River Conglomerate
Upper Sixmile Canyon Formation (Indianola Group)
0
10
20
30
40
50
60
70
80
90
100
110
120
130
140
150
160
170
180
190
200
210
220
230
240
250
260
270
280
290
300
n=10
n=14
n=3
n=5
n=11
n=7
n=6
n=8
n=18
n=10
n=12
n=12
n=8
n=12
n=10
n=5
10.1 N39 15 11.4, W111 49 00.9 Elevation = 1809 m
10.2 N39 15 09.8, W111 49 01.6 Elevation = 1784 m
10.3 N39 15 08.8, W111 49 01.9 Elevation = 1770 m
Appearance of a massive quartzite-dominated fanglomerate with interspersed channel sand/gravel lenses.
10.4 N39 15 07.5, W111 49 04.4 Elevation = 1751 m
10.5 N39 15 00.8, W111 42 04.2 Elevation = 1744 m
10.6 N39 15 05.2, W111 49 04.8 Elevation = 1732 m
10.7 N39 15 03.3, W111 49 06.6 Elevation = 1721 m
10.8 N39 15 02.3, W111 49 07.3 Elevation = 1715 m
12.1 N39 15 00.7, W111 49 05.8 Elevation = 1711 m
12.2 N39 15 00.0, W111 49 09.8 Elevation = 1701 m
12.3 N39 14 59.6, W111 49 15.3
12.4 N39 14 59.8, W111 49 23.6 Elevation = 1691 m
12.5 N39 14 58.0, W111 49 25.0 Elevation = 1683 m

APPENDIX C: *Supplement to* Field evidence for disequilibrium dynamics in preserved fluvial cross-strata: A record of discharge variability or morphodynamic hierarchy?[1]

Contents:

[1] A version of this appendix is published in ***Earth and Planetary Science Letters***:

Lyster, S. J., Whittaker, A. C., Hajek, E. A., and Ganti, V. (2022) Field evidence for disequilibrium dynamics in preserved fluvial cross-strata: A record of discharge variability or morphodynamic hierarchy? ***Earth and Planetary Science Letters***, 579, 117355, DOI: 10.1016/j.epsl.2021.117355

C1 Field localities

Table C1 | Field localities visited in this study. Localities are grouped by field area (e.g., Price Canyon, Wattis Road; see Figure 4.1 in Chapter 4) and subdivided by formation (i.e., Blackhawk Formation, Castlegate Sandstone and Ferron Sandstone).

Location and stratigraphic interval		Field sites	Elevation, m (±3–4)
Last Chance Creek	Ferron Sandstone	N38 40 18.9, W111 24 52.5	2255
		N38 40 20, W111 24 45.3	2241
		N38 40 21.7, W111 24 17.1	2218
		N38 40 17.5, W111 24 12	2209
		N38 40 12, W111 24 2.5	2190
		N38 40 7.7, W111 23 50.3	2179
		N38 40 9.1, W111 23 44.8	2187
		N38 40 8.9, W111 23 53.6	2215
Link Canyon	Blackhawk Formation	N38 57 42.1, W111 19 57.4	2363
		N38 57 39.7, W111 19 53.9	2383
		N38 57 41.4, W111 19 53.0	2398
		N38 57 44.3, W111 19 53.8	2421
		N38 57 48.4, W111 19 53.9	2473
		N38 57 58.3, W111 19 57.3	2538
		N38 57 52.8, W111 19 55.8	2509
		N38 57 51.4, W111 19 55.0	2500
	Castlegate Sandstone	N38 58 05.9, W111 19 56.6	2572
		N38 58 08.0, W111 19 55.8	2584
		N38 58 10.6, W111 19 54.2	2600
Price Canyon	Blackhawk Formation	N39 44 11.0, W110 50 47.7	1932
		N39 44 08.4, W110 50 46.9	1947
	Castlegate Sandstone	N39 45 05.1, W110 53 10.3	1920
		N39 44 48.5, W110 49 58.1	1969
		N39 44 52.6, W110 49 55.4	1983
		N39 45 01.3, W110 49 43.5	2000
		N39 45 03.0, W110 49 40.6	1999
		N39 45 10.5, W110 49 35.8	2008
		N39 45 12.0, W110 49 34.8	2003
Salina Canyon	Blackhawk Formation	N38 54 00.8, W111 39 53.8	1861
		N38 53 51.5, W111 39 02.3	1885
		N38 54 29.6, W111 41 46.8	1802
		N38 54 13.8, W111 39 05.9	1926
	Castlegate Sandstone	N38 54 52.9, W111 38 06.5	2036
		N38 54 52.3, W111 38 08.7	2017
		N38 54 50.6, W111 38 18.1	2009
		N38 54 52.6, W111 38 20.2	2030
		N38 54 53.7, W111 38 ~20.2	2035
		N38 54 33.0, W111 42 32.7	1779
		N38 54 57.1, W111 38 20.3	2076
		N38 54 59.4, W111 38 13.1	2111

Straight Canyon	Blackhawk Formation	N39 16 56.6, W111 13 58.0	2027
		N39 16 46.2, W111 13 41.9	2010
		N39 16 29.1, W111 13 11.9	1996
		N39 17 16.2, W111 14 37.5	2047
		N39 17 15.7, W111 14 30.4	2043
		N39 17 05.7, W111 14 10.5	2037
		N39 17 36.5, W111 16 16.7	2146
		N39 17 19.3, W111 16 00.0	2129
		N39 17 20.9, W111 15 19.8	2102
	Castlegate Sandstone	N39 17 51.9, W111 16 18.0	2161
		N39 18 28.6, W111 16 13.2	2181
		N39 18 55.2, W111 16 06.2	2238
Wattis Road	Blackhawk Formation	N39 31 45.5, W111 02 16.0	2577
		N39 31 11.9, W111 01 56.9	2692
		N39 31 19.8, W111 01 58.4	2655
		N39 31 20.7, W111 02 37.2	2798
		N39 31 14.3, W111 02 13.8	2765
	Castlegate Sandstone	N39 31 28.6, W111 02 44.9	2844
		N39 31 31.7, W111 02 50.6	2877
		N39 31 30.2, W111 02 46.4	2861
		N39 31 33.5, W111 02 53.2	2889
Willow Basin	Ferron Sandstone	N38 34 50.9, W111 28 6.2	2668
		N38 34 49, W111 28 6.5	2636
		N38 34 48.9, W111 28 4.5	2631
		N38 34 47.6, W111 28 5.4	2592
		N38 34 35.1, W111 27 48.4	2537
Willow Creek	Ferron Sandstone	N38 44 0.4, W111 18 47.2	1965
		N38 43 37.4, W111 18 46.5	1926
		N38 43 25.2, W111 18 45.9	1895

C2 Extended methodology: Estimation of bedform turnover timescale

We propagated mean thicknesses of individually measured cross-sets (and their respective grain-sizes) through a well-established quantitative framework (c.f. Ganti et al., 2019; Chapter 3 (Lyster et al., 2021)) to reconstruct a variety of palaeohydraulic parameters and, eventually, bedform turnover timescales, T_t. We first reconstructed mean original bedform (i.e., dune) height, h_d, as a function of mean cross-set thickness, h_{xs}, using the relation of Leclair and Bridge (2001),

$$h_d = 2.9(\pm 0.7)h_{xs}, \qquad \text{Eq. C1}$$

where 2.9 is the mean (μ) and 0.7 is the standard deviation (σ). The above relation was experimentally derived for steady-state conditions, i.e., bedform preservation ratio (h_{xs}/h_d) of ~0.3. However, bedform preservation in disequilibrium conditions may imply that h_{xs}/h_d is higher (Jerolmack & Mohrig, 2005; Reesink et al., 2015; Ganti et al., 2020; Leary & Ganti, 2020). Initially, we assumed h_{xs}/h_d of ~0.3, which means that T_t estimates are maximum values. We subsequently evaluated the sensitivity of T_t to h_{xs}/h_d (see Section 4.3 in Chapter 4). Finally, we estimated likely values of h_{xs}/h_d for each geologic formation using available data (Section C3), which broadly range from 0.3–0.7, and used these values to contextualise the implications of this sensitivity on our results (Figure 4.8 in Chapter 4).

We used a Monte Carlo uncertainty propagation method to estimate uncertainty (c.f. Chapter 3 (Lyster et al., 2021)). In doing so, we offer plausible spreads of values for the median of each reconstructed parameter. From Equation C1, we generated 10^6 random samples of the model parameter between bounds defined by $\mu-\sigma$ and $\mu+\sigma$. To avoid introduction of additional assumptions, we generated these samples from a uniform distribution as the shape and the scale of the full distribution of the data is unknown. These 10^6 samples were used to calculate 10^6 values of h_d, and these results were propagated through subsequent calculations. Given that Equation C1 assumes steady-state flow conditions and a h_{xs}/h_d value of ~0.3, and that we randomly sampled the model parameter between $\mu-\sigma$ and $\mu+\sigma$, we note that our uncertainty analysis analytically accounts for some variability in h_{xs}/h_d, between ~0.28 and ~0.45.

To reconstruct formative flow depth, H, we used the bedform height−flow depth scaling relation of Bradley and Venditti (2017), which was derived using >380 empirical data. Bradley and Venditti (2017) presented a non-parametric relation which characterized their data, which did not assume an underlying distribution for the scaling parameter. In this relation, median H is given as

$$H = 6.7h_d, \qquad \text{Eq. C2}$$

with a probabilistic uncertainty estimator in which the 1st and 3rd quartiles of H are given by $H=4.4h_d$ and $H=10.1h_d$, respectively (Bradley & Venditti, 2017). We generated 10^6 random samples between 4.4 and 10.1, again from a uniform distribution, and reconstructed 10^6 values of H in these ancient fluvial systems using

Equation C2. These values were then used to estimate bedform wavelength, λ, as λ=7.3H, following van Rijn (1984).

To reconstruct palaeoslope, we used the empirical method of Trampush et al. (2014). Palaeoslopes may also be calculated by a Shields stress inversion where the dimensionless Shields stress is known (or where it can be estimated using, e.g., bedform stability diagrams; Carling, 1999). However, we implemented the method of Trampush et al. (2014) for consistency with the method that Mahon and McElroy (2018) used to derive Equations C4 and C5. In addition, previous studies have shown that both palaeoslope methods recover similar values for sand-grade grain-sizes (Ganti et al., 2019; Chapter 3 (Lyster et al., 2021)). Trampush et al. (2014) expressed palaeoslope, S, as

$$\log S = \alpha_0 + \alpha_1 \log D_{50} + a_2 \log H, \quad \text{Eq. C3}$$

where $\alpha_0 = -2.08 \pm 0.036$, $\alpha_1 = 0.254 \pm 0.016$, and $\alpha_2 = -1.09 \pm 0.044$ are constants. We randomly sampled 10^6 values of a_0, a_1, and a_2 (uniformly distributed between $\mu-\sigma$ and $\mu+\sigma$) and reconstructed 10^6 values of S.

To calculate characteristic bedform migration velocity, V_c, and therefore unit bedload flux, q_b, we used the bedform-scale (as opposed to grain-scale) approach of Mahon and McElroy (2018), in which q_b is estimated geometrically, per unit width, as a function of bedform migration velocity, V_c. These variables are given as:

$$\log V_c = \beta_0 + \beta_1 \log S, \quad \text{Eq. C4}$$

$$q_b = (1-\varphi)\frac{h_d V_c}{2}, \quad \text{Eq. C5}$$

where $\beta_0 = 0.6113 \pm 0.144$ and $\beta_1 = 1.305 \pm 0.0515$ are constants, and φ is a dimensionless bed porosity of 0.5 (Mahon & McElroy, 2018). To reconstruct V_c, we randomly sampled 10^6 values for the model parameters, β_0 and β_1, from a uniform distribution between bounds defined by $\mu-\sigma$ and $\mu+\sigma$. These values were then used to estimate q_b (Equation C5).

Having calculated 10^6 values of h_d, H, λ, S, V_c, and q_b, we reconstructed bedform turnover timescales, T_t, i.e., the time taken to displace the volume of sediment of the bedform (per unit width), following Martin and Jerolmack (2013), Myrow et al. (2018), and Leary and Ganti (2020) as:

$$T_t = \frac{\lambda h_d \beta}{q_b}, \quad \text{Eq. C6}$$

where $\beta \sim 0.55$ is the bedform shape factor. We highlight that this approach to calculate T_t approximates λ / V_c.

This recovered 10^6 values of T_t in units of seconds which we converted to days. From these values, we extracted median T_t, the 25–75 percentile range of T_t (or the 1st–3rd interquartile range of T_t), and the 10–90 percentile range of T_t. Given that the errors and uncertainties associated with Equations C2–C6 are propagated through the methodology, and that these errors and uncertainties are compounded on top of each other, we suggest that the 10–90 percentile range of T_t offers plausible minimum and maximum values for median T_t, with the 25–75 percentile range of T_t highlighting where true values of median T_t are most likely to occur between these bounds.

C3 Constraints on bedform preservation ratios

As discussed in the Chapter 4, and above, the scaling relation of Leclair and Bridge (2001) (Equation C1) is derived for steady-state conditions, which implies that reconstructed H values are also steady-state estimates. However, it is expected that h_{xs}/h_d is higher in disequilibrium conditions (see Chapter 4). The ability to constrain h_{xs}/h_d from geological outcrop would be useful for evaluating the nature of bedform preservation, however this is difficult in practice.

In order to accurately constrain h_{xs}/h_d, we ideally require systematic measurements of cross-set heights and knowledge of their original bedform heights, however it is not possible to know original bedform heights in ancient fluvial systems. Instead, we can contrast cross-set heights with independent proxies of H, e.g., barform heights. If H values reconstructed from mean cross-set heights using steady-state assumptions agree with independent proxies of H, then this might imply that h_{xs}/h_d was truly ~0.3. However, this approach requires us to assume the relationship between the original bedform height and the palaeoflow depth (Equation C2) in order to recover a value for h_{xs}/h_d. Reconstructions of h_{xs}/h_d are therefore estimates. Moreover, barform heights are a proxy for maximum bankfull depths which, given the possibility that mean bankfull depths are smaller, will act to decrease the estimated value of h_{xs}/h_d. This is particularly true where the heights of point bar deposits are used as independent proxies of H, as flow depths in meandering systems are typically greater on meander bends. One further issue with this approach is that the barforms themselves may not be fully preserved (Chamberlin & Hajek, 2019).

In this study, despite our detailed data collection, we do not have the desired spatiotemporal resolution of field measurements to accurately constrain h_{xs}/h_d., i.e., we do not have a mean cross-set height and the mean height of the associated barform for each measured cross-set. However, as a starting point, we compared mean cross-set heights across our field areas (Figure 4.1 in Chapter 4) with mean barform heights in published literature. Based on stratigraphic observations, detailed below, we predict that values of h_{xs}/h_d likely ranged between 0.3 and 0.7. This suggests that uncertainty margins in Equation C1, which analytically account for variability in h_{xs}/h_d between ~0.28 and ~0.45, are reasonable. It is unlikely that h_{xs}/h_d is much smaller than ~0.3 because, as mentioned in the main text, if h_{xs}/h_d is much smaller than ~0.3 then T_t rapidly increases from 10^1 to 10^5 days (Equations C1 and C2), which are implausible bedform migration timescales.

We recovered median values of h_{xs} equal to ~0.13–0.14 m for the Blackhawk Formation and Castlegate Sandstone, but which broadly span 0.1–0.2 m. H values reconstructed using steady-state assumptions have previously been verified for the Blackhawk Formation and Castlegate Sandstone in Chapter 3 (Lyster et al., 2021). The authors reconstructed median H values of 2–4 m from cross-sets spanning the Blackhawk Formation and Castlegate Sandstone at localities along the eastern front of the Wasatch Plateau (Chapter 3 (Lyster et al., 2021)). These H values are in broad agreement with H values independently inferred from bar-scale clinoform heights, which have means of ~3–3.5 m, but which typically span 1–8 m (Adams & Bhattacharya, 2005; Lynds & Hajek, 2006; McLaurin & Steel, 2007; Hajek & Heller, 2012; Chamberlin &

Hajek, 2019; Chapter 3 (Lyster et al., 2021)). Assuming the model parameter in Equation C3 is true, we might expect values of h_{xs}/h_d up to 0.6–0.7.

Meanwhile, for the Ferron Sandstone, H values reconstructed using steady-state assumptions have not previously been verified. Here, from individually measured cross-sets (n=190), we recovered median values of 0.15 m for mean cross-set heights, which broadly span 0.1–0.3 m. Using Equation C3 we project median values for H of ~3 m, but which broadly span 1–10 m (Equation C3). Independent proxies of H are limited for the Ferron Sandstone. As such, in the field we obtained new measurements of independent H proxies, e.g., laterally accreted point bar deposit heights, which we made using a Haglof Laser Geo laser range finder to a precision of ±5 cm, and which we used to supplement limited secondary data (Table C2). In the Ferron Sandstone, previous work has documented channel-fill deposits and laterally accreted point bars with heights of order 8–9 m (Cotter, 1971; Gardner et al., 2004; Garrison & Bergh, 2004). Here we report a broader range of heights for independent H proxies (Table C2). Across 35 measurements of point bar/lateral accretion set heights (Table C2), we recover a mean height of 4.7 m, with a 1st–3rd interquartile range spanning 2.9–6.5 m. Minimum and maximum heights are 1.1 and 10 m, respectively (Table C2). Similarly, if we assume the model parameter in Equation C3 is true, then we might expect h_{xs}/h_d values up to 0.6–0.7.

Table C2 | Independent measurements of palaeoflow depth indicators in the Ferron Sandstone

Palaeoflow depth proxy	Thickness (m)	Source
Laterally accreted point bar deposit	9.1	Cotter (1971)
Laterally accreted point bar deposit	<8	Gardner et al. (2004)
Maximum thickness of channel-fill deposits	~9	Gardner et al. (2004)
Maximum thickness of channel-fill deposits	~9	Garrison and Bergh (2004)
Laterally accreted point bar deposits	8, 7.5, 9, 3.2, 4.8, 3.6, 6.5, 7.5, 3.6, 4.1, 2.7, 6.4, 5.5, 2.8, 1.1, 1.9, 7.5, 2.7, 7.1, 1.2, 4.4, 3.7, 3.1, 3.4, 3, 2.5, 5.9, 2.5, 4.7, 10, 4.2, 1.6, 3, 6.5, 10	**This study (Chapter 4)**
Maximum thickness of single channel storeys	8.6, 11.1, 12.2, 9, 7.6, 7.1, 3.9, 5.6, 2.6, 7.3, 12, 9.3	**This study (Chapter 4)**

C4 Data tables

The following data tables contain field results and a selection of reconstructed palaeohydrologic parameters for the Blackhawk Formation, Castlegate Sandstone, and Ferron Sandstone. Field data and results are reported per field area (see Figure 4.1 in Chapter 4).

BLACKHAWK FORMATION	FIELD DATA				RECONSTRUCTED PALAEOHYDRAULIC PARAMETERS							
	Mean cross-set height, m	Maximum cross-set height, m	CV(hxs)	Median grain size, m	Minimum plausible flow depth, m	Median flow depth, m	Maximum plausible flow depth, m	10th percentile of palaeoslope	25th percentile of palaeoslope	Median palaeoslope	75th percentile of palaeoslope	90th percentile of palaeoslope
SALINA CANYON	0.175	0.26	0.333009	0.00075	1.69553636	3.6060487	6.356994667	0.000224282	0.000265979	0.00033144	0.000421306	0.000515544
	0.124444444	0.19	0.434804	0.0005	1.20640424	2.5644985	4.520734474	0.000293396	0.000347813	0.0004336	0.000550975	0.000674477
	0.135	0.2	0.283389	0.0005	1.30867018	2.7802884	4.90375036	0.000268992	0.000318937	0.00039702	0.000504732	0.000617489
	0.153333333	0.23	0.397212	0.0005	1.48769526	3.1618369	5.56932235	0.000234192	0.000277518	0.00034534	0.000439146	0.000537525
	0.12	0.15	0.228218	0.0005	1.16218038	2.4731614	4.36154305	0.000306006	0.000362479	0.00045134	0.000574016	0.000701557
	0.134545455	0.21	0.389567	0.001	1.30405739	2.7749046	4.890971704	0.000322137	0.000381692	0.00047432	0.000602969	0.000736356
	0.14625	0.21	0.320582	0.001	1.4165669	3.013532	5.315167329	0.000294286	0.000348717	0.00043398	0.000551351	0.000673991
	0.13375	0.22	0.506992	0.001	1.29655719	2.7573089	4.861922476	0.000324508	0.000384273	0.00047825	0.000608109	0.000743146
	0.15625	0.24	0.398856	0.001	1.51358509	3.2223143	5.678733003	0.000273953	0.000324481	0.00040358	0.000512964	0.000626624
	0.107142857	0.17	0.440135	0.001	1.04094149	2.2092972	3.893793461	0.000413159	0.000488792	0.00060807	0.00077343	0.000945708
STRAIGHT CANYON	0.1575	0.2	0.232047	0.000375	1.52584228	3.242664	5.719899922	0.000211073	0.000250395	0.00031236	0.000397241	0.000486162
	0.15125	0.22	0.298699	0.000375	1.46453888	3.1134282	5.496194007	0.000220678	0.000261639	0.00032626	0.000415171	0.000507888
	0.1225	0.17	0.26452	0.000375	1.18802327	2.523313	4.453500173	0.000277693	0.000329347	0.00041035	0.000521901	0.000638536
	0.180909091	0.25	0.262146	0.000375	1.75352002	3.7274887	6.575761572	0.00018129	0.000215179	0.00026849	0.000341544	0.000417707
	0.126666667	0.16	0.257841	0.000375	1.22793646	2.6109994	4.603810649	0.000267718	0.000317306	0.00039539	0.000502665	0.000614575
	0.163333333	0.21	0.304075	0.0005	1.58249421	3.3667422	5.935139077	0.000218319	0.000258804	0.00032268	0.000410472	0.000502568
	0.162222222	0.22	0.273566	0.0005	1.57218029	3.3437906	5.896675908	0.000219837	0.000260727	0.00032499	0.000413145	0.000505261

	0.138181818	0.21	0.348299	0.000375	1.33992904	2.8482868	5.022227729	0.000243298	0.0002886	0.00035958	0.000457686	0.000560232
	0.18625	0.24	0.286902	0.000375	1.80569092	3.8353465	6.767874615	0.000175852	0.000208702	0.00026009	0.000330657	0.000404702
	0.16	0.21	0.3125	0.000375	1.550378	3.2974623	5.813946822	0.000207531	0.000246264	0.00030699	0.000390191	0.000477151
	0.127142857	0.18	0.326552	0.000375	1.23228285	2.6183692	4.621900706	0.000266499	0.000316025	0.00039408	0.000501562	0.000613668
	0.10375	0.16	0.378376	0.000375	1.00452327	2.1396088	3.771428693	0.000332806	0.000394683	0.00049142	0.000624792	0.000764482
	0.168333333	0.19	0.165557	0.000375	1.63266768	3.4693891	6.11615316	0.000196259	0.000232705	0.0002899	0.000368763	0.000451307
	0.077142857	0.1	0.256154	0.000188	0.74876883	1.5885297	2.802911843	0.000384752	0.000456317	0.0005692	0.000724118	0.0008873
	0.145555556	0.22	0.362093	0.000188	1.4131465	2.9996863	5.288486601	0.000192657	0.000228702	0.00028534	0.000362993	0.000444494
	0.114285714	0.15	0.306696	0.000188	1.10724176	2.3565486	4.152743563	0.000250947	0.000297618	0.00037098	0.000472307	0.000578396
	0.1	0.14	0.275681	0.000188	0.96891516	2.0612803	3.634456374	0.000290023	0.000343916	0.00042888	0.00054535	0.000667419
	0.206666667	0.28	0.232056	0.000188	2.00333252	4.2629193	7.508916638	0.000131071	0.000155671	0.00019439	0.000247507	0.000303519
	0.213529412	0.31	0.220869	0.000375	2.06928999	4.4043396	7.760037023	0.000151152	0.000179348	0.0002236	0.000284535	0.00034861
	0.282222222	0.38	0.275954	0.0005	2.73195781	5.819131	10.25591923	0.000119982	0.000142478	0.00017765	0.000225954	0.000276707
	0.133	0.19	0.309095	0.0005	1.29041653	2.7404957	4.832098077	0.00027323	0.000323822	0.00040336	0.000512648	0.000627609
	0.13875	0.18	0.286837	0.000375	1.3444735	2.8602592	5.042949484	0.000242465	0.000287363	0.00035789	0.000454897	0.000556368
	0.213333333	0.23	0.050301	0.000375	2.06601145	4.3969985	7.744357925	0.000151422	0.000179704	0.00022407	0.0002849	0.000348702
	0.195	0.25	0.255476	0.000375	1.8904352	4.0195779	7.08281435	0.000166889	0.000197936	0.00024707	0.000314408	0.000385266
	0.208571429	0.28	0.332668	0.000375	2.02049938	4.298896	7.57902058	0.000155184	0.000184144	0.00022964	0.000292238	0.000357924
	0.128333333	0.19	0.371231	0.000375	1.24455772	2.6458421	4.661561199	0.000263962	0.000312921	0.0003901	0.000495971	0.000606046
PRICE CANYON	0.123333333	0.17	0.22205	0.00025	1.19495557	2.5416565	4.479258232	0.000248216	0.000294519	0.0003674	0.000467099	0.00057226
	0.097142857	0.13	0.283255	0.00025	0.94106852	2.0015444	3.527882242	0.000322605	0.000382387	0.00047654	0.000605903	0.000741848

	0.138	0.17	0.207505	0.00025	1.33689797	2.8452964	5.016585457	0.000219724	0.000260576	0.00032498	0.000413333	0.000505433
	0.113333333	0.13	0.164285	0.00025	1.09775417	2.3353651	4.119795283	0.00027258	0.000323194	0.00040295	0.000512574	0.000627241
	0.12	0.16	0.263523	0.00025	1.16291117	2.4726343	4.358266824	0.000255729	0.000303489	0.00037846	0.000481896	0.000589317
	0.118571429	0.16	0.305749	0.000375	1.14939477	2.4453751	4.30853723	0.000287779	0.000341043	0.00042485	0.000539993	0.000660329
	0.109	0.15	0.261105	0.000375	1.05529256	2.2468449	3.962511061	0.000315278	0.000373859	0.00046569	0.000592038	0.000724622
	0.1475	0.18	0.129398	0.00025	1.42869329	3.0387878	5.3602594	0.000204259	0.000242303	0.00030223	0.000384372	0.000470666
	0.10875	0.16	0.362648	0.00025	1.05425841	2.2409753	3.950846958	0.000285224	0.000338157	0.00042149	0.000536053	0.000656187
	0.127692308	0.17	0.235274	0.00025	1.23643807	2.6304081	4.639651193	0.000239209	0.000283792	0.00035392	0.000450533	0.0005515
	0.1025	0.14	0.206958	0.00025	0.99372866	2.1118452	3.724448616	0.000304065	0.000360923	0.00044973	0.000571588	0.000699574
	0.09	0.13	0.337931	0.00025	0.87240502	1.855449	3.270595322	0.000350619	0.00041542	0.00051777	0.000658124	0.000805156
WATTIS ROAD	0.141428571	0.21	0.303927	0.00075	1.37153157	2.9137444	5.138396462	0.000283544	0.000336013	0.0004183	0.000531636	0.000649467
	0.088181818	0.12	0.276934	0.00075	0.85397362	1.8169119	3.204470581	0.000474424	0.00056142	0.00069927	0.000888857	0.001086994
	0.0975	0.13	0.224372	0.00075	0.94487237	2.009446	3.543137243	0.000425507	0.000503819	0.00062717	0.000797055	0.00097436
	0.120833333	0.18	0.365807	0.00075	1.1707558	2.4905715	4.391645339	0.000336681	0.000398644	0.00049601	0.000630797	0.00077113
	0.145454545	0.21	0.333085	0.00075	1.4088605	2.9972064	5.287394354	0.000274913	0.000325905	0.00040608	0.000516202	0.000630857
	0.154444444	0.21	0.377698	0.000375	1.49554818	3.1878011	5.60875062	0.000215314	0.000255331	0.00031844	0.000404886	0.00049538
	0.118888889	0.16	0.315965	0.000375	1.15273223	2.4488569	4.31907252	0.00028696	0.000340159	0.00042409	0.000539421	0.000659695
	0.1	0.13	0.334664	0.000375	0.96943708	2.0624682	3.635062795	0.000346233	0.000410174	0.00051139	0.000650835	0.000796326
	0.095714286	0.13	0.240201	0.000375	0.92826596	1.9721642	3.477581792	0.000363546	0.000431057	0.00053674	0.000682047	0.000834481
	0.128571429	0.17	0.299313	0.000375	1.24676041	2.6496481	4.672130115	0.000263319	0.000312216	0.00038911	0.000495287	0.000606066
	0.1625	0.21	0.2273	0.000375	1.57535379	3.3500082	5.905220763	0.000203933	0.000241973	0.0003015	0.000383706	0.000469605

	0.115	0.16	0.293456	0.000375	1.11512277	2.3702845	4.179194823	0.000297282	0.000352473	0.00043901	0.000558075	0.000683727
	0.094285714	0.13	0.279654	0.000375	0.91280828	1.9425612	3.424246398	0.000369335	0.000437743	0.00054551	0.000693575	0.000848688
	0.13	0.16	0.250106	0.000375	1.25930062	2.6802509	4.726404	0.000260064	0.000308189	0.00038391	0.00048839	0.000597218
	0.131428571	0.16	0.230065	0.000375	1.2736555	2.7089329	4.773334578	0.000257111	0.000304923	0.00037982	0.000482886	0.000591578
LINK CANYON	0.15375	0.3	0.508504	0.00075	1.49079363	3.1677728	5.5864087	0.000258797	0.000306643	0.00038201	0.000485603	0.000593655
	0.152857143	0.26	0.484752	0.00075	1.48017302	3.1510322	5.551970614	0.000260495	0.000308426	0.00038417	0.000487894	0.000596448
	0.125	0.16	0.338467	0.00075	1.21089964	2.5783995	4.540574724	0.000324226	0.000384128	0.00047841	0.000608141	0.000743297
	0.141	0.22	0.411443	0.0005	1.3651672	2.9042897	5.125491966	0.000256415	0.000304041	0.00037899	0.000481878	0.000589573
	0.161666667	0.27	0.460261	0.0005	1.56665833	3.3311373	5.873361992	0.000220683	0.000261692	0.00032597	0.000415077	0.000507992
	0.142857143	0.2	0.273252	0.0005	1.38462809	2.9421903	5.192080165	0.000252646	0.000299552	0.0003734	0.000474601	0.00058043
	0.19	0.27	0.40198	0.0005	1.84228533	3.9226342	6.905662492	0.000184757	0.000219149	0.00027336	0.000347894	0.000425753
	0.171428571	0.25	0.408928	0.0005	1.66057438	3.5372194	6.226972687	0.000206959	0.000245353	0.00030574	0.000388443	0.000475659
	0.121	0.16	0.300389	0.0005	1.17251778	2.4927509	4.396092917	0.000303034	0.000359336	0.00044754	0.000568632	0.000695184
	0.091666667	0.13	0.361265	0.0005	0.88770123	1.8890634	3.331375123	0.000410245	0.000485628	0.0006053	0.000769614	0.000940732
	0.112	0.16	0.386103	0.0005	1.08482282	2.3091117	4.071495878	0.000329782	0.000390565	0.00048621	0.000618034	0.000755824
	0.126666667	0.16	0.242905	0.0005	1.2292122	2.610558	4.604587633	0.000288417	0.000341768	0.00042589	0.000541383	0.00066218
	0.076666667	0.11	0.401321	0.0005	0.74323545	1.5808932	2.785592845	0.000498446	0.000590294	0.00073508	0.000934191	0.001142089
	0.28875	0.38	0.294118	0.0005	2.7983842	5.9552413	10.49724933	0.00011691	0.000138862	0.00017318	0.000220319	0.000269794
	0.144444444	0.22	0.349789	0.0005	1.39974376	2.9780785	5.250517697	0.000249641	0.000295986	0.0003686	0.000468435	0.000572687
	0.13875	0.2	0.362286	0.0005	1.34394275	2.8584193	5.038990068	0.000260899	0.000309344	0.00038538	0.000489692	0.00059912
	0.156666667	0.26	0.462491	0.0005	1.51759816	3.2302507	5.695846182	0.000228279	0.000270582	0.00033748	0.000429315	0.000525019

	0.1825	0.22	0.154289	0.0005	1.77011399	3.7596253	6.634656661	0.000193706	0.000229607	0.00028603	0.000363894	0.000444782

CASTLEGATE SANDSTONE	**FIELD DATA**				**RECONSTRUCTED PALAEOHYDRAULIC PARAMETERS**							
	Mean cross-set height, m	**Maximum cross-set height, m**	**CV(hxs)**	**Median grain size, m**	**Minimum plausible flow depth, m**	**Median flow depth, m**	**Maximum plausible flow depth, m**	**10th percentile of palaeoslope**	**25th percentile of palaeoslope**	**Median palaeoslope**	**75th percentile of palaeoslope**	**90th percentile of palaeoslope**
SALINA CANYON	0.15	0.3	0.648645	0.00075	1.45398019	3.0910532	5.446789213	0.000266236	0.000315345	0.00039251	0.000498887	0.000609871
	0.172222222	0.24	0.332007	0.002	1.66892277	3.549146 5	6.259218963	0.000293577	0.000347476	0.00043262	0.000549616	0.000671317
	0.114	0.2	0.60647	0.0015	1.1050769	2.347235 1	4.142533366	0.000428841	0.000507265	0.0006308	0.000801764	0.000979997
	0.228888889	0.31	0.382403	0.0005	2.21754488	4.712709 4	8.315583368	0.000151021	0.000179161	0.0002235	0.000284086	0.000347379
	0.11125	0.16	0.379655	0.00075	1.07872411	2.291953 6	4.043547867	0.000367871	0.000436114	0.00054311	0.000690818	0.000844716
	0.165454545	0.22	0.225114	0.000375	1.6039371	3.414545 7	6.013670741	0.000199783	0.000236827	0.00029522	0.000375598	0.000459836
	0.14	0.23	0.474999	0.0005	1.35639332	2.886262 9	5.086514752	0.000258286	0.000306185	0.00038157	0.000485539	0.000593289
	0.162857143	0.23	0.381352	0.0015	1.58087653	3.354962 3	5.92023184	0.000290301	0.000343655	0.00042763	0.000543362	0.000664196
	0.145555556	0.21	0.327889	0.00075	1.41014504	3.001939 7	5.288248623	0.000274776	0.00032518	0.0004049	0.000514716	0.000628915
	0.20375	0.31	0.36909	0.00075	1.97329117	4.196928 6	7.406722544	0.000190237	0.000225652	0.00028109	0.000357699	0.000437511
	0.1	0.15	0.412311	0.00075	0.96885491	2.060420 2	3.634608923	0.000414347	0.000490242	0.00061042	0.000775077	0.000946336
	0.114	0.15	0.385366	0.001	1.10558437	2.349456 9	4.144775925	0.000386533	0.000457612	0.00056944	0.000723051	0.000883782
	0.138333333	0.18	0.327835	0.0015	1.34146542	2.849062 7	5.025819063	0.000346983	0.00041085	0.00051131	0.000649552	0.000793453

	0.128	0.18	0.33784	0.002	1.23942617	2.6368567	4.652411643	0.00040653	0.000480957	0.00059803	0.000760147	0.000929044
	0.098	0.14	0.39123	0.003	0.95130718	2.0224046	3.560343081	0.000602957	0.000712134	0.00088433	0.001124451	0.001373455
	0.152105263	0.21	0.2446	0.00075	1.47379302	3.1375002	5.525248463	0.000261673	0.000310069	0.00038602	0.000490756	0.000600141
	0.116666667	0.2	0.457589	0.003	1.13091776	2.4051053	4.239933807	0.000498807	0.000589912	0.00073282	0.00093168	0.001137776
	0.127777778	0.15	0.128463	0.000375	1.23844938	2.6357713	4.643059975	0.000265078	0.000314337	0.00039166	0.0004979	0.000609309
	0.10625	0.14	0.313922	0.000375	1.02993618	2.1876177	3.860313137	0.000324451	0.000384475	0.00047957	0.000609943	0.000745211
	0.102	0.13	0.252291	0.000375	0.98811798	2.1022461	3.708088578	0.000339197	0.000402166	0.00050087	0.0006369	0.000778838
	0.07125	0.1	0.217915	0.0005	0.69055347	1.4695645	2.589787331	0.000539739	0.000639046	0.00079551	0.001011007	0.001237214
	0.115714286	0.13	0.097991	0.000375	1.12181279	2.3848191	4.204914172	0.000295529	0.000350363	0.00043656	0.000555059	0.000679373
	0.13625	0.22	0.500772	0.0015	1.32047687	2.8064138	4.952096063	0.000352412	0.000417333	0.0005195	0.000659922	0.000806221
	0.125	0.2	0.481901	0.00075	1.21222218	2.5779912	4.543460308	0.000324359	0.000384148	0.00047824	0.000607552	0.000742683
	0.125454545	0.2	0.413209	0.0015	1.21523061	2.5866772	4.558902154	0.000385667	0.000456542	0.00056783	0.000721303	0.000881423
	0.17375	0.27	0.444682	0.00075	1.68338329	3.5771025	6.313350675	0.000226525	0.000268648	0.00033464	0.000425208	0.000519705
	0.141428571	0.22	0.411133	0.00075	1.36950517	2.913919	5.141671827	0.000283569	0.000336017	0.00041808	0.000531314	0.000649566
	0.116	0.15	0.25117	0.000375	1.12460942	2.3923557	4.214845576	0.000294609	0.000348875	0.00043481	0.00055313	0.00067701
	0.124444444	0.16	0.300967	0.00075	1.20608573	2.5654426	4.522688769	0.00032615	0.000386223	0.00048075	0.000610968	0.00074645
	0.092	0.14	0.372326	0.00075	0.89131707	1.8959652	3.341164352	0.00045309	0.00053649	0.00066752	0.00084843	0.001036939
	0.068888889	0.11	0.37324	0.00075	0.66752022	1.4202851	2.503395421	0.000622181	0.000736091	0.00091526	0.001163678	0.001422557
	0.097	0.13	0.228206	0.001	0.94026741	1.9994002	3.523451051	0.000460508	0.000545348	0.00067844	0.00086161	0.001051953
	0.12	0.18	0.30429	0.00075	1.16461324	2.4724763	4.359596756	0.000339435	0.000402074	0.00050017	0.000635262	0.000776799
	0.112857143	0.17	0.408346	0.00075	1.09553601	2.325934	4.101052066	0.000362778	0.000429763	0.00053511	0.000680128	0.000831418

	0.14	0.17	0.202031	0.00075	1.35760472	2.8836548	5.086427104	0.000286667	0.000339904	0.00042303	0.000538142	0.000658311
	0.12	0.16	0.283823	0.0005	1.1630816	2.472175	4.362521927	0.000305664	0.000362168	0.00045116	0.000573937	0.000702252
	0.088	0.12	0.246358	0.0005	0.8525517	1.8136318	3.199219717	0.000428814	0.000508054	0.00063239	0.000804035	0.000982972
	0.129	0.16	0.315309	0.00075	1.24934075	2.6593011	4.688835524	0.00031323	0.000370955	0.00046164	0.000586758	0.000717218
	0.078571429	0.1	0.186308	0.00075	0.76234123	1.6194292	2.855733952	0.000537975	0.000636989	0.00079267	0.001007681	0.001232087
	0.153	0.21	0.270451	0.00075	1.4821895	3.1534835	5.560308747	0.000259886	0.00030803	0.00038352	0.000487698	0.000596808
	0.106666667	0.14	0.204323	0.00075	1.03402981	2.1989701	3.876335707	0.00038606	0.000457197	0.00056877	0.000722561	0.000883228
	0.103	0.13	0.204934	0.00075	0.9974273	2.1226044	3.743319461	0.000400627	0.000474129	0.0005904	0.000750889	0.000918289
STRAIGHT CANYON	0.154444444	0.24	0.399281	0.00075	1.49602109	3.185927	5.613203747	0.000257192	0.000304546	0.00037933	0.000482465	0.000590471
	0.127142857	0.18	0.316939	0.00075	1.23107695	2.6195807	4.620619726	0.000318406	0.000377393	0.00046993	0.000596966	0.000729658
	0.148571429	0.18	0.297041	0.00075	1.43932664	3.0627421	5.396310422	0.000268884	0.000318458	0.00039623	0.00050378	0.000616696
	0.134444444	0.18	0.276087	0.00075	1.30345795	2.7705955	4.887894756	0.000299598	0.00035485	0.00044199	0.000561477	0.000686424
	0.1425	0.22	0.381003	0.00075	1.38139653	2.9333761	5.178235808	0.000281518	0.000333491	0.00041546	0.00052798	0.000645048
	0.1975	0.28	0.347541	0.00075	1.91260471	4.0698082	7.173151963	0.000196723	0.000233208	0.0002906	0.00036962	0.000452212
	0.162222222	0.23	0.280425	0.00075	1.57255305	3.3436355	5.894464375	0.000244079	0.000289318	0.0003602	0.000457606	0.000559454
	0.172857143	0.19	0.079842	0.00075	1.6749765	3.5661897	6.282532117	0.000227533	0.000269682	0.0003357	0.000426536	0.000521775
	0.1275	0.16	0.186311	0.00075	1.23495441	2.6253006	4.633558917	0.000317678	0.000376293	0.00046853	0.000595678	0.000728105
	0.23	0.28	0.155248	0.00075	2.2310396	4.7394915	8.362345022	0.000166496	0.000197661	0.00024631	0.000313028	0.000382774
	0.204285714	0.23	0.154428	0.00075	1.98249098	4.2097612	7.421492513	0.000189645	0.000224953	0.00028035	0.00035659	0.000436095
	0.175	0.23	0.248142	0.00075	1.69673615	3.6067361	6.360712839	0.000224763	0.000266406	0.00033159	0.000421193	0.000515136
	0.148571429	0.2	0.281377	0.00075	1.43875101	3.0600228	5.401067968	0.000268918	0.000318491	0.00039692	0.00050413	0.000615975

	0.215	0.25	0.127377	0.00075	2.08250761	4.4282906	7.814069577	0.000179293	0.000212702	0.00026504	0.00033726	0.000411931
	0.131428571	0.18	0.318078	0.00075	1.27296654	2.7080098	4.77390983	0.000307251	0.000364146	0.00045333	0.000576	0.000703864
	0.235714286	0.29	0.162209	0.00075	2.28665692	4.8581573	8.566585361	0.000162281	0.000192452	0.00023983	0.000305057	0.000373228
	0.13	0.2	0.482433	0.0015	1.25942281	2.6813809	4.724035711	0.00037084	0.000439072	0.00054593	0.000693991	0.000847918
	0.09	0.13	0.366113	0.0015	0.87253601	1.8546162	3.269818634	0.000554231	0.000655543	0.00081515	0.001036394	0.001265933
	0.118571429	0.16	0.313407	0.002	1.14859929	2.443351	4.306820428	0.000441723	0.000522823	0.00064995	0.000825985	0.001009082
	0.1	0.13	0.264575	0.002	0.96905362	2.0595249	3.632559149	0.000532123	0.000629776	0.00078286	0.000994888	0.001213408
	0.174444444	0.19	0.111419	0.00075	1.69194563	3.5968863	6.337786911	0.000225275	0.000266938	0.00033256	0.000422632	0.000516766
	0.103333333	0.14	0.38548	0.00075	1.00079719	2.1302961	3.754682448	0.000399342	0.000472878	0.00058822	0.000747481	0.000913521
	0.095	0.13	0.297729	0.00075	0.91993414	1.9568164	3.451130328	0.000438123	0.000518286	0.0006458	0.000820248	0.001002041
	0.118333333	0.14	0.124391	0.003	1.14600339	2.4379093	4.30004746	0.000491555	0.000580909	0.00072159	0.000917816	0.001120555
	0.11	0.14	0.314918	0.003	1.06674662	2.2658246	3.99582535	0.000531792	0.000629197	0.00078219	0.000993114	0.001212186
	0.11	0.18	0.39775	0.001	1.06511749	2.2663778	3.998186984	0.000401336	0.000475636	0.00059146	0.000751588	0.000918573
	0.1075	0.13	0.237164	0.0015	1.04313943	2.2156163	3.906284046	0.000456839	0.000540386	0.00067246	0.000854578	0.001043756
	0.116666667	0.15	0.263725	0.0015	1.130319	2.404343	4.237500102	0.000417728	0.000494666	0.00061518	0.000781912	0.000954961
	0.15	0.18	0.183787	0.0015	1.45375087	3.0891359	5.45000717	0.000317318	0.000375777	0.00046792	0.00059478	0.000725501
	0.105	0.15	0.339401	0.0015	1.01769742	2.1657799	3.813616125	0.000468908	0.000554561	0.00068935	0.000876245	0.00106956
PRICE CANYON	0.108888889	0.16	0.288389	0.00025	1.05478625	2.2442217	3.95618714	0.000284394	0.000337271	0.00042075	0.000535311	0.000655072
	0.10125	0.16	0.396602	0.00025	0.98099589	2.0890843	3.680593189	0.000308101	0.00036516	0.00045493	0.0005787	0.000708711
	0.1375	0.2	0.395965	0.000375	1.33330885	2.8350569	4.997144581	0.000244567	0.000289967	0.00036126	0.000459162	0.000562311
	0.131428571	0.18	0.321097	0.00025	1.27322812	2.7081151	4.774772644	0.000231703	0.000275091	0.00034317	0.000436491	0.000534025

	0.183	0.21	0.08942	0.000375	1.77275449	3.7717775	6.651599154	0.000179074	0.000212427	0.00026482	0.00033689	0.000412031
	0.185	0.23	0.242073	0.000375	1.79309106	3.8091407	6.721682329	0.000177041	0.000210097	0.00026202	0.000333373	0.000408216
	0.17	0.23	0.32676	0.000375	1.64686111	3.5015073	6.178438994	0.000194218	0.000230415	0.00028711	0.000365026	0.000446688
	0.114444444	0.16	0.299873	0.000375	1.10986172	2.3595797	4.158019382	0.000299006	0.000354575	0.00044157	0.000561351	0.000687199
	0.153636364	0.19	0.204326	0.000375	1.4884743	3.1658357	5.583752987	0.000216787	0.000257304	0.0003206	0.00040746	0.00049837
	0.146428571	0.21	0.310779	0.000375	1.41820594	3.0176267	5.317855314	0.000228383	0.000270934	0.00033774	0.000429465	0.000525321
	0.120909091	0.14	0.158894	0.000375	1.17285506	2.4933001	4.39530882	0.000281374	0.000333455	0.00041574	0.000529023	0.000647017
	0.115555556	0.14	0.184142	0.000375	1.12024596	2.3801552	4.198911955	0.000295835	0.000350702	0.00043686	0.000555728	0.000679433
	0.115555556	0.15	0.248981	0.0005	1.11955136	2.3811428	4.200344063	0.000318666	0.000377546	0.00047011	0.000597861	0.00073122
	0.124166667	0.16	0.262565	0.0005	1.20314673	2.55848	4.514094468	0.000294822	0.000349344	0.00043491	0.000552581	0.000675533
	0.131	0.18	0.332643	0.0005	1.26906696	2.7005371	4.760525067	0.000277793	0.00032915	0.00041025	0.000521409	0.000637621
	0.105555556	0.13	0.222738	0.0005	1.02285879	2.1774973	3.835807333	0.000351177	0.000416252	0.00051812	0.000658522	0.000805586
	0.137	0.22	0.384782	0.0005	1.32866483	2.8238155	4.980651842	0.00026456	0.000313493	0.00039073	0.000496834	0.000607799
	0.117777778	0.18	0.305477	0.000375	1.14210963	2.4254399	4.280681682	0.000289965	0.000343833	0.0004283	0.000544229	0.000666067
	0.08125	0.11	0.290043	0.000375	0.78719969	1.6745014	2.950199121	0.0004348	0.000515316	0.0006416	0.000815196	0.000997252
	0.088	0.13	0.302082	0.000375	0.85224743	1.8147625	3.199127752	0.000398353	0.000471799	0.00058738	0.000746933	0.000915299
	0.116	0.16	0.30735	0.00025	1.12340756	2.3929344	4.217440204	0.000265664	0.000314968	0.00039239	0.000498781	0.000610574
	0.13375	0.2	0.385272	0.00025	1.29610584	2.7581997	4.860622522	0.000227232	0.000269465	0.00033616	0.000427592	0.000523655
	0.144444444	0.21	0.328593	0.00025	1.40082973	2.9765113	5.249261724	0.000209013	0.000247983	0.00030952	0.000393782	0.000481816
	0.105555556	0.15	0.28068	0.00025	1.02382005	2.1759373	3.835545915	0.000294236	0.000349087	0.00043537	0.000553711	0.000678284
	0.14875	0.2	0.244874	0.00025	1.4420335	3.0665837	5.40553335	0.000202297	0.000240039	0.00029935	0.000380807	0.000466489

	0.102	0.12	0.212544	0.00025	0.98889348	2.1013068	3.704353322	0.000305573	0.000362671	0.00045229	0.000575291	0.000704291
	0.125	0.16	0.28365	0.00025	1.21130883	2.5740867	4.541039375	0.000244894	0.000290615	0.0003624	0.000460888	0.000564371
	0.095	0.14	0.417276	0.00025	0.91998896	1.9569283	3.451121778	0.000330669	0.000392077	0.00048893	0.000621628	0.000760317
	0.12	0.16	0.280542	0.00025	1.16299596	2.4755309	4.36210928	0.00025554	0.000303181	0.00037821	0.000480966	0.000588966
	0.102222222	0.14	0.275732	0.000375	0.99058561	2.1055477	3.71590445	0.000338576	0.000401271	0.00049947	0.00063558	0.000777502
	0.115714286	0.17	0.326636	0.000375	1.12233998	2.3834179	4.205009194	0.000295672	0.000350578	0.00043704	0.000555469	0.000679363
	0.081428571	0.1	0.193248	0.000375	0.78983093	1.6788698	2.958582299	0.000434029	0.000514062	0.00064039	0.000813827	0.000996431
	0.128571429	0.2	0.429374	0.000375	1.24543691	2.6484623	4.672005202	0.000263296	0.000312226	0.00038901	0.000494263	0.000604482
	0.143333333	0.2	0.281242	0.000375	1.39000508	2.9530328	5.20740996	0.000233771	0.000277337	0.00034593	0.0004397	0.000538425
	0.104285714	0.14	0.281517	0.000375	1.01010354	2.1496946	3.790596794	0.000331072	0.000392216	0.00048866	0.000620714	0.000759417
	0.158571429	0.2	0.168543	0.000375	1.53740935	3.2683976	5.76256591	0.000209375	0.000248524	0.00031	0.000394494	0.000482467
	0.17375	0.23	0.242113	0.000375	1.68410432	3.5812975	6.314154378	0.000189685	0.000225013	0.00028026	0.000356418	0.000436426
	0.110909091	0.14	0.233225	0.00025	1.07538821	2.2825816	4.031079472	0.000279102	0.000331284	0.00041327	0.000525527	0.00064265
	0.133846154	0.21	0.288618	0.00025	1.29685519	2.7586798	4.861842106	0.000227131	0.000269573	0.00033614	0.000427528	0.000523779
	0.098571429	0.16	0.376997	0.00025	0.95527072	2.0332482	3.580038296	0.000317105	0.000376038	0.00046903	0.000596776	0.000730826
WATTIS ROAD	0.1175	0.16	0.286812	0.0005	1.13807991	2.4219554	4.270163651	0.000312699	0.000370207	0.00046151	0.000586914	0.000718074
	0.09375	0.13	0.284722	0.0005	0.90766858	1.9328001	3.407094386	0.000400079	0.000474082	0.00059056	0.00075031	0.000917523
	0.132222222	0.19	0.331347	0.0005	1.28188968	2.7237121	4.80363225	0.000274871	0.000325893	0.00040595	0.000516219	0.000631161
	0.15375	0.21	0.257683	0.0005	1.49059884	3.1688408	5.585668865	0.00023309	0.000276233	0.00034424	0.000438137	0.000535968
	0.133333333	0.18	0.313449	0.0005	1.29229848	2.7451638	4.846035249	0.000272367	0.000323029	0.00040287	0.000512194	0.00062653
	0.098	0.14	0.303465	0.000375	0.94916079	2.0204822	3.560982973	0.000354221	0.000419504	0.00052263	0.000665089	0.000813837

	0.11125	0.15	0.273646	0.000375	1.07771198	2.2950134	4.041296478	0.000308355	0.00036563	0.00045546	0.000578875	0.000708799
	0.09	0.13	0.366113	0.0005	0.87134194	1.8563441	3.269958383	0.000418675	0.000495971	0.00061763	0.000784902	0.000959451
	0.107272727	0.2	0.435432	0.000375	1.03866226	2.2106097	3.89982216	0.000320918	0.000380348	0.00047376	0.00060266	0.000737275
	0.119285714	0.19	0.411304	0.0015	1.15594438	2.4602691	4.33370777	0.000407562	0.000482259	0.00059971	0.000761932	0.000930899
	0.111818182	0.16	0.389447	0.00075	1.08445301	2.3054974	4.065082918	0.000366349	0.000433779	0.0005399	0.000686435	0.000838718
	0.134444444	0.2	0.399012	0.00075	1.30349686	2.7697971	4.882883207	0.000299702	0.000355027	0.000442	0.000561655	0.000687062
	0.065	0.09	0.333531	0.00075	0.6294416	1.3381558	2.362517696	0.000662765	0.000784469	0.0009767	0.001242138	0.00151805
	0.087777778	0.12	0.203617	0.00075	0.85126733	1.8098163	3.191345303	0.000476841	0.000564777	0.00070226	0.000892716	0.001091278
LINK CANYON	0.15	0.24	0.42339	0.0005	1.45298535	3.0902339	5.452708093	0.000239626	0.000284061	0.00035386	0.000449606	0.000550267
	0.15375	0.2	0.262331	0.0005	1.49002454	3.1680543	5.585424587	0.000233383	0.000276649	0.00034459	0.000437891	0.000535844
	0.200909091	0.33	0.452068	0.0005	1.94674253	4.1405995	7.301174949	0.000174027	0.000206386	0.00025732	0.000326905	0.000400028
	0.184	0.31	0.458444	0.0005	1.78227935	3.79153	6.688872835	0.000191662	0.000227172	0.00028329	0.000360311	0.000440909
	0.133	0.22	0.394767	0.0005	1.29122482	2.7419803	4.831993282	0.000273197	0.000323962	0.00040366	0.000513133	0.000627507
	0.16125	0.23	0.332211	0.0005	1.56278607	3.3236452	5.859580068	0.00022141	0.000262592	0.00032711	0.000416174	0.000509047
	0.187142857	0.32	0.462468	0.0005	1.81464022	3.8564701	6.80177209	0.000188049	0.000223142	0.00027806	0.000353759	0.000432494
	0.17	0.29	0.455645	0.0005	1.64779499	3.5037281	6.178157932	0.000208969	0.000247846	0.00030883	0.000392621	0.000480248
	0.144285714	0.2	0.350799	0.0005	1.39846742	2.9734267	5.245334157	0.000249929	0.000296524	0.00036974	0.00046987	0.000574261
	0.143333333	0.25	0.4725	0.0005	1.38784545	2.9539702	5.210985367	0.000251805	0.000298599	0.00037215	0.000473175	0.00057859
	0.125714286	0.19	0.425543	0.0015	1.21860443	2.5913212	4.567350156	0.000384724	0.000455705	0.00056661	0.000719986	0.00088007
	0.16375	0.23	0.278779	0.00075	1.58708662	3.3760864	5.951547942	0.000241555	0.000286142	0.00035621	0.000452969	0.000553839
	0.15	0.21	0.33665	0.00075	1.45252876	3.0928319	5.451314747	0.000265884	0.000314997	0.00039214	0.000498783	0.000609697

	0.097142857	0.15	0.401841	0.00075	0.94188654	2.0009878	3.529823104	0.000427486	0.000506152	0.00062997	0.000800332	0.000977395
	0.204444444	0.26	0.200351	0.00075	1.9823915	4.217818	7.429436164	0.000189391	0.000224623	0.0002799	0.000355664	0.000434913
	0.153636364	0.18	0.140425	0.00075	1.48947997	3.1636519	5.585326896	0.000259119	0.000307205	0.00038271	0.000486391	0.000594156
	0.1075	0.16	0.305503	0.002	1.04238267	2.2166662	3.906387446	0.000491169	0.000580918	0.00072212	0.000917674	0.001120675
	0.116666667	0.16	0.296923	0.002	1.13136747	2.4037413	4.239533233	0.000449859	0.000532155	0.00066187	0.000841162	0.00102606
	0.135	0.2	0.387943	0.002	1.30714462	2.7802175	4.905679698	0.000383591	0.000454149	0.0005646	0.000717543	0.000875576
	0.111111111	0.15	0.306676	0.0015	1.0766686	2.2893422	4.037711222	0.000440449	0.000521366	0.00064836	0.000824502	0.001006884

FERRON SANDSTONE	**FIELD DATA**				**RECONSTRUCTED PALAEOHYDRAULIC PARAMETERS**							
	Mean cross-set height, m	**Maximum cross-set height, m**	**CV(hxs)**	**Median grain size, m**	**Minimum plausible flow depth, m**	**Median flow depth, m**	**Maximum plausible flow depth, m**	**10th percentile of palaeoslope**	**25th percentile of palaeoslope**	**Median palaeoslope**	**75th percentile of palaeoslope**	**90th percentile of palaeoslope**
LAST CHANCE CREEK	0.252727273	0.45	0.522269	0.0015	2.45050397	5.2112508	9.184084561	0.000179393	0.000212591	0.0002649	0.000337176	0.000411869
	0.324545455	0.51	0.464513	0.000375	3.14502297	6.6891429	11.79571094	9.57E-05	0.000113724	0.00014209	0.000180922	0.000221712
	0.297777778	0.48	0.389385	0.002	2.88299088	6.1375071	10.8176095	0.000161432	0.000191308	0.00023823	0.000302922	0.000370543
	0.391666667	0.52	0.349878	0.0015	3.79402237	8.068606	14.23796947	0.000111076	0.000131891	0.00016446	0.000209241	0.000255724
	0.312222222	0.5	0.429043	0.002	3.02325532	6.4369554	11.349822	0.000153167	0.000181687	0.00022638	0.000287863	0.000351653
	0.25625	0.43	0.565878	0.00075	2.48266651	5.2805584	9.314353569	0.000148023	0.000175656	0.00021897	0.000278439	0.000340796
	0.11	0.23	0.655555	0.00075	1.06671797	2.2670742	3.998815343	0.000372776	0.000441598	0.00054939	0.000697962	0.00085382

	0.127142857	0.19	0.415477	0.00075	1.23106884	2.6202692	4.620677692	0.000318467	0.000377487	0.00046962	0.000596676	0.000729653
	0.127142857	0.21	0.48428	0.0015	1.23262009	2.6190467	4.622247228	0.000380248	0.000450103	0.00056002	0.000711041	0.000868582
	0.21	0.35	0.536217	0.0015	2.03522753	4.3255453	7.632321164	0.000219902	0.000260366	0.00032437	0.000412278	0.000503864
	0.217777778	0.36	0.547073	0.0015	2.11246885	4.4858611	7.9156732	0.000211275	0.000250463	0.00031187	0.00039643	0.000484344
	0.171	0.28	0.522657	0.0015	1.65688551	3.5253792	6.211525594	0.000274889	0.000325693	0.0004054	0.00051579	0.00063054
	0.208	0.28	0.306714	0.0015	2.0142143	4.2854201	7.556666931	0.000222208	0.000263187	0.00032767	0.000416397	0.000509136
	0.202857143	0.35	0.483164	0.00075	1.96594741	4.1837951	7.370078999	0.000190976	0.000226468	0.00028229	0.000358692	0.000438729
	0.130909091	0.23	0.499112	0.00075	1.26890077	2.6938968	4.758301666	0.000308605	0.000365687	0.00045536	0.000578914	0.000707867
	0.23875	0.4	0.403263	0.00075	2.31156277	4.9210432	8.678715249	0.000159892	0.000189637	0.00023646	0.000300812	0.000367746
	0.335	0.64	0.682569	0.001	3.24824043	6.9022764	12.17087915	0.000118857	0.000141057	0.00017599	0.000223622	0.000273343
	0.21875	0.42	0.572244	0.001	2.11918084	4.5091279	7.952039245	0.000189618	0.000224586	0.00027969	0.000355757	0.000435004
	0.205714286	0.28	0.28325	0.001	1.99299855	4.2404406	7.468797793	0.000202537	0.000240044	0.00029901	0.00038026	0.000464899
	0.274285714	0.41	0.309257	0.001	2.65618315	5.6500997	9.966979624	0.000148002	0.000175509	0.00021888	0.00027845	0.000340515
	0.225	0.3	0.261052	0.00075	2.1801993	4.6392618	8.176580392	0.000170694	0.000202413	0.00025211	0.000320429	0.000392018
	0.216	0.34	0.370499	0.00075	2.09484861	4.4579109	7.848247748	0.000178344	0.000211404	0.00026315	0.000334625	0.000409391
	0.147142857	0.23	0.483296	0.00075	1.42766914	3.0338901	5.348358613	0.000271523	0.000321748	0.00040038	0.00050872	0.000621916
	0.192	0.35	0.477857	0.000375	1.85979179	3.9548758	6.978719526	0.000169876	0.000201758	0.00025157	0.000320087	0.000391941
	0.202222222	0.3	0.531322	0.00075	1.96121197	4.1660215	7.347883901	0.000191697	0.000227329	0.00028324	0.000360251	0.000440315
	0.088571429	0.12	0.27213	0.00075	0.8580326	1.8269906	3.218299073	0.000472079	0.000558619	0.00069544	0.000884312	0.001081237
	0.103333333	0.13	0.209056	0.00075	1.00128679	2.1282349	3.75509256	0.000399144	0.000472972	0.00058927	0.000748752	0.000914083
	0.128571429	0.17	0.312497	0.00075	1.24674884	2.649012	4.669611738	0.000315007	0.000372886	0.00046397	0.000589386	0.000721074

	0.1375	0.2	0.407254	0.0015	1.33305824	2.8347415	4.996809816	0.000348911	0.000412909	0.0005143	0.00065362	0.000798716
	0.3325	0.49	0.437828	0.00075	3.22031444	6.8517615	12.08484752	0.000111249	0.000132144	0.00016495	0.000209631	0.000256558
	0.13	0.29	0.56825	0.00075	1.25921841	2.6785755	4.723801253	0.000311034	0.000368301	0.00045828	0.000582779	0.000712004
	0.201428571	0.35	0.491822	0.0015	1.95375172	4.153074	7.320961696	0.000229981	0.000272402	0.00033877	0.000430298	0.000525534
	0.228	0.3	0.318398	0.0015	2.21364491	4.7000238	8.285675009	0.000200821	0.000237943	0.00029639	0.000376806	0.000460336
	0.371666667	0.62	0.539806	0.000375	3.60159323	7.655998 4	13.50911627	8.24E-05	9.81E-05	0.00012251	0.000155886	0.000190947
	0.124166667	0.19	0.414174	0.00075	1.20258103	2.5589577	4.514532767	0.000326863	0.000387166	0.00048201	0.000613335	0.000749866
	0.305	0.44	0.380479	0.000375	2.95597958	6.2850147	11.08434924	0.000102402	0.00012174	0.00015194	0.000193246	0.000236612
	0.4475	0.59	0.229371	0.00075	4.33609718	9.229318	16.2577794	8.04E-05	9.56E-05	0.0001193	0.000151759	0.000185738
	0.290714286	0.42	0.374744	0.0005	2.81747107	5.9931057	10.5645532	0.000116155	0.000137894	0.00017206	0.000219084	0.000268049
	0.293076923	0.54	0.486821	0.0005	2.8398357	6.0424181	10.65237081	0.000115207	0.000136678	0.00017065	0.000217147	0.000265931
	0.1325	0.24	0.46829	0.000375	1.28316354	2.7303237	4.81686251	0.000254855	0.000302108	0.00037679	0.000479068	0.000586143
	0.0675	0.1	0.489487	0.0005	0.65361788	1.3918696	2.453521051	0.000572774	0.000678108	0.00084488	0.001074702	0.001313565
	0.085555556	0.12	0.274807	0.0005	0.83034142	1.7643557	3.109942992	0.000442157	0.000523513	0.000652	0.000828168	0.001012121
	0.083333333	0.13	0.427083	0.00075	0.80768108	1.7168146	3.02808995	0.000505164	0.000597916	0.00074405	0.000944977	0.001155157
	0.094285714	0.12	0.317339	0.00075	0.91378153	1.9428383	3.427732267	0.000441234	0.000522288	0.00065016	0.000826414	0.001010648
	0.09	0.12	0.30089	0.00075	0.87151603	1.8545611	3.270246415	0.000464731	0.000550179	0.00068456	0.000870113	0.001063518
	0.095555556	0.12	0.203405	0.00075	0.92597668	1.9693483	3.473630692	0.000434865	0.000514936	0.00064082	0.000814072	0.000995258
	0.070833333	0.11	0.353369	0.00075	0.68580935	1.4606409	2.573310637	0.000602696	0.000712817	0.00088723	0.001126625	0.001378344
	0.059090909	0.08	0.306999	0.00075	0.57298033	1.2181625	2.148123931	0.000735247	0.000869649	0.00108117	0.001374318	0.001679738
	0.299	0.41	0.273735	0.0015	2.89972971	6.1627143	10.85427026	0.000149232	0.000177097	0.00022075	0.000280633	0.000343181

	0.124	0.26	0.631806	0.003	1.20200467	2.5545008	4.50651278	0.000466637	0.000551584	0.00068554	0.00087097	0.001063552
	0.19	0.26	0.225062	0.0015	1.84069953	3.9191192	6.898675077	0.000245347	0.000290638	0.00036135	0.000459627	0.000561462
	0.263636364	0.57	0.755061	0.0005	2.55510409	5.4344736	9.579913161	0.000129246	0.000153504	0.00019162	0.000243748	0.000298376
	0.293333333	0.4	0.265712	0.0005	2.84035041	6.0408682	10.66096647	0.000115176	0.000136734	0.00017081	0.00021724	0.000265763
	0.14625	0.25	0.363539	0.00075	1.41616506	3.0111762	5.315833327	0.000273496	0.000324031	0.00040358	0.000513017	0.000626817
	0.096666667	0.14	0.324944	0.0005	0.93754884	1.9913033	3.512942901	0.000386969	0.000458643	0.00057103	0.000725494	0.000887922
	0.105	0.15	0.334013	0.0005	1.01658137	2.1636775	3.815508144	0.000353938	0.000418933	0.00052184	0.00066384	0.000811908
	0.121666667	0.19	0.400694	0.0005	1.17943188	2.5053482	4.421783952	0.0003013	0.000357171	0.00044456	0.000565285	0.000691152
	0.145	0.19	0.342752	0.0005	1.40443858	2.9894119	5.268077491	0.000248781	0.000294786	0.00036713	0.000466666	0.000571675
	0.128333333	0.19	0.379878	0.00075	1.24423517	2.6456396	4.665042837	0.000315114	0.000373576	0.00046505	0.000591648	0.000723158
	0.17875	0.23	0.24374	0.0005	1.73277501	3.6825924	6.49871059	0.000197876	0.000234784	0.0002924	0.000371779	0.000455002
	0.085714286	0.12	0.284638	0.0005	0.83062776	1.7682096	3.115076562	0.000441077	0.000522312	0.00065036	0.000827453	0.001012371
	0.10875	0.15	0.279937	0.000375	1.05390579	2.2406741	3.95082051	0.00031656	0.000374872	0.00046713	0.000593878	0.000727232
	0.116666667	0.2	0.489898	0.0005	1.12990388	2.4049236	4.239304526	0.000315161	0.000373559	0.00046539	0.000591801	0.000723679
	0.10125	0.13	0.327302	0.00075	0.98362627	2.0903026	3.678416479	0.0004078	0.000482954	0.00060102	0.00076409	0.000934673
	0.142222222	0.22	0.514025	0.00075	1.37782604	2.9294461	5.169761739	0.000281809	0.000333952	0.00041598	0.000528915	0.000646506
	0.092857143	0.13	0.386865	0.00075	0.89973384	1.912318	3.375123345	0.000449016	0.000531965	0.00066148	0.000840389	0.001027127
	0.209230769	0.32	0.389975	0.00075	2.02761818	4.31192	7.604269263	0.00018482	0.000219197	0.00027289	0.00034718	0.000424816
	0.1475	0.22	0.444941	0.00075	1.43004736	3.0408296	5.361196721	0.000271068	0.000320931	0.00039971	0.000507607	0.000620422
	0.051428571	0.09	0.543385	0.00075	0.49797522	1.0606433	1.868625597	0.000854106	0.001010624	0.00125719	0.001599832	0.001955103
	0.1075	0.15	0.288865	0.00075	1.04154633	2.2158173	3.905769731	0.000382925	0.000453564	0.00056389	0.000717081	0.000876201

	0.07	0.11	0.521641	0.00075	0.67819942	1.4430721	2.543693632	0.000610632	0.00072294	0.00089938	0.001143856	0.001397813
	0.1	0.2	0.7	0.00075	0.96879301	2.0614979	3.632945841	0.000413825	0.000489796	0.0006096	0.000774897	0.000947616
	0.082	0.1	0.234578	0.00075	0.79405813	1.6898921	2.979048851	0.00051362	0.000607792	0.00075598	0.000962373	0.001177424
	0.114285714	0.17	0.377561	0.00075	1.10764027	2.3552293	4.153517788	0.000357554	0.00042337	0.00052742	0.000670226	0.000819211
	0.1	0.16	0.44376	0.00075	0.9691017	2.0609322	3.632094011	0.00041406	0.000490043	0.00060982	0.000775419	0.000947686
	0.138333333	0.17	0.206583	0.00075	1.34098358	2.8509652	5.027936314	0.000290416	0.000343926	0.00042816	0.000544613	0.000666201
	0.096666667	0.12	0.232854	0.00075	0.93721744	1.9904304	3.51238324	0.000429661	0.000508825	0.00063329	0.000804853	0.000983378
	0.17	0.22	0.294118	0.00075	1.64659354	3.5070004	6.175829463	0.000231791	0.000274828	0.00034204	0.000434935	0.000531845
	0.165714286	0.23	0.317135	0.00075	1.60627319	3.4140108	6.024486181	0.000238279	0.000282404	0.00035192	0.00044754	0.000547308
	0.133333333	0.22	0.449166	0.00075	1.29161346	2.7475689	4.846164245	0.000302234	0.000358125	0.00044593	0.000566625	0.000692912
	0.145	0.2	0.389518	0.00075	1.40453984	2.9850961	5.269137349	0.000275709	0.000327004	0.00040732	0.000517549	0.000632592
	0.188333333	0.35	0.563349	0.00075	1.82568407	3.8834673	6.840916184	0.000207203	0.000245736	0.00030607	0.000389433	0.000475977
	0.195	0.29	0.37789	0.0005	1.89117791	4.019977	7.089343969	0.000179784	0.00021323	0.00026579	0.000337961	0.000413564
	0.1175	0.17	0.377194	0.0005	1.13862982	2.4209908	4.270595482	0.000312893	0.000370609	0.00046172	0.000587016	0.00071733
	0.108333333	0.18	0.375712	0.0005	1.04935234	2.2336015	3.937770739	0.000341615	0.000404698	0.00050375	0.00064074	0.000783898
	0.1925	0.3	0.495747	0.0005	1.86706905	3.9691569	6.994243446	0.000182271	0.000216209	0.00026951	0.000342758	0.000419488
	0.13125	0.22	0.416193	0.0005	1.27225548	2.7024855	4.768946403	0.000277309	0.000328823	0.00040974	0.000520625	0.000636575
	0.127777778	0.22	0.50534	0.0005	1.23767213	2.6321206	4.644198729	0.000285529	0.000338348	0.00042146	0.000535542	0.000655139
	0.265714286	0.45	0.564456	0.0005	2.57360907	5.4710592	9.652861153	0.0001284	0.000152431	0.0001901	0.000241971	0.000295864
	0.18125	0.3	0.461075	0.0005	1.75685628	3.7337121	6.587386738	0.000194942	0.000231259	0.00028809	0.000366378	0.000448426
	0.255	0.33	0.25587	0.00075	2.47546212	5.2569213	9.265922495	0.000148795	0.000176457	0.00022014	0.000279913	0.00034232

	0.4225	0.53	0.232163	0.00075	4.09625171	8.7114971	15.34807815	8.56E-05	0.000101695	0.00012688	0.000161443	0.000197846
	0.132	0.17	0.259131	0.00075	1.27893732	2.7194131	4.796192475	0.000305871	0.000362508	0.00045113	0.000573574	0.000701303
	0.12625	0.21	0.500843	0.0005	1.22358851	2.6038358	4.587960489	0.000289072	0.00034257	0.00042675	0.000542349	0.000663252
	0.1125	0.18	0.382326	0.001	1.09018023	2.3162737	4.087810349	0.000392099	0.000464551	0.00057774	0.000733792	0.000896837
	0.204444444	0.29	0.331845	0.00075	1.98064837	4.2147673	7.432395613	0.000189303	0.000224559	0.00027991	0.000355823	0.000435415
	0.315	0.37	0.18036	0.00075	3.0546273	6.4948774	11.45018594	0.000118174	0.00014022	0.00017487	0.000222413	0.000272211
	0.151666667	0.19	0.265106	0.00075	1.47070862	3.1275044	5.50720308	0.000262761	0.000311398	0.00038745	0.000492439	0.000601844
	0.108571429	0.17	0.514001	0.00075	1.05218097	2.2382772	3.946216343	0.000378179	0.000447792	0.00055724	0.000708527	0.000866221
	0.057142857	0.08	0.345808	0.0015	0.55362053	1.178659	2.077122334	0.000909649	0.001075745	0.00133664	0.001699637	0.002075981
	0.38	0.64	0.473475	0.00075	3.68122575	7.827909	13.80698752	9.62E-05	0.000114222	0.0001425	0.000181273	0.000221932
	0.19625	0.3	0.440814	0.00075	1.90260638	4.0460101	7.128510663	0.000198207	0.000234857	0.00029255	0.000371646	0.000454457
	0.25	0.42	0.489244	0.00075	2.42448527	5.1510938	9.086765544	0.000152131	0.000180501	0.00022502	0.000286111	0.000349743
	0.195714286	0.3	0.428362	0.00075	1.89702672	4.0291211	7.112887427	0.000198895	0.000235912	0.00029374	0.000373561	0.000457002
	0.241	0.32	0.287111	0.00075	2.33496753	4.9665222	8.758347318	0.00015827	0.000187705	0.00023409	0.000297645	0.000363867
WILLOW BASIN	0.07375	0.11	0.389883	0.0005	0.7140648	1.5187742	2.680282097	0.000520195	0.000615697	0.00076679	0.000974577	0.001192029
	0.06375	0.09	0.277297	0.00075	0.61727652	1.314386	2.315235477	0.000676613	0.000800525	0.00099514	0.001264057	0.001546289
	0.1	0.13	0.244949	0.00075	0.96982069	2.059896	3.633212914	0.000413788	0.000489958	0.00060989	0.000775012	0.000947193
	0.07	0.09	0.267261	0.0005	0.67828326	1.4434504	2.544469105	0.00055081	0.000652158	0.0008117	0.001032633	0.001262463
	0.061428571	0.08	0.256166	0.0005	0.59528073	1.2663905	2.230856104	0.000635085	0.00075185	0.00093575	0.001189919	0.001454599
	0.08875	0.12	0.258612	0.0005	0.85919143	1.8276067	3.225165595	0.000425104	0.000503625	0.00062724	0.000797112	0.000974943
	0.09	0.14	0.456194	0.0005	0.87297816	1.8568585	3.268283982	0.000418139	0.00049547	0.00061642	0.00078306	0.000958695

	0.128333333	0.16	0.248456	0.0005	1.24475939	2.6449611	4.665467476	0.00028431	0.00033702	0.00041969	0.00053335	0.000651754
	0.15	0.18	0.152023	0.0005	1.45295084	3.0916764	5.450702277	0.000239481	0.000284095	0.00035398	0.000450074	0.000550741
	0.091666667	0.12	0.252721	0.0005	0.88779999	1.888659	3.330500398	0.0004103	0.000486267	0.00060548	0.000769527	0.000940806
	0.085	0.11	0.235294	0.0005	0.82416552	1.7508158	3.089539111	0.0004455	0.00052788	0.00065724	0.000835704	0.001021891
	0.198333333	0.22	0.074216	0.00075	1.92166289	4.0877912	7.208741567	0.000195875	0.000232256	0.00028929	0.000367605	0.000449665
	0.125	0.2	0.476655	0.00075	1.21157475	2.5770639	4.540799209	0.000324496	0.000384174	0.00047847	0.000608095	0.000742859
	0.121666667	0.18	0.433102	0.0005	1.17892695	2.506314	4.421526088	0.00030127	0.000357069	0.00044492	0.000565707	0.000690825
	0.145555556	0.17	0.091603	0.00075	1.41137735	2.9996257	5.288668493	0.000274599	0.000325219	0.00040525	0.000515168	0.000629967
	0.186666667	0.29	0.441761	0.0005	1.80998846	3.8491341	6.785347821	0.000188511	0.000223724	0.00027883	0.000354724	0.000434242
	0.105714286	0.17	0.561909	0.0005	1.02424025	2.1784186	3.842590529	0.000351186	0.000416215	0.00051799	0.000659044	0.000805817
	0.114444444	0.16	0.330168	0.0005	1.10876765	2.3591422	4.159129106	0.000322192	0.000381752	0.00047544	0.000603703	0.000739092
	0.071428571	0.13	0.501066	0.0005	0.6920164	1.4716849	2.59662942	0.000539134	0.000638097	0.00079464	0.001009327	0.001233596
	0.196666667	0.28	0.411519	0.0005	1.90693379	4.0500493	7.146975787	0.000178288	0.000211499	0.00026387	0.000335478	0.000410037
	0.133333333	0.2	0.37687	0.00075	1.29281565	2.7487277	4.847586067	0.000302037	0.000357821	0.00044562	0.000566766	0.00069376
	0.21	0.25	0.134687	0.00075	2.03519421	4.3280797	7.629898053	0.000183969	0.000218229	0.00027215	0.00034591	0.000422774
	0.166666667	0.24	0.344674	0.00075	1.61444571	3.4372858	6.058149305	0.00023707	0.000280839	0.0003496	0.000444519	0.000543891
	0.194285714	0.3	0.541345	0.00075	1.88249938	4.0037348	7.059126528	0.000200236	0.000237356	0.00029584	0.000376317	0.000460148
	0.1775	0.27	0.465307	0.00075	1.71872725	3.6566494	6.447964676	0.000221274	0.000262245	0.00032661	0.000415771	0.00050867
	0.17875	0.26	0.295177	0.0005	1.73310918	3.6851173	6.496159732	0.000197827	0.000234513	0.00029205	0.000371946	0.000455143
	0.18625	0.34	0.546746	0.00075	1.80550013	3.8366514	6.767416244	0.000209711	0.000248879	0.00030992	0.000394306	0.000482154
	0.178888889	0.3	0.460497	0.00075	1.73398953	3.6829332	6.499943137	0.000219477	0.000260062	0.00032421	0.000412298	0.000503716

	0.166666667	0.33	0.619677	0.00075	1.61591346	3.4358696	6.054276474	0.000236796	0.000280604	0.00034955	0.000444458	0.000543864
	0.144285714	0.25	0.502745	0.00075	1.39762091	2.9731471	5.244884256	0.000277361	0.000328572	0.00040899	0.000520324	0.000636758
	0.19875	0.35	0.478413	0.0005	1.92781663	4.0977427	7.222814562	0.000176107	0.000208795	0.00026038	0.00033122	0.000405479
	0.233333333	0.35	0.445384	0.00075	2.25991384	4.8094419	8.479450213	0.000164014	0.000194524	0.00024252	0.000308332	0.000377222
	0.165	0.25	0.422072	0.00075	1.59830028	3.4003737	5.996316842	0.000239707	0.000283895	0.00035362	0.000449502	0.000549804
	0.122	0.2	0.482842	0.0015	1.18206537	2.5145747	4.433983306	0.000397282	0.000470275	0.00058536	0.00074405	0.000909516
	0.1975	0.3	0.493694	0.0005	1.91385104	4.0717255	7.178771004	0.000177362	0.000210434	0.00026242	0.000333776	0.000408307
	0.251	0.4	0.470821	0.0005	2.43285054	5.168667	9.120328543	0.000136531	0.000162091	0.00020222	0.00025711	0.000314897
	0.111666667	0.16	0.364497	0.0005	1.08283849	2.3035869	4.059057643	0.0003307	0.00039166	0.00048748	0.000619416	0.000757952
	0.092222222	0.13	0.30563	0.00075	0.89330962	1.9005873	3.351686313	0.000452325	0.000535434	0.00066612	0.000847208	0.00103603
	0.057142857	0.07	0.241523	0.00075	0.55365581	1.1783545	2.076869302	0.000762904	0.000901474	0.0011215	0.001425673	0.001744147
	0.091666667	0.13	0.293583	0.00075	0.88869192	1.8902614	3.330596341	0.000454683	0.000538701	0.00066998	0.000851156	0.001041038
	0.1	0.15	0.454606	0.0005	0.96834424	2.0592089	3.632461677	0.000373148	0.000442258	0.00055053	0.000699569	0.000855458
	0.0775	0.12	0.369814	0.0005	0.75194473	1.5964835	2.815060395	0.000492839	0.000583661	0.00072655	0.000923718	0.001129017
	0.085714286	0.11	0.218092	0.0005	0.83158384	1.7658415	3.115678959	0.000441386	0.000522872	0.00065128	0.000827396	0.001012908
	0.13	0.19	0.251942	0.00075	1.25863434	2.6767035	4.725218406	0.000310986	0.00036845	0.00045931	0.000583647	0.000712811
	0.073333333	0.1	0.294579	0.00075	0.71062098	1.5114875	2.66424158	0.000580958	0.000687637	0.00085543	0.001087491	0.001329035
	0.288571429	0.42	0.459917	0.0005	2.79453176	5.944133	10.48582225	0.000117129	0.000139046	0.00017364	0.000220847	0.000270255
	0.28125	0.5	0.520979	0.0005	2.72674951	5.7974562	10.21910789	0.000120502	0.000143096	0.0001784	0.000227027	0.000277933
	0.206	0.32	0.418434	0.0005	1.99605852	4.2465641	7.487018014	0.000169405	0.000201114	0.00025069	0.000318742	0.000389892
	0.198	0.29	0.383639	0.0005	1.92031737	4.0814481	7.196830629	0.000176835	0.000209702	0.00026155	0.000332583	0.000406686

	0.20375	0.36	0.542698	0.0005	1.97540565	4.199852 8	7.40323740 1	0.000171555	0.000203363	0.00025346	0.000322291	0.000393888
	0.24166666 7	0.35	0.360182	0.00075	2.3409495	4.980232 2	8.78273906	0.000157658	0.000187011	0.0002331	0.000296435	0.000362794
	0.18	0.3	0.576012	0.00075	1.74586872	3.708526 9	6.53514011	0.0002177	0.000258245	0.00032189	0.000409382	0.000500636
	0.24571428 6	0.45	0.651102	0.0005	2.38063691	5.066415 1	8.92414593 6	0.000139662	0.000165828	0.00020675	0.000262828	0.000321945
	0.21333333 3	0.3	0.365104	0.0005	2.06532233	4.39785	7.75337963 7	0.000162915	0.000193289	0.00024101	0.000306522	0.000375049
	0.1825	0.29	0.465638	0.00075	1.76794187	3.762341 7	6.63287027 6	0.000214612	0.000254287	0.00031663	0.000402485	0.000491927
WILLOW CREEK	0.12	0.19	0.430331	0.0005	1.16344161	2.474312 4	4.36307719 1	0.000305719	0.000362063	0.00045125	0.000573822	0.000701982
	0.21	0.38	0.582434	0.0005	2.0371084	4.327575 3	7.63218712 7	0.000165839	0.000196726	0.00024528	0.000311877	0.000381627
	0.12166666 7	0.2	0.417213	0.0015	1.17894086	2.508286 9	4.42074995 7	0.000398941	0.000472147	0.00058734	0.000747002	0.000911344
	0.105	0.14	0.274378	0.0015	1.01759714	2.164026 6	3.81471148	0.000469204	0.000554885	0.00068965	0.000876576	0.001069997
	0.185	0.3	0.450631	0.0015	1.79534712	3.808715	6.71864357	0.000252346	0.000299211	0.00037241	0.000473072	0.00057815
	0.18	0.29	0.539776	0.0005	1.74336728	3.707788 9	6.54017696	0.00019631	0.000232826	0.00029038	0.000369249	0.000451689
	0.10833333 3	0.19	0.479349	0.0005	1.0496826	2.231759	3.93682599 5	0.000342131	0.000405276	0.00050485	0.000641257	0.000783821
	0.08625	0.14	0.471723	0.0015	0.83557162	1.777358 4	3.13428769 5	0.000580635	0.000687127	0.000855	0.001086093	0.001325327
	0.072	0.1	0.316715	0.00075	0.69742178	1.483700 7	2.61681988 7	0.000592493	0.000700708	0.00087226	0.001108878	0.00135582
	0.2225	0.47	0.688242	0.0015	2.15589381	4.581397 2	8.08281166 3	0.000206569	0.000244885	0.00030481	0.000387206	0.000473027
	0.11833333 3	0.18	0.386952	0.00075	1.14617292	2.439757 9	4.29833464 5	0.000344523	0.000407887	0.00050756	0.000645344	0.000788152
	0.18375	0.3	0.43434	0.00075	1.7800551	3.788431 9	6.67812111 1	0.000212869	0.000252167	0.00031438	0.000399946	0.000488522
	0.158	0.25	0.503155	0.00075	1.5316793	3.256200 7	5.74016942 3	0.000250946	0.000297654	0.00037061	0.000471092	0.000576388
	0.15666666 7	0.3	0.561799	0.00075	1.51790509	3.230089 1	5.69188465	0.000253565	0.000300366	0.00037414	0.000475619	0.000581776
	0.08714285 7	0.12	0.262636	0.00075	0.84458157	1.795497 6	3.16639077 4	0.000480754	0.000569044	0.00070847	0.000900758	0.00110176

	0.13888889	0.2	0.349857	0.00075	1.34545177	2.8633476	5.044117475	0.000289114	0.000342486	0.00042624	0.000541886	0.000661928
	0.108571429	0.14	0.273376	0.00075	1.05309885	2.237264 3	3.944709301	0.000378367	0.000447918	0.00055749	0.000708598	0.000867047
	0.148571429	0.22	0.424676	0.001	1.44078326	3.061579 8	5.397723677	0.000289124	0.000342397	0.00042621	0.000541572	0.000662232
	0.156666667	0.28	0.580348	0.00075	1.52094092	3.227677	5.695666706	0.000253394	0.000300313	0.00037442	0.000475965	0.000581716
	0.131666667	0.25	0.606486	0.001	1.27615087	2.711620 7	4.784806042	0.000329983	0.000390931	0.00048695	0.000618844	0.000755915
	0.075	0.12	0.475161	0.00037 5	0.72735376	1.545549 3	2.72674828	0.000474457	0.000561838	0.00069966	0.000889163	0.001088059
	0.095555556	0.14	0.343565	0.00037 5	0.92662256	1.968416 2	3.47249696	0.000364289	0.00043183	0.00053771	0.000684027	0.000837126
	0.145714286	0.19	0.306546	0.0005	1.41229451	3.002817 7	5.296092004	0.00024719	0.000293138	0.00036518	0.000464072	0.000567789
	0.083333333	0.13	0.339411	0.00037 5	0.80786807	1.717741 6	3.026104363	0.000422598	0.000500823	0.00062397	0.00079378	0.00097063
	0.137777778	0.21	0.411824	0.0005	1.33426206	2.839149 4	5.005909473	0.000262862	0.000311689	0.00038812	0.000493684	0.000603563
	0.192857143	0.25	0.268955	0.00075	1.86893906	3.975451 7	7.003978032	0.000201973	0.000239612	0.00029841	0.000378983	0.000463698
	0.082	0.13	0.505767	0.0005	0.79520234	1.690566 9	2.978367941	0.000463004	0.000548079	0.00068296	0.000868479	0.001062183
	0.064	0.09	0.450152	0.00075	0.62050195	1.318378 3	2.325148655	0.00067383	0.000797623	0.00099242	0.001261134	0.001541651
	0.11125	0.14	0.260685	0.0005	1.07887772	2.290737 4	4.043285834	0.000332178	0.000393299	0.00049002	0.000622799	0.000761811
	0.132	0.19	0.492133	0.00075	1.27874645	2.720981	4.797928484	0.000305681	0.000362186	0.00045083	0.000572528	0.000699561

APPENDIX D: *Supplement to* The problem of palaeo-planforms[1]

Contents:

[1] A version of this appendix has been accepted for publication in ***Geology***.

D1 Methodological details

D1.1 Field methods

We collected cross-set and grain-size data from fluvial strata of the Blackhawk Formation, Castlegate Sandstone and Ferron Sandstone at multiple localities in Utah, USA (Chapter 5; Figure 5.1). These data are the same as those previously presented in Chapter 3 (Lyster et al., 2021) and Chapter 4 (Lyster et al., 2022). For individual cross-sets, we delineated bounding surfaces and measured the cross-set thickness at regular intervals along the entire width of the cross-set dip-section (vertical precision = ±5 mm; n = 5–15 measurements per cross-set; Chapter 5; Figure 5.1e), and we used the thickness distribution to establish the mean cross-set thickness, h_{xs} (c.f. Ganti et al., (2019); Chapter 3 (Lyster et al., 2021); Chapter 4 (Lyster et al., 2022). We also estimated the median grain-size (D_{50}) of each cross-set using the Wentworth (1922) classification (Chapter 5; Figure 5.1d). For each size term in the Wentworth (1922) classification we assigned the middle value, e.g., D_{50} of medium-grade sand = 0.375 mm, or, where grain-size straddled two size terms, we used the boundary value, e.g., D_{50} of medium–coarse-grade sand = 0.5 mm (Wentworth, 1922). We repeated this protocol for multiple cross-sets within co-sets at localities (Chapter 5; Figure 5.1a).

D1.2 Hydraulic geometry reconstruction

For each cross-set, we reconstructed the original bedform (i.e., dune) height, h_d, using the relation of Leclair and Bridge (2001):

$$h_d = 2.9(\pm 0.7)h_{xs}, \quad \text{Eq. D1}$$

where 2.9 is the mean (μ) and 0.7 is the standard deviation (σ). We estimated and propagated uncertainty using a Monte Carlo approach. In Equation D1, we generated 10^6 random samples of the model parameter between bounds defined by $\mu-\sigma$ and $\mu+\sigma$. To avoid introduction of additional assumptions, we generated samples from a uniform distribution because the shape and scale of the full data distribution is unknown. Using 10^6 samples of the model parameter, we calculated 10^6 values of h_d and propagated these values through Equations D2–D8. We then reconstructed paleoflow depths, H, using the empirically derived relation of Bradley and Venditti (2017), where median H is given as

$$H = 6.7h_d. \quad \text{Eq. D2}$$

Bradley and Venditti (2017) also presented a probabilistic uncertainty estimator in which the 25th and 75th percentiles of H are given by $H=4.4h_d$ and $H=10.1h_d$, respectively. We generated 10^6 random samples between 4.4 and 10.1, again from a uniform distribution, and used these values to reconstruct 10^6 values of H. We highlight that estimates of H derived using Equations D1 and D2 have previously been verified for the Blackhawk Formation, Castlegate Sandstone and Ferron Sandstone using independent paleoflow depth proxies, e.g., bar heights (c.f. Chapter 3 (Lyster et al., 2021); Chapter 4 (Lyster et al., 2022)).

To reconstruct paleoslope, we used the empirical approach of Trampush et al., (2014) which, for sand-grade deposits, has previously been shown to recover paleoslope values that are similar to those recovered using a Shields stress inversion (Ganti et al., 2019; Chapter 3 (Lyster et al., 2021)). Trampush et al., (2014) expressed paleoslope, S, as

$$\log S = \alpha_0 + \alpha_1 \log D_{50} + a_2 \log H, \quad \text{Eq. D3}$$

where $\alpha_0 = -2.08 \pm 0.036$, $\alpha_1 = 0.254 \pm 0.016$, and $\alpha_2 = -1.09 \pm 0.044$ are constants. We randomly sampled 10^6 values of a_0, a_1, and a_2 (uniformly distributed between $\mu-\sigma$ and $\mu+\sigma$) and used these values to generate 10^6 values of S.

With 10^6 values of H and S, we used Manning's equation to calculate 10^6 values flow velocity, U, as

$$U = \frac{1}{n} H^{\frac{2}{3}} S^{\frac{1}{2}}, \quad \text{Eq. D4}$$

where n is Manning's constant (set as 0.03), and 10^6 values of Froude number, Fr, as:

$$Fr = \frac{U}{\sqrt{gH}}, \quad \text{Eq. D5}$$

where g is acceleration due to gravity. As the errors and uncertainties associated with Equations D1–D5 are propagated forwards, we suggest that, of the 10^6 values recovered for each hydraulic parameter for each cross-set, median values offer plausible values for the mean, and 10–90 percentile ranges offer plausible minimum–maximum values for the mean.

D1.3 Channel width estimation

Each planform predictor requires the channel aspect ratio, H/W (Equations D6–D8). However, W can be difficult to constrain from geological outcrop. Relations that scale H with W are often used to estimate W (e.g., Bridge & Mackey, 1993; Leopold & Maddock Jr., 1953), but these estimates are very tentative and, where systems are multi-thread, subject to further uncertainty regarding the number of active threads. To address the difficulty of constraining W, we: (1) implemented plausible lower and upper estimates of W (W_{min} and W_{max}) for each formation (Chapter 5; Figure 5.2); (2) evaluated the sensitivity of each predictor to H/W for a given h_{xs} and D_{50} (Chapter 5; Figure 5.2). Below we outline how we selected W_{min} and W_{max} for each geologic formation.

Ferron Sandstone

The Turonian Ferron Sandstone, Utah, USA, preserves major meandering trunk channels that fed the Last Chance deltaic complex. For these terrestrial fluvial strata, Bhattacharya and Tye (2004) reported valley-scale channels with widths of 250 m. Further, Garrison and Bergh (2004) measured channel-belt widths, which did not exceed 2 km, and noted that, within channel belts, channels had average widths of 250 m. The authors found no evidence to suggest that channel widths exceeded a few hundred metres. Alternatively, Cotter (1971) documented point bars with widths of order 60 m, and recent observations

suggest that channel widths are ~2.34 times greater than bar width (c.f. Greenberg et al., 2021), which would suggest a channel width nearer to 150 m. Nonetheless, as the average channel width is reported to be 250 m, we prescribe W_{min} = 200 m and W_{max} = 300 m.

Blackhawk Formation

For terrestrial fluvial strata of the Campanian Blackhawk Formation, Utah, USA, Flood and Hampson (2015) reported the apparent widths of channelized fluvial sandbodies, which offer a maximum cap on channel widths, for six cliff-face panels. Mean apparent widths for each of these panels were 370 m, 360 m, 750 m, 190 m and 250 m. Whereas, when the authors instead presented results for a series of time intervals during Blackhawk deposition, the mean apparent widths were 390 m, 420 m, 370 m and 350 m (Flood & Hampson, 2015). Given these values, we assign W_{min} = 300 m. However, Flood and Hampson (2015) also documented many larger channelized sandbodies with widths up to and in excess of 1000 m. We therefore assign W_{max} = 1000 m. As the Blackhawk Formation preserves both single-thread and multi-thread channels, we anticipate that these values of W_{min} and W_{max} will capture both planforms.

Castlegate Sandstone

The Campanian Castlegate Sandstone is a channel-dominated deposit and has been widely interpreted to preserve braided fluvial systems, albeit with more sinuous/meandering channels in the middle Castlegate Sandstone (Miall, 1993; 1994). Architecturally, the Castlegate Sandstone is dominated by barforms, which are well documented (Adams & Bhattacharya, 2005; McLaurin & Steel, 2007; Hajek & Heller, 2012; Chamberlin & Hajek, 2019). Chamberlin and Hajek (2019) reported mean bar package widths of 58 m, 180 m and 87 m, for three localities along the eastern Wasatch Plateau, Utah, USA, which might point to channel widths of order tens to hundreds of metres. However, we still do not know total wetted channel widths as we do not know the number of active threads in ancient Castlegate rivers. We tentatively assign W_{min} = 300 m and W_{max} = 1000 m, and we intend for these widths to capture a spread of possible scenarios, from possession of a few active threads to possession of many active threads.

D1.4 Planform reconstruction

For each measured cross-set, we implemented three approaches to estimate planform. These predictors were either theoretically or empirically derived and were each tested on empirical observations of modern rivers. However, they all differ in their approach and/or the parameters on which they depend. First, we used the predictor of Parker (1976) who theoretically derived planform stability fields, which are expressed as:

$$\epsilon = \frac{S}{Fr}\,\frac{H}{W'}, \qquad \text{Eq. D6}$$

where $\epsilon < 1$ for single-thread rivers, $\epsilon > 1$ for multi-thread rivers with 1–10 threads, and $\epsilon > 10$ for multi-thread rivers with more than 10 threads. Second, we used the theoretically derived predictor of Crosato and Mosselman (2009) in which the likely bar mode, m, of a river is estimated as:

$$m^2 = 0.17g \frac{b-3}{\sqrt{RD_{50}}} \frac{W^3 S}{CQ}, \quad \text{Eq. D7}$$

where b is the degree of nonlinearity of the dependence of sediment transport on flow velocity, assumed to be 4 in sand-bed rivers, R is the dimensionless submerged specific density of sediment in water (1.65 for quartz), C is Chezy's coefficient ($m^{1/2}/s$), which can be calculated by $U = C\sqrt{HS}$, and Q is water discharge (m^3/s). Here, $m \leq 1.5$ for single-thread rivers, $m \geq 2.5$ for multi-thread rivers, and $1.5 < m < 2.5$ for transitional rivers (Crosato & Mosselman, 2009). Finally, we implemented the empirically derived predictor of van den Berg (1995), who derived a "potential" specific stream power parameter, ω, in sand-bed rivers that can be expressed as

$$\omega = 2.1\, S\sqrt{Q} \quad \text{Eq. D8}$$

where ω is in units of kW/m^2. Here, the potential specific stream power at the transition between single-thread and multi-thread rivers is defined as $\omega_t = 900\, {D_{50}}^{0.42}$ (van den Berg, 1995) and we expect $\omega/\omega_t < 1$ for single-thread rivers and $\omega/\omega_t > 1$ for multi-thread rivers.

D1.5 Dataset compilation

We compiled data of hydraulic geometries in natural rivers. We excluded data from manmade channels, e.g., irrigation canals, or laboratory flume experiments as these are difficult to apply and/or upscale to geologic settings. Further, focus on natural rivers maximises the potential for empirical data to indirectly account for important planform controls, e.g., bank stability and vegetation (Ielpi, 2018; Ielpi & Lapôtre, 2019b; Lapôtre et al., 2019; Dunne & Jerolmack, 2020; Ielpi & Lapôtre, 2020). As we are interested in geologic applications of planform predictors, we have specific data selection criteria, which are outlined below:

(1) Net-erosional regions in fluvial landscapes are inherently not preserved in the rock record (Romans & Graham, 2013; Weissmann et al., 2015; Romans et al., 2016). Therefore, data collection should ideally focus on rivers in net-depositional regions, however this is non-trivial given the limited global extent of modern sedimentary basins (Nyberg & Howell, 2015; Weissmann et al., 2015). To alleviate this as best as possible, and to ensure that data are from rivers that can be considered appropriate modern analogues for preserved ancient rivers, we excluded data from mountain rivers and bedrock rivers (where stated in the data source and/or inferred from Google Earth).

(2) We did not restrict data collection to a specific flow stage (e.g., bankfull or mean flow conditions) as this would have been biased against braided multi-thread rivers, which are the less stable form of multi-thread river (as opposed to more stable anastomosing multi-thread rivers) and are often only multi-

thread during low flow stages (Makaske, 2001; Eaton et al., 2010; Carling et al., 2014). Moreover, it is still unclear whether fluvial strata preserve a record of bankfull/flood events or more ordinary flow conditions (Leclair, 2011; Paola et al., 2018; Ganti et al., 2020; Leary & Ganti, 2020; Chapter 4 (Lyster et al., 2022)).

(3) We excluded data from sources that reported hydraulic geometries of natural rivers in response to river regulation or restoration. Ideally, our data would exclude all anthropogenically-impacted rivers, however this not feasible. At minimum, we avoided data that had been collected within the vicinity of dams.

(4) Studies that present hydraulic geometries of multi-thread rivers commonly report data for individual threads; we exclude these data as individual threads of multi-thread rivers have been frequently shown to share the same hydraulic geometries as single-thread rivers (Parker et al., 2007; Gaurav et al., 2015; Gaurav et al., 2017).

As we compiled data, we categorized rivers as single-thread or multi-thread; single-thread rivers were then subcategorized as meandering or sinuous/straight, and multi-thread rivers were subcategorized as braided, anastomosing, or transitional. The subcategory of transitional rivers comprises: (1) rivers characterized as transitional in the data source; (2) rivers identified on Google Earth as possessing 1–3 threads that vary at reach-scale in space and/or time; (3) rivers that were characterized as multi-thread in the data source, but where the process (i.e., braiding or anastomosing) was not described. If rivers with single-thread planforms were not subcategorized as either meandering or sinuous/straight, we classified them as meandering where the data source classified the river as C-type or E-type (according to the Rosgen stream classification) or reported a channel sinuosity in excess of 1.5.

To contrast observations of natural rivers with existing planform predictors, and with stratigraphic observations, the minimum parameters that we required for each data point were the channel width, channel depth, slope, flow velocity, and water discharge. These data were typically obtained from field surveys, where channel geometries could be measured and flow velocity and discharge could either be obtained from stream gauge data or measured *in situ* using, e.g., acoustic doppler current profilers. Less frequently, flow velocity and discharge data were obtained using satellite observations, which are commonly used to assess rivers that are ungauged and/or inaccessible. Where hydraulic geometries for bankfull flow conditions are reported, we note that these geometries are usually calculated by identifying bankfull flow indicators (e.g., floodplain breaks, inflection points, point bars, depositional benches, and scour lines). If one of the minimum required parameters was absent in the data source, often flow velocity, this could often be back calculated from field measurements of discharge and channel cross-sectional area. We also required Froude number to implement the predictor of Parker (1976) (Equation D6), which is straightforward to calculate (Equation D5).

To ensure our dataset includes rivers from a variety of climate and vegetative regimes, we permitted inclusion of data for dryland rivers, which are often ungauged. Here, channel geometries can be measured

in the field, but flow velocities must instead be calculated using field-based measures of bed roughness and flow transport equations, e.g., Equation D4. This is potentially a limitation of our dataset, as there are uncertainties involved with including data that have not been explicitly measured. However, we feel it is important to include these data as dryland rivers are crucial analogues for unvegetated rivers on early Earth and other planets (e.g., Ielpi, 2018; Ielpi & Lapôtre, 2019b, 2019a; Lapôtre et al., 2019; Lapôtre & Ielpi, 2020). Our dataset contains 61 datapoints for dryland rivers, which constitute only 3.6% of the entire dataset. Therefore, we do not anticipate that these data impact our proposed thresholds. Moreover, for studies of dryland rivers in which flow velocities were calculated, we found that authors usually noted that channel cross-sections were carefully surveyed and, in some instances, visual estimates of Manning's n were derived using back calculated examples from similar dryland river locations that are gauged (e.g., Nanson & Huang, 2017).

D2 Dataset

Due to the size of the dataset, I have made the full dataset available online and it can be accessed via **https://figshare.com/s/4c098d0f0964bda4875b** (DOI:**10.6084/m9.figshare.17938085**).

At minimum, for each data point we provide the following:

1. Data source, which includes a shorthand reference and a working URL.
2. River name and, where available, whether the river is broadly considered "gravel-bed", "gravel–sand-bed" or "sand-bed".
3. The location of the river, including the region/country and the continent.
4. The location where measurements were collected and, where available, stream gauge information and the date of measurement.
5. Hydraulic geometries: width and depth or the width/depth ratio, slope, flow velocity, water discharge, Froude number.
6. Planform information, including whether the river is: (1) single-thread or multi-thread; (2) anastomosing, braided, transitional, meandering, or sinuous/straight.

*We additionally include a column containing either "b", "m", or "i" to broadly categorize the flow conditions that measurements reflect. (1) b denotes bankfull measurements. (2) m denotes mean measurements (often mean annual). (3) i denotes instantaneous measurements (the dates of measurement are provided where available).

D3 Field localities

Table D1 | Field localities from which data were collected. Localities are grouped by field area (e.g., Price Canyon, Wattis Road; see Figure 5.1 in Chapter 5) and are subdivided by formation (i.e., Blackhawk Formation, Castlegate Sandstone, and Ferron Sandstone). This table is a replica of Table C1 in Appendix C (Lyster et al. (2022)).

Location and stratigraphic interval		Field sites	Elevation, m (±3–4)
Last Chance Creek	Ferron Sandstone	N38 40 18.9, W111 24 52.5	2255
		N38 40 20, W111 24 45.3	2241
		N38 40 21.7, W111 24 17.1	2218
		N38 40 17.5, W111 24 12	2209
		N38 40 12, W111 24 2.5	2190
		N38 40 7.7, W111 23 50.3	2179
		N38 40 9.1, W111 23 44.8	2187
		N38 40 8.9, W111 23 53.6	2215
Link Canyon	Blackhawk Formation	N38 57 42.1, W111 19 57.4	2363
		N38 57 39.7, W111 19 53.9	2383
		N38 57 41.4, W111 19 53.0	2398
		N38 57 44.3, W111 19 53.8	2421
		N38 57 48.4, W111 19 53.9	2473
		N38 57 58.3, W111 19 57.3	2538
		N38 57 52.8, W111 19 55.8	2509
		N38 57 51.4, W111 19 55.0	2500
	Castlegate Sandstone	N38 58 05.9, W111 19 56.6	2572
		N38 58 08.0, W111 19 55.8	2584
		N38 58 10.6, W111 19 54.2	2600
Price Canyon	Blackhawk Formation	N39 44 11.0, W110 50 47.7	1932
		N39 44 08.4, W110 50 46.9	1947
	Castlegate Sandstone	N39 45 05.1, W110 53 10.3	1920
		N39 44 48.5, W110 49 58.1	1969
		N39 44 52.6, W110 49 55.4	1983
		N39 45 01.3, W110 49 43.5	2000
		N39 45 03.0, W110 49 40.6	1999
		N39 45 10.5, W110 49 35.8	2008
		N39 45 12.0, W110 49 34.8	2003
Salina Canyon	Blackhawk Formation	N38 54 00.8, W111 39 53.8	1861
		N38 53 51.5, W111 39 02.3	1885
		N38 54 29.6, W111 41 46.8	1802
		N38 54 13.8, W111 39 05.9	1926

	Castlegate Sandstone	N38 54 52.9, W111 38 06.5	2036
		N38 54 52.3, W111 38 08.7	2017
		N38 54 50.6, W111 38 18.1	2009
		N38 54 52.6, W111 38 20.2	2030
		N38 54 53.7, W111 38 ~20.2	2035
		N38 54 33.0, W111 42 32.7	1779
		N38 54 57.1, W111 38 20.3	2076
		N38 54 59.4, W111 38 13.1	2111
Straight Canyon	Blackhawk Formation	N39 16 56.6, W111 13 58.0	2027
		N39 16 46.2, W111 13 41.9	2010
		N39 16 29.1, W111 13 11.9	1996
		N39 17 16.2, W111 14 37.5	2047
		N39 17 15.7, W111 14 30.4	2043
		N39 17 05.7, W111 14 10.5	2037
		N39 17 36.5, W111 16 16.7	2146
		N39 17 19.3, W111 16 00.0	2129
		N39 17 20.9, W111 15 19.8	2102
	Castlegate Sandstone	N39 17 51.9, W111 16 18.0	2161
		N39 18 28.6, W111 16 13.2	2181
		N39 18 55.2, W111 16 06.2	2238
Wattis Road	Blackhawk Formation	N39 31 45.5, W111 02 16.0	2577
		N39 31 11.9, W111 01 56.9	2692
		N39 31 19.8, W111 01 58.4	2655
		N39 31 20.7, W111 02 37.2	2798
		N39 31 14.3, W111 02 13.8	2765
	Castlegate Sandstone	N39 31 28.6, W111 02 44.9	2844
		N39 31 31.7, W111 02 50.6	2877
		N39 31 30.2, W111 02 46.4	2861
		N39 31 33.5, W111 02 53.2	2889
Willow Basin	Ferron Sandstone	N38 34 50.9, W111 28 6.2	2668
		N38 34 49, W111 28 6.5	2636
		N38 34 48.9, W111 28 4.5	2631
		N38 34 47.6, W111 28 5.4	2592
		N38 34 35.1, W111 27 48.4	2537
Willow Creek	Ferron Sandstone	N38 44 0.4, W111 18 47.2	1965
		N38 43 37.4, W111 18 46.5	1926
		N38 43 25.2, W111 18 45.9	1895